R-07-57

Hydrogeological pre-modelling exercises

Assessment of impact of the Äspö Hard Rock Laboratory

Sensitivities of palaeo-hydrogeology

Development of a local near-surface Hydro-DFN for KLX09B–F

Site descriptive modelling SDM-Site Laxemar

Lee Hartley, Peter Jackson, Steve Joyce
David Roberts, John Shevelan, Ben Swift
Serco Assurance

Björn Gylling, Niko Marsic
Kemakta Konsult AB

Jan Hermanson, Johan Öhman
Golders Associates

December 2007

Svensk Kärnbränslehantering AB
Swedish Nuclear Fuel
and Waste Management Co
Box 250, SE-101 24 Stockholm
Tel +46 8 459 84 00

ISSN 1402-3091
SKB Rapport R-07-57

Hydrogeological pre-modelling exercises

Assessment of impact of the Äspö Hard Rock Laboratory

Sensitivities of palaeo-hydrogeology

Development of a local near-surface Hydro-DFN for KLX09B–F

Site descriptive modelling SDM-Site Laxemar

Lee Hartley, Peter Jackson, Steve Joyce
David Roberts, John Shevelan, Ben Swift
Serco Assurance

Björn Gylling, Niko Marsic
Kemakta Konsult AB

Jan Hermanson, Johan Öhman
Golders Associates

December 2007

Summary

Impact of the Äspö Hard rock laboratory (HRL)

Numerical modelling has been used to investigate the potential impact of the Äspö HRL on regional groundwater flow and hydro-geochemistry in the Laxemar study area. The numerical models have been adapted for this application from the ones use in the site-descriptive modelling (SDM) and SR-Can assessment modelling based on Laxemar version 1.2. In order to test the robustness of the simulation results, sensitivities were studied with respect to different flow boundary conditions and the hydraulic properties of the Quaternary deposits, particularly those beneath the sea around the Äspö island.

The simulations show that the Äspö HRL has a local effect on the groundwater situation. Typically, in the simulations, the rock under the Äspö island, the bays around it and the Ävrö area (mainly western part of the islands of Ävrö, Mjälen and Hålö) are influenced. In the sensitivity study, visualisations of the drawdown caused by the HRL tunnel system show small differences in the results for head versus flux top boundary conditions, little sensitivity to a change in the surface infiltration rate, but most sensitivity to the contact between the sea and the bedrock beneath the seabed sediments. For all simulation cases considered, results suggest that the Äspö HRL has not been in operation sufficiently long to have affected the chemistry of samples collected at Laxemar and Simpevarp, though there is some possibility that Ävrö samples have been altered, at least for boreholes in the western part of Ävrö, Mjälen and Hålö. The distribution of flow and discharge areas around the bay at Äspö is clearly affected by the HRL for all cases.

Using the drawdown in percussion drilled boreholes around Äspö as an interference test suggests that there is a partial reduction in the hydraulic contact between the sea and the groundwater system in the bedrock beneath. It is recommended that the conclusions about appropriate hydraulic properties for Quaternary sediments beneath the sea be carried forward into future regional groundwater flow modelling studies.

Sensitivities of palaeo-hydrogeology and hydro-geochemistry

In the SDM and SR-Can calculations for Laxemar version 1.2, hydro-geochemical data (the concentrations of various groundwater constituents) and interpreted mixing proportions of certain reference waters were used to test and calibrate the models, and some sensitivity studies were undertaken. It was considered that further sensitivity studies would be valuable in developing understanding, and would provide a foundation for future work. A further study was therefore carried out:

- To examine the variability in the modelled groundwater composition, by considering a number of realisations of the Hydro-DFN model.
- To explore the sensitivity of the modelled composition to key hydraulic properties, boundary and initial conditions.
- To develop the approach for using hydro-geochemical data to test and calibrate the flow models.

It is considered that the match of the predicted concentrations of various groundwater constituents to observations is acceptable for the SR-Can reference case apart from the following. The predicted values of Br/Cl ratio in the top 400 m of bedrock are close to 0 whereas the observed values are significant (about 0.005) suggesting that the Br/Cl ratio is too low for the recharging water. Also, there is an indication that the modelled oxygen isotope ratio, $\delta^{18}O$, is more negative

than the observations for depths between 800 m and 1,200 m, which may suggest that the assumed initial condition of a mix of Brine (with $\delta^{18}O$ about –9) and Glacial (with $\delta^{18}O$ about –17) in this region may not be right, but should be a mix of Brine and a water with less negative $\delta^{18}O$ than the Glacial reference water. One possible interpretation of this is that the water at 800 m and 1,200 m depths is a mixture of old warm climate freshwaters some of which pre-date the most recent glaciation, i.e. inter-glacial meteoric water. Such a hypothesis about the origin of the freshwater at depth would also imply that glacial water was not generally injected to depths much below 700 m whilst ice sheets covered or past over the site during the last ice age.

Calculations were carried out for a suite of 10 realisations of the Hydro-DFN model, to examine the variability in the modelled groundwater composition. In most cases, the profiles of a particular quantity in a borehole have a fairly similar but slightly displaced shape for the different realisations. The results for some boreholes may be significantly influenced by the presence of nearby transmissive deformation zones.

After the first calculations had been undertaken, revised specifications for the reference waters were provided by the ChemNET group and all subsequent calculations were carried out with the revised reference waters. The main differences in the new reference water compositions are that the Glacial water has a more negative $\delta^{18}O$ (–21 rather than –17) and the Dilute granitic water (DGW) is slightly more saline, and in particular, has a non-zero Br/Cl ratio (similar to that of Brine in fact). The revised reference waters led to an improved match to the observed Br/Cl ratios, but the possible discrepancy in between the predicted and observed values of $\delta^{18}O$ at depth between 800 m and 1,200 m was more apparent, adding weight to the suggestion that the assumed initial condition was not right at these depths.

Further calculations were undertaken for a suite of variants in which the properties of the hydraulic conductor domains (HCDs) were taken to vary spatially within the deformation zones according to a stochastic process. The results for these variants generally varied less than the results for the suite of variants for different realisations of the Hydro-DFN. However, for the highest level of variability considered, numerical convergence of the flow simulations were only obtained for one of the three realisations considered due to the extreme degree of heterogeneity.

It was found that the results were not very sensitive to the value of the kinematic porosity except for the highest value considered. It was also found that the results were not very sensitive to the depth dependence in hydraulic conductivity, except for the highest values considered. Further, it was found that the results were not very sensitive to the boundary condition for the groundwater head imposed on the top surface. However, only variations in the specified head were considered, and the range of variations may not have been large. Variations in, for example, the chemistry of the recharging water were not considered.

The greatest sensitivity found was that to the assumed initial conditions. In particular, the initial distribution of salinity plays a very important role. It appears that the initial distribution largely remains at depths below about 1,000 m. The initial conditions for the reference case give the best match to observations of salinity. The match to the observations of $\delta^{18}O$ may not be as good for this variant, but as discussed above, the assumption of an initial fraction of Glacial water at depth between 800 m and 1,200 m may not be right.

The Br/Cl ratio may provide a useful indicator of the origin of salinity, in particular the presence of Littorina water. Mg provides a consistency check on the interpretation of Littorina water, but can only be used qualitatively due to it being non-conservative.

It is considered that it was more useful to compare the predictions with the observation for the concentrations of major ions and isotope ratios than with the inferred M3 mixing fractions, since the latter introduce addition interpretation uncertainties that in some circumstances can be large /Gómez et al. 2007/.

In summary, the modelling of palaeo-hydrogeology in the Laxemar subarea is most sensitive to the hydro-geochemical conceptual model of the origin and composition of groundwater, and the depth dependency of the hydraulic conductivity. Hence, it provides a useful calibration of these two aspects of the site descriptive model. Other aspects of the model and parameters, such as deformation zone transmissivities and porosities, seem to give results consistent with the hydro-geochemical data for all values considered within their ranges of uncertainity, and so these parameters cannot be calibrated to a fine degree this type of data.

Near surface Hydro-DFN for Ävrö Granite based on KLX09B–F

A Hydro-DFN model for the near surface Ävrö Granite has been developed based on one vertical and four inclined boreholes around the KLX09 drill site area and integrating core descriptions, borehole image and outcrop data together with hydraulic data from single-hole and multi-hole PFL-f tests. Fracture set classification and orientation models were provided by a local Geo-DFN model. Based on the power-law concept for fracture size, distribution parameters have been determined for DFN models consistent with the intensity of open fractures in the core-drilled boreholes, the intensity of deformation zones on the regional scale, and the frequency of connected fractures that provide the flows seen in the PFL-f tests. Briefly, the size models for open fractures that give the best overall performance are ones with a location parameter, r_0, similar to the borehole radius, 0.04 m, and an exponent k_r around 2.6. This is broadly consistent with the Geo-DFN model for the size distribution of all fractures in the sub-horizontal and NW sets, but quite different for the ENE and NS sets.

An analysis of the orientations of flow-anomalies suggests the sub-horizontal and NW (NE plunge) oriented fractures are responsible for the majority of higher flow-rates. This is reasonable since the sub-horizontal set is the most abundant and the NW set correlates with the direction of maximum horizontal in situ stress /SKB 2006a/, (Hakami 2007, personal communication based on KLX12A data).

Inspecting the interference tests revealed that the majority of the flow measured corresponds with only about 5 fractures intercepted by the boreholes. Two of these are sub-horizontal belonging to set S_df (HZ), and 3 NW striking sub-vertical belonging to set S_C. Of the boreholes they intercept, 2 are in KLX09C, 1 in KLX09E, and 2 in KLX09F. These 3 boreholes correspond to the ones with the highest total inflow during the single-hole tests, and the highest drawdown responses seen in the monitoring holes during the interference tests. Therefore, it may be asserted that these 5 fractures with transmissivities around 10^{-4} m^2/s are responsible for the different magnitudes of flow and head response seen when pumping different boreholes. A local structural model of deformation zones was not available for the area around the boreholes, and hence the modelling did not aim to reproduce the exact responses in particular boreholes, but tried to find model settings that gave models that agreed with several statistics quantifying the nature of the flow system such as frequency, magnitudes and variability in flow-rates and head responses.

The fracture size distribution parameters were finely calibrated to obtain a good statistical match to the frequency and distribution in magnitudes of flows seen in the PFL-f tests for each fracture set based on numerical DFN simulations of connectivity and flow. The ultimate models were conditioned, based on several statistics that quantified the nature of flow in both the single-hole and multi-hole PFL-f tests, to give a recommended Hydro-DFN parameterisation. Different relationships between fracture transmissivity and size were considered varying from direct correlations to completely uncorrelated. Due to an abundance of hydraulic data from a range of borehole orientations, different relationships were considered for different sets. It is hard to give a definitive answer as to which sort of relationship works best. The correlated model tends to predict a distribution of flow-rates in PFL-anomalies that it is narrower than that measured, and that has too much variability between the flow-rates at individual boreholes, while the uncor-

related model has slightly too little variability, and so a semi-correlated model is marginally the most realistic. The main actions taken to obtain a satisfactory stochastic model were to choose the size distribution for the NW set to give a slightly higher intensity of long fractures than was suggested by matching to the L 1.2 deformation zone model, and have a strong correlation between size and transmissivity with exponent 1.5; while the sub-horizontal set requires a weak correlation between size and transmissivity or heterogeneity within fracture planes on the scale of about 10 m, or so.

In summary, the KLX09 interference test data has allowed us to analyse differences between the geometrical and hydraulic properties between the different fracture sets much more thoroughly than has been possible using mainly vertical boreholes and single-hole tests. Key findings are a tendency toward distinctly more extensive and transmissive fracturing in the NW direction. It has also pointed towards possible subtleties such as that the relationship between transmissivity and size may be different for different sets with strong correlations in sub-vertical sets parallel to the maximum in situ stress (NW), while fractures in other directions (ENE and NS and sub-horizontal) are less well correlated or may be spatially heterogeneous It should be remembered that these remarks are based on the hydrogeology of fractures near the surface, so as yet it is not clear if such conclusions apply at depth.

Contents

1 Introduction

As a precursor to the site descriptive modelling (SDM) for the complete site investigations (CSI) numerical modelling has been used to investigate the following three issues:

1. What effect may the Äspö Hard Rock Laboratory (HRL) have had on groundwater flow and hydro-geochemical situations in the Simpevarp area and especially the Laxemar investigation subarea.
2. What are the key sensitivities for the numerical simulations of palaeo-hydrogeology and hydro-geochemistry in the Simpevarp area.
3. What is an appropriate hydrogeological DFN (Hydro-DFN) model for the top 100 m of Ävrö granite based on the Posiva flow log (PFL) single hole and interference test performed in KLX09B–F.

To investigate the impact of the Äspö HRL the equivalent continuum porous medium (ECPM) reference case from the SR-Can L 1.2 report by /Hartley et al. 2006a/ is extended to include the hydraulic effects of the tunnel system of the Äspö HRL. Numerical simulation cases are calculated using both pressure and flux boundary conditions on the top of the model. The flux boundary condition is used with different models for the Hydraulic Soil Domains (HSD) and sensitivities are considered to both the infiltration rate and hydraulic properties of the various soil types, in particular the sub-sea sediments. Measured water-levels and drawdowns around Äspö are used to identify which parameter settings may best characterise the hydrogeological system.

In the SDM and SR-Can simulations of palaeo-hydrogeology for Laxemar 1.2 /Hartley et al. 2006ab/, hydro-geochemical data (the concentrations of various groundwater constituents) and interpreted mixing proportions of certain reference waters were used to test and calibrate the models, and some sensitivity studies were undertaken. It was considered that further sensitivity studies would be valuable in developing understanding, and would provide a foundation for future work. Therefore, further sensitivity studies were carried out here. The overall objectives of the study were:

- To examine the variability in the modelled groundwater composition, by considering a number of realisations of the Hydro-DFN model.
- To explore the sensitivity of the modelled composition to key hydraulic properties, boundary and initial conditions.
- To develop the approach for using hydro-geochemical data to test and calibrate the flow models.

The objectives of near-surface Hydro-DFN study were to develop a methodology for simulating hydraulic tests in an array of closely spaced boreholes of varying inclination, and then derive a parameterisation of the upper Ävrö Granite based on the measured flows and drawdowns. The region of interest contains the KLX09B to KLX09F shallow core drilled boreholes in the Laxemar subarea. The region also contains the KLX09 deep cored borehole. A set of DFN modelling simulations were performed to attempt to match geometric measurements from borehole and outcrop data, as well as single-hole flow measurements and interference test results. Key issues of interest for this study were the derivation of a Hydro-DFN modelling for the upper 100 m of rock since this is usually cased in the other deep cored drilled holes, and the identification of any anisotropy in the fracture geometrical and hydraulic properties.

1.1 Coordinate system

The coordinate system employed is the RT 90 system with X (eastings) and Y (northings) and the Z coordinate expressed as elevation in “metres above sea level”. The latter implies that all data (whether surface of subsurface) are normalised to one common datum (mean sea level). Hence, the majority of subsurface vertical positions in the tables and figures of this report have the format: “- XXX m”.

2 Modelling of the influence of the Äspö hard rock laboratory (HRL) on groundwater flow

A number of simulations have been carried out to investigate if the Äspö Hard Rock Laboratory (HRL) has an impact on the groundwater flow situation at Äspö and the area around it. As a platform for the calculations, the equivalent continuum porous medium (ECPM) reference case from the SR-Can L 1.2 report by /Hartley et al. 2006a/ is used. In the calculations performed in the current study, the results from the SR-Can simulations are used to provide initial conditions. Construction of the Äspö HRL started in October 1990 and was completed summer of 1995, and so the new simulations were started well before this time taking initial conditions from the SR-Can simulations at 1960 AD, since a 20 year time-step was used there. Here, a one year time-step is used until the year 2006 with a fully implicit time-stepping scheme for stability. For each case, one simulation is calculated with the HRL present, and another simulation is performed without the HRL. Thereafter, these two simulations are compared to assess the impact of the HRL from the natural undisturbed flow.

To be able to perform the simulations, developments of the ConnectFlow code were necessary. Using these enhancements, the main tunnel and the main shaft in the model are represented in a simplified manner. The HRL is included as line segments with prescribed inflows from those measured in the tunnels. The interaction between the line segment and the finite-element it intersects can be modified as no contact, flow spread over the whole segment, or distributed according to the local permeability. Skin effects may be included, but that option is not developed yet, but could be useful if e.g. pressure is used as a boundary condition in the tunnel.

Cases have been calculated using both pressure and flux boundary conditions on the top of the model. The flux boundary condition used specified a maximum potential infiltration of either 165 or 80 mm/year. However, the boundary condition does not force a uniform flux inflow equal to this maximum into the model everywhere. Instead, the flux is adjusted on each finite-element and in time according to the relative levels of the groundwater head and the ground surface. If the head is well below ground surface, then the full maximum potential infiltration is used. However, when the modelled head at the top of the model is close to ground surface, the infiltration is reduced in proportion to the difference, and if the head is above ground surface, then an outflow (discharge) is specified to reduce the head back down to ground surface. Hence, this flux boundary condition is non-linear in head, and effectively implements a specified flux in recharge areas and automatically switches to a specified head equal to topography in discharge areas. The flux boundary condition was used for models with both a homogeneous soil domain model, and that was built up from different soil materials and spatial varying thickness.

It is not expected that the interim storage facility Clab will have more than a localised effect on hydrogeology given its superficial depth (circa 50 m of rock cover) and the inflow to Clab was a maximum in 1987 of about 80 m^3/day compared with a maximum for the HRL in 1998 of about 2,200 m^3/day.

2.1 Objectives of study

The overall objective of this modelling study is to test the current hypothesis that the underground openings of the Äspö HRL do not significantly affect the hydraulic and chemical conditions in the Laxemar and Simpevarp subareas. So far, there are no direct evidences that the inflow to Äspö HRL (present total inflow rate ca 0.018 m^3/s or 1,100 L/min), present since 1990, have significantly altered the hydraulic or chemical conditions in the Laxemar and Simpevarp subareas. However, it is considered necessary to make some scoping calculations with the current regional groundwater flow model (L 1.2) to quantify possible effects such as changes in groundwater chemistry, flow-rates and discharge patterns.

2.2 Hydrogeological concepts, methodology and data

In this study an ECPM approach is used to simulate the conditions surrounding the Äspö Island. The hydrogeological model has been developed for some time now and refined even more in the Laxemar 1.2 SDM project described in /Hartley et al. 2006b/. A slightly improved model was also used in the SR-Can temperate simulations of Laxemar /Hartley et al. 2006a/. The model domain is limited by water divides onshore and major fracture zones offshore. The hydraulic conductor domains, HCD, are modelled by including the deformation zones specified in the official L 1.2 data delivery. The deformation zones are modelled with depth dependent hydraulic properties. The hydraulic properties were calibrated to available hydraulic and chemical data. The properties of the hydraulic rock domains, HRD, were obtained by a Hydro-DFN approach. Also, the properties of the rock domains are depth dependent. The bedrock is divided into several rock domains. A simplified hydraulic soil domain, HSD, concept was used in the ECPM reference case in the SR-Can study based on 3 layers with different hydraulic properties. Previously in the SDM studies, a method for including more elaborate soil domains has been developed /Hartley et al. 2006b/ that uses several different cover types of spatial varying thickness and each with different hydraulic properties. Both HSD model were considered in this study, along with variants on the more elaborate model to quantify sensitivities to the soil types and properties making up the sea bed.

The data used for the HCD, HRD and HSD are detailed in the SDM report by /Hartley et al. 2006b/. Summaries of the data used may be found in Section 2.3 of this report. The used HRL data are described below.

2.2.1 Äspö hard rock laboratory (HRL) data used

Tunnel geometry

In the delivered data set, the geometry of the tunnels and shafts are given. The names of the different Äspö HRL tunnel objects are given in Table 2-1 and Table 2-2. More information may be found in Appendix A. The Äspö HRL is illustrated in Figure 2-1.

Table 2-1. The main tunnel objects that are included in the model.

Name	Object
TASA	The main tunnel, A.
TASH	Elevator shaft, H
TASV	Ventilation-in shaft, V
TASW	Ventilation-out shaft, W

Table 2-2. The diameters of the drilled parts.

Object	Diameter
TBM tunnel	5.0 m
Elevator shaft, H	3.8 m
Ventilation-in shaft, V	1.5 m
Ventilation-out shaft, W	1.5 m

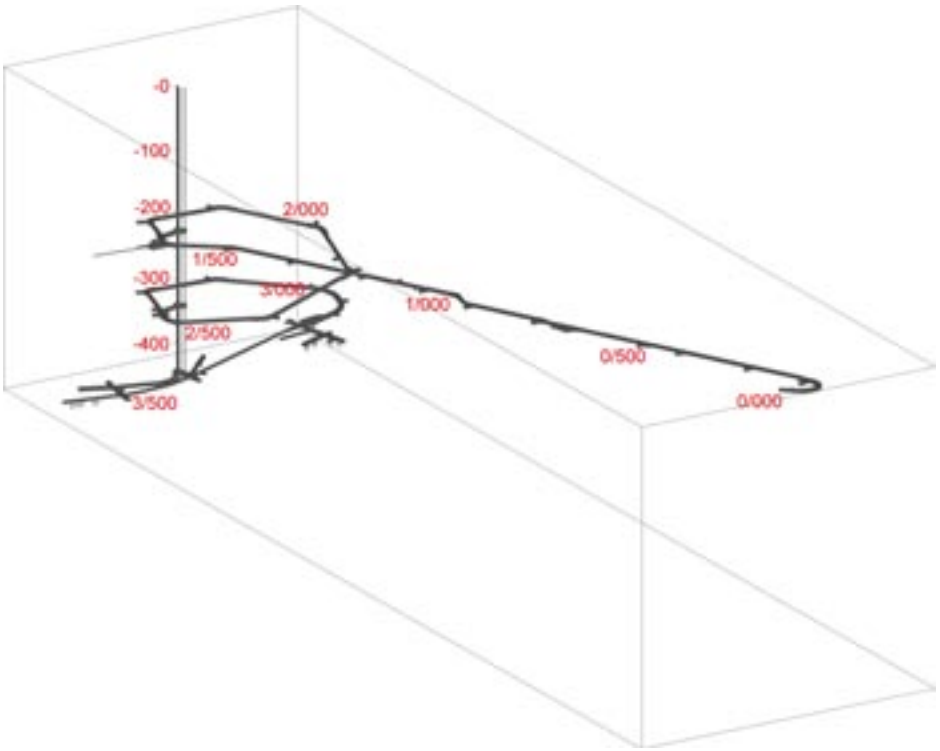

Figure 2-1. *An illustration of the tunnels and shafts at the Äspö HRL.*

The influences of the ventilation shafts are included into the elevator shaft. The inflows to Tunnel G and F, which run parallel and close to Tunnel A (approximately at section 3,400–3,510 m and 3,510–3,600 m) are added to the last part of tunnel A (TASA), and thus tunnels G and F are not modelled geometrically. All other short tunnels are excluded in the modelling. The coordinates for the tunnel line for tunnel A is 0.25 m above the tunnel floor in the drill and blasted tunnel (tunnel section 0–3,191 m) and 0.8 m above the tunnel floor in the TBM tunnel (tunnel section 3,191–3,600 m). An observation or measurement in the tunnel is linked to a ”Tunnel section”. ”Tunnel section” is defined as the length of the projection of the tunnel line on a horizontal plane, called SECTION in the tables for tunnel A and other tunnel parts. All flow rates are related to SECTION for the tunnels. The cross-section area of the drill and blasted tunnel is about 25 m^2 in the straight parts of the tunnel and about 43 m^2 in the bends. In the TBM assembly hall, the cross-sectional area is about 100 m^2.

Figure 2-2 show some illustrations of the location of the Äspö HRL tunnel and information on rock types, major deformation zones and boreholes. The information is obtained from /SKB 2006a/. Information is also available on which deformation zones that intersect the HRL system. This may be seen in Appendix A.

Flow into the Äspö HRL

Data on the measured flow rates at weir positions are available. This gives information on the total inflow, and inflow at different sections of the HRL as monthly averaged values. Data are available at the weirs along the Äspö tunnel during the excavation of the Äspö Hard Rock Laboratory (HRL) and operation of the Äspö HRL, for the time period May 1991 until December 2004.

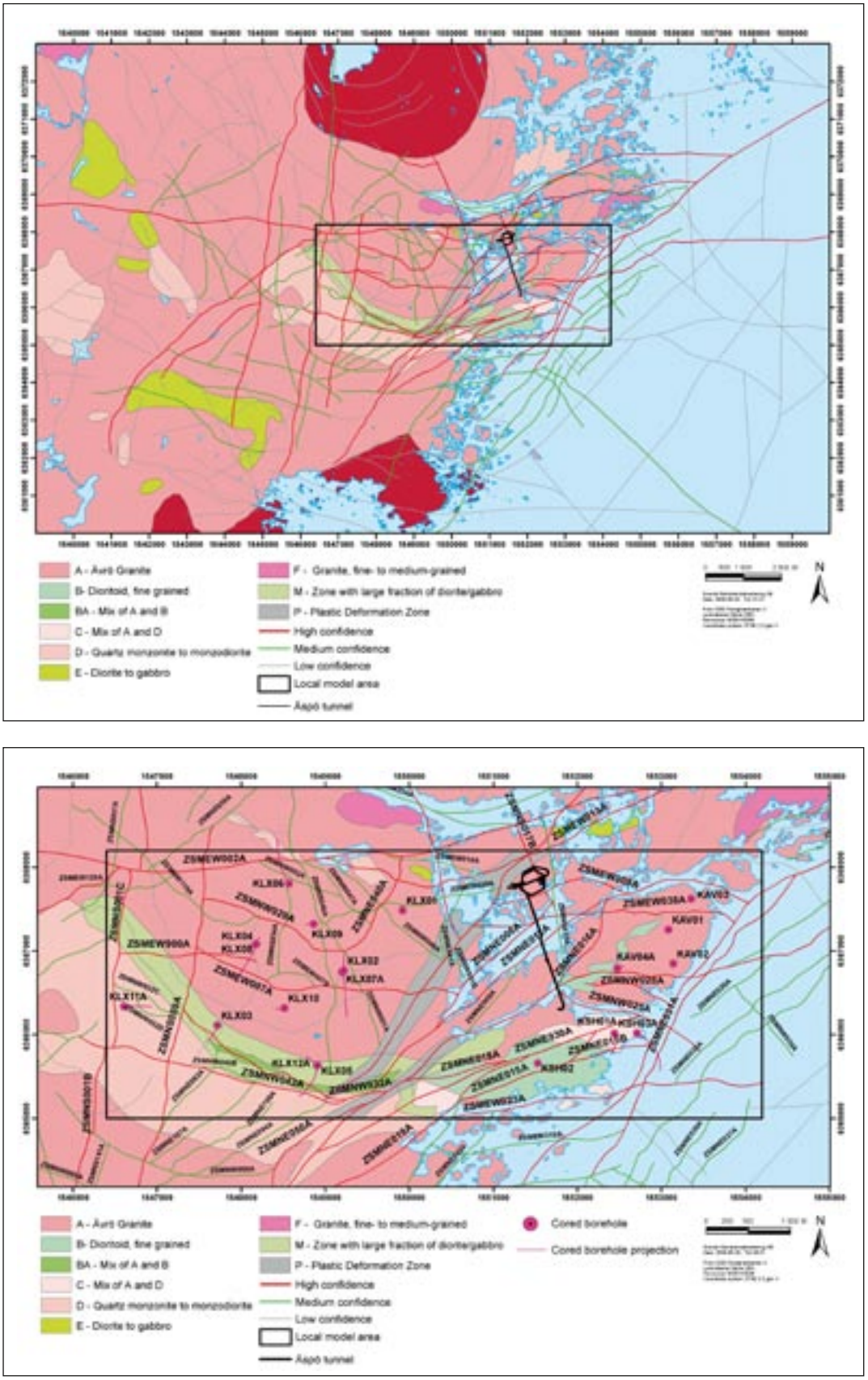

Figure 2-2. *Modelling areas from L 1.2 SDM modelling showing rock types, deformation zones and the Äspö HRL tunnel /SKB 2006a/. Top: regional-scale area; Bottom: local-scale area. The black box is the L 1.2 local-scale modelling area.*

Details about the flow measurements may be found in Appendix A. Tunnel F and G are parallel and close to tunnel A, approximately section 3,400–3,510 m and 3,510–3,600 m. Hence, the flow rates in tunnels F and G are included in the main tunnel. Data from May 1991 to January 1994 are from the Task 5 modelling exercise with the Äspö HRL Task Force /Rhén and Smellie 2003/. Data from later periods are monthly mean values, calculated from SICADA data. Some spikes of inflow rates, with short duration, have been removed, as generally they can be assumed to be related to drill water when excavating new tunnels. It is possible that some of these spikes, totally or partly, can be related to true inflow from the rock, due e.g. hydraulic tests. No attempt has been made to sort this out as it was judged that it would only result in smaller changes of the total flow rate. At some occasions data are missing after 1995 or there is an indication that a weir has been clogged. Linear interpolation has been used to estimate flow rates for months with missing or erroneous data. Flow rates are missing for 2005, but can be assumed to be more or less as December 2004. The total inflow to the HRL is shown in Figure 2-3, the inflow to the upper part of the shaft in Figure 2-4, and one example of the flow rate at one weir position is shown in Figure 2-5. The rest of the weir measurements are given in Appendix A.

Hydrochemistry data

In addition, hydrochemistry data at the weirs are available. The information contains data on Chloride, pH and electrical conductivity measured at the weirs along the Äspö tunnel during the excavation of Äspö Hard Rock Laboratory for the time period May 1991 to about end of 2003. Based on Cl and electrical conductivity (Cond) measured, TDS has been calculated.

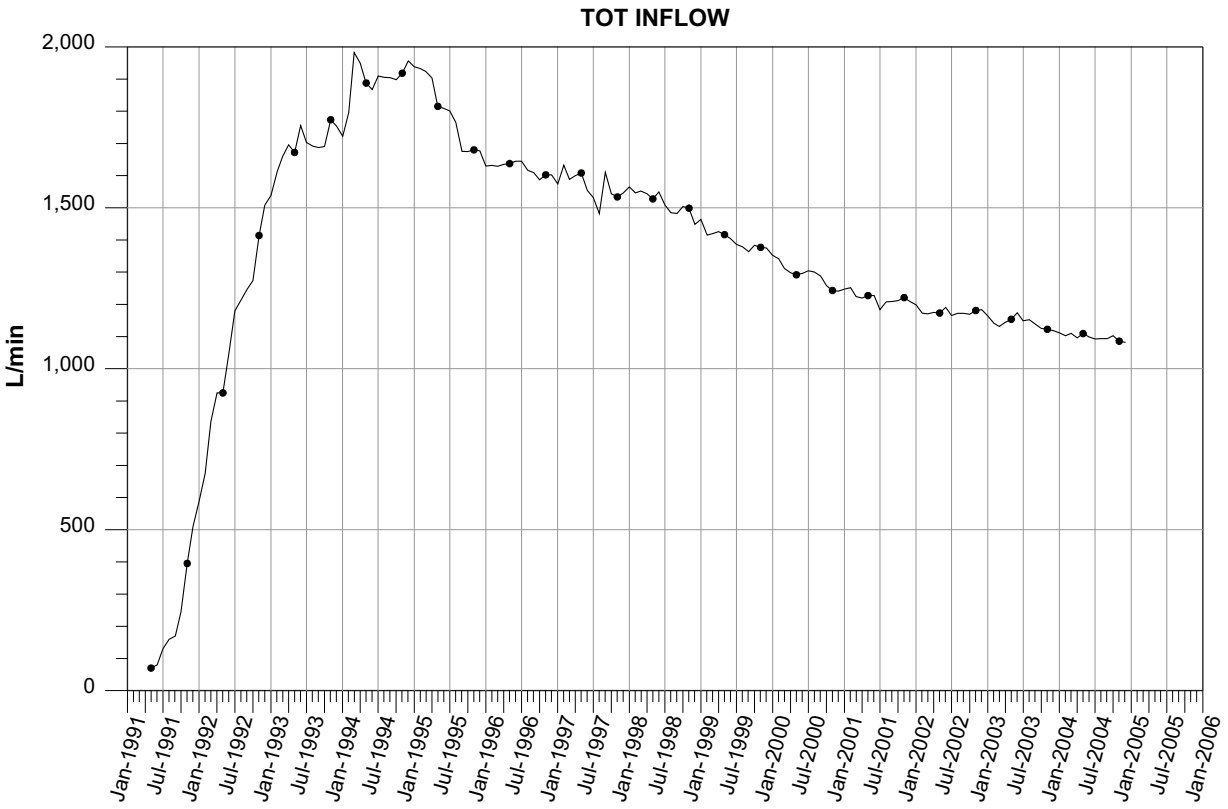

Figure 2-3. *The evolution of total water inflow to the tunnel.*

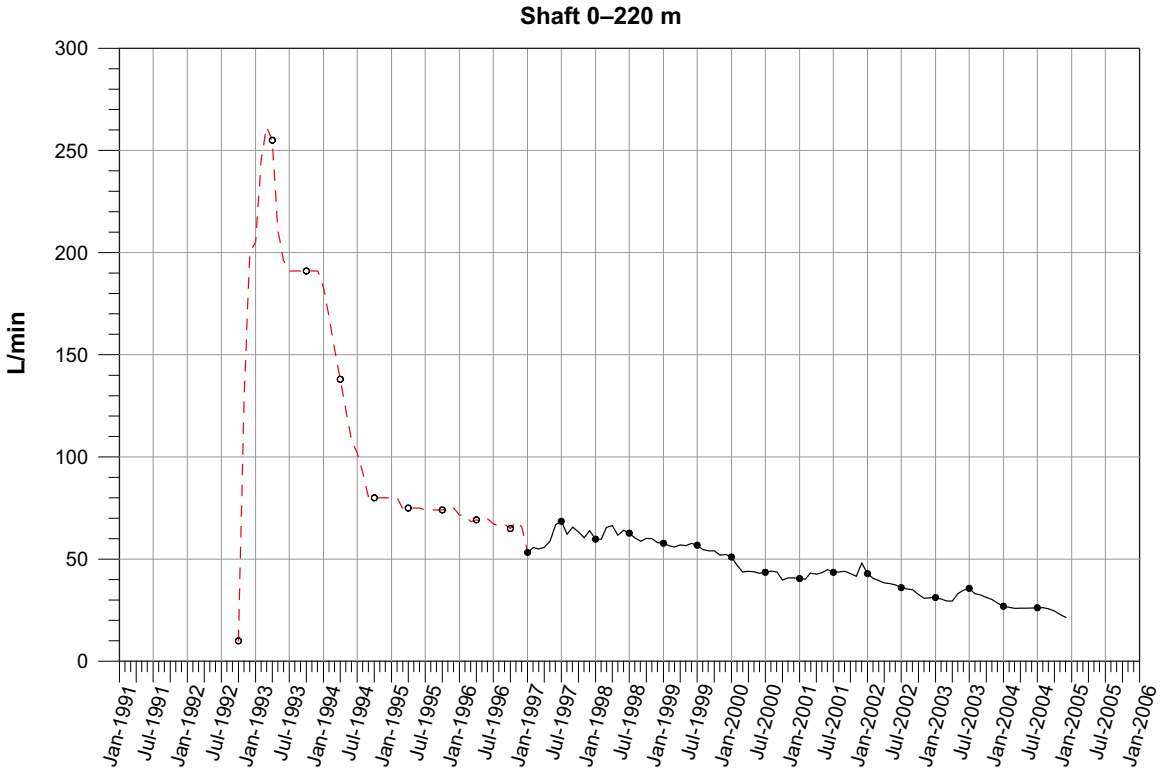

Figure 2-4. *Inflow to the upper part of the shaft. The red dashed line is Äspö Task Force, Task 5 data /Rhén and Smellie 2003/.*

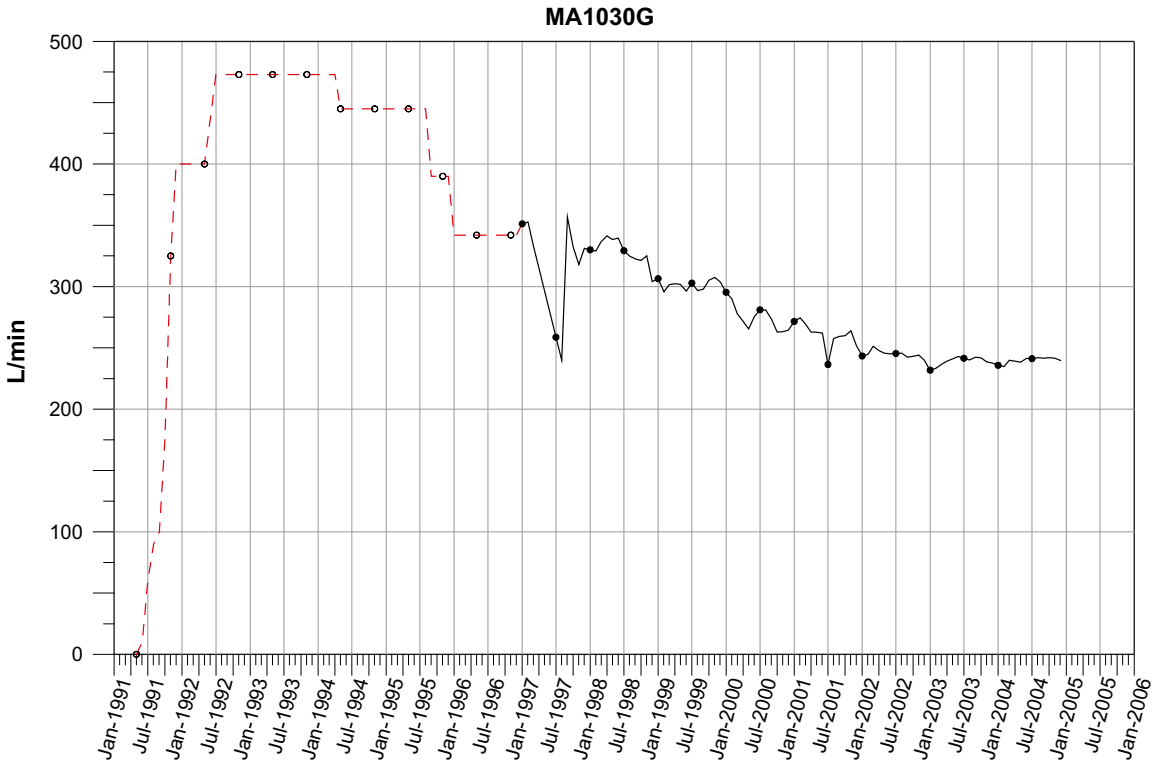

Figure 2-5. *Example of one weir measurement. The red dashed line is Äspö Task Force, Task 5 data /Rhén and Smellie 2003/.*

Water table at Äspö

There are modelling results from other studies available showing e.g. the head distribution at Äspö. /Vidstrand 2003/ gives some illustration on the transient development. Some examples may be found in Figure 2-6 and Figure 2-7. /Rhén et al. 1997b/ illustrates the difference in head between undisturbed condition and a situation with the HRL present. This may be seen in Figure 2-8.

Water table at Ävrö and Laxemar

Drawdown observations that may be related to the inflow to the Äspö HRL, have been measured in the western part of Ävrö and close to the southern coast of Laxemar. Significant drawdowns at the western part of Ävrö, about 2–5 m, and in the strait between Ävrö and Mjälen, about 8.5 m, have been observed in 1996 (Rhén 2006, personal communication). Then there is a slight recovery in the drawdown, and the drawdown in the strait goes down to 7 m in the year 2000. Mjälen is located north-west of Ävrö.

In HLX02, which intersects the Mederhult zone (EW002) near Äspö, there is a drawdown of 0.5 m. No other percussion boreholes in the Laxemar subarea seem to show any significant drawdown. Estimated water levels and calculated drawdowns are given in Table A-5 in Appendix A.

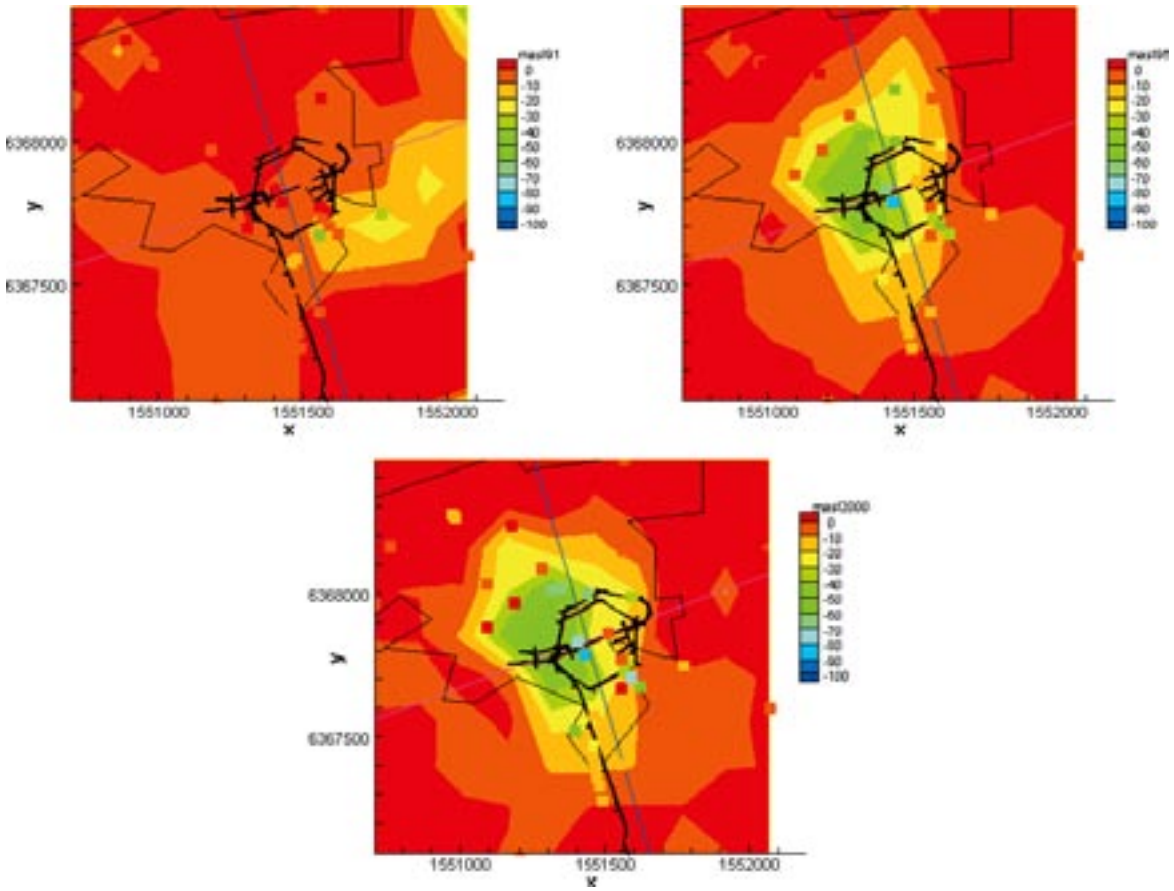

Figure 2-6. *A previous model of the development of the hydraulic head with time shown at 1991 (upper left), 1995 (upper right), and 2000 (lower), according to /Vidstrand 2003/.*

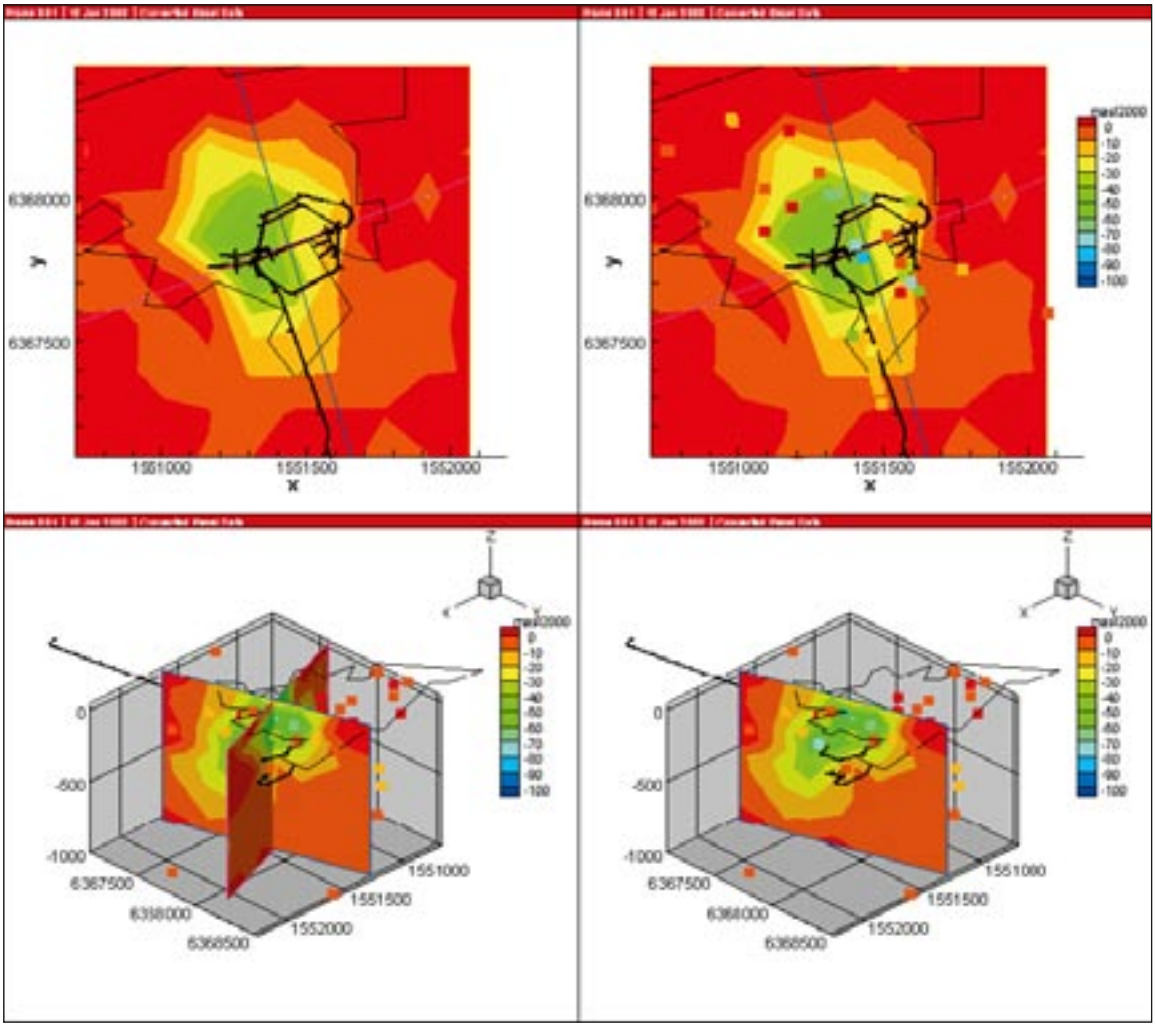

Figure 2-7. *A previous model of the hydraulic head distribution at year 2000. Interpolated values /Vidstrand 2003/.*

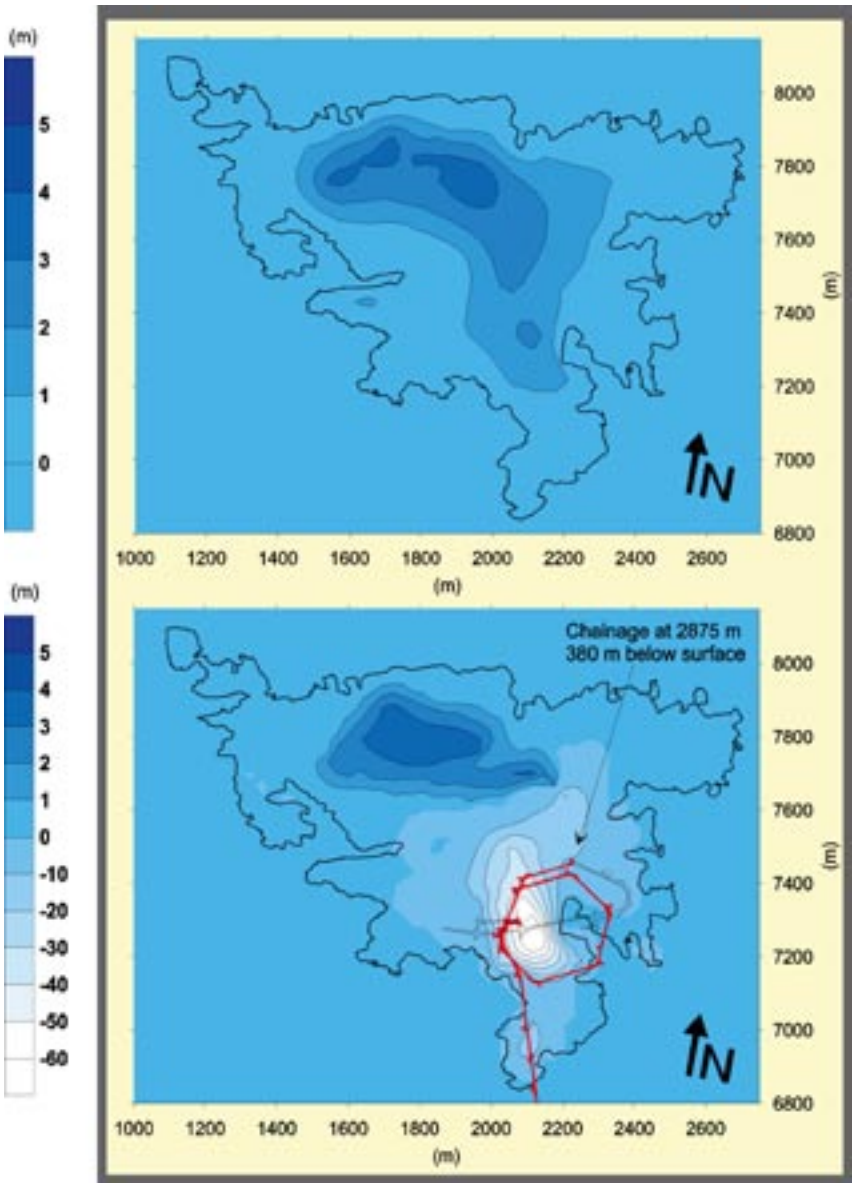

Figure 2-8. *Results from a previous study of tunnel drawdown at the surface, i.e. watertable /Rhén et al. 1997b/. Top figure: undisturbed conditions. Bottom figure: Tunnel face position 2,875 m: c. 1994-01-25.*

2.3 Regional-scale modelling

The model developed in the Laxemar 1.2 SR-Can project is used as base for this study. In the simulations, two types of flow boundary conditions have been used for the top surface, head or flux, respectively. In the simulations using a head boundary condition on the top surface, the model is the same as the ECPM reference case in /Hartley et al. 2006a/. Approximations to the elevation of the watertable were derived from too files provided: surface topography and a "simulated watertable" obtained by interpolation between measured surface water heights from the Simpevarp study area, e.g. lakes and streams. In the reference case, the top-surface head equals the simulated watertable plus 30% of the difference between the simulated watertable and the topographic surface /see Rhén et al. 2006/. The same properties are used here, and may be seen below in Table 2-3, and the size of the model is shown in Figure 2-9 below. A simplistic model of the Quaternary cover is used in the reference case model that has three parallel soil layers each 1 m thick and with hydraulic properties based on silty till. Hence, a specified head boundary condition is coupled with a relatively high conductivity to soil to give a good contact between the boundary condition and the underlying crystalline rock.

By contrast, the flux boundary condition was always used in combination with the more complicated L 1.2 HSD model, which has three layers of varying thickness and varying spatial distribution of soil types varying from Sandy Till to much tighter clays. Hence, in this case the hydraulic contact between the surface flow boundary condition and the bedrock varies according to the local soil types. The soil types and hydraulic properties of the Quaternary cover beneath the sea are uncertain in some areas of the L 1.2 HSD model. In particular it was not certain whether the base of the sea sediments was mainly highly permeable Till, or the much tighter Gyttja Clay. This was felt to be an important consideration for this project since it would affect whether the water inflow to the tunnel was mainly of marine or meteoric origin. The flux boundary condition used specified a maximum potential infiltration of either 165 or 80 mm/year.

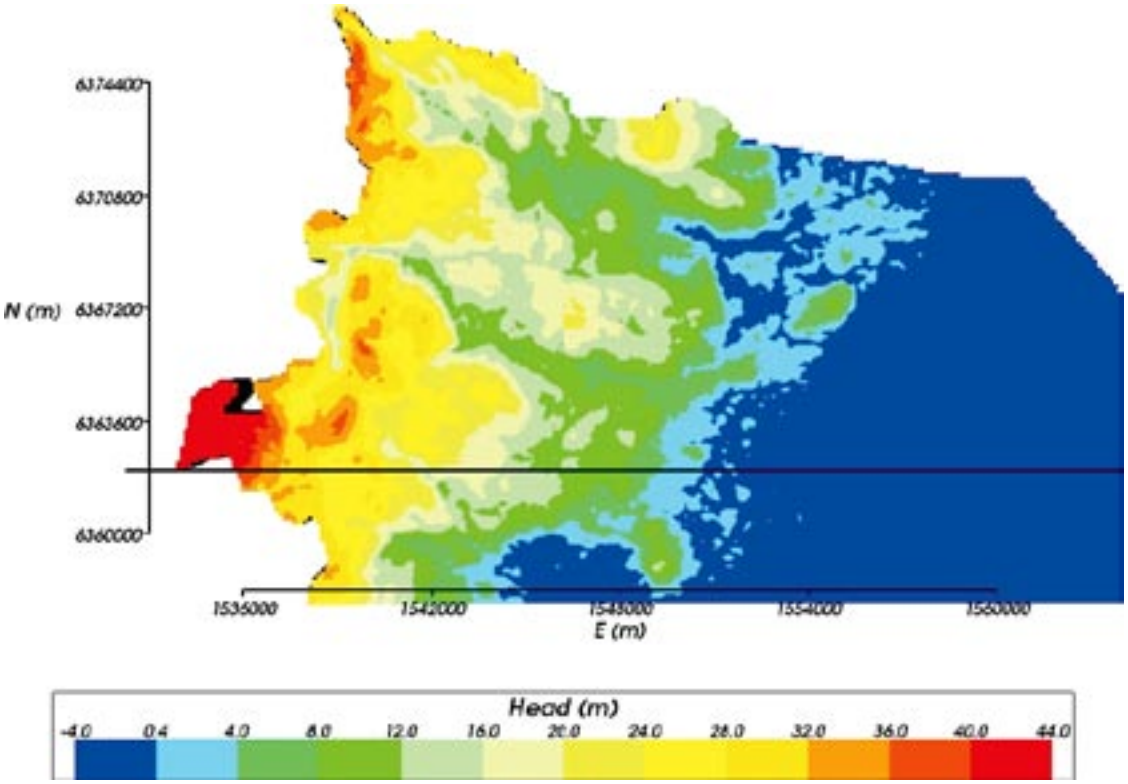

Figure 2-9. *The model domain based on identified water divides for the reference case model as in /Hartley et al. 2006a/. Here, the model is coloured by groundwater head at 2005 AD for a case without the Äspö HRL. The black E-W line indicates where the position of the southern boundary for the cases with a flux boundary condition on the top surface.*

Table 2-3. Description of the reference case in /Hartley et al. 2006a/.

Property	Description
Domain	Extended regional model domain with 50 m element-size embedded grid in Laxemar, Simpevarp and Ävrö release areas, and 100 m element-size elsewhere.
Initial condition[1)]	Initial condition is set to full glacial melt water conditions between ground surface and an elevation of –700 m; then linear gradient to no Glacial and full Brine at –1,500 m elevation. Between –700 m and –1,500 m elevation, the Brine increases linearly from 0 to 100%. Below –1,500 m elevation, a full Brine condition is applied.
Top surface flow boundary condition	Top-surface head equals simulated watertable + 30% of the difference between the simulated watertable and the topographic surface /see Rhén et al. 2006/.
Top surface waters	Surface groundwaters are: Glacial and Littorina during early Baltic Ice Lake, Yoldia Sea and Ancylus Lake periods; Meteoric water and Littorina during the Littorina Sea and current Baltic Sea phases. The provided sea-water salinity history is used to determine relative fractions of Littorina and Meteoric waters at the top surface of the model offshore.
Density and viscosity	Density and viscosity are functions of salinity (transient), temperature (fixed), and total pressure (transient).
Transmissivity model	Hydraulic properties obtained from an upscaled regional-scale DFN that is based on the semi-correlated cases of the Hydro-DFN models.
Anisotropy	Anisotropy has been introduced by decreasing the transmissivity of fracture sets Set_A and Set_B by a factor of 10.
HCD confidence	HCD included all zones.
Depth dependency	HRD: The underlying DFN has a step change in properties according to the Hydro-DFN, although a transition elevation of –200 m is used instead of –300 m. For all HRD except HRD(A2), the upscaled conductivity is then reduced by an order of magnitude below an elevation of –600 m. HCD: Implemented as a step function in elevation (0 to –300 m, –300 m to –600 m, < –600 m), conditioned at boreholes against measured transmissivities.
HSD	Homogeneous 3 layer HSD of uniform 1 m thickness per layer.
Flow-wetted surface and salinity matrix diffusion length	Flow-wetted-surface (FWS) per unit volume for rock matrix diffusion (RMD) above –200 m elevation: a_r = 2.0 m^2/m^3.for HRD(A2), a_r = 1.0 m^2/m^3 for HRD(D,E,M), a_r = 1.5 m^2/m^3 elsewhere. For all rock domains below –200 m elevation, a_r = 1.0 m^2/m^3 /see Hartley et al. 2006b/. Matrix diffusion length into matrix blocks: $L_D = 1/a_r$
Kinematic porosity of flowing fractures	HRD kinematic porosity is taken from the upscaled regional-scale DFN that is based on the semi-correlated cases of the Hydro-DFN models. However, the 10th percentile values for the 20 m block scale kinematic porosity obtained from the appropriate Hydro-DFN are used as minima of $n_{e,b}$. HCD porosity 10^{-3} for zone thickness $W < 100$ m and 10^{-2} for $W \geq 100$ m.
Diffusion accessible porosity (excluding the kinematic porosity)	Diffusion accessible porosity from /Byegård et al. 2006/ upper limit $n_m = 5.9\ 10^{-3}$.
Diffusion coefficient	Intrinsic diffusion coefficient into intact rock matrix $D_e = 1.5\ 10^{-13}$ m^2/s.
Dispersion lengths	a_l = 40 m, a_t = 5 m

[1)] This describes the initial condition of the SR-Can reference case. In this study, the values from the time step representing 1960 AD are used as initial condition.

However, the boundary condition does not force a uniform flux inflow to the model everywhere. Instead, the flux is adjusted on each finite-element and in time according to the relative levels of the groundwater head at the top of the model and the ground surface. If the modlled head well below ground surface, then the full potential infiltration is used. Then as the head approaches ground surface the infiltration is reduced, and if the head is above ground surface, then an outflow (discharge) is specified to reduce the head back down to ground surface. Hence, this flux boundary condition is non-linear in head, and effectively implements a specified flux in recharge areas and automatically switches to a specified head equal to topography in discharge areas. This boundary condition was found to encounter some numerical difficulties in the far south of the L 1.2 model, which are thought to have arisen from some soil layers having zero thickness, or near zero, in some places as a result of different interpolations used for the digital elevation of the surface and the Quaternary deposit layers. These problems were remedied by trimming off the southern 3 km of the domain as shown in Figure 2-9.

For the specified head boundary condition, the watertable is fixed, and so the tunnel cannot cause any drawdown at the surface, only below the surface around the tunnel. For the flux boundary condition, there will be a drawdown at the surface.

Some examples of imposing different top surface flow boundary conditions and for different maximum potential infiltration of 40, 80 and 165 mm/year are given in Section 2.3.4.

In addition, the storage coefficient is set to zero for simplicity, since the time-step size of a year is large enough for hydraulic storage not to be a factor, i.e. pressure disturbances can be assumed to be dissipated within one time-step.

2.3.1 Hydraulic conductor domain (HCD) model

This section summarises the description of the HCD model, which is used in /Hartley et al. 2006a/. The HCD model is based on the L 1.2 data delivery from the discipline Geology in the Analysis group for the Site Investigations (a full account of the models is given in /Hermanson et al. 2005, Rhén et al. 2006/), and a calibration of the hydraulic properties of the HCD model against PSS data and chemistry data. The data delivery from the disciplines Geology and Hydrogeology in the Analysis group for the Site Investigations included the following.

- Rock Visualisation System (RVS) data file in XML format.
- Supporting documents and spreadsheets defining:
  - Properties (transmissivity and kinematic porosity) for deformation zones.
  - Three different depth dependency models for transmissivity of HCD.

The HCD model contains 37 deformation zones (DZ) that have been classified as high confidence zones. 65 zones are classified as intermediate confidence zones, and in total there are 200 DZs in the data set. This is illustrated in Figure 2-10. Hydraulic thickness is based on geological estimates of the width of the DZ. If no value is given by the geologist, the thickness is approximated with a default value of 20 m. For 24 of the zones, an explicit transmissivity is estimated on the basis of the hydraulic tests in the HCDs.

Transmissivity

All RVS Deformation Zones (DZs) in the data delivery are assumed to have a depth dependency according to a step change variation of properties within each RVS DZ as the reference case. This depth dependency model is shown as solid lines showing the piecewise constant variation in Figure 2-11 along with other alternative models such as power-law or exponential. The step change model is given by:

- $-300 \le z \le 0$: $T = 2.0\ 10^{-5}\ m^2\ s^{-1}$
- $-600 \le z \le -300$: $T = 1.2\ 10^{-5}\ m^2\ s^{-1}$
- $-2{,}100 \le z \le -600$: $T = 7.1\ 10^{-7}\ m^2\ s^{-1}$

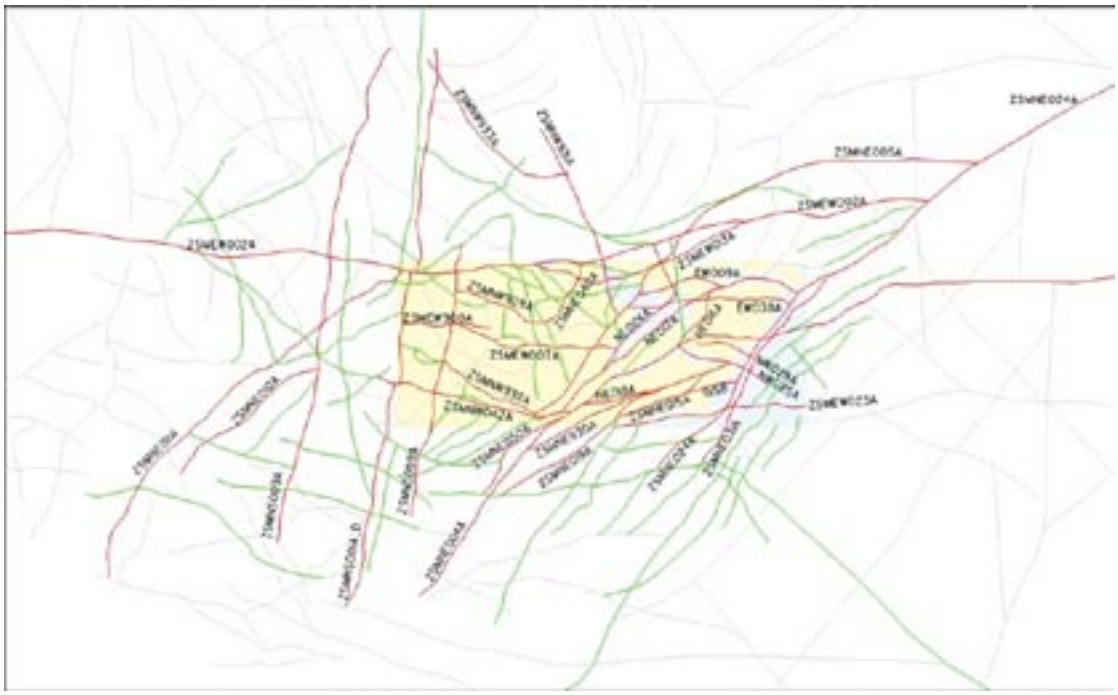

Figure 2-10. *HCD for regional-scale modelling. Deformation zones coloured red have been verified and are assigned high confidence. Lineaments are coloured green or grey and have been assigned intermediate (green) or low confidence (grey).*

A figure showing the data and fitting of transmissivities in the HCD performed in /Rhén et al. 2006/ is reproduced in Figure 2-11.

For these RVS DZs with one or more measured transmissivities (for 25 HCDs hydraulic test data are available) the geometric mean *T* and the representative 'mean elevation' of these observations are used to modify the suggested depth trend curves for transmissivity (*T*) defined above, by adding/subtracting a number to/from the given depth trend so that it passes through the given point. For RVS DZs without any measurements, the given depth trends for *T* are used. Global maximum and minimum *T* values are also provided and these are used to limit the resulting *T* values.

After the depth trends are implemented, the values are calibrated against pipe string transient injection test data (PSS). Where there is a discrepancy between the modelled and observed transmissivity, the properties of the zones are modified individually to obtain a better match. Based on the data, intersections of the boreholes with the deformation zones were identified and the intersected horizontal segment of the zone was calibrated against corresponding PSS data. The depth trend was represented by 3 horizontal segments (> –300 m, –300 to –600 m, < –600 m) in which the transmissivity is uniform. Therefore, for each intersected deformation zone with PSS data, the transmissivity of the horizontal segment where the borehole intercepts the zone was modified to match the measured value, whilst checking that the transmissivities remained within the suggested range. For those RVS DZs where no PSS data is available, the transmissivity specification follows the provided general HCD depth dependency profile for the site. An example of the implementation of the HCD model is illustrated in Figure 2-12. It is also stipulated that all HCDs should be in hydraulic contact with the overburden (the modelled HSD's).

The deformation zones are usually divided into triangles. Presently, no tool has been developed to identify all of the triangles within a given radius of the calibration point. In the current study, a horizontal segment of the deformation zone is modified to fit the calibration value, i.e. only the horizontal segment with the PSS data is modified.

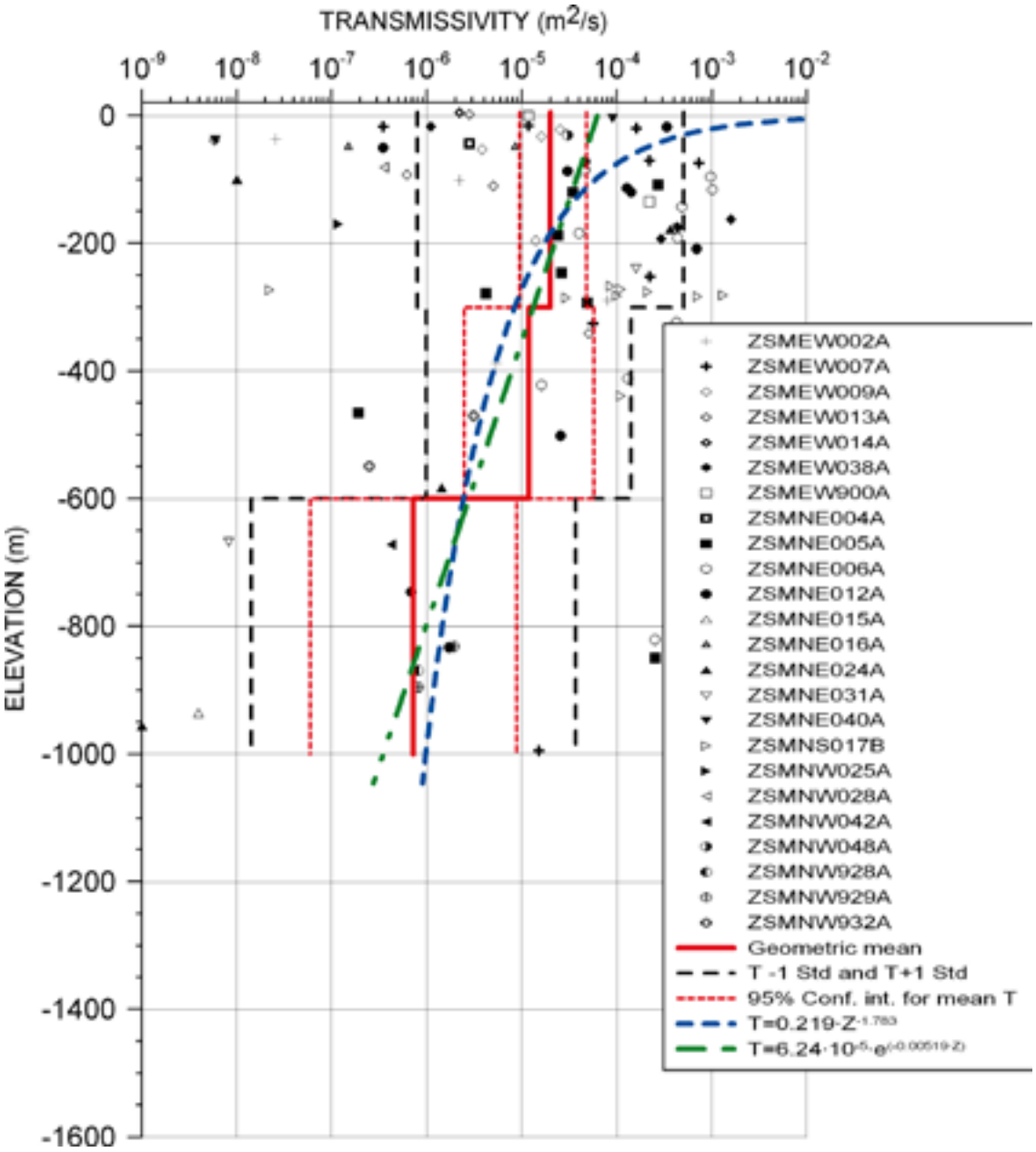

Figure 2-11. *Zone transmissivity values versus depth and three interpreted depth dependency models (given in the legend where Z (= –z) is the depth): Step change (Geometric mean); Power-law ($T = 0.219\ (-z^{-1.783})$); Exponential ($T = 6.24\ 10^{-5}\ e^{-0.00519\ z}$).*

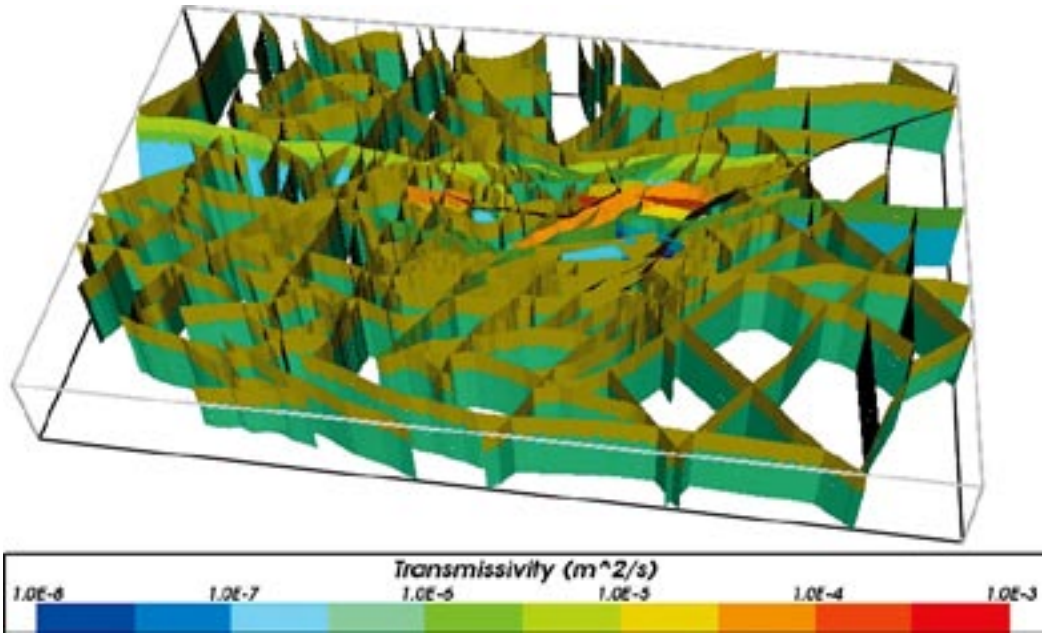

Figure 2-12. *HCD for regional-scale modelling in 3D. The zones are coloured by transmissivity, where red is high and blue is low.*

2.3.2 Hydraulic rock domain (HRD) model

The development of the HRD model is detailed in /Hartley et al. 2006a/. A summary is given below. The Hydraulic Rock Domain (HRD) model for L 1.2, as provided by Geology, is illustrated in Figure 2-13. To create a simplified HRD model, domains with similar geological properties were grouped and the HRD's listed below were defined (The Original HRD names and groupings are given in brackets.

- HRD(A) (A – Ävrö granite).
- HRD(A2) (A in an area east of Äspö shear zone (Rock domain P) that forms a more conductive part of HRD(A)).
- HRD(B,C) (B and C).
- HRD(D,E,M) (M, BA, D and E).
- HRD(F,G) (F and G).

The domain was also subdivided into four layers according to the elevation intervals 0 m to –100 m, –100 m to –200 m, –200 m to –600 m, and below –600 m. A dummy HRD was added as an extra layer at the bottom of the model (elevation –2,100 to –2,300 m) to act as a buffer between the bottom of the HCD's and the lower (no flow) boundary of the model. The extent of the regional model domain is based on the water catchment area. The resulting model is illustrated in Figure 2-14.

HRD models based on the Hydro-DFN

The treatment of HRD properties was based on an underlying Hydro-DFN that derived properties for the different rock domains based on detailed fracture and flow logging in boreholes located in each domain. The methodology is to create a stochastic realisation of the DFN model on a regional-scale, and then convert the properties of the DFN model to an equivalent continuum porous medium representation element by element. This method of "upscaling" calculates the equivalent properties based on DFN flow simulations through the fracture network within each finite-element volume. The ECPM reference case and the model in the current use

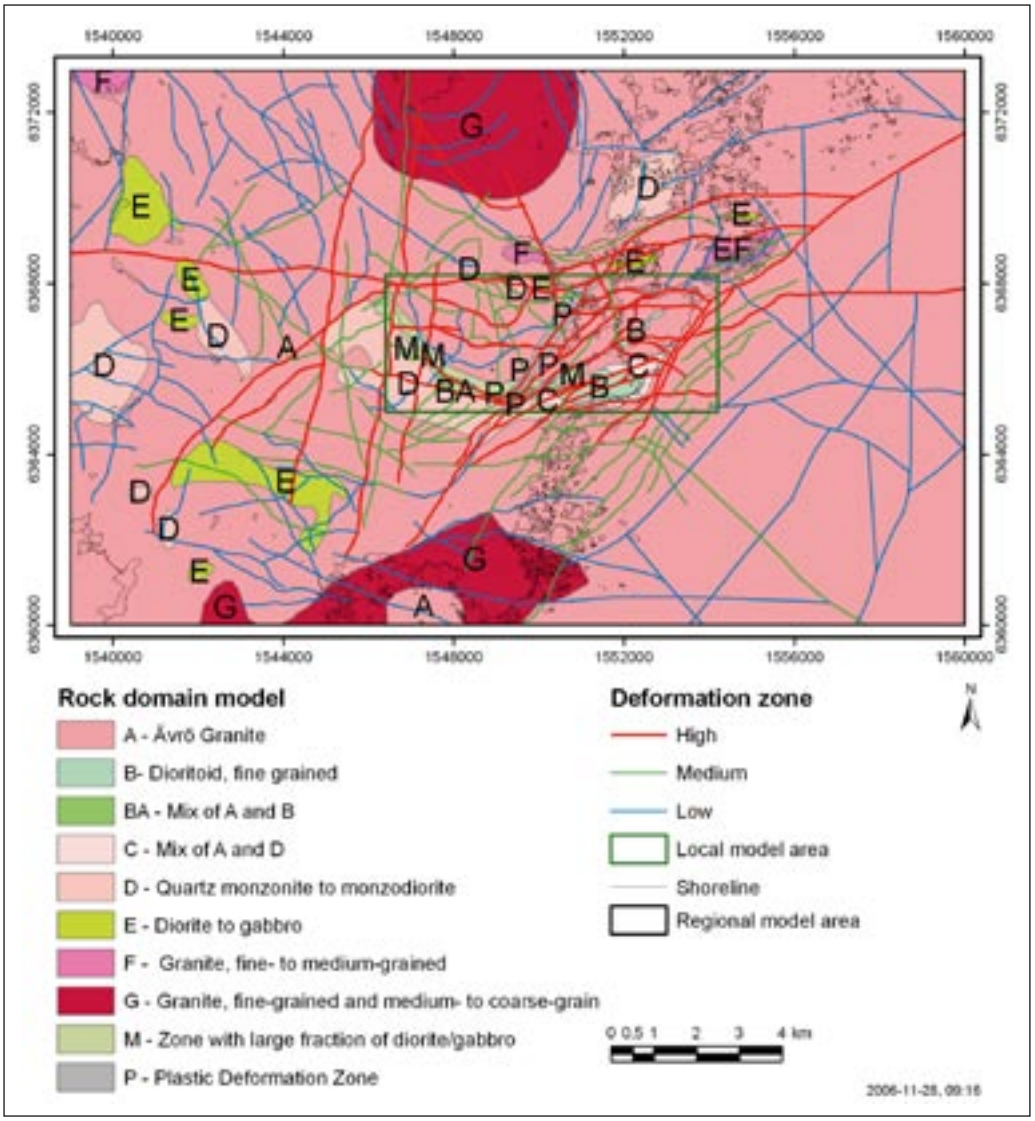

Figure 2-13. *Rock domain model for the regional model area.*

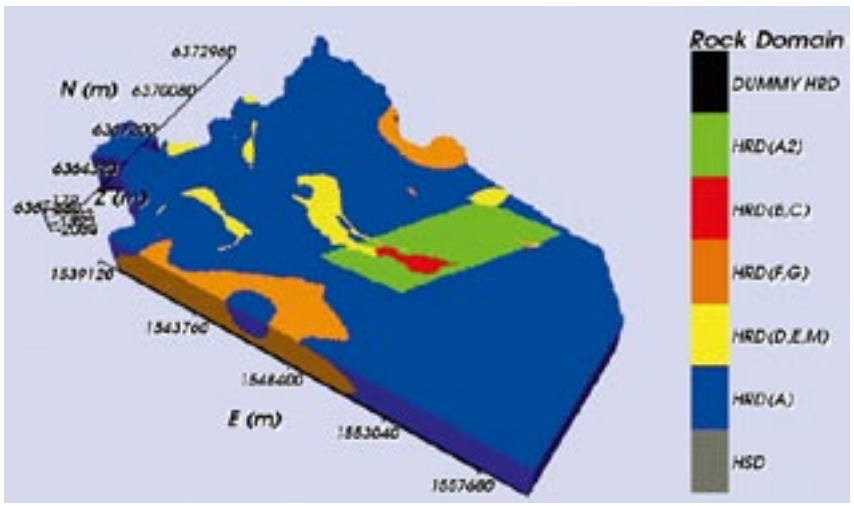

Figure 2-14. *HRD model. The regional model domain is divided into the HRDs: HRD(A), HRD(A2), HRD(B,C), HRD(D,E,M) and HRD(F,G). The key gives the name of the HRD. The HRD in the depth interval 2,100 m to 2,300 m provides a buffer between the bottom of the HCDs and the bottom of the model. The HSD layers have been removed.*

the properties from one realisation of the Hydro-DFN with a semi-correlation between fracture size and transmissivity, i.e. the mean transmissivity scales with fracture size, but some random perturbation is added to the correlation.

Hydro-DFN models were defined for four boreholes that traverse different rock domains in the Laxemar, Simpevarp and Ävrö subareas. For the models described in this section, each rock domain in the simplified HRD model (see Figure 2-14) is associated with one of the Hydro-DFN models.

The HRD's are listed below; each is followed by the borehole for which the associated Hydro-DFN model was defined and, in brackets, the rock domains traversed by the borehole. The Hydro-DFN parameters are given in /Hartley et al. 2006a/.

- HRD(A) and HRD(F,G): KLX04 (Laxemar RD A).
- HRD(A2): KAV04A (Ävrö RDs A and C).
- HRD(B,C): KSH01A (Simpevarp RDs B and C).
- HRD(D,E,M): KLX03 (Laxemar RDs M(A), M(D) and D).

For the Hydro-DFN, two intervals were considered separately, above –200 m and below –200 m, to reflect a depth trend observed in the PFL-f and PSS data for the Laxemar subarea, with flow occurring mainly in the region above –200 m. However, site data suggested some variability between –200 m and –300 m in the elevation at which this reduction in flow takes place. An elevation of –200 m was used ultimately in the SR-Can L 1.2 reference case regional-scale model, so it was also used in this study. Also, there is an uncertainty in extrapolating the properties of a whole rock domain from a single borehole. Considerations of the variability of the mean measured 100 m PSS interval data without deformation zones within the Laxemar sub-area suggests a variability of about half an order of magnitude between boreholes, and KLX04 is probably toward the high-end compared with newer boreholes such as KLX08. Hence, the current model probably over-estimates hydraulic conductivity in the Ävrö granite. In addition, an extra depth zonation was introduced at –600 m, such that the mean hydraulic conductivity is an order of magnitude lower below –600 m. Finally, some anisotropy between the sub-vertical sets was introduced such that fractures oriented ENE and NS have an order of magnitude lower transmissivity than those oriented NW (this direction coinciding with the orientation of maximum principal stress).

The transport aperture was calculated using the empirical relationship $e_t = aT^b$, $a = 0.46$, $b = 0.5$ based on Äspö Task Force 6c results /Dershowitz et al. 2003/. The kinematic porosity, $n_{e,b}$, for a block was then calculated as the sum of products of connected fracture area within the block and the transport aperture, and then divided by the volume of the block.

Based on the findings of block-scale upscaling in a previous study /Hartley et al. 2005/, the minimum fracture length sampled should be no more than one quarter of the element size. Hence, $r_{min} = 14$ m was used (equivalent to a fracture length of 25 m) throughout the regional domain. The full regional DFN model, which has over ten million fractures, is too large to visualise and so a smaller regional domain is shown here as an illustration. One realisation of the regional-scale DFN model is shown in Figure 2-15 as the full 3D model in plan view, and as a horizontal cross-section at $z = –500$ m (i.e. a trace map) in Figure 2-16 with the deterministic HCD model superimposed. It is apparent from this cross-section that different fracture parameters – mainly fracture intensity and transmissivity – are used in different rock domains. Note that based on a regional-scale connectivity analysis, the isolated fractures, isolated fracture clusters and dead-end fractures are removed, so the fractures shown are only those that form part of the connected network. Even for a Poisson spatial process this can result in a very heterogeneous distribution of connected fractures. The resulting upscaled hydraulic conductivity and kinematic porosity on the full regional-scale model are shown in Figure 2-17 and Figure 2-18, respectively. The kinematic porosity is based on the connected fracture volume (area times transport aperture) per unit volume based on stochastic fractures of radius greater than 14 m and the deterministic deformation zones.

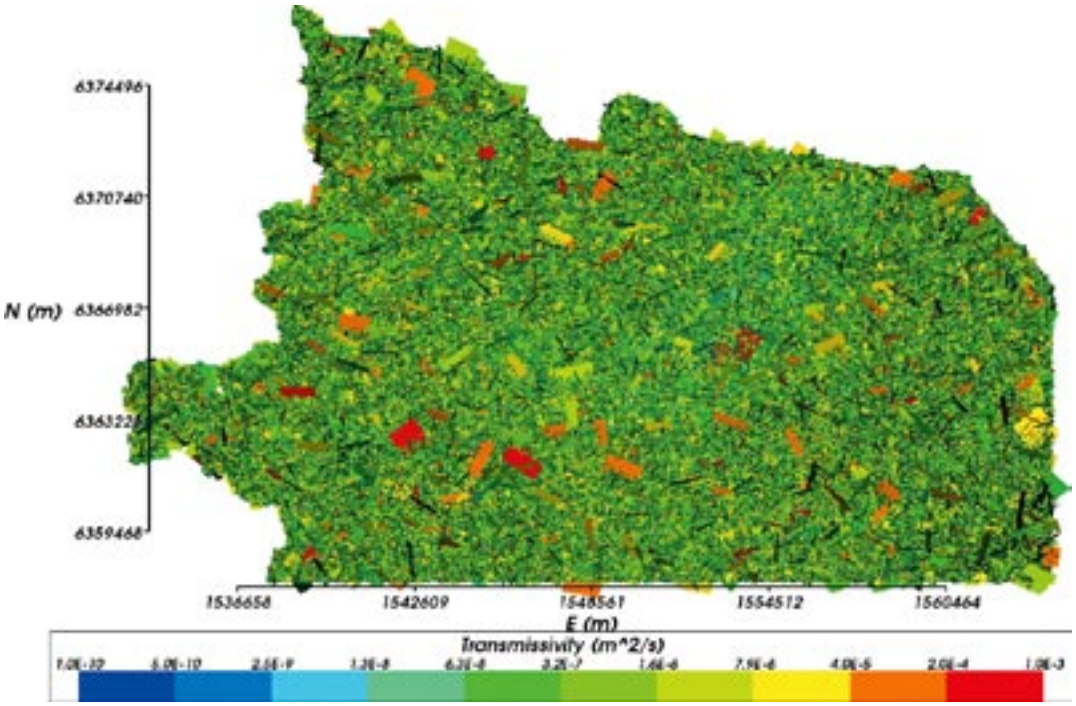

Figure 2-15. *Map view of the DFN model for the regional-scale domain showing all connected stochastic fractures (in 3D) coloured by Log(transmissivity).*

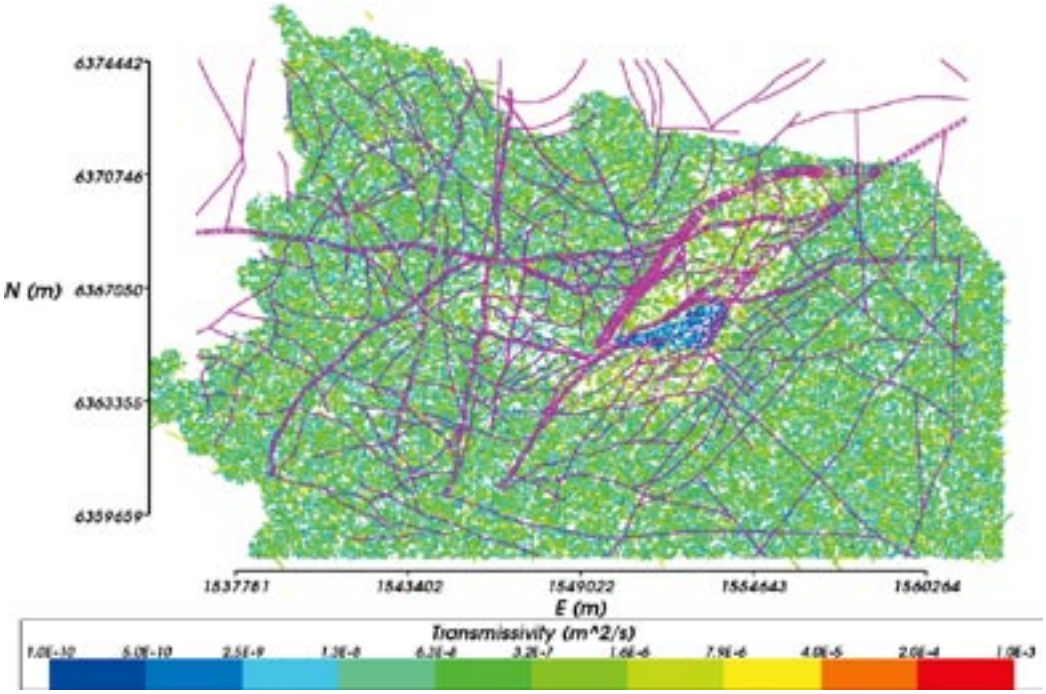

Figure 2-16. *Map view of the DFN model for the regional-scale domain showing stochastic fractures cutting a horizontal slice at z = –500 m coloured by Log(transmissivity) and the HCD model superimposed (purple).*

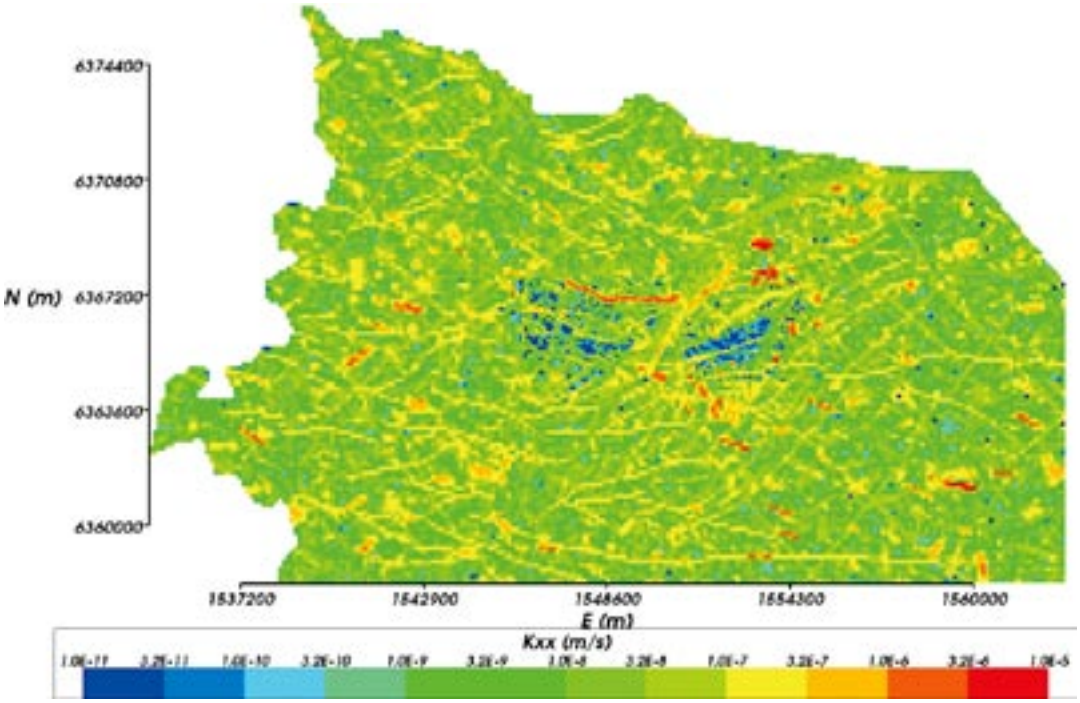

Figure 2-17. *Regional-scale ECPM model showing upscaled hydraulic conductivity on a horizontal slice at z = –500 m through the model.*

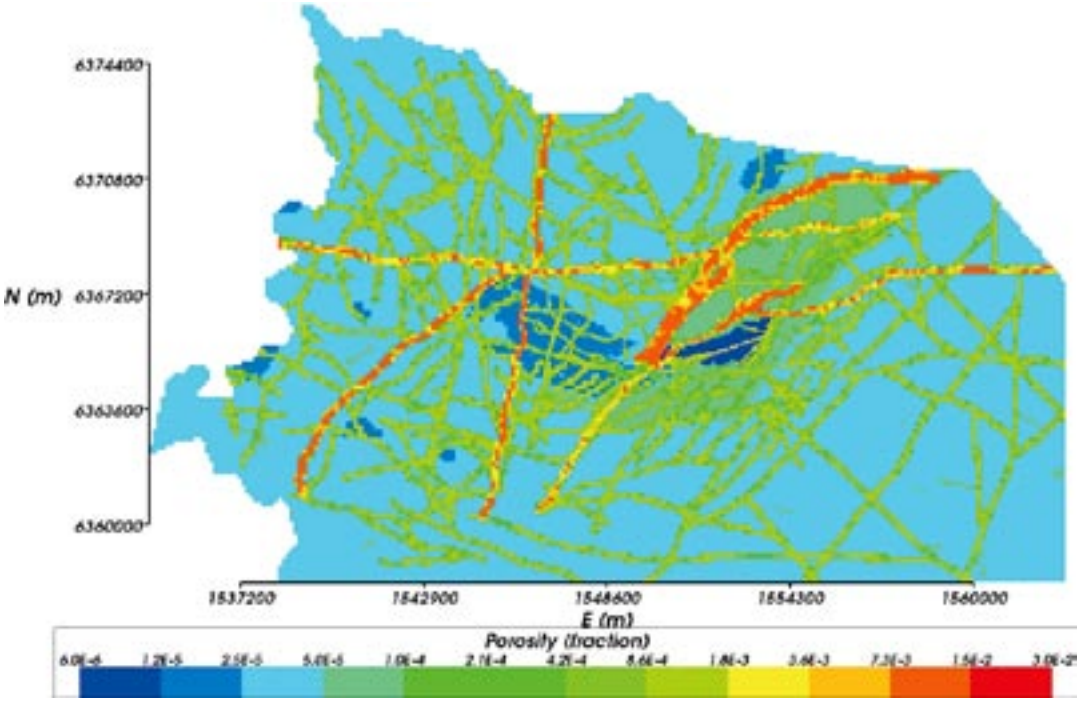

Figure 2-18. *Regional-scale ECPM model showing upscaled kinematic porosity on a horizontal slice at z = –500 m through the model.*

2.3.3 Hydraulic soil domain (HSD) model

The approach used for modelling the HSD is described in /Hartley et al. 2006a/. A summary is given below. The overburden in the Simpevarp area is dominated by sandy till but in several valleys the till is overlain by clay deposits, and on top of hills the thickness of the till is small or the rock is out-cropping. In minor parts of the area, eskers with coarse-grained material are found.

In the L 1.2 reference case modelling, it was assumed that the entire area is covered by a 3 m thick layer of silty till, with the upper 1 m more porous due to soil forming processes. This was represented explicitly in the model as three very thin layers of finite-elements of thickness 1 m at the top surface of the model. The HSD properties within each layer are uniform. The HSD overlay all HCD's providing a hydraulic contact between the soil layers and the deformation zones. This approach to model the soil domain is called HSD1 in this study.

A heterogenous model for the distribution of Quaternary Deposits (QD) was also provided /Nyman 2005/. The QD depth model is based on three layers, Z1, Z2 and Z3. The upper layer (Z1) is characterised by the impact of surface processes, e.g. roots and biological activity. The bottom layer (Z3) is characterised by contact with the bedrock and is dominated by till. The middle layer (Z2) is assumed to have different hydraulic qualities to the upper and bottom layers and is dominated by clay. The soil type assigned to QD layer Z1 at a certain location is taken directly from detailed maps of QD. The soil types assigned to QD layers Z2 and Z3 at a certain location also depend on the soil type in QD layer Z1. This approach to model the soil domain is called HSD2 in this study. Three additional layers, M1, M2 and M3, are superimposed on the layers Z1, Z2, Z3 as illustrated in Figure 2-19. Layer M1 corresponds to peat, M2 to glacio-fluvial sediments, M3 to artificial fill. All layers can have thickness zero.

QD maps were provided, which indicate the soil type at each node on a uniform grid with 10 m spacing. In addition, stratigraphy maps were provided for the top surface and for each of the six layers Z1, Z2, Z3, M1, M2 and M3. These maps provide the surface topography (with lake bathymetry) and depths of the layers on a uniform grid with 10 m spacing. Twelve different soil types were defined for the current study.

The regional model is composed of 100 m and 50 m elements and so the QD distribution and stratigraphy had to be mapped on to these elements in some way. Firstly, to set the soil type of each element, the QD maps were used to assign the most frequently occurring soil type within each 100 m or 50 m element to the entire element. The ConnectFlow implementation of the QD maps is illustrated in Figure 2-20. The soil type was used to set the QD in the layers Z1, Z2 and Z3 based on the 'stratigraphy rules' of /Werner et al. 2005/. For each node on the top surface of the regional model domain, the elevation was then approximated by taking a linear interpolation of the elevations of the four corners of the appropriate cell in the stratigraphy maps. The stratigraphy maps for the six layers were used in a similar way to assign a thickness to each element corresponding to each layer. The resulting model is illustrated in Figure 2-20. The data provided specifies mostly Gyttja under the sea as a default, although where data is available

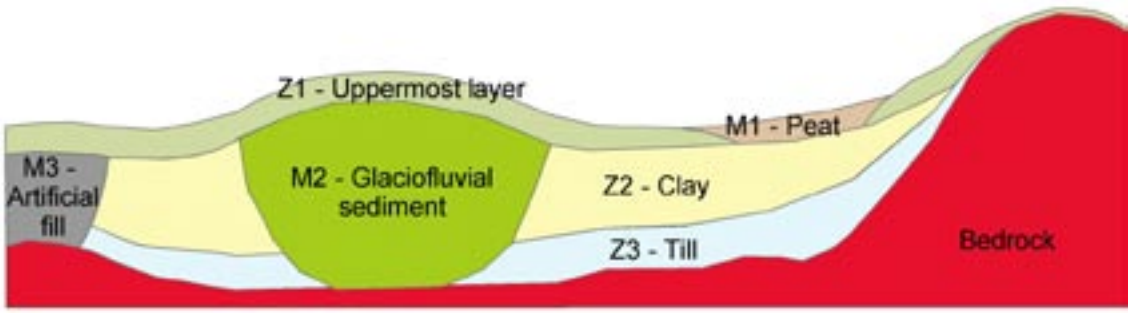

Figure 2-19. *Illustration of the layers Z1, Z2 and Z3, and M1, M2 and M3 in the overburden model. From /Nyman 2005/.*

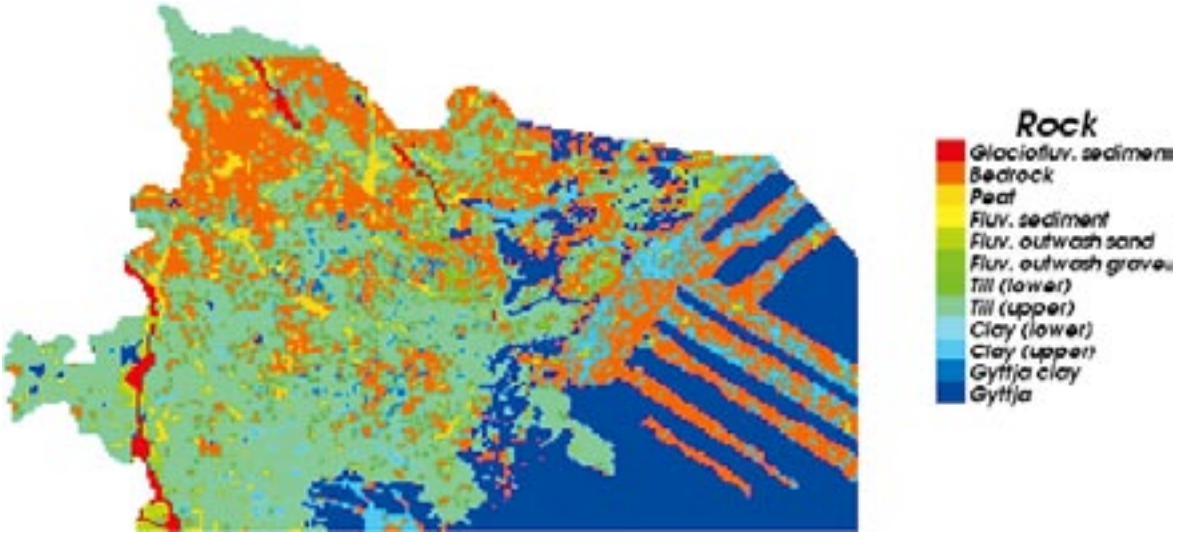

Figure 2-20. *The ConnectFlow implementation of the QD map for the extended regional model domain. The long thin strips offshore correspond to data available from ship traverses.*

from ship traverses, shown as long thin strips offshore in Figure 2-20, the QD is either Clay or Till. One vertical cross-section through the regional model with the overburden model is shown in Figure 2-21. The figure illustrates the thinner surface layers on top of hills and thicker surface layers in valleys and in the bays around Äspö. This figure also illustrates a key feature of the L 1.2 HSD model in that there is always a thick layer of Lower Till beneath the Gyttja and Clay, and so even if the top layer of sediments limits vertical flow from the surface, there is in effect a highly conductive horizontal aquifer beneath it. This is an important point for this study since the hydraulic contact between the sea and the bedrock determines where the water flowing into the tunnel originates. To try to quantify the sensitivity to the hydraulic properties of the sea sediments variants were considered initially by reducing the hydraulic conductivity of the Gyttja and Gyttja clay, but this had almost no effect. The reason was that although the Gyttja and clay was made tighter, the underlying high conductivity Lower Till beneath provided a hydraulic conduit

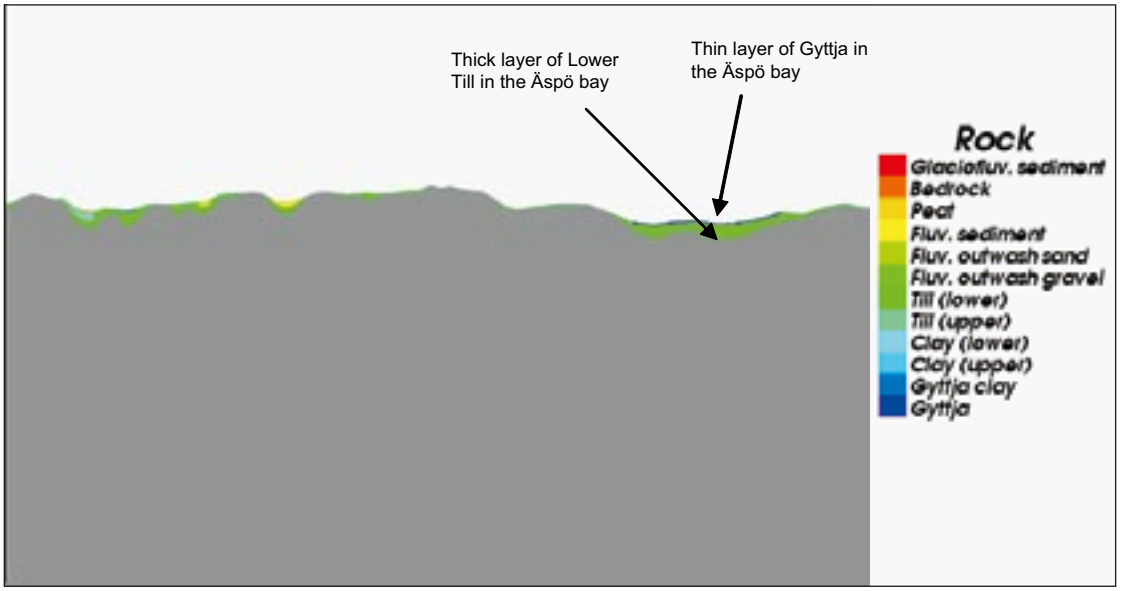

Figure 2-21. *Cross-section through the regional model illustrating thicker QD layers in valleys, and thinner layers on top of hills. HRD layers are coloured grey. The model has been stretched 10:1 in the z-direction to exaggerate the surface topography.*

beneath the Gyttja that can bring water from land, essentially maintaining the head below the sea equal to the head at the coast, i.e. 0 m. Hence, in effect whatever properties were set for the top Gyttja and clay layers, the boundary condition on the top of the bedrock beneath the sea was the specified head at the coast, i.e. zero head. For this reason, a more drastic set of variants had to be constructed to study the sensitivity to the sea sediments, by changing the L 1.2 HSD model such that the Lower Till was changed to Gyttja, and then varying the hydraulic conductivity of the Gyttja, Gyttja clay and clay by reducing them by one or two orders of magnitude.

The properties of the two HSD layers for the homogenous HSD model and for the twelve soil types for the heterogeneous HSD model are summarised in Table 2-4. These properties are taken from the report /Werner et al. 2005/. For the heterogeneous HSD model, the thickness of a soil type depends on which of the layers, Z1, Z2, Z3, M1, M2 or M3, it lies in. Z1 is up to 0.5 m thick; Z2 is up to 3.8 m thick; Z3 is at least 3.6 m thick; M1 has a thickness of 0.9 m; M2 has a thickness of 5.0 m or 15 m; and M3 has a thickness of 4 m. Comparing these hydraulic conductivities with those of the homogeneous HRD model shows that they are generally higher than the HRD, and even the Clay has a similar hydraulic conductivity to the Laxemar HRD near the surface. Comparing with the HCD, only the Gyttja, Gyttja clay and Clay (lower) have a lower hydraulic conductivity than the HCD. Hence, the overburden is not expected to affect infiltration to the deep bedrock significantly. The hydraulic conductivity of the clay would have to be reduced by about an order of magnitude for it to act as a semi-impermeable cover

2.3.4 Top surface flow boundary condition

The reference case model used in SR-Can L 1.2 used a specified head boundary condition for flow through the top surface based on a simulated watertable plus 30% of the difference between the simulated watertable and the topographic surface since this was found to a reasonable approximation to piezometric head data /see Rhén et al. 2006/. The head on the top surface at 2000 AD for this case is shown in Figure 2-22. For this case, there was no drawdown at the surface of Äspö due to the head being fixed here. In fact some drawdown at the surface will have occurred, and so alternative boundary conditions were tried with a mixture of specified maximum potential infiltration on the inland top surface, and specified head offshore. Initially,

Table 2-4. Surface hydraulic domain properties /from Werner et al. 2005/. In HSD2 the hydraulic thicknesses vary spatially across the whole model and may be zero.

HSD case	Geological description	Hydraulic Thickness (m)	Hydraulic conductivity (m/s)	Kinematic porosity
HSD1	Till/artificial fill , near surface	1	$4\ 10^{-5}$	$1.5\ 10^{-1}$
	Till/artificial fill, below HSD1	2	$4\ 10^{-5}$	$5\ 10^{-2}$
HSD2	Gyttja	–	$1\ 10^{-8}$	$3\ 10^{-2}$
	Gyttja clay	–	$1\ 10^{-7}$	$3\ 10^{-2}$
	Clay (upper)	–	$1\ 10^{-6}$	$3\ 10^{-2}$
	Clay (lower)	–	$1\ 10^{-8}$	$3\ 10^{-2}$
	Till (upper)	–	$4\ 10^{-5}$	$1.5\ 10^{-1}$
	Till (lower)	–	$4\ 10^{-5}$	$5\ 10^{-2}$
	Fluv. outwash gravel	–	$1\ 10^{-4}$	$2.5\ 10^{-1}$
	Fluv. outwash sand	–	$1\ 10^{-4}$	$2.5\ 10^{-1}$
	Fluv. sediment	–	$1\ 10^{-6}$	$3\ 10^{-2}$
	Peat	–	$1.5\ 10^{-6}$	$2.4\ 10^{-1}$
	Bedrock	–	$1.05\ 10^{-7}$	$5\ 10^{-3}$
	Glaciofluv. sediment	–	$1\ 10^{-4}$	$2.5\ 10^{-1}$

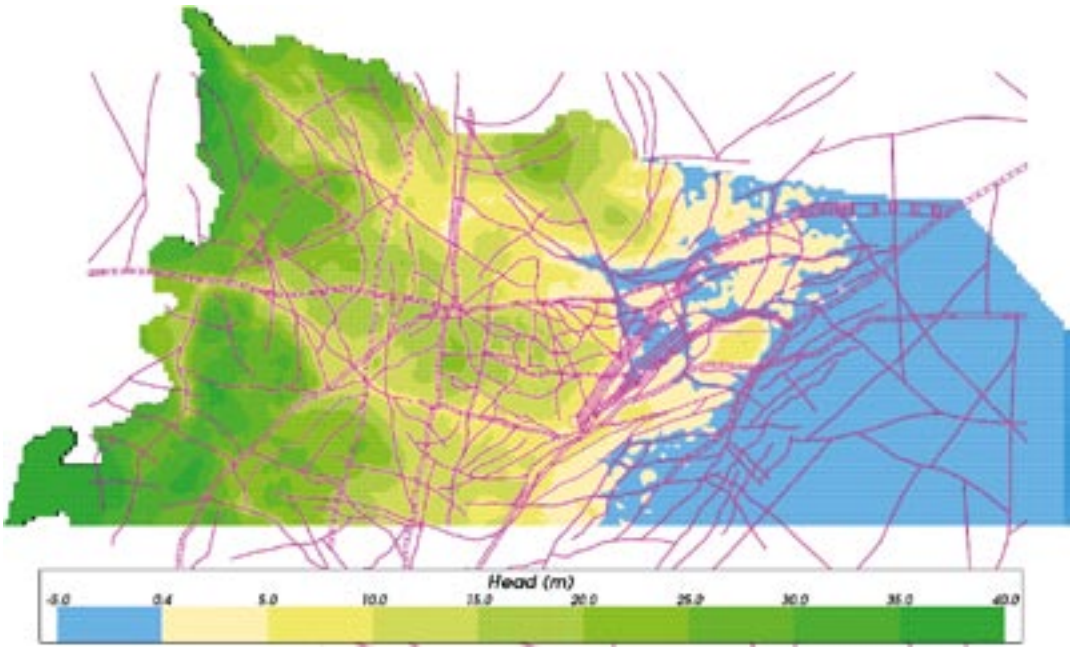

Figure 2-22. *Distribution of head at 2000 AD in the regional model with a specified head on the surface without pumping based on watertable + 30% of the difference between the simulated watertable and the topographic surface /see Rhén et al. 2006/. A horizontal-section through the top of the HCD is superimposed in purple.*

maximum infiltration rates of 165, 80 and 40 mm/year were considered resulting in the heads shown in Figure 2-23 to Figure 2-25. As can be seen, an infiltration of 165 mm/year gives heads similar to the SR-Can reference case, while 40 mm/year gives much lower heads. Therefore, 165 mm/year was considered as the most realistic case with 80 mm/year as a variant, and 40 mm/year was not considered further in these simulations.

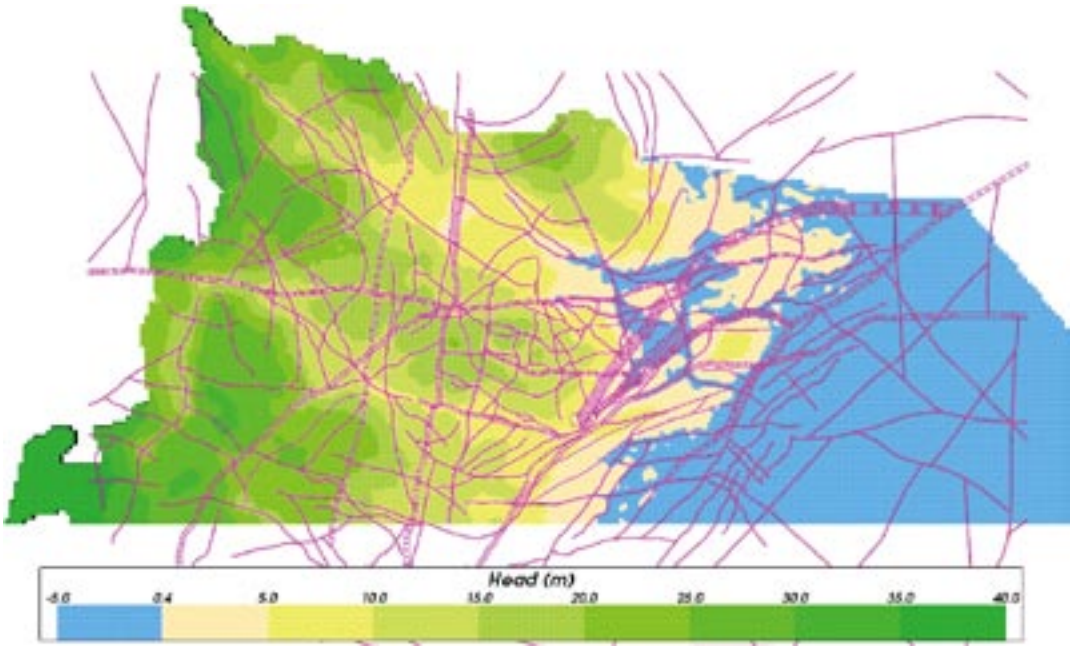

Figure 2-23. *Distribution of head on the surface without pumping at 2000 AD in the regional model with a specified maximum potential infiltration of 165 mm/year. A horizontal-section through the top of the HCD is superimposed in purple.*

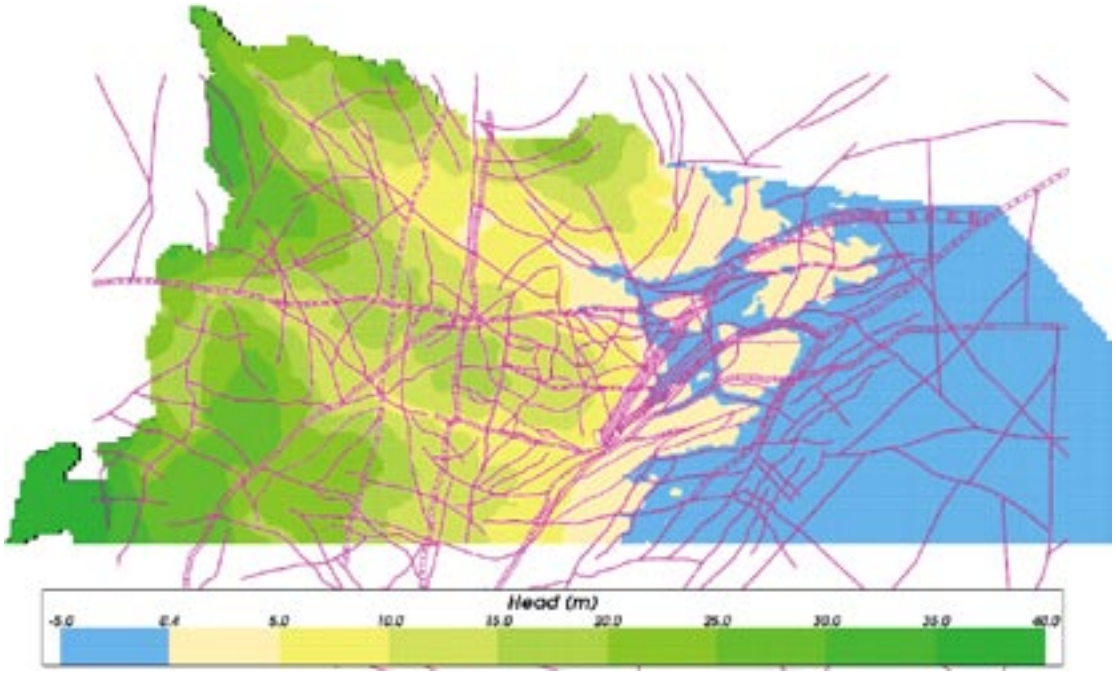

Figure 2-24. *Distribution of head on the surface without pumping at 2000 AD in the regional model with a specified maximum potential infiltration of 80 mm/year. A horizontal-section through the top of the HCD is superimposed in purple.*

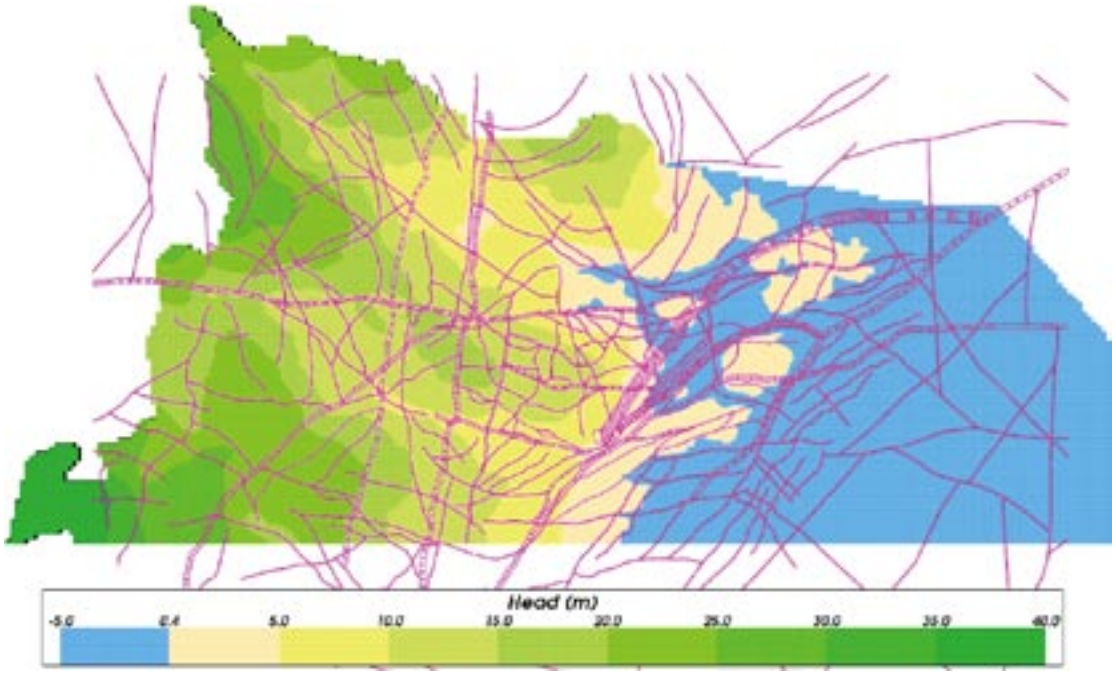

Figure 2-25. *Distribution of head on the surface without pumping at 2000 AD in the regional model with a specified maximum potential infiltration of 40 mm/year. A horizontal-section through the top of the HCD is superimposed in purple.*

2.4 Results

In previous simulations for SR-Can based on L 1.2, using head or flux as top boundary conditions, variables are saved for time steps representing 1960 to be used as an initial condition for these simulations before the construction of the HRL. In the new simulations the length of the time step is one year.

Cases are set up for the different boundary conditions on the top surface. For each approach one case is calculated without Äspö HRL and another case is performed including the Äspö HRL. The results are then compared.

Figure 2-26 shows the location of a verticals section used to illustrate the Darcy velocity. The Äspö HRL underground tunnels are simplified as one tunnel and one shaft. This is illustrated in Figure 2-27. Some parallel sections of the tunnel are included in the main tunnel in terms of geometry and inflow. Also, the two ventilation shafts are included in the main elevator shaft. In this pre-modelling exercise the geometry of the tunnel is simplified so that the tunnel is represented by the endpoints for each weir segment. This means that the line that represents the tunnel is not exactly following the Äspö HRL tunnel contours.

2.4.1 Reference case with top head boundary condition

The model from the reference case of SR-Can Laxemar 1.2 /Hartley et al. 2006a/ was used as a platform for this case. It uses a head boundary condition on the top surface. Two simulations are carried out from 1960 to 2006 using one year time-steps. In one of the simulations, the Äspö HRL is represented as a tunnel and a shaft with a time-varying specified inflow based on measured values. In the other case, the tunnel is removed, i.e. undisturbed flow conditions. Below some illustrations of the difference between the case with HRL and without may be seen as drawdown, change in Darcy velocity and change in four types of reference waters. The properties of the HCD, HRD and HSD are described above.

The drawdown induced by the Äspö HRL at 2006 may be seen in Figure 2-28 below. The result is shown for a slice at an elevation –450 m around the base of the HRL spiral. It may be seen that the region beneath the western side of Ävrö is influenced whereas the Laxemar subarea and the remainder of Simpevarp subarea are much less affected with drawdowns of less than 1 decimetre apart from near KLX01.

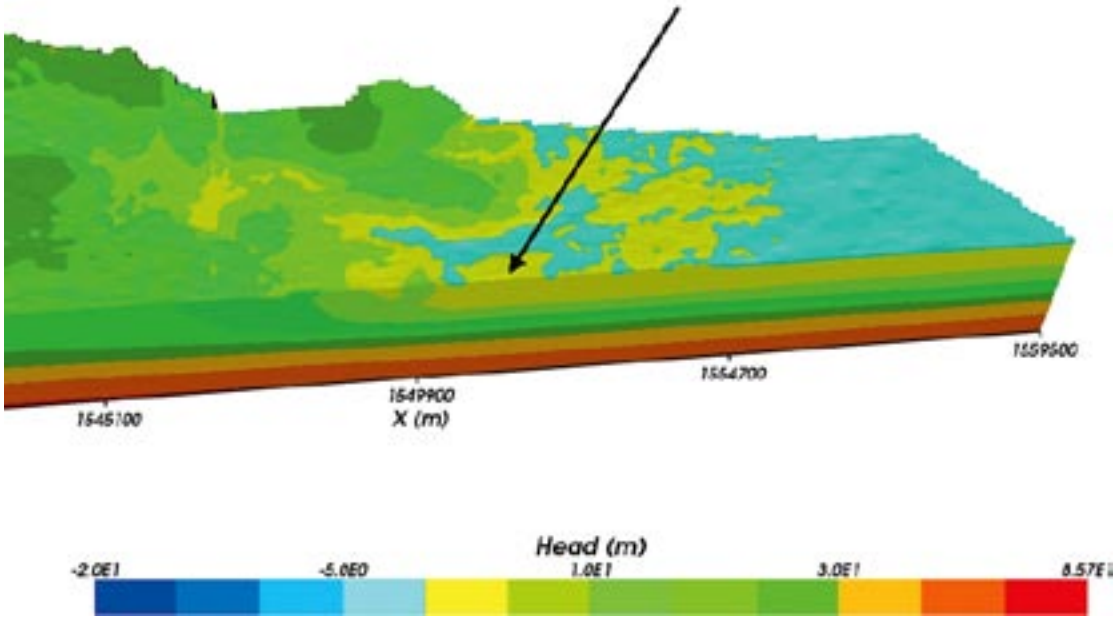

Figure 2-26. *Location of the slice through KLX01 used in the visualisations of Darcy velocity for a case with undisturbed conditions showing freshwater head. The arrow indicates the Äspö island.*

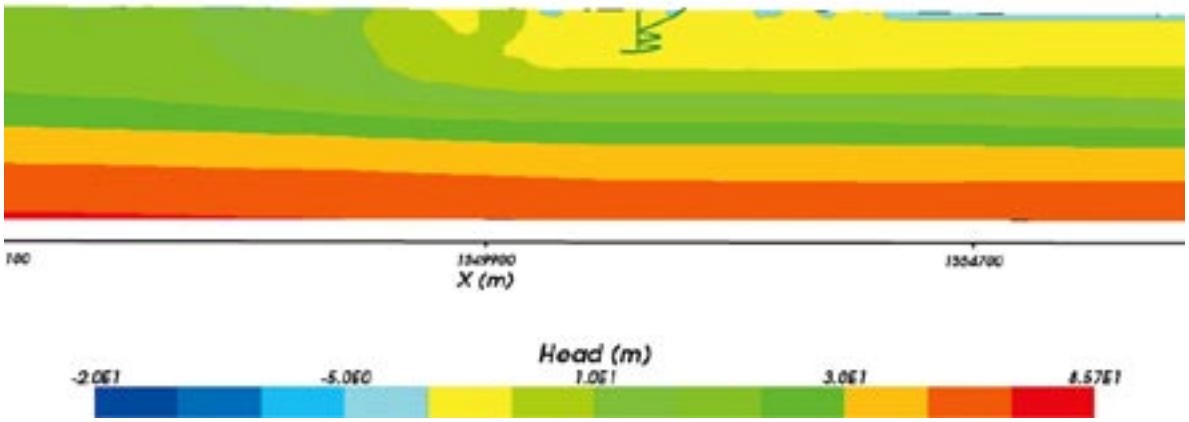

Figure 2-27. *The same profile as Figure 2-26, but with the modelled Äspö HRL in the upper middle parts of the figure. The freshwater head field is for a case with undisturbed conditions.*

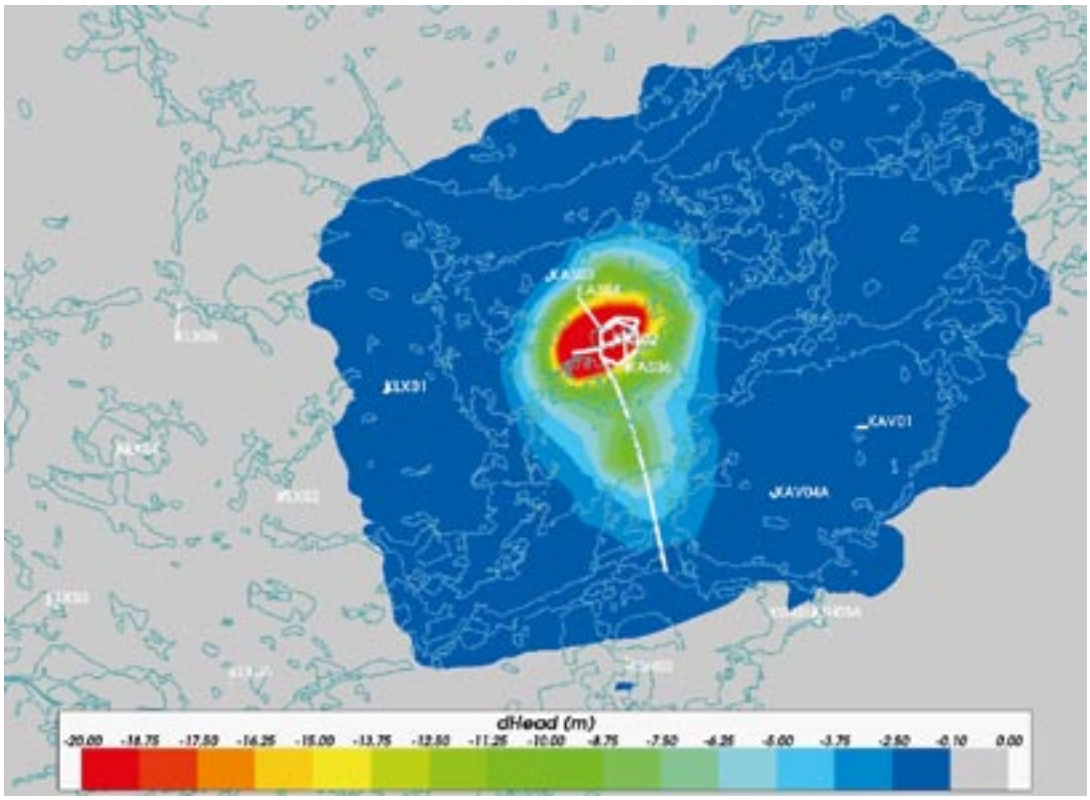

Figure 2-28. *The magnitude of drawdown of the Äspö HRL shown as the difference between a case with the HRL and a case without the HRL for a fixed top surface head. The slice is shown for 2006 AD at –450 m elevation and the boundary of surface waterbodies may be seen.*

The magnitude of the change in the Darcy velocity may be seen in Figure 2-29. The increase in Darcy velocity is larger near the Äspö HRL and the imprint of deformation zones may be seen. The deformation zones in which the change in flow is largest are the ones connecting East to Ävrö, and also south and south west toward Laxemar around KLX02. The change in the direction of flow and the distribution of discharge areas are illustrated in Figure 2-30 on a vertical E-W slice through KLX01, Äspö and the ZSMEW038A deformation zone extending East to Ävrö. On this slice, flow converges towards the bay around Äspö from both Laxemar and Ävrö, but discharges around the shoreline. However, with the tunnel present flow is drawn from Ävrö in the East along the zone ZSMEW038A down toward the tunnel, although a large part of the flow from the West still seems to discharge at the coast. The change in Darcy velocity near the surface on a horizontal slice at an elevation of –20 m is shown in Figure 2-31. This shows that the largest effect on near-surface flow rates is in the bay surrounding the Äspö island, and slightly more to the South and East, which suggests that the tunnel is drawing water from the sea directly above it.

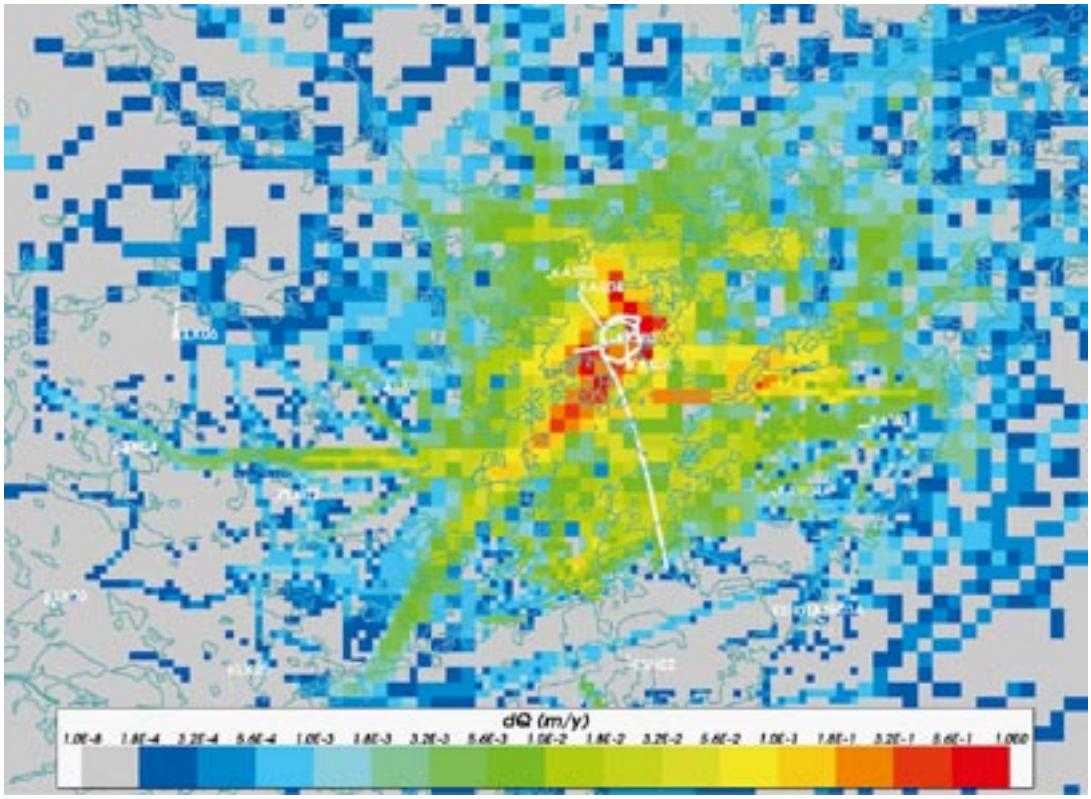

Figure 2-29. *The magnitude of difference in Darcy velocity between a case with the Äspö HRL and a case without the HRL for a fixed top surface head. The slice is shown for 2006 AD at –450 m elevation and the boundary of surface waterbodies may be seen.*

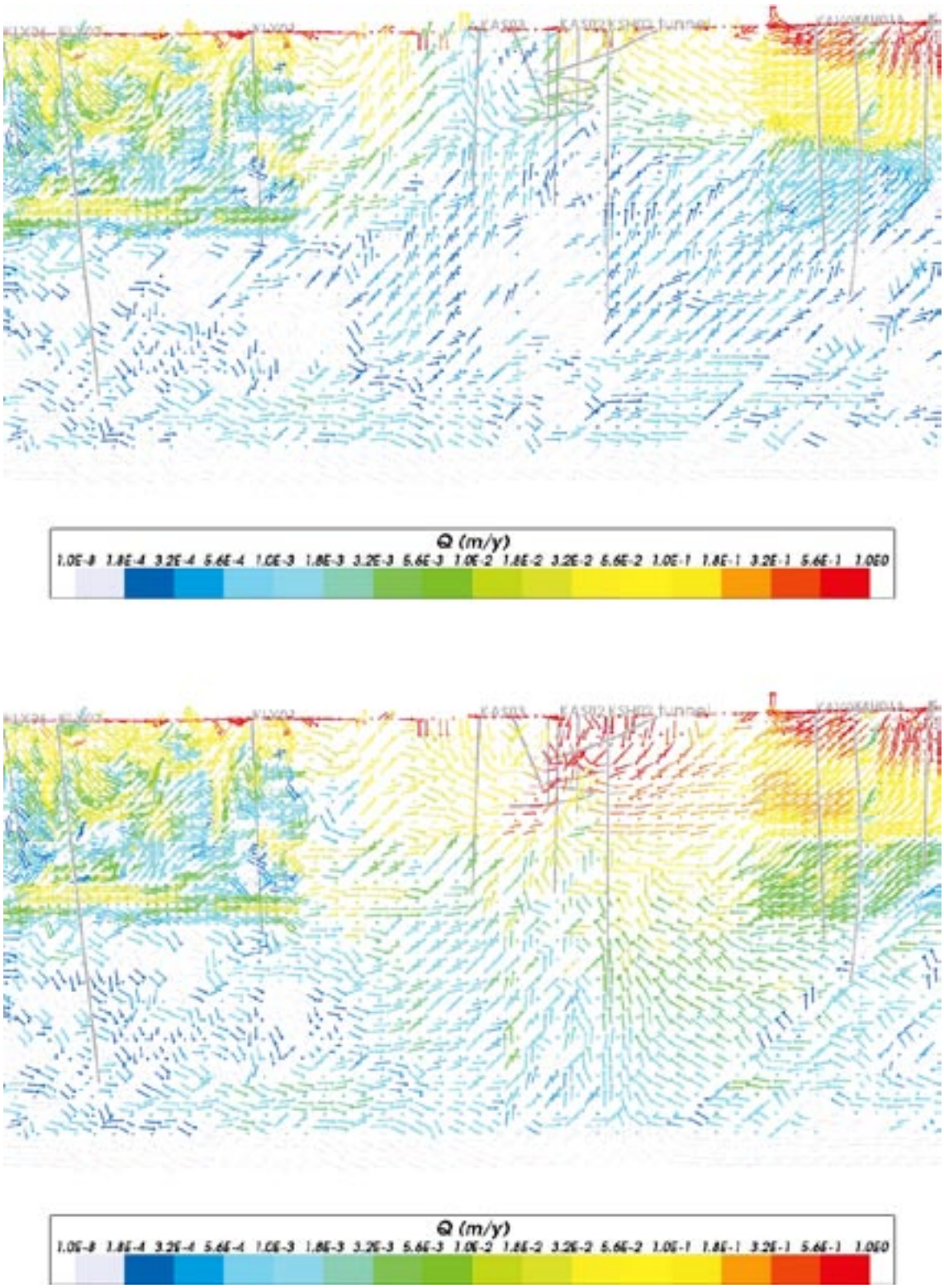

Figure 2-30. *The direction of Darcy velocity on a vertical E-W slice through KLX01 and Äspö for a fixed top surface head. The dimensions are about 4 km E-W and 2.3 km top to bottom. The two simulations are shown without the Äspö HRL (top) and with the HRL (bottom). The velocity is shown for 2006 AD.*

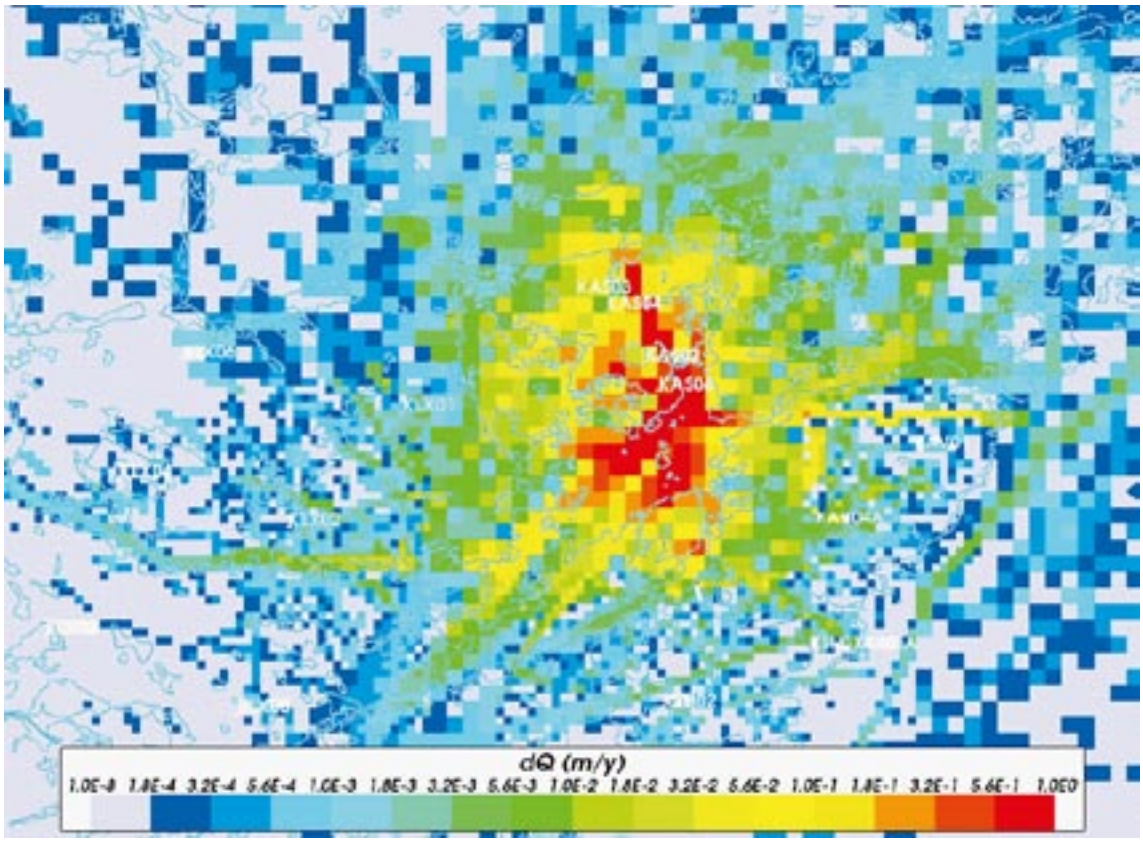

Figure 2-31. *The magnitude of difference in Darcy velocity between a case with the Äspö HRL and a case without the HRL for a fixed top surface head. The slice is shown for 2006 AD at –20 m elevation and the boundary of surface waterbodies may be seen.*

The change in the reference water fraction of meteoric water at 2006 is shown in Figure 2-32 with positive (red-yellow) indicating an increase in meteoric water due to the Äspö HRL, and negative (blue-green) indicating a decrease. The changes in the other reference water fractions: Brine, Glacial and Littorina are shown in Figure 2-33 to Figure 2-35, respectively. The content of meteoric water is less with the HRL in the immediate vicinity of the HRL spiral, due to a displacement by Brine water upconed from below (see Figure 2-33). Further out, the meteoric water fraction is significantly higher as marine water has been replaced by meteoric water. Localised upconing of brine also occurs around a major NE striking zone that intersects the access tunnel to the south.

The difference in Brine reference water fraction between a case with the HRL and a case without the HRL are shown in Figure 2-36. The slices are shown for the year 2006 at –300 m, –450 m, –700 m and –1,000 m elevations. This shows that Brine is drawn up from below –1,000 m underneath the southern half of the Äspö island and the bay due south of the island.

The transient evolution is illustrated in Figure 2-37 using the difference in head (drawdown) for time-steps representing 1993, 1994, 1995 and 1999 AD. The maximum drawdown occurs about 1995, then reduces by about 1999, and continues to very slowly reduce to 2006 as seen in Figure 2-28.

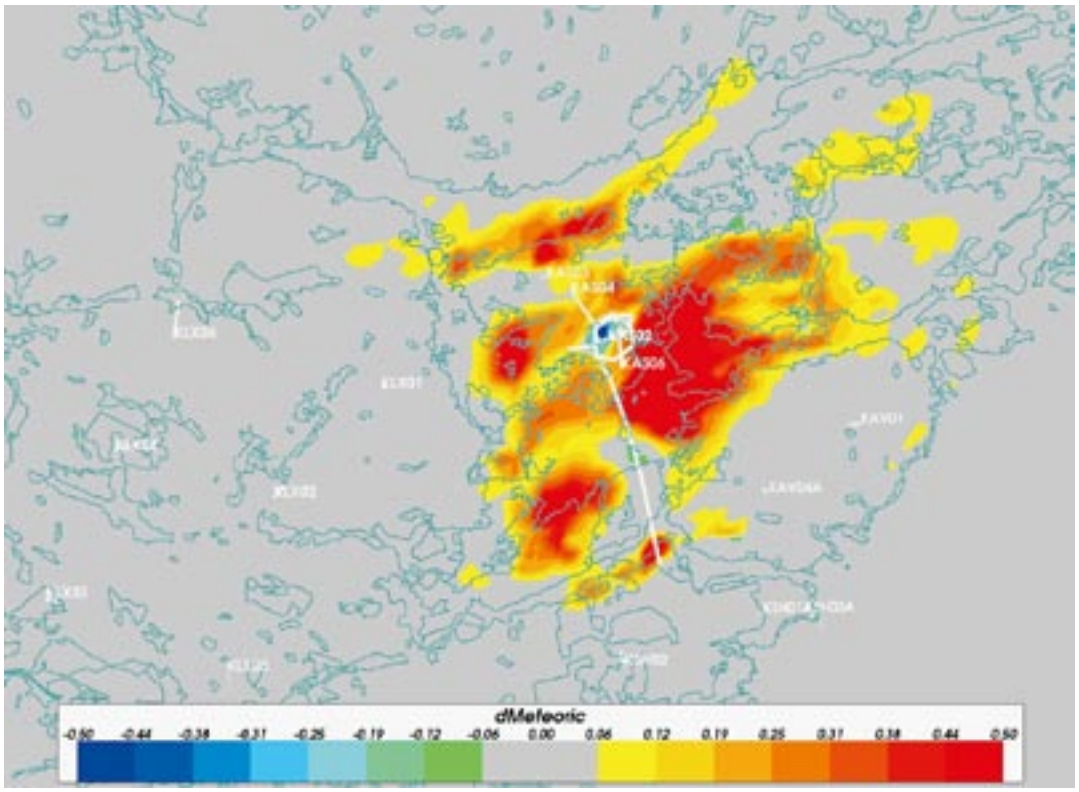

Figure 2-32. *The difference in the Meteoric reference water fraction between a case with the Äspö HRL and a case without the HRL for a fixed top surface head. The slice is shown for 2006 AD at an elevation of –450 m and the boundary of surface waterbodies may be seen.*

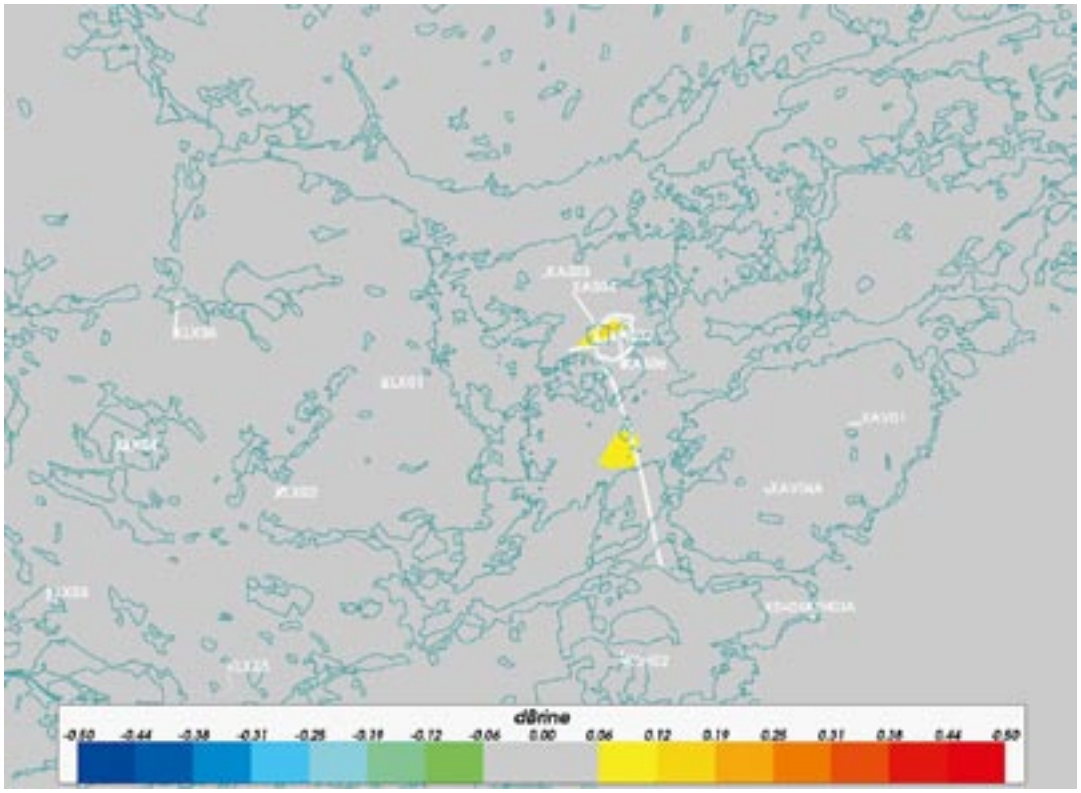

Figure 2-33. *The difference in the Brine reference water fraction between a case with the Äspö HRL and a case without the HRL for a fixed top surface head. The slice is shown for 2006 AD at an elevation of –450 m and the boundary of surface waterbodies may be seen.*

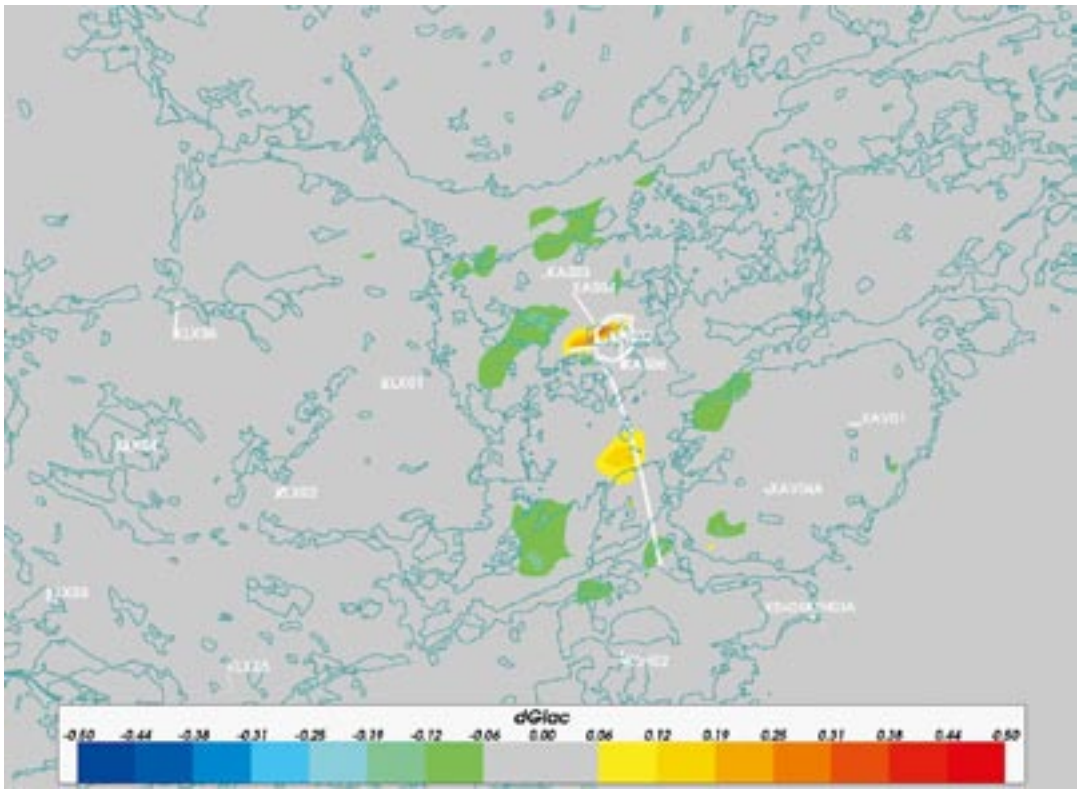

Figure 2-34. *The difference in the Glacial reference water fraction between a case with the Äspö HRL and a case without the HRL for a fixed top surface head. The slice is shown for 2006 AD at an elevation of –450 m and boundary of surface waterbodies may be seen.*

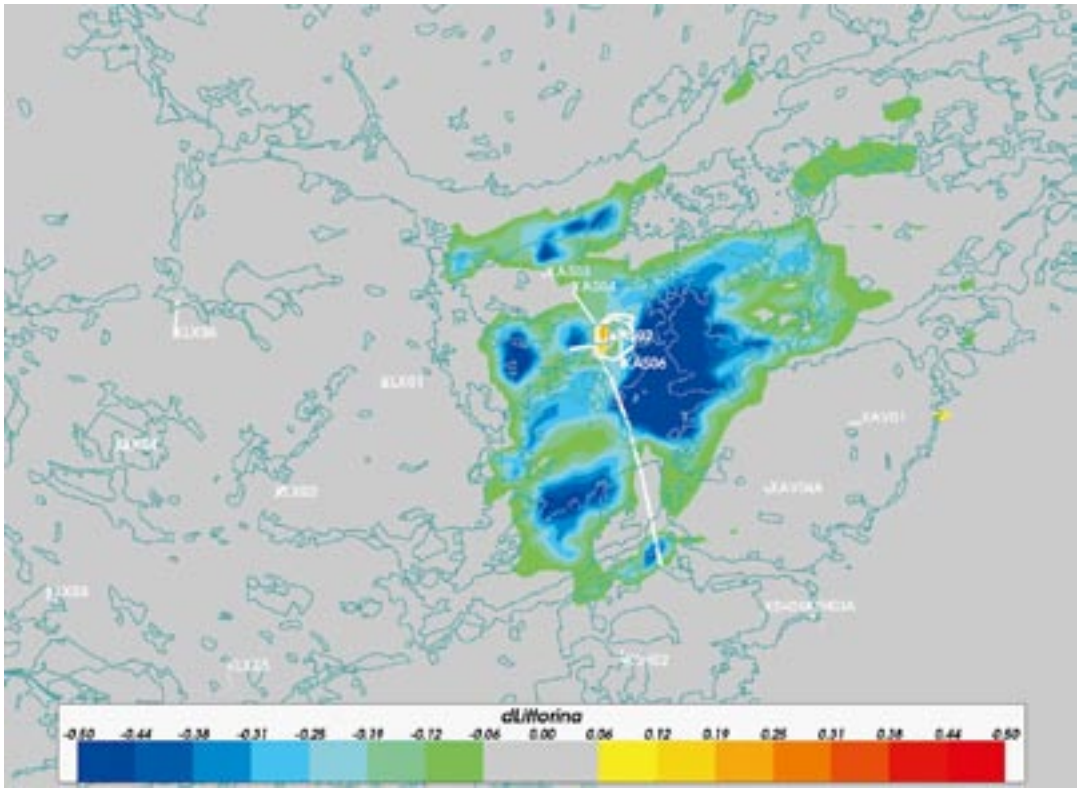

Figure 2-35. *The difference in the Littorina reference water fraction between a case with the Äspö HRL and a case without the HRL for a fixed top surface head. The slice is shown for 2000 AD at an elevation of –450 m and the boundary of surface waterbodies may be seen.*

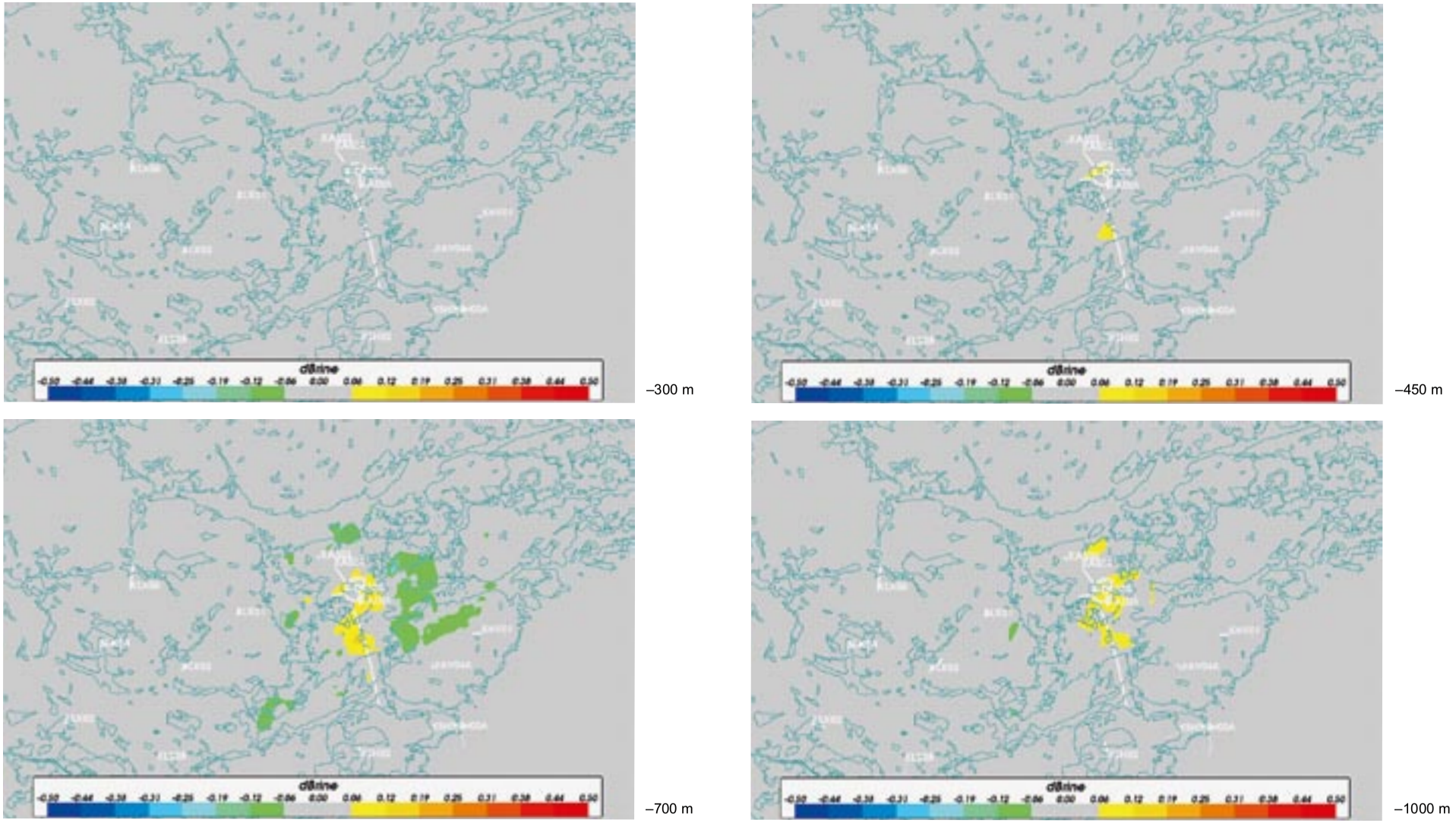

Figure 2-36. *The differences in fraction of the Brine reference water fraction for different depths at the year 2006 for a fixed top surface head.*

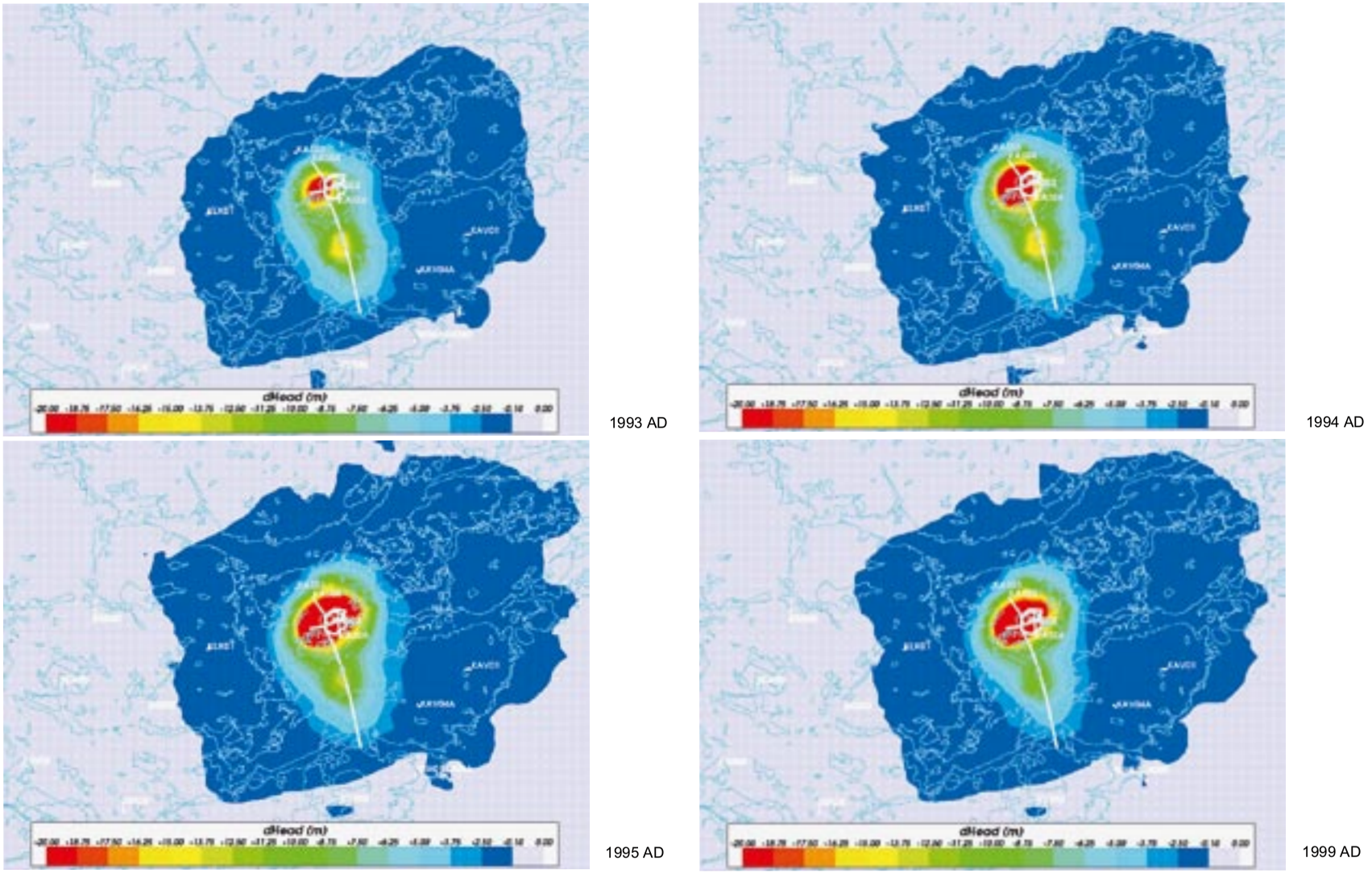

Figure 2-37. *The differences in head with and without the Äspö HRL at –450 m elevation for different times for a fixed top surface head.*

2.5 Sensitivities

2.5.1 Summary of applied regional model cases

In order to test the robustness of the results and conclusions, a number of variants have been simulated. For a reference point, a base case was created called SC_HCD1P3_HRD3a_ ddKhalf_ani_HSD1_BC3_MD1_IC1_ASPO, which has identical hydraulic properties to the reference case from SR-Can L 1.2 in /Hartley et al. 2006a/, but uses the simulated conditions at 1960 AD from that previous study as initial conditions. The features of the model are summarised in Table 2-5.

In order to explain the model name: SC stands for SR-Can, HCD1 represents a deformation zone model that has a step change in transmissivity; P3 is the porosity approach used; HRD3a indicates that the properties of the rock domains are obtained by upscaling fracture properties for a specific realisation of a regional DFN model using a semi-correlated T-model (The underlying DFN has a step change in properties at –200 m and below –600 m elevation for all HRD, except HRD(A2), and there is anisotropy in the transmissivity between sets in the DFN model); HSD1 indicates that the simplified soil domain is used, whereas HSD2 indicates that the elaborate soil domain is used; BC3 represents the head boundary condition used in the SR-Can reference case, i.e. head based on the watertable plus 30% of the difference of the topography and watertable (BC4d indicates that a flux boundary condition is used on the top surface. In this specific case, the inflow rate is 165 mm/year); MD1 stands for the large model domain, and MD3 means that a smaller domain is used. (The size of the smaller model is shown in Figure 2-38. ASPO is added to indicate undisturbed conditions, whereas ASPOHRL is added to show that the Äspö HRL is present).

2.5.2 Sensitivity to the top surface flow boundary condition

As mentioned at the beginning of Section 2.3, a specified flux boundary condition based on a maximum infiltration through the unsaturated zone of either 165 mm/year or 80 mm/year was implemented as a variant. The same hydraulic properties for the rock mass and deformation zones are used in this case as for the reference case of SR-Can Laxemar 1.2, but the more elaborate soil model developed by the SurfaceNet Group /Nyman 2005/ is implemented at the top of the model. It was felt important that in order to represent infiltration to the groundwater system realistically, then a specified flux type boundary condition should be coupled with a realistic distribution of Quaternary cover and its properties. The Quaternary model is based on three layers, but each having variable thickness and soil type. Two alternative rates of maximum

Table 2-5. Summary of the simulated cases. All the case names start with the stem SC_HCD1P3_HRD3a_ddKhalf_ani, and therefore the stem is replaced by Ψ. For each case, one simulation is performed without the Äspö HRL, and one simulation is carried out with the HRL present.

Simulated cases	Properties or characteristics
Ψ_HSD1_BC3_MD1_IC1_ASPO	Adopted from the reference case in /Hartley et al. 2006a/.
Ψ_HSD2_BC4d_MD3_IC1_ASPO	Elaborate soil model, flux boundary conditions, and smaller model domain.
Ψ_HSD2_BC4c_MD3_IC1_ASPO	Elaborate soil model, flux boundary conditions (80 mm/ year), and smaller model domain.
Ψ_HSD2I3_BC4d_MD3_IC1_ASPO	The lower till below z = 0 is changed to Gyttja Clay ($K = 10^{-8}$ m/s).
Ψ_HSD2I_BC4d_MD3_IC1_ASPO	The lower till below z = 0 is changed to Gyttja Clay, and reduce K by 10 ($K = 10^{-9}$ m/s).
Ψ_HSD2I2_BC4d_MD3_IC1_ASPO	The lower till below z = 0 is changed to Gyttja Clay, and reduce K by 100 ($K = 10^{-10}$ m/s).

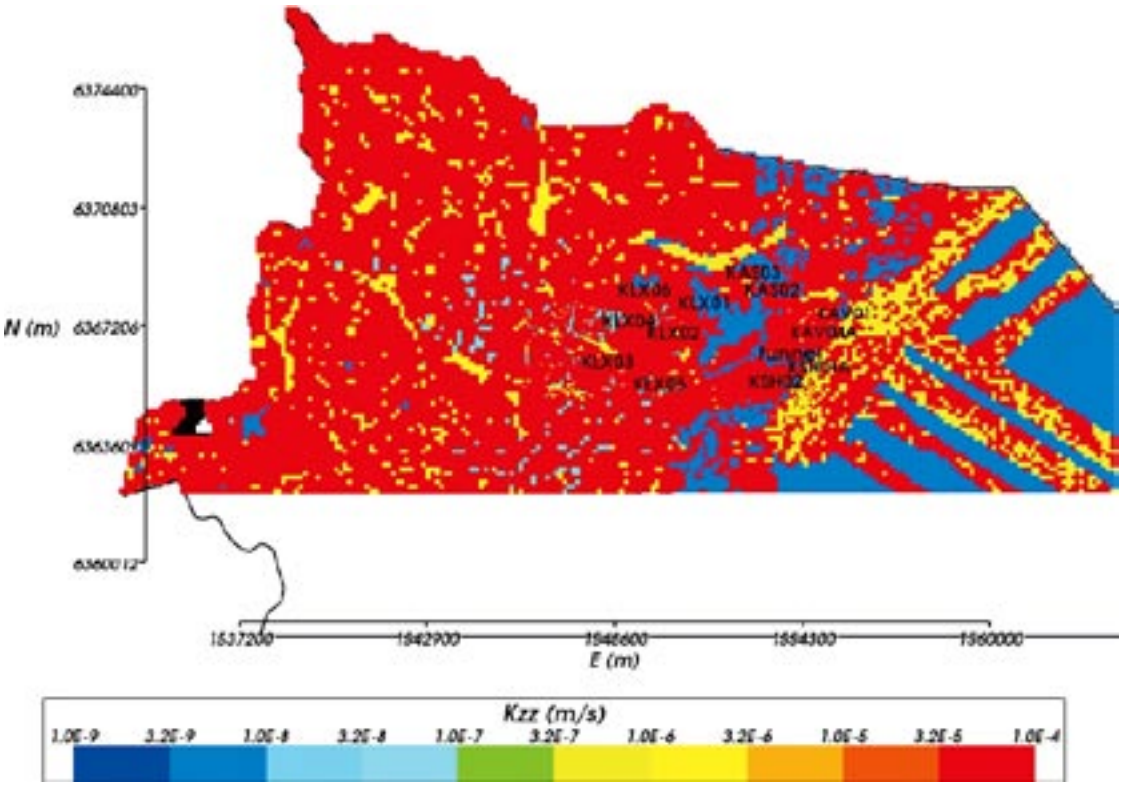

Figure 2-38. *The model domain (MD3) for which the elaborate soil domain model HSD2 was implemented. A black line showing the extent of the MD1 domain that extends south is superimposed. Here, the top surface of the model is coloured by log(vertical hydraulic conductivity). The red colours are associated with Till soil type, and the blue is associated with Gyttja. The long red and yellow strips offshore correspond to data available from ship traverses.*

infiltration to the saturated zone were considered: 165 mm/year, based P-E (precipitation minus evapo-transpiration), and 80 mm/year over the entire inland surface as a lower figure to allow for water loss to overland flow. Some numerical difficulties were encountered in running palaeo-hydrogeological simulations for the full regional domain using this combination of complex soil model and non-linear boundary condition. It is suspected the problem was due to some inconsistency in the modelled soil domain surface layers in the south of the model which has probably lead to layers crossing or vanishing to zero thickness. Anyway, a pragmatic approach was to remove around 3 km from the south of the model, which is far enough from Äspö that it is not thought to affect the hydrogeology. Figure 2-38 shows the model domain (MD3) used for the simulations with the elaborate soil model and top surface flux boundary condition. The plot also shows the dominance of the highly conductive Till soil type over much the model domain. It should also be pointed out that even where there is lower hydraulically conductive Gyttja and Clay in the soil model, it tends to be underlain by the Lower Till which is also very conductive.

Again, the impact of the Äspö HRL is shown by the difference between two simulations with and without the Äspö HRL present. Figure 2-39 shows the drawdown; Figure 2-40 and Figure 2-41 shows the effect on Darcy velocity; Figure 2-42 to Figure 2-45 show the effect on the groundwater chemistry composition in terms of changes in reference water fractions. For all these quantities, the changes are very similar to those for the case with a specified top surface head boundary condition.

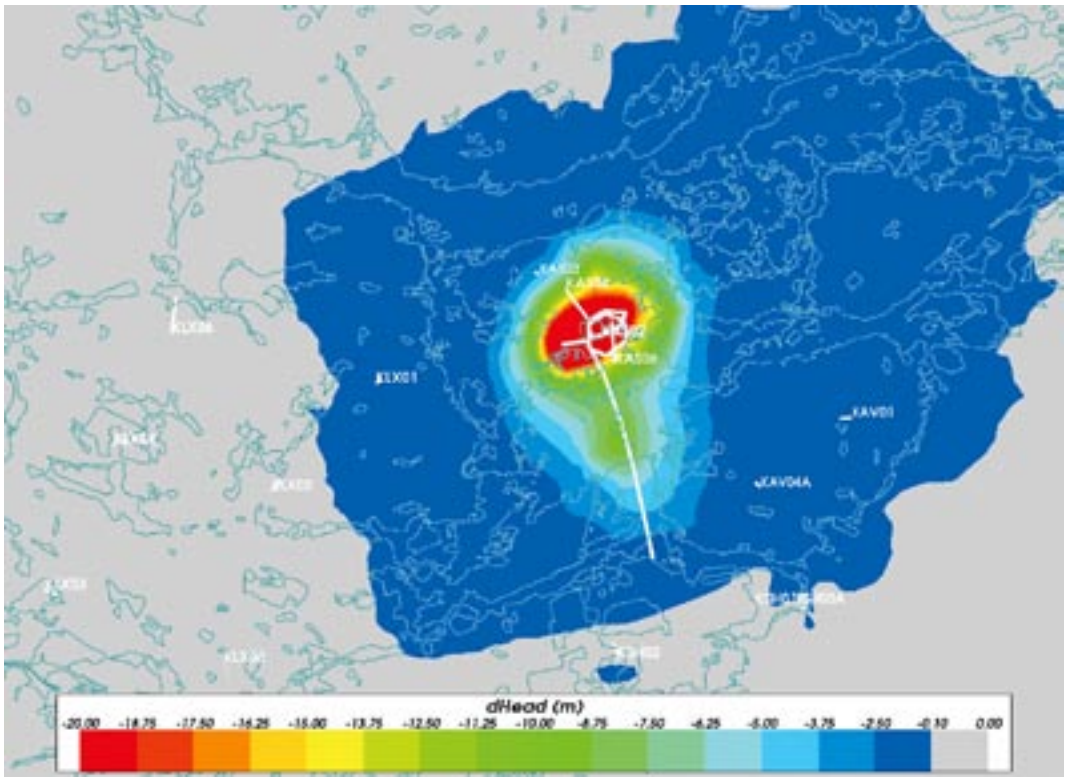

Figure 2-39. *The drawdown of the Äspö HRL shown as the difference between a case with the HRL and a case without the HRL for an infiltration rate of 165 mm/year and elaborate soil model (HSD2). The slice is shown for 2006 AD at –450 m and the boundary of surface waterbodies may be seen.*

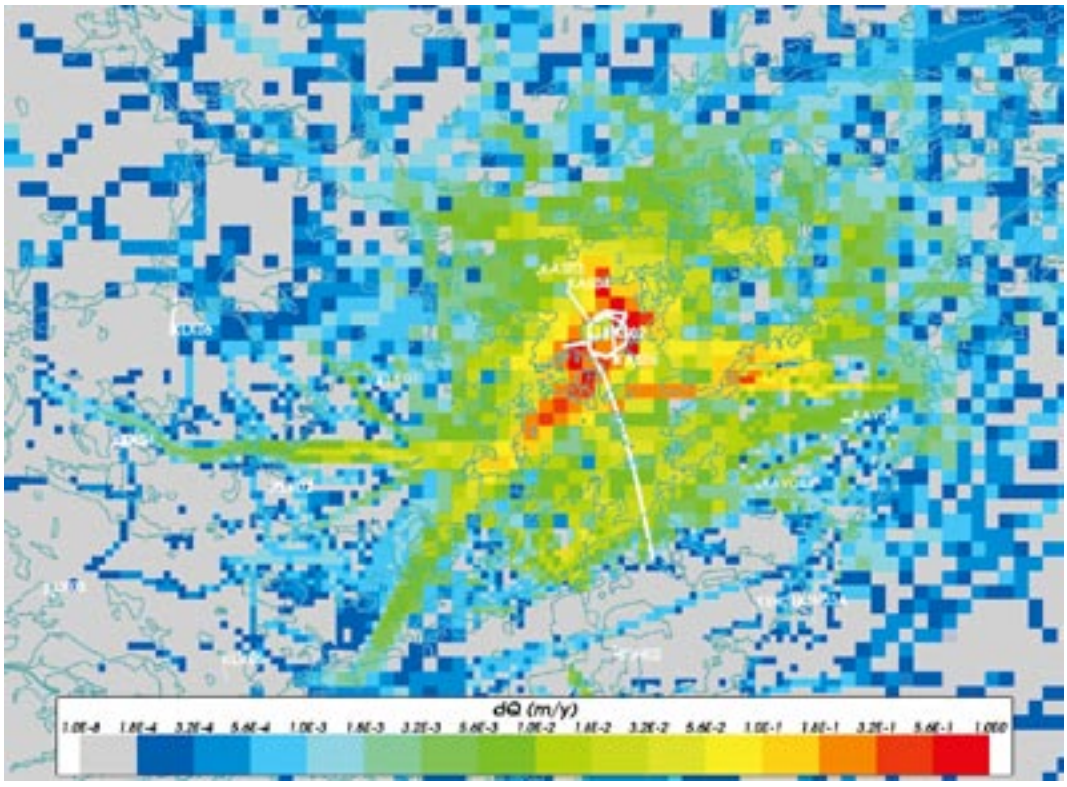

Figure 2-40. *The difference in Darcy velocity between a case with the Äspö HRL and a case without the HRL for an infiltration rate of 165 mm/year and elaborate soil model (HSD2). The slice is shown for 2006 AD at –450 m and the boundary of surface waterbodies may be seen.*

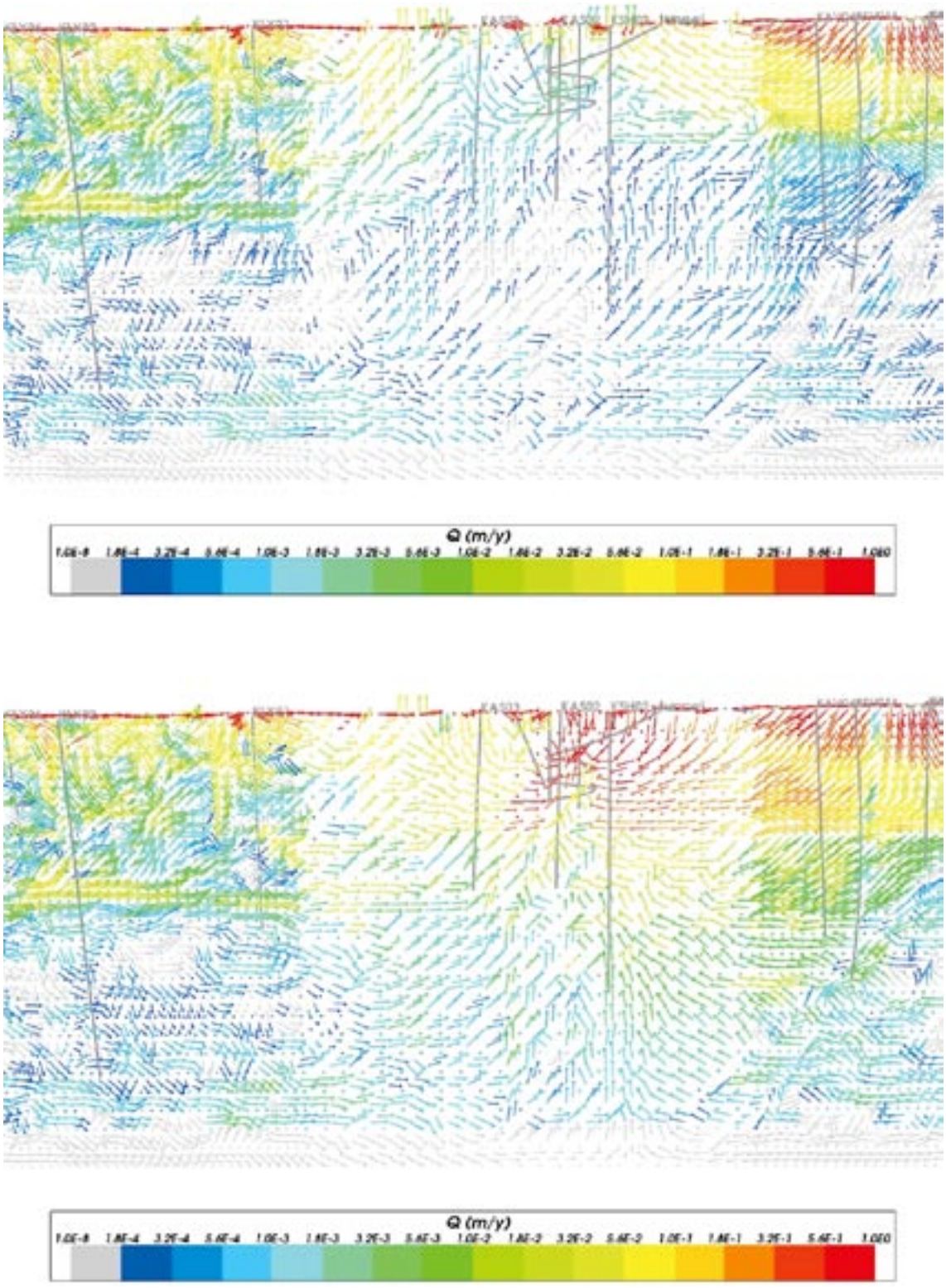

Figure 2-41. *The direction of Darcy velocity on a vertical E-W slice through KLX01 and the Äspö island for an infiltration rate of 165 mm/year and elaborate soil model. The dimensions are about 4 km E-W and 2.3 km top to bottom. The two simulations are shown without the Äspö HRL (top) and with the HRL (bottom). The velocity is shown for the year 2006.*

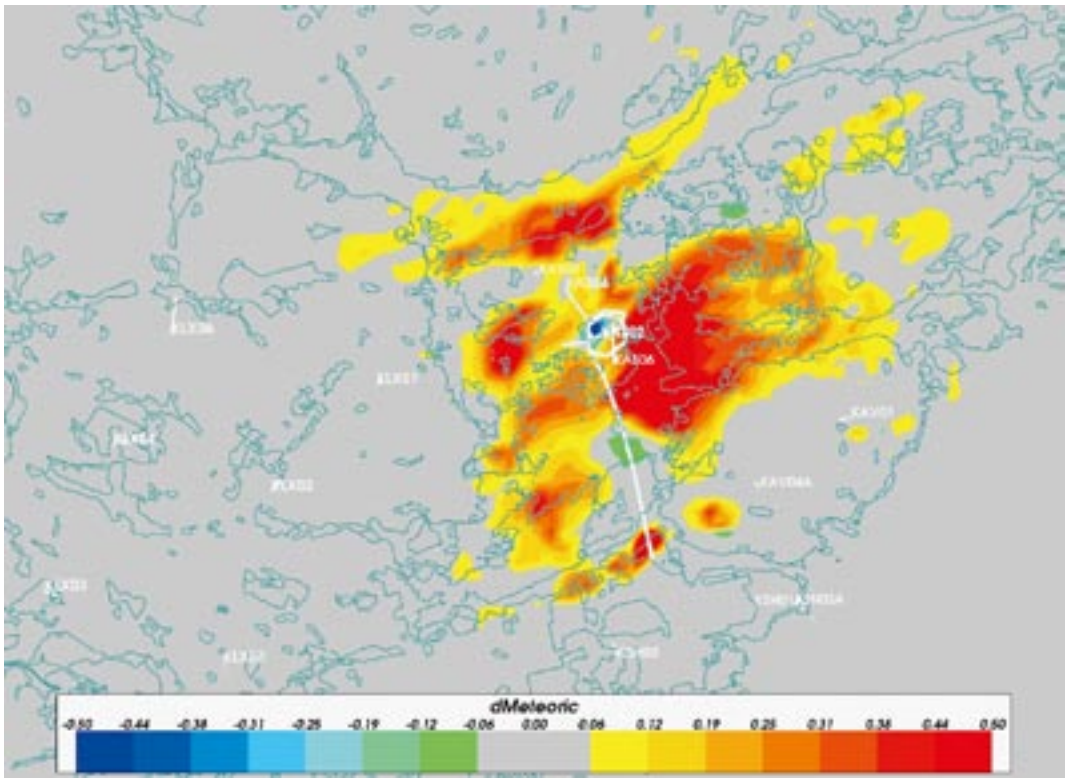

Figure 2-42. *The difference in Meteoric reference water fraction between a case with the Äspö HRL and a case without the HRL for an infiltration rate of 165 mm/year and elaborate soil model. The slice is shown for 2006 AD at –450 m and the boundary of surface waterbodies may be seen.*

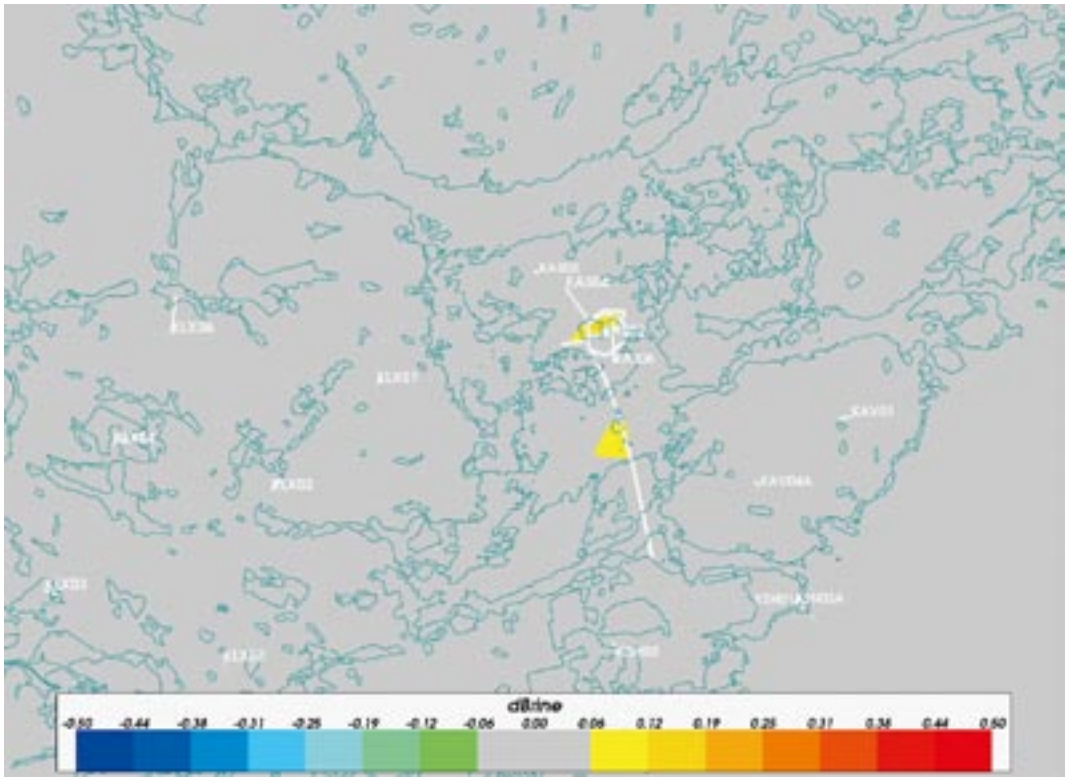

Figure 2-43. *The difference in Brine reference water fraction between a case with the Äspö HRL and a case without the HRL for an infiltration rate of 165 mm/year and elaborate soil model. The slice is shown for 2006 AD at –450 m and the boundary of surface waterbodies may be seen.*

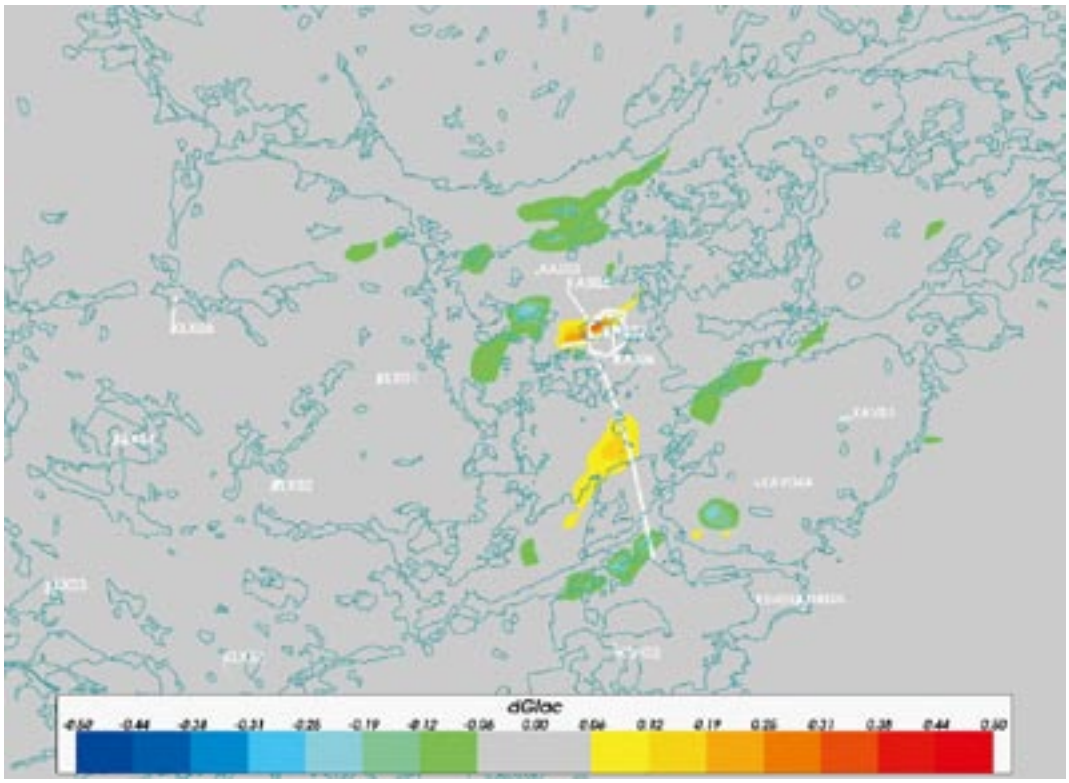

Figure 2-44. *The difference in Glacial reference water fraction between a case with the Äspö HRL and a case without the HRL for an infiltration rate of 165 mm/year and elaborate soil model. The slice is shown for 2006 AD at –450 m and the boundary of surface waterbodies may be seen.*

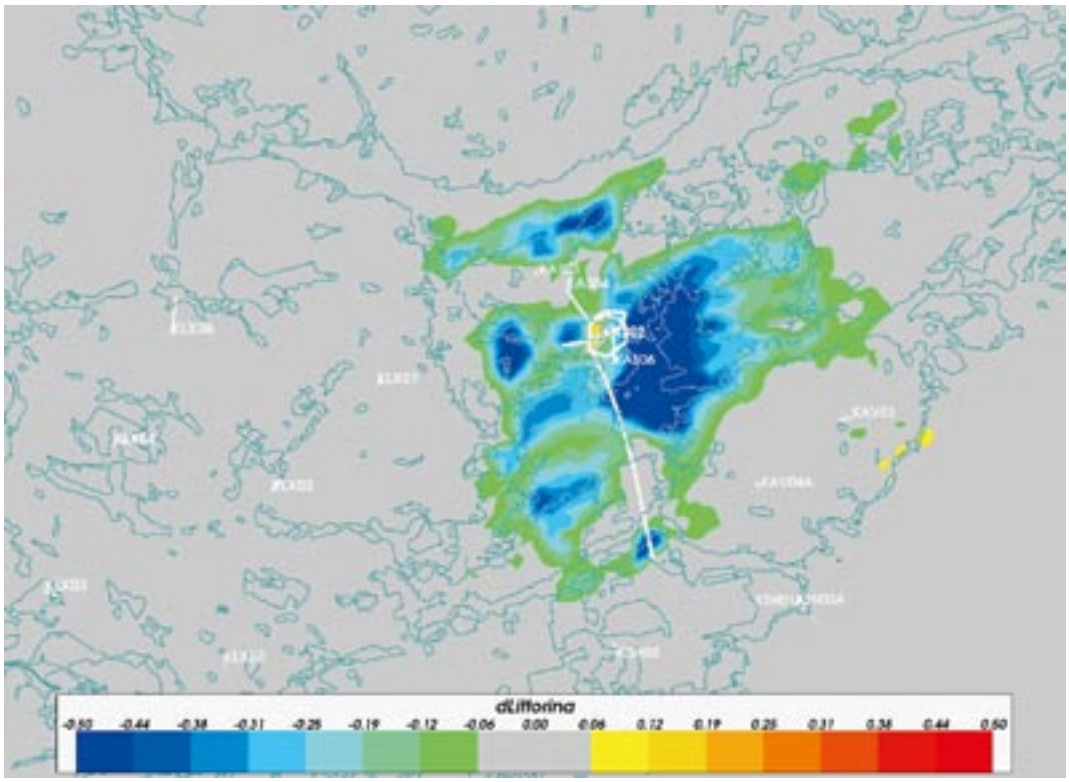

Figure 2-45. *The difference in Littorina reference water fraction between a case with the Äspö HRL and a case without the HRL for an infiltration rate of 165 mm/year and elaborate soil model. The slice is shown for 2006 AD at –450 m and the boundary of surface waterbodies may be seen.*

2.5.3 Sensitivity to groundwater infiltration rate

Inflow rate 80 mm/year

An amount of water to represent percolation into the saturated system appropriate to a regional-scale model is uncertain. In the model, the maximum potential infiltration is specified, but the actual infiltration is calculated automatically based on the relative elevations of the calculated groundwater head and the surface topographic elevation. For a maximum infiltration of 165 mm/year, it is assumed that the full P-E percolates through to the saturated zone on the regional-scale. As a sensitivity test, a lower maximum infiltration of 80 mm/year was also tried. The drawdown for this case is shown in Figure 2-46. There is only a very slight increase in the area of the 0.1 m drawdown contour (cf. Figure 2-39). This suggests that a lot of the inflow to the tunnel comes from sea around Äspö where there is a specified head boundary condition. It is also likely that since the land immediately around the Äspö HRL is generally low lying, then it becomes fully saturated in both values of infiltration, and hence the low sensitivity to the range of infiltration considered. The sensitivities of the changes in hydro-geochemistry are illustrated in Figure 2-47 to Figure 2-50. These show broadly the same pattern of changes mainly focussed on the area to the east of the HRL, but here there is less impact to the south on the northern edge of the Simpevarp peninsula than for the top surface head boundary condition. The effects on Darcy velocity for this variant were also very similar to the reference fixed head condition.

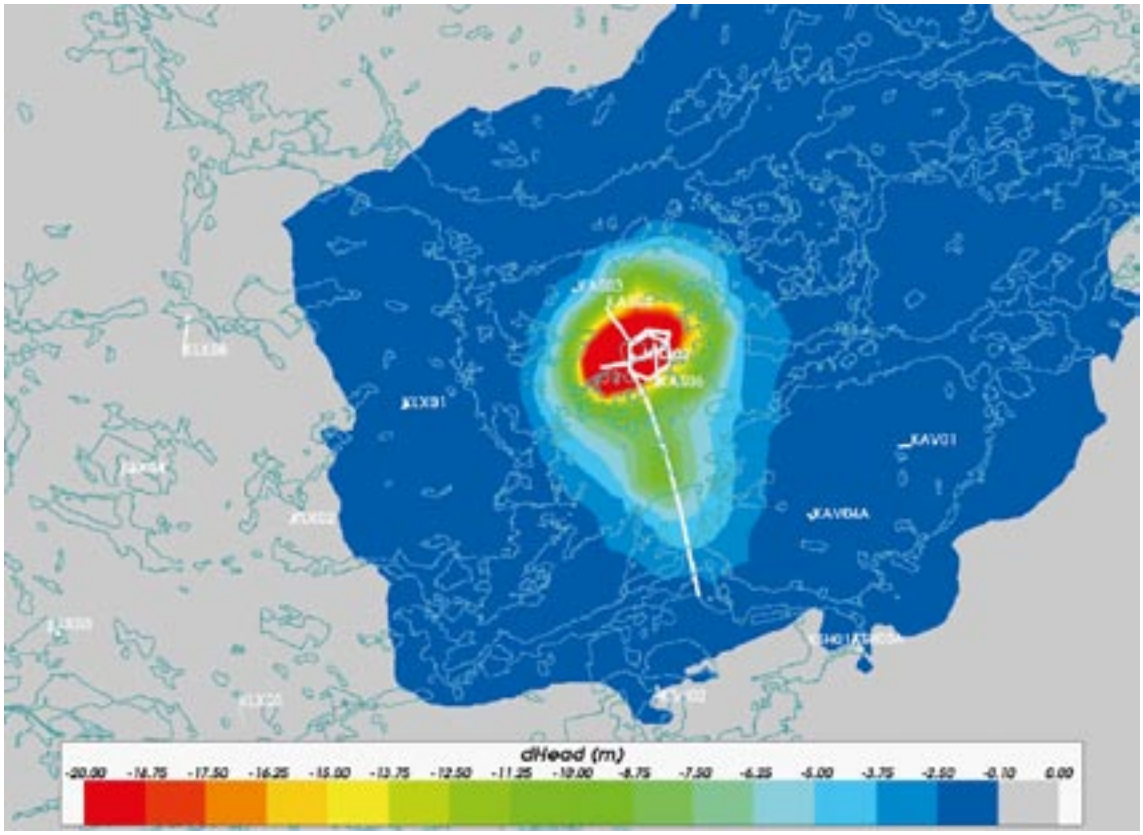

Figure 2-46. *The drawdown of the Äspö HRL shown as the difference between a case with the HRL and a case without the HRL for an infiltration rate of 80 mm/year and elaborate soil model. The slice is shown for 2006 AD at –450 m and the boundary of surface waterbodies may be seen.*

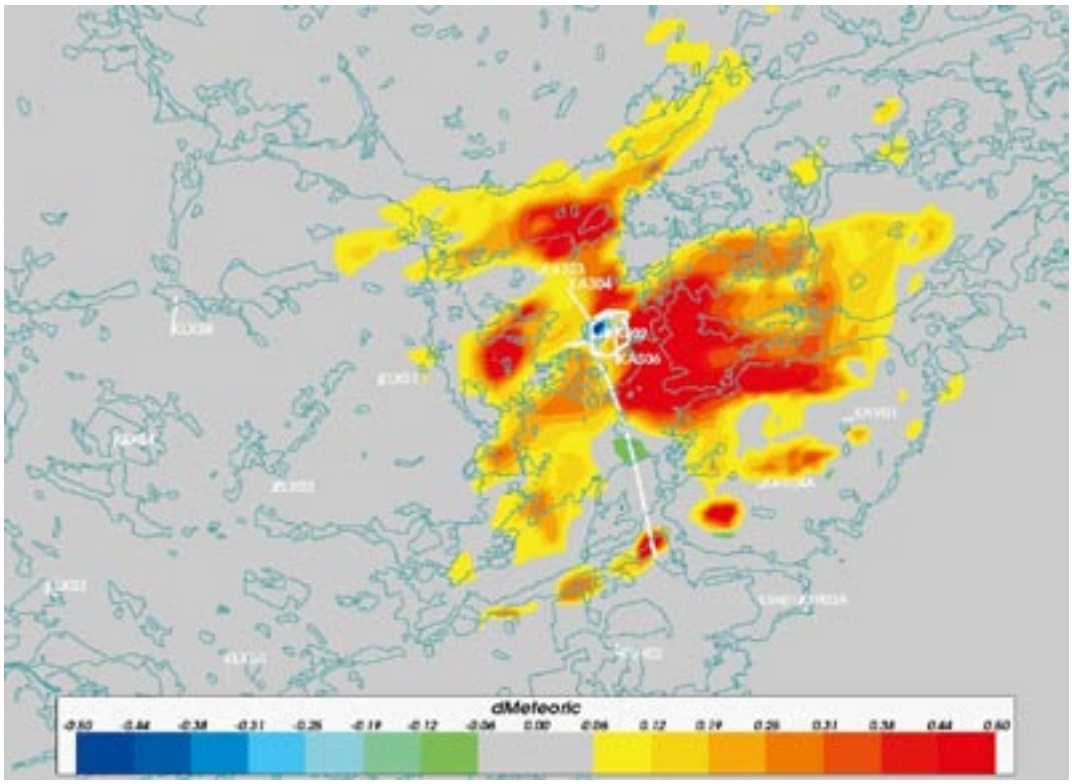

Figure 2-47. *The difference in Meteoric reference water fraction between a case with the Äspö HRL for an infiltration rate of 80 mm/year and elaborate soil model. The slice is shown for 2006 AD at –450 m and the boundary of surface waterbodies may be seen.*

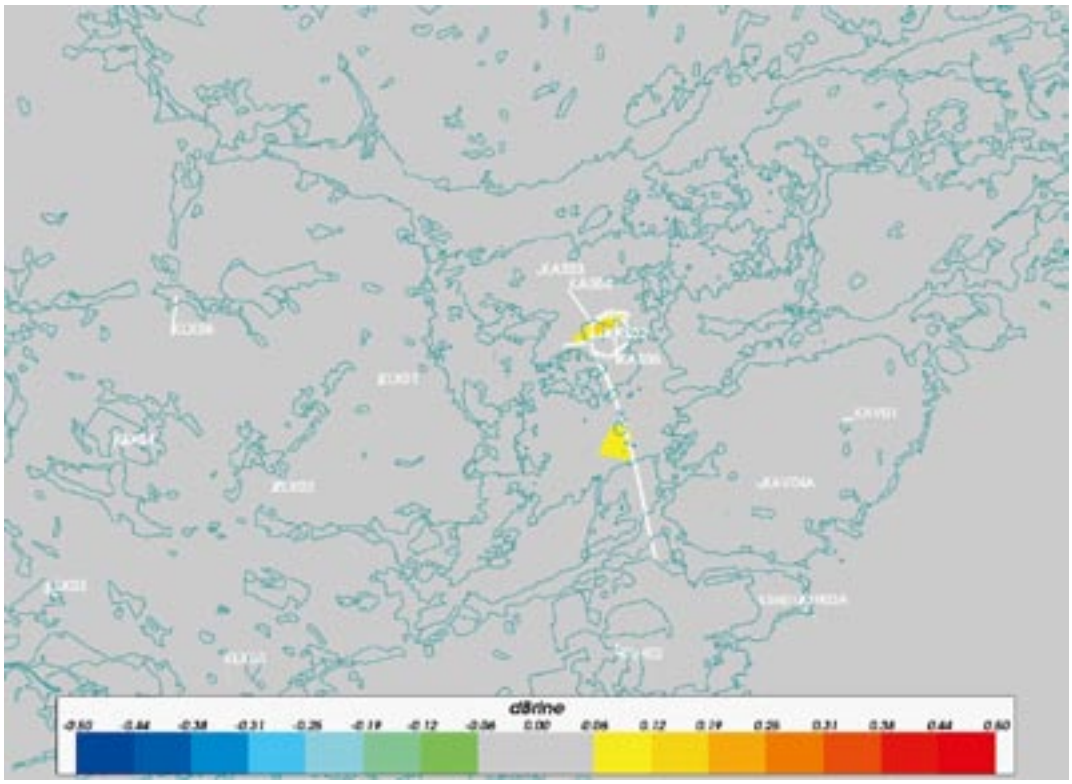

Figure 2-48. *The difference in Brine reference water fraction between a case with the Äspö HRL and a case without the HRL for an infiltration rate of 80 mm/year and elaborate soil model. The slice is shown for 2006 AD at –450 m and the boundary of surface waterbodies may be seen.*

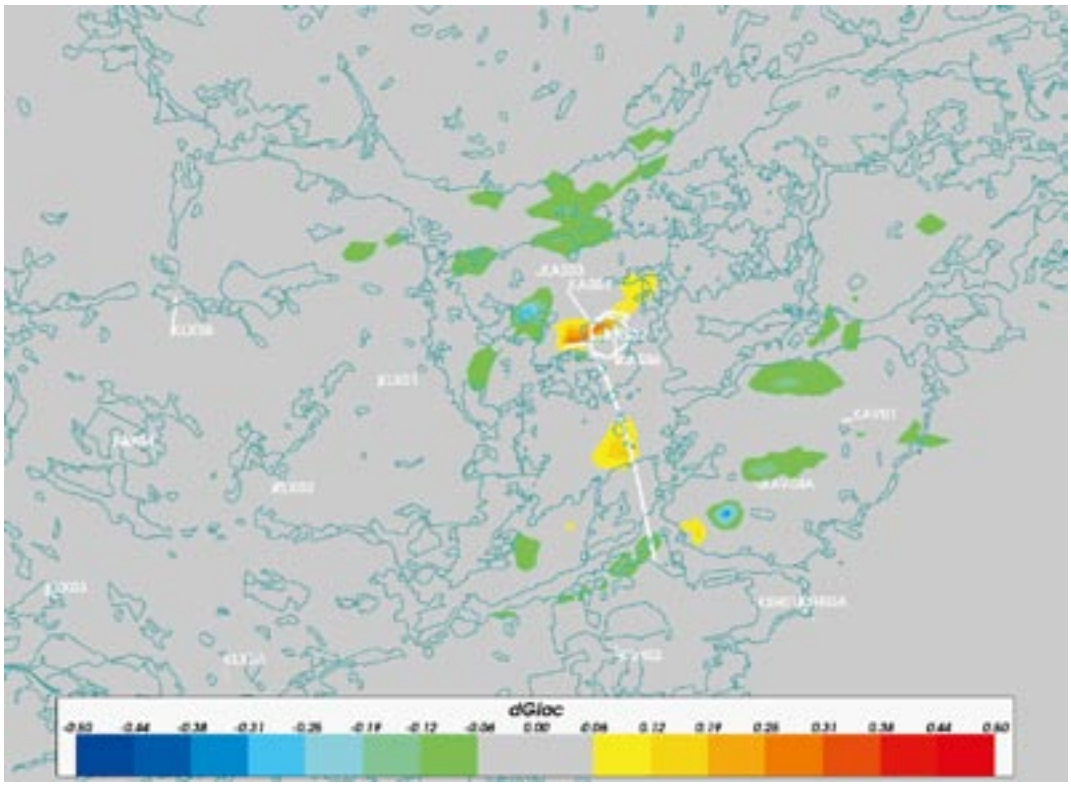

Figure 2-49. *The difference in Glacial reference water fraction between a case with the Äspö HRL and a case without the HRL for an infiltration rate of 80 mm/year and elaborate soil model. The slice is shown for 2006 AD at –450 m and the boundary of surface waterbodies may be seen.*

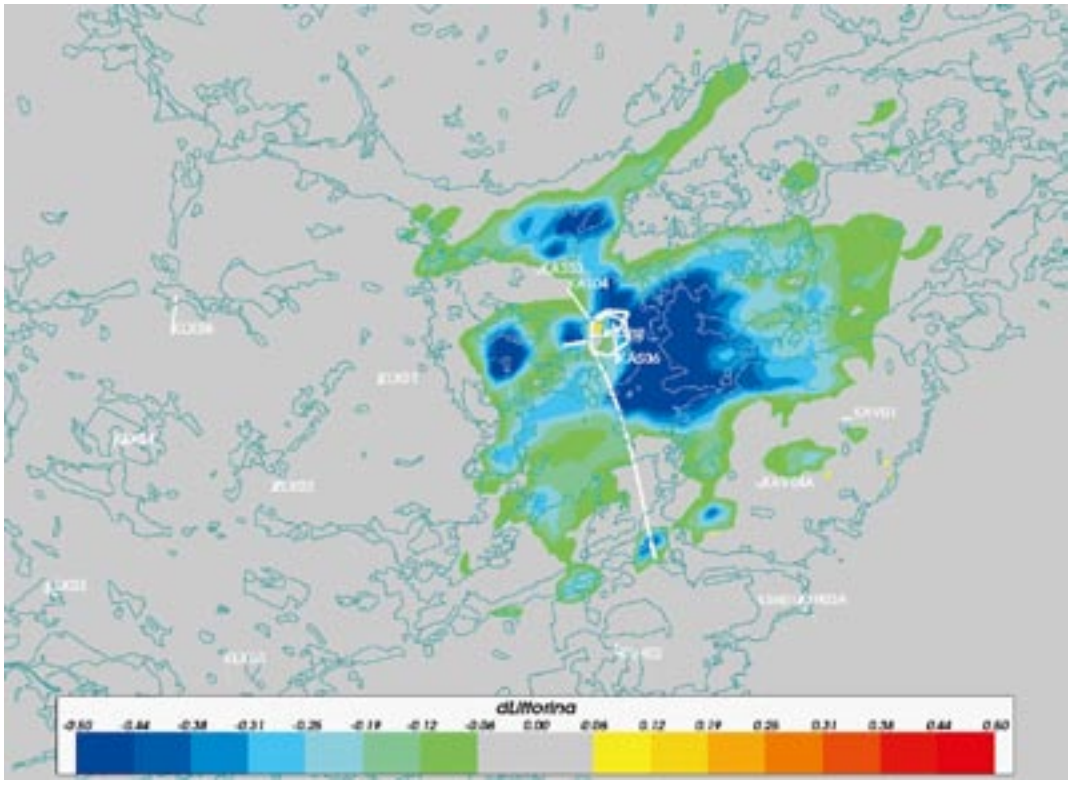

Figure 2-50. *The difference in Littorina reference water fraction between a case with the Äspö HRL and a case without the HRL for an infiltration rate of 80 mm/year and elaborate soil model. The slice is shown for 2006 AD at –450 m and the boundary of surface waterbodies may be seen.*

2.5.4 Sensitivity to hydraulic soil domain (HSD) Properties

The elaborate soil domain represents a best guess of the distribution, thickness and hydraulic properties of the Quaternary cover. However, this is subject to considerable uncertainty in the extrapolation of the HSD model over the regional-scale, as well as the actual hydraulic properties. To test the robustness of any conclusions drawn about the impact of the Äspö HRL, several variants of the case with a maximum infiltration of 165 mm/year and the HSD model from SurfaceNet were constructed. The key uncertainty investigated was the hydraulic communication between groundwater in the bedrock and the sea bottom, since this determines whether the water inflow to the tunnel originates from the sea immediately above the HRL, or from meteoric water around the shoreline to the east, south and west of Äspö. Some simulations were tried with the hydraulic conductivity of the Gyttja and Clay lowered by a factor 10 or 100 of their original value, but this made very little difference. The reason is thought to lie in the fact that the three-layer HSD model always had a thick layer of very conductive Lower Till underneath the Gyttja in the bay around Äspö. This meant that even when the Gyttja layer was made quite impermeable, the very conductive Lower Till still acted like an aquifer channelling water from around the shore to the bedrock beneath the sea, and in effect setting a zero head boundary condition on top of the bedrock beneath the sea. Therefore, more dramatic changes to the HSD model were implemented. The main difference was to change the soil type of all areas defined as Lower Till beneath the Baltic sea to the much less conductive Gyttja. In the first variant only this change to the soil type below the Gyttja was made. A second variant was made where the hydraulic conductivities for Gyttja, Gyttja Clay, Clay(upper) and Gyttja(lower) were all reduced by a factor 10. Finally, in a third simulation the hydraulic conductivities for Gyttja, Gyttja Clay, Clay(upper) and Gyttja(lower) are all reduced by a factor 100.

Reducing the hydraulic contact between the sea and the bedrock beneath by having a tight soil domain has a dramatic effect on the drawdown in the bedrock. Even by just switching the Lower Till soil to Gyttja beneath the sea causes the 0.1 m drawdown to extend to KLX02 and nearly KLX05 and the entire Simpevarp peninsula. Reducing the hydraulic conductivity of the Gyttja, and other tight soils, extends the drawdown contours even further inland such that KLX01 and the Ävrö boreholes see drawdowns of around 5 m or more. A comparison of the cases is shown in Figure 2-51.

The effects on Darcy velocity are also quite dramatic even for the case where only the soil type of Lower Till is switched to Gyttja as shown in Figure 2-52 and Figure 2-53. Figure 2-52 shows that on this slice the velocity beneath the sea is increased dramatically in the deformation zone to the east through which it passes, such that water is drawn to the tunnel from the land to the east. This is also shown in the horizontal cross-section at different elevations in Figure 2-53. At –450 m the general velocity increases, especially in the area to the east of the spiral tunnel. Near the surface (–20 m is shown) the increase in flow spreads out significantly further south and east than in cases with a good contact between the sea and the bedrock, since here water has to be brought from the surrounding land rather than the sea directly above to provide the measured inflows.

Changes in hydro-geochemistry are shown in Figure 2-54 to Figure 2-57. Here, it is seen the reduced contact between the bedrock hydrogeology and the sea results in greater upconing of Brine and glacial waters from deep, and a higher degree of replacement of marine water by meteoric water beneath the bay around Äspö since there is less infiltration by Baltic seawater.

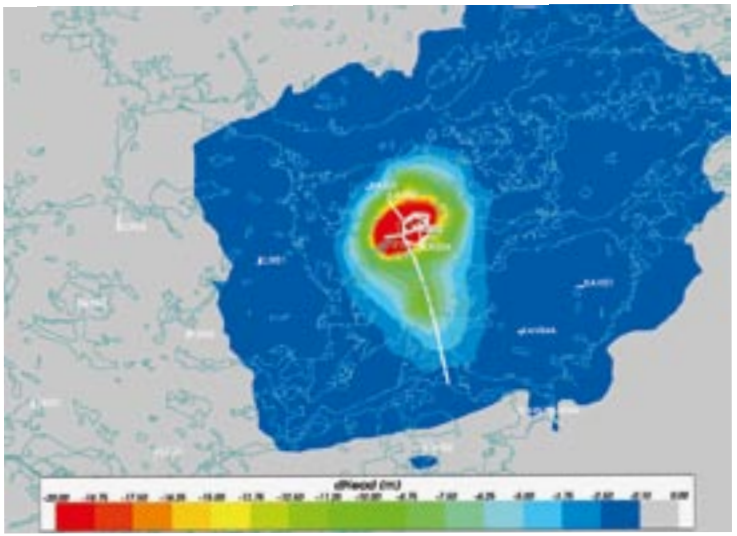

The unmodified HSD2, i.e. Figure 2-39 repeated.

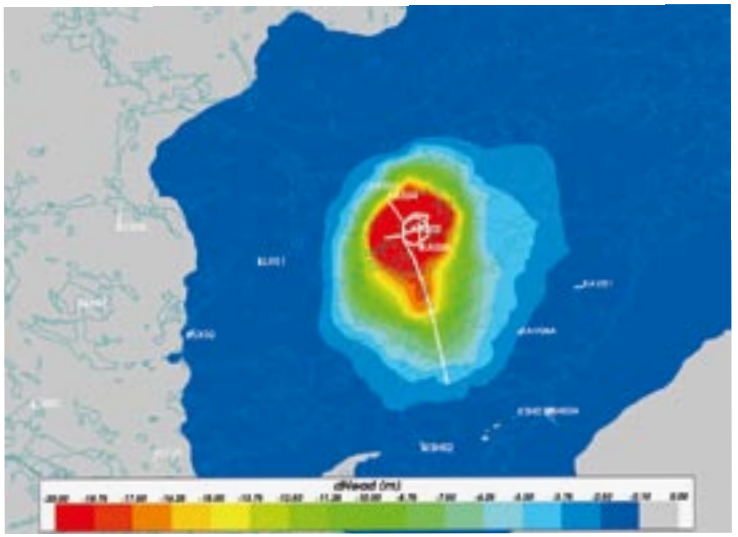

Lower Till underneath the sea is changed to Gyttja.

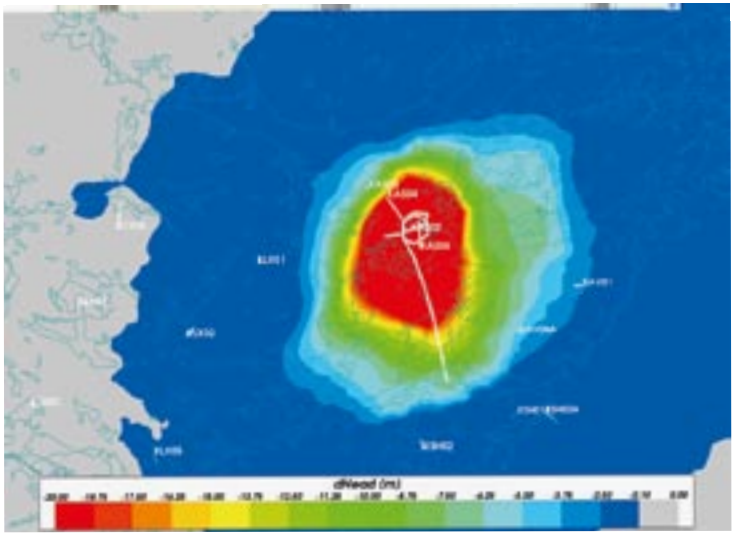

Lower Till underneath the sea is changed to Gyttja, and hydraulic conductivity for Gyttja, Gyttja Clay, Clay(upper) and Gyttja(lower) are all reduced by a factor 10.

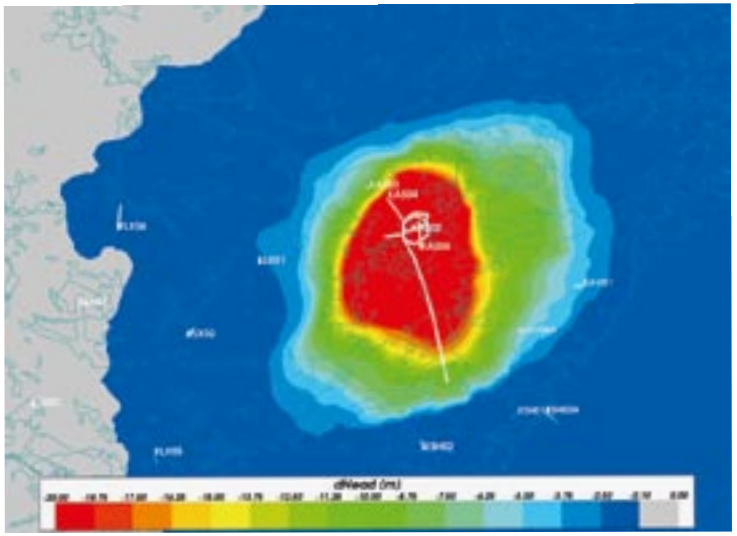

Lower Till underneath the sea is changed to Gyttja, and hydraulic conductivity for Gyttja, Gyttja Clay, Clay(upper) and Gyttja(lower) are all reduced by a factor 100.

Figure 2-51. *Sensitivity study of the drawdown at –450 m elevation and 2006 AD to properties of HSD.*

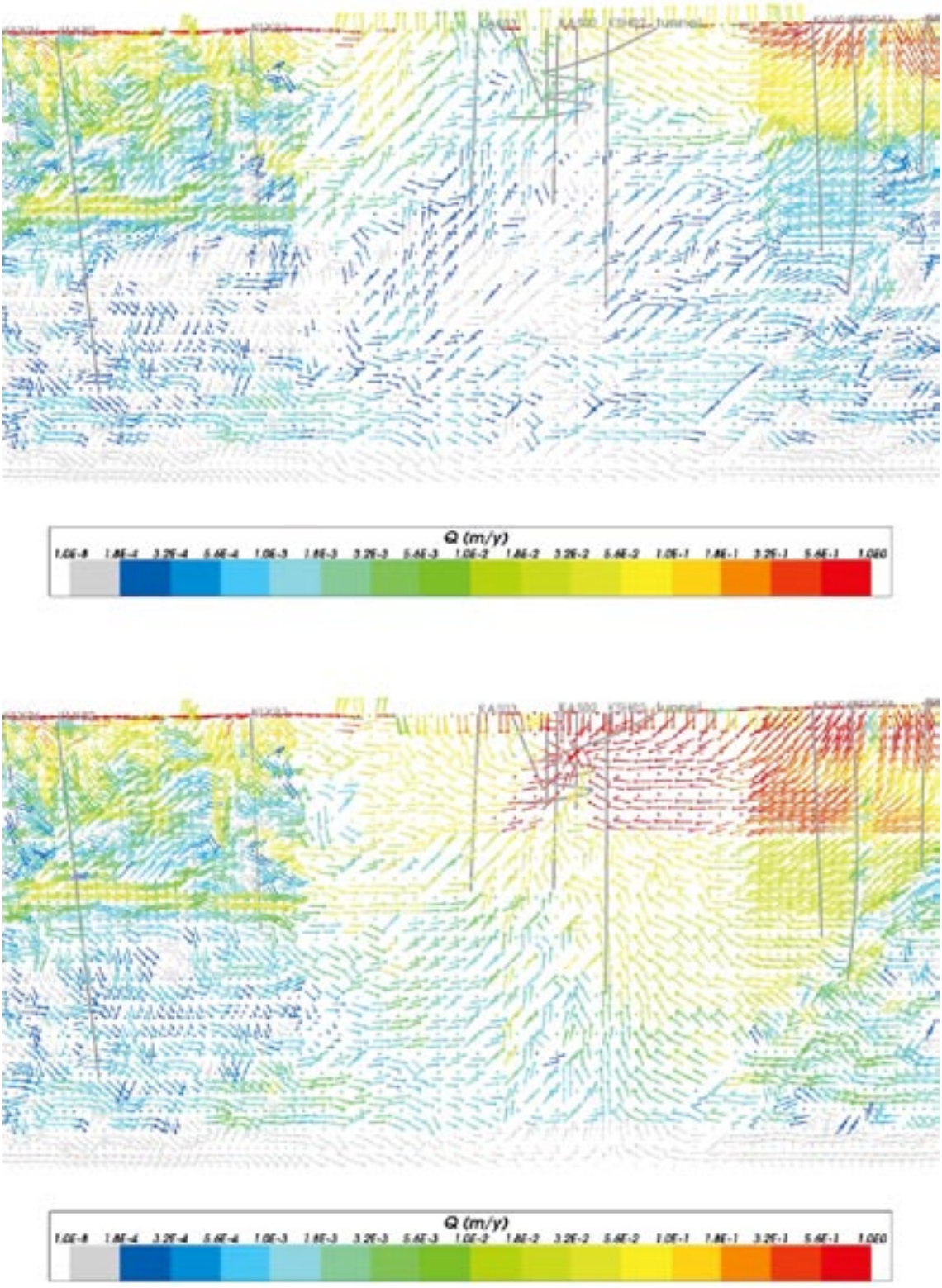

Figure 2-52. *The direction of Darcy velocity on a vertical E-W slice through KLX01 and Äspö for an infiltration rate of 165 mm/year and elaborate soil model with Lower Till changed to Gyttja below the sea. The dimensions are about 4 km E-W and 2.3 km top to bottom. The two simulations are shown without the Äspö HRL (top) and with the HRL (bottom). The velocity is shown for 2006 AD.*

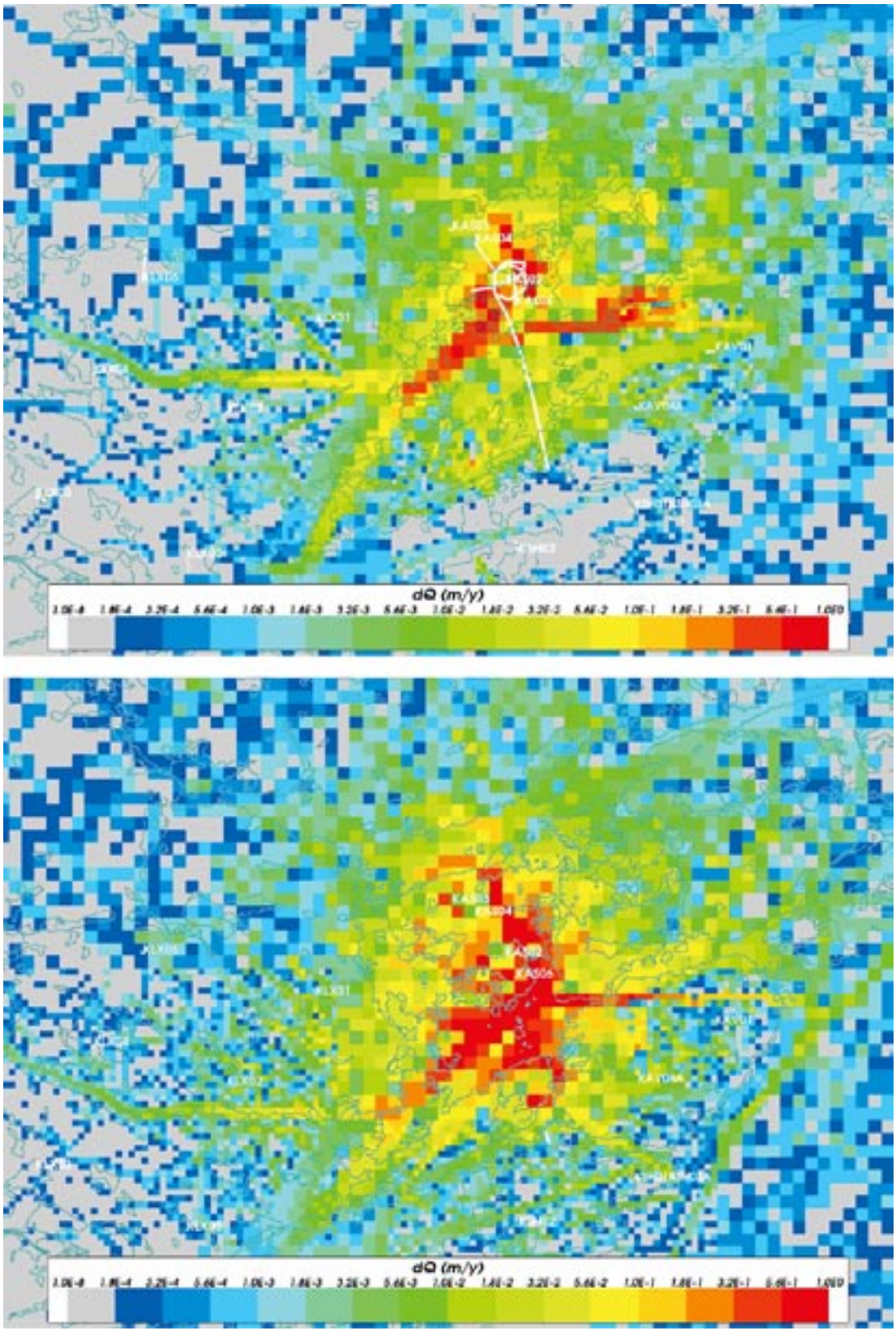

Figure 2-53. *The magnitude of difference in Darcy velocity between a case with the Äspö HRL and a case without the HRL with an infiltration rate of 165 mm/year and elaborate soil model with Lower Till changed to Gyttja below the sea. Top: –450 m elevation; Bottom: –20 m elevation. The slices are shown for 2006 AD, and the boundary of surface waterbodies may be seen.*

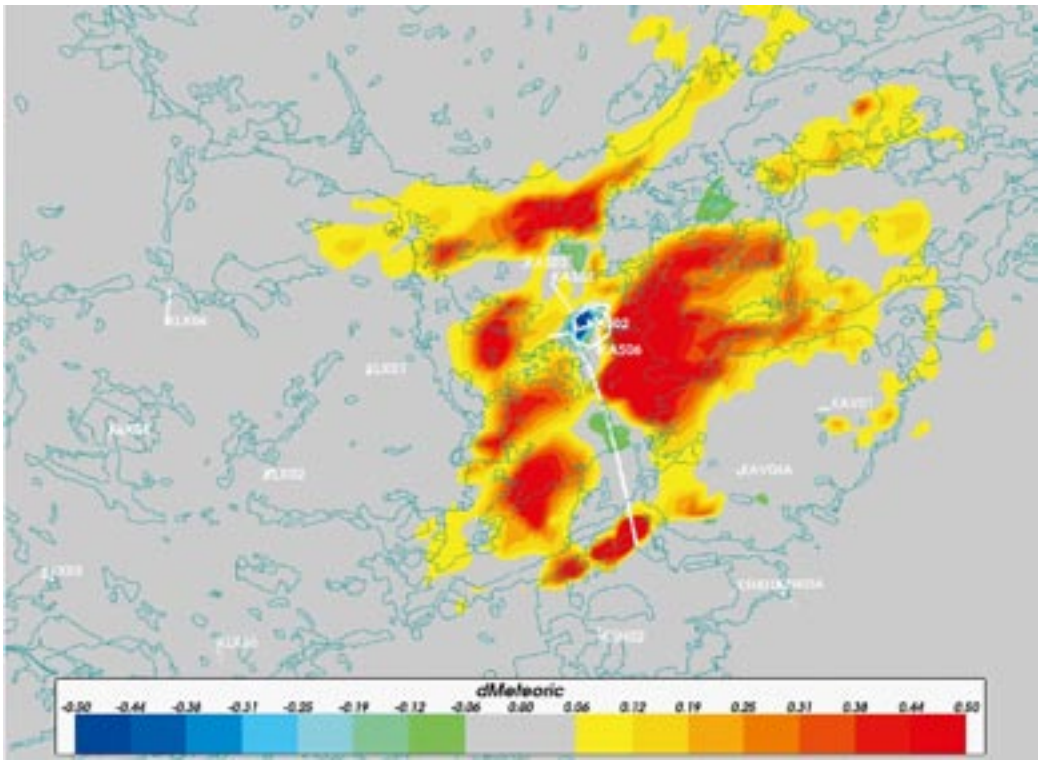

Figure 2-54. *The difference in Meteoric reference water fraction between a case with the Äspö HRL for an infiltration rate of 165 mm/year and elaborate soil model with Lower Till changed to Gyttja below the sea. The slice is shown for 2006 AD at –450 m and the boundary of surface waterbodies may be seen.*

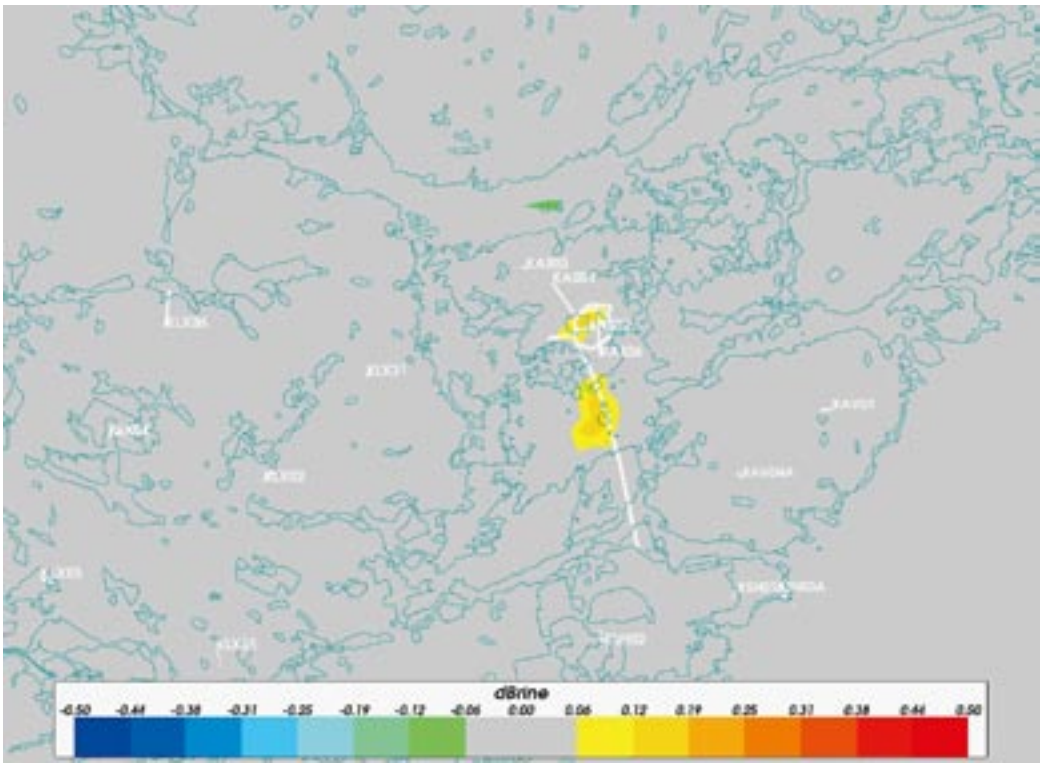

Figure 2-55. *The difference in Brine reference water fraction between a case with the Äspö HRL and a case without the HRL for an infiltration rate of 165 mm/year and elaborate soil model with Lower Till changed to Gyttja below the sea. The slice is shown for 2006 AD at –450 m and the boundary of surface waterbodies may be seen.*

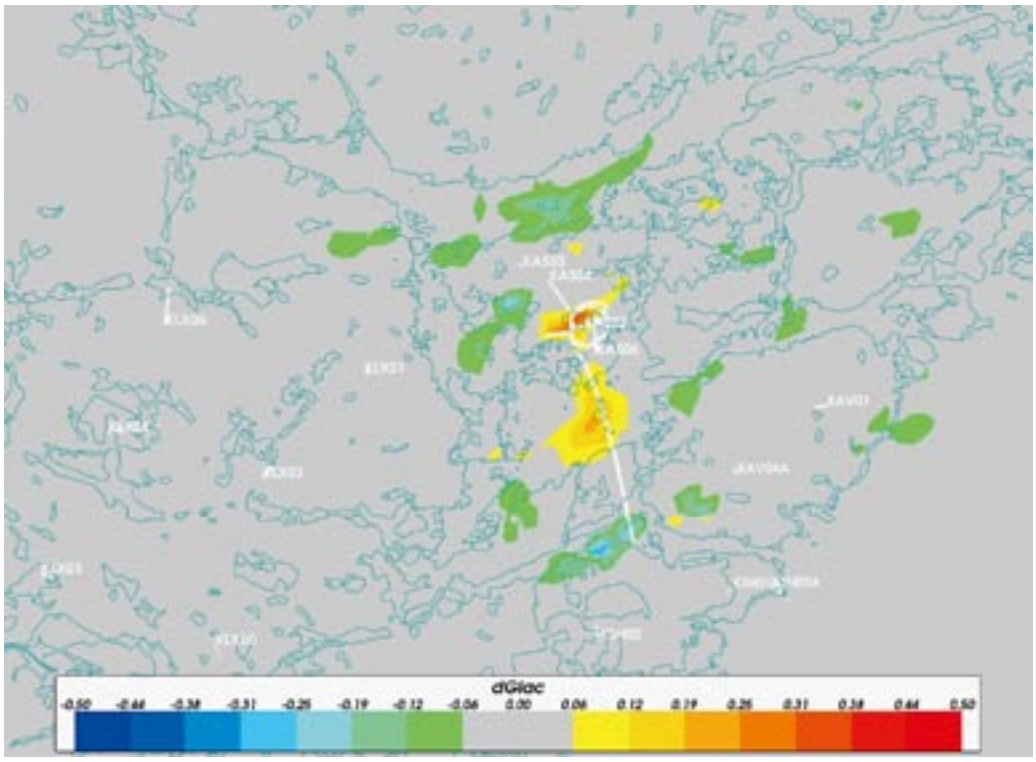

Figure 2-56. *The difference in Glacial reference water fraction between a case with the Äspö HRL and a case without the HRL for an infiltration rate of 165 mm/year and elaborate soil model with Lower Till changed to Gyttja below the sea. The slice is shown for 2006 AD at –450 m and the boundary of surface waterbodies may be seen.*

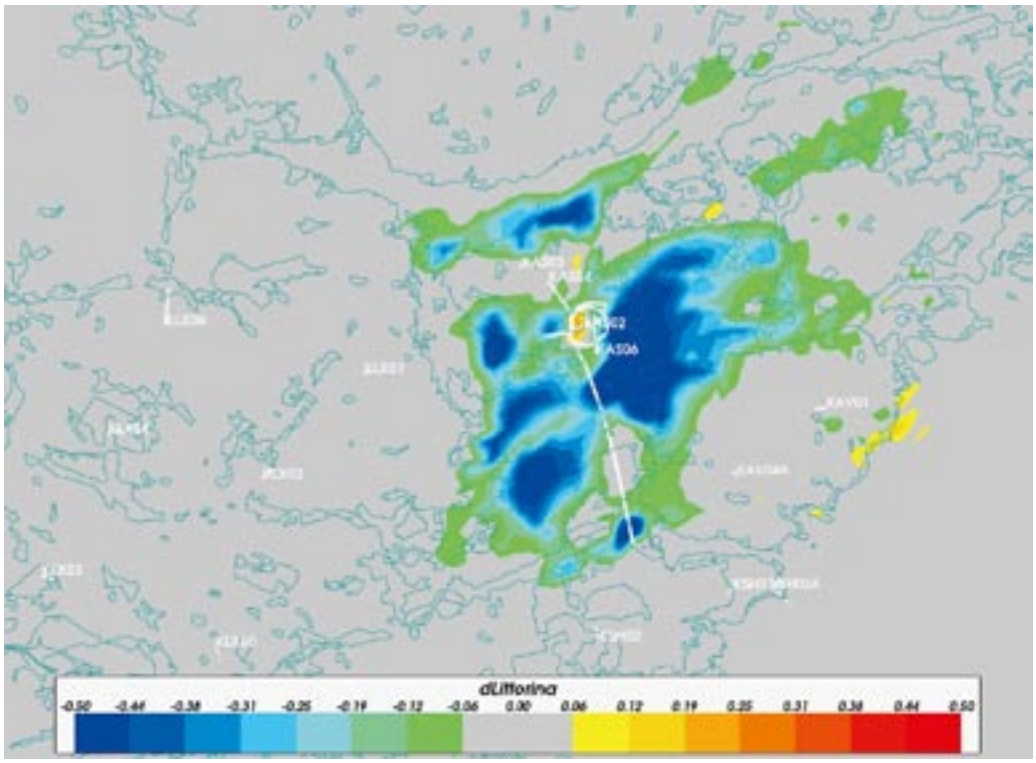

Figure 2-57. *The difference in Littorina reference water fraction between a case with the Äspö HRL and a case without the HRL for an infiltration rate of 165 mm/year and elaborate soil model with Lower Till changed to Gyttja below the sea. The slice is shown for 2006 AD at –450 m and the boundary of surface waterbodies may be seen.*

2.6 Affect of Äspö hard rock laboratory (HRL) on flow-paths

In order to illustrate the flow field, pathlines were simulated. The simulated pathlines are started at canister positions in tentative repository layout from the SR-Can study /Hartley et al. 2006a/. The starting positions may be seen in Figure 2-62. Even though the particles are released under present day conditions and the water residence time from repository depth is on average in the 1,000 year range, the pathlines may reveal something on the prevailing gradients. In Figure 2-58, exit locations are shown for the case with un-modified elaborate HSD model, maximum infiltration of 165 mm/year and un-disturbed conditions. It may be seen that many particles exit in the bays near Äspö. Figure 2-59 shows the pathlines from the starting position to some of the exit locations. For illustration purposes, the southern part of the model is removed.

For the same model set-up, except that the Äspö HRL is present, pathlines were simulated and it may be seen in Figure 2-60 that the exit locations near Äspö seem to have disappeared. This may be explained in Figure 2-61, where it may be possible to see that the particles are attracted by the Äspö HRL instead.

Table 2-6. Log_{10} travel times (t_r) for particles starting at repository depth and exiting at the ground surface or the Äspö HRL if applicable. In each case 7,483 particles are released.

Case	Exit at top Surface		Exit at HRL	
	Median $Log_{10}(t_r)$ (years)	Percentage of pathlines	Median $Log_{10}(t_r)$ (years)	Percentage of pathlines
Elaborate HSD, 165 mm/year, un-disturbed conditions	3.08	95%	Not applicable	Not applicable
Elaborate HSD, 165 mm/year, HRL present	2.93	50%	3.74	50%
Elaborate HSD, 165 mm/year, HRL present, modified HSD, Lower Till is switched to Gyttja and K is 10^{-10} m/s for Gyttja	2.72	19%	3.57	81%

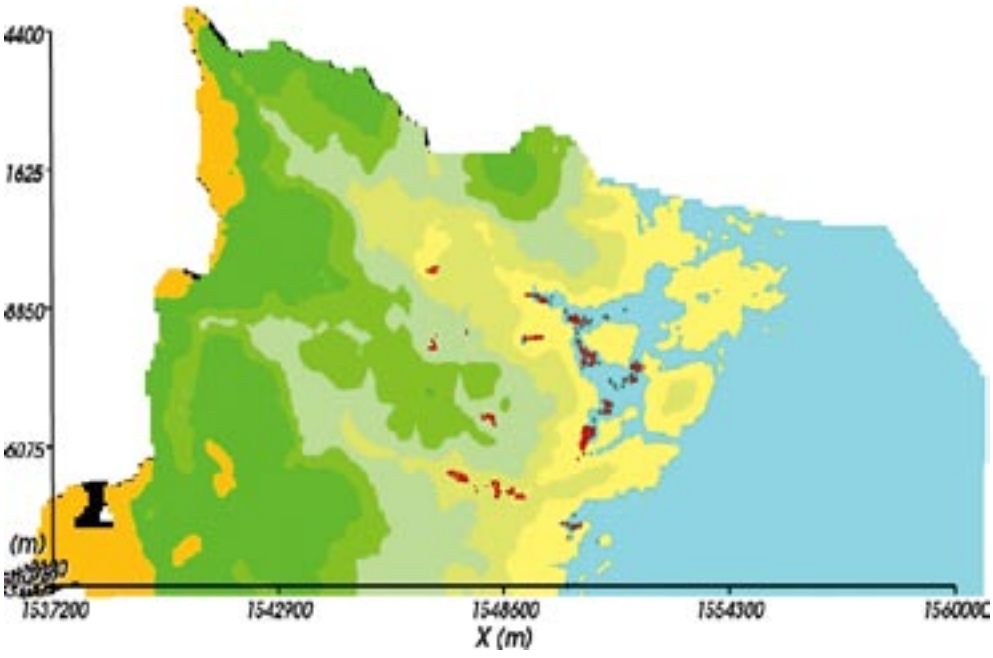

Figure 2-58. *Exit locations as red markers for the case with elaborate HSD model, maximum infiltration rate of 165 mm/year, and without the Äspö HRL present.*

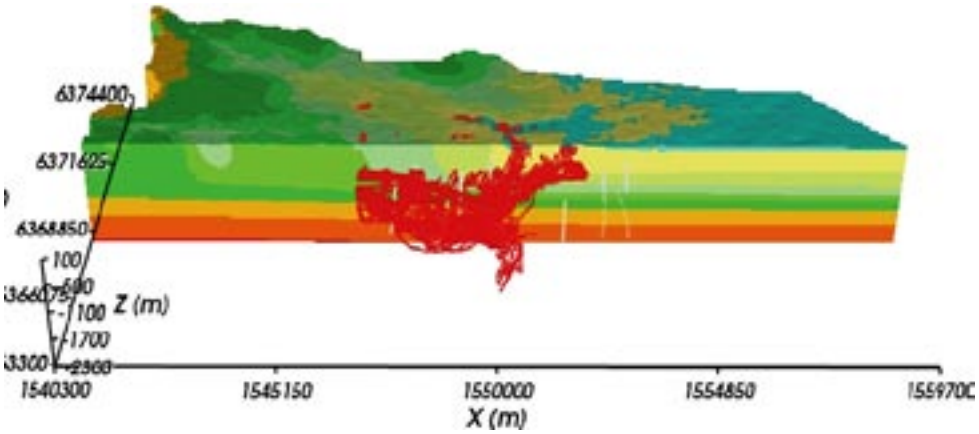

Figure 2-59. *Pathlines for the case with elaborate HSD model, maximum infiltration rate of 165 mm/year, and without the Äspö HRL present. The southern part of model is removed for illustration purposes.*

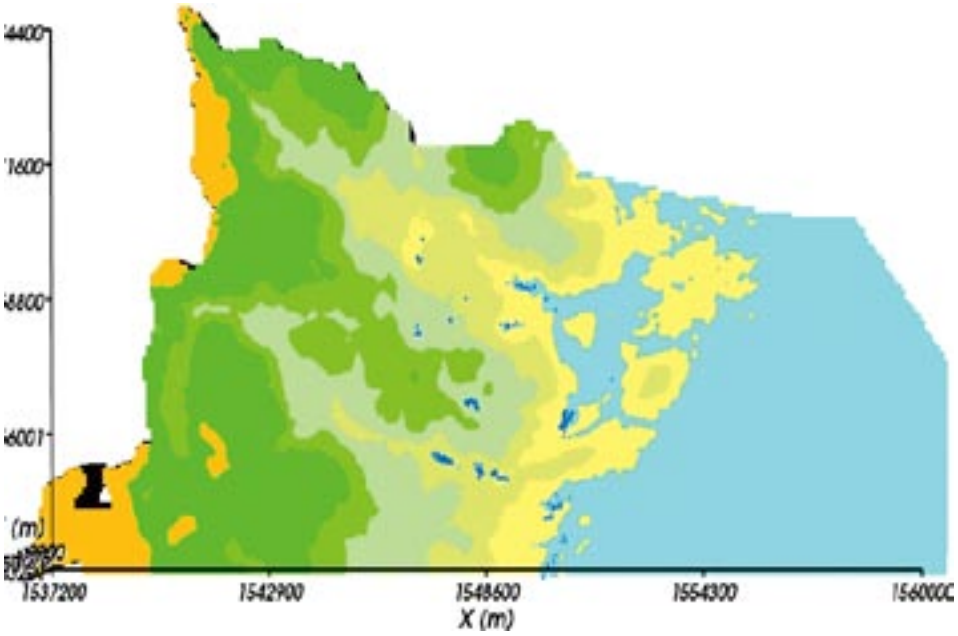

Figure 2-60. *Exit locations as blue markers for the case with elaborate HSD model, maximum infiltration rate of 165 mm/year, and with the Äspö HRL present.*

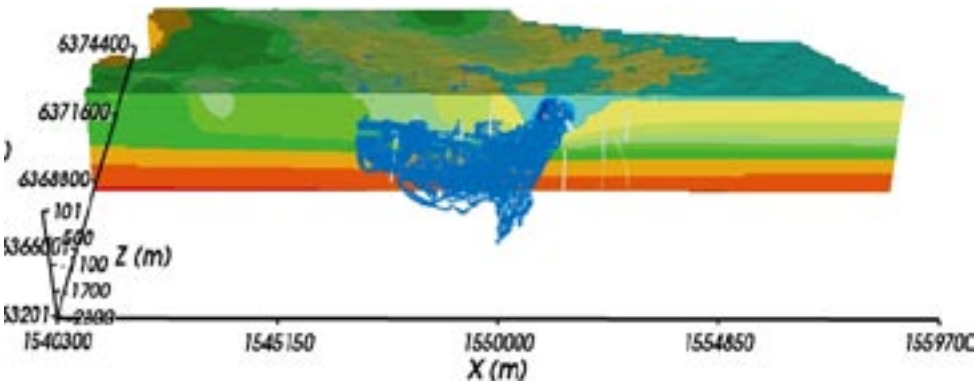

Figure 2-61. *Pathlines for the case with the elaborate HSD model, maximum infiltration rate of 165 mm/year, and with the Äspö HRL present. The southern part of model is removed for illustration purposes.*

In Figure 2-62, the particle starting positions that end up in the Äspö HRL are marked with red. This is shown for the case with un-modified HSD2 and infiltration rate 165 mm/year. In this case, about 50% of all released particles are going to the HRL. This may be compared with the case with the Lower Till switched to Gyttja under Z = 0 m and the permeability reduced to 10^{-10} m/s, there about 81% of the particles are going to the Äspö HRL. This is illustrated in Figure 2-63.

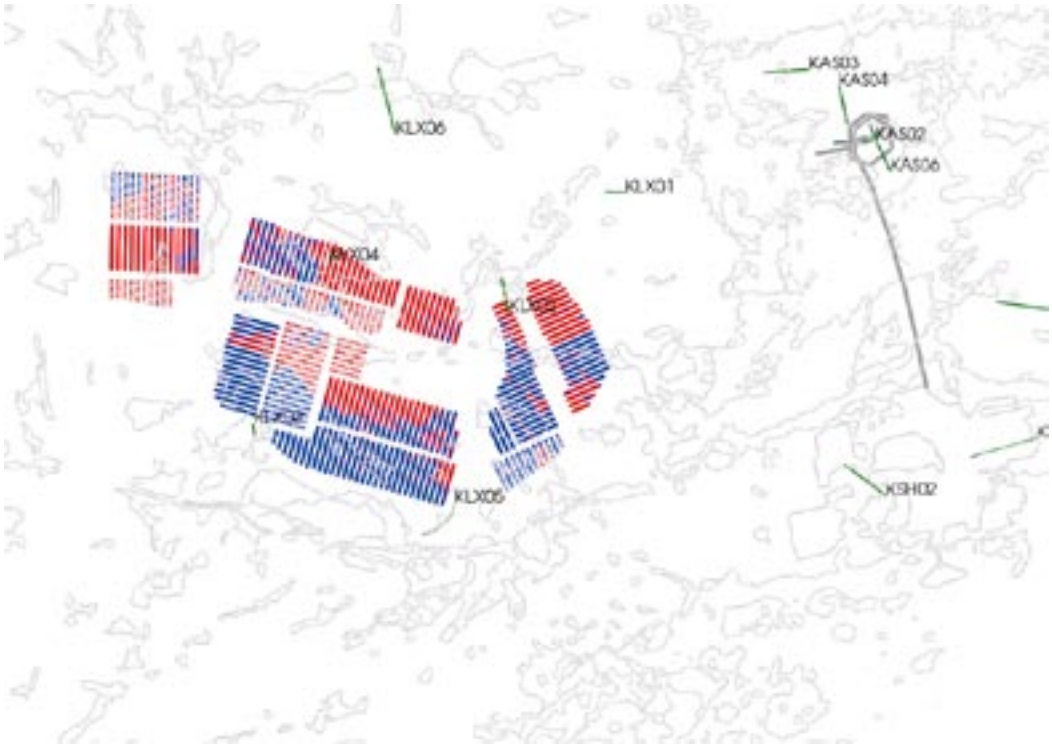

Figure 2-62. *Roughly 50% of the starting positions (red) end up in the Äspö HRL, and the blue positions exit at the ground surface for the case with elaborate HSD model, unmodified HSD, and infiltration rate 165 mm/year.*

Figure 2-63. *Roughly 81% of the starting positions (red) end up in the Äspö HRL, and the blue positions exit at the ground surface for the case with elaborate HSD model, modified HSD (Lower Till is switched to Gyttja below Z = 0 and K for Gyttja is 10^{-10} m/s), and infiltration rate 165 mm/year.*

2.7 Summary and conclusions

A number of simulations have been carried out to investigate if the Äspö Hard Rock Laboratory has an impact on the groundwater flow situation at Äspö and the area around it. As a platform for the calculations, the ECPM reference case from the SR-Can Laxemar 1.2 calculations /Hartley et al. 2006a/ was used. In the reference case case, a specified head boundary condition was set on the top surface. For this study, two simulations were performed for each set of hydraulic properties and boundary conditions considered: one with the Äspö HRL present and water abstracted according to the inflow rates measured in the tunnel weirs; and a simulation under undisturbed conditions. In both simulations, the calculations start at 1960 using appropriate models of palaeo-hydrogeology without any disturbance for the initial condition and then the models are run until 2006 with a one year time-step. The cases were compared in terms of modelled drawdown, and changes to the Darcy velocity and hydro-geochemistry. Sensitivities of the results were considered in relation to the top surface boundary condition including a maximum infiltration of 165 mm/year or 80 m/year, and varying the hydraulic contact between the sea and the bedrock beneath.

A number of comparisons with field data can be made to assess which of the variants is considered to best reflect site conditions and to possibly inform future developments of the site descriptive model. Data are available for both drawdowns around the Simpevarp area and for salinity of the water collected in the weirs within the tunnel. Drawdown measurements are available for several percussion drilled boreholes whose locations are shown in Figure 2-64. Essentially, this can be used as a long-term interference test with the Äspö HRL as the sink and the percussion drilled boreholes as monitoring points.

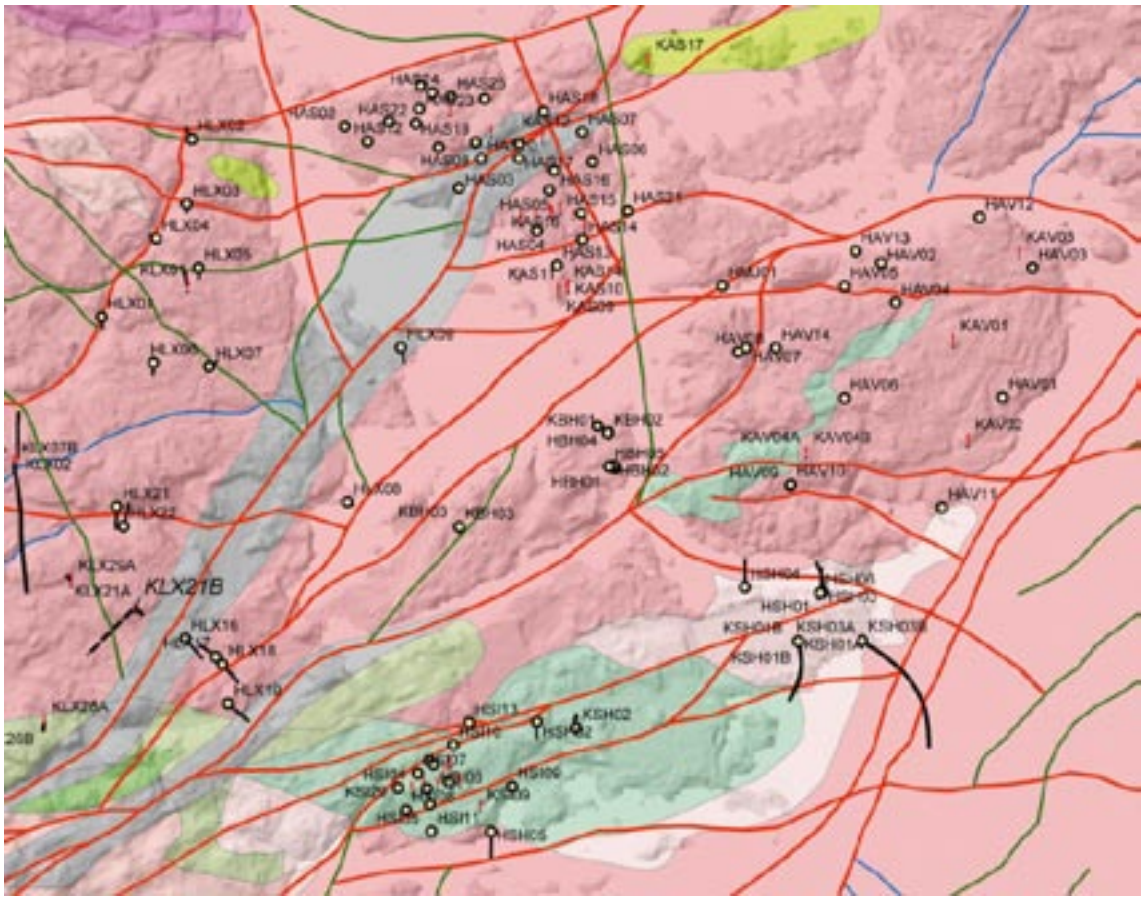

Figure 2-64. *Locations of percussion and core drilled boreholes around Äspö, in some of which long term water-level monitoring was performed.*

A comparison of the modelled and measured drawdowns is given for each model variant in Table 2-7. The measured drawdowns are based on the difference between groundwater levels before the Äspö HRL and measurements taken between 1993 and1995 when the inflows reached a maximum. Some drawdowns are small, less than 0.5 m, and so it is hard to say if this is a response to the HRL or just seasonal variations etc. An extra column is included to indicate in which boreholes it is thought a response to the HRL was seen or not. When comparing with the model, it is suggested that drawdowns of less than 0.5 m are to be regarded as no response. The drawdowns in the tunnel and shaft are also included. It can be seen the model gives consistent predictions of the drawdown around the tunnel for all cases apart from those where the Lower Till was changed to Gyttja, and the Gyttja hydraulic conductivity was significantly reduced. The variant that agrees best is probably the case with a flux boundary condition of 165 mm/year and the Lower Till switched to Gyttja. The variants where the sea sediments are made very tight, less than 10^{-9} m/s, seem to give drawdowns too large and the cases where there is good contact between the sea and bedrock give drawdowns too small. Hence, this hints at the sea sediments being moderately tight, i.e. 10^{-8} m/s, but without a thicker layer of high conductivity Lower Till beneath. The plots of changes in Darcy velocity and reference water fractions for the case with a flux boundary condition of 165 mm/year and the Lower Till switched to Gyttja are given in Figure 2-52 to Figure 2-57.

Otherwise, switching from the specified head boundary condition derived for L 1.2 to a specified flux does not impact significantly on the results. Reducing the infiltration to 80 mm/year also does not have a large affect. It may have been interesting to combine this lower infiltration with the Lower Till being switched to Gyttja to obtain an optimal set of drawdown predictions.

Table 2-7. A comparison of modelled and measured drawdowns (m) for 1995 AD in percussion drilled boreholes. The drawdown predicted by each variant is given: specified top surface head (Head); specified maximum infiltration of 165 mm/year (Flux 165); specified maximum infiltration of 80 mm/year(Flux 80); specified maximum infiltration of 165 mm/year and Lower Till switched to Gyttja (Flux 165, Gyttja), specified maximum infiltration of 165 mm/year and Lower Till switched to a lower conductivity Gyttja (Flux 165, Gyttja 10^{-9} m/s); specified maximum infiltration of 165 mm/year and Lower Till switched to very low conductivity Gyttja (Flux 165, Gyttja 10^{-10} m/s).

Borehole	Measured drawdown	Response?	Modelled drawdown for variants					
			Head	Flux (165)	Flux (80)	Flux (165), Gyttja	Flux (165), Gyttja (10^{-9})	Flux (165), Gyttja (10^{-10})
HAV01	0.3	possibly small	0.1	0.1	0.2	0.3	0.7	1.3
HAV02	1.5	yes	0.2	0.3	0.4	1.1	2.9	4.6
HAV03	0.0	no	0.0	0.1	0.2	0.4	0.9	1.6
HAV04	0.2	possibly small	0.1	0.3	0.5	0.7	1.6	2.5
HAV05	2.4	yes	0.1	0.4	0.6	1.2	3.0	4.6
HAV06	3.2	yes	0.4	0.7	0.9	1.7	3.4	4.7
HAV07	?	?	0.5	0.8	0.9	2.9	7.2	10.1
HAV08	4.5	yes	0.6	0.9	1.0	3.2	7.5	10.2
HMJ01	8.5	yes	0.8	1.0	1.3	5.8	15.3	21.7
HLX01	0.0	no	0.0	0.0	0.0	0.0	0.1	0.2
HLX02	0.5	possibly	0.0	0.0	0.0	0.1	0.3	0.5
HLX03	0.0	no	0.0	0.0	0.1	0.1	0.2	0.4
HLX04	0.0	no	0.0	0.0	0.1	0.1	0.2	0.3
HLX05	0.0	no	0.0	0.1	0.1	0.2	0.6	1.1
HLX06	0.0	no	0.0	0.0	0.1	0.1	0.3	0.6
HLX07	0.0	no	0.0	0.1	0.1	0.2	0.6	1.1
HLX08	1.0	possibly	0.1	0.1	0.2	1.4	6.6	10.9
HLX09	1.7	yes	0.5	0.7	0.7	4.9	17.6	32.6
Tunnel	70	yes	69.0	70.7	71.2	81.7	92.7	100.5
Shaft	70	yes	79.4	78.2	78.7	90.1	102.3	110.9

Figure 2-65 shows a comparison of the modelled and measured profiles of salinity in the tunnel and shaft. The model predictions are broadly in line with the trends observed. However, there are only moderate differences between the different simulation variants, and so it is hard to promote a particular case based on the salinity data alone.

Some plots of the Darcy velocity in vertical slices are given in Figure 2-66 to Figure 2-69 fro iluustration and to satisfy a request from the ChemNET group. The velocities are calculated in the model case with a specified infiltration rate of 165 mm/year, the elaborate soil model with Lower Till changed to Gyttja below the sea, and with inflows at the Äspö HRL. Four E-W vertical slices are given through selected boreholes, and 4 N-S slices.

In summary, the simulations show that the Äspö HRL has a significant local effect on the groundwater situation. Typically, in the simulations, the rock under the Äspö island, the bays around it and the Ävrö area (mainly western part of the islands of Ävrö, Mjälen and Hålö) are influenced. In the sensitivity study, the visualisations of drawdown show small differences in the results for head versus flux top boundary conditions, little sensitivity to the change of infiltration rate, but most sensitivity to the contact between the sea and the bedrock beneath the seabed sediments. The primary objective of this work was to assess whether the operation of the Äspö HRL could have disturbed the hydro-geochemical conditions significantly from there natural state. For all simulation cases considered here, the Äspö HRL has not been in operation sufficiently long to have affected the chemistry of samples collected in the Simpevarp study area,

though there is some possibility that Ävrö samples have been altered, at least for boreholes in the western part of Ävrö, Mjälen and Hålö. The distribution of flow and discharge areas around the bay surrounding the Äspö island is clearly affected by the HRL for all cases.

Using the drawdown in percussion drilled boreholes around Äspö as an interference test suggests that there is a partial reduction in the hydraulic contact between the sea and the groundwater system in the bedrock beneath. It is recommended that the conclusions about appropriate hydraulic properties for Quaternary sediments beneath the sea be carried forward into future regional groundwater flow modelling studies.

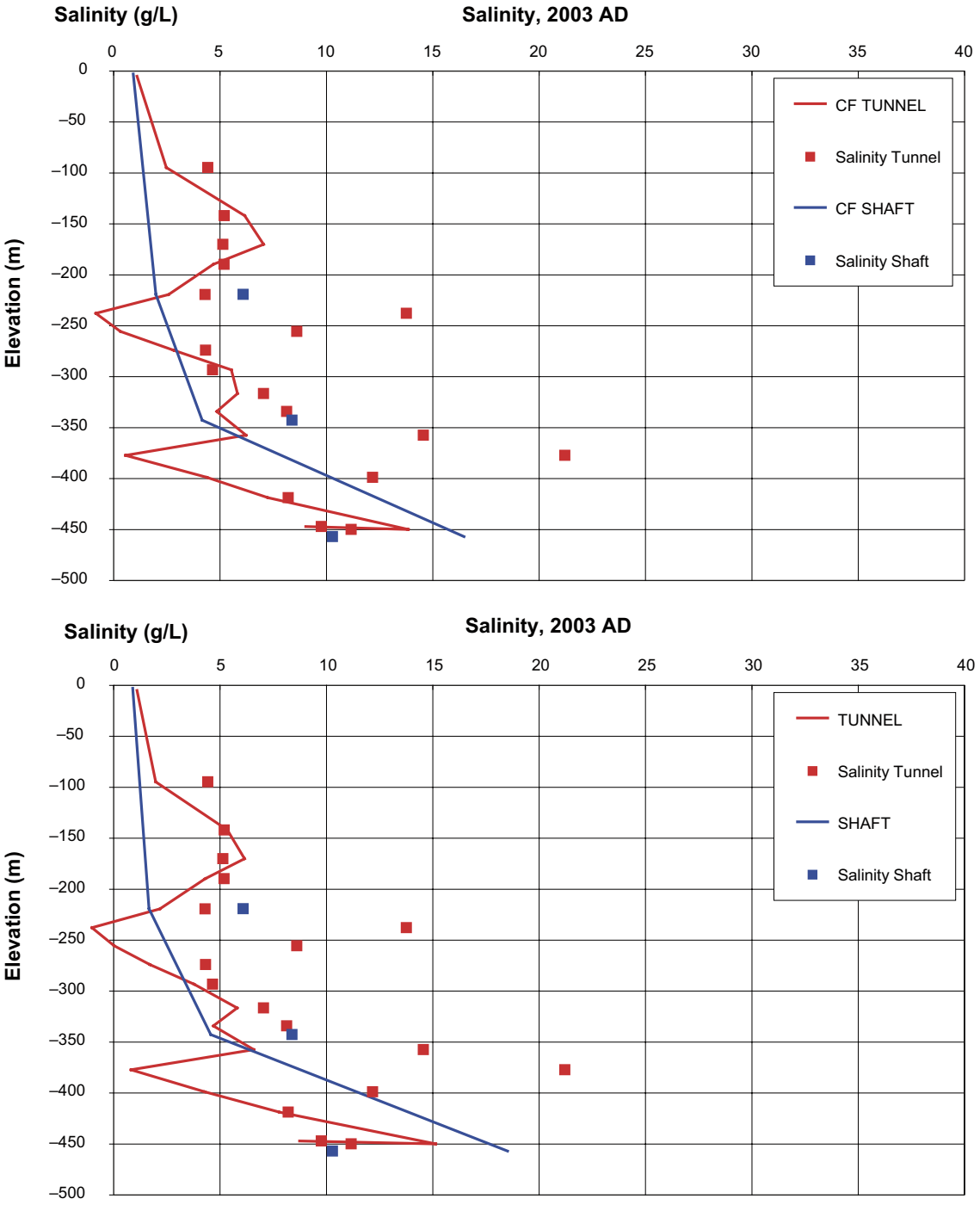

Figure 2-65. *Comparison of modelled and measured salinity in the tunnel and shaft as a function of elevation. Top: case with a specified maximum infiltration of 165 mm/year; Bottom: case with a specified maximum infiltration of 165 mm/year and Lower Till switched to Gyttja beneath the sea. (CF is an abbreviation for ConnectFlow).*

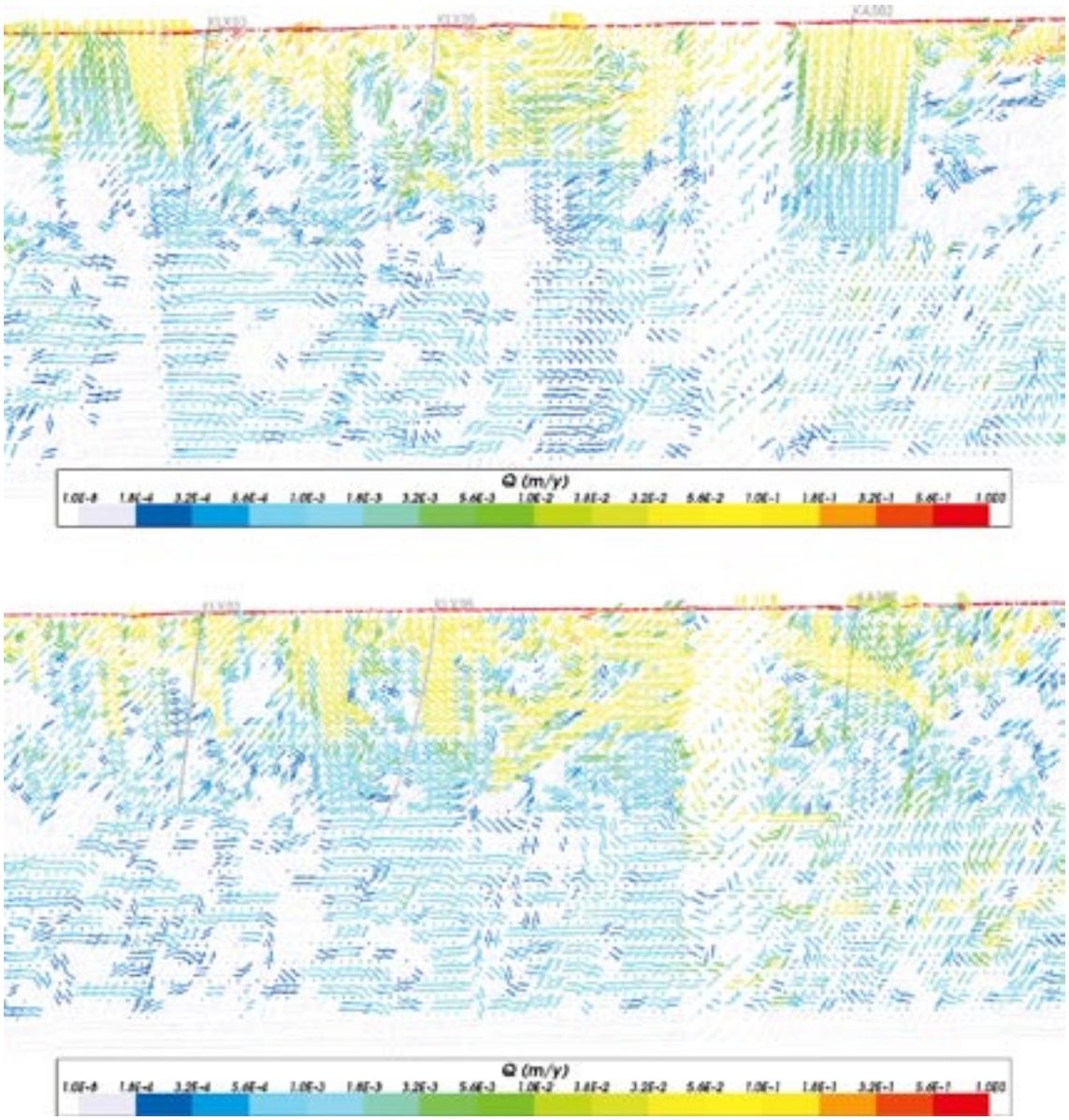

Figure 2-66. *The direction and magnitude of Darcy velocity on vertical E-W slices for an infiltration rate of 165 mm/year and elaborate soil model with Lower Till changed to Gyttja below the sea, and with inflows at the Äspö HRL. The dimensions are about 4 km E-W and 2.3 km top to bottom. The slices are through KLX05 (top) and KLX03 (bottom). The velocity is shown for 2006 AD. Selected borehole trajectories are superimposed, but these do not necessary lie along the vertical section shown, and hence there can be a perspective effect when viewing in 3D.*

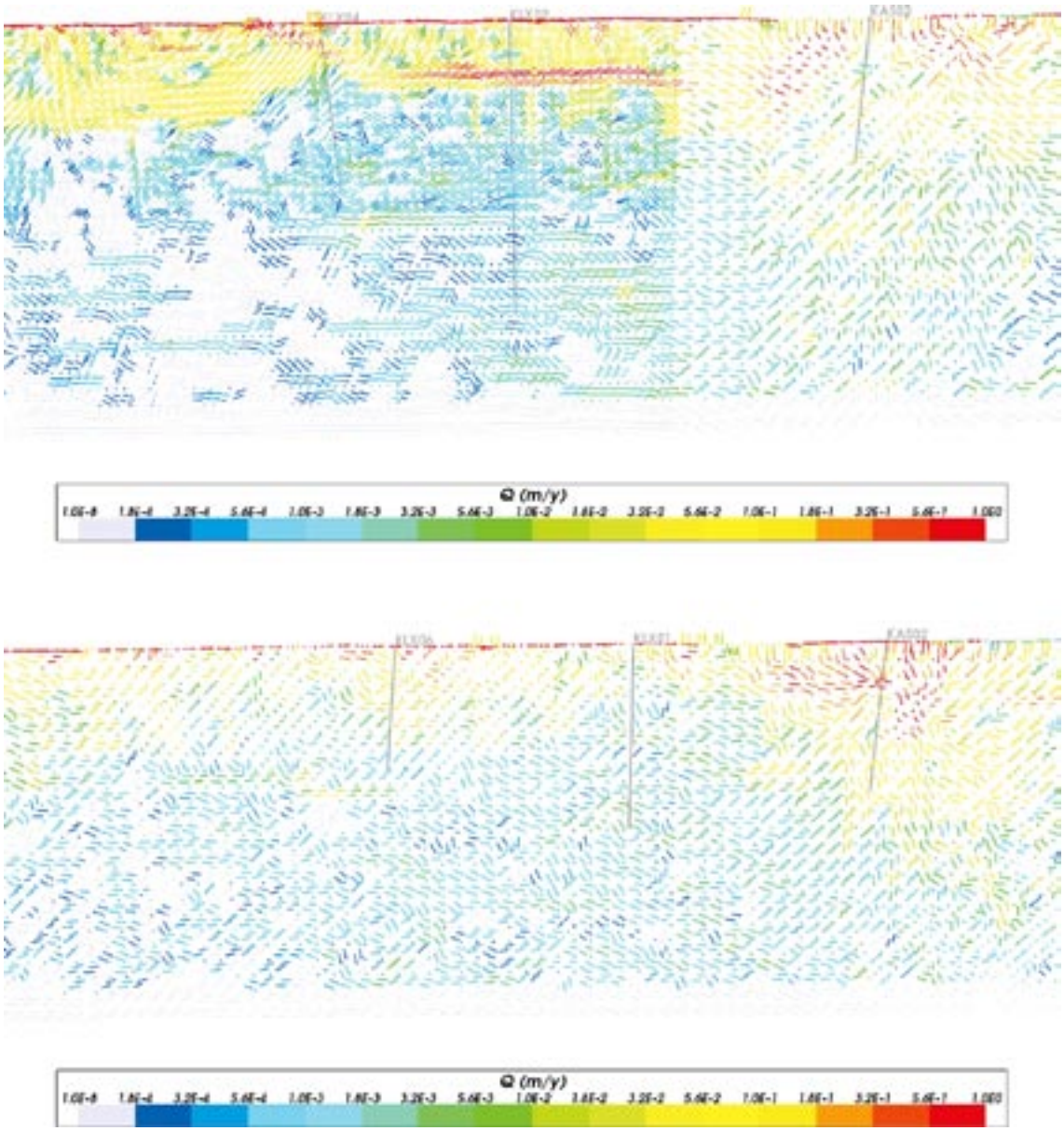

Figure 2-67. *The direction and magnitude of Darcy velocity on vertical E-W slices for an infiltration rate of 165 mm/year and elaborate soil model with Lower Till changed to Gyttja below the sea, and with inflows at the Äspö HRL. The dimensions are about 4 km E-W and 2.3 km top to bottom. The slices are through KLX02 (top) and KLX06 (bottom). The velocity is shown for 2006 AD. Selected borehole trajectories are superimposed, but these do not necessary lie along the vertical section shown, and hence there can be a perspective effect when viewing in 3D.*

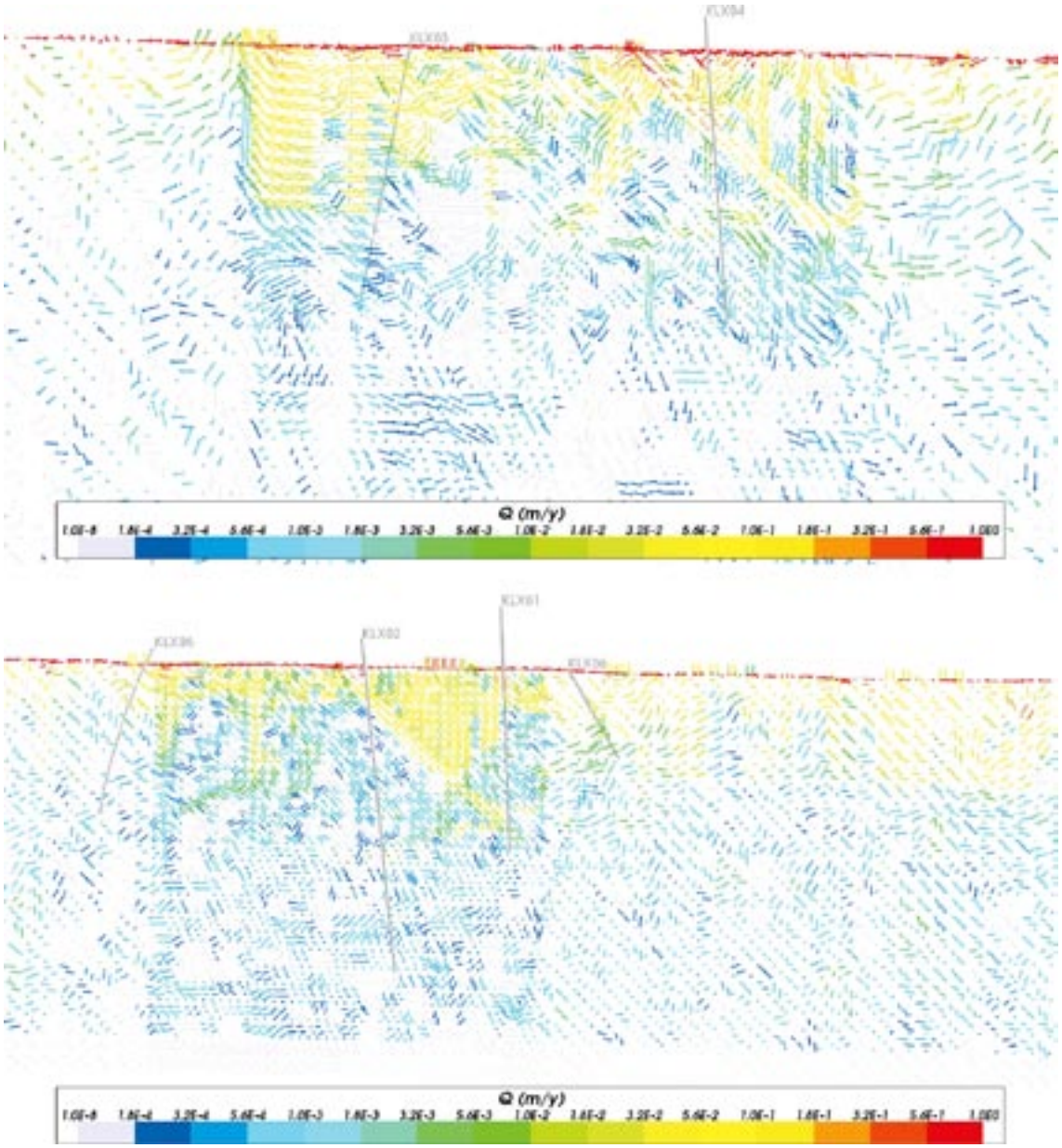

Figure 2-68. *The direction and magnitude of Darcy velocity on vertical N-S slices for an infiltration rate of 165 mm/year and elaborate soil model with Lower Till changed to Gyttja below the sea, and with inflows at the Äspö HRL. The dimensions are about 3.5–4 km N-S and 2.3 km top to bottom. The slices are through KLX03 (top) and KLX06 (bottom). The velocity is shown for 2006 AD. Selected borehole trajectories are superimposed, but these do not necessary lie along the vertical section shown, and hence there can be a perspective effect when viewing in 3D.*

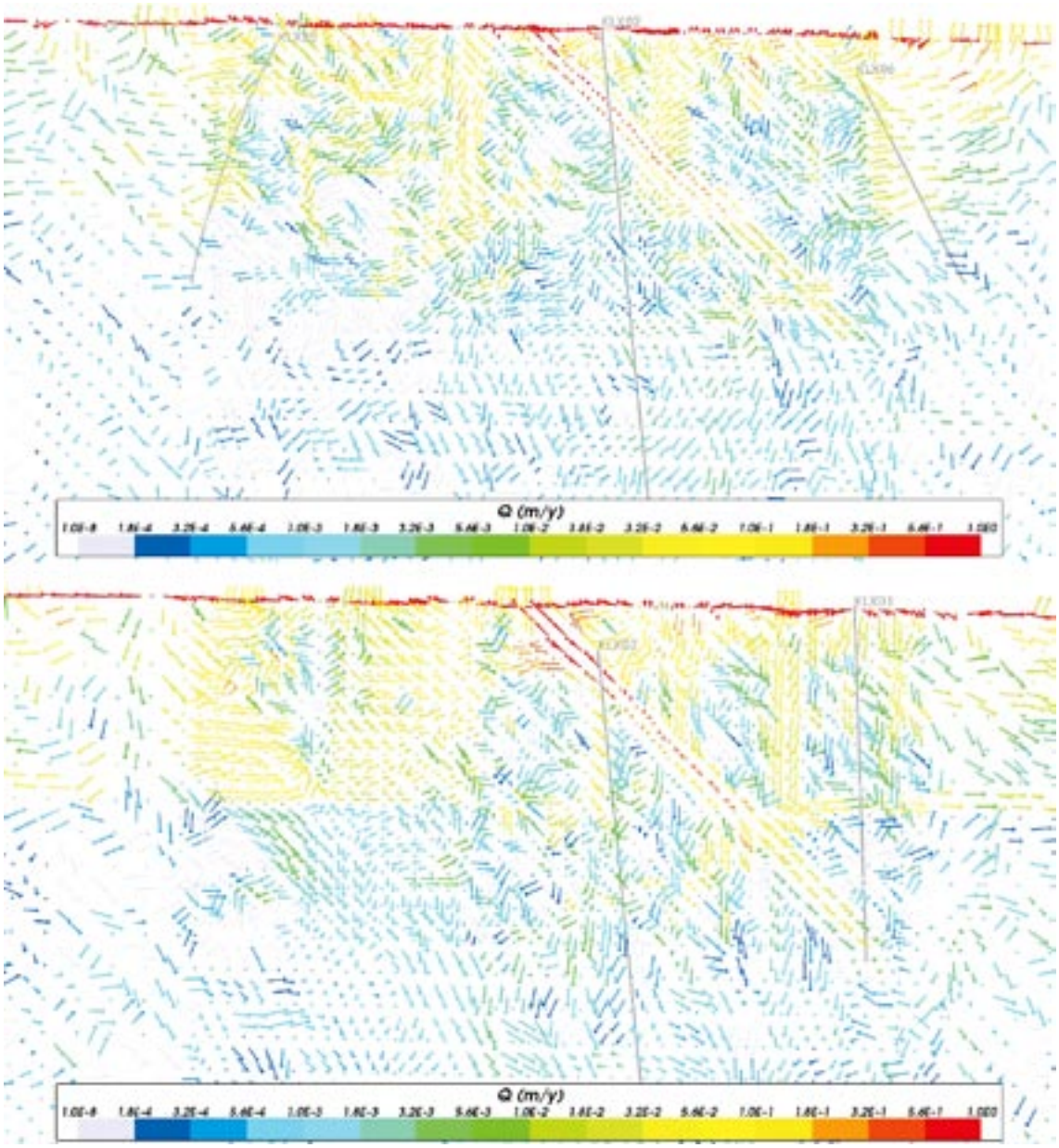

Figure 2-69. *The direction and magnitude of Darcy velocity on vertical N-S slices for an infiltration rate of 165 mm/year and elaborate soil model with Lower Till changed to Gyttja below the sea, and with inflows at the Äspö HRL. The dimensions are about 3.5 km N-S and 2.3 km top to bottom. The slices are through KLX02 (top) and KLX01 (bottom). The velocity is shown for 2006 AD. Selected borehole trajectories are superimposed, but these do not necessary lie along the vertical section shown, and hence there can be a perspective effect when viewing in 3D.*

3 Sensitivity study of modelled chemistry using L 2.1 hydro-geochemistry data

In the SR-Can and SDM calculations for Laxemar 1.2 /Hartley et al. 2006ab/, hydro-geochemical data (the concentrations of various groundwater constituents) and interpreted mixing proportions of certain reference waters were used to test and calibrate the models, and some sensitivity studies were undertaken. It was considered that further sensitivity studies would be valuable in developing understanding, and would provide a foundation for future work. The additional studies are documented in this section. The modelling was based on the reference case from the Laxemar 1.2 modelling. The sensitivities considered are detailed in Section 3.3. Comparisons were made with L 2.1 hydro-geochemistry data, which is discussed in Section 3.2.

3.1 Objectives of the study

The overall objectives of the studies were:

- To examine the variability in the modelled groundwater composition, by considering a number of realisations of the Hydro-DFN model.
- To explore the sensitivity of the modelled composition to key hydraulic properties, boundary and initial conditions.
- To develop the approach for using hydro-geochemical data to test and calibrate the flow models.

Presently it is hypothesised that the groundwater composition is largely the result of mixing rather than reaction /SKB 2006a, pp. 435/, and it is therefore appropriate to compare the observed groundwater composition with the modelled composition in a flow model that represents only transport and mixing, but not reactions. It is considered that the most suitable data for use in this way are those for Total Dissolved Solids (TDS) or salinity, $\delta^{18}O$, and the interpreted presence of marine water (which is mainly based on the ratio Br/Cl augmented by a qualitative interpretation of Mg).

It is recognized that it is difficult to make direct comparisons between modelled groundwater compositions and observations. The rock is heterogeneous. The relatively limited number of water samples come from levels in boreholes where the transmissivity is high enough that sufficient water can be obtained. However, the flow model was not conditioned to match the transmissivities of the sampled horizons. Therefore, it is the trends and larger features in the profiles of groundwater composition that should be considered when comparing model results and observations. The variation between different realisations of the stochastic model of the heterogeneity should be taken into account.

It is expected that this study may improve the foundation for using hydro-geochemical data to test the hydrogeological model, and the approach for making this comparison, and help to understand the limitations of this.

3.2 Geochemistry data

The primary data used in this study were the L 2.1 hydro-geochemistry data available from boreholes in the regional model area. This includes measurements of salinity, ratios of environmental isotopes (Oxygen-18 ($\delta^{18}O$) and Deuterium (δD)), analyses of the rock matrix pore-water and inferred mixing fractions of certain reference waters, down boreholes KLX01, KLX02, KLX03, KLX04, KLX05, KLX06, KLX07, KLX08, KSH01A, KSH02, KSH03A, KAV01, KAV04, KAS02, KAS03, KAS04 and KAS06, under present-day conditions. However, it should be noted that not all types of data were available for all boreholes. In Table 3-1, a summary is presented of the available data for the different boreholes. Figure 3-1 shows the relative location of these boreholes with reference to the road network.

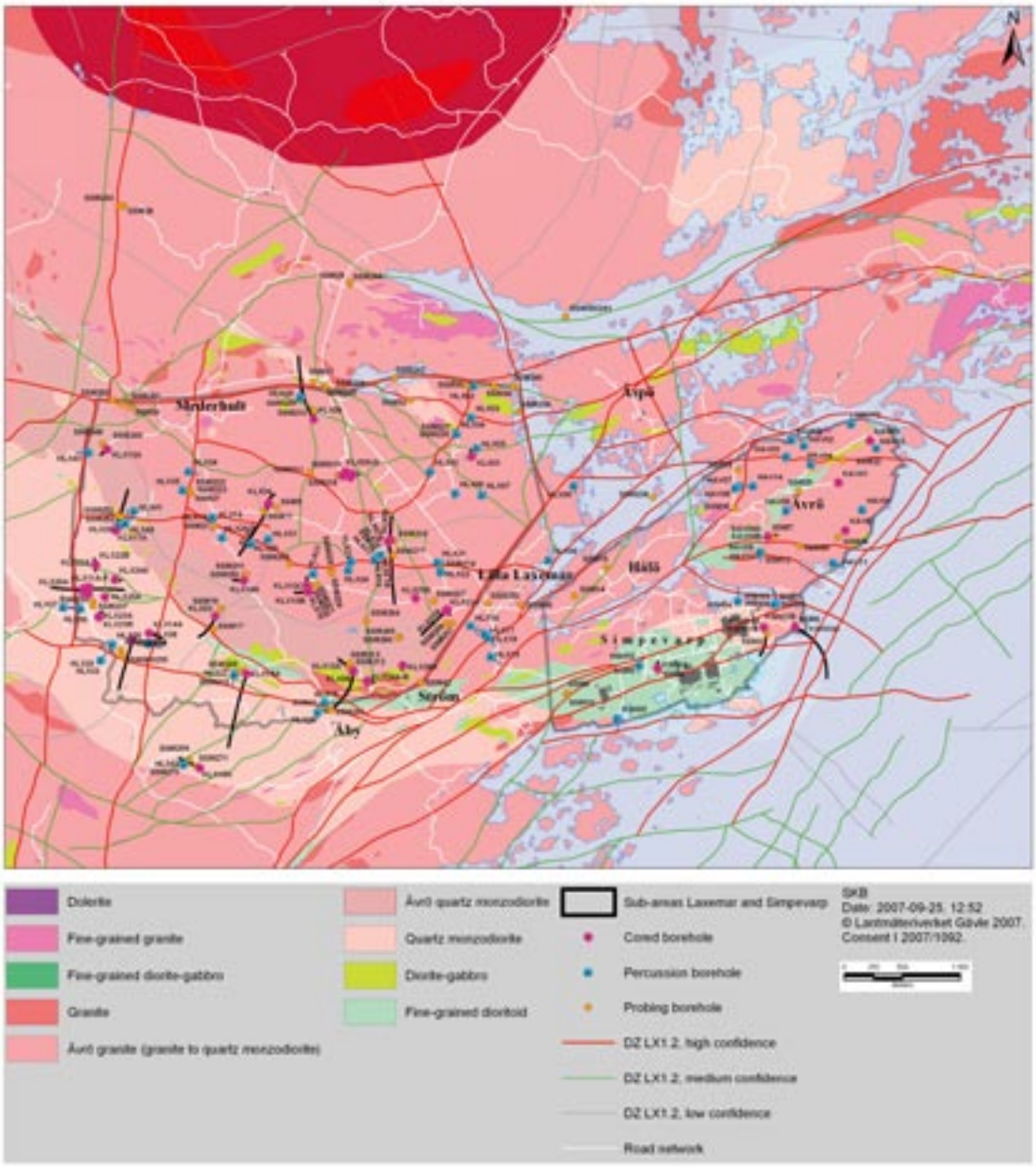

Figure 3-1. *Map showing the location of the sampling points and boreholes in the Simpevarp and Laxemar subareas.*

Table 3-1. Coverage of hydro-geochemistry data of the boreholes used as calibration targets. *) See Table 3-2 for a detailed specification of the quality classification system used for data samples.

Name	Easting	Northing	Salinity	Major ions	Isotopes	Pore water	Water types	No. of samples *) [representative/less representative/ alternative/total nr]	Highest elevation of data (m)	Lowest elevation of data (m)
KLX01	1549923	6367486	yes	yes	yes	–	yes	0/7/3/10	–163	–1,020
KLX02	1549224	6366769	yes	yes	yes	–	yes	0/9/15/24	–2	–1,531
KLX03	1547719	6366113	yes	yes	yes	yes	yes	2/2/8/12	–1	–922
KLX04	1548172	6367077	yes	yes	yes	–	yes	0/3/7/10	7	–944
KLX05	6365633	1548909	yes	yes	yes	–	yes	0/0/10/10	0	–715
KLX06	6367807	1548567	yes	yes	yes	–	yes	0/0/11/11	0	–646
KLX07	6366752	1549207	yes	–	–	–	–	0/0/13/13	6	–598
KLX08	6367079	1548177	yes	–	–	yes	–	0/0/3/3	–62	–285
KSH01A	1552443	6366014	yes	yes	yes	–	yes	0/1/11/12	–68	–843
KSH02	1551529	6365658	yes	yes	yes	–	yes	1/1/12/14	–15	–950
KSH03A	1552711	6366019	yes	yes	yes	–	yes	0/1/11/12	–13	–762
KAV01	1553085	6367258	yes	yes	yes	–	yes	0/1/3/4	–408	–675
KAV04	1552475	6366796	yes	yes	yes	–	yes	1/0/2/3	–40	–761
KAS02	1551420	6367796	yes	yes	yes	–	yes	5/0/0/5	–200	–881
KAS03	1551005	6368217	yes	yes	yes	–	yes	3/5/0/8	–122	–914
KAS04	1551185	6368121	yes	yes	yes	–	yes	2/0/2/4	–119	–377
KAS06	1551509	6367621	yes	yes	yes	–	yes	3/1/0/4	–200	–433

Most of the L 2.1 geochemistry data delivery is the same as the L 1.2 data delivery. Some changes have been made to the classification of how representative samples are for a few measurements. The data in question are for KLX05, KLX06, KLX07 and KLX08 /SKB 2006c/. These data were originally judged by ChemNet to be unsuitable because data were not obtained for all the major ions. However, this meant that there was a lack of data for these four boreholes, and it was therefore decided to use samples that could be representative for TDS. The selected samples all meet the criterion that the drilling water content is less than or close to 5%, which is the same criterion as used by ChemNet for less representative samples. In addition, the L 2.1 delivery also includes representative data samples for Br for many of the boreholes, and there are new rock-matrix pore water data for KLX03 and KLX08.

Limiting the data used to those that met criteria such as a low level of drilling water residue and full coverage of major ions and isotopes would leave a large number of unused samples. Some of these samples are found at elevations where more representative data are missing. It was therefore decided to use some of these samples as supplementary data in this study in order to provide more data for the comparison. Samples with drilling water residue less than 20% were selected, but only if there were no other data available for that particular elevation. Samples having such high contents of drilling water must of course be used with a great deal of caution and may serve only as indicative data.

The delivery of geochemistry data makes use of a colour code in order to show the degree of how representative samples are. In Table 3-2, these codes are defined for samples taken from the ored boreholes.

For ease of presentation, and to allow results for different boreholes to be combined in a plot with colours used to distinguish the values for the different boreholes, a modified scheme is used in the plots here.

- Data samples considered representative or less representative (orange and green colour coding) were grouped together and indicated by large filled squares in the plots.
- The supplementary data (yellow, grey and purple colour coding) were grouped together and indicated by small filled circles in the plots.
- The pore water data are indicated by unfilled circles or a cross (for those boreholes where such data are available).

In the present study, the main focus has been on the results for salinity, Br/Cl-ratio and $\delta^{18}O$, primarily in boreholes KLX01, KLX02, KLX03 and KSH01A.

Table 3-2. Colour coding of geochemistry data used with respect to the degree of how representative samples are in the hydrogeochemistry data set 2.1.

Colour coding	Specification
Orange	Considered representative or suitable. A charge balance of ± 5%. Less than or close to 1% drilling water.
Green	Less representative or of a limited suitability. A charge balance of ± 5%. Less than or close to 5% drilling water. Should be used with caution.
Yellow	Supplementary data used as representative sample for TDS. Less than or close to 5% drilling water (judgement by Ingvar Rhén).
Grey	Supplementary data for elevations where no representative data is present. Less representative or of a limited suitability. Less than or close to 20% drilling water. Should be used with great caution.
Purple	Supplementary data with some problems with Bromide data.
White	Not used in calibration.

3.2.1 Reference waters

Based on the analysis of Hydro-geochemistry data delivery L 2.1 /SKB 2006c/, groundwater compositions were described using a simplified system of four reference waters, which have been used previously in Multivariate mixing and mass-balance (M3) /Laaksoharju et al. 1999, Gómez et al. 2006/ geochemical modelling:

- **Brine water (Brine 1)** corresponds to the most saline sample found inside the Laxemar subarea and is characterised by a very high sulphate content. It represents the sampled deep brine type (Cl = 47,000 mg/L) of water found in KLX02. An old age for the Brine is suggested by the measured ^{36}Cl values indicating a minimum residence time of 1.5 Ma for the Cl component.
- **Glacial water (Glacial 1)** represents a possible melt-water composition from the last glaciation > 11,000 BC. Sampled modern glacial melt water from Norway is used for the major elements and the $\delta^{18}O$ isotope value (−21 ‰ SMOW) is based on measured values of $\delta^{18}O$ in surficial calcite coatings (subglacial $CaCO_3$ deposits precipitates on present rock surface on the Swedish west coast /Tullborg and Larson 1984/. The δD value (−158 ‰ SMOW) is a modelled value based on the equation ($\delta D = 8 \times \delta^{18}O + 10$ for the meteoric water line /Craig 1961/.
- **Littorina water (Littorina 1)** corresponds to the theoretical composition of the Littorina Sea, so it represents an old Baltic sea water.
- **Dilute granitic groundwater (DGW HLX14)** corresponds to a sample from borehole HLX14 within the Laxemar subarea. It was sampled between 17 and –91 m elevation and represents the shallow end member for the local hydro-geochemical model in the Simpevarp area.

In Table 3-3, the major ion components and stable isotope composition for the reference waters modelled in the initial reference case are specified. In the L 1.2 hydro-geochemical site description /SKB 2006b/ alternative compositions are given for each end member. These alternatives were explored in the Forsmark versions 2.2 pre-modelling exercises /Follin et al. 2007/ and the findings of that study guided the following choice of end-members: Brine was set to Brine 1, Littorina is set to Littorina1, Glacial was set to Glacial 2, and Dilute groundwater was based on a groundwater sample from a percussion drilled borehole (HFM03). These reference waters were used in initial work for this sensitivity study.

The compositions of the reference waters were modified slightly for L 2.1. The DGW was based on data from HLX14 (from the top interval of 0–116 m length of borehole) suggesting a slightly higher salinity, and the glacial water was taken to have a more negative value of $\delta^{18}O$ and hence also a more negative value of δD. Alternative samples appropriate to DGW from the top of KLX04 and HLX10 have TDS values of 0.51 and 0.32 g/L, respectively. The modified compositions are shown in Table 3-4. The revised reference waters were used in the later part of the current study.

The equations used to represent the transport of fractions of reference waters, with rock-matrix diffusion, are described in /Hartley et al. 2006b/.

Table 3-3. Groundwater analytical or modelled data used as reference waters for the reference case based on L1.2 /SKB 2006a, Table 9-2/ and F2.1 /Follin et al. 2007/.

	TDS (g/L)	Cl (g/L)	Na (g/L)	K (g/L)	Ca (g/L)	Mg (g/L)	HCO_3 (g/L)	SO_4 (g/L)	Br (g/L)	δD (‰)	$\delta^{18}O$ (‰)
Brine	76.0	47.2	8.5	0.045	19.3	0.002	0.014	0.906	0.323	–44.9	–8.9
Littorina	11.9	6.5	3.674	0.134	0.151	0.448	0.093	0.89	0.022	–38	–4.7
DGW	0.50	0.016	0.064	0.010	0.062	0.014	0.310	0.019	0	–79.6	–11.8
Glacial	0.00	0.001	0	0	0	0	0	0.001	0	–125	–17

Table 3-4. Groundwater analytical or modelled data used as reference waters for Laxemar 2.1 /Gómez et al. 2006/.

	TDS (g/L)	Cl (g/L)	Na (g/L)	K (g/L)	Ca (g/L)	Mg (g/L)	HCO_3 (g/L)	SO_4 (g/L)	Br (g/L)	δD (‰)	$\delta^{18}O$ (‰)
Brine	76.0	47.2	8.5	0.045	19.3	0.002	0.014	0.906	0.323	–44.9	–8.9
Littorina	11.9	6.5	3.674	0.134	0.151	0.448	0.093	0.89	0.022	–38	–4.7
DGW	0.57	0.070	0.138	0.003	0.019	0.005	0.302	0.031	0.000	–78.6	–11.2
Glacial	0.00	0.001	0.000	0.000	0.000	0.000	0.000	0.001	0.000	–158	–21

3.2.2 Salinity profiles in boreholes

Data

Salinity data are available for all of the boreholes of interest (see Table 3-1).

Calibration targets

Salinity is a very important natural tracer because variations in salinity lead to one of the driving forces for groundwater flow.

The salinity for a given water composition in the model is calculated as the sum of the products of each reference water fraction and the salinity of that reference water. The salinities for the reference waters were calculated from the TDS in Table 3-3 or Table 3-4, as appropriate. The modelled salinities were compared with those observed through a visual comparison of the profiles along the boreholes, comparing the trends and major features in the boreholes (see Section 3.1). The modelled reference waters do not minor ions such as Si and Sr. For groundwater samples these generally contribute less than 1% of TDS for saline groundwater samples greater than about 1 g/L, which rises to about 10% of TDS in some samples for very dilute water less than about 0.1 g/L. Hence, ignoring the contribution to TDS from minor ions to TDS is unlikely to have any significant effect on density driven flow or the calibration made here.

Uncertainties in data

Compared to Laxemar 1.2, additional data from more boreholes is available in Laxemar 2.1. For KLX01-KLX04, some supplementary data were included to aid the comparison in regions where no representative data was found. For KLX05-KLX08, it was judged that the salinities of some data samples which were not classified as representative by the ChemNet group, could nevertheless be used. Data from below 1 km is only available for KLX02 (down to an elevation of –1,531 m) and a single sample from KLX01 at –1,020 m. Since Brine is not seen in significant proportion until about –900 m, the data on the dense saline water is quite sparse.

The observed salinity is calculated from the sum of the major ion concentrations. The analytical error on each major ion concentration is about ± 5% except for Cl for which the error is ± 10% to 15% and bromide for which the error is ± 15%. The errors in the Br/Cl ratio are therefore shown as ± 25%.

3.2.3 Water types, major ions and isotopes in boreholes

The reference water mixing fractions provide several different tracers that have entered the groundwater system at different times and with different densities. This provides additional information for testing the model, beyond that provided by salinity alone.

Data

Transport of four reference waters (assumed to be chemically non-reactive fluids) was simulated in the ConnectFlow groundwater flow model. That is, a transport equation is solved for the mass fractions of each of the four reference waters, which describes advection, dispersion and rock matrix diffusion. Together, these mass fractions of reference waters describe the chemical composition of the groundwater at any point, such that dependent quantities such as fluid density, salinity, and ion concentrations. These reference waters have been identified by the hydrogeochemistry group from previous site investigations as well as by Oskarshamn site-specific data /SKB 2006c/. Their compositions are given in Table 3-3 and Table 3-4.

The concentrations of the major ions and the isotope ratios (and the salinity) can be readily determined from the fractions of the reference waters. In this study, these concentrations were compared with those observed, which represent in a sense raw data. This was considered preferable to comparing the calculated mixing fractions of the reference waters with the M3 mixing fractions inferred from the data (using a principal component analysis), because there are additional interpretation uncertainties than can be substantial (at least 10%) associated with the M3 mixing fractions /Gómez et al. 2007/.

It is perhaps worth noting that ConnectFlow could have directly simulated the transport of the major ions and isotopes individually. However, it was more convenient to specify the boundary and initial conditions in terms of the reference waters and formulate the equations in terms of their mass fractions. Also, although some chemical constituents, such as Cl and $\delta^{18}O$, are transported conservatively (i.e. no chemical reaction takes place during transport), others are likely to be non-conservative, such as SO_4, which can be affected by chemical and microbial processes. Mg is not strictly a conservative tracer either, but it is a useful indicator to differentiate between Brine at depth (low Mg concentration) and shallower Littorina water with high Mg concentration. The environmental isotopes δD and $\delta^{18}O$ help to differentiate between Glacial and DGW reference waters (Glacial has lower values), and to some extent $\delta^{18}O$ can be used to distinguish the saline reference waters (Brine from Littorina).

Calibration targets

The main comparison of the results of the flow model with observation is a visual comparison of the trends of salinity, Br/Cl-ratio and $\delta^{18}O$ along the boreholes with interpreted field data. The comparison is made in this way, rather than in terms of a quantitative measure defined at the data points for the reasons discussed in Section 3.1.

Uncertainties in data

The analytical error on each major ion concentration is about ± 5% except for Cl for which the error is ± 10 to 15% and bromide for which the error is ± 15%. The errors in the Br/Cl ratio are therefore shown as ± 25%.

3.2.4 Rock matrix pore water

Data

In L 2.1, new rock matrix pore water data has been delivered for KLX03 and KLX08 /Waber and Smellie 2006ab/ but only for $\delta^{18}O$, δD and Cl. For KLX03, a depth profile of 14 matrix pore water samples, down to an elevation of –932 m, have been reported for the Cl concentration and 11 samples for the components $\delta^{18}O$ and δD. In the very shallow levels in KLX03, in the Ävrö granite, pore water and groundwater from nearby fractures intercepted by the borehole have identical stable isotope compositions. This indicates equilibrium between pore water and groundwater. At greater depth, the pore water isotope composition is strongly enriched in the heavy isotopes compared to the fracture groundwater. Pore water isotope compositions from these depths appear to be more of brine-type composition. The lack of equilibrium between

pore water and fracture groundwater suggests that the pore water contains a component that is significantly older than the fracture groundwater (because the groundwater is predominantly flowing in the fractures), possibly corresponding the remnants of inter-glacial meteoric water.

The behaviour of the chloride concentration in KLX03 is consistent with that of $\delta^{18}O$ and δD. For all three quantities, an equilibrium between the pore water and the fracture water seem to have been established in the shallower bedrock levels within the Ävrö granite, while deeper down (at depths greater than about 450 m) the pore water is more saline than the fracture groundwater /Waber and Smellie 2006a/ suggesting remnants of Littorina water in the matrix.

For KLX08, a depth profile of 18 matrix pore water samples, down to an elevation of –817 m, have been reported for the Cl concentration and 15 samples for the components $\delta^{18}O$ and δD. The situation in KLX08 is different from that in KLX03. At shallow depths, the isotope ratios in the pore water are somewhat less negative than in the groundwater in nearby fractures. This indicates the presence of warm climate water in the rock matrix associated with either Littorina water or older pre-glacial meteoric water. If this water is of Littorina origin, and given that the Littorina period occurred between 6,000 BC and 2,000 BC, then this would suggest rock matrix diffusion is sufficiently slow that the fractures and matrix are far from equilibrium. Based on the diffusion coefficient and matrix porosity in Table 3-6, it implies a diffusion length of about 4 m or more, i.e. matrix blocks between interconnected fractures of 8 m.

Uncertainties in data

In Table 3-5, the number of samples and the estimated error for each of the measured components in the two boreholes are given.

3.3 The Laxemar version 1.2 reference case

The model used in the present sensitivity study was based on the reference case for L 1.2 used in SR-Can /Hartley et al. 2006a/. The properties and conditions for that case are summarised in Table 3-6. A detailed description of the general conditions of the model and the calibration of the reference case is presented in the preliminary site description of the Laxemar subarea version 1.2 /Hartley et al. 2006b/.

In the reference case, and in all the variants considered here, the same top–surface boundary conditions for the water chemistry were used. During early Baltic Ice Lake, Yoldia Sea and Ancylus Lake periods, which were taken to end in 4,500 BC, the recharging water onshore was considered to be a cold climate water, i.e. glacial meltwater. During this period, the offshore water was taken to be a mix of Littorina and cold climate water (Glacial). The mix was determined by the seawater salinity, whose variation over time was specified. The variation over time of the sea-level, which determines which regions are offshore, was also specified. During the subsequent Littorina Sea and current Baltic sea phases, the recharging water onshore was taken to be DGW, and offshore the water was taken to be a mix of Littorina and DGW. Again, the mix was determined by the specified seawater salinity.

Table 3-5. Pore water measurement error of studied components /Waber and Smellie 2006ab/.

Component	KLX03 Pore water error	Nr of samples	KLX08 Pore water error	Nr of samples
$\delta^{18}O$	± 2.1 (‰)	11	± 1.7 (‰)	15
δD	± 23 (‰)	11	± 9.7 (‰)	15
Cl	/Waber and Smellie 2006a/	14	/Waber and Smellie 2006b/	18

Table 3-6. Description of the L 1.2 reference case /Hartley et al. 2006a/.

Property	Description
Domain	Extended regional model domain with 50 m element-size embedded grid in Laxemar, Simpevarp and Ävrö release areas, and 100 m element-size elsewhere.
Initial condition	Initial condition is set to full glacial melt water conditions between ground surface and an elevation of –700 m; then linear gradient to no Glacial and full Brine at –1,500 m elevation. Between –700 m and –1,500 m elevation, the Brine increases linearly from 0 to 100%. Below –1,500 m elevation, a full Brine condition is applied.
Top surface flow boundary condition	Top-surface head equals simulated water table +30% of the difference between the simulated water table and the topographic surface.
Top surface waters	Surface groundwaters are: Glacial and Littorina during early Baltic Ice Lake, Yoldia Sea and Ancylus Lake periods; Meteoric water and Littorina during the Littorina Sea and current Baltic Sea phases. The provided sea-water salinity history is used to determine relative fractions of Littorina and Meteoric waters at the top surface of the model offshore.
Density and viscosity	Density and viscosity calculated as functions of salinity (transient), temperature (fixed), and total pressure (transient).
Transmissivity model	Hydraulic properties obtained from an upscaled regional-scale DFN that is based on the semi-correlated cases of the Hydro-DFN models.
Anisotropy	Anisotropy has been introduced by decreasing the transmissivity of fracture sets Set_A and Set_B by a factor of 10.
HCD confidence	HCD included all zones.
Depth dependency	HRD: The underlying DFN has a step change in properties according to the Hydro-DFN, although a transition elevation of –200 m is used instead of –300 m. For all HRD except HRD(A2), the upscaled conductivity is then reduced by one order of magnitude below an elevation of –600 m.[1)]
	HCD: Implemented as a step function in elevation (0 to –300 m, –300 m to –600 m, < –600 m), conditioned at boreholes against measured transmissivities.
HSD	Homogeneous 3 layer HSD of uniform 1 m thickness per layer.
Flow-wetted surface and Matrix diffusion length	Flow-wetted-surface (FWS) per unit volume for rock matrix diffusion (RMD) above –200 m elevation: a_r = 2.0 m²/m³ for HRD(A2), a_r = 1.0 m²/m³.for HRD(D,E,M), a_r = 1.5 m²/m³ elsewhere. For all rock domains below –200 m elevation, a_r = 1.0 m²/m³.
	Matrix diffusion length into matrix blocks above –200 m elevation, L_D = 0.5 m for HRD(A2), L_D = 1.0 m for HRD(D,E,M), L_D = 0.7 m elsewhere, and L_D = 1.0 m for all rock domains below –200 m elevation.
Kinematic porosity	HRD kinematic porosity is taken from the upscaled regional-scale DFN that is based on the semi-correlated cases of the Hydro-DFN models. However, the 10th percentile values for the 20 m block scale kinematic porosity obtained from the appropriate Hydro-DFN are used as minima of $n_{e,b}$. HCD porosity 10^{-3} for zone thickness W < 100 m and 10^{-2} for $W \geq 100$ m
Diffusion accessible porosity	Diffusion accessible porosity from Byegård upper limit $n_m = 5.9\ 10^{-3}$.
Diffusion coefficient	Intrinsic diffusion coefficient into matrix $D_e = 1.5\ 10^{-13}$ m²/s.
Dispersion lengths	a_l = 40 m, a_t = 5 m.

[1)] In the description of the L 1.2 reference case in /Hartley et al. 2006ab/, it is stated that the reduction was half an order of magnitude, but it was in fact one order of magnitude.

In the development of the L 1.2 flow model, a number of key issues were identified:

- Model domain size.
- Initial and boundary conditions for flow and reference water transport.
- Hydro-DFN parameters.
- Hydraulic properties of HRD and HCD.
- Transport parameters for rock matrix diffusion (RMD) and flow-path calculations.

A significant number of models were created during the L1.2 model development to gain an understanding of how individual model parameters affected the model, and ultimately what ranges of parameters gave a reasonable match to the field data. Based on the findings, a reference case that gave a reasonable match was defined. It should be noted that to obtain a good fit of the hydrochemistry, the conductivity of all HRDs, except HRD(A2), were reduced by one order of magnitude (not half an order of magnitude as stated in /Hartley et al. 2006a/). That work is continued here in a more comprehensive sensitivity analysis.

Some results of the SDM reference case

Some comparisons of the measured data with the simulated constituents for the reference case are shown in Figure 3-2 to Figure 3-6. The calculated profiles of salinity, $\delta^{18}O$, Br/Cl and Cl and Br separately in various boreholes are plotted together with the corresponding observations. As discussed in Section 3.2, the representativity classification of each observation is indicated by the symbol used. The representative and less representative data are indicated by large filled squares, and the supplementary data are indicated by small filled circles. The uncertainties, both in the measured value and in sampling depth, are indicated by error bars. In addition, the characteristic signature values of Brine, Littorina, Glacial, DGW and Modern rain are indicated by dashed vertical lines.

The match of the predicted salinity to observations shown in Figure 3-2 is considered to be about as good as can reasonably be expected, bearing in mind that there will be variations between different realisations of the Hydro-DFN.

The match of the predicted Br/Cl ratio to observations shown in Figure 3-3 is reasonable at depth. However the model predicts a Br/Cl ratio of 0 in the top few hundred metres, whereas, although the observed Br/Cl ratio may fall off from values at depth of about 0.007 (characteristic of Brine) to lower values in the top few hundred metres, the value does not appear to fall off much below 0.003 (a value characteristic of Littorina). It is considered that this difference is probably because in this model the recharging water in recent times (after the Littorina period) is the DGW, which is taken to have a Br concentration of 0 (see Table 3-3). If the recharging water were to be taken to have a Br/Cl ratio about 0.003 (or higher), albeit still with a very low concentration of Cl and therefore also Br, then it would be expected that the predicted values of the Br/Cl ratio in the top few hundred metres would be about 0.003 or higher, and therefore in much better agreement with observations. Figure 3-4 and Figure 3-5 give comparisons of the predicted and observed concentrations of Cl and Br separately.

If all the observations for $\delta^{18}O$, including the supplementary data, are considered (Figure 3-6) there is an indication that there is a feature in the modelled values for KLX02 that is not present in the observations. Although the match of the predicted and modelled values of $\delta^{18}O$ is probably acceptable in the top few hundred metres and at great depth, the modelled value of $\delta^{18}O$ is predicted to drop significantly between about –700 m and –1,400 m elevation, but this behaviour is not shown by the supplementary data for KLX02. However, the small number of data classified as representative and less representative may have a similar trend to that predicted.

It is considered that this possible difference between the predictions and observations may be the result of the assumed initial condition for the groundwater composition in the model. At the start of the simulations (about 10,000 years before the present day), the groundwater water was taken to be Glacial (with $\delta^{18}O$ of about –17) above 700 m, to be a mix of Glacial and Brine (with $\delta^{18}O$ of about –9) with the fraction of Brine increasing linearly with depth between 700 m and 1,500 m, and to be Brine below 1,500 m. Over the 10,000 years simulated, the Glacial component, equivalently the more negative $\delta^{18}O$ component, is flushed out of the region above 700 m, but this component remains below about 700 m.

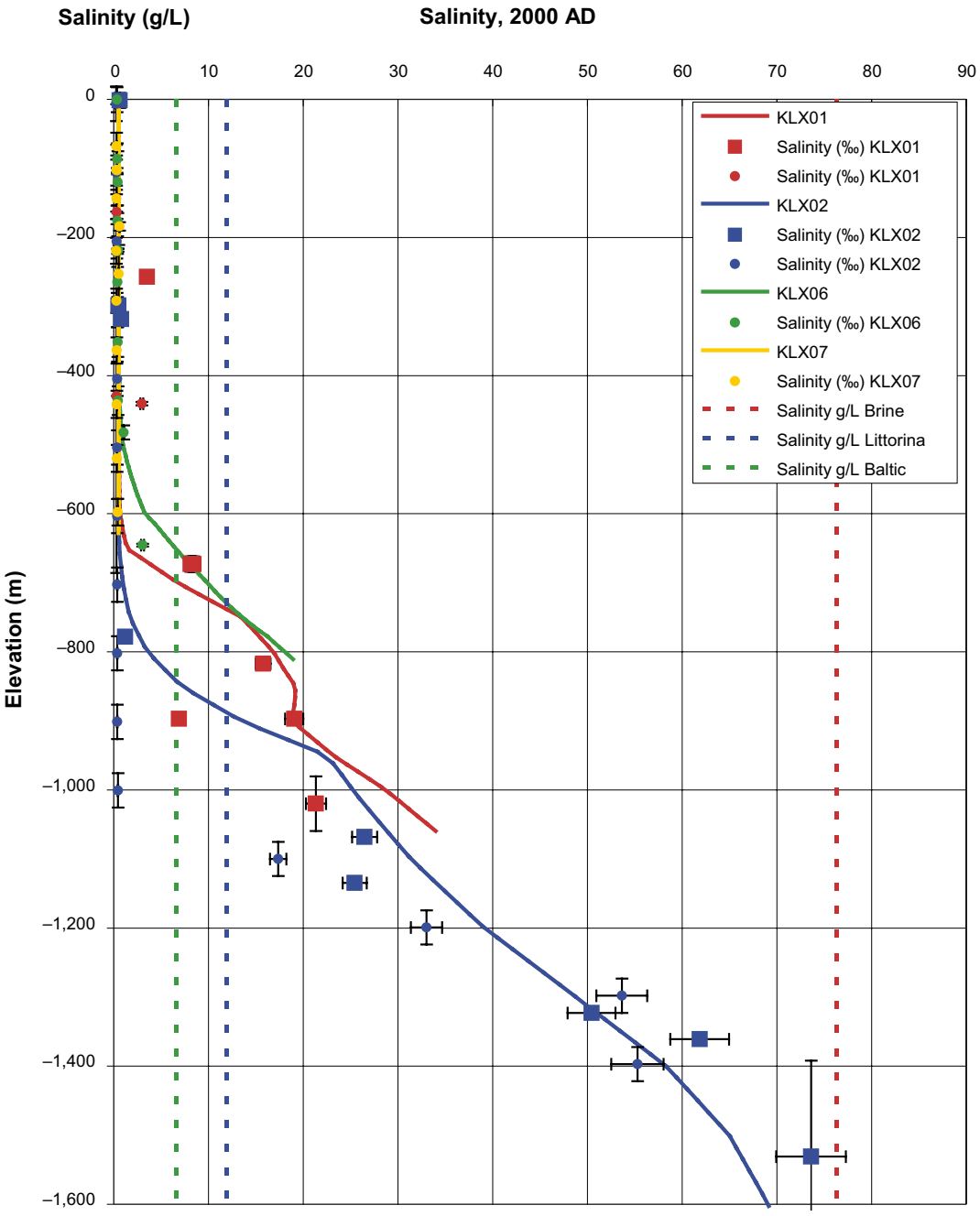

Figure 3-2. *Calculated salinity profiles in the boreholes KLX01, KLX02, KLX06 and KLX07 for the reference case compared to data. Squares correspond to water samples that are representative (Table 3-2: orange) and less representative data (Table 3-2: green), and round dots represent fairly representative TDS data (Table 3-2: yellow) and supplemental data (Table 3-2: grey). The uncertainties in data are indicated with horizontal error bars. The vertical "error bars" indicate elevation interval for sample. In addition, the signature values of salinity for Brine, Littorina and Baltic Sea water are shown. For all displayed boreholes, values are shown from 0 m.a.s.l. down to the full depth of the boreholes. Where the results are very similar for different boreholes, the profiles may be hidden.*

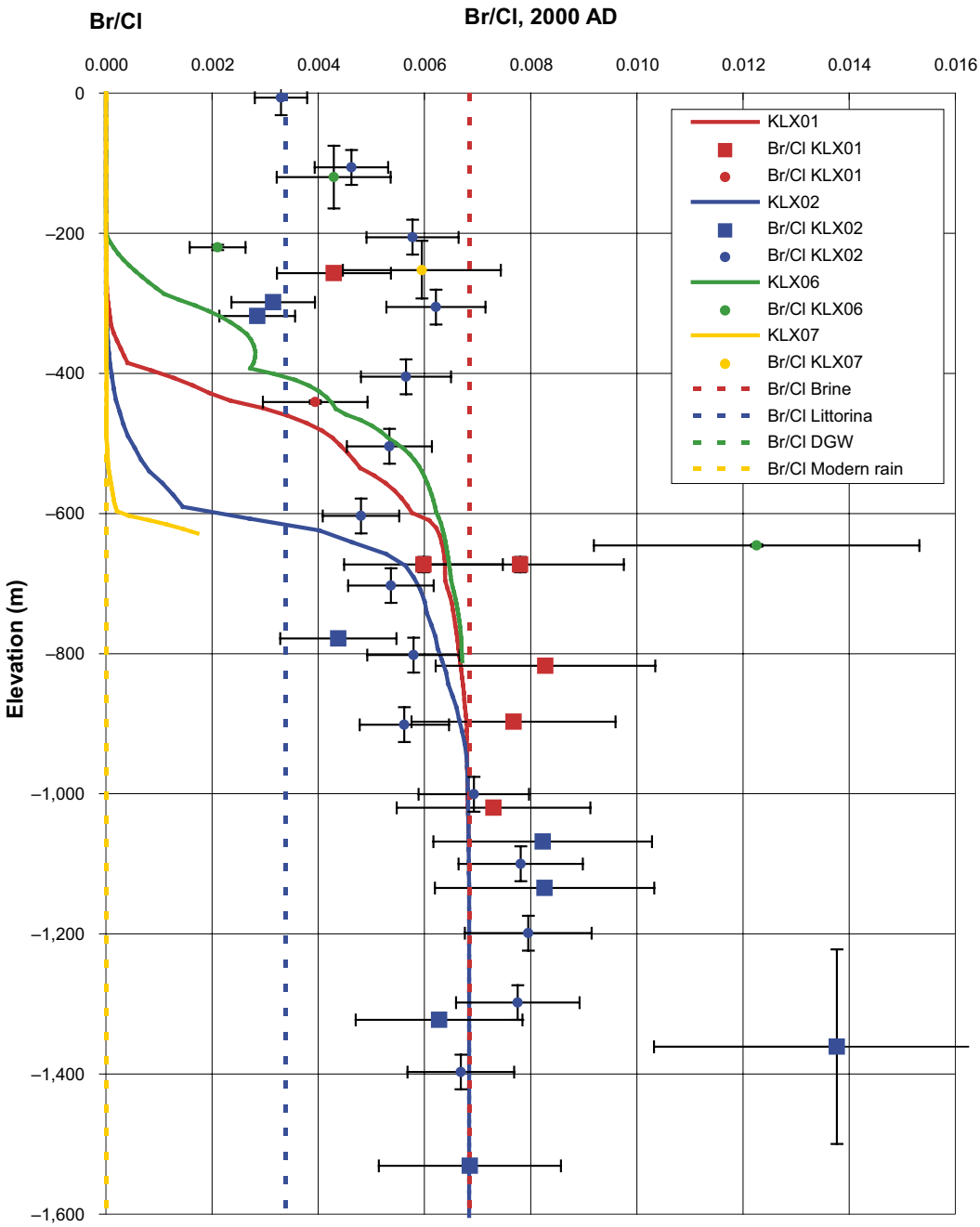

Figure 3-3. *Calculated profiles of the ratio Br/Cl in the boreholes KLX01, KLX02, KLX06 and KLX07 for the reference case compared to data. Squares represent representative (Table 3-2: orange) and less representative data (Table 3-2: green), and round dots represent supplemental data (Table 3-2: grey). The uncertainties in data are indicated with horizontal error bars. The vertical "error bars" indicate elevation interval for sample. In addition, the signature values for Brine, Littorina, Dilute Groundwater, and Modern rain water are shown. The signature value for DGW is 0. For all displayed boreholes, values are shown from 0 m.a.s.l. down to the full depth of the boreholes. Where the results are very similar for different boreholes, the profiles may be hidden.*

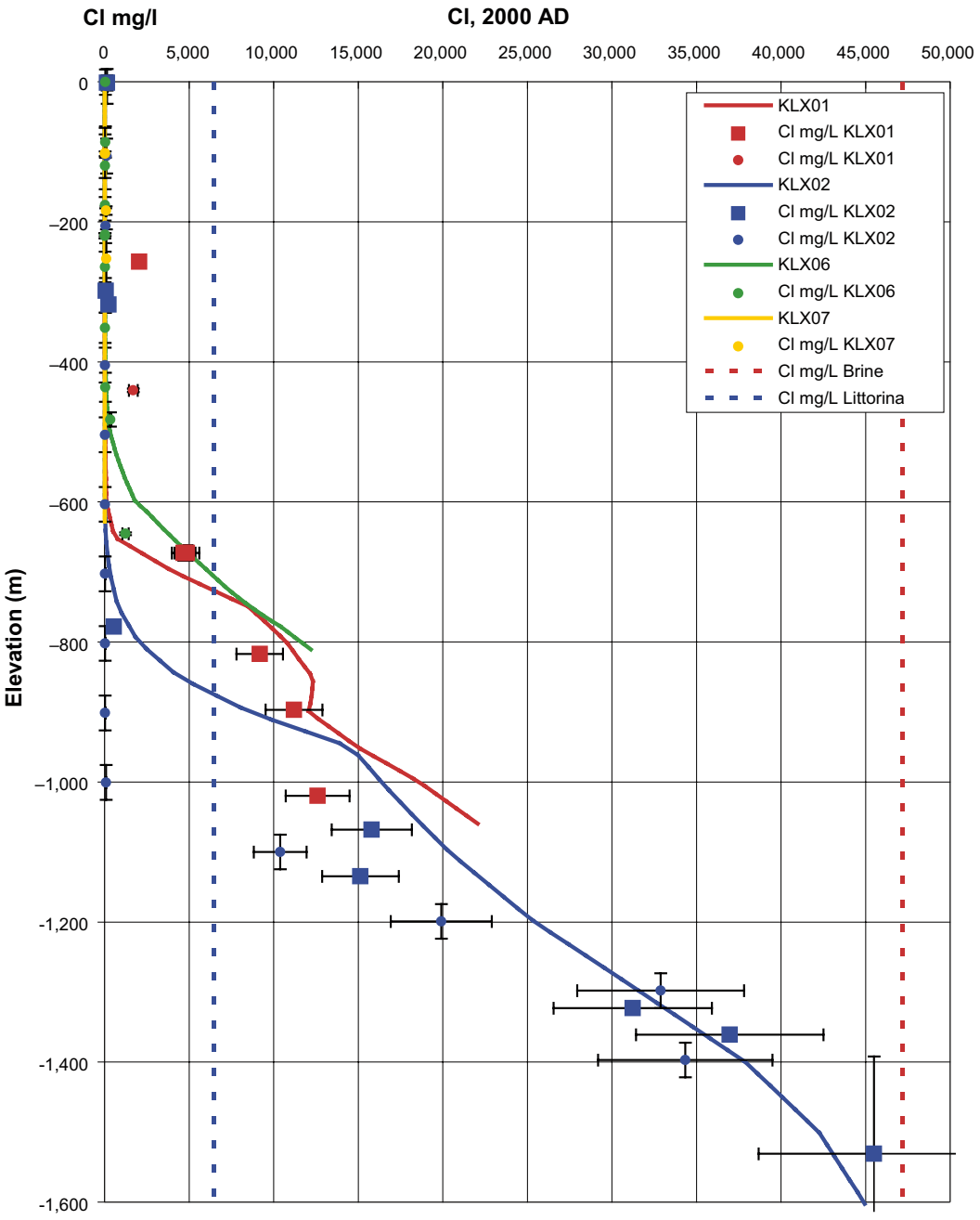

Figure 3-4. *Calculated profiles of Cl in the boreholes KLX01, KLX02, KLX06 and KLX07 for the reference case compared to data. Squares represent representative (Table 3-2: orange) and less representative data (Table 3-2: green), and round dots represent supplemental data (Table 3-2: grey). The uncertainties in data are indicated with horizontal error bars. The vertical "error bars" indicate elevation interval for sample. In addition, the signature values for Brine and Littorina are shown. For all displayed boreholes, values are shown from 0 m.a.s.l. down to the full depth of the boreholes. Where the results are very similar for different boreholes, the profiles may be hidden.*

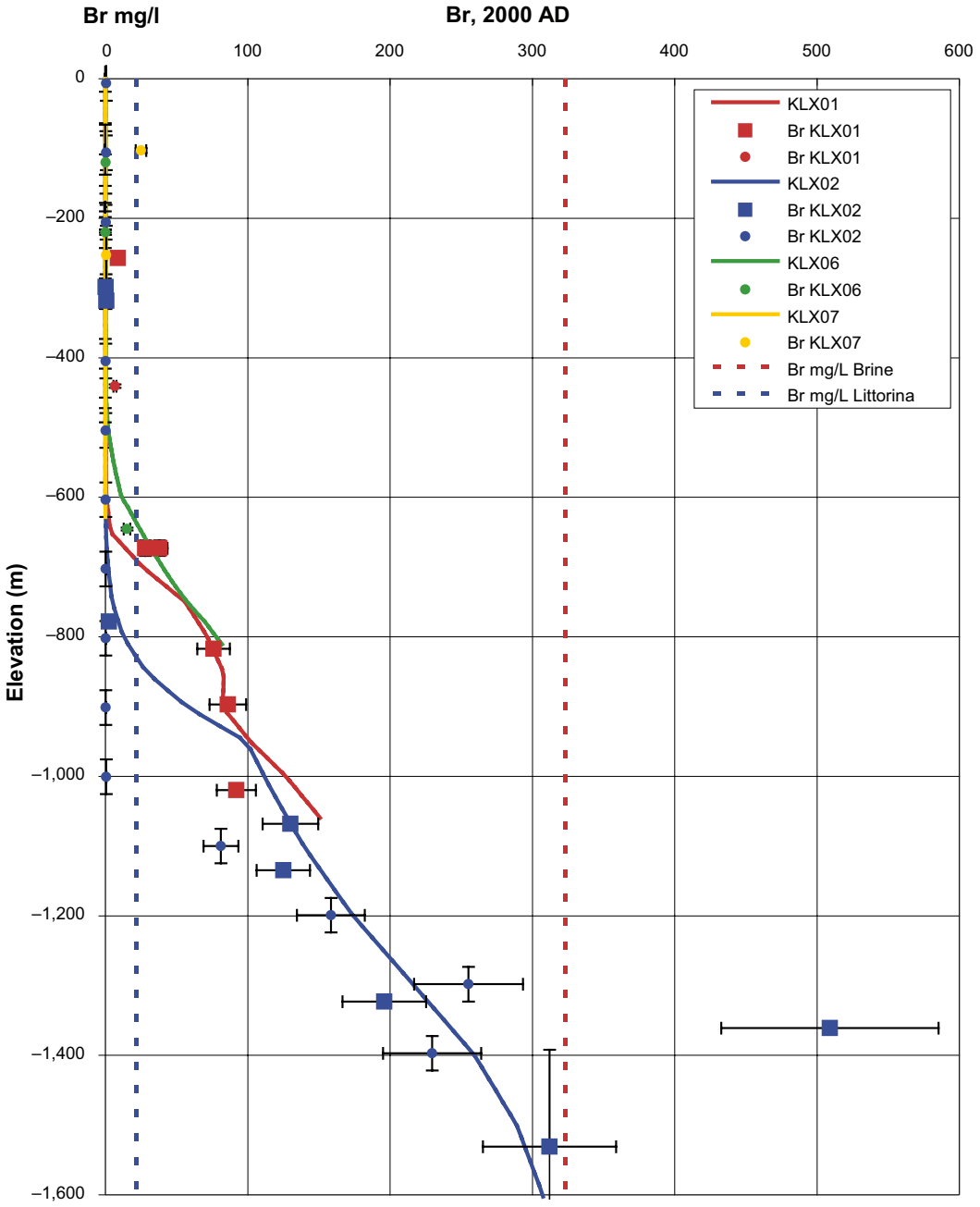

Figure 3-5. *Calculated profiles of Br in the boreholes KLX01, KLX02, KLX06 and KLX07 for the reference case compared to data. Squares represent representative (Table 3-2: orange) and less representative data (Table 3-2: green), and round dots represent supplemental data (Table 3-2: grey). The uncertainties in data are indicated with horizontal error bars. The vertical "error bars" indicate elevation interval for sample. In addition, the signature values for Brine and Littorina are shown. For all displayed boreholes, values are shown from 0 m.a.s.l. down to the full depth of the boreholes. Where the results are very similar for different boreholes, the profiles may be hidden.*

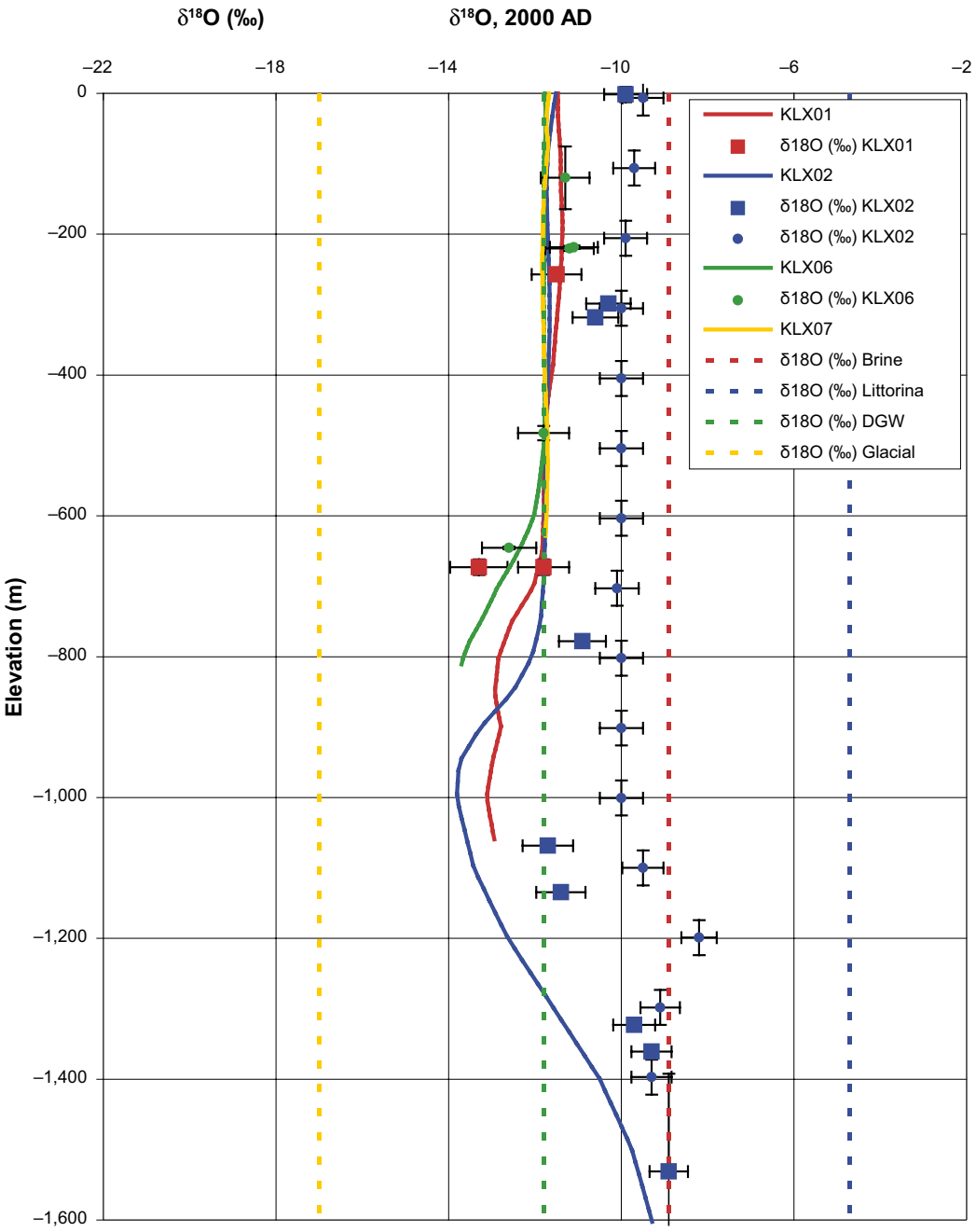

Figure 3-6. *Calculated profiles of $\delta^{18}O$ in the boreholes KLX01, KLX02, KLX06 and KLX07 for the reference case compared to data. Squares represent representative (Table 3-2: orange) and less representative data (Table 3-2: green), and round dots represent supplemental data (Table 3-2: grey). The uncertainties in data are indicated with horizontal error bars. The vertical "error bars" indicate elevation interval for sample. In addition, the signature values for Brine, Littorina, Dilute Groundwater, and Glacial melt water are shown. For all displayed boreholes, values are shown from 0 m.a.s.l. down to the full depth of the boreholes. Where the results are very similar for different boreholes, the profiles may be hidden.*

Had the initial condition between about 700 m and 1,500 m depth corresponded to a water with $\delta^{18}O$ about –11, then it would be expected that, because this water would not have been flushed out during the period simulated, the value of the $\delta^{18}O$ between about 700 m and 1,500 m depth would be in much better agreement with observations. Given that in the simulations carried out, the Glacial component does not appear to have been flushed out over the last 10,000 years, it is not unreasonable that the water at this depth might date from well before the most recent glacial period, i.e. warm climate inter-glacial water. It is also possible that the initial water in the rock matrix might play an important role in controlling the composition of the water in the depth range of interest, and it is likely that the initial water in the rock matrix is older than that in the fractures.

It also appears that the water in the top few hundred metres has a slightly more negative value of $\delta^{18}O$ than that observed (about –12 rather than –10). This may be because the recharging water has slightly too negative a value of $\delta^{18}O$. However, it should be noted that many of the data that suggest that the value of $\delta^{18}O$ in the top few hundred metres is about –10 are the supplementary data, and care should be taken in drawing conclusions on the basis of this data alone.

3.4 Sensitivities

In order to address the objectives of the study,

(i) calculations were undertaken for a number of realisations of the Hydro-DFN and

(ii) various sensitivity studies were carried out in which the hydraulic properties, boundary or initial conditions were varied. These studies addressed the sensitivities to:

- The heterogeneity of the Hydraulic Conductor Domains (HCD). Different values of the standard deviation of the transmissivity distribution were considered.
- The kinematic porosity.
- The depth dependence of the hydraulic conductivity.
- The boundary and initial conditions.

It had been hoped that it might be possible to consider some combined variants, but this was not practicable in the time available.

The calculations carried out are listed in Table 3-7 and Table 3-8 which indicate the main differences from the L 1.2 reference case.

Table 3-7. Performed simulation cases. The symbol (*) indicates that Laxemar 1.2 reference case properties are used; L12_HCD1P3_HRD3a_ddKhalf_ani_HSD1_BC3_MD1_IC1 /Hartley et al. 2006a/.

Sensitivity	HCD	Porosity	Depth dependence	BC	IC	Description
SC_HCD1P3_HRD3a_ddKhalf_ani_HSD1_BC3_MD1_IC1_p.dat SC_HCD1P3_HRD3b_ddKhalf_ani_HSD1_BC3_MD1_IC1_p.dat SC_HCD1P3_HRD3c_ddKhalf_ani_HSD1_BC3_MD1_IC1_p.dat SC_HCD1P3_HRD3d_ddKhalf_ani_HSD1_BC3_MD1_IC1_p.dat SC_HCD1P3_HRD3f_ddKhalf_ani_HSD1_BC3_MD1_IC1_p.dat SC_HCD1P3_HRD3g_ddKhalf_ani_HSD1_BC3_MD1_IC1_p.dat SC_HCD1P3_HRD3h_ddKhalf_ani_HSD1_BC3_MD1_IC1_p.dat SC_HCD1P3_HRD3i_ddKhalf_ani_HSD1_BC3_MD1_IC1_p.dat SC_HCD1P3_HRD3j_ddKhalf_ani_HSD1_BC3_MD1_IC1_p.dat SC_HCD1P3_HRD3k_ddKhalf_ani_HSD1_BC3_MD1_IC1_p.dat SC_HCD1P3_HRD3a_ddKhalf_ani_HSD1_BC3_MD1_IC1_p_refwat_L 1.2.dat	(*)	(*)	(*)	(*)	(*)	10 realisations of the HydroDFN based on Laxemar 1.2 reference case. One realisation is selected for the following sensitivity study. The selected reference case (A) has been re-run with new reference water compositions (L 2.1) in order to be comparable to the remaining variants.
SC_HCD1P3_SD0.5r1_HRD3a_ddKhalf_ani_HSD1_BC3_MD1_IC1_p.dat SC_HCD1P3_SD0.5r2_HRD3a_ddKhalf_ani_HSD1_BC3_MD1_IC1_p.dat SC_HCD1P3_SD0.5r3_HRD3a_ddKhalf_ani_HSD1_BC3_MD1_IC1_p.dat	SD0.5	(*)	(*)	(*)	(*)	Heterogeneous transmissivity distribution within HCD. Lower STD. 3 realisations.
SC_HCD1P3_SD1.0r1_HRD3a_ddKhalf_ani_HSD1_BC3_MD1_IC1_p.dat SC_HCD1P3_SD1.0r2_HRD3a_ddKhalf_ani_HSD1_BC3_MD1_IC1_p.dat SC_HCD1P3_SD1.0r3_HRD3a_ddKhalf_ani_HSD1_BC3_MD1_IC1_p.dat	SD1.0	(*)	(*)	(*)	(*)	Heterogeneous transmissivity distribution within HCD. Medium STD. 3 realisations.
SC_HCD1P3_SD2.0r1_HRD3a_ddKhalf_ani_HSD1_BC3_MD1_IC1_p.dat SC_HCD1P3_SD2.0r2_HRD3a_ddKhalf_ani_HSD1_BC3_MD1_IC1_p.dat SC_HCD1P3_SD2.0r3_HRD3a_ddKhalf_ani_HSD1_BC3_MD1_IC1_p.dat	SD2.0	(*)	(*)	(*)	(*)	Heterogeneous transmissivity distribution within HCD. Higher STD. 3 realisations.
SC_HCD1P3_HRD3a_ddKhalf_ani_HSD1_BC3_MD1_IC1_S21_p.dat	(*)	S21	(*)	(*)	(*)	Increased kinematic porosity.
SC_HCD1P3_HRD3a_ddKhalf_ani_HSD1_BC3_MD1_IC1_S22_p.dat	(*)	S22	(*)	(*)	(*)	Slightly decreased kinematic porosity.
SC_HCD1P3_HRD3a_ddKhalf_ani_HSD1_BC3_MD1_IC1_S23_p.dat	(*)	S23	(*)	(*)	(*)	Decreased kinematic porosity.
SC_HCD1P3_HRD3a_ddKhalf_ani_HSD1_BC3_MD1_IC1_S31_p.dat	(*)	(*)	S31	(*)	(*)	Increased depth dependence of hydraulic conductivity.
SC_HCD1P3_HRD3a_ddKhalf_ani_HSD1_BC3_MD1_IC1_S32_p.dat	(*)	(*)	S32	(*)	(*)	Moderately increased depth dependence of hydraulic conductivity.
SC_HCD1P3_HRD3a_ddKhalf_ani_HSD1_BC3_MD1_IC1_S33_p.dat	(*)	(*)	S33	(*)	(*)	Moderately decreased depth dependence of hydraulic conductivity.
SC_HCD1P3_HRD3a_ddKhalf_ani_HSD1_BC3_MD1_IC1_S34_p.dat	(*)	(*)	S34	(*)	(*)	Decreased depth dependence of hydraulic conductivity.

Sensitivity	HCD	Porosity	Depth dependence	BC	IC	Description
SC_HCD1P3_HRD3a_ddKhalf_ani_HSD1_BCS41_MD1_IC1_p.dat	(*)	(*)	(*)	BCS41	(*)	Higher water table.
SC_HCD1P3_HRD3a_ddKhalf_ani_HSD1_BCS42_MD1_IC1_p.dat	(*)	(*)	(*)	BCS42	(*)	Moderately higher water table.
SC_HCD1P3_HRD3a_ddKhalf_ani_HSD1_BCS43_MD1_IC1_p.dat	(*)	(*)	(*)	BCS43	(*)	Lower water table.
SC_HCD1P3_HRD3a_ddKhalf_ani_HSD1_BC3_MD1_ICS41_p.dat	(*)	(*)	(*)	(*)	ICS41	Higher Brine.
SC_HCD1P3_HRD3a_ddKhalf_ani_HSD1_BCS41_MD1_ICS41_p.dat	(*)	(*)	(*)	BCS41	ICS41	
SC_HCD1P3_HRD3a_ddKhalf_ani_HSD1_BCS42_MD1_ICS41_p.dat	(*)	(*)	(*)	BCS42	ICS41	
SC_HCD1P3_HRD3a_ddKhalf_ani_HSD1_BCS43_MD1_ICS41_p.dat	(*)	(*)	(*)	BCS43	ICS41	
SC_HCD1P3_HRD3a_ddKhalf_ani_HSD1_BC3_MD1_ICS42_p.dat	(*)	(*)	(*)	(*)	ICS42	Lower Brine.
SC_HCD1P3_HRD3a_ddKhalf_ani_HSD1_BCS41_MD1_ICS42_p.dat	(*)	(*)	(*)	BCS41	ICS42	
SC_HCD1P3_HRD3a_ddKhalf_ani_HSD1_BCS42_MD1_ICS42_p.dat	(*)	(*)	(*)	BCS42	ICS42	
SC_HCD1P3_HRD3a_ddKhalf_ani_HSD1_BCS43_MD1_ICS42_p.dat	(*)	(*)	(*)	BCS43	ICS42	
SC_HCD1P3_HRD3a_ddKhalf_ani_HSD1_BC3_MD1_ICS43_p.dat	(*)	(*)	(*)	(*)	ICS43	Higher Brine. Gradual transition.
SC_HCD1P3_HRD3a_ddKhalf_ani_HSD1_BCS41_MD1_ICS43_p.dat	(*)	(*)	(*)	BCS41	ICS43	
SC_HCD1P3_HRD3a_ddKhalf_ani_HSD1_BCS42_MD1_ICS43_p.dat	(*)	(*)	(*)	BCS42	ICS43	
SC_HCD1P3_HRD3a_ddKhalf_ani_HSD1_BCS43_MD1_ICS43_p.dat	(*)	(*)	(*)	BCS43	ICS43	

Table 3-8. Properties of simulation cases performed.

Parameter	Value	Description	Comments
HCD	SD 0.5	STD $Log_{10}(T)$ = 0.5	
HCD	SD 1.0	STD $Log_{10}(T)$ = 1.0	
HCD	SD 2.0	STD $Log_{10}(T)$ = 2.0	
Porosity	S21	$5 \cdot n_{ref}$	
Porosity	S22	$0.5 \cdot n_{ref}$	
Porosity	S23	$0.2 \cdot n_{ref}$	
Depth dependence	S31	A1 = $10 \cdot K_{ref}$ A2 = $5 \cdot K_{ref}$ A3 = $2 \cdot K_{ref}$	
Depth dependence	S32	A1 = $5 \cdot K_{ref}$ A2 = $2.5 \cdot K_{ref}$ A3 = $1 \cdot K_{ref}$	
Depth dependence	S33	A1 = $1/5 \cdot K_{ref}$ A2 = $1/2.5 \cdot K_{ref}$ A3 = $1 \cdot K_{ref}$	
Depth dependence	S34	A1 = $1/10 \cdot K_{ref}$ A2 = $1/5 \cdot K_{ref}$ A3 = $1/2 \cdot K_{ref}$	
BC	(*)	Water table – 0.3	L 1.2 reference case
BC	BCS41	DEM	
BC	BCS42	Water table – 0.6	
BC	BCS43	Water table – base	
IC	(*)	Glacial: 0 to –700 m.a.s.l. Brine: below –1,500 m.a.s.l. Linear transition in between	L 1.2 reference case
IC	ICS41	Glacial: 0 to –200 m.a.s.l. Brine: below –1,000 m.a.s.l. Linear transition in between	
IC	ICS42	Glacial: 0 to –1,100 m.a.s.l. Brine: below –1,900 m.a.s.l. Linear transition in between	
IC	ICS43	Glacial: 0 to –200 m.a.s.l. Brine: below –1,900 m.a.s.l. Linear transition in between	

3.4.1 Sensitivity to stochastic Hydro-DFN realisations

In the Site Descriptive Modelling (SDM) of Laxemar version 1.2, hydro-geochemical data and interpreted mixing fractions were used to test and calibrate the models. The hydraulic properties of the rock mass, i.e. the HRD regions, were derived using a methodology based on Hydro-DFN models. In the SDM study, the Hydro-DFN models were based on borehole data. A number of hydraulic rock domains were identified based on variations in fracture properties between boreholes that intercept the different rock domains. Different geological and hydraulic fracture properties were interpreted for the different rock domains to obtain the model parameters, and some uncertainties were quantified explicitly such as the relationship between fracture size and transmissivity. The best fit to observations was found for a semi-correlated transmissivity model. The reference case ECPM model described in the SDM work and one of the realisations in this sensitivity section use HRD hydraulic conductivities from an upscaled DFN model divided into several volumes. The hydraulic properties (hydraulic conductivity tensor, kinematic porosity and flow-wetted surface) of the HRD of the reference case are obtained from one realisation of the Hydro-DFN.

In this study, calculations were made for 10 realisations of the Hydro-DFN model in order to better understand the variability in the modelled groundwater composition. The calculations used the reference waters given in Table 3-3.

Some of the results for the 10 realisations are presented in Figure 3-7 to Figure 3-18. The calculated profiles of salinity, $\delta^{18}O$ and Br/Cl in boreholes KLX01, KLX02, KLX03 and KSH01A are plotted together with the corresponding observations. As discussed in Section 3.2, the representativity classification of each observation is indicated by the symbol used. The representative and less representative data are indicated by large filled squares, and the supplementary data are indicated by small filled circles. The uncertainties, both in the measured value and in sampling depth, are indicated by error bars. In addition, the characteristic signature values of Brine, Littorina, Glacial, DGW and Modern rain are indicated by dashed lines.

For each borehole, the predicted results for the different realisations have very similar trends. In most cases, the profiles of a particular quantity in a borehole have a fairly similar but slightly displaced shape for the different realisations. However, this does mean that in regions where a quantity is changing the value at a particular depth may vary significantly between realisations. This highlights the difficulty of making point-wise comparisons of predicted and observed concentrations. For $\delta^{18}O$, the pattern above about –600 m elevation in KLX01, KLX02 and KLX03 (Figure 3-15 to Figure 3-17) varies little between realisations by flushing closer to the surface, resulting in similar patterns between all realizations. Below the $\delta^{18}O$ profile is controlled by the Hydro-DFN, resulting in variability between realisations. $\delta^{18}O$ variations between different realisations are larger in KSH01A (Figure 3-19). KSH01A has no deterministic DZs, and so it may be that the chemistry is this borehole is more susceptible to the particular realisation of the lower hydraulic background HRD compare to other boreholes where the local hydrogeology is dominated by the HCD they intersect.

Overall, the match of the different realisations to the observations is very similar to the match for the reference case discussed in Section 3.3, which is not surprising since it is identical to Realisation 1 in this set of Hydro-DFN simulations. The plots for salinity and Br/Cl ratio demonstrate that the depth at which saline water occurs and the transition from Littorina water to Brine dominated salinity can vary by 100 m between realisations, so we should be careful not calibrate models on the position of the saline interface to less than 100 m without considering multiple realisations of the underlying HRD properties.

A demonstration of how the model performs for a complete range of major ions and stable isotopes in comparison to water samples from both fractures and pore water is given in Appendix B. The plots shown there are for a single realisation of the reference case, but with a modified reference water composition as described in Section 3.4.2 since this improved the match.

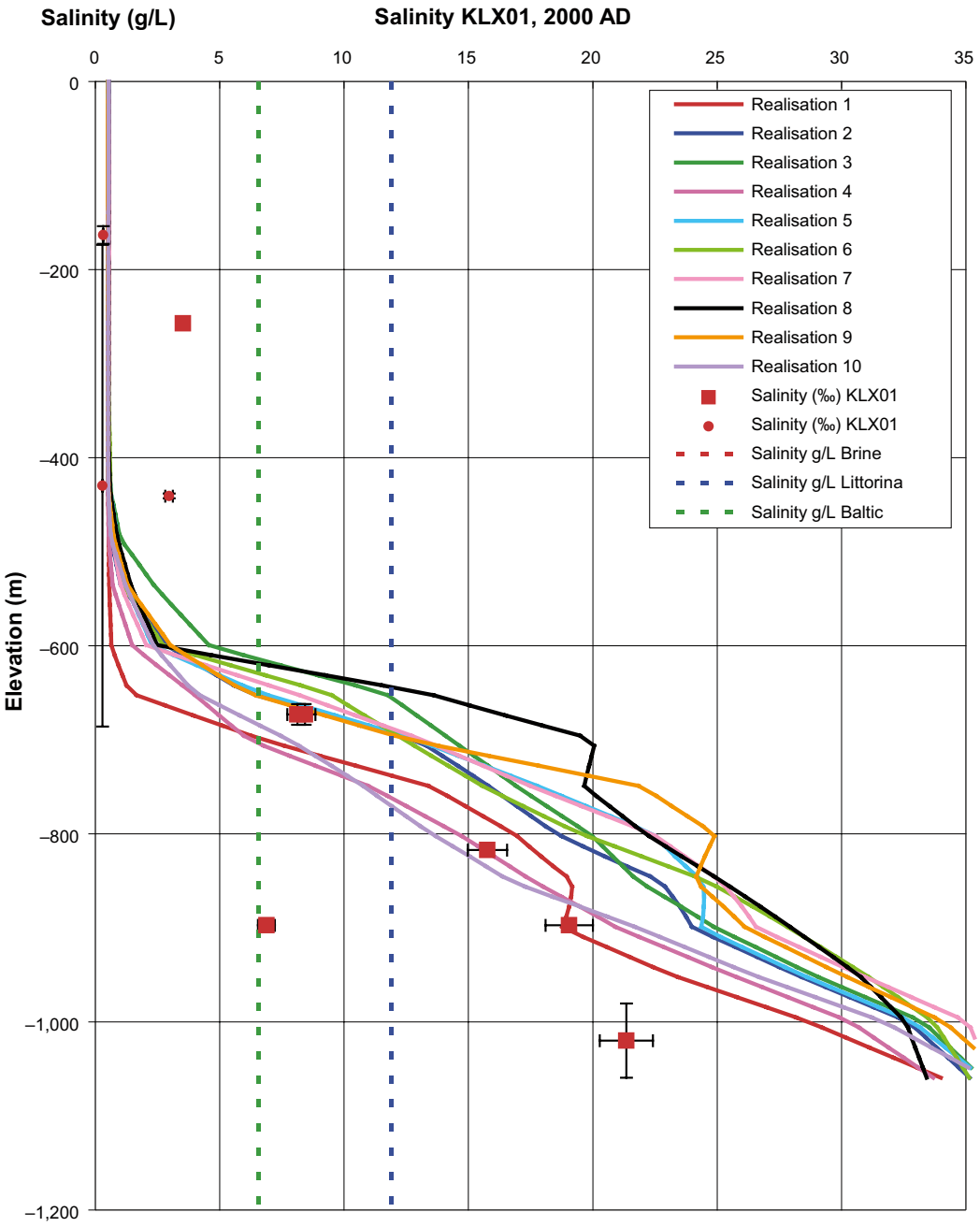

Figure 3-7. *Calculated salinity profiles in the borehole KLX01 for ten realisations of the Hydro-DFN concept compared to data. Squares correspond to water samples that are representative (Table 3-2: orange) and less representative data (Table 3-2: green), and round dots represent fairly representative TDS data (Table 3-2: yellow) and supplemental data (Table 3-2: grey). The uncertainties in data are indicated with horizontal error bars. The vertical "error bars" indicate elevation interval for sample. In addition, the signature values of salinity for Brine, Littorina and Baltic Sea water are shown. The Brine value is out of range.*

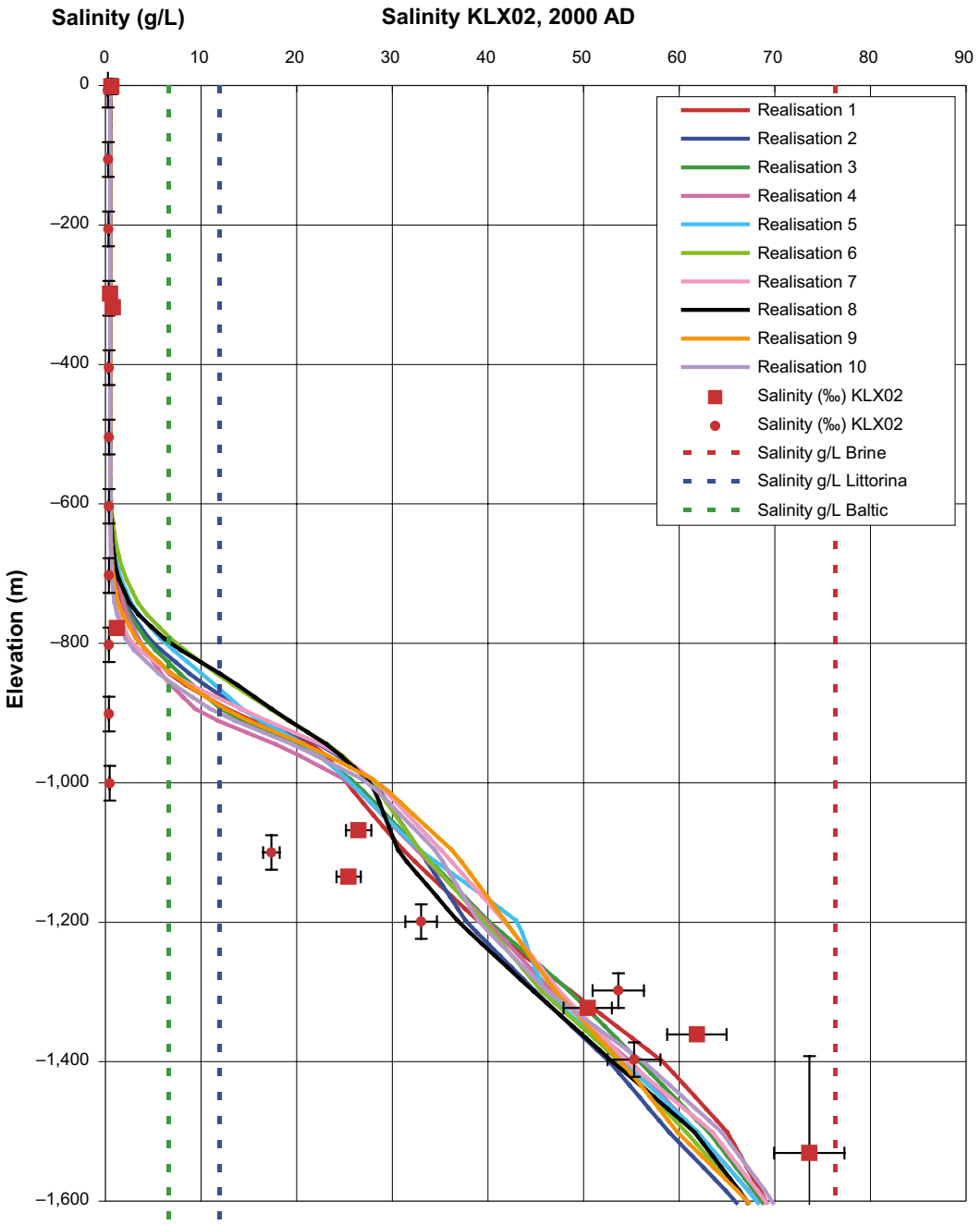

Figure 3-8. *Calculated salinity profiles in the borehole KLX02 for ten realisations of the Hydro-DFN concept compared to data. Squares correspond to water samples that are representative (Table 3-2: orange) and less representative data (Table 3-2: green), and round dots represent fairly representative TDS data (Table 3-2: yellow) and supplemental data (Table 3-2: grey). The uncertainties in data are indicated with horizontal error bars. The vertical "error bars" indicate elevation interval for sample. In addition, the signature values of salinity for Brine, Littorina and Baltic Sea water are shown.*

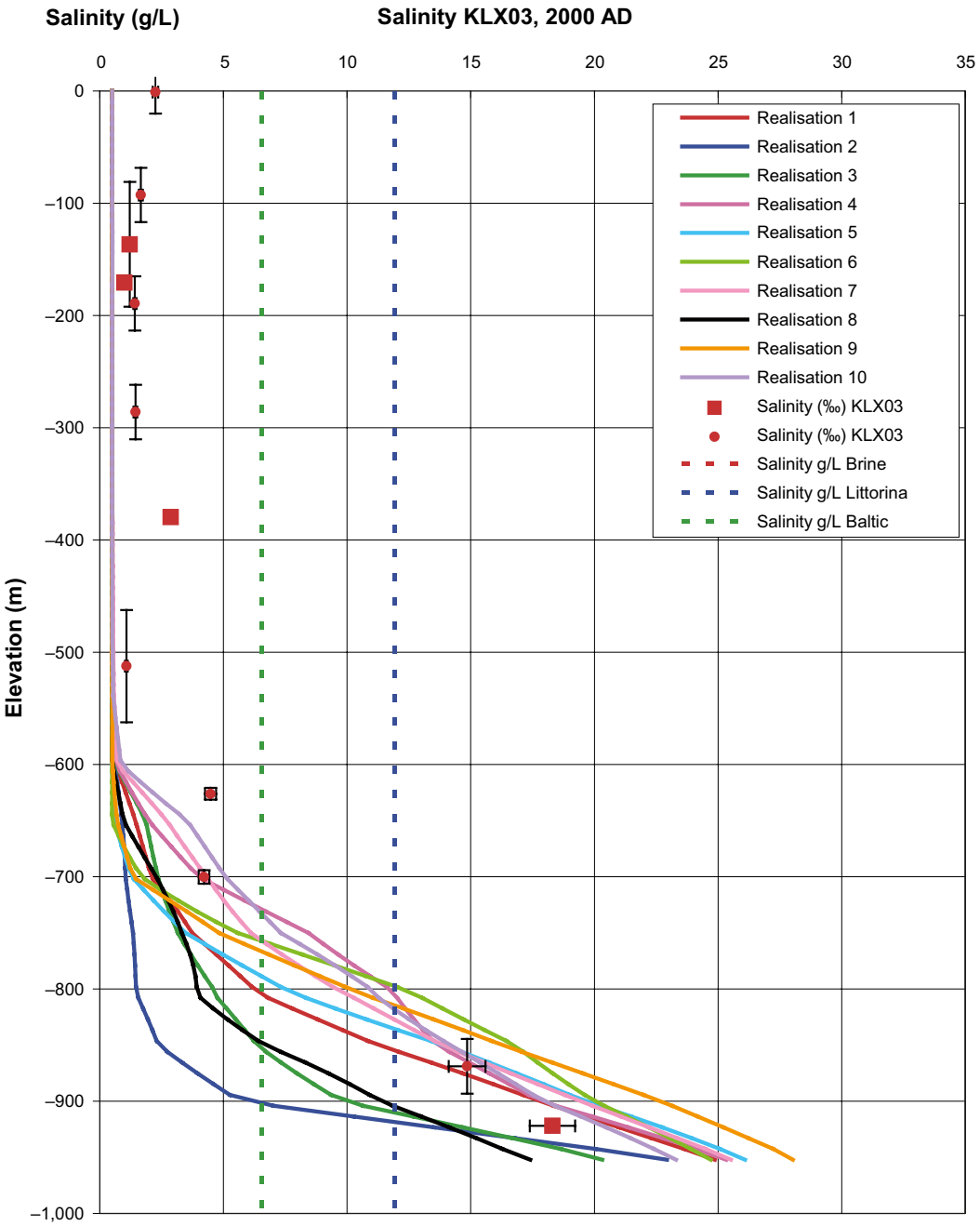

Figure 3-9. *Calculated salinity profiles in the borehole KLX03 for ten realisations of the Hydro-DFN concept compared to data. Squares correspond to water samples that are representative (Table 3-2: orange) and less representative data (Table 3-2: green), and round dots represent fairly representative TDS data (Table 3-2: yellow) and supplemental data (Table 3-2: grey). The uncertainties in data are indicated with horizontal error bars. The vertical "error bars" indicate elevation interval for sample. In addition, the signature values of salinity for Brine, Littorina and Baltic Sea water are shown. The Brine value is out of range.*

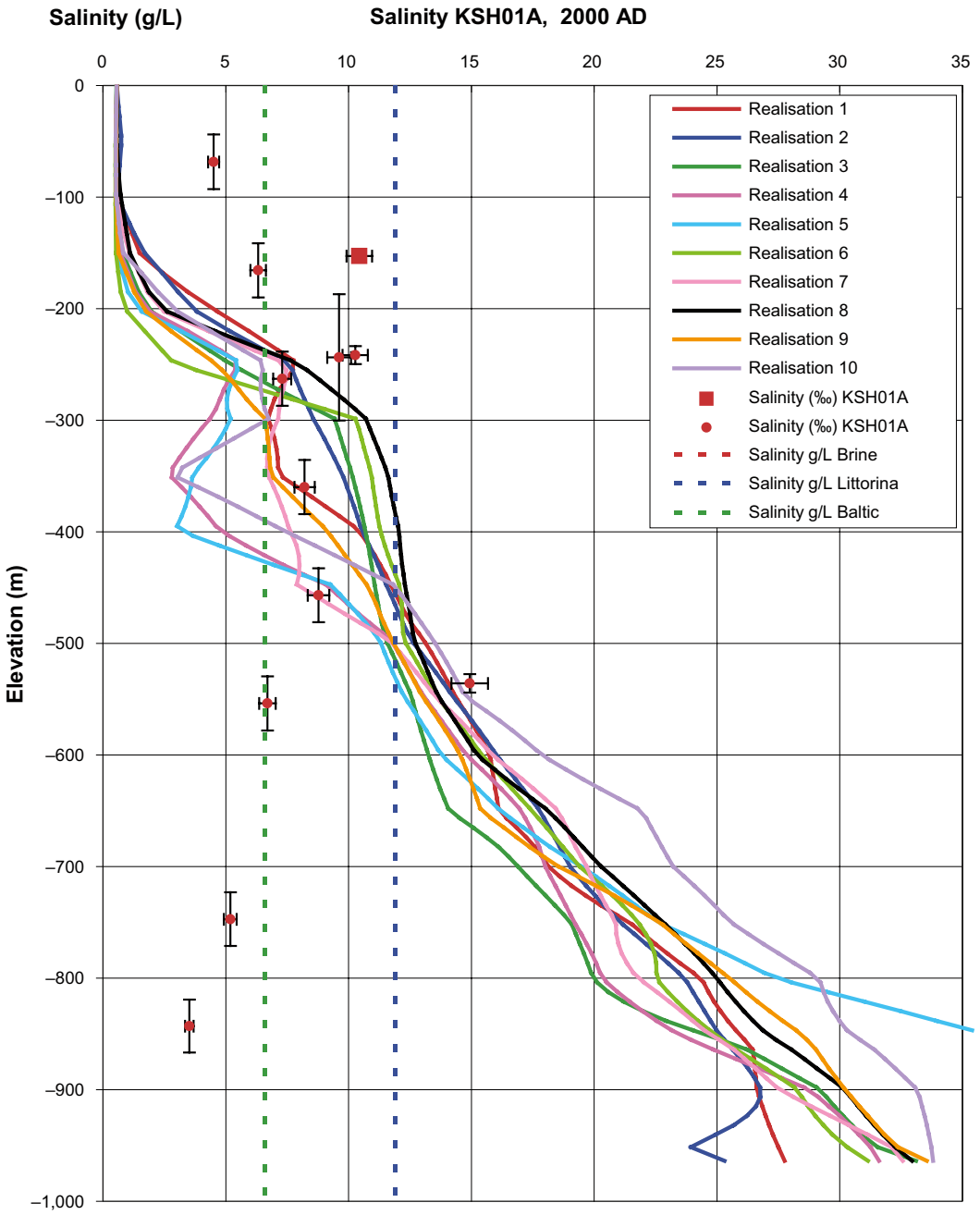

Figure 3-10. *Calculated salinity profiles in the borehole KSH01A for ten realisations of the Hydro-DFN concept compared to data. Squares correspond to water samples that are representative (Table 3-2: orange) and less representative data (Table 3-2: green), and round dots represent fairly representative TDS data (Table 3-2: yellow) and supplemental data (Table 3-2: grey). The uncertainties in data are indicated with horizontal error bars. The vertical "error bars" indicate elevation interval for sample. In addition, the signature values of salinity for Brine, Littorina and Baltic Sea water are shown. The Brine value is out of range.*

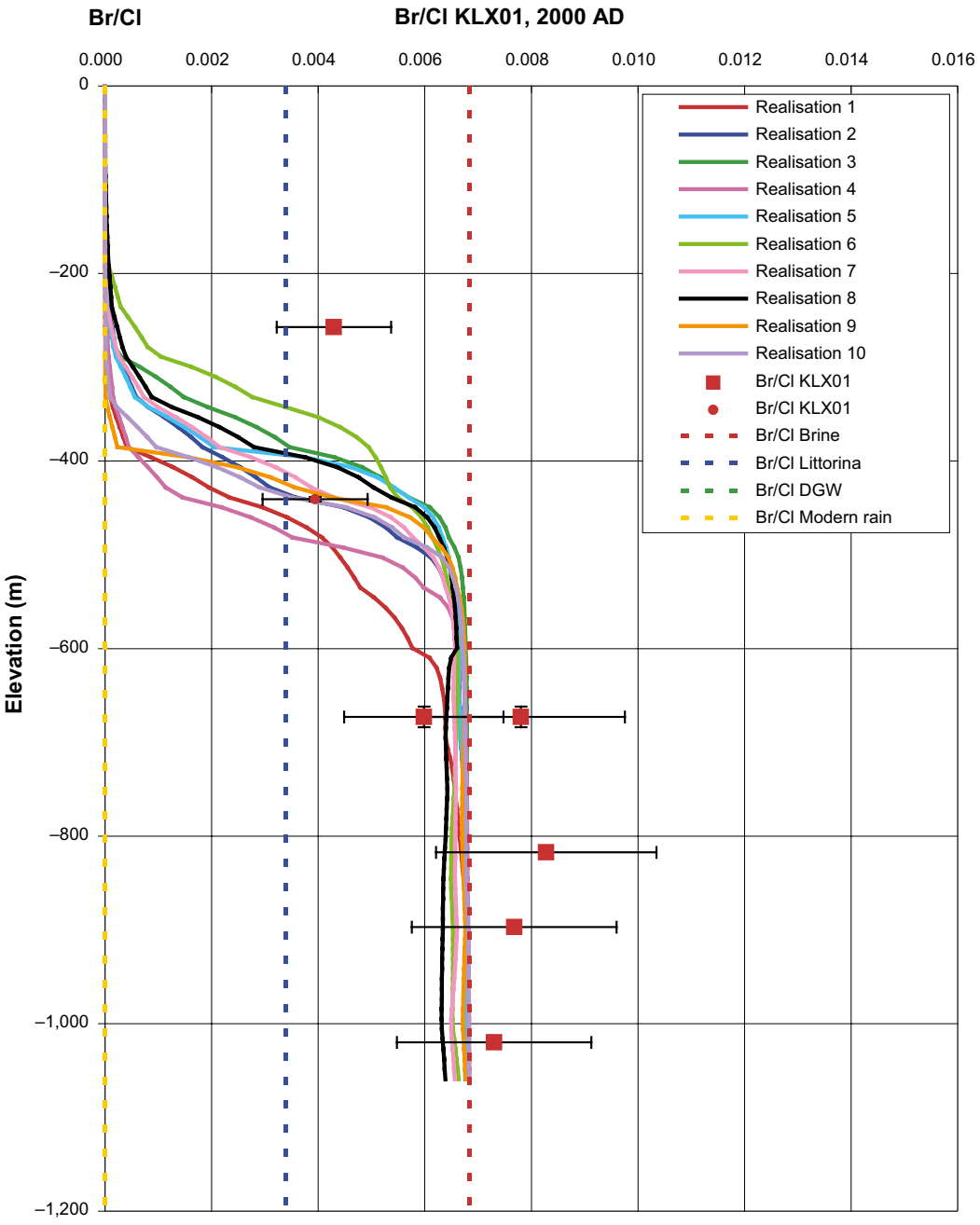

Figure 3-11. *Calculated profiles of the ratio Br/Cl in the borehole KLX01 for ten realisations of the Hydro-DFN concept compared to data. Squares correspond to water samples that are representative (Table 3-2: orange) and less representative data (Table 3-2: green), and round dots represent supplemental data (Table 3-2: grey). The uncertainties in data are indicated with horizontal error bars. The vertical "error bars" indicate elevation interval for sample. In addition, the signature values of salinity for Brine, Littorina, DGW and Modern rain water are shown. The value for DGW is 0.*

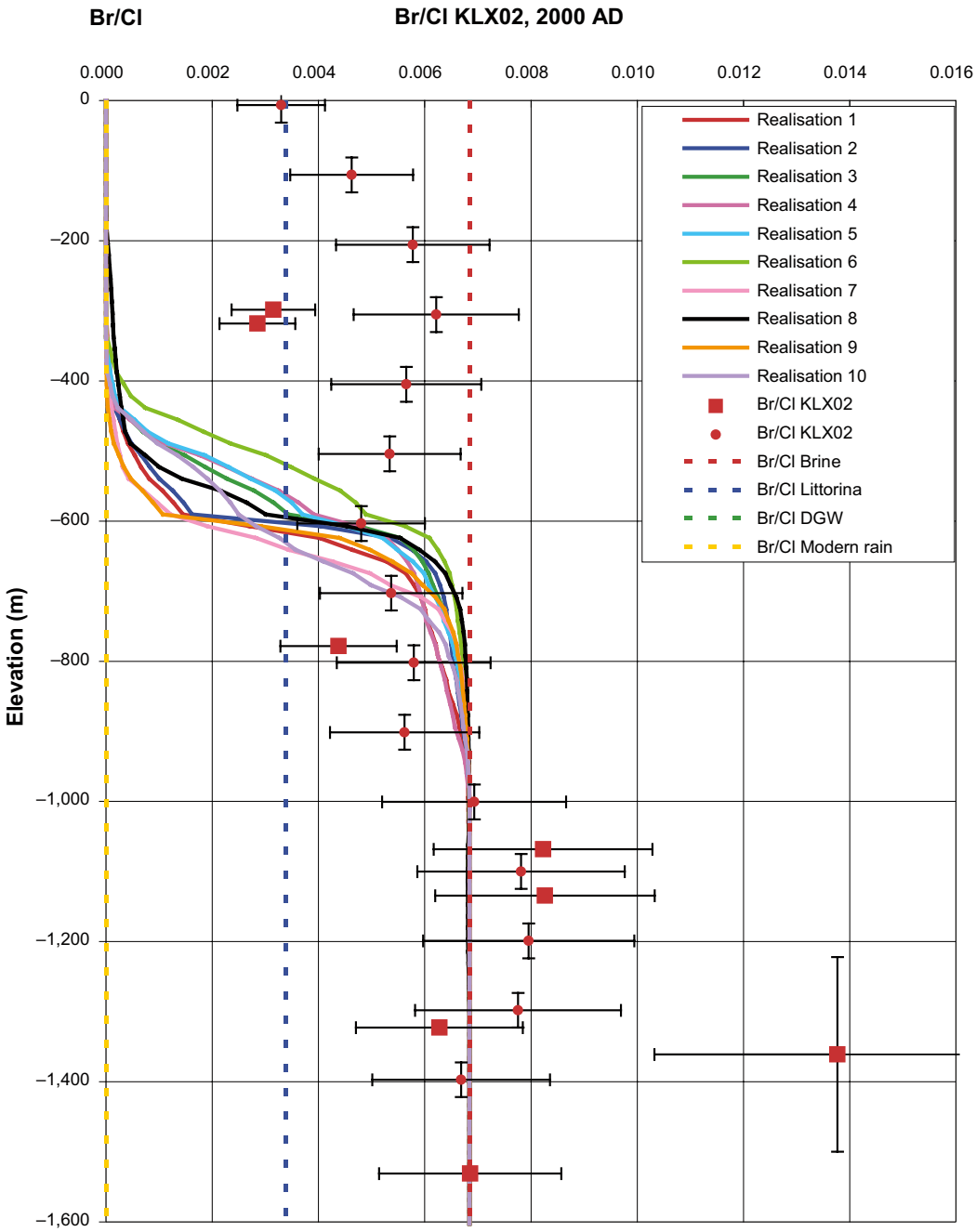

Figure 3-12. *Calculated profiles of the ratio Br/Cl in the borehole KLX02 for ten realisations of the Hydro-DFN concept compared with data. Squares correspond to water samples that are representative (Table 3-2: orange) and less representative data (Table 3-2: green), and round dots represent supplemental data (Table 3-2: grey). In addition, signature values for Brine, Littorina, Dilute Groundwater, and Modern rain water are shown. The value for DGW is 0.*

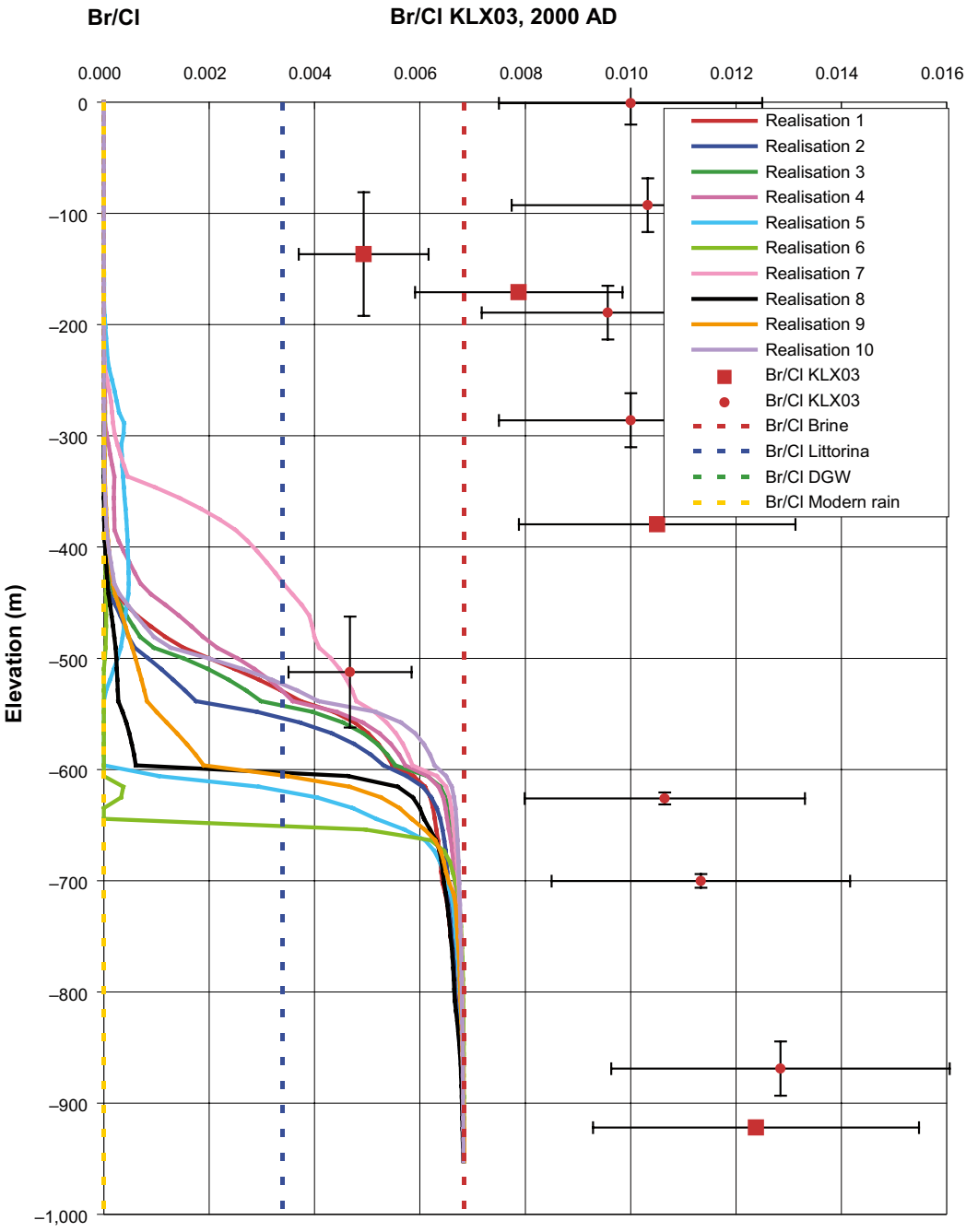

Figure 3-13. *Calculated profiles of the ratio Br/Cl in the borehole KLX03 for ten realisations of the Hydro-DFN concept compared with data. Squares correspond to water samples that are representative (Table 3-2: orange) and less representative data (Table 3-2: green), and round dots represent supplemental data (Table 3-2: grey). In addition, signature values for Brine, Littorina, Dilute Groundwater, and Modern rain water are shown. The value for DGW is 0.*

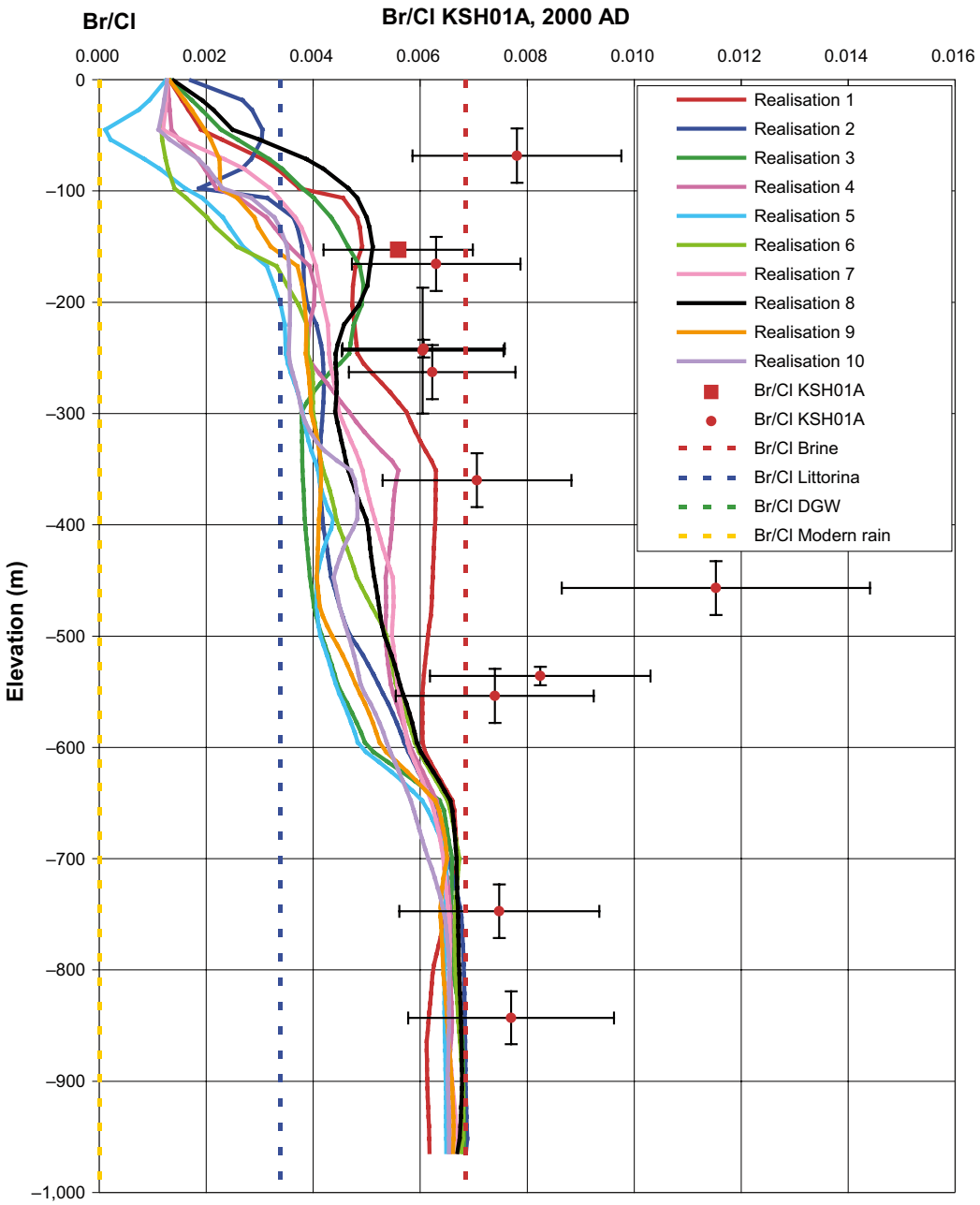

Figure 3-14. *Calculated profiles of the ratio Br/Cl in the borehole KSH01A for ten realisations of the Hydro-DFN concept compared with data. Squares correspond to water samples that are representative (Table 3-2: orange) and less representative data (Table 3-2: green), and round dots represent supplemental data (Table 3-2: grey). In addition, the signature values for Brine, Littorina, Dilute Groundwater, and Modern rain water are shown. The value for DGW is 0.*

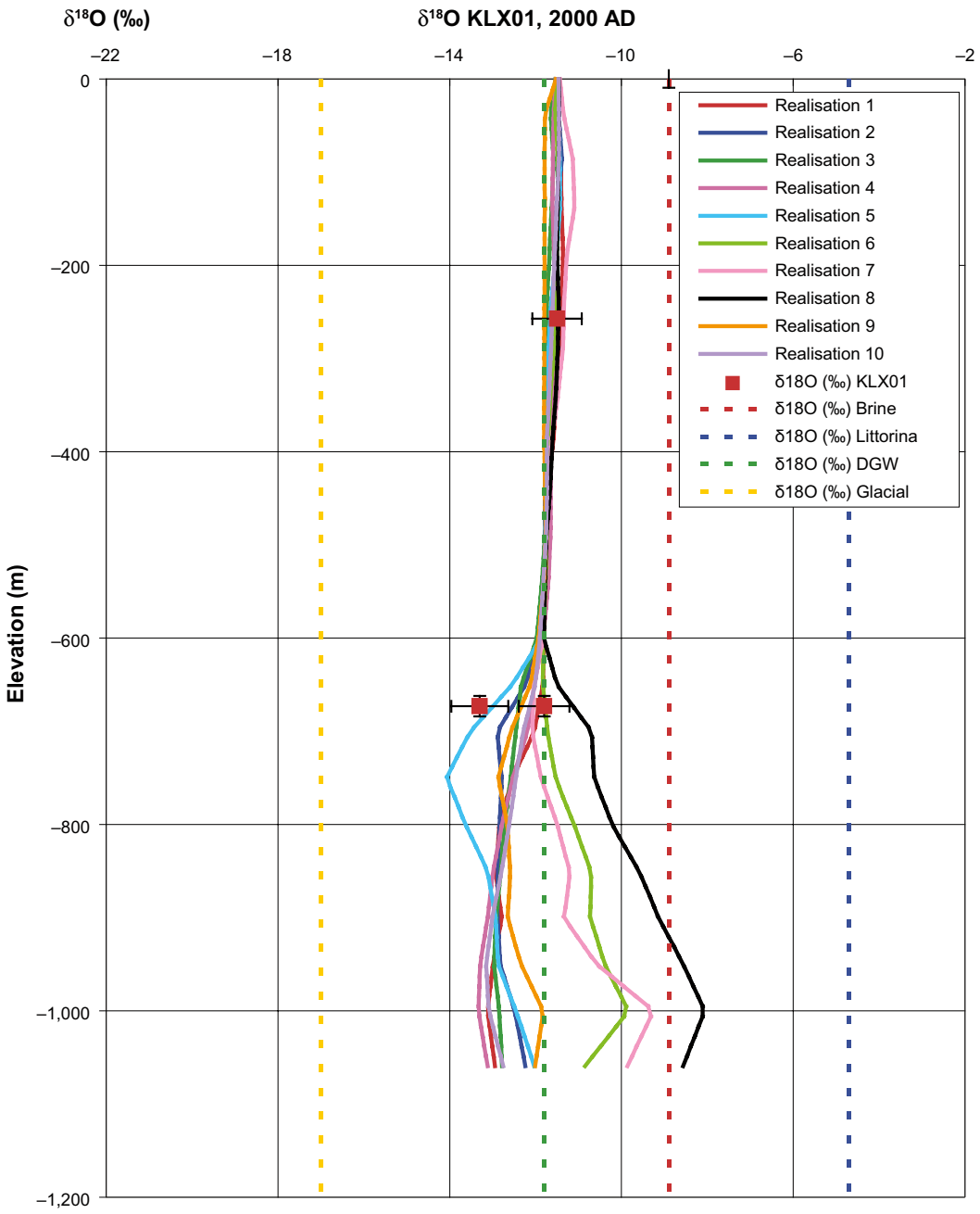

Figure 3-15. *Calculated profiles of $\delta^{18}O$ in the borehole KLX01 for ten realisations of the Hydro-DFN concept compared with data. Squares correspond to water samples that are representative (Table 3-2: orange) and less representative data (Table 3-2: green), and round dots represent supplemental data (Table 3-2: grey). In addition, signature values for Brine, Littorina, Dilute Groundwater, and Glacial water are shown.*

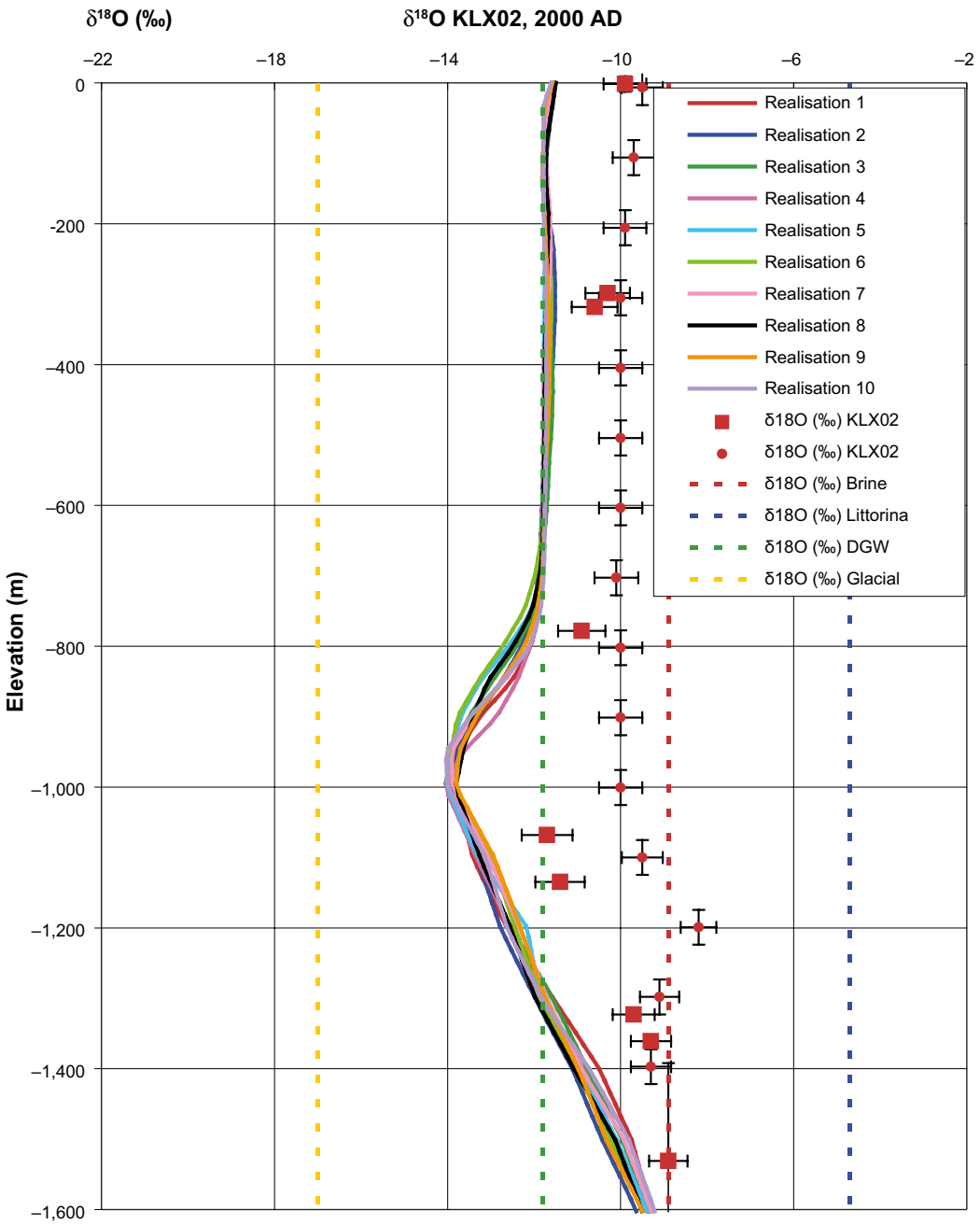

Figure 3-16. *Calculated profiles of $\delta^{18}O$ in the borehole KLX02 for ten realisations of the Hydro-DFN concept compared with data. Squares correspond to water samples that are representative (Table 3-2: orange) and less representative data (Table 3-2: green), and round dots represent supplemental data (Table 3-2: grey). In addition, signature values for Brine, Littorina, Dilute Groundwater, and Glacial water are shown.*

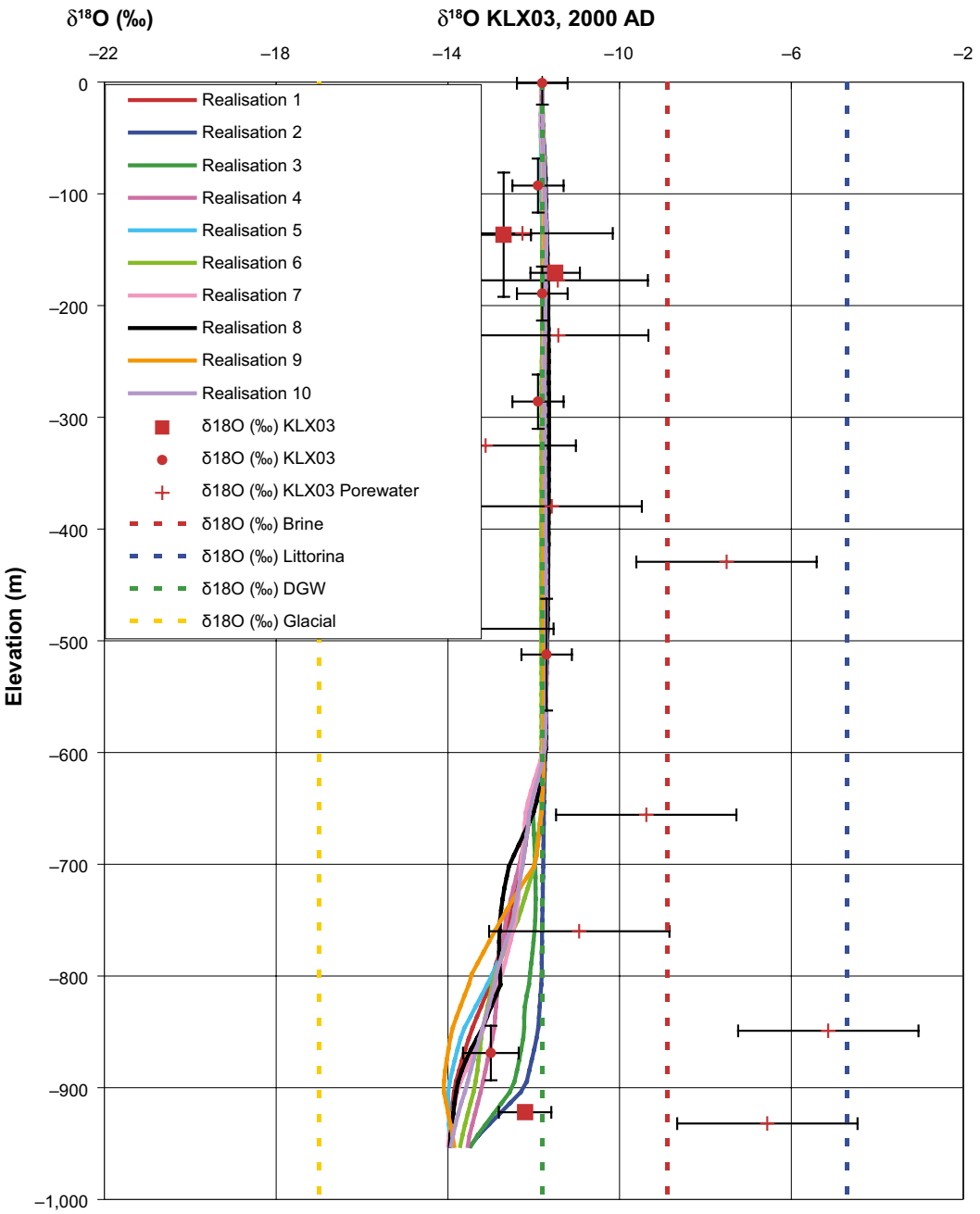

Figure 3-17. *Calculated profiles of $\delta^{18}O$ in the borehole KLX03 for ten realisations of the Hydro-DFN concept compared with data. Squares correspond to water samples that are representative (Table 3-2: orange) and less representative data (Table 3-2: green), and round dots represent supplemental data (Table 3-2: grey). In addition, signature values for Brine, Littorina, Dilute Groundwater, and Glacial water are shown.*

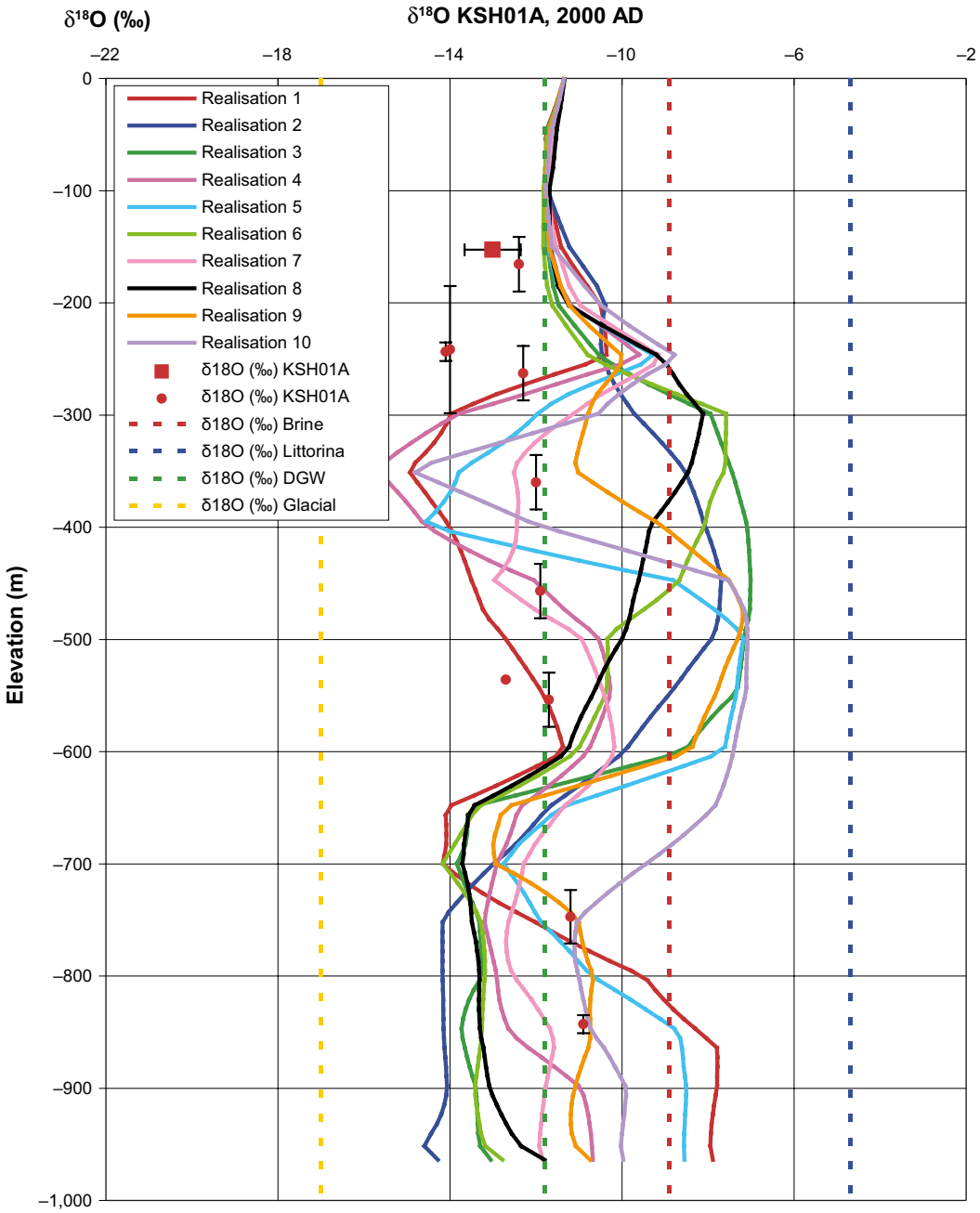

Figure 3-18. *Calculated profiles of $\delta^{18}O$ in the borehole KSH01A for ten realisations of the Hydro-DFN concept compared with data. Squares correspond to water samples that are representative (Table 3-2: orange) and less representative data (Table 3-2: green), and round dots represent supplemental data (Table 3-2: grey). In addition, signature values for Brine, Littorina, Dilute Groundwater, and Glacial water are shown.*

3.4.2 Revised reference waters

After the initial calculation for 10 different realisations of the Hydro-DFN, the reference waters were revised to the waters shown in Table 3-4. This study aimed to use Laxemar 2.1 data or the most recent data, so the reference case was re-run using the revised reference waters, and all subsequent calculations used the revised reference waters.

The calculated profiles of salinity, Br/Cl and $\delta^{18}O$ in various boreholes for the revised calculation are shown in Figure 3-19 to Figure 3-21 together with the corresponding observations.

As for the calculation with the original reference waters, the match of the predicted salinity to observations shown in Figure 3-19 is considered to be about as good as can reasonably be expected within the constraints of reference water composition defined and bearing in mind the variations between different realisations of the Hydro-DFN.

For the revised calculation, the match of the predicted Br/Cl ratio to observations shown in Figure 3-20 is now significantly improved in the top few hundred metres. This reflects the non-zero Br/Cl ratio of the recharging DGW in the revised calculation (see Table 3-4).

The possible discrepancy between the predicted and observed values of $\delta^{18}O$ (Figure 3-21) at depths between about 700 m and 1,500 m is much more apparent for the revised calculations. In KLX02, the predicted value of $\delta^{18}O$ drops to about –16 in this depth range, whereas the data are no lower than about –12, and the supplementary data appear to indicate an even higher value of about –10. As discussed in Section 3.3, it is considered that this discrepancy may be because the assumed initial condition (about 10,000 years ago) took the water between 700 m and 1,500 m to be a mix of Glacial (with $\delta^{18}O$ of about –21 for the revised calculation) and Brine (with $\delta^{18}O$ of about –9), whereas a mix of Brine and a water with a less negative value of $\delta^{18}O$ than the revised Glacial water (i.e. an older warm climate inter-glacial water) would lead to a much better match to the observations. This hypothesis about the origin of the freshwater at depth also implies that glacial water was not generally injected to depths much below 700 m whilst ice sheets covered or past over the site during the last ice age. Ongoing work with the SKB programme is considering the hydrogeological conditions that may have occurred under perma-frost and glacial condition (/Jansson et al. 2007/ and /Vidstrand et al. 2006/ for example).

A complete range of major ions and stable isotopes model results and comparison to water samples from both fractures and pore water is given in Appendix B for this case. These show good agreement in the profiles of Cl, Na and Ca for most boreholes. Both data and models are consistent in a lack of Mg in the Laxemar KLX boreholes, i.e. no remnant of Littorina water. Significant Mg is present under the Simpevarp peninsula, KSH, Ävrö island, KAV, and Äspö island, KAS, in both the model and data, although concentrations are lower in the measurements, partly due to reactions. Br/Cl ratio also confirms the lack of a significant Littorina pulse apart from in Äspö boreholes. The penetration of HCO_3 gives a non-conservative marker for meteoric water and suggests more variability in the depth of meteoric penetration in the data than in the model perhaps pointing to greater spatial heterogeneity. If anything, the data indicates less overall penetration of meteoric water, i.e. lower hydraulic conductivity in higher kinematic porosity. There are significant levels of SO_4 at depth confirming the hydro-geochemical model for Brine. This is in contrast to the Brine composition for deep water at Forsmark which suggests low SO_4.

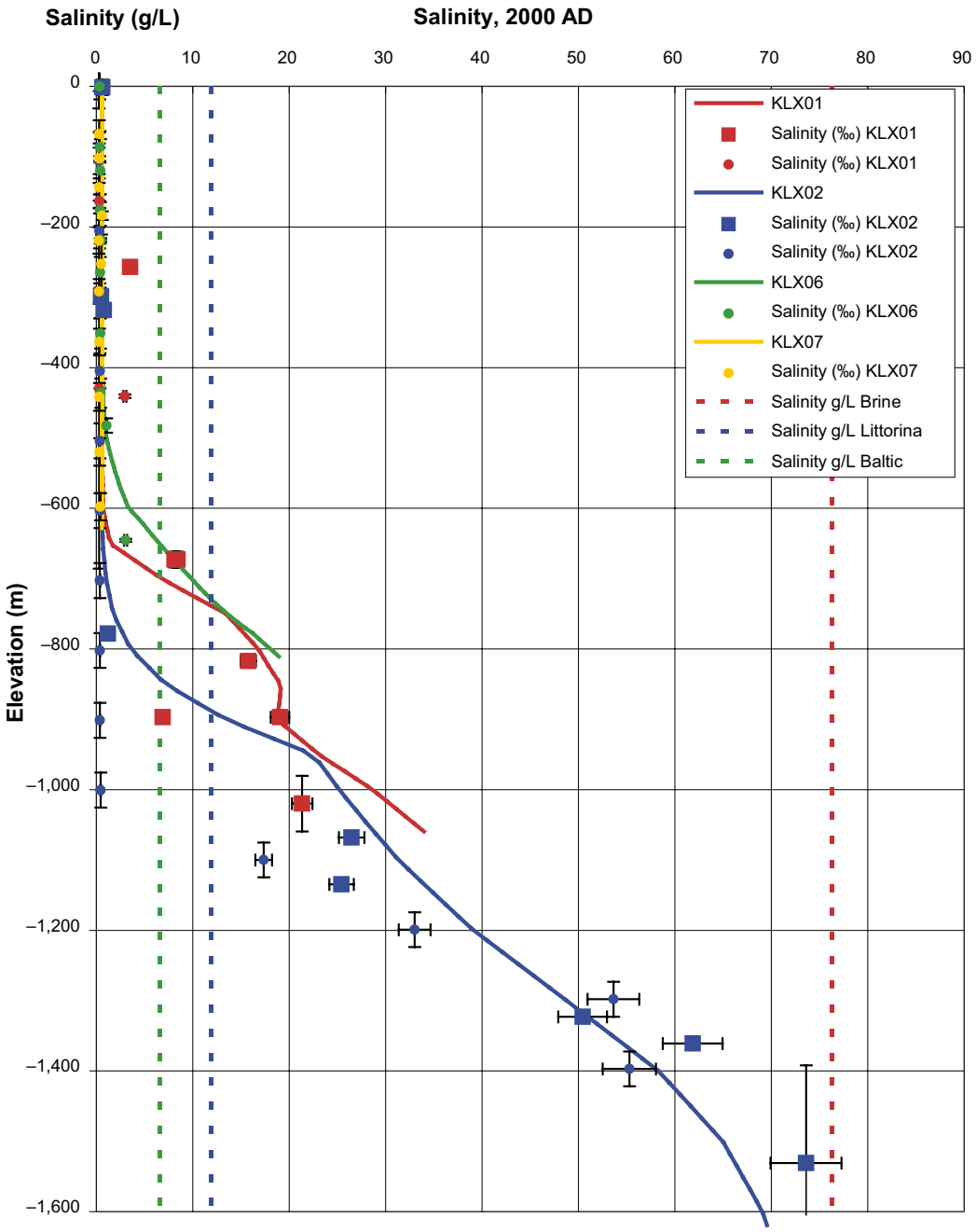

Figure 3-19. *Calculated salinity profiles in the boreholes KLX01, KLX02, KLX06 and KLX07 for the Revised reference case compared to data. Squares correspond to water samples that are representative (Table 3-2: orange) and less representative data (Table 3-2: green), and round dots represent fairly representative TDS data (Table 3-2: yellow) and supplemental data (Table 3-2: grey). The uncertainties in data are indicated with horizontal error bars. The vertical "error bars" indicate elevation interval for sample. In addition, the signature values of salinity for Brine, Littorina and Baltic Sea water are shown. For all displayed boreholes, values are shown from 0 m.a.s.l. down to the full depth of the boreholes. Where the results are very similar for different boreholes, the profiles may be hidden.*

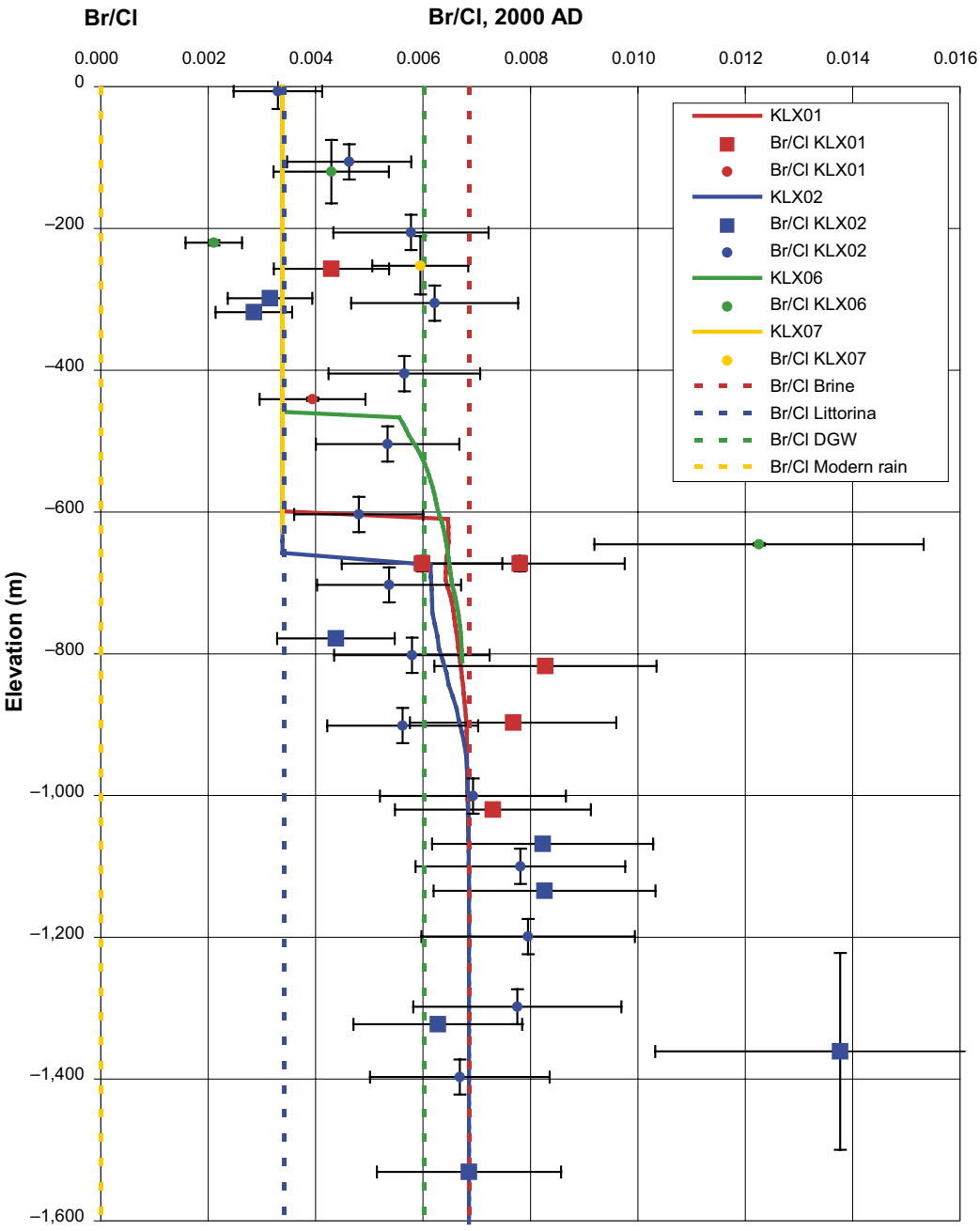

Figure 3-20. *Calculated profiles of the ratio Br/Cl in the boreholes KLX01, KLX02, KLX06 and KLX07 for the Revised reference case compared to data. Squares correspond to water samples that are representative (Table 3-2: orange) and less representative data (Table 3-2: green), and round dots represent supplemental data (Table 3-2: grey). In addition, the signature values for Brine, Littorina, Dilute Groundwater, and Modern rain water are shown. The signature value for DGW is 0. For all displayed boreholes, values are shown from 0 m.a.s.l. down to the full depth of the boreholes. Where the results are very similar for different boreholes, the profiles may be hidden.*

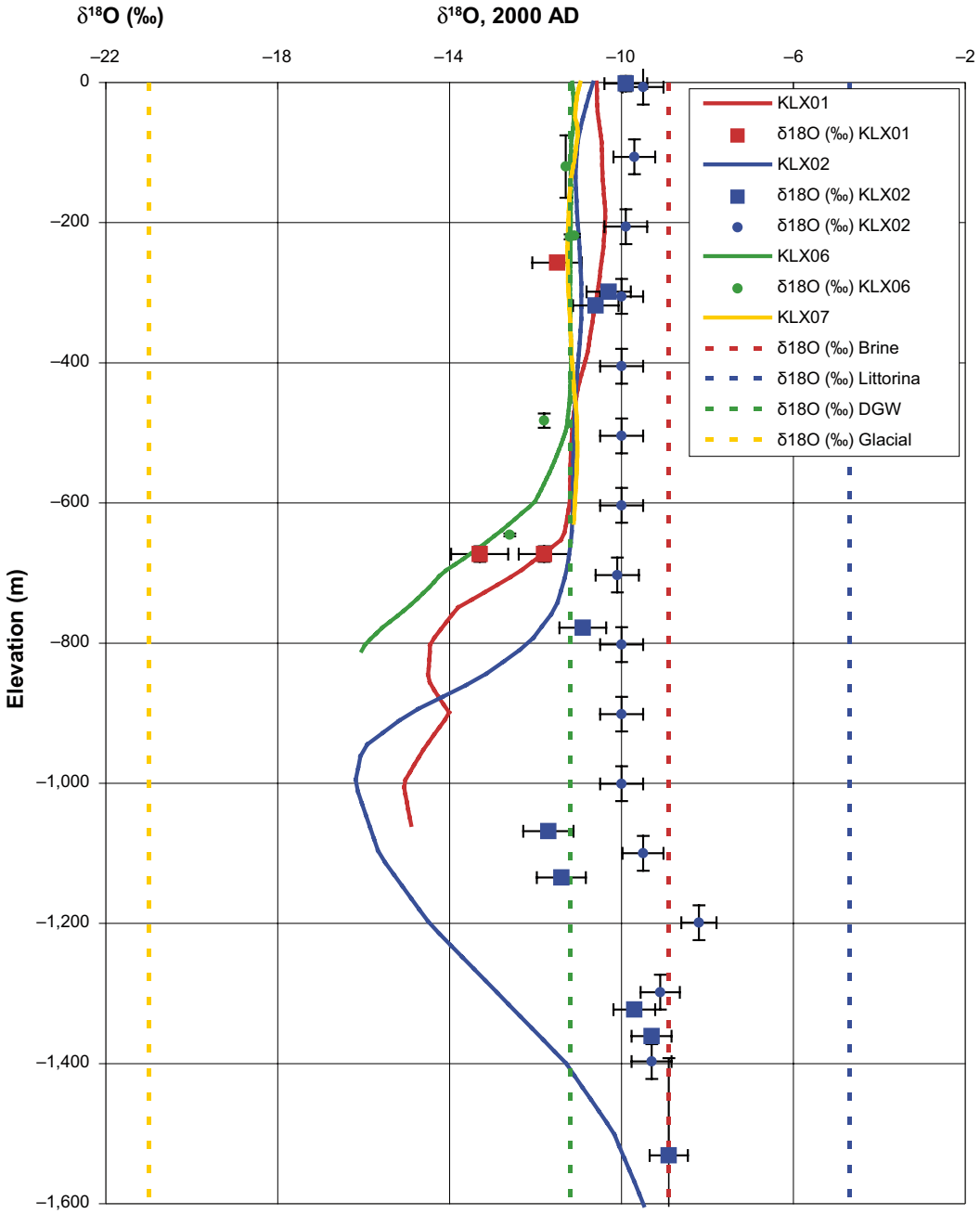

Figure 3-21. *Calculated profiles of $\delta^{18}O$ in the boreholes KLX01, KLX02, KLX06 and KLX07 for the Revised reference case compared to data. Squares correspond to water samples that are representative (Table 3-2: orange) and less representative data (Table 3-2: green), and round dots represent supplemental data (Table 3-2: grey). In addition, the signature values for Brine, Littorina, Dilute Groundwater, and Glacial melt water are shown. For all displayed boreholes, values are shown from 0 m.a.s.l. down to the full depth of the boreholes. Where the results are very similar for different boreholes, the profiles may be hidden.*

3.4.3 Sensitivity to heterogeneity within HCD

In the L 1.2 reference case, uniform properties were used within each HCD. As a sensitivity study in /Hartley et al. 2006a/, calculations were performed for a few additional cases with stochastic HCD properties. It was found that this had some impact on the reference water profiles and hence further investigations were recommended.

To study this further in the current project, calculations were carried out for three sets of stochastic realisations of the HCD model. The three sets had different levels of variability. In the first set, the standard deviation of Log_{10} transmissivity is 0.5, in the second set, it is 1.0, and in the third set, it is 2.0.

The stochastic deformation zones are created by the RvsInfo tool. RvsInfo reads in the deformation zone topology definition file produced by the Rock visualisation System (RVS) tool which defines all the deformation zones. Each deformation zone can be divided into sub-triangles of a specified size with different transmissivities. The transmissivities of each sub-triangle are independently randomly sampled from a specified Gaussian distribution, i.e. a pure nugget spatial process on the scale of the sub-triangles. In the current case, 200 m triangles were used and the logarithm of the transmissivity was sampled from a Gaussian distribution with specified mean and standard deviation. This is illustrated below. Figure 3-22 shows the HCDs in the reference case (where there is only a variation with depth) and Figure 3-23 shows a case with stochastic HCDs.

The HCDs are taken into account in the flow calculations with the permeability and porosity of each finite element crossed by HCDs being an effective permeability and porosity that represent the combined effect of the background rock and the HCDs.

Flow calculations were carried out using the revised reference waters given in Table 3-4. It was found that these calculations converged for all the realisations with standard deviations of Log_{10} transmissivity of 0.5 and 1.0, but only converged for one realisation with standard deviation of Log_{10} transmissivity of 2.0.

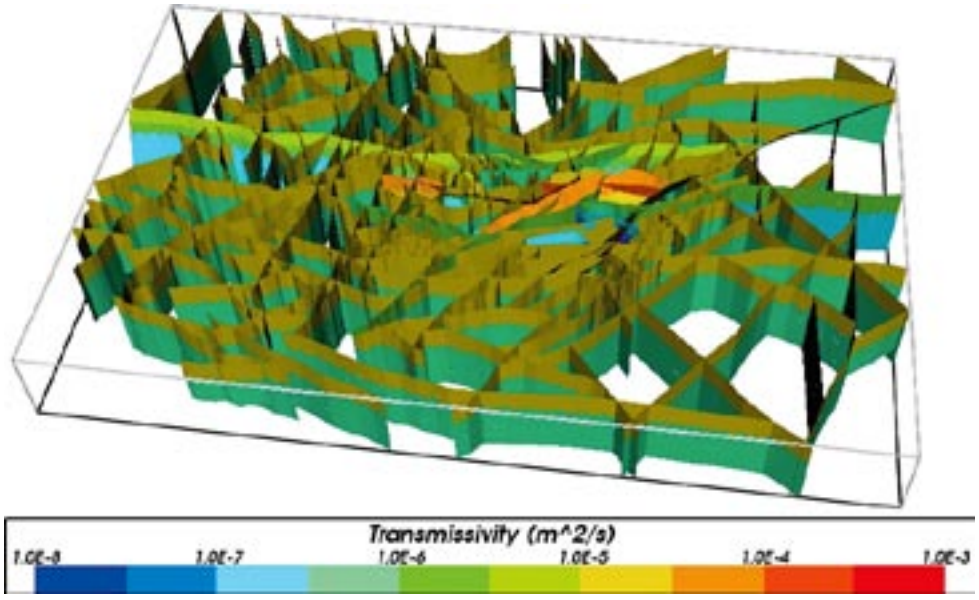

Figure 3-22. *HCD for regional-scale modelling in 3D. The zones are coloured by transmissivity, where red is high and blue is low /Hartley et al. 2006b/.*

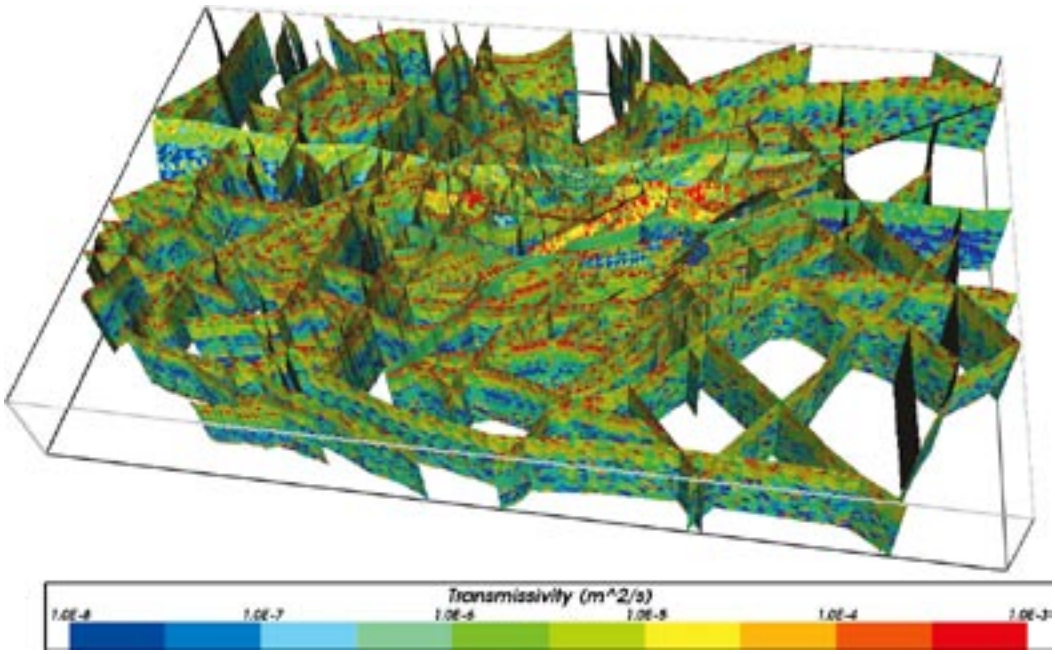

Figure 3-23. *HCD model with all zones and stochastic hydraulic properties. The zones are coloured by transmissivity, where red is high and blue is low /Hartley et al. 2006b/.*

The calculated profiles of salinity, $\delta^{18}O$ and Br/Cl in KLX01, KLX02, KLX03 and KSH01A for the calculations are shown in Figure 3-24 to Figure 3-35 together with the corresponding observations. Generally, there appears to be relatively little variation between the results for the different realisations, which are similar to the results for the reference case with the revised reference waters. The largest variations are probably those for $\delta^{18}O$ in KSH01a.

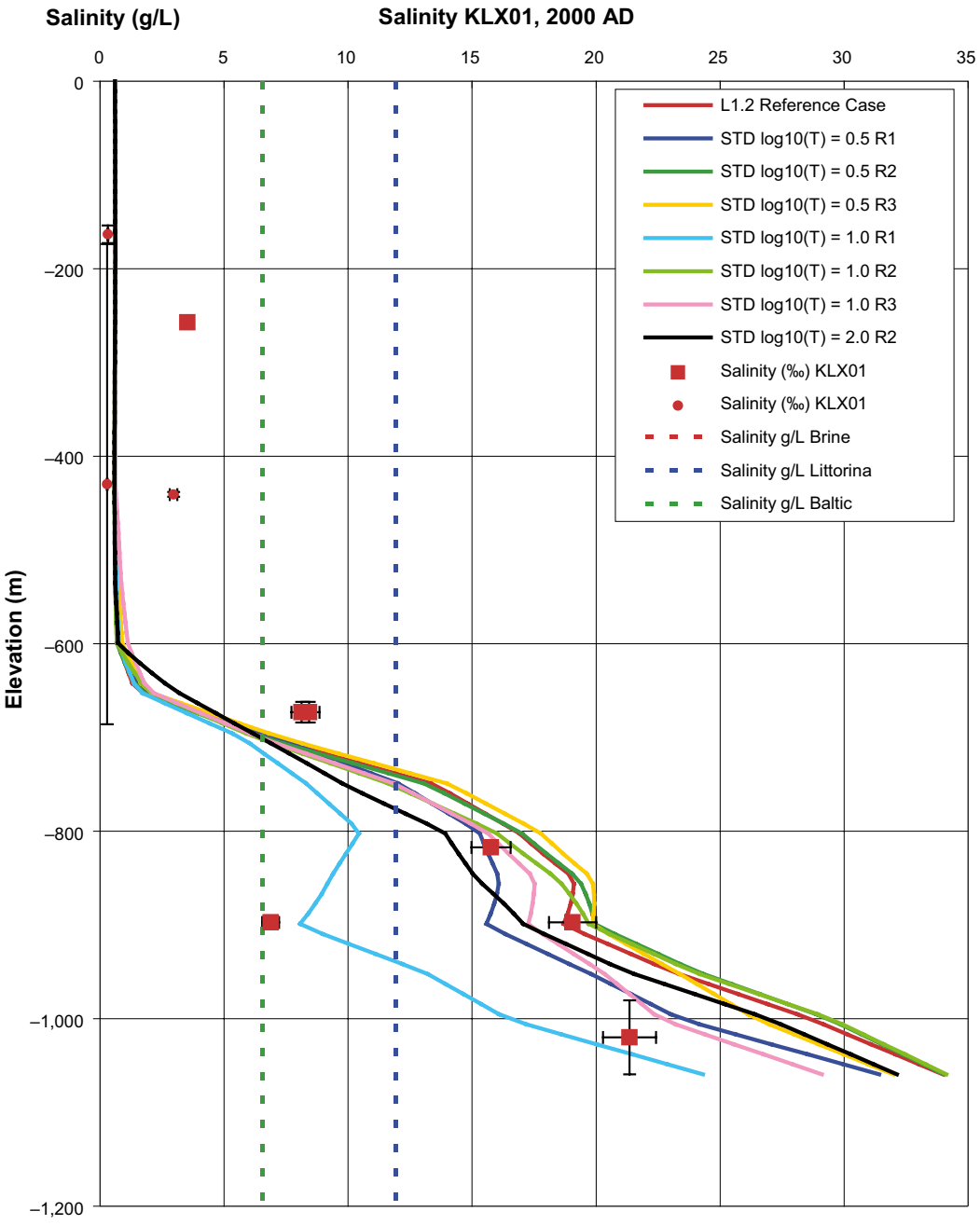

Figure 3-24. *Calculated salinity profiles in the borehole KLX01 for different realisations of cases using stochastic HCD properties. Three different standard deviations in Log_{10} K are used. Squares correspond to water samples that are representative (Table 3-2: orange) and less representative data (Table 3-2: green), and round dots represent fairly representative TDS data (Table 3-2: yellow) and supplemental data (Table 3-2: grey). The uncertainties in data are indicated with horizontal error bars. The vertical "error bars" indicate elevation interval for sample. In addition, the signature values of salinity for Brine, Littorina and Baltic Sea water are shown. The Brine value is out of range.*

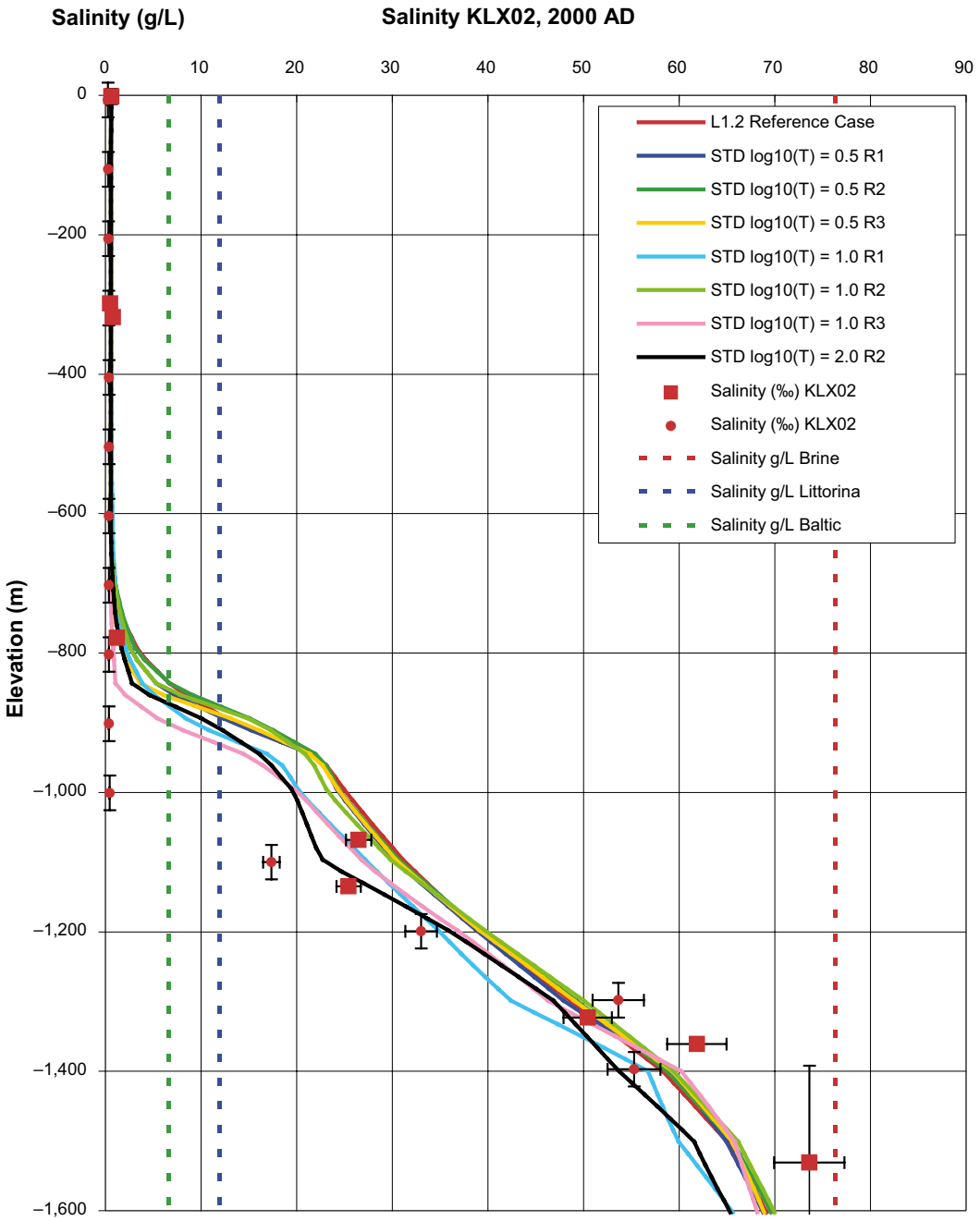

Figure 3-25. *Calculated salinity profiles in the borehole KLX02 for different realisations of cases using stochastic HCD properties. Three different standard deviations in Log_{10} K are used. Squares correspond to water samples that are representative (Table 3-2: orange) and less representative data (Table 3-2: green), and round dots represent fairly representative TDS data (Table 3-2: yellow) and supplemental data (Table 3-2: grey). The uncertainties in data are indicated with horizontal error bars. The vertical "error bars" indicate elevation interval for sample. In addition, the signature values of salinity for Brine, Littorina and Baltic Sea water are shown.*

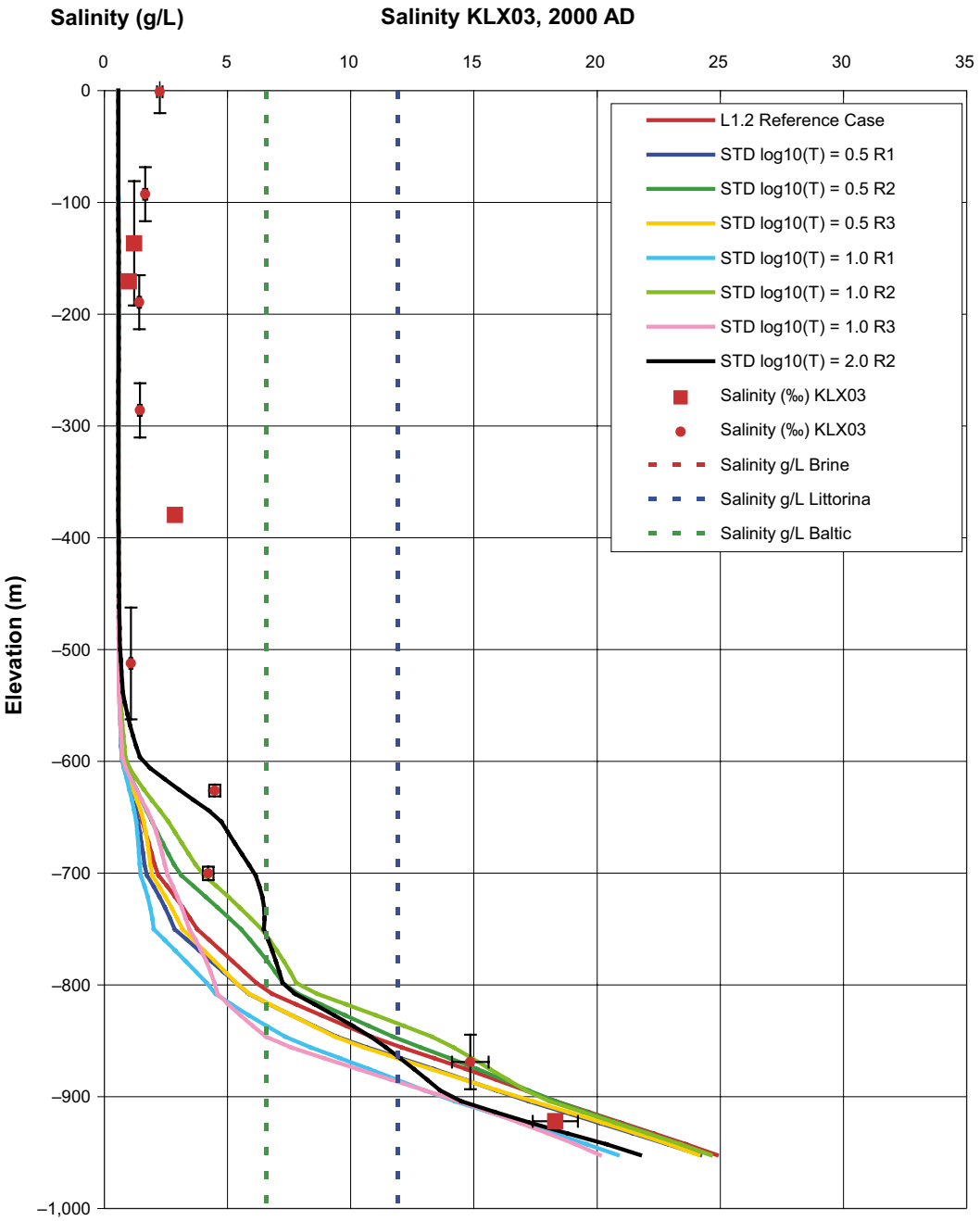

Figure 3-26. *Calculated salinity profiles in the borehole KLX03 for different realisations of cases using stochastic HCD properties. Three different standard deviations in Log_{10} K are used. Squares correspond to water samples that are representative (Table 3-2: orange) and less representative data (Table 3-2: green), and round dots represent fairly representative TDS data (Table 3-2: yellow) and supplemental data (Table 3-2: grey). The uncertainties in data are indicated with horizontal error bars. The vertical "error bars" indicate elevation interval for sample. In addition, the signature values of salinity for Brine, Littorina and Baltic Sea water are shown. The Brine value is out of range.*

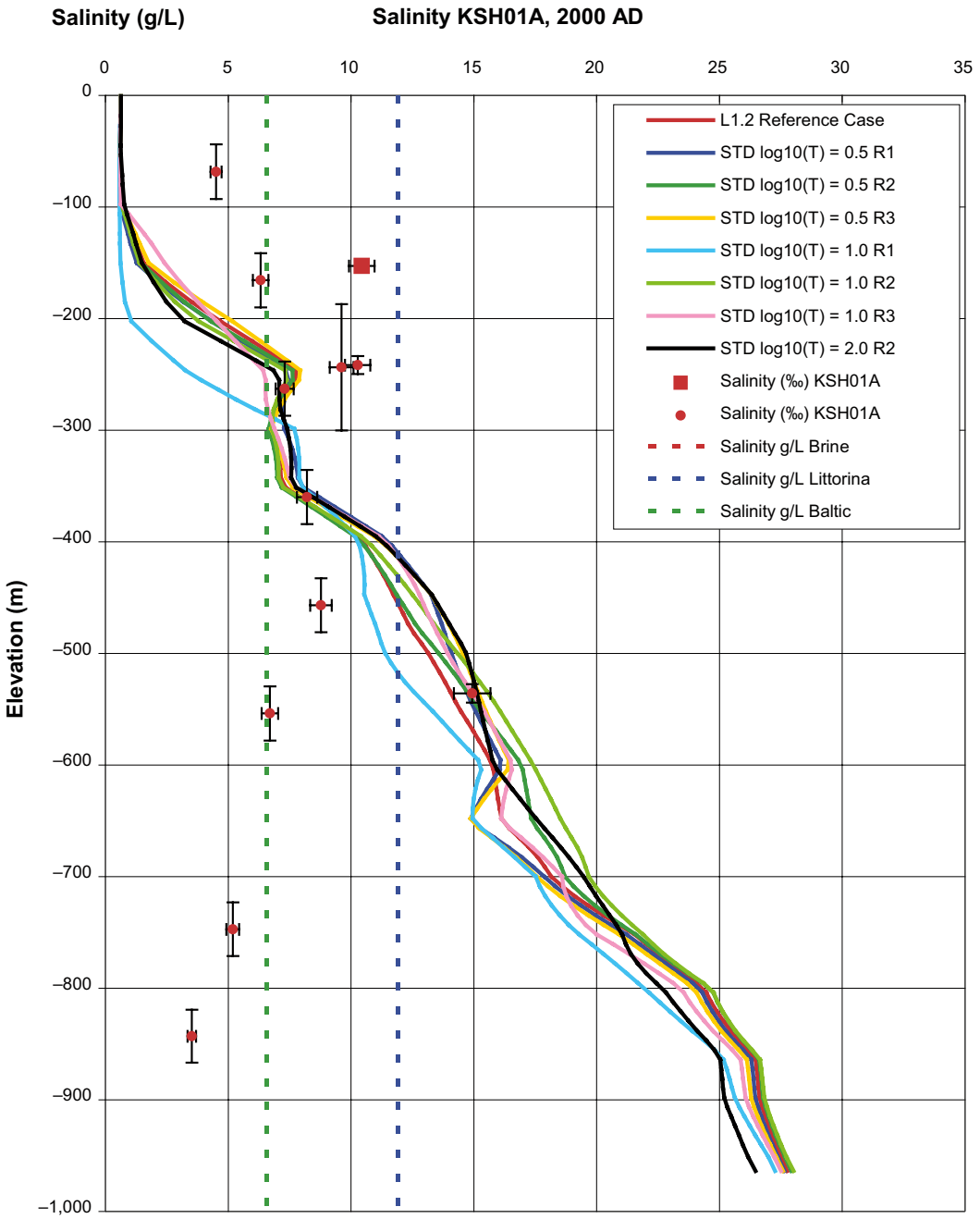

Figure 3-27. *Calculated salinity profiles in the borehole KSH01A for different realisations of cases using stochastic HCD properties. Three different standard deviations in Log_{10} K are used. Squares correspond to water samples that are representative (Table 3-2: orange) and less representative data (Table 3-2: green), and round dots represent fairly representative TDS data (Table 3-2: yellow) and supplemental data (Table 3-2: grey). The uncertainties in data are indicated with horizontal error bars. The vertical "error bars" indicate elevation interval for sample. In addition, the signature values of salinity for Brine, Littorina and Baltic Sea water are shown. The Brine value is out of range. Note: the 3 supplemental values below –550 m elevation correspond to tube samples and are probably unrepresentative.*

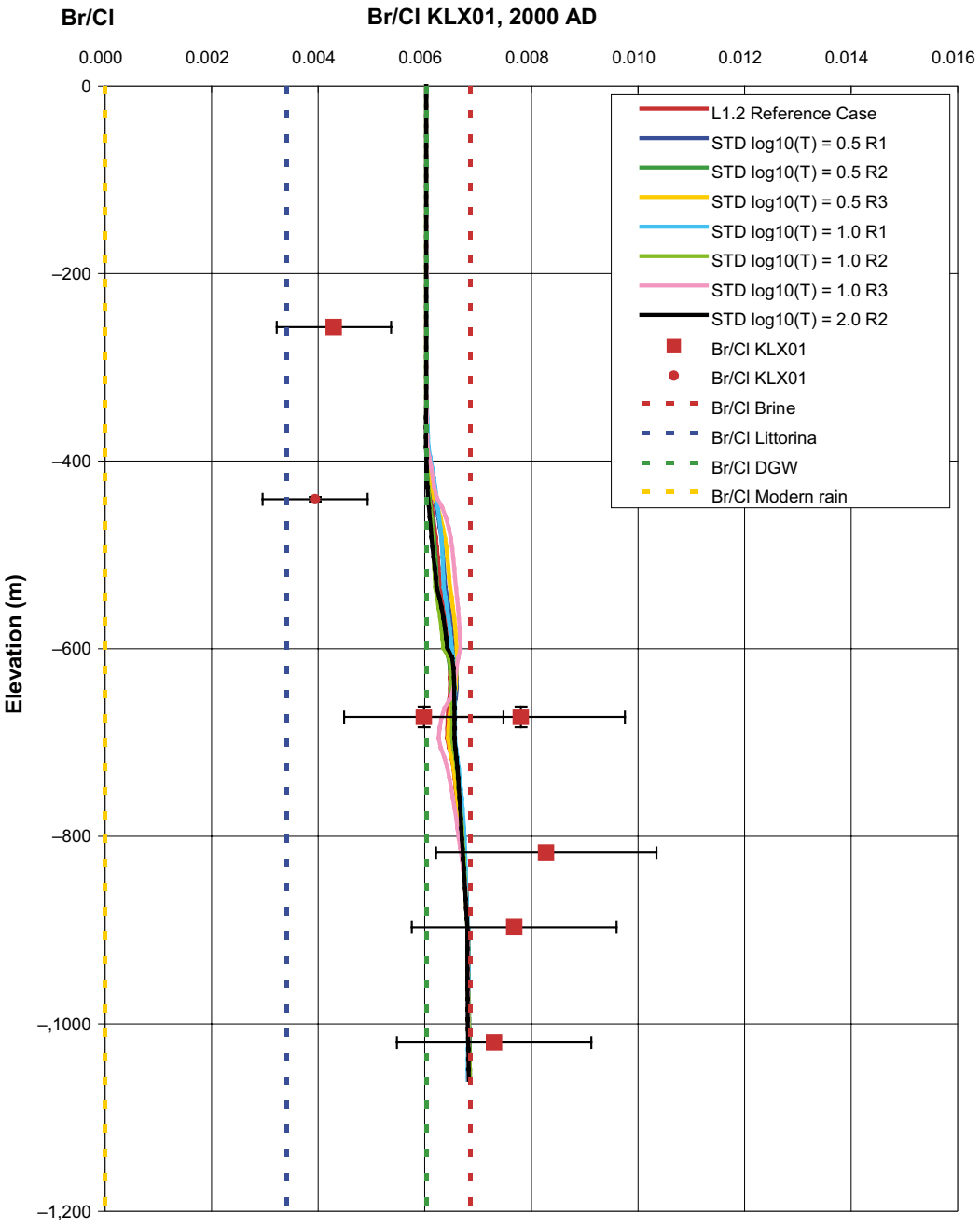

Figure 3-28. *Calculated profiles of the ratio Br/Cl in the borehole KLX01 for different realisations of cases using stochastic HCD properties. Three different standard deviations in Log_{10} K are used. In addition, measured values and the signature values for Brine, Littorina, Dilute Groundwater, and Modern rain water are shown. Squares correspond to water samples that are representative (Table 3-2: orange) and less representative data (Table 3-2: green), and round dots represent supplemental data (Table 3-2: grey). The uncertainties in data are indicated with horizontal error bars. The vertical "error bars" indicate elevation interval for sample.*

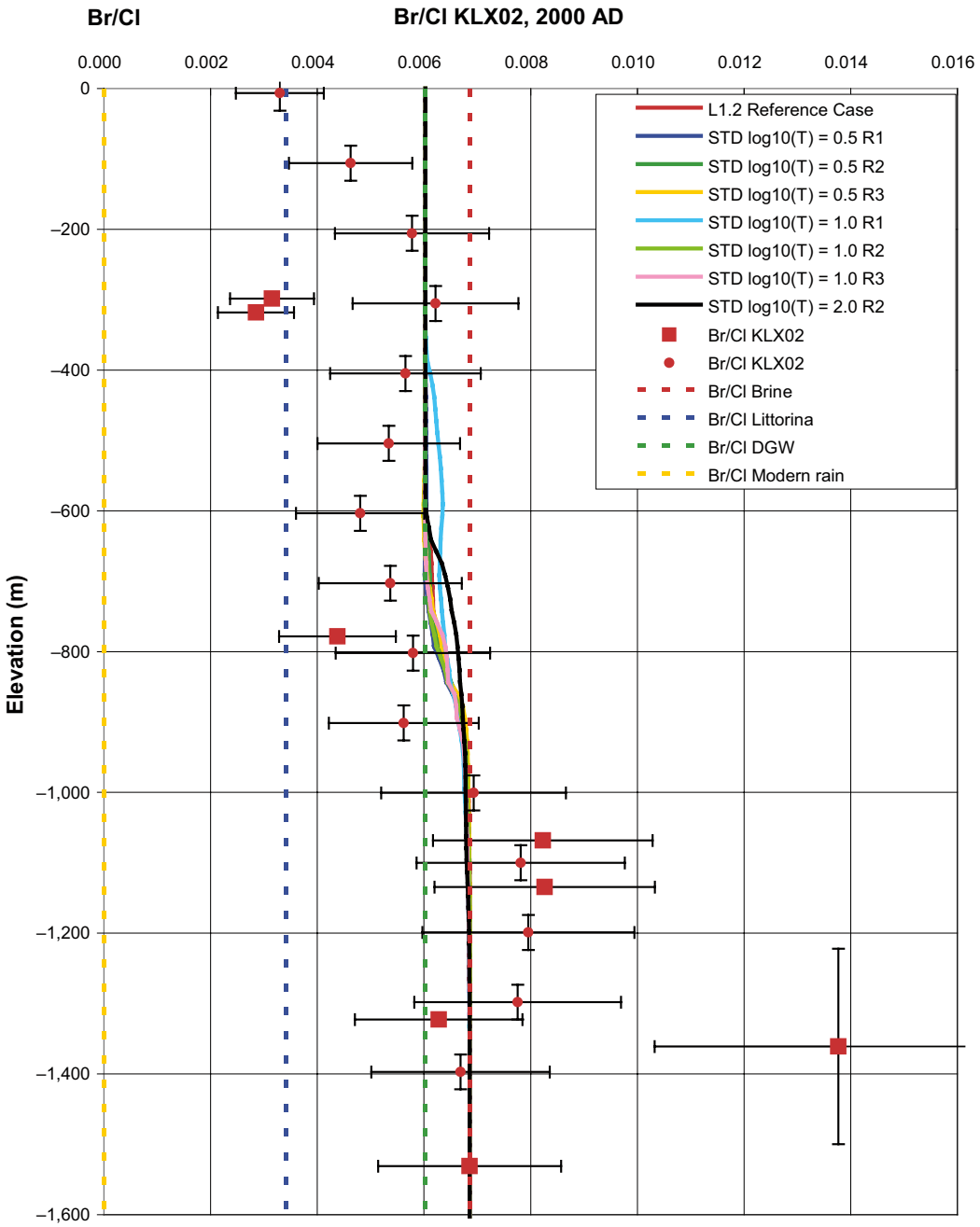

Figure 3-29. *Calculated profiles of the ratio Br/Cl in the borehole KLX02 for different realisations of cases using stochastic HCD properties. Three different standard deviations in Log_{10} K are used. In addition, measured values and the signature values for Brine, Littorina, Dilute Groundwater, and Modern rain water are shown. Squares correspond to water samples that are representative (Table 3-2: orange) and less representative data (Table 3-2: green), and round dots represent supplemental data (Table 3-2: grey). The uncertainties in data are indicated with horizontal error bars. The vertical "error bars" indicate elevation interval for sample.*

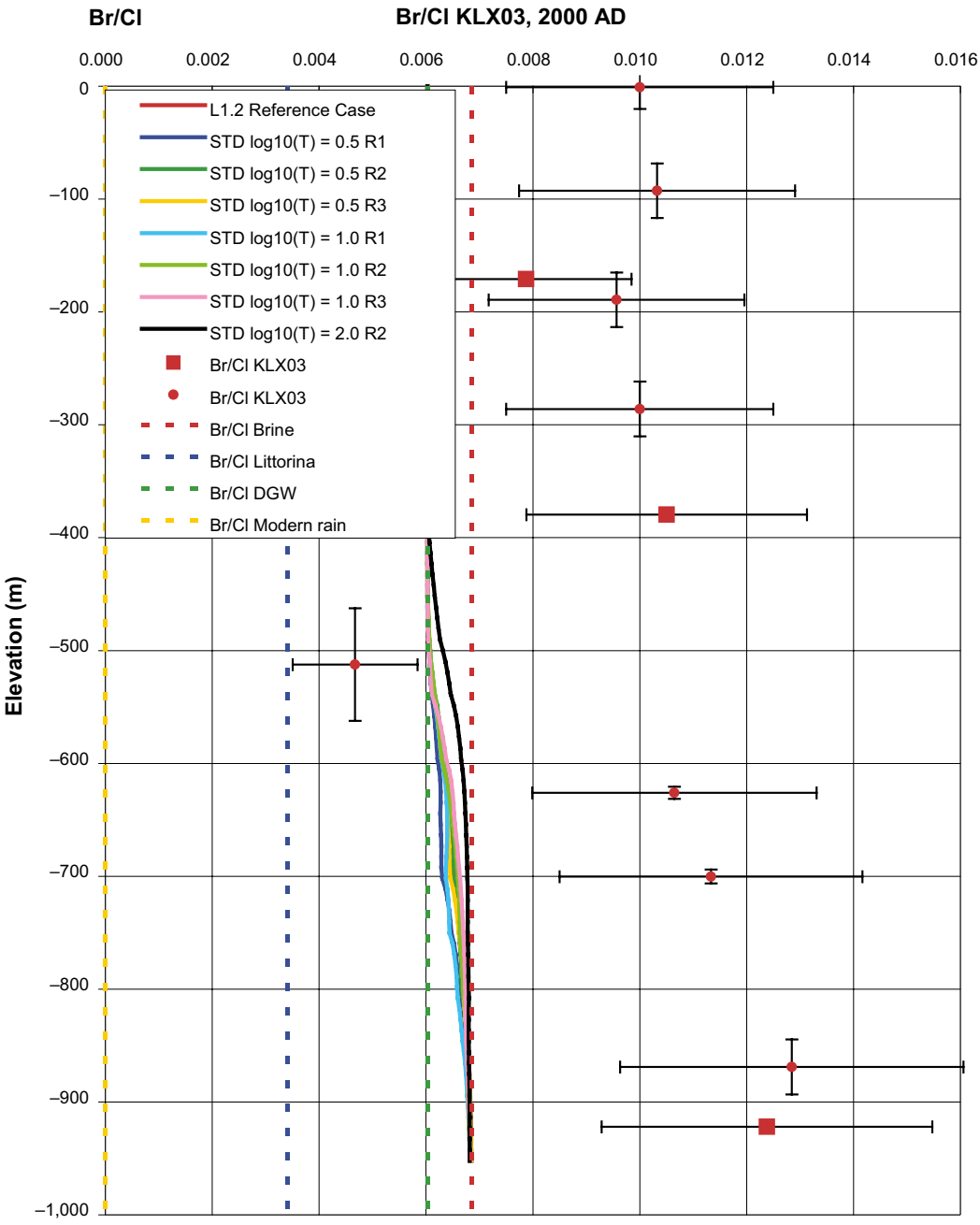

Figure 3-30. *Calculated profiles of the ratio Br/Cl in the borehole KLX03 for different realisations of cases using stochastic HCD properties. Three different standard deviations in Log_{10} K are used. In addition, measured values and the signature values for Brine, Littorina, Dilute Groundwater, and Modern rain water are shown. Squares correspond to water samples that are representative (Table 3-2: orange) and less representative data (Table 3-2: green), and round dots represent supplemental data (Table 3-2: grey). The uncertainties in data are indicated with horizontal error bars. The vertical "error bars" indicate elevation interval for sample.*

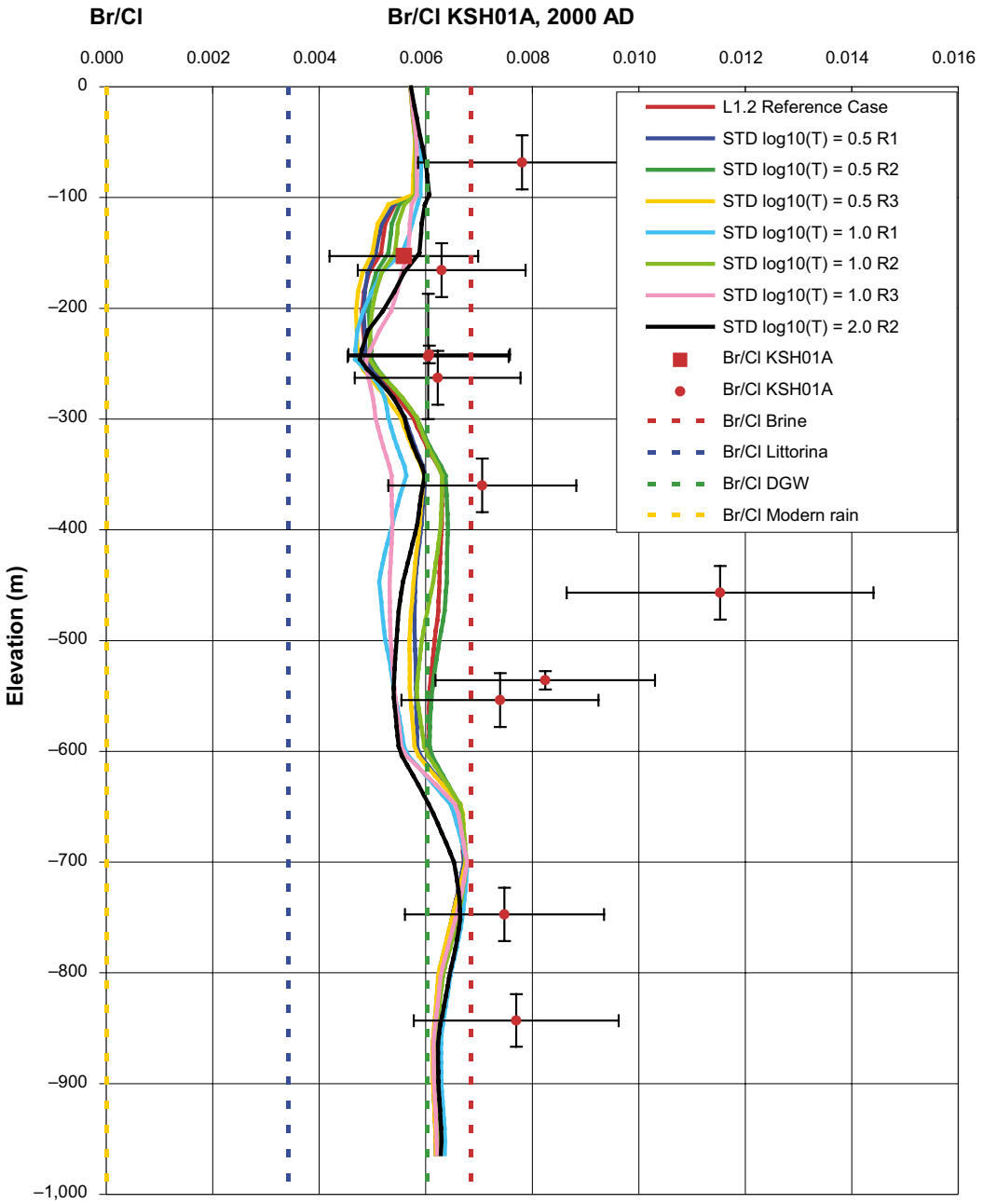

Figure 3-31. *Calculated profiles of the ratio Br/Cl in the borehole KSH01A for different realisations of cases using stochastic HCD properties. Three different standard deviations in Log_{10} K are used. In addition, measured values and the signature values for Brine, Littorina, Dilute Groundwater, and Modern rain water are shown. Squares correspond to water samples that are representative (Table 3-2: orange) and less representative data (Table 3-2: green), and round dots represent supplemental data (Table 3-2: grey). The uncertainties in data are indicated with horizontal error bars. The vertical "error bars" indicate elevation interval for sample.*

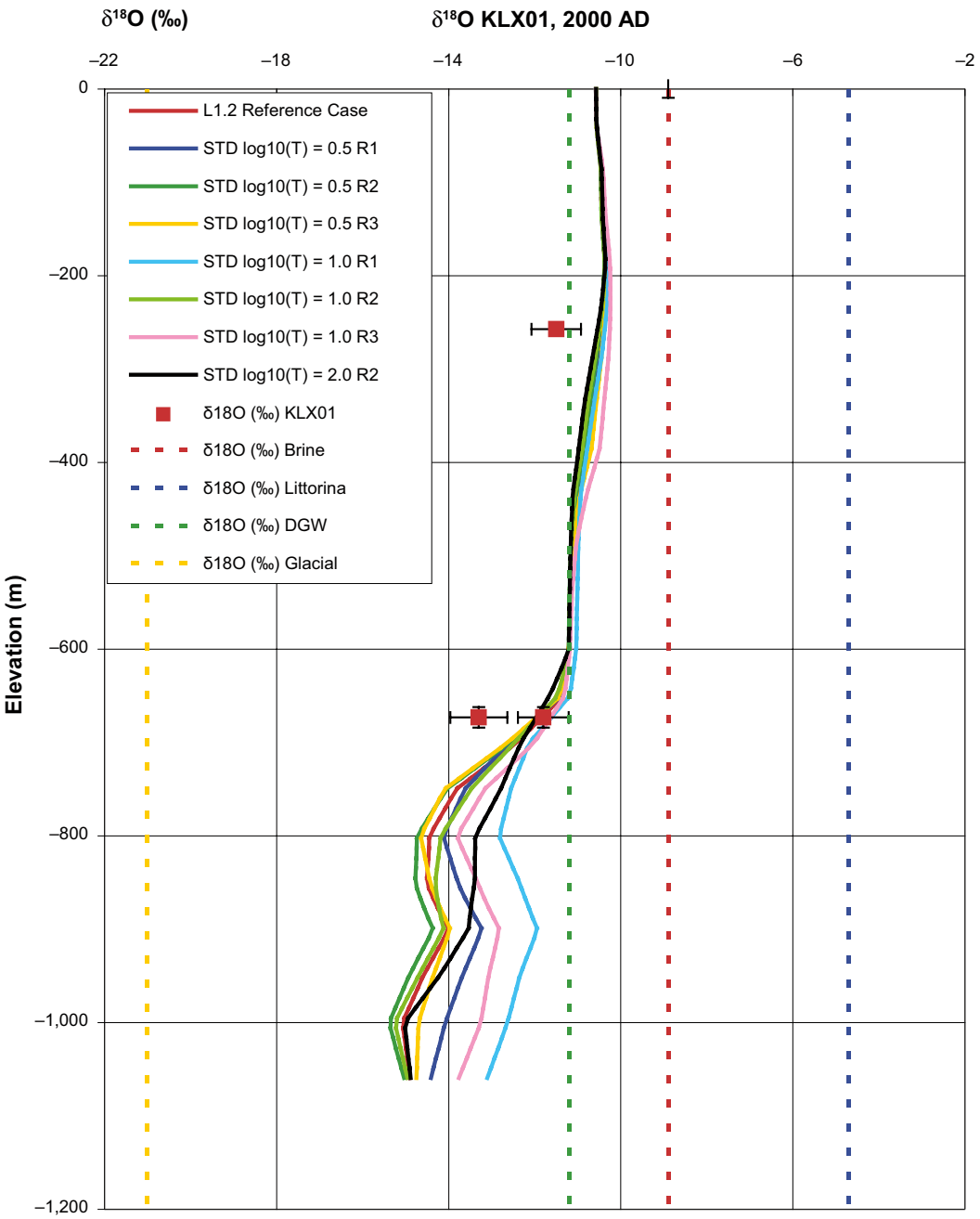

Figure 3-32. *Calculated profiles of $\delta^{18}O$ in the borehole KLX01 for different realisations of cases using stochastic HCD properties. Three different standard deviations in Log_{10} K are used. In addition, measured values and the signature values for Brine, Littorina, Dilute Groundwater, and Glacial water are shown. Squares correspond to water samples that are representative (Table 3-2: orange) and less representative data (Table 3-2: green), and round dots represent supplemental data (Table 3-2: grey). The uncertainties in data are indicated with horizontal error bars. The vertical "error bars" indicate elevation interval for sample.*

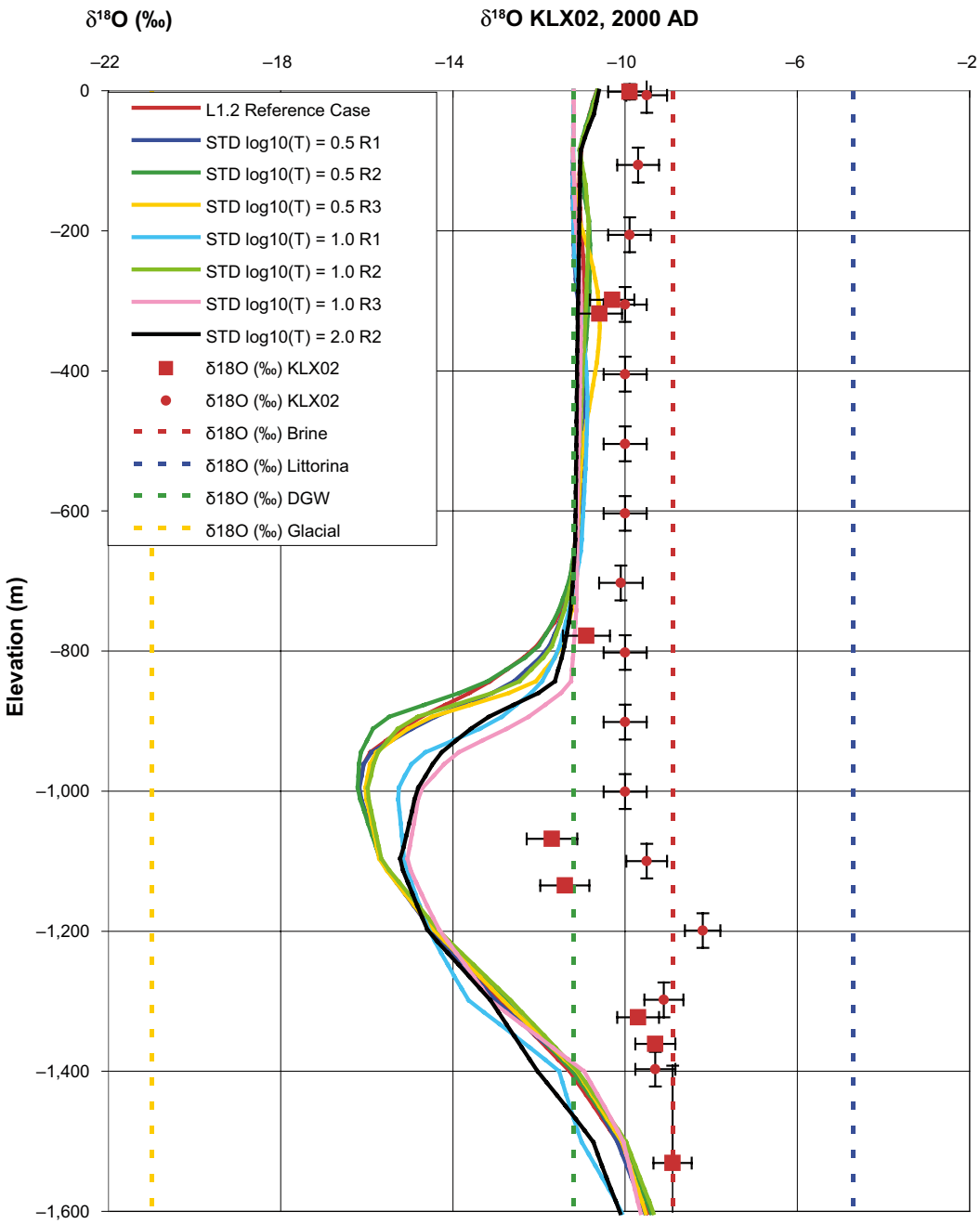

Figure 3-33. *Calculated profiles of $\delta^{18}O$ in the borehole KLX02 for different realisations of cases using stochastic HCD properties. Three different standard deviations in Log_{10} K are used. In addition, measured values and the signature values for Brine, Littorina, Dilute Groundwater, and Glacial water are shown. Squares correspond to water samples that are representative (Table 3-2: orange) and less representative data (Table 3-2: green), and round dots represent supplemental data (Table 3-2: grey). The uncertainties in data are indicated with horizontal error bars. The vertical "error bars" indicate elevation interval for sample.*

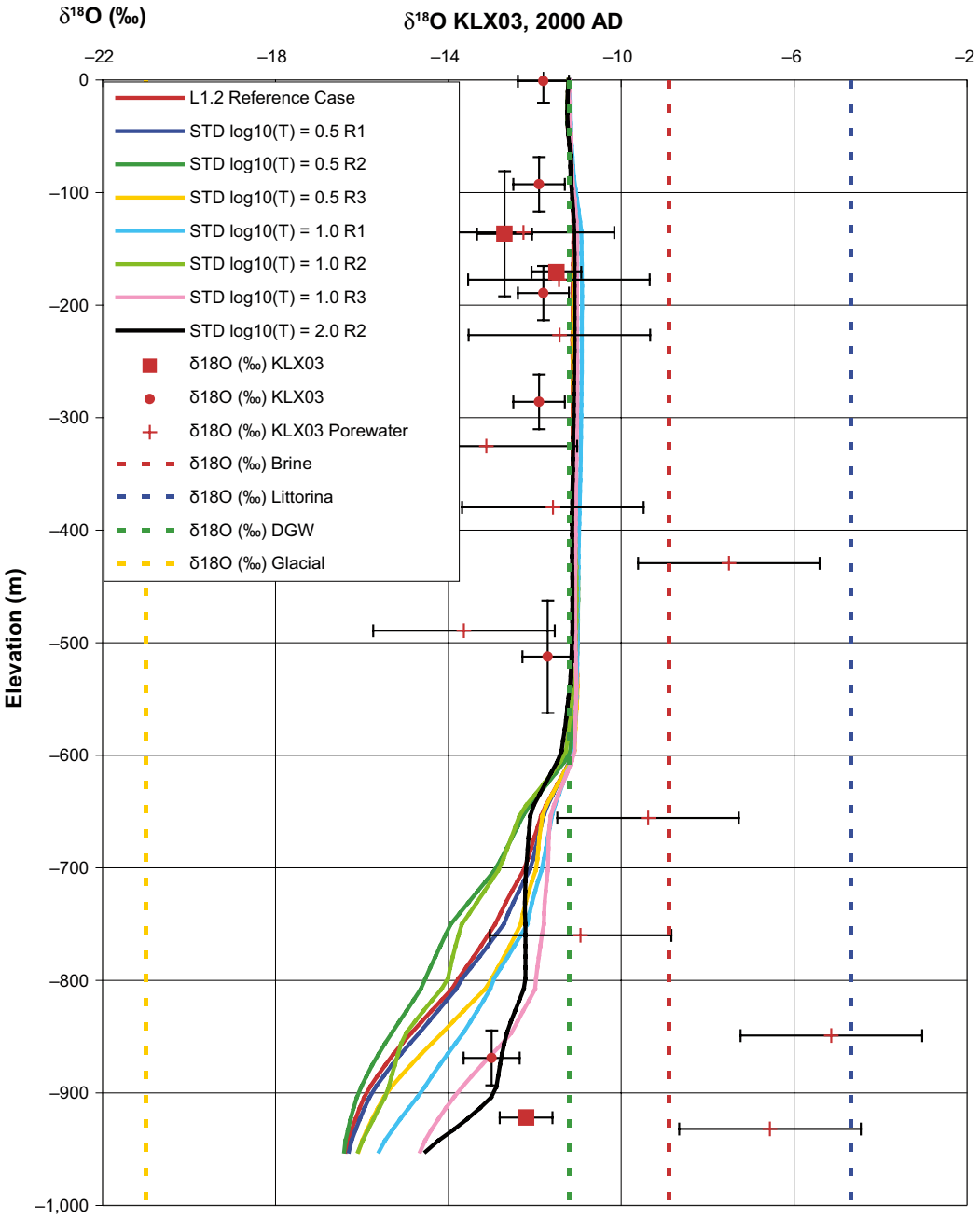

Figure 3-34. *Calculated profiles of $\delta^{18}O$ in the borehole KLX03 for different realisations of cases using stochastic HCD properties. Three different standard deviations in Log_{10} K are used. In addition, measured values and the signature values for Brine, Littorina, Dilute Groundwater, and Glacial water are shown. Squares correspond to water samples that are representative (Table 3-2: orange) and less representative data (Table 3-2: green), and round dots represent supplemental data (Table 3-2: grey). The uncertainties in data are indicated with horizontal error bars. The vertical "error bars" indicate elevation interval for sample.*

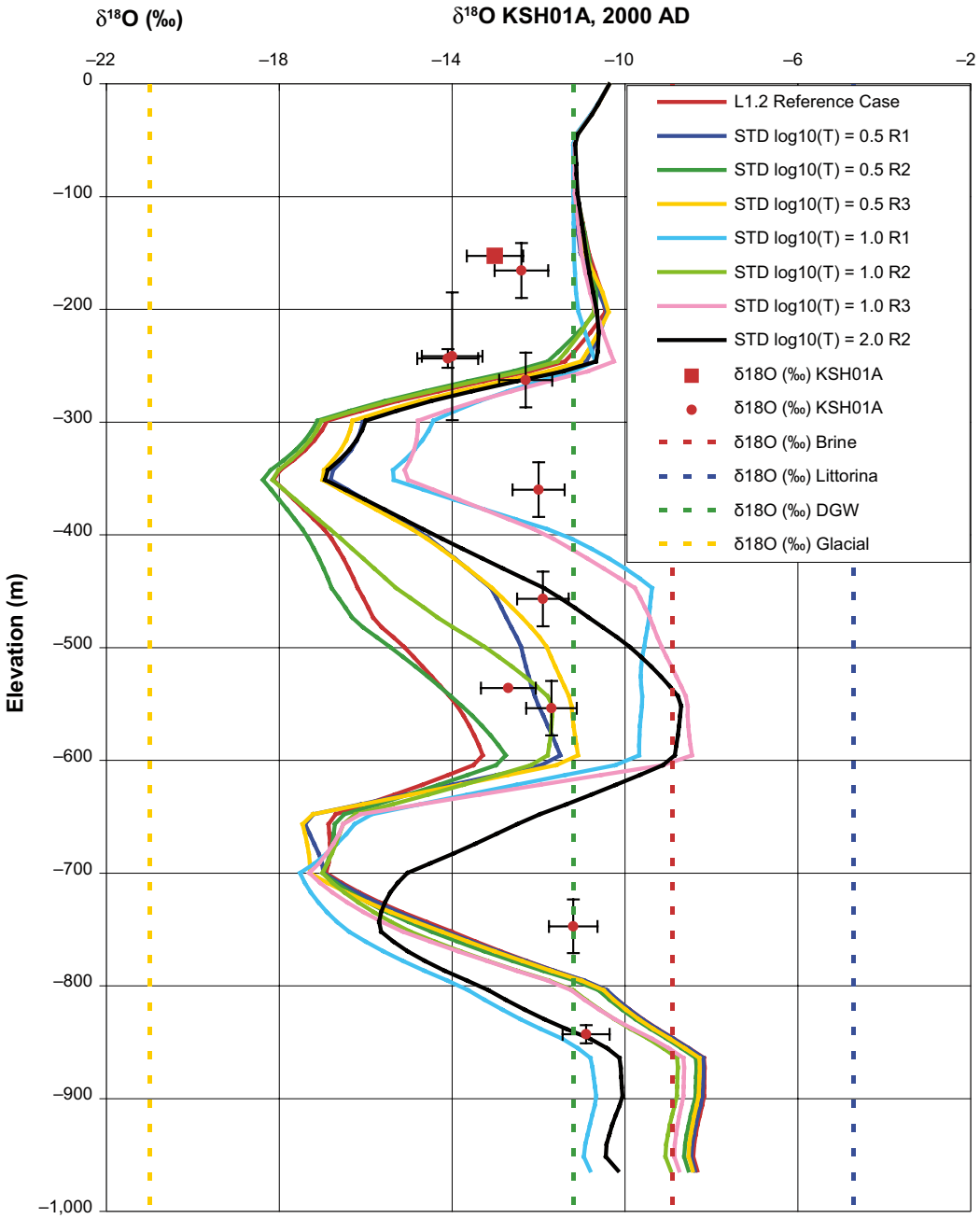

Figure 3-35. *Calculated profiles of $\delta^{18}O$ in the borehole KSH01A for different realisations of cases using stochastic HCD properties. Three different standard deviations in Log_{10} K are used. In addition, measured values and the signature values for Brine, Littorina, Dilute Groundwater, and Glacial water are shown. Squares correspond to water samples that are representative (Table 3-2: orange) and less representative data (Table 3-2: green), and round dots represent supplemental data (Table 3-2: grey). The uncertainties in data are indicated with horizontal error bars. The vertical "error bars" indicate elevation interval for sample.*

3.4.4 Sensitivity to kinematic porosity

In the L 1.2 reference case, the HRD kinematic porosity is obtained from the upscaled regional-scale DFN based on the semi-correlated transmissivity-model. In order to assess the sensitivity to the kinematic porosity, 3 cases with different kinematic porosity were considered. In the different cases the kinematic porosities in the reference case were scaled linearly, by factors of 0.2, 0.5 and 5 respectively. The calculations used the revised reference waters given in Table 3-4.

The calculated profiles of salinity, Br/Cl and $\delta^{18}O$ in the borehole KLX02 for the reference case and the different values of kinematic porosity are shown in Figure 3-36 to Figure 3-38 together with the observations and the signature values for Brine, Littorina, Dilute Groundwater, and Glacial water.

Generally there is relatively little variation between the results for the different values of kinematic porosity. The main difference is that for the highest value of the kinematic porosity the region in KLX02 where $\delta^{18}O$ is more negative than –12 extends to shallower depths. This is presumably a consequence of the transport velocity being about 5 times lower for the 5 times higher kinematic porosity and therefore it taking longer for the assumed initial Glacial water to be flushed out from the region below about –600 m. Since reducing the porosity makes little difference to the simulated geochemical profiles in the Laxemar subarea, it implies that the situation is approaching a steady-state.

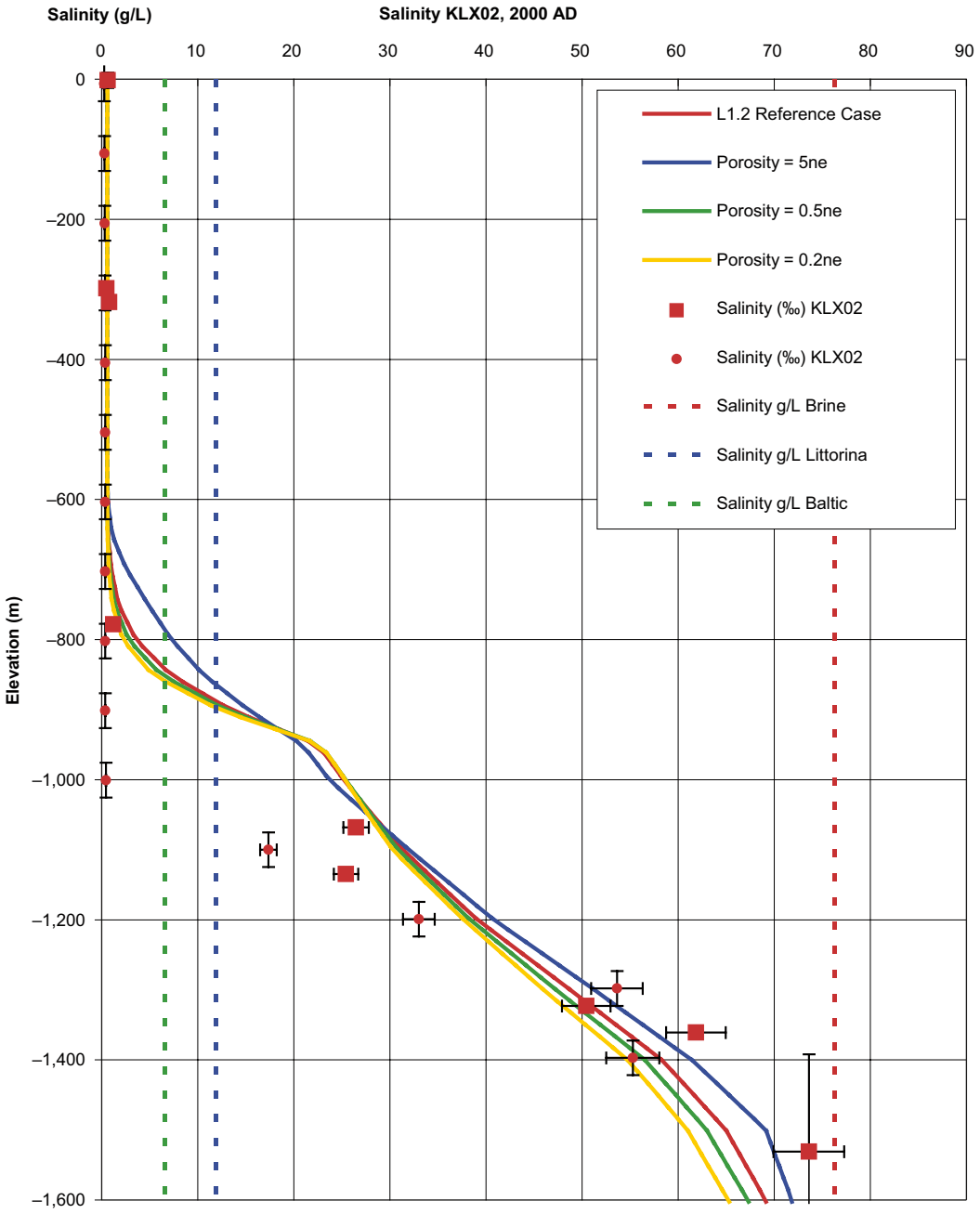

Figure 3-36. *Calculated salinity profiles in the borehole KLX02 for cases using different kinematic porosity approaches. The reference case, one case with increased porosity and two cases with decreased porosity are shown. The case with the porosity upscaled five times is denoted 5 n_e, the case with the porosity halved is denoted 0.5 n_e and the case with the porosity downscaled 5 times is denoted 0.2 n_e. In addition, measured values and the signature values for Brine, Littorina and Baltic Sea water are shown. Squares correspond to water samples that are representative (Table 3-2: orange) and less representative data (Table 3-2: green), and round dots represent fairly representative TDS data (Table 3-2: yellow) and supplemental data (Table 3-2: grey). The uncertainties in data are indicated with horizontal error bars. The vertical "error bars" indicate elevation interval for sample.*

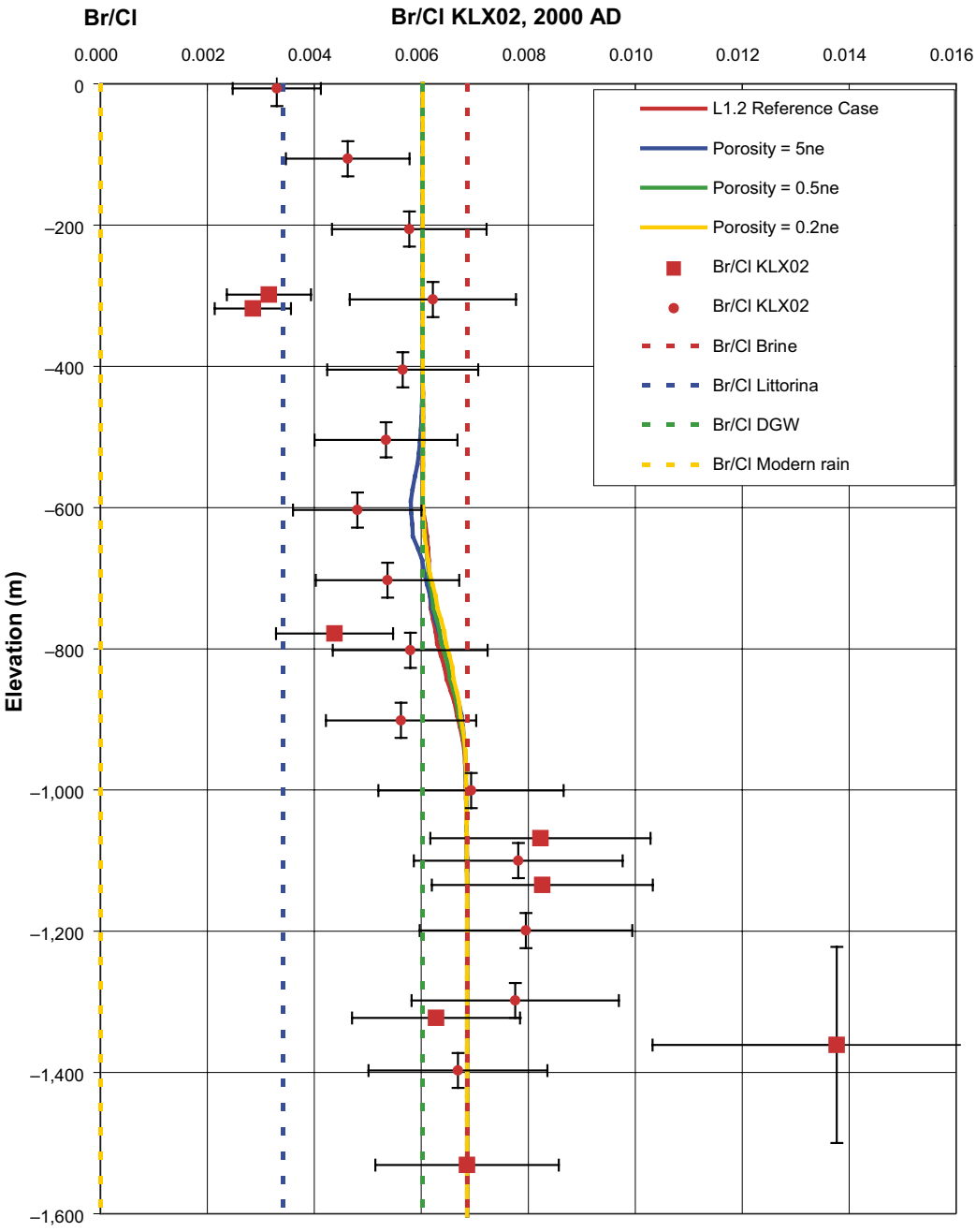

Figure 3-37. *Calculated profiles of the ratio Br/Cl in the borehole KLX02 for cases using different kinematic porosity approaches. The reference case, one case with increased porosity and two cases with decreased porosity are shown. The case with the porosity upscaled five times is denoted 5 n_e, the case with the porosity halved is denoted 0.5 n_e and the case with the porosity downscaled 5 times is denoted 0.2 n_e. In addition, measured values and the signature values for Brine, Littorina, Dilute Groundwater, and Modern rain water are shown. Squares correspond to water samples that are representative (Table 3-2: orange) and less representative data (Table 3-2: green), and round dots represent supplemental data (Table 3-2: grey). The uncertainties in data are indicated with horizontal error bars. The vertical "error bars" indicate elevation interval for sample.*

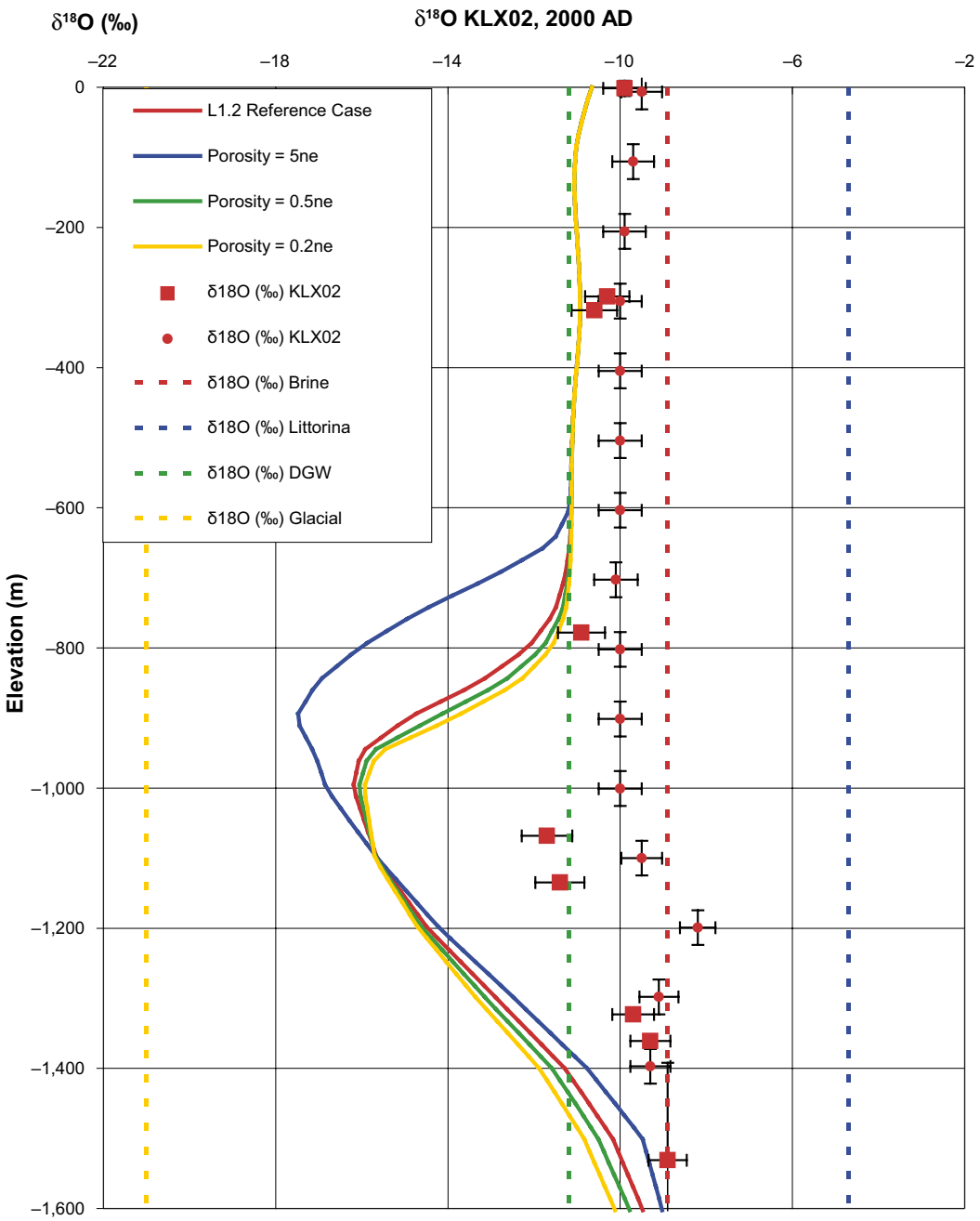

Figure 3-38. *Calculated profiles of $\delta^{18}O$ in the borehole KLX02 for cases using different kinematic porosity approaches. The reference case, one case with increased porosity and two cases with decreased porosity are shown. The case with the porosity upscaled five times is denoted 5 n_e, the case with the porosity halved is denoted 0.5 n_e and the case with the porosity downscaled 5 times is denoted 0.2 n_e. In addition, measured values and the signature values for Brine, Littorina, Dilute Groundwater, and Glacial water are shown. Squares correspond to water samples that are representative (Table 3-2: orange) and less representative data (Table 3-2: green), and round dots represent supplemental data (Table 3-2: grey). The uncertainties in data are indicated with horizontal error bars. The vertical "error bars" indicate elevation interval for sample.*

3.4.5 Sensitivity to depth dependence of hydraulic conductivity

The sensitivity to the depth dependency of the hydraulic conductivity was investigated. In the reference case, the hydraulic conductivities of the HRDs and the HCDs were taken to be depth dependent. Three depth intervals were identified: 0 to –300 m, –300 m to –600 m and < –600 m; and the properties in each interval were taken to be different. The DFN underlying the HRD is taken to have a step change in properties at a depth of 200 m, although in the modelling this change is taken to occur at –300 m. In addition, for all HRDs apart from A2, the upscaled conductivity derived from a realisation of the DFN is reduced by an order of magnitude below –600 m. (In /Hartley et al. 2006a/, it is stated that the reduction is half an order of magnitude.) Likewise, in the reference case, the transmissivities of the HCDs are taken to vary in a stepwise manner, conditioned at boreholes against measured transmissivities (see Figure 3-22).

In this sensitivity study, the hydraulic conductivities of the HRDs and the transmissivities of the HCDs in the different depth intervals were scaled by various factors, which are given in Table 3-9 and illustrated in Figure 3-39. In each case, the same scale factor is applied to the HRDs and HCDs. The calculations used the revised reference waters given in Table 3-4.

The calculated profiles of salinity, Br/Cl and $\delta^{18}O$ in the borehole KLX02 for the reference case and the variants are shown in Figure 3-40 to Figure 3-42, together with the observations and the signature values for Brine, Littorina, Dilute Groundwater, and Glacial water.

Table 3-9. The scaling factors for three depth intervals for the simulation cases.

	Depth interval			Comment
Case	0 to –300 m	–300 m to –600 m	< –600 m	
S31	$10 \cdot K_{ref}$	$5 \cdot K_{ref}$	$2 \cdot K_{ref}$	Increased conductivity
S32	$5 \cdot K_{ref}$	$2.5 \cdot K_{ref}$	$1 \cdot K_{ref}$	Moderately increased conductivity
S33	$0.2 \cdot K_{ref}$	$0.4 \cdot K_{ref}$	$1 \cdot K_{ref}$	Moderately decreased conductivity
S34	$0.1 \cdot K_{ref}$	$0.2 \cdot K_{ref}$	$0.5 \cdot K_{ref}$	Decreased conductivity

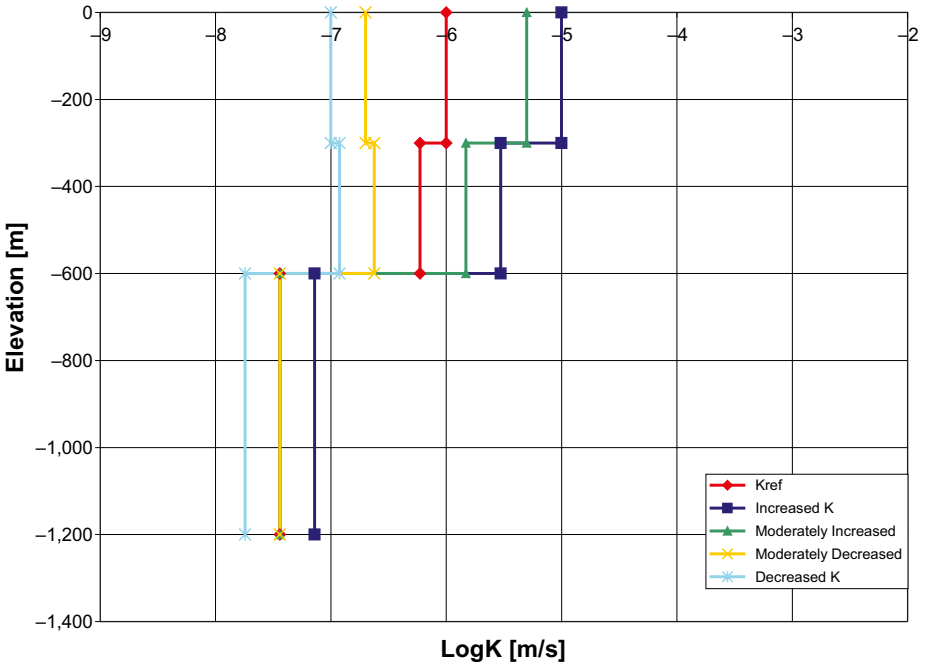

Figure 3-39. *Illustration of an example of the changes in conductivity for HCD due to the used depth dependency variants together with the step change that is used in the reference case.*

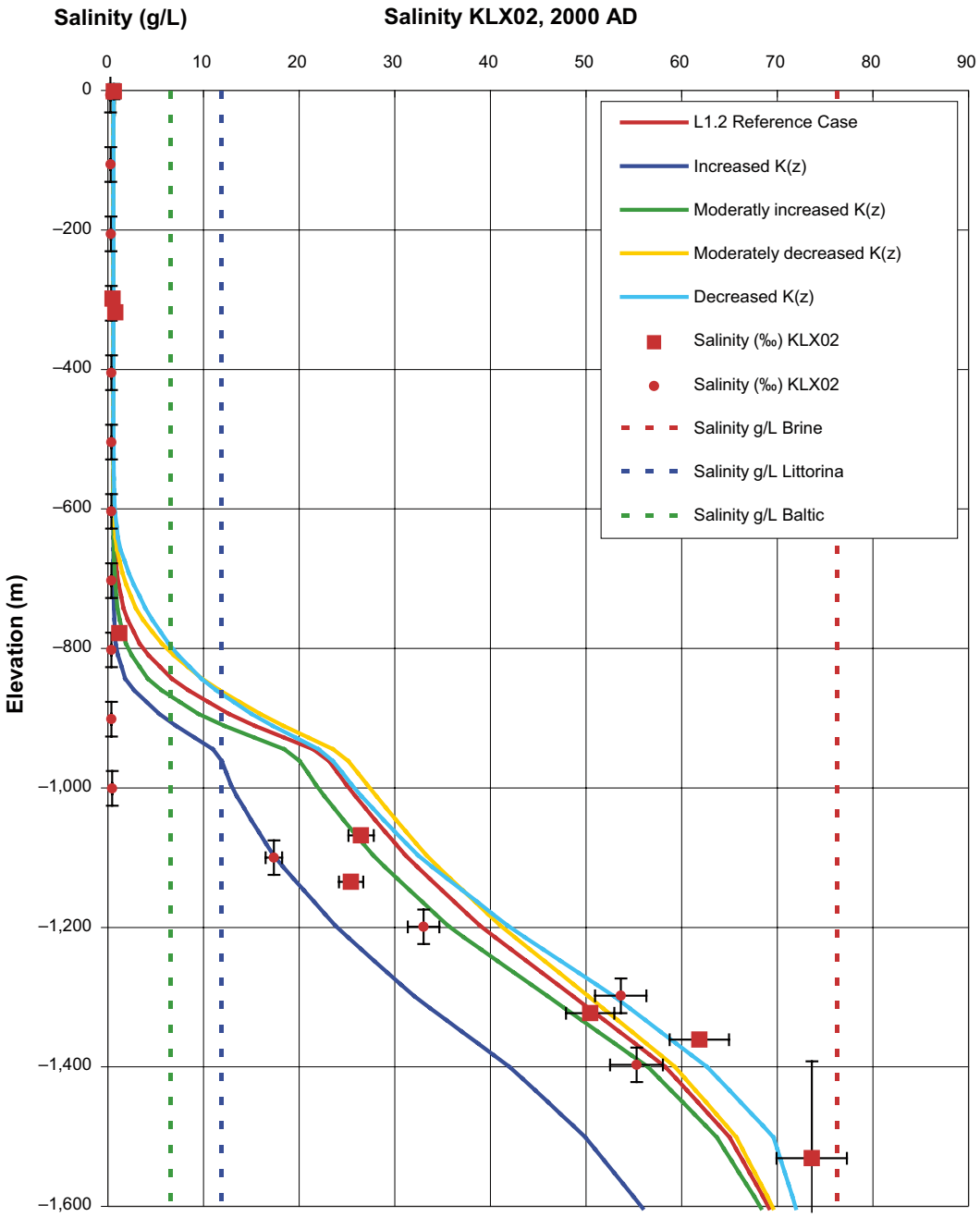

Figure 3-40. *Calculated salinity profiles in the borehole KLX02 for cases using different hydraulic conductivity approaches. In addition, measured values and the signature values for Brine, Littorina and Baltic Sea water are shown. Squares correspond to water samples that are representative (Table 3-2: orange) and less representative data (Table 3-2: green), and round dots represent fairly representative TDS data (Table 3-2: yellow) and supplemental data (Table 3-2: grey). The uncertainties in data are indicated with horizontal error bars. The vertical "error bars" indicate elevation interval for sample.*

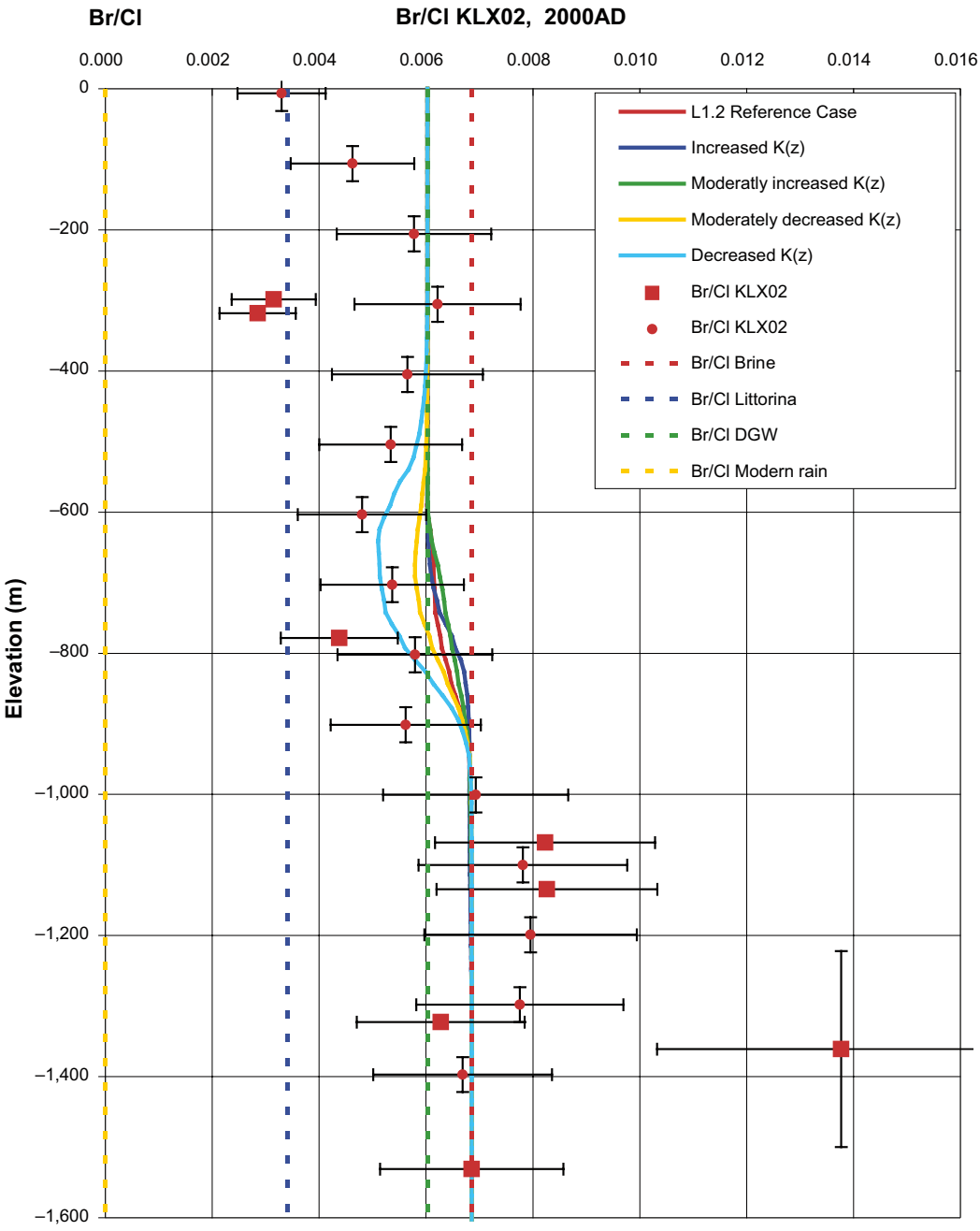

Figure 3-41. *Calculated profiles of the ratio Br/Cl in the borehole KLX02 for cases using different hydraulic conductivity approaches. In addition, measured values and the signature values for Brine, Littorina, Dilute Groundwater, and Modern rain water are shown. Squares correspond to water samples that are representative (Table 3-2: orange) and less representative data (Table 3-2: green), and round dots represent supplemental data (Table 3-2: grey). The uncertainties in data are indicated with horizontal error bars. The vertical "error bars" indicate elevation interval for sample.*

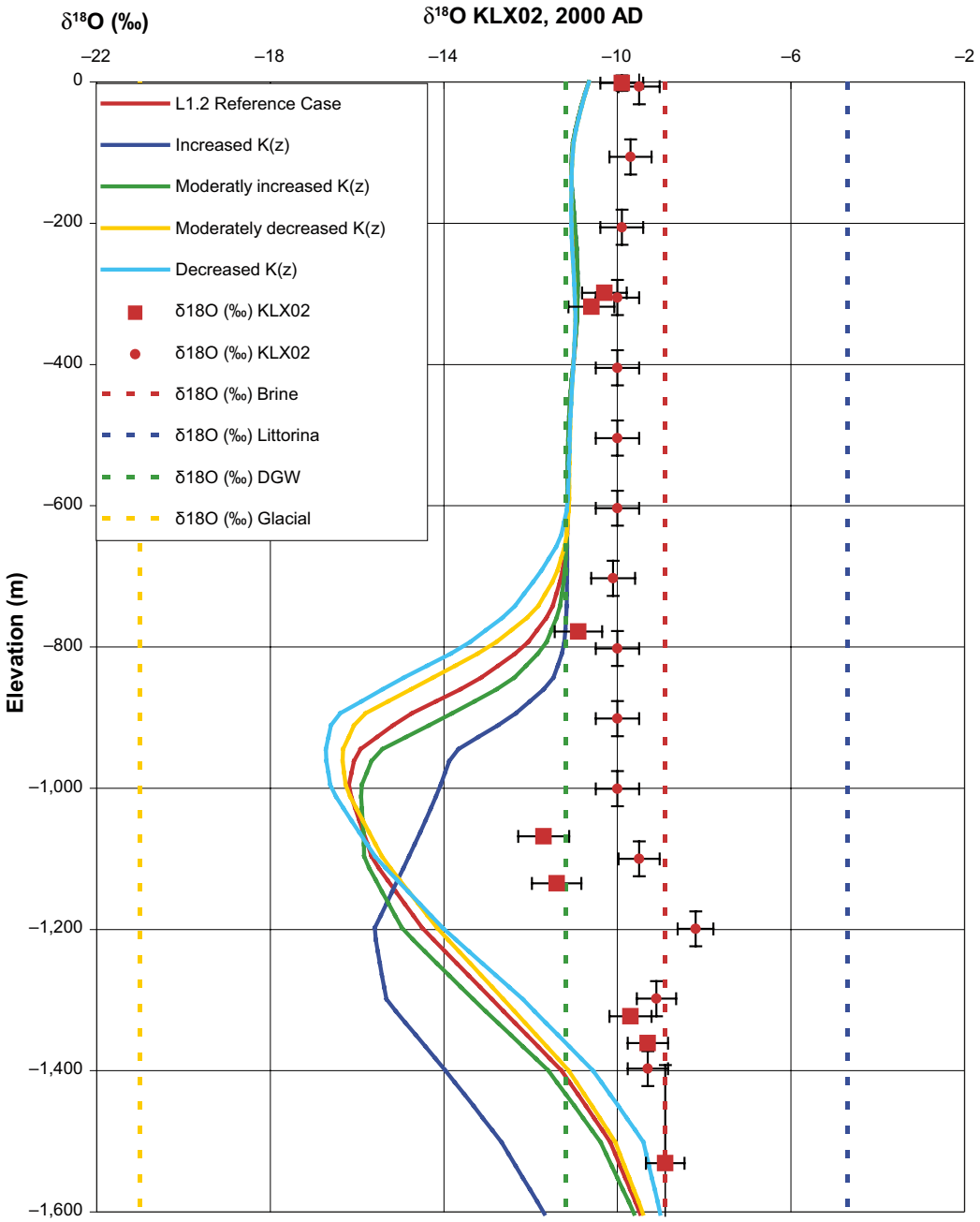

Figure 3-42. *Calculated profiles of $\delta^{18}O$ in the borehole KLX02 for cases using different hydraulic conductivity approaches. In addition, measured values and the signature values for Brine, Littorina, Dilute Groundwater, and Glacial water are shown. Squares correspond to water samples that are representative (Table 3-2: orange) and less representative data (Table 3-2: green), and round dots represent supplemental data (Table 3-2: grey). The uncertainties in data are indicated with horizontal error bars. The vertical "error bars" indicate elevation interval for sample.*

Apart from the case with the largest increase in conductivity and transmissivity, there is relatively little variation between the results for the different cases. In the former case, the regions of higher salinity and more negative $\delta^{18}O$ are displaced about 200 m downwards. This presumably is a consequence of the region that can be readily flushed by the less saline water with a less negative value of $\delta^{18}O$ being increased if the conductivity of the rocks is increased.

3.4.6 Sensitivity to boundary and initial conditions

The sensitivities to variations on the boundary and initial conditions were also considered. Four different hydraulic top boundary conditions were considered:

- In the reference case (boundary condition BC3), the head on the top surface onshore was taken to be equal to the water table plus 30% of the difference between the topography and the water table.
- For boundary condition BCS41, the head on the top surface onshore was taken to be equal to the topography.
- For boundary condition BCS42, the head on the top surface onshore was taken to be equal to the water table plus 60% of the difference between the topography and the water table.
- For boundary condition BCS43, the head on the top surface onshore was taken to be equal to the water table.

Four different initial conditions were also considered. In each case, at the start of the simulations (about 10,000 years before the present day), the groundwater was taken to be Glacial above a certain depth, d1, say, to be a mix of Glacial and Brine with the fraction of Brine increasing linearly with depth between d1 and another depth d2, and to be Brine below d2. The different initial conditions correspond to different values of d1 and d2.

- In the reference case (initial condition IC1) d1 = –700 m and d2 = –1,500 m.
- For initial condition ICS41, d1 = –200 m and d2 = –1,000 m.
- For initial condition ICS42, d1 = –1,100 m and d2 = –1,900 m.
- For initial condition ICS43, d1 = –200 and d2 = –1,900 m.

These initial conditions are illustrated in Figure 3-43.

Calculations were carried out for all combinations of the different boundary and initial conditions. The calculations used the revised reference waters given in Table 3-4. The calculated profiles of salinity, Br/Cl, Cl, Br and $\delta^{18}O$ in the boreholes KLX02 and KSH02 for the reference case and the variants are shown in Figure 3-44 to Figure 3-53, together with the observations and the signature values for Brine, Littorina, Dilute Groundwater, and Glacial water.

For a particular initial condition, there is little variation between the results for the different boundary conditions. However, there is considerable variation between the results for the different initial conditions. These variations are the largest for any of the sensitivities considered.

It appears that the reference case initial condition (IC1) gives the best match to the observed distribution of salinity in KLX02. The match for initial condition ICS43 is not quite as good, but probably still acceptable. The salinities for initial conditions ICS41 and ICS452 do not match the observed salinities at all well. Initial conditions IC1, ICS41 and ICS43 all lead to similar acceptable matches to the observed Br/Cl ratio, whereas the match for initial condition ICS42 is significantly poorer at depths between 800 m and 1,200 m.

The best match to the observed values of $\delta^{18}O$ is for initial condition ICS41. The matches for initial conditions IC1, ICS42 and ICS43 are much poorer, all having regions where the predicted value of $\delta^{18}O$ is about –16, which is much more negative than any of the observed values. It is considered that the ICS41 leads to a better match to $\delta^{18}O$ because this initial condition does not include any component of Glacial water (with very negative $\delta^{18}O$) below 1,000 m depth. However, as discussed above, initial condition ICS41 leads to a much poorer match to salinity. These observations strongly suggest that the initial fraction of Brine for initial condition IC1 is about right, but that, at least below about 700 m depth, the initial water should not be a mix of Glacial and Brine, but a mix of a Brine and a water with a much less negative $\delta^{18}O$ than Glacial water and a low salinity. It appears that the initial condition for the water composition above about 700 m depth is less important (for the reference case parameters) because this water is flushed out and replaced by more recent water, and therefore, the initial condition above about 700 m depth is not really constrained by the available data.

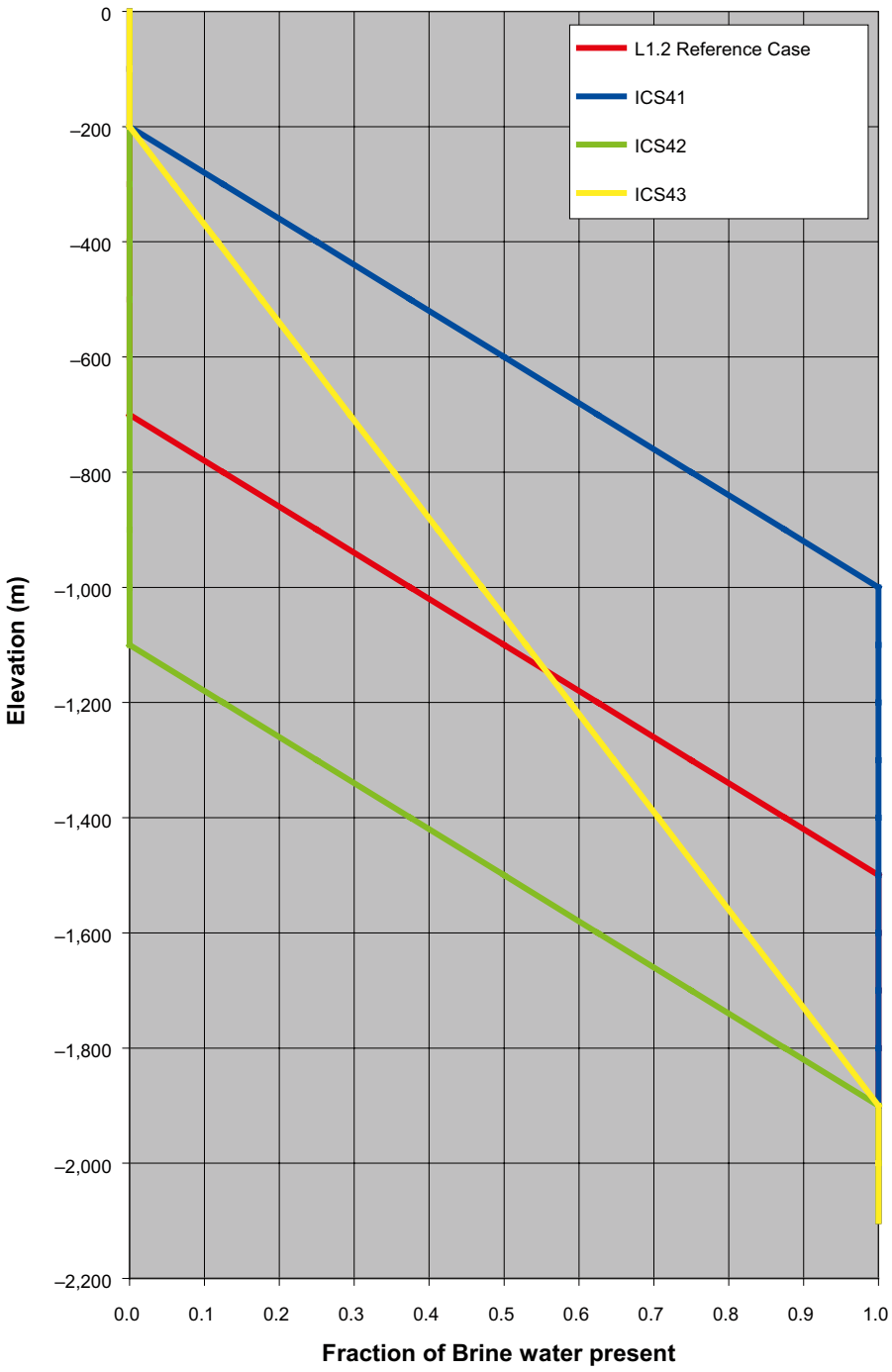

Figure 3-43. *Illustration of the four different initial conditions for reference water transport at –8000 AD, used in the sensitivity study. The graph is showing the content of Brine as a function of depth. The content of Glacial water is the complementary amount.*

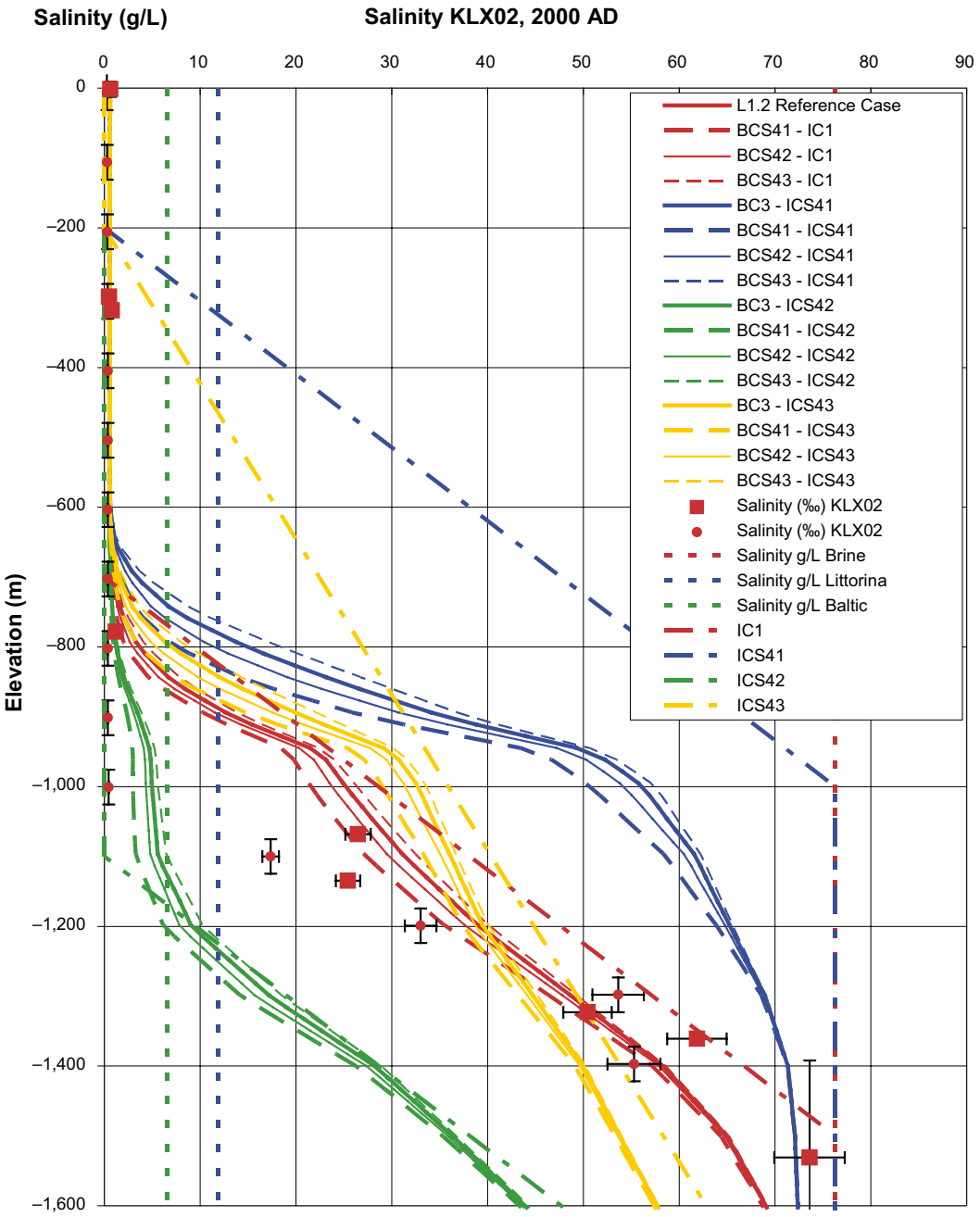

Figure 3-44. *Calculated salinity profiles in the borehole KLX02 for cases using different boundary and initial conditions. Four different boundary conditions are combined with four different initial conditions. In addition, measured values and the signature values for Brine, Littorina and Baltic Sea water are shown. Lines representing the initial conditions are also shown. Squares correspond to water samples that are representative (Table 3-2: orange) and less representative data (Table 3-2: green), and round dots represent fairly representative TDS data (Table 3-2: yellow) and supplemental data (Table 3-2: grey). The uncertainties in data are indicated with horizontal error bars. The vertical "error bars" indicate elevation interval for sample.*

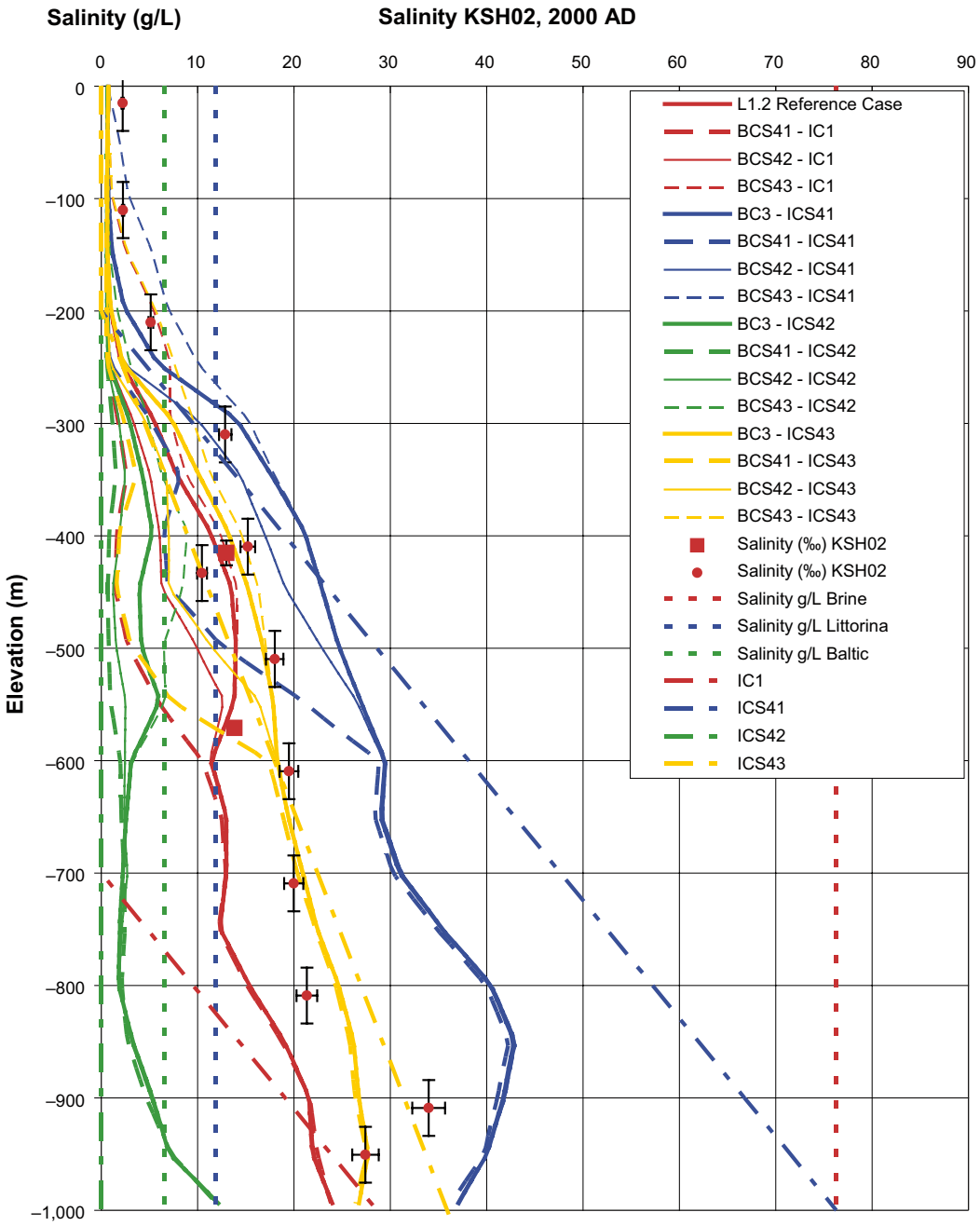

Figure 3-45. *Calculated salinity profiles in the borehole KSH02 for cases using different boundary and initial conditions. Four different boundary conditions are combined with four different initial conditions. In addition, measured values and the signature values for Brine, Littorina and Baltic Sea water are shown. Lines representing the initial conditions are also shown. Squares correspond to water samples that are representative (Table 3-2: orange) and less representative data (Table 3-2: green), and round dots represent fairly representative TDS data (Table 3-2: yellow) and supplemental data (Table 3-2: grey). The uncertainties in data are indicated with horizontal error bars. The vertical "error bars" indicate elevation interval for sample.*

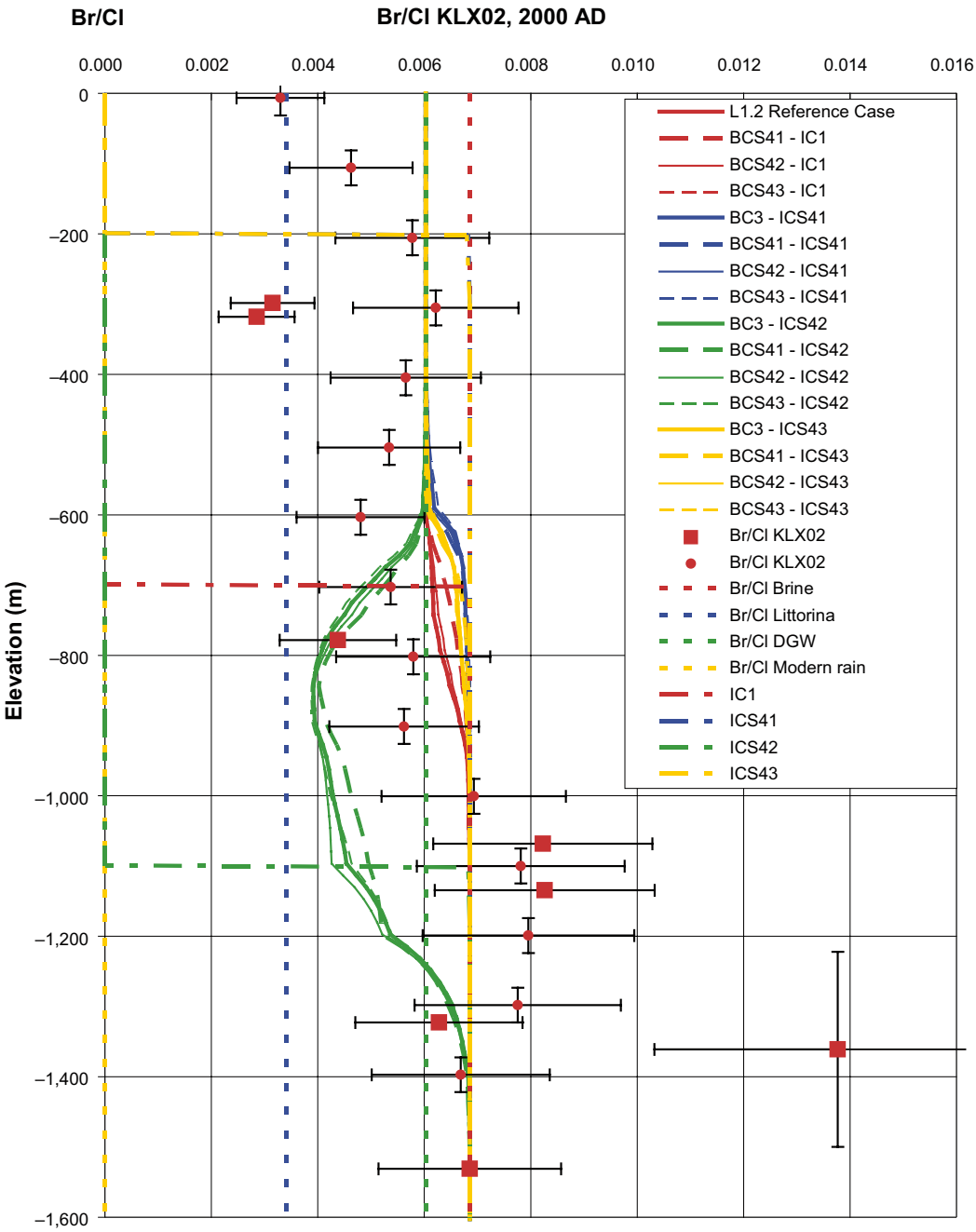

Figure 3-46. *Calculated profiles of the ratio Br/Cl in the borehole KLX02 for cases using different boundary and initial conditions. Four different boundary conditions are combined with four different initial conditions. In addition, measured values and the signature values for Brine, Littorina, Dilute Groundwater, and Modern rain water are shown. Lines representing the initial conditions are also shown. Squares correspond to water samples that are representative (Table 3-2: orange) and less representative data (Table 3-2: green), and round dots represent supplemental data (Table 3-2: grey). The uncertainties in data are indicated with horizontal error bars. The vertical "error bars" indicate elevation interval for sample.*

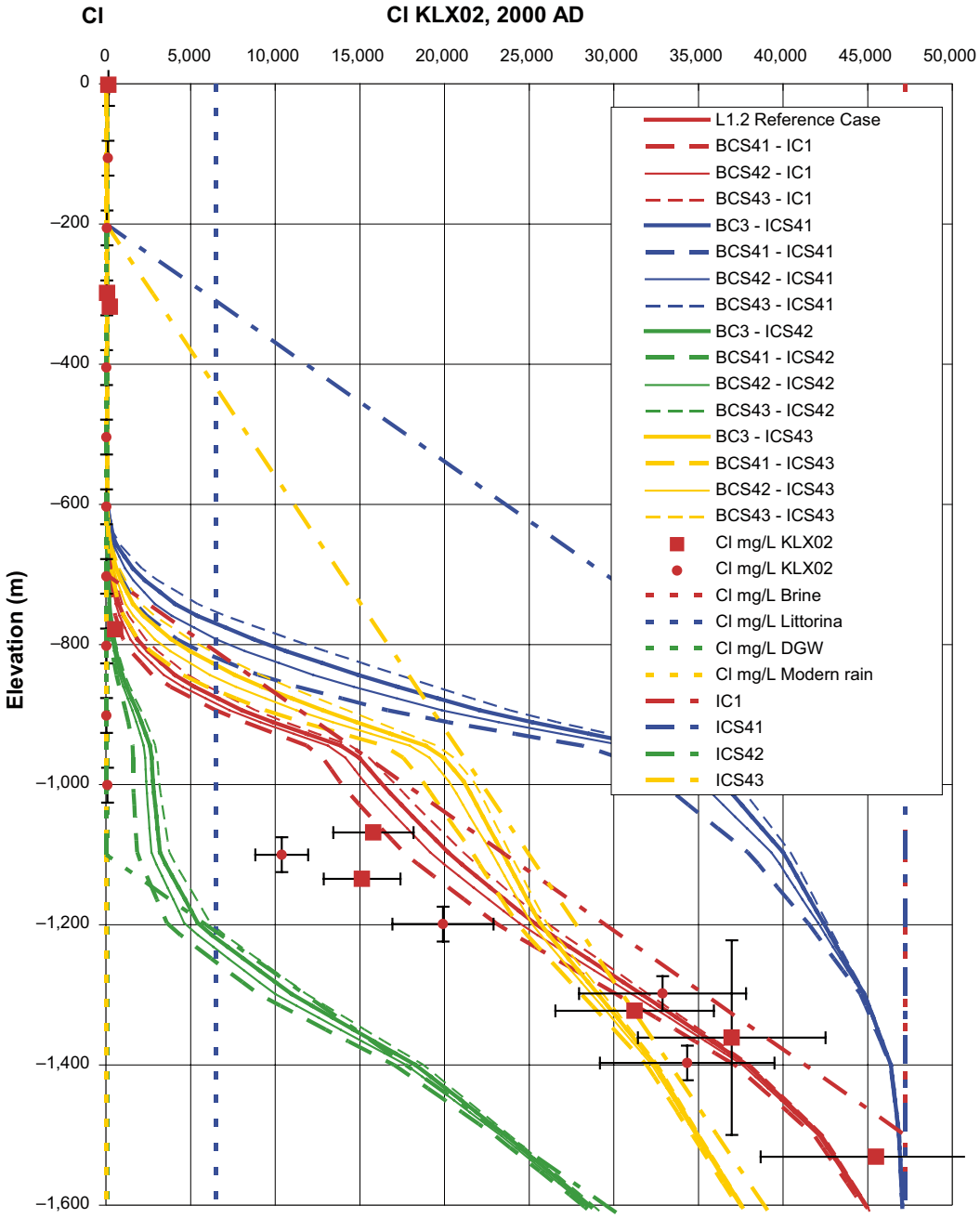

Figure 3-47. *Calculated profiles of Cl in the borehole KLX02 for cases using different boundary and initial conditions. Four different boundary conditions are combined with four different initial conditions. In addition, measured values and the signature values for Brine, Littorina, Dilute Groundwater, and Modern rain water are shown. Lines representing the initial conditions are also shown. Squares correspond to water samples that are representative (Table 3-2: orange) and less representative data (Table 3-2: green), and round dots represent and supplemental data (Table 3-2: grey). The uncertainties in data are indicated with horizontal error bars. The vertical "error bars" indicate elevation interval for sample.*

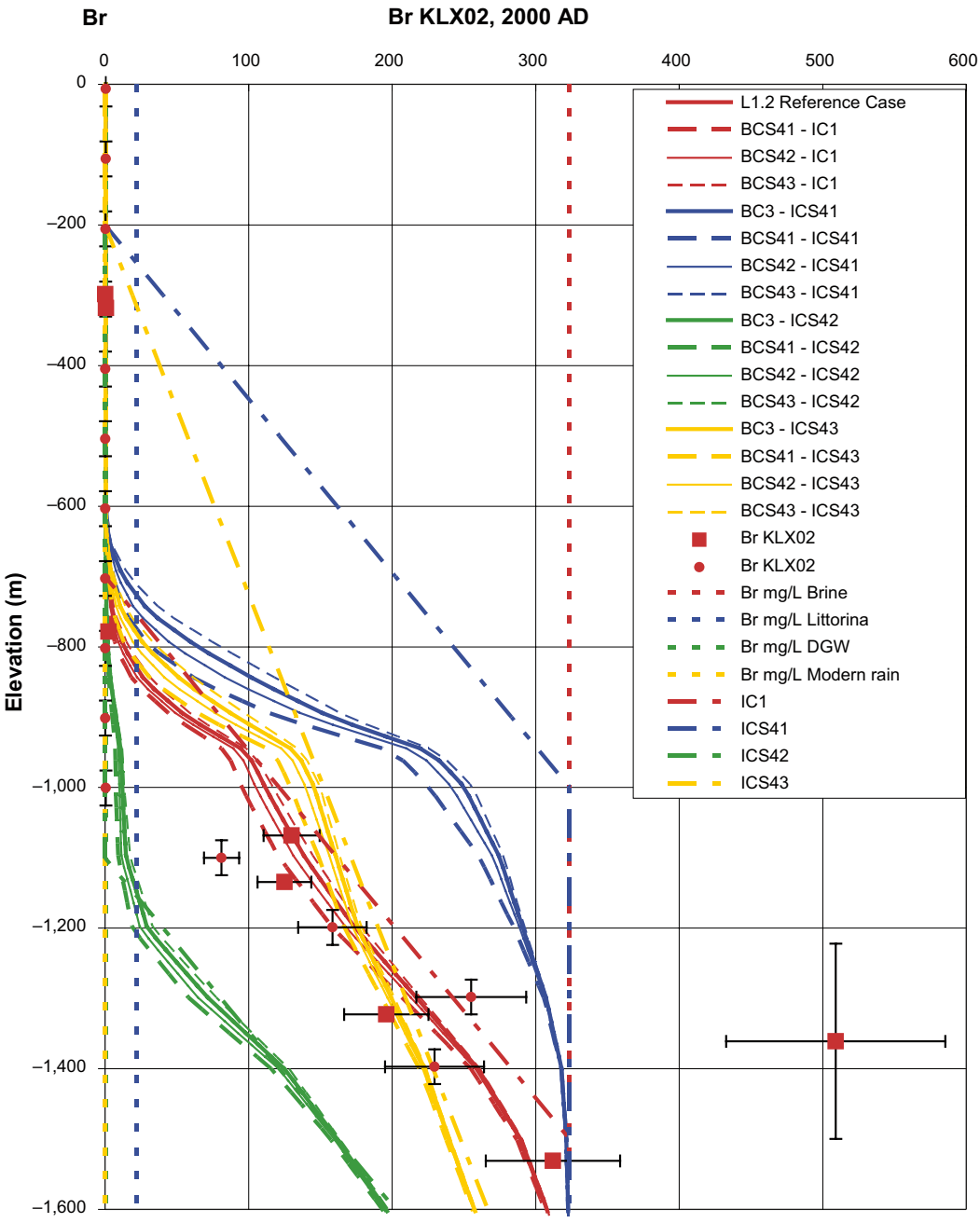

Figure 3-48. *Calculated profiles of Br in the borehole KLX02 for cases using different boundary and initial conditions. Four different boundary conditions are combined with four different initial conditions. In addition, measured values and the signature values for Brine, Littorina, Dilute Groundwater, and Modern rain water are shown. Lines representing the initial conditions are also shown. Squares correspond to water samples that are representative (Table 3-2: orange) and less representative data (Table 3-2: green), and round dots represent supplemental data (Table 3-2: grey). The uncertainties in data are indicated with horizontal error bars. The vertical "error bars" indicate elevation interval for sample.*

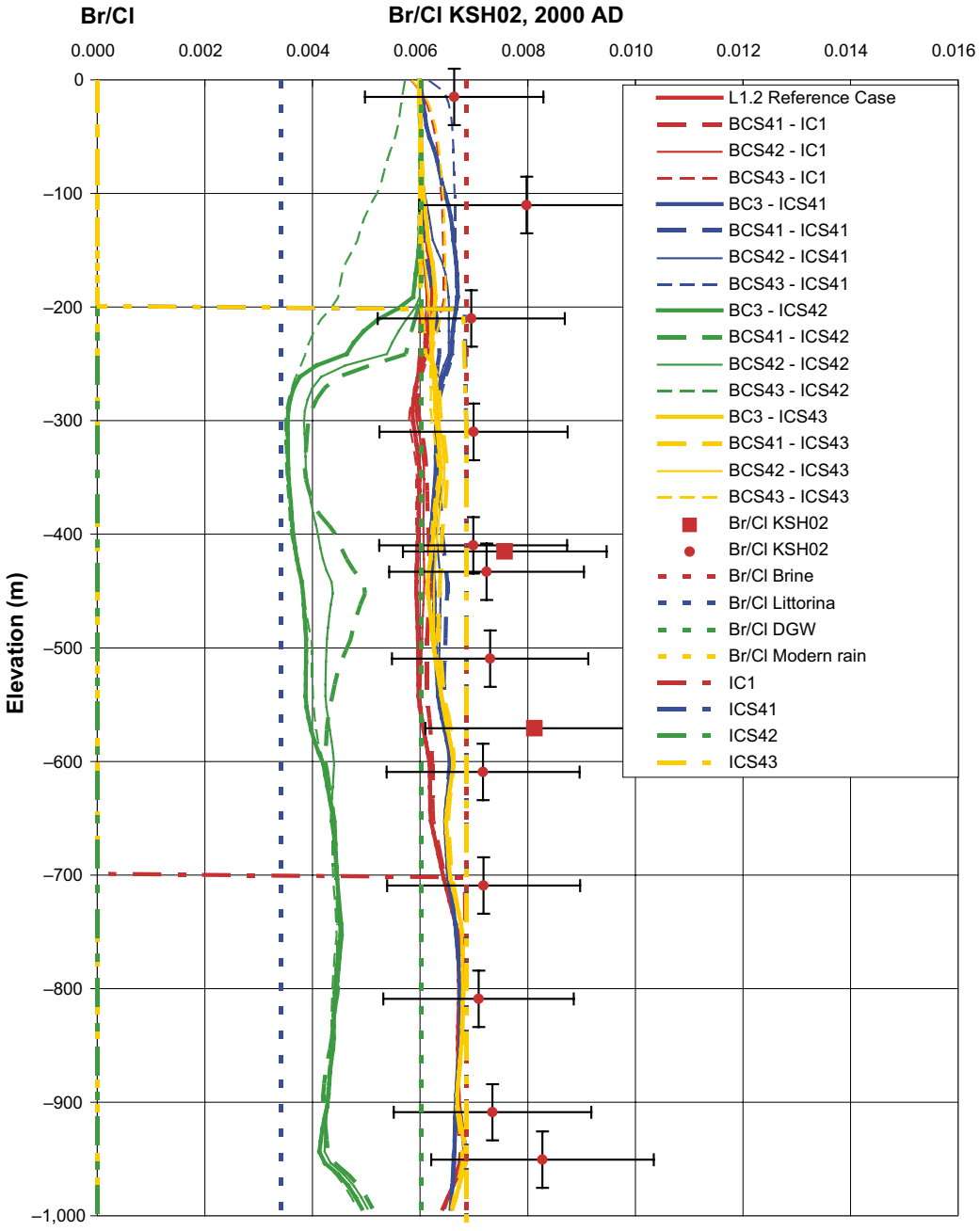

Figure 3-49. *Calculated profiles of the ratio Br/Cl in the borehole KSH02 for cases using different boundary and initial conditions. Four different boundary conditions are combined with four different initial conditions. In addition, measured values and the signature values for Brine, Littorina, Dilute Groundwater, and Modern rain water are shown. Lines representing the initial conditions are also shown. Squares correspond to water samples that are representative (Table 3-2: orange) and less representative data (Table 3-2: green), and round dots represent supplemental data (Table 3-2: grey). The uncertainties in data are indicated with horizontal error bars. The vertical "error bars" indicate elevation interval for sample.*

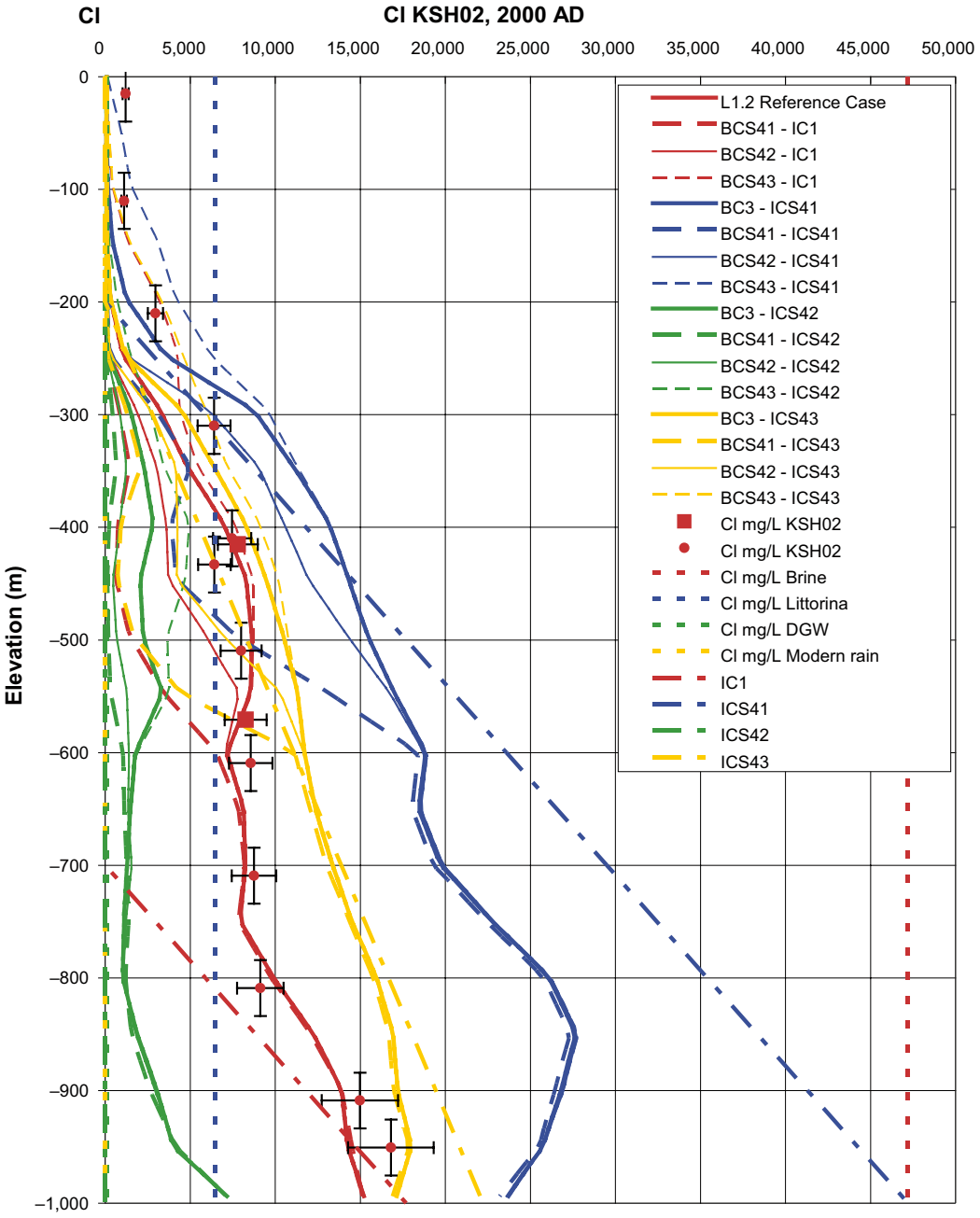

Figure 3-50. *Calculated profiles of Cl in the borehole KSH02 for cases using different boundary and initial conditions. Four different boundary conditions are combined with four different initial conditions. In addition, measured values and the signature values for Brine, Littorina, Dilute Groundwater, and Modern rain water are shown. Lines representing the initial conditions are also shown. Squares correspond to water samples that are representative (Table 3-2: orange) and less representative data (Table 3-2: green), and round dots represent supplemental data (Table 3-2: grey). The uncertainties in data are indicated with horizontal error bars. The vertical "error bars" indicate elevation interval for sample.*

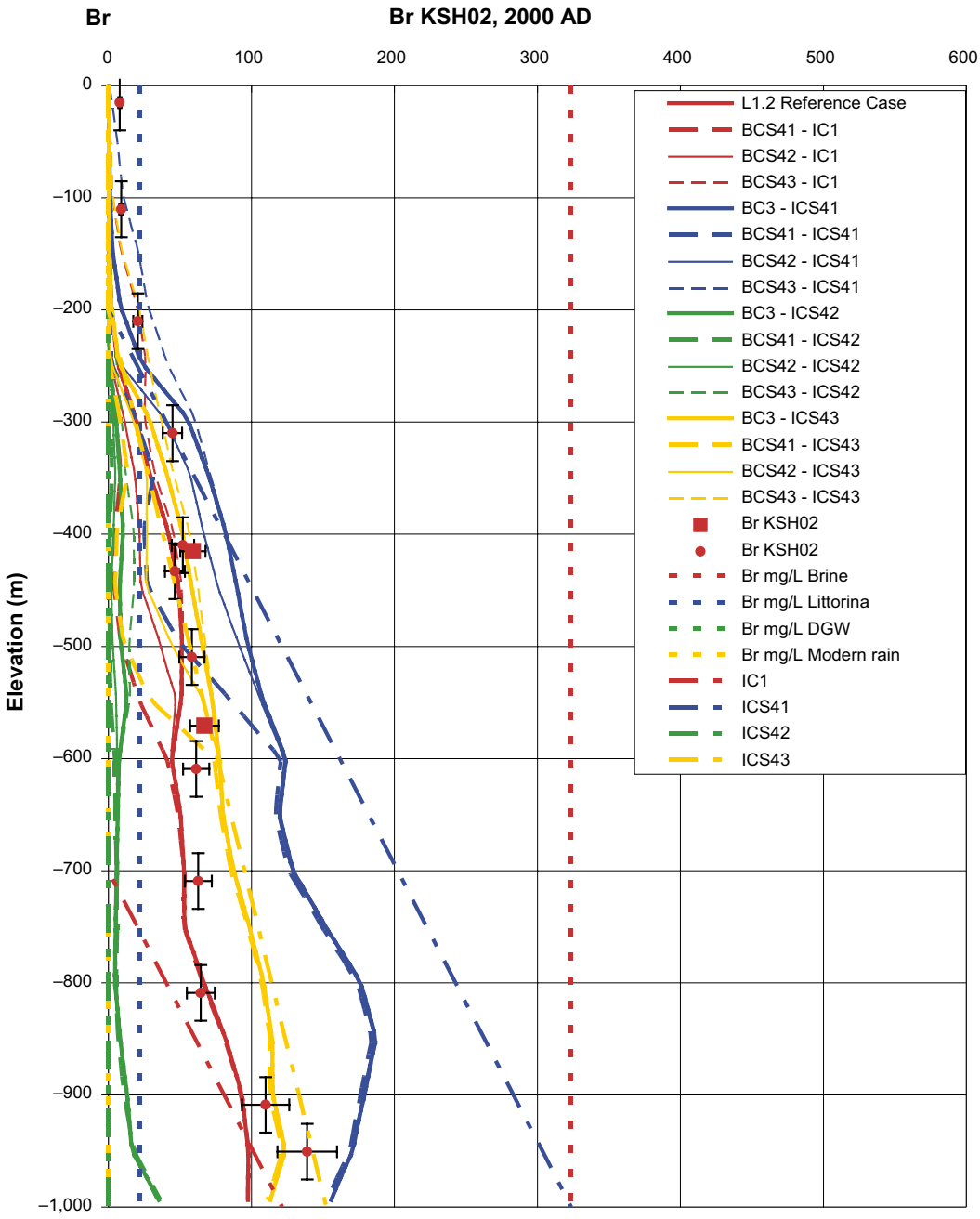

Figure 3-51. *Calculated profiles of Br in the borehole KSH02 for cases using different boundary and initial conditions. Four different boundary conditions are combined with four different initial conditions. In addition, measured values and the signature values for Brine, Littorina, Dilute Groundwater, and Modern rain water are shown. Lines representing the initial conditions are also shown. Squares correspond to water samples that are representative (Table 3-2: orange) and less representative data (Table 3-2: green), and round dots represent supplemental data (Table 3-2: grey). The uncertainties in data are indicated with horizontal error bars. The vertical "error bars" indicate elevation interval for sample.*

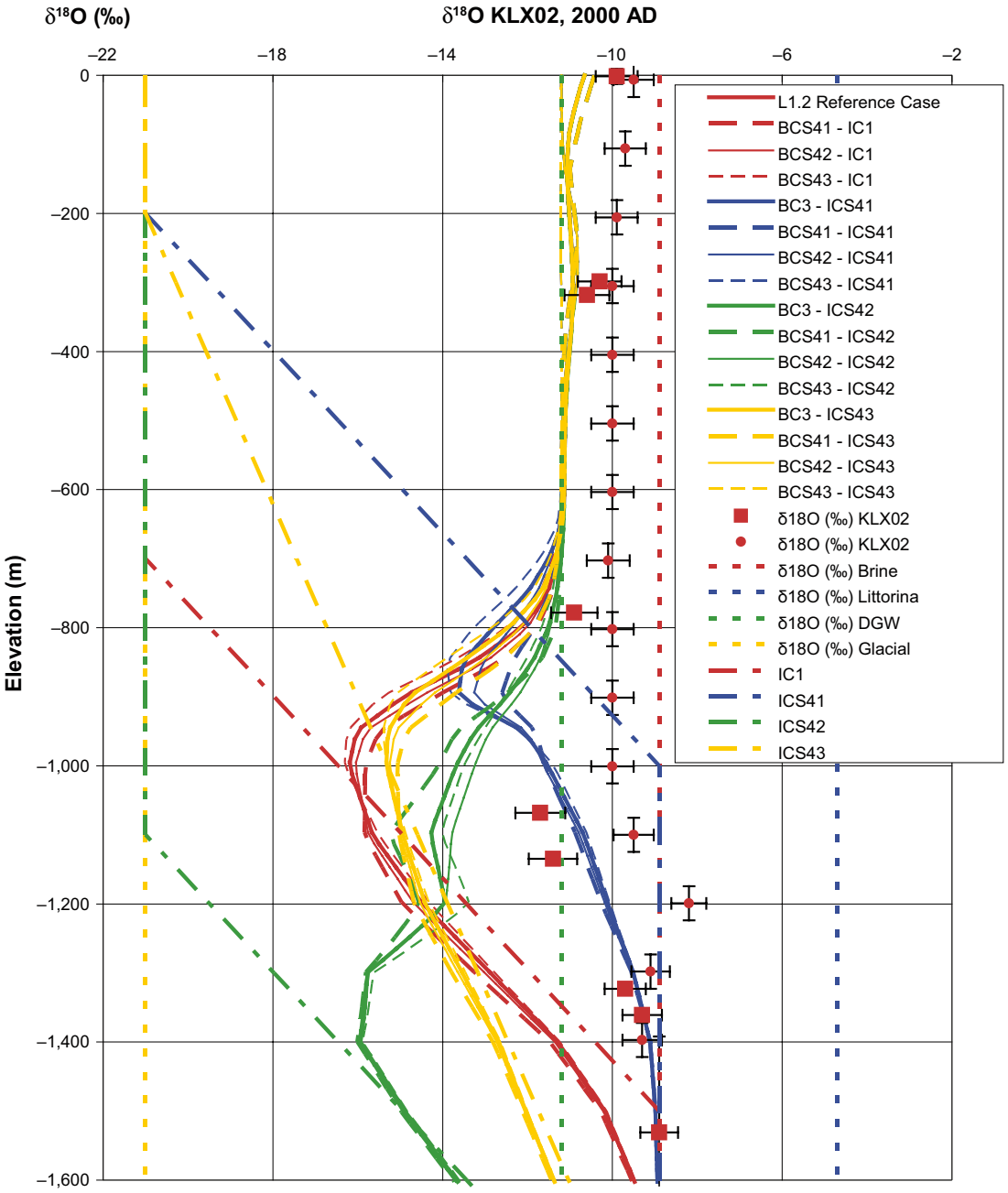

Figure 3-52. *Calculated profiles of $\delta^{18}O$ in the borehole KLX02 for cases using different boundary and initial conditions. Four different boundary conditions are combined with four different initial conditions. In addition, measured values and the signature values for Brine, Littorina, Dilute Groundwater, and Glacial water are shown. Lines representing the initial conditions are also shown. Squares correspond to water samples that are representative (Table 3-2: orange) and less representative data (Table 3-2: green), and round dots represent supplemental data (Table 3-2: grey). The uncertainties in data are indicated with horizontal error bars. The vertical "error bars" indicate elevation interval for sample.*

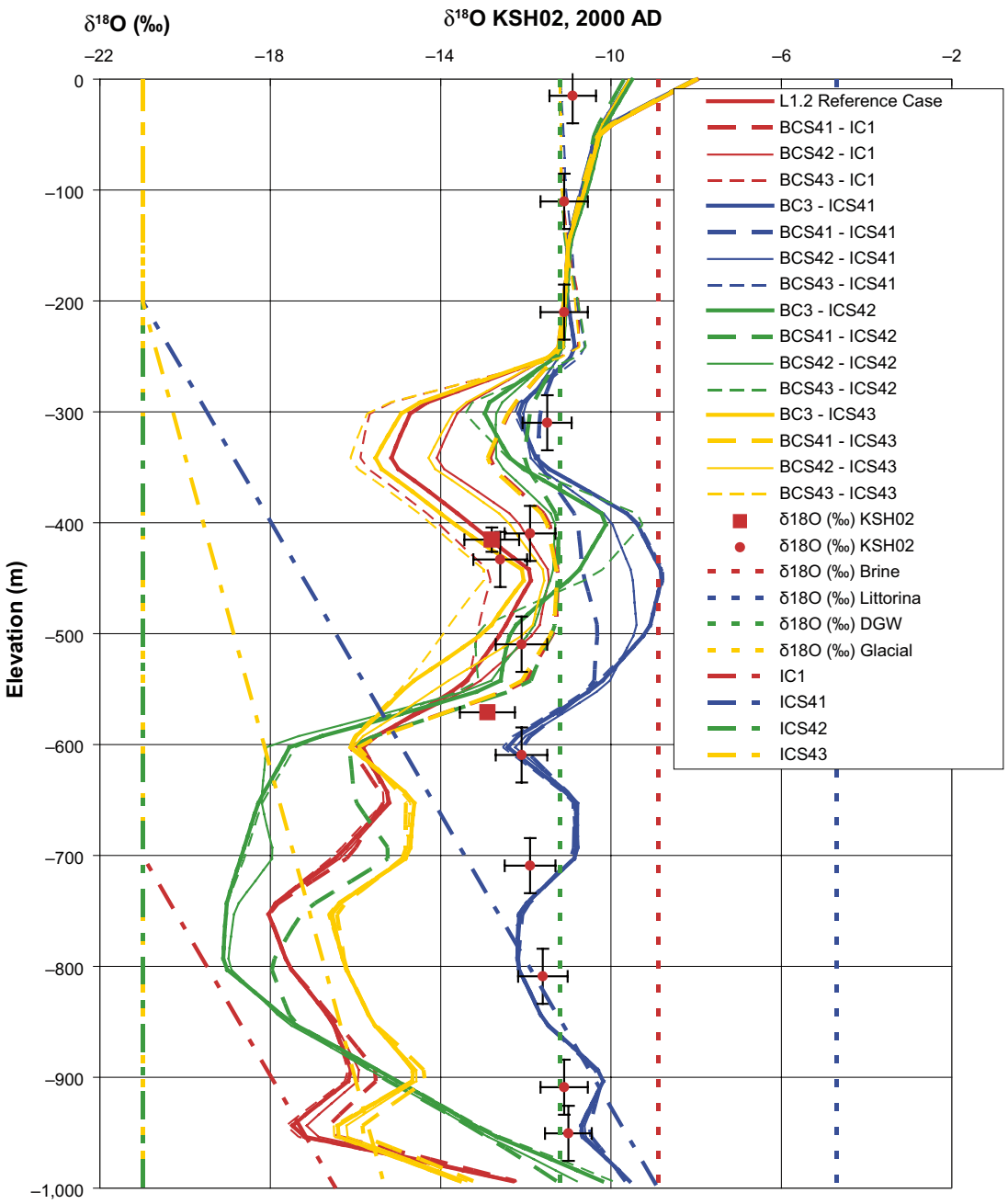

Figure 3-53. *Calculated profiles of $\delta^{18}O$ in the borehole KSH02 for cases using different boundary and initial conditions. Four different boundary conditions are combined with four different initial conditions. In addition, measured values and the signature values for Brine, Littorina, Dilute Groundwater, and Glacial water are shown. Lines representing the initial conditions are also shown. Squares correspond to water samples that are representative (Table 3-2: orange) and less representative data (Table 3-2: green), and round dots represent supplemental data (Table 3-2: grey). The uncertainties in data are indicated with horizontal error bars. The vertical "error bars" indicate elevation interval for sample.*

The match to the observed values of the Br/Cl ratio is very similar and probably acceptable for initial conditions IC1, ICS41 and ICS43, but significantly poorer for initial condition ICS42.

Although the match to observations is not as good for initial condition ICS42, the results for this initial condition are very helpful in understanding the flow, although careful consideration is required to develop this understanding. The initial condition for the Br/Cl ratio is actually very close to a step function for each initial condition considered. This is because the initial water composition is a mix of Brine, with high chloride and bromide concentrations, and Glacial with very small chloride concentration and zero bromide concentration (for the revised reference waters). If the mix contains even a small fraction of Brine, then the concentrations of chloride and bromide are dominated by the contribution from the Brine and the Br/Cl ratio is essentially equal to that for the Brine.

The calculated distribution of Br/Cl at the end of the simulation differs significantly from the initial distribution above about 1,400 m. Clearly the initial water has been flushed out and replaced by a different water above this depth. The question is 'what is this water?'. Above about 600 m, the replacement water is clearly DGW because it has zero salinity and $\delta^{18}O$ equal to that for DGW. The more interesting question is 'what is the water between about 700 m depth and 1,200 m depth where the Br/Cl is significantly lower than elsewhere?'. This cannot be a mix of Glacial, DGW and Brine with a significant fraction of Brine because this would have the Br/Cl signature of Brine, for a reason similar to that discussed above. This water must be mainly Littorina in order to give the predicted Br/Cl ratio and the predicted non-zero salinity. Thus the low value of Br/Cl in the region is providing a strong indication of the presence of Littorina water.

The question is then 'why is Littorina present for this variant?'. It is considered that the reason is as follows. For all variants, a fraction of Littorina enters the model in the region that is offshore, which varies over time. The Littorina is significantly more saline, and hence denser, than either the Glacial or DGW and the density of the Littorina provides a force driving it into the domain. In all the variants, the groundwater flows are very low in the region where there is a significant fraction of Brine, because of the density gradient. The Littorina therefore only flows down to a depth where the density of the water is less than or equal to that of Littorina, which is about 1,200 m for the variant with initial condition ICS42. Subsequent to the Littorina entering the model in the region of KLX02, the top 700 m are flushed out by DGW because KLX02 is then onshore. This leads to the observed distribution for Br/Cl in KLX02.

This pattern is not shown for the other variants because the Littorina does not penetrate to as great a depth for the other variants. This is because the region where there is a mix of Brine and hence a density gradient suppressing flow extends closer to the top of the model for these variants. The Littorina therefore only migrates into the upper and middle depths of bedrock down to a depth of about 600 m that have a relatively high hydraulic conductivity, from where it is subsequently flushed out by the recharging DGW.

3.5 Summary and conclusions

In the SDM and SR-Can calculations for Laxemar 1.2 /Hartley et al. 2006ab/, hydro-geochemical data (the concentrations of various groundwater constituents) and interpreted mixing proportions of certain reference waters were used to test and calibrate the developed flow models, and some sensitivity studies were undertaken. It was considered that further sensitivity studies would be valuable in developing understanding, and would provide a foundation for future work. The current study was therefore carried out. The overall objectives of the study were:

- To examine the variability in the modelled groundwater composition, by considering a number of realisations of the Hydro-DFN model.
- To explore the sensitivity of the modelled composition to key hydraulic properties, boundary and initial conditions.
- To develop the approach for using hydro-geochemical data to test and calibrate the flow models.

It is considered that the match of the predicted concentrations of various groundwater constituents to observations is acceptable for the SR-Can reference case apart from the following. The predicted values of Br/Cl in the top 400 m are close to 0 whereas the observed values are significant (about 0.005) suggesting that the Br/Cl ratio is too low for the recharging water. There is an indication that the modelled $\delta^{18}O$ is more negative than the observations for depths between about 700 m and 1,500 m, which may suggest that the assumed initial condition of a mix of Brine (with $\delta^{18}O$ about –9) and Glacial (with $\delta^{18}O$ about –17) in this region may not be right, but should be a mix of Brine and a water with less negative $\delta^{18}O$ than the Glacial reference water, i.e. an older warm climate inter-glacial water. Such a hypothesis about the origin of the freshwater at depth would also imply that glacial water was not generally injected to depths much below 700 m whilst ice sheets covered or past over the site during the last ice age.

Calculations were carried out for a suite of 10 realisations of the Hydro-DFN model, to examine the variability in the modelled groundwater composition. For each borehole, the predicted results for the different realisations have very similar trends. In most cases, the profiles of a particular quantity in a borehole have a fairly similar but slightly displaced shape for the different realisations. However, this does mean that in regions where a quantity is changing the value at a particular depth may vary significantly between realisations. This highlights the difficulty of making pointwise comparisons of predicted and observed concentrations. The results for some boreholes may be significantly influenced by the presence of nearby transmissive deformation zones.

After the first calculations had been undertaken, revised specifications for the reference waters were provided and all subsequent calculations were carried out with the revised reference waters. The main differences in the reference water compositions are that the Glacial water has a more negative $\delta^{18}O$ (–21 rather than –17) and the DGW is slightly more saline, and in particular, has a non-zero Br/Cl ratio (similar to that of Brine in fact).The revised reference waters led to an improved match to the observed Br/Cl ratios, but the possible discrepancy in between the predicted and observed values of $\delta^{18}O$ at depth between 800 m and 1,200 m was more apparent, adding weight to the suggestion that the assumed initial condition was not right in this region.

Calculations were undertaken for a suite of variants in which the properties of the HCDs were taken to vary stochastically. The results for these variants generally varied less than the results for the suite of variants for different realisations of the Hydro-DFN. However, for the highest level of variability considered, the flow calculations only converged for one of the three realisations considered. In the L1.2 modelling, it was commented that stochastic HCD properties gave significant changes in the predicted chemistry profiles. However, having complete a more comprehensive sensitivity study here, this appears less important than the assumed initial condition and depth dependency in the hydraulic conductivity.

It was found that the results were not very sensitive to the value of the kinematic porosity except for the highest value considered. It was also found that the results were not very sensitive to the hydraulic conductivity, except for the highest values considered. Further, it was found that the results were not very sensitive to the boundary condition for the groundwater head imposed on the top surface. However, only variations in the specified head were considered, and the range of variations may not have been large. Variations in, for example, the chemistry of the recharging water were not considered.

The greatest sensitivity found was that to the assumed initial conditions. In particular, the initial distribution of salinity plays a very important role. It appears that the initial distribution largely remains at depths below about 1,000 m. The initial conditions for the reference case give the best match to observations of salinity. The match to the observations of $\delta^{18}O$ may not be as good for this variant, but as discussed above, the assumption of an initial fraction of Glacial water at depth between 800 m and 1,200 m may not be right.

It is suggested that the specified infiltration boundary condition be used in future and sensitivities to the properties of the Quaternary deposits be quantified.

The Br/Cl ratio may provide a useful indicator of the presence of Littorina. Mg can be used as consistency check on the interpretation of Littorina water, but only in qualitative way as it is non-conservative.

It is considered that it was more useful to compare the predictions with the observation for the concentrations of major ions and isotope ratios than with the inferred M3 mixing fractions, since the latter introduce addition interpretation uncertainties that in some circumstances can be large /Gómez et al. 2007/.

The help from ChemNet is gratefully acknowledged, and it is suggested that the data and simulation results should be discussed even more in the future. It may be possible to utilise the data with higher levels of drilling fluid contamination if this can be compensated for.

In summary, the modelling of palaeo-hydrogeology in the Laxemar subarea is most sensitive to the hydro-geochemical conceptual model of the origin and composition of groundwater, especially the assumptions made about the initial hydro-geochemical conditions appropriate at 8,000 BC after the most recent glaciation event, and the depth dependency of the hydraulic conductivity. Hence, it provides a useful calibration of these two aspects of the site descriptive model. Other aspects of the model and parameters, such as deformation zone transmissivities and porosities, seem to give results consistent with the hydro-geochemical data for all values considered within their ranges of uncertainity, and so these parameters cannot be calibrated to a fine degree this type of data.

4 Development of a Hydro-DFN model for the near-surface from boreholes KLX09B–F

4.1 Background and objectives of study

A methodology for deriving Hydro-DFN models has been developed primarily based on borehole geological and hydraulic logging, for example /Hartley et al. 2006b/. The purpose of this study is to assess this methodology more thoroughly by simulating the hydrogeology of a region containing a number of closely spaced boreholes of varying trajectory using a discrete fracture network (DFN) concept. The region of interest contains the KLX09B to KLX09F shallow core drilled boreholes of the Laxemar subarea. The region also contains the KLX09 deep cored borehole. A set of DFN modelling simulations were performed to attempt to match geometric measurements from borehole and outcrop data, as well as single-hole flow measurements and interference test results. Key issues of interest for this study were the derivation of hydrogeological DFN (Hydro-DFN) model for the upper 100 m of rock since this depth interval is usually cased in the other deep cored drilled holes, and the identification of any anisotropy in the fracture geometrical and hydraulic properties.

4.1.1 Borehole layout

The boreholes lie in fairly close proximity to one another, as shown in Figure 4-1.

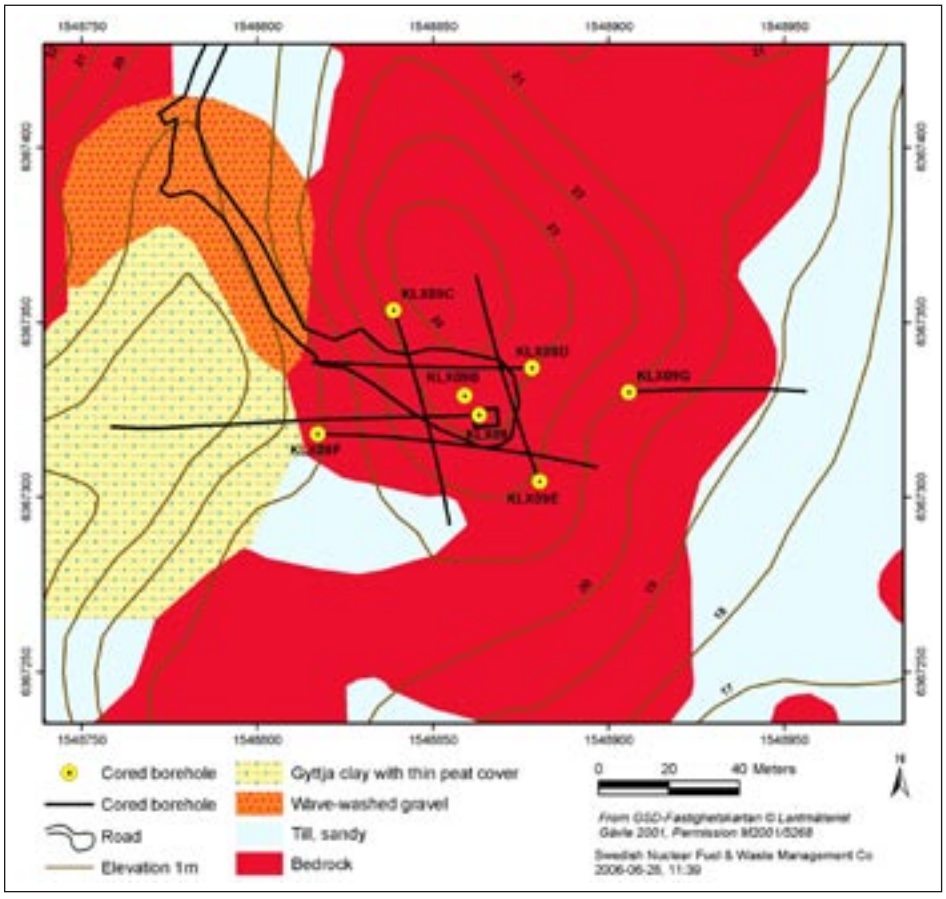

Figure 4-1. Layout of the KLX09 boreholes along with the Quaternary deposits map.

Borehole KLX09B lies in the centre of the region and is vertical. Boreholes KLX09C to KLX09F are inclined at approximately 60 degrees to the horizontal and run in different directions (as indicated by the black lines in Figure 4-1). Boreholes KLX09B to KLX09F are approximately 100 m to 150 m long; with casing in the top 13 m to 16 m beneath the surface. Borehole KLX09 is near-vertical and approximately 900 m long with casing in about the first 12 m. Borehole KLX09 provides mainly geological data and was not involved in the hydraulic tests in the same way as the near surface boreholes. Neither pumping nor PFL-f tests were performed in KLX09 in time for this modelling (PFL measurements have since been made). During the tests, KLX09 was packed-off and pressures were registered in the intervals; 0–33 m, 34–66 m, 67–103 m and 104–880 m. KLX09 was included in the simulations as an open hole since it does provide extra potential hydraulic connections between fractures.

Details of how the single-hole and interference tests were performed are documented in /Sokolnicki and Väisäsvaara 2006, Sokolnicki and Pöllänen 2006/.

4.1.2 Definitions

Here, some of the concepts and terminology used in this section are defined.

Fracture classifications

Each of the fractures mapped in the cores are classified according to a range of different properties. One main classification used in this study is an indication of whether the fracture corresponds with some void space in the borehole core indicating a potential contribution to flow:

- Sealed fractures – fractures mapped in the core that do not correspond with a visible natural break in the core.
- Open – fractures mapped in the core that correspond with a natural complete break in the core.
- Partly open – fractures mapped in the core that correspond with a partial natural break in the core.

The term “All fractures” will be used here to denote fractures which are sealed, open or partly open, whereas “Open fractures” will be used to denote only those fractures which are either open or partly open. The numbers of partly open fractures is generally very small, only 0.3% of all fractures.

Another key classification used in this study is

- PFL-anomaly fracture – a fracture which is judged to be the most likely to be associated with an observed flow-anomaly in a PFL-f hydraulic test. The word “anomaly” is used here, and elsewhere in the site descriptions, to described the discrete changes in flow along the pumped borehole located by the PFL-f difference logging technique.

Conceptually, it is assumed that open fractures form potential conduits for groundwater flow, whether they actually provide paths for flow depending on their connectivity and transmissivity. Such that, the PFL-anomaly fractures represent a sub-set of the open fractures that are both connected to a wider network and have a transmissivity above a threshold which will give flow measurable by the PFL-f method.

Fracture size distribution

One of the most difficult characteristics of fractures to measure directly in the sub-surface rock is fracture size. Fracture trace length can be measured on outcrops for fractures on the scale of metres to tens of metres, and data is available for lineaments on the scale of 1 km to several kilometres, but this leaves a gap between the scales. (The minimum lineament length mapped at Laxemar is around 1 km). A widely used assumption is one of a continuous scale of fracturing that spans all scales in a continuous manner which can be described by a power-law relationship between fracture intensity and fracture size. The key parameters for a power-law distribution for fractures of different sizes, measured in terms of the radius of a disc, are the shape parameter (k_r) and the location parameter (r_0). The distribution, $f(r)$, is often defined only in a truncated range, between r_{min} and r_{max}.

$$f(r) = \frac{k_r \, r_0^{k_r}}{r^{k_r+1}} \qquad \text{Equation 4-1}$$

where $r_{max} \geq r \geq r_{min} \geq r_0$, $r_0 > 0$, and $k_r > 0$.

The outcrop and lineament fracture size data can be used to derive measures of fracture frequency by using so called area-normalised frequency plots to combine structural data gathered on different scales of observation so as to guide the choice of fracture size parameters. Fracture frequency is also measured along core-drilled boreholes, which gives another scale of measurement resolution. Small scale fractures generally show up well on the surfaces of cored rock cylinder, so it is possible to observe fractures on the scale of the borehole diameter, 0.076 m. Figure 4-2 illustrates the fracture size windows measured by each of the fracture characterisation techniques used in SKB's site investigations.

For the KLX09 drill site area, a local-scale geological DFN model, or Geo-DFN, was derived with the fracture size parameters determined from combining fracture frequency data for outcrop maps and borehole core. Such models were developed based on all fractures mapped in the cores and outcrop without consideration for the flow characteristics of the interpreted fracture system.

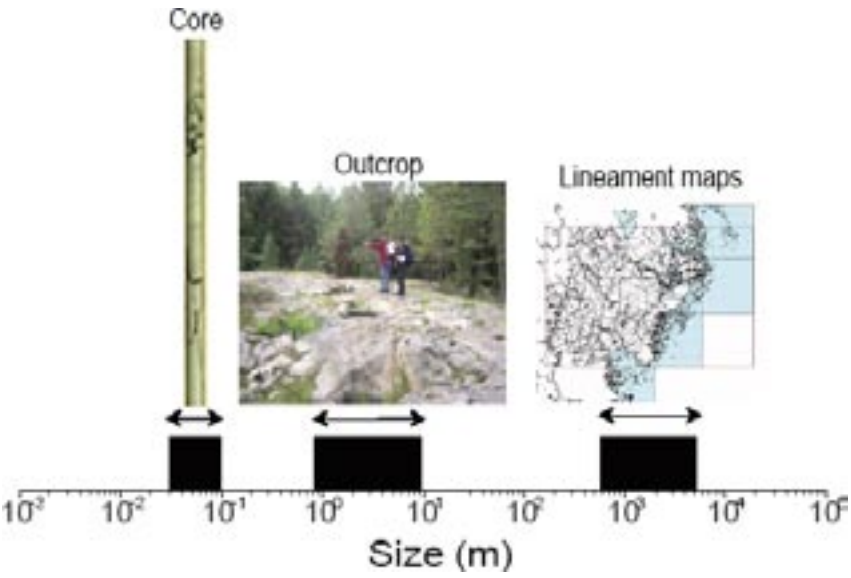

Figure 4-2. *Three scales of fracture trace observations. Only Outcrop and Lineament traces are used for the construction of a fracture size model in the geological DFN. Part of the aim of this study is to derive fracture size models that honour the fracture frequency data from core and hydraulic tests in boreholes.*

In this study, we are interested in the fracture size distribution of only those fractures that contribute to the hydrogeological system, i.e. open fractures and PFL-anomaly fractures. Clearly this will be a sub-set of all fractures, but the parameter distributions of this sub-set do not necessarily bare a simple relationship to those for all fractures. Since, the distribution of fracture sizes for open fractures cannot be measured directly; here we develop methods for calibrating the size distribution of open fractures based on characteristics such as the observed frequency of PFL-anomaly fractures, since this indicates the connectivity of the fracture system which is strongly dependent on the fracture size distribution given the measured frequency of open fractures.

Fracture intensity

The intensity of fracturing can be measured in several ways usually depending on the method by which fractures are mapped. The main ones are defined as:

- P_{10} – average fracture frequency along a borehole or scan-line,
- P_{21} – average fracture trace length per unit area, e.g. on an outcrop or lineament map,
- P_{32} – average fracture area per unit volume of rock.

The first two of these are used commonly to collate field data since they can be computed readily. However, both are subject to bias introduced by the orientation in which a measurement is made relative to the orientation of fractures. Measurements along a scanline or borehole preferentially detect fractures orthogonal to the scanline than at an oblique angle, which will bias measures of fracture intensity such as frequency or stereographic concentration contour plots heavily in favour of fracture sets orthogonal to the borehole. To compensate for this bias, calculations of fracture intensity can be accumulated in terms of a weighted sum rather than a simple count with a geometrical weighting factor calculated and applied to each fracture measured. This weighting, W, is used in calculating statistics such as the corrected linear fracture intensity, $P_{10,corr}$, when comparing between different borehole orientations, or can be applied to concentration plots for identifying sets. The process is called Terzaghi correction /Terzaghi 1965/ and is illustrated in Figure 4-3.

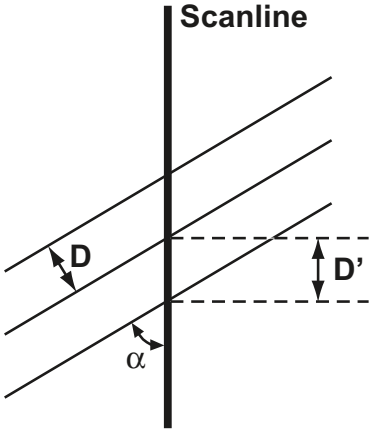

Figure 4-3. *α = minimum angle between plane and traverse, D' = apparent spacing along traverse, D = D' sin(α) = D' (1/W) = true spacing of discontinuity set, W = cosec(α) = weighting applied to individual pole before density calculation.*

The last measure, P_{32}, is an unbiased fracture intensity statistic, although it is obviously difficult to measure in the field directly. Still, it is used to parameterise fracture intensity in models because of its independence from the definition of orientations. In practice, P_{32} can be estimated from $P_{10,corr}$ and adjusted if necessary by calibration against numerical simulations.

For the power-law size distribution it is useful to be able to calculate the P_{32} fracture intensity associated with different ranges of fracture size using the following formulae. If $P_{32}[r > r_0]$ denotes the fracture surface area of all fractures greater than the location parameter, r_0, we can write:

$$P_{32}[r > r_1] = P_{32}[r > r_0]\left(\frac{r_0}{r_1}\right)^{(r_0-2)} \qquad \text{Equation 4-2}$$

where $P_{32}[r > r_1]$ is the fracture surface area of all fractures r greater than the size r_1. From a modelling point of view, it is necessary to decide the size range $[r_{max}, r_{min}]$ that will be used in the numerical simulations and, equally important, the intensity value $P_{32}[r > r_0]$ that corresponds to the smallest value of the underlying data set. For fractures in the size interval $[r_{min}, r_{max}]$, the fracture intensity of a DFN model is given by

$$P_{32}[r_{min}, r_{max}] = P_{32}[r > r_0]\left(\frac{(r_{min})^{(2-k_r)} - (r_{max})^{(2-k_r)}}{(r_0)^{(2-k_r)}}\right) \qquad \text{Equation 4-3}$$

In modeling a hydrogeological DFN, it is important to quantify both the geometrical connectivity of the network and the distribution of fractures that conduct flow. Figure 4-4 illustrates the concept of fracture connectivity and flow as modelled in a borehole. Here, N_{CAL} is the number of all open fractures seen in the borehole section; N_{CON} is the number of open connected fractures; and N_{PFL} is the number of PFL-anomaly fractures observed with flow above the detection limit, typically corresponding to a transmissivity above about 10^{-9} m^2/s. Then the corresponding measures of fracture intensity would be:

- $P_{10} = N_{CAL}/D$ – the linear intensity of all fractures,
- $P_{10,cof} = N_{CON}/D$ – the linear intensity of connected open fractures (cof),
- $P_{10,PFL} = N_{PFL}/D$ – the linear intensity of fractures associated with PFL-anomalies,

where D is the length of borehole section mapped.

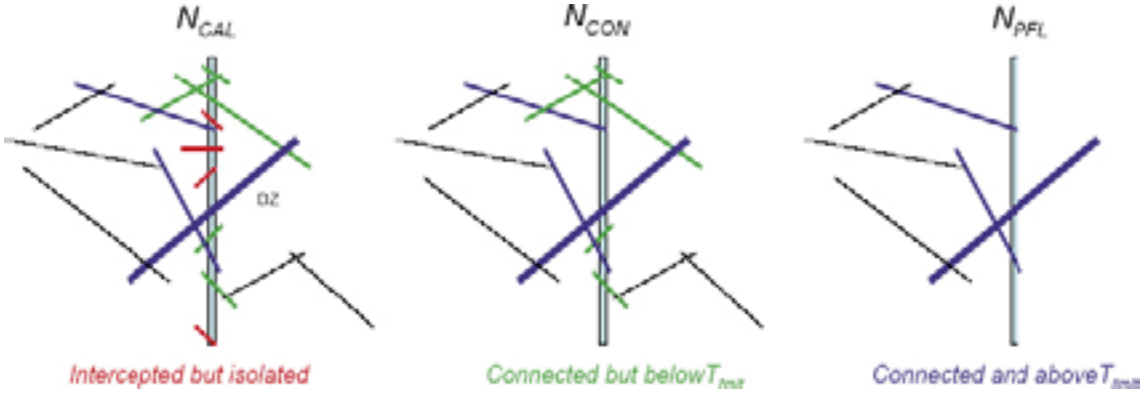

Figure 4-4. *The definition of NCAL, NCON and NPFL of Open fractures. T_{limit} denotes the lower measurement limit for transmissivity, which is typically around 10^{-9} m^2/s for the Posiva Flow Log (PFL-f).*

4.1.3 Measured and interpreted data

The following measured and interpreted data were provided for the KLX09 area:

- Borehole geometries.
- Boremap files, including interpretations of the Posiva Flow Log (PFL) anomalies for boreholes KLX09B to KLX09F.
- Flow rates, freshwater heads and transmissivity values from single-hole tests for boreholes KLX09B to KLX09F.
- Flow rates and drawdowns in observation and pumping boreholes KLX09B to KLX09F.
- Initial and final hydraulic head in the monitored sections of KLX09.
- Data from the ASM100234 outcrop, giving surface P21 fracture intensity values.

There was some slightly greater uncertainty in the accuracy of the orientation data for the vertical KLX09B borehole than the inclined boreholes, and so this borehole was not used in some of the data analysis and simulations.

To help interpret the flow data measured by the Posiva Flow Log (PFL), borehole fractures that correspond to the borehole lengths at which flow anomalies have been identified in the PFL-f tests have been identified by SWECO VIAK. This allows identified flows to be linked to particular fractures seen in the borehole core and image logs. The methodology followed is described in /Forsmann et al. 2005/. The methodology followed by Forsmann and co-authors when assigning a fracture orientation to each flow anomaly is described below.

For each anomaly, the fracture (or fractures) most 'consistent' with the anomaly is (are) selected. If there is more than one equally consistent fracture associated with an anomaly, then the orientations of each of the fractures are used. Generally, there are only one or two consistent fractures, but sometimes there are 3–5 equally consistent fractures. The assumptions made by Forsmann and co-authors when correlating the Boremap data to the PFL-anomalies were:

- As a first assumption, the open and partly-open fractures as well as crush zones are assumed to be possible flowing features. This is an important assumption on which all subsequent analysis relies. Alternative possibilities, which were not considered in this work, include the suggestion that fractures mapped as sealed could contain flow. For instance, fractures that are considered sealed when viewed from the Boremap data within the diameter of the borehole may have a conductive (flowing) section further away from the borehole.
- It is assumed that the precision of the position (L) in the borehole of the PFL-anomaly is not on the 1 dm level. If an open, partly-open fracture or crush zone is within ± 0.5 m of a PFL-anomaly it is assumed that it could potentially correspond to the PFL-anomaly (in a few cases larger differences have been accepted). The nearest distance in dm from the fractures trace (a sinus-shape line) on the borehole wall to depth L is judged and documented in the database (PFL-anom. Confidence). This distance is estimated in dm as the deviation of each potential open, partly-open fractures or crush zones from L, defined positive if the fracture is located below L.
- A few **sealed fractures** were indicated as possible flowing features if the core has been broken AND adjusted secup (Boremap) ≈ L (Borehole length) for the PFL-anomaly AND that no open fracture was < 0.6 m from L OR that the nearest open fracture is positioned closer than 0.6 m but matches another anomaly very well. When interpreting these broken/sealed fractures, only the ones located ± 0.1 m from the anomaly have been mapped. These are fractures considered to be very uncertain and may be excluded from the analysis. "PFL-Confidence" is set to zero (0) in the database for these cases.

- Occasionally, several **open fractures** are within ± 0.1–0.2 m of *L* for the PFL-anomaly and it is judged that one or all of them may be flowing features. If "FRACT_INTERPRET" is used in the database, the "Certain, Probable, Possible" entries can be used to decide whether one is more likely to be the flowing feature. In a few cases, the mapped open fractures are so close (< 1 cm) that possibly one could consider them as one fracture. In some cases where open fractures have been identified within ± 0.1–0.2 m of *L*, there may be more open fractures at a distance ± 0.2–0.5 m that are not included in the database as possible flowing features.
- In a few cases several PFL-anomalies may be connected to a single geological feature, generally a crush zone but sometimes also an open fracture.
- Some open, possibly flowing, fractures have very high amplitudes in the BIPS log, stretching over up to several meters of the borehole wall. These fractures can, because of their shape, have an influence on the flow conditions quite a long distance from the level indicated by the fractures "secup"-value. When evaluating the data, these fractures are given a lower "PFL-confidence" than suggested only by the distance between the fractures secup and the level of the PFL-anomaly. If the fracture cuts the level of the PFL-anomaly, the PFL-confidence is set to one (1, which is the highest confidence), independent of how long the distance between the secup value and the level of the anomaly is. In consequence, some fractures with high amplitudes that almost (± 0.2 m) cut the PFL-anomaly level are also included in the analysis. The PFL-confidence has been set to 2 in these cases.
- If several fractures are considered as possible objects for the PFL-f flow anomaly, as option for the modeller, one fractures chosen as "Best Choice" (BC) based on mainly mapping parameters as the confidence for if the fracture is open or not and the distance to the PFL-f anomaly as well as the fracture appearance in the BIPS image /Teurneau et al. 2007/.

4.2 Fracture sets and the Geo-DFN

A further input to this study was a description of a geological DFN (Geo-DFN) model for the KLX09 area with associated parameters (See Appendix C). This model provided fracture set definitions based on the geometric data from the KLX09 site measures. The initial fracture sets used in the Geo-DFN were the hard-sectors from the Laxemar Version 1.2 Geo-DFN model /Hermanson et al. 2005/. For the KLX09 Geo-DFN model, it was decided that fracture sets S_d and S_f had been erroneously divided and should be merged into a single set, S_df. Also, a soft-sector fracture set definition was used, with the orientation, size and intensity parameters adjusted to fit the measured P_{10} values from the boreholes and the P_{21} outcrop data. The two fracture set definitions are compared in Table 4-1 and Table 4-2. As part of the Geo-DFN, fracture parameters were derived based on DFN geometrical simulations to obtain distributions for orientation, size and intensity. The parameter settings for the local Geo-DFN are shown in Table 4-3.

Table 4-1. General set definitions for all fractures for Laxemar subarea, RSMA, L 1.2 (taken from /Hermanson et al. 2005/).

Fracture set	Orientation			Data	
	Trend	Plunge	Fisher κ	No. fractures in outcrop	No. fractures in boreholes
S_A (ENE)	338	5	13	393	409
S_B (NS)	100	0	20	199	373
S_C (NW)	212	1	10	250	557
S_d (HZ)	3	62	10	164	2,075
S_f (NW)	243	24	24	122	778

Table 4-2. Local Geo-DFN set definitions for all fractures estimated for the KLX09-drilling-site data (cf. Appendix C, Section C.3).

Fracture set	Orientation			Data	
	Trend	Plunge	Fisher κ	No. fractures in outcrop	No. fractures in borehole
S_A (ENE)	350	12	19	397	464
S_B (NS)	92	1	17	231	499
S_C (NW)	213	5	13	293	712
S_df (HZ)	250	77	15	207	2,517

Table 4-3. Calibrated parameters local KLX09 Geo-DFN model for all fractures (cf. Appendix C, Section C.4).

Fracture set	Orientation			Size		Intensity		
	Trend	Plunge	Fisher κ	k_r	r_0 [m]	P_{32} ($r_{min} = r_0$) [m^2/m^3]	P_{32} ($r_{min} = 0.56$) [m^2/m^3]	P_{32} ($r_{min} = 1.0$) [m^2/m^3]
S_A (ENE)	350	12	19	2.35	0.11	2.40	1.03	0.64
S_B (NS)	92	1	17	1.8	0.04	1.90	1.18	0.93
S_C (NW)	213	5	13	2.5	0.04	1.18	0.65	0.43
S_df (HZ)	250	77	15	2.6	0.065	5.48	0.94	0.48

4.2.1 Validity of the Geo-DFN sets for fracture flow

The Geo-DFN model and parameters were based on analysing all fractures irrespective of any consideration of their physical nature or flow. Hence, for the Hydro-DFN it is important to assess whether the defined fracture sets can be applied usefully when considering hydraulic characteristics.

Figure 4-5 shows a stereonet plotted for all fractures taken from KLX09C–F borehole core and image logs. Figure 4-6 shows a stereonet for only the open and partly-open fractures, and Figure 4-7 shows only the fractures associated with PFL-anomalies identified in the single-hole hydraulic tests. The stereonets are coloured according to the fracture sets defined by the Geo-DFN. The stereonets seem to indicate that the set definitions provide a useful framework for describing all fractures, for open (and partly-open) fractures and for the PFL-anomaly fractures. That is, in all three cases, fracture poles seem to cluster in broadly the same 4 areas. In the case of the PFL-anomaly fractures, set S_B (NS) seems to become insignificant and sets S_df (HZ) and S_C (NW) are dominant. The trend values given in Table 4-3 are consistent with the clusters of poles for each set.

4.2.2 Anisotropy in flow

Figure 4-8 shows the Log_{10}(transmissivity) values in m^2/s for the PFL-anomaly fractures interpreted from the single-hole flow tests plotted on a stereonet pole plot. The higher transmissivities, shown by hot colours, tend to correlate with the sub-horizontal set S_df (HZ) and the NW striking (NE plunge) sub-vertical set S_C (NW). This is not an absolute rule, since there are a few high and moderate transmissivities in set S_A (ENE), but still sets S_df and S_C seem to have the majority of the high flows. Set S_B (NS) seems to contribute very little to the flow. Interestingly, this correlation of flow is consistent with the known stress field in this region that has a maximum horizontal NW component /SKB 2006a/, (Hakami 2007, personal communication based on KLX12A data), suggesting the anisotropy demonstrated in Figure 4-8 may reflect the overall pattern of in situ stress conditions.

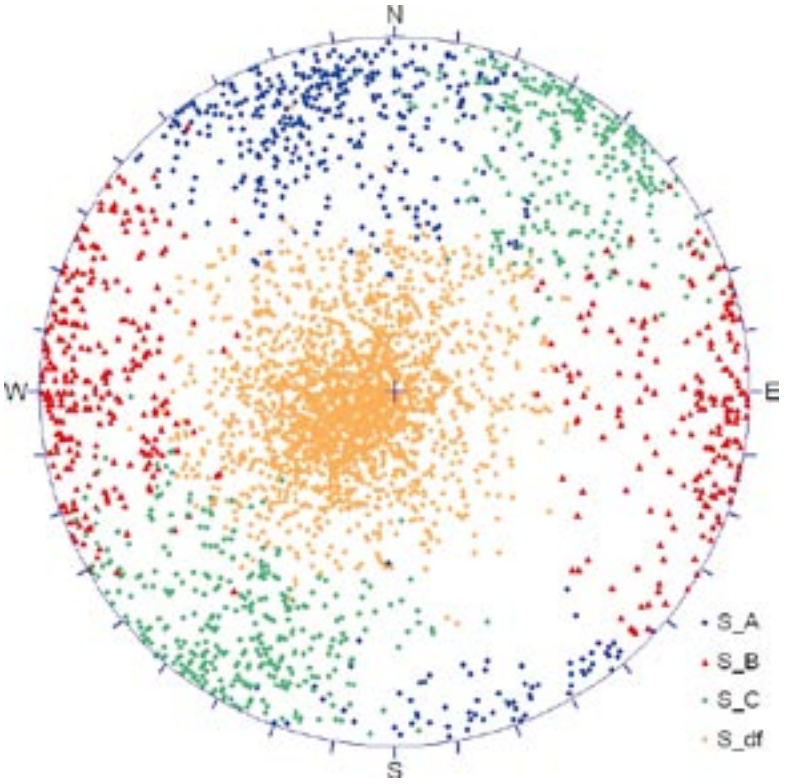

KLX09C–F, all fractures (equal area, lower hemisphere)

Figure 4-5. *Pole plot stereonets for all fractures intersecting boreholes KLX09C to KLX09F.*

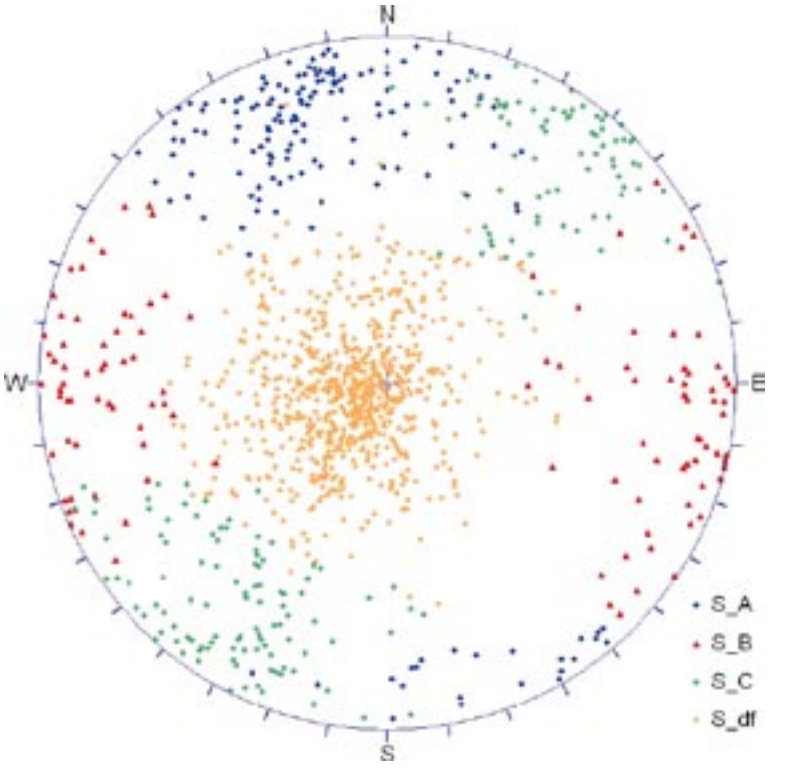

KLX09C–F, open and partly open fractures (equal area, lower hemisphere)

Figure 4-6. *Pole plot stereonets for open and partly open fractures intersecting boreholes KLX09C to KLX09F.*

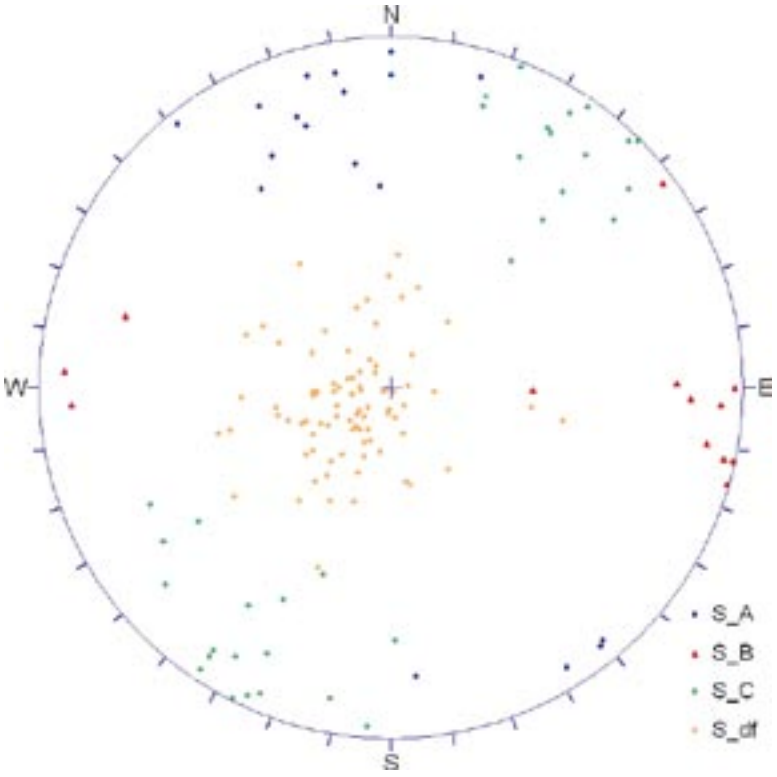

KLX09C–F, PFL-anomaly fractures (equal area, lower hemisphere)

Figure 4-7. *Pole plot stereonets for fractures associated with PFL-anomalies intersecting boreholes KLX09C to KLX09F.*

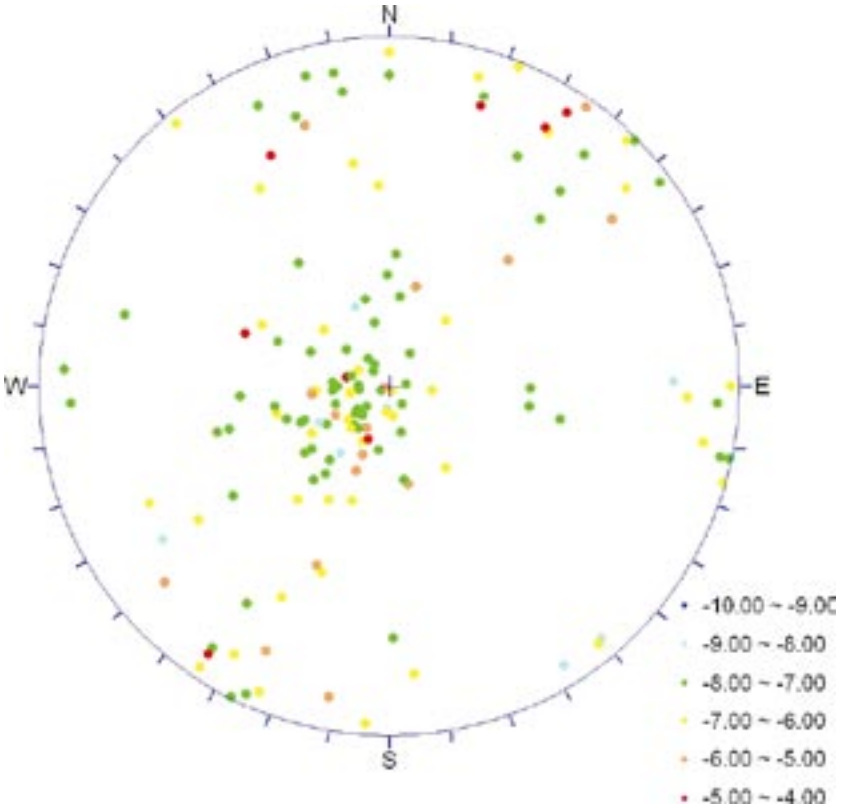

KLX09C–F, PFL-anomaly fractures coloured by log(transmissivity) [m^2/s] (equal area, lower hemisphere)

Figure 4-8. *Symbolic pole plot stereonet showing log(transmissivity) for PFL-anomaly fractures intersecting boreholes KLX09C to KLX09F. Fracture are coloured by the interpreted Log_{10}(transmissivity) associated with each PFL-anomaly.*

4.3 Analysis of fractures in boreholes

The measured borehole data was collated and P_{10} calculated by fracture set and by borehole, with a Terzaghi correction (to give $P_{10,corr}$) applied to compensate for the sampling bias of the borehole /Terzaghi 1965/. These values are given in Table 4-4, along with the values for boreholes KLX09C to KLX09F combined. The P_{32} values for the Geo-DFN from Table 4-3, where $r_{min} = r_0$ are approximately equal to the $P_{10,corr}$ values. However, S_C (NW) is the most intense of the vertical sets here, whereas it is much less intense than S_A (ENE) and S_B (NS) in the Geo-DFN.

The reason for the underestimate in the intensity in S_C (NW) in the Geo-DFN is not known. However, based on the analysis of flow-anomalies in Figure 4-8, it would seem more consistent that set S_C is the dominant vertical set in terms of fracture intensity and flow. Table 4-5 shows the P_{10} values (uncorrected) by fracture set for all fractures, for open and partly-open fractures and for PFL-anomaly fractures. The values for the open and partly-open and the PFL-anomaly fractures are calculated on the basis of the percentages given in the table. Again, taking the intensity of open and partly-open fractures also points to S_C being the predominant vertical set. Significantly, the percentages of open fractures that correspond to PFL-anomalies is consistently about 12-13% for sets S_A (ENE), S_B (NS) and S_df (HZ), but is much higher at 18% for set S_C. This may indicate that set S_C fractures are statistically more likely to have been subjected to reactivation by in situ stress than the other sets since they are parallel to the maximum horizontal stress /SKB 2006a/, (Hakami 2007, personal communication based on KLX12A data).

Table 4-6 shows the percentage of open PFL-anomaly fractures according to the certainty with which they were assigned as being open or partly-open. As can be seen the PFL-anomalies are almost equally distributed between open fractures that were characterised as certain, probable and possible in the core logging.

Table 4-4. Calculated P_{10} values for all fractures for each borehole and fracture set with Terzaghi correction applied.

$P_{10,corr}$ [m^{-1}]	S_A (ENE)	S_B (NS)	S_C (NW)	S_df (HZ)
KLX09B	1.32	1.47	2.74	5.41
KLX09C	2.07	1.37	3.20	5.28
KLX09D	1.94	1.94	2.79	4.91
KLX09E	2.78	2.03	4.32	6.54
KLX09F	1.71	2.93	3.07	5.88
KLX09C–F	2.08	2.13	3.30	5.65

Table 4-5. Calculated P_{10} values for fracture sets for all, open and PFL-anomaly fractures.

KLX09C–F: P_{10} [m^{-1}]	S_A (ENE)	S_B (NS)	S_C (NW)	S_df (HZ)
All	0.88	0.95	1.34	4.33
Open + partly open	0.34	0.24	0.38	1.49
(% of all)	(39%)	(25%)	(28%)	(34%)
PFL-anomaly	0.04	0.03	0.07	0.18
(% of open)	(12%)	(13%)	(18%)	(12%)

Table 4-6. Percentages of open or partly open PFL anomaly fractures by certainty.

PFL-anomalies that are:	Open + certain	Open + probable	Open + possible
	29%	37%	32%

4.4 Simulations of fracture geometry

4.4.1 Modelling approach

In line with our standard Hydro-DFN modelling approach, the initial stage of the modelling was focussed on attempts to simulate the geometry and connectivity of fractures within the KLX09 area. For this part of the study, hydraulic flow was not considered. The software used was ConnectFlow Version 9.3 with DFN-only models.

The model domain chosen was centred on borehole KXL09B and was sufficiently large to encompass all the boreholes, with approximately a 20 m margin on the sides and bottom. The top surface was mapped to the actual topography of the area. This gave a model domain with dimensions of approximately 150 m by 150 m by 200 m. Note that the bottom of KLX09 passes below the bottom of this region, but no measurements for this borehole are considered. It is present only to simulate potential hydraulic connections. The fracture generation region extended an additional 100 m in the horizontal directions and 50 m in the vertical beyond the model domain in order to avoid reduced fracture intensities at the model boundaries. The boreholes were modelled as straight lines. A borehole radius of 0.04 m was used. Figure 4-9 shows the DFN model domain and position of boreholes KLX09B to KLX09C. Also shown are the neighbouring deformation zones. The deformation zones are only for illustration and were not included in the models. Figure 4-10 shows an example of the smaller fractures that were generated around each borehole, coloured by log of transmissivity. In this example, fractures of up to 1 m radius were generated within a cylinder of 4 m diameter around the borehole.

The fractures were generated stochastically using specified power-law size distributions, as described in Section 4.4.2. Four sets of fractures were generated based on the Geo-DFN (S_A, S_B, S_C and S_df). The orientation parameters for each set were based on the Geo-DFN given in Table 4-3. The size and intensity parameters were set according to the case being simulated (see Section 4.4.2). Due to the high number of fractures being generated, the smallest fractures were only generated in a cylinder around each borehole in order to make the calculations

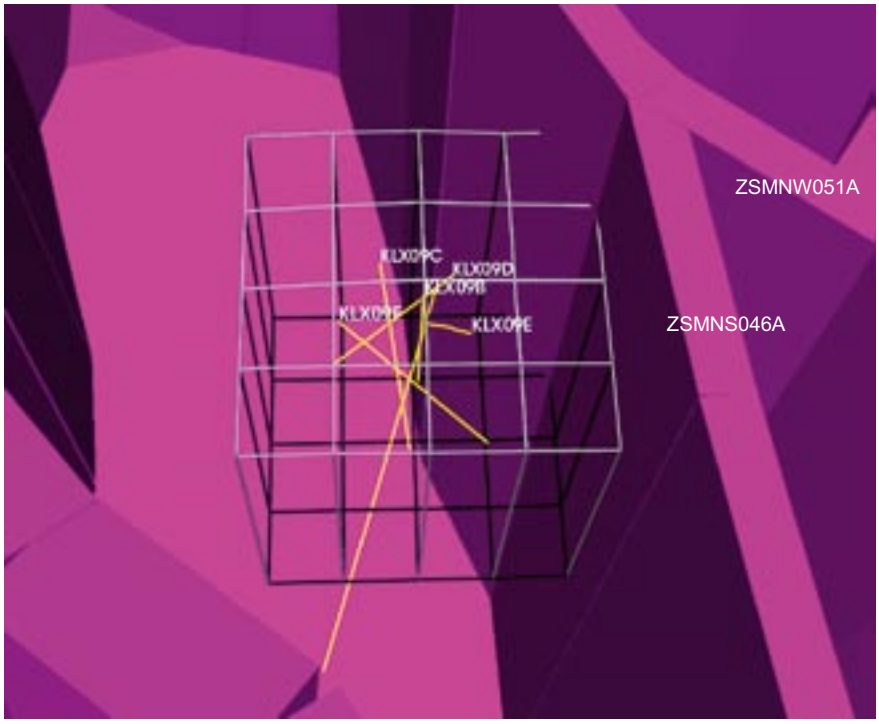

Figure 4-9. *DFN model domain showing the 5 pumped boreholes and set in the context of the L 1.2 deformation zones.*

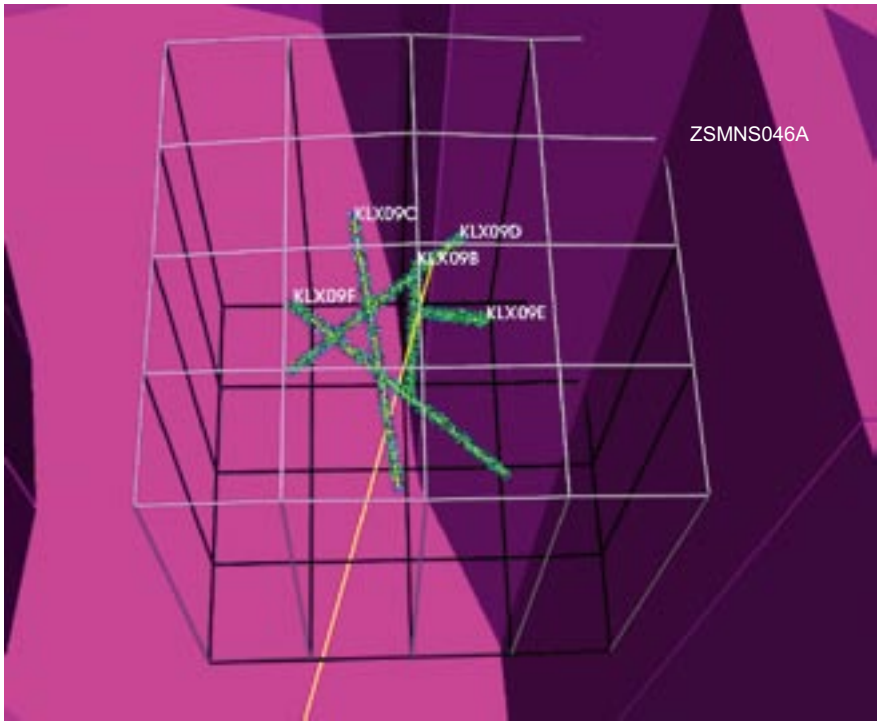

Figure 4-10. *Smaller fractures generated around each of the 5 pumped boreholes and set in the context of the L 1.2 deformation zones.*

feasible. The radius of each cylinder was chosen so that the centre of the largest fracture that could be generated in the cylinder and intersect the borehole would be contained within the cylinder. The larger fractures were generated throughout the whole model domain. Figure 4-11 shows an example of some generated fractures, coloured by Log_{10} of transmissivity.

Figure 4-11. *All fractures generated within the simulation domain and set in the context of the L 1.2 deformation zones. The fractures are coloured by Log_{10} transmissivity.*

4.4.2 Fracture size cases

The commonly used power-law distribution was used to relate fracture intensity to fracture radius using the formulae given in Equations 4-1 to 4-3. Note that ConnectFlow represents fractures as rectangles of specified side lengths, rather than discs of specified radius. Assuming a consistent area between both representations and square fractures, then

$$r = \frac{L}{\sqrt{\pi}} \qquad \text{Equation 4-4}$$

where r is the disc radius and L is the square side length.

Initially, the modelling considered possible fracture size models for all fractures, primarily for comparison with Geo-DFN, since that study determined fracture size models only for all fractures. Three size cases were considered using a power-law distribution. The first case, "BH_DZ_min" used $r_{min} = r_0$, where r_0 was taken to be the borehole radius of 0.04 m. The second case, "BH_DZ_max" used $r_0 = 0.28$ m, corresponding to a fracture length of 0.5 m, which has previously been the smallest size considered for flow simulations and is a typical minimum trace length mapped on outcrops. The third case, "BH_DZ_outcrop", used r_0 values in the range 0.06 m to 0.18 m chosen to match the outcrop data from ASM100234. All cases used a r_{max} value of 564 m (1 km length) based on the approximate minimum size of a deterministic deformation zone mapped in the L 1.2 structural model. The k_r value in each case was determined by fitting the $P_{32}(r > r_0)$ to be $P_{10,corr}$ from cored boreholes KLX09C–F, and $P_{32}(r > 564$ m) to the P_{32} for the deformation zones in model version L 1.2 from RVS (SKB's Rock Visualisation System). Given these two reference points for fracture intensity, it is straightforward to calculate appropriate choices of k_r using Equation (4-3). The $P_{10,corr}$ values from KLX09C–F cores are given in Table 4-4. The resulting size parameters for all fractures are given in Table 4-7, and a comparison of the $P_{32}(r > 564$ m) values from the L 1.2 DZ's and the 3 fracture size models are given for each fracture set in Table 4-8. Note that very few sub-horizontal deformation zones were mapped for L 1.2 since it was largely based on surface lineaments, and hence it was only possible to derive k_r values for the sub-vertical sets. For the S_df (HZ) set, the k_r value of set S_C (NW) was used as this was the dominant sub-vertical set.

In order to obtain suitable size parameters from the BH_DZ_outcrop case to also match the outcrop data from ASM100234, DFN simulations were performed. To do this, a horizontal trace map on a 20 m by 20 m slice through the simulation models was calculated at an elevation of 0.0 m, about 20 m below the top surface. The smallest fractures (1 m $> r > r_0$) were generated from the top surface to a depth of –5.0 m and the larger fractures were generated throughout the model domain, but all traces less than 0.5 m in length were discarded for consistency with the resolution of the outcrop mapping. The DFN simulation approach is described further in Section 4.4.3. Ten realisations of stochastically generated fractures for each of the fracture size cases were calculated. The measured P_{21} from ASM100234 and resulting simulated P_{21} values are also given in Table 4-8. Since the BH_DZ_outcrop case was calibrated to the outcrop P_{21}, this obviously gives the best agreement with the measured values. The agreement is less good for the other two cases, especially the BH_DZ_max case.

The same procedure was followed to estimate fracture size parameters appropriate to open and partly-open fractures. That is, (r_0, k_r) pairs were calculated for each set for the equivalent cases BH_DZ_min and BH_DZ_max based on $P_{32}(r > r_0) = P_{10,corr}$ for open fractures given in Table 4-5, and the $P_{32}(r > 564$ m) for the L 1.2 DZ's. This assumes that all mapped deformation zones can be considered as open fractures. For the BH_DZ_outcrop case it was assumed that proportions of fractures mapped on the ASM100234 outcrop corresponding to open fractures could be estimated from the proportions of open fractures mapped in the borehole cores given in Table 4-5. This turned out to give r_0 values essentially identical to the equivalent case for all fractures. The parameters derived for open and partly-open fractures based on the three cases are given in Table 4-9.

A comparison of the $P_{32}(r > 564$ m) values from the L 1.2 DZ's and the 3 fracture size models are given for each fracture set in Table 4-10. This table also compares predictions of P_{21} for the simulations with the assumed open P_{21} on ASM100234.

Table 4-7. Power-law size parameters for all fractures by fracture set for each of the fracture size model cases considered.

Case	Size parameters	S_A (ENE)	S_B (NS)	S_C (NW)	S_df (HZ)
BH_DZ_min	r_0	0.04 m	0.04 m	0.04 m	0.04 m
	k_r	2.71	2.78	2.75	2.75
BH_DZ_max	r_0	0.28 m	0.28 m	0.28 m	0.28 m
	k_r	2.90	2.99	2.96	2.96
BH_DZ_outcrop	r_0	0.18 m	0.12 m	0.06 m	0.06 m
	k_r	2.85	2.89	2.79	2.79

Table 4-8. Comparison of modelled P_{32} for deformation zones, 5,640 m > r > 564 m, with the L 1.2 deformation zone model; and P_{21}, r > 0.28 m, with the ASM100234 outcrop data for each of the fracture size model cases for all fractures.

Case	Calibration parameters	S_A (ENE)	S_B (NS)	S_C (NW)	S_df (HZ)
ASM100234 outcrop data	P_{21} outcrop	1.23	0.93	0.85	0.52
L 1.2 DZ data	P_{32} DZ model	$2.0\ 10^{-3}$	$1.0\ 10^{-3}$	$2.0\ 10^{-3}$	–
BH_DZ_min	P_{21} (r > 0.28 m)	0.49	0.43	0.71	0.48
	P_{32} (5,640 m > r > 564 m)	$2.0\ 10^{-3}$	$1.0\ 10^{-3}$	$2.1\ 10^{-3}$	$4.5\ 10^{-3}$
BH_DZ_max	P_{21} (r > 0.28 m)	1.85	2.00	3.01	1.93
	P_{32} (5,640 m > r > 564 m)	$1.9\ 10^{-3}$	$1.0\ 10^{-3}$	$2.0\ 10^{-3}$	$4.4\ 10^{-3}$
BH_DZ_outcrop	P_{21} (r > 0.28 m)	1.29	0.94	0.87	0.58
	P_{32} (5,640 m > r > 564 m)	$2.0\ 10^{-3}$	$1.0\ 10^{-3}$	$2.0\ 10^{-3}$	$4.5\ 10^{-3}$

Table 4-9. Power-law size parameters for open and partly-open fractures by fracture set.

Case	Length parameters	S_A (ENE)	S_B (NS)	S_C (NW)	S_df (HZ)
BH_DZ_min	r_0	0.04 m	0.04 m	0.04 m	0.04 m
	k_r	2.59	2.62	2.60	2.60
BH_DZ_max	r_0	0.28 m	0.28 m	0.28 m	0.28 m
	k_r	2.76	2.79	2.77	2.77
BH_DZ_outcrop	r_0	0.18 m	0.12 m	0.06 m	0.06 m
	k_r	2.71	2.71	2.63	2.63

Table 4-10. Comparison of modelled P_{32} for deformation zones, 5,640 m > r > 564 m, with the L 1.2 deformation zone model; and P_{21}, r > 0.28 m, with the ASM100234 outcrop data for each of the fracture size model cases for open and partly-open fractures.

Case	Calibration parameters	S_A (ENE)	S_B (NS)	S_C (NW)	S_df (HZ)
ASM100234 outcrop data	P_{21} outcrop (estimate open fractures based on Table 4-5)	0.48	0.23	0.27	0.16
L 1.2 DZ data	P_{32} DZ model	$2.0\ 10^{-3}$	$1.0\ 10^{-3}$	$2.0\ 10^{-3}$	–
BH_DZ_min	P_{21} (r > 0.28 m)	0.20	0.14	0.24	0.18
	P_{32} (5,640 m > r > 564 m)	$1.9\ 10^{-3}$	$1.0\ 10^{-3}$	$2.1\ 10^{-3}$	$3.7\ 10^{-3}$
BH_DZ_max	P_{21} (r > 0.28 m)	0.72	0.78	0.87	1.71
	P_{32} (5,640 m > r > 564 m)	$1.9\ 10^{-3}$	$1.0\ 10^{-3}$	$2.0\ 10^{-3}$	$3.6\ 10^{-3}$
BH_DZ_outcrop	P_{21} (r > 0.28 m)	0.49	0.24	0.29	0.24
	P_{32} (5,640 m > r > 564 m)	$1.9\ 10^{-3}$	$1.0\ 10^{-3}$	$2.0\ 10^{-3}$	$3.4\ 10^{-3}$

4.4.3 Calibration of fracture intensity and connectivity

The geometrical DFN simulations were carried out using 10 realisations of stochastically generated fractures for each of the fracture size cases. The mean P_{10} values for all fractures calculated by the simulations for all fractures are given in Table 4-11, along with the measured values, for each borehole and fracture set. All cases seemed to be in reasonable agreement with the measured data, and there is little difference between the modelled cases with respect to fracture intensities in boreholes. This is to be expected since they all use the same sets, orientation parameters and areal fracture intensities. The only difference is how the size of individual fractures is distributed, which has little effect on fracture occurrence along a borehole, but has impact on fracture connectivity and the occurrence of flow.

To identify the fractures capable of bearing flow, as detected by the PFL-f measurements, models were created containing only open or partly-open fractures and then a connectivity analysis was performed for each fracture size case. For this study, the P_{32} values for each set were taken from $P_{10,corr}$ for open fractures in Table 4-5 and fracture size from Table 4-9. Initially, the models are generated with only fractures, but no boreholes. Then, a connectivity analysis is performed to identify any open fractures without a connection to one of the boundary surfaces of the model, which are then removed. The boreholes are then re-inserted in the model and the frequency of occurrence of connected open fractures in the boreholes is calculated. Table 4-12 gives the simulated P_{10} values for connected open fractures, $P_{10,cof}$, and the P_{10} values for the PFL flow-anomalies. The BH_DZ_min case seems to give the best agreement with the PFL-f measurements, whereas the BH_DZ_max case seems to consistently calculate too many connected open fractures. Note that the simulated P_{10} values for open and connected fractures are expected to be higher than the P_{10} values for the PFL flow-anomalies, because some of the simulated fractures would have flows below the detection limit of the PFL instruments.

Table 4-11. Measured and simulated P_{10} values for all fractures by borehole and fracture set.

Borehole	Case P_{10} [m^{-1}]	S_A (ENE)	S_B (NS)	S_C (NW)	S_df (HZ)
KLX09B	Measured	0.41	0.47	0.78	4.89
	Model BH_DZ_min	0.54	0.39	0.77	5.33
	Model BH_DZ_max	0.46	0.39	0.74	4.80
	Model BH_DZ_outcrop	0.51	0.42	0.75	5.38
KLX09C	Measured	0.79	0.46	1.50	4.02
	Model BH_DZ_min	0.71	0.48	1.36	4.63
	Model BH_DZ_max	0.73	0.51	1.51	4.51
	Model BH_DZ_outcrop	0.69	0.51	1.40	4.60
KLX09D	Measured	0.69	1.02	1.18	4.21
	Model BH_DZ_min	0.58	0.96	1.08	4.94
	Model BH_DZ_max	0.57	0.89	0.99	4.53
	Model BH_DZ_outcrop	0.61	1.00	1.16	5.00
KLX09E	Measured	1.70	0.75	1.65	5.10
	Model BH_DZ_min	1.46	0.51	1.01	4.85
	Model BH_DZ_max	1.33	0.47	0.98	4.30
	Model BH_DZ_outcrop	1.51	0.51	1.08	5.02
KLX09F	Measured	0.53	1.42	1.11	4.10
	Model BH_DZ_min	0.41	1.07	0.81	3.78
	Model BH_DZ_max	0.37	1.06	0.78	3.69
	Model BH_DZ_outcrop	0.40	1.11	0.83	3.83

Table 4-12. Measured and simulated $P_{10,cof}$ values for connected open fractures by borehole and fracture set.

Borehole	Case $P_{10,cof}$ [m^{-1}]	S_A (ENE)	S_B (NS)	S_C (NW)	S_df (HZ)
KLX09B	PFL-f	0.04	0.02	0.10	0.32
	Model BH_DZ_min	0.05	0.05	0.09	0.50
	Model BH_DZ_max	0.19	0.08	0.18	1.70
	Model BH_DZ_outcrop	0.15	0.03	0.10	0.95
KLX09C	PFL-f	0.05	0.02	0.11	0.15
	Model BH_DZ_min	0.08	0.07	0.16	0.42
	Model BH_DZ_max	0.21	0.07	0.37	1.68
	Model BH_DZ_outcrop	0.19	0.10	0.15	0.78
KLX09D	PFL-f	0.04	0.05	0.06	0.19
	Model BH_DZ_min	0.08	0.07	0.16	0.50
	Model BH_DZ_max	0.25	0.27	0.31	1.45
	Model BH_DZ_outcrop	0.20	0.12	0.12	0.86
KLX09E	PFL-f	0.05	0.01	0.05	0.21
	Model BH_DZ_min	0.14	0.07	0.07	0.42
	Model BH_DZ_max	0.48	0.17	0.22	1.58
	Model BH_DZ_outcrop	0.54	0.07	0.20	0.82
KLX09F	PFL-f	0.01	0.03	0.07	0.19
	Model BH_DZ_min	0.03	0.03	0.04	0.34
	Model BH_DZ_max	0.19	0.35	0.20	1.38
	Model BH_DZ_outcrop	0.06	0.13	0.07	0.60

4.5 Simulation of single-hole tests

The first step in developing a Hydro-DFN model consistent with the measured hydrogeological response seen in the PFL-f tests is to calibrate against the flow-rates measured at the abstraction boreholes. This section describes the methodology and results derived from this initial step.

4.5.1 Modelling approach

PFL-f hydraulic testing was performed in each of the 5 boreholes KLX09B–F with a delay of about 5 days between each to allow the hydraulic system to recover /Sokolnicki and Väisäsvaara 2006/. Flow-rates and heads were measured at each location associated with a PFL-anomaly before pumping and then during pumping. The drawdown and flow difference were calculated as the difference between the natural and pumped values based on an assumption that the system was in steady-state when both measurements were made. 198 PFL-anomalies were identified in all over the 5 boreholes. Each of these tests can be considered as a single-hole pumping test, although while any one borehole is being pumped, the other boreholes may have an impact on flow since they are open holes and hence provide additional paths for communication between fractures.

A methodology to parameterise a Hydro-DFN model for single-hole tests has been developed in previous studies, /Hartley et al. 2006b/ for example. The primary calibration targets in those studies were the distribution of flow-rates per unit drawdown in the abstraction borehole, and the total flow to the borehole. In previous studies, the boreholes were predominantly vertical, and so it was difficult to identify any clear evidence for anisotropy in flow between the sub-vertical sets since the flow-anomalies tended to be mainly associated with the sub-horizontal set. Here, we have flow data for 1 vertical and 4 inclined borehole, which offers the possibility to analyse anisotropy between sets in a less biased way. Therefore, extra effort was placed in matching not only the overall distribution of flow-rates from individual fractures, but also the flow-rates associated with individual fracture sets, and in consequence, a fine-tuning of the fracture sizes and transmissivities

was carried out for each set. Another new feature of the methodology was to test the sensitivity of the Hydro-DFN to the fracture size distribution more rigorously than in previous studies. This involved testing quite different assumptions about the (r_0, k_r) size parameters in a similar way to that promoted by /Follin and Stigsson 2007/.

The simulation procedure was to generate either 5 or 10 realisations of a DFN model in a domain surrounding all 5 boreholes together with the deep borehole KLX09. During a preliminary testing only 5 realisations were used, but the number was increased to 10 realisations for fine-tuning the models. The domain is 150 m east-west, 150 m north-south, and 170 m deep. The simulations are identical to those described in Section 4.4, except fractures smaller than 0.28 m radii were discarded from the simulations for practical reasons. The sensitivity to this action was tested, and it was found that adding in smaller fractures only added some very small additional flows well below the measurement limit, and hence had little influence on the matching process. For each borehole, boundary conditions were specified as a fixed drawdown of –10 m head in the abstraction borehole, and 0 m head on the top and 4 vertical surfaces. The steady-state flow-field is then calculated using a DFN flow model to obtain the inflows to the boreholes at each fracture intersected by the borehole. The borehole is represented by a line with approximately the top 12 m of borehole below ground-surface removed since this section of the borehole is cased. 10 realisations are performed to simulate the pumping at each borehole. An example of a flow simulation is shown in Figure 4-12 which is a case with KLX09B being pumped. Here, the fractures are coloured by head, or coloured grey where they are not connected to the network. Having run 5-10 realisations of a particular set of DFN parameters, the inflow to the abstraction borehole is calculated for each fracture intersecting it for each realisation. To assess the 'goodness of fit', the following statistics are calculated:

- Average total flow to the abstraction borehole over the 5-10 realisations.
- Histogram of flux to borehole divided by drawdown (notated *Q/s*) as an average over 5–10 realisations.
- Box and whisker plot of minimum, mean minus standard deviation, mean, mean plus standard deviation, maximum of $Log_{10}(Q/s)$ for the inflows within each fracture set taken over all realisations.
- The average numbers of fractures within each set giving inflows to the abstraction borehole above the measurement limit for the PFL-f tests.

Initially, the BH_DZ_min and BH_DZ_outcrop cases were assessed in this way to appraise which fracture size distribution gave the best agreement with the PFL-f data. The key statistic to match here is the numbers of inflow points. Another key issue to assess in these initial simulations was to establish appropriate choices for the parameters in the correlated, semi-correlated and uncorrelated relationships between size and transmissivity that gave a match to the magnitude of the inflows. In the beginning, the same transmissivity parameters were assigned to all fracture sets, but eventually fine-tuning of the parameters was performed to reproduce the distribution of inflows associated with individual fracture sets.

4.5.2 Calibration

Initially, two sets of simulations were performed for the BH_DZ_min and BH_DZ_outcrop alternative models for fracture size distribution since these gave fracture intensity of connected open fractures,$P_{10,cof}$, most consistent with the intensity of PFL-anomalies. As a starting point, the transmissivity parameters used in the L 1.2 Hydro-DFN for the upper section (above –300 m) of the Ävrö granite as detailed in Table 4-13 were used. These relationships between fracture transmissivity and radius are illustrated in Figure 4-13. Initially, the same transmissivity settings were used for all 5 fracture sets, and then the parameters were modified slightly to improve the match to the total flow magnitude. Relative to the L 1.2 Hydro-DFN, the correlated and semi-correlated transmissivity models, the magnitude, *a*, was increased by a factor 2, while the mean was reduced slightly and the standard deviation increased significantly in the uncorrelated transmissivity model. As will be seen later in Table 4-20, further changes were made to the transmissivity parameters to match the flow in individual fracture sets.

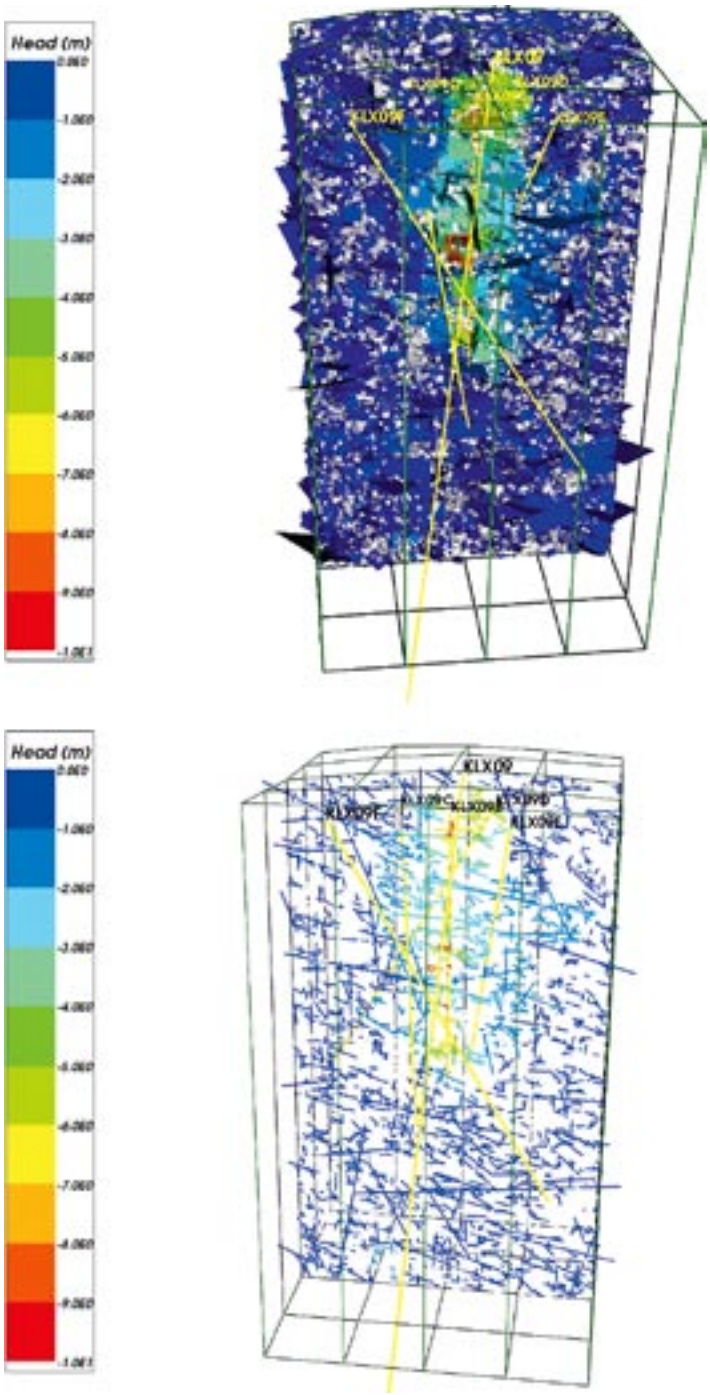

Figure 4-12. *Example of simulations of flow in one realisation showing the distribution of head for pumping at KLX09B. Top: full 3D model with fractures at the front removed (grey fractures are not connected). Bottom: vertical section through KLX09B.*

Table 4-13. Initial transmissivity parameters used for all sets when matching PFL-f flow distribution in single-hole tests.

Type	Description	Relationship	Parameters
Semi-correlated	Log-normal distribution about a correlated mean	$Log_{10}T = Log_{10}(a \times r^b) + \sigma N(0,1)$	a = 6.9 10^{-8}, b = 1.0, σ = 0.9
Correlated	Power-law relationship	$T = a \times r^b$	a = 6.3 10^{-8}, b = 1.2
Uncorrelated	Log-normal distribution about a specified mean	$Log_{10}T = \mu + \sigma N(0,1)$	μ = –6.5, σ = 1.2

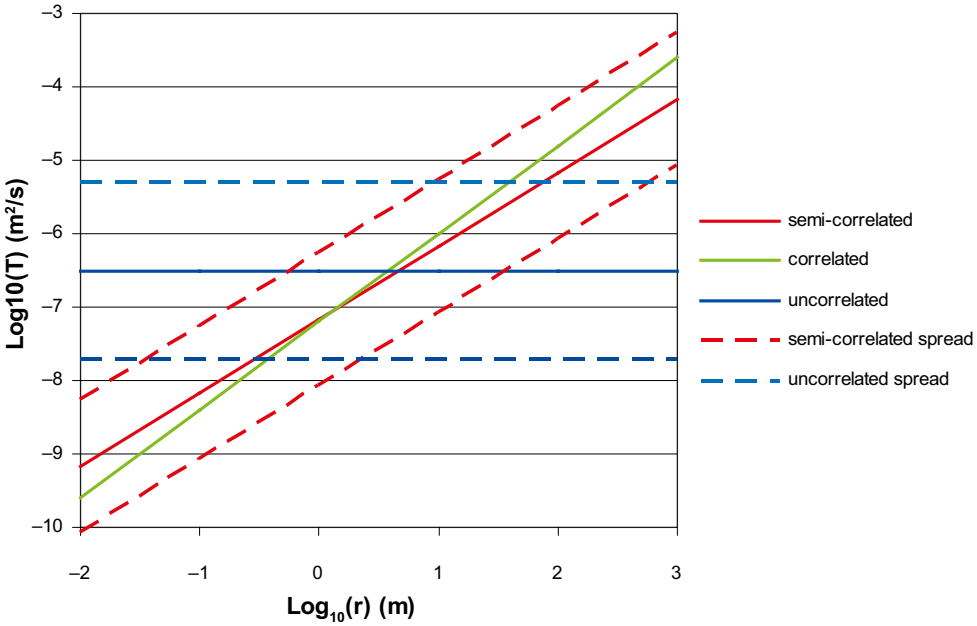

Figure 4-13. *Initial transmissivity model relationships from Table 4-13. For the semi-correlated and uncorrelated cases, the spread is displayed by the standard deviation,* ± σ.

The calibration of the fracture size distributions and transmissivity models was developed based on plots of distributions of inflows from individual fractures to the boreholes, the total flow, and the flow associated with individual fracture sets. The inflow fluxes, Q, were normalised with respect to the drawdown, s, in the abstraction borehole to allow a sensible comparison between boreholes, since the drawdowns were about 10 m for KLX09B and KLX09D, 5 m for KLX09C, 5.8 m for KLX09E and 3.5 m for KLX09F. Plots were made for each borehole KLX09B–F to show the responses in individual boreholes. A plot combining the distributions over boreholes KLX09C–F was also made to collate statistics over a larger ensemble. A decision was made to collect statistics for the inclined boreholes KLX09C–F only, since there was some indication that the fracture orientations interpreted in the vertical KLX09B may be subject to more uncertainty. Figure 4-14 shows an example of a comparison between the PFL-f inflow rate distribution for KLX09C–F compared with the simulated distribution for the BH_DZ_min fracture size model and semi-correlated transmissivity. Here, statistics for the simulations are calculated over an ensemble of 5 realisations and the 4 boreholes (10 realisations were used later in the fine-tuning of models). The solid bars indicate measured or simulated flows that are above the reliable measurement limits, while the error bars indicate values that are below. For the PFL-f data, some anomalies have a measured flow, but the values are recorded as being uncertain. Also, of course there may be flows from fractures that are below the measurement limit. It should be noted that the measurement limit varies from borehole to borehole. The measurement limit was assumed to be the minimum Q/s value interpreted in the abstraction borehole as given in Table 4-14. A second value was calculated, phrased as the "reliability limit", as the maximum uncertain value of Q/s interpreted. In Figure 4-14 the **error bars on the measured PFL-f values** indicate values that are between these two limits, **and may actually be less than those interpreted**. The error bars on the simulations indicate inflows that were calculated, but fell below the measurement threshold for that borehole (The assumed measurement limits are given in Table 4-14). The difference in measurement limit between the boreholes is the cause of the uncertain values being distributed over several histogram bins. The graph shows the distribution of measured inflows to be spread over about four orders of magnitude with a mode around 10^{-7} m^2/s. Below 10^{-7} m^2/s, the data probably suffers from a lack of resolution of small flow-rates, and the simulations suggest what the idealised distribution may look like.

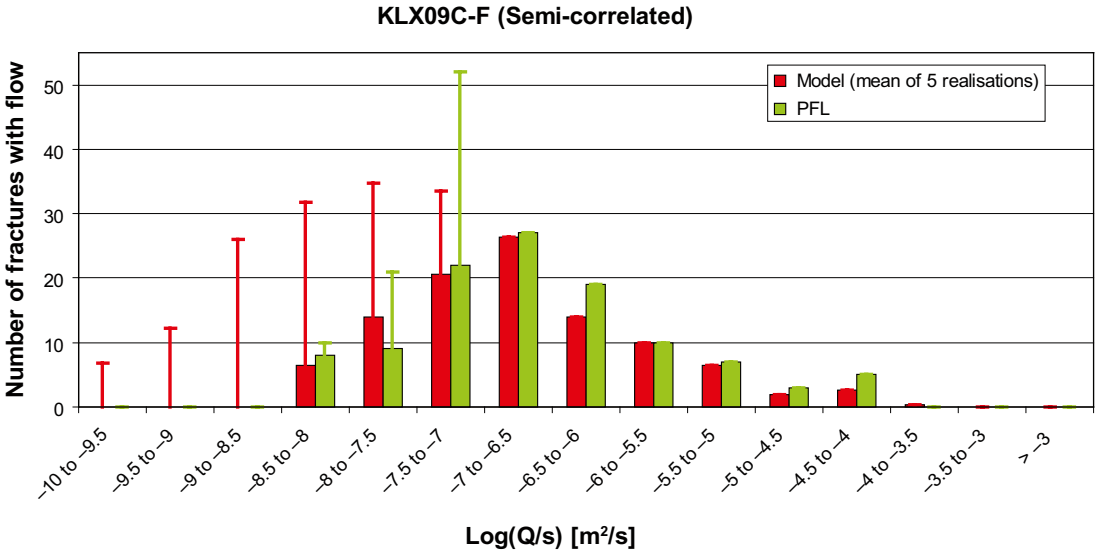

Figure 4-14. *A comparison of the distributions of individual fracture inflows, Q/s, for the PFL-f measurements from KLX09C–F against the mean over 5 realisations of the BH_DZ_min fracture size model and a semi-correlated transmissivity to size. For the PFL-f data, the error bars indicate values close to the detection limit which are estimated. For the model, the error bars indicate predicted flows below the measurement limit (Note the measurement limit varies between boreholes).*

Table 4-14. Assumed measurement and "reliability limits" used in plotting the uncertainty in the distribution of fracture inflows.

Borehole	Assumed measurement limit (minimum value measured)	Assumed "reliability limit" (maximum uncertain value)
KLX09B	$1\ 10^{-9}$ m²/s	$2\ 10^{-9}$ m²/s
KLX09C	$5\ 10^{-8}$ m²/s	$1\ 10^{-7}$ m²/s
KLX09D	$3\ 10^{-9}$ m²/s	$5\ 10^{-9}$ m²/s
KLX09E	$1\ 10^{-8}$ m²/s	$2\ 10^{-8}$ m²/s
KLX09F	$3\ 10^{-8}$ m²/s	$5\ 10^{-8}$ m²/s

The corresponding plots for the correlated and uncorrelated models are given in Figure 4-15 and Figure 4-16, respectively. The correlated model is characterised by a more triangular shaped distribution since there is no stochastic component in the transmissivities generated. The uncorrelated model based on a log-normal distribution gives a Gaussian shaped distribution with which it is quite difficult to reproduce the shape of the inflow distribution. Of the three cases, the semi-correlated model reproduces the shape of the distribution most closely, and it is probably the most realistic.

The next stage was to check the distribution of flow corresponding with individual sets using plots such as Figure 4-17 and Figure 4-18. Based on the BH_DZ_min fracture size model, the distribution of flow-rates, *Q/s*, is shown for each set in Figure 4-17 for the semi-correlated and correlated transmissivity relationships. The equivalent plot for the uncorrelated relationship is shown in Figure 4-18. In these plots, the distribution of the flow-rates is shown as a bar and whisker plot. The centre of the bar indicates the mean; the left-end of the bar is the mean minus one standard deviation; and the right-end of the bar is the mean plus one standard deviation. The ends of the whiskers correspond to the minimum and maximum flow-rates. For each set, a bar and whisker is shown for the PFL-f data at the top, and then a bar and whisker is plotted for the model just below. For the PFL-f data, statistics are calculated over the ensemble of flow-rates measured in the boreholes. Obviously, this will exclude any flow values below the measurement values, and so in order to compare with the model, any flow-rates computed in the simulations below the measurement limits given in Table 4-14 are excluded from the model statistics.

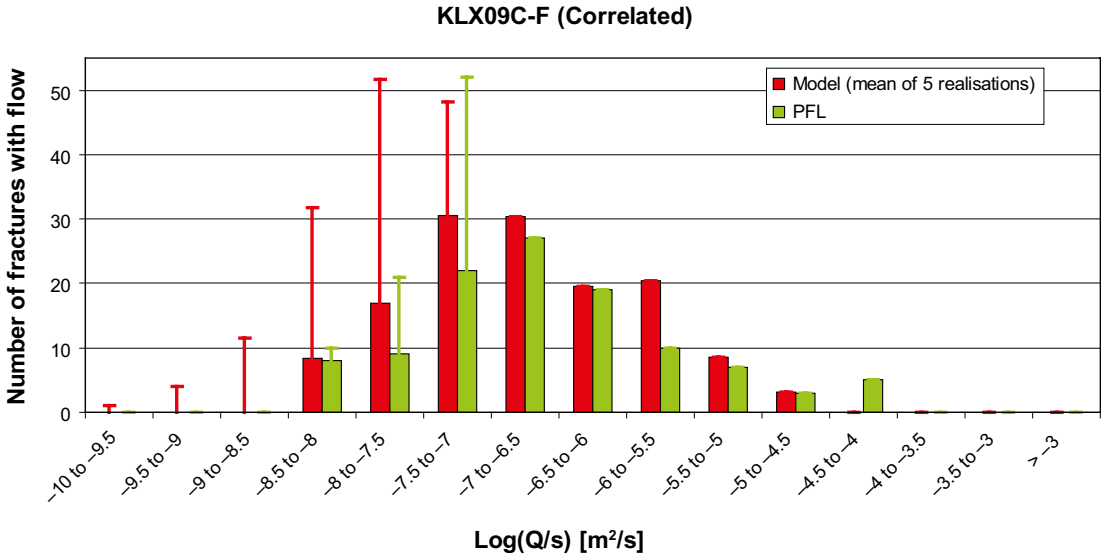

Figure 4-15. *A comparison of the distributions of individual fracture inflows, Q/s, for the PFL-f measurements from KLX09C–F against the mean over 5 realisations of the BH_DZ_min fracture size model and a correlated transmissivity to size. For the PFL-f data, the error bars indicate values close to the detection limit which are estimated. For the model, the error bars indicate predicted flows below the measurement limit (Note the measurement limit varies between boreholes).*

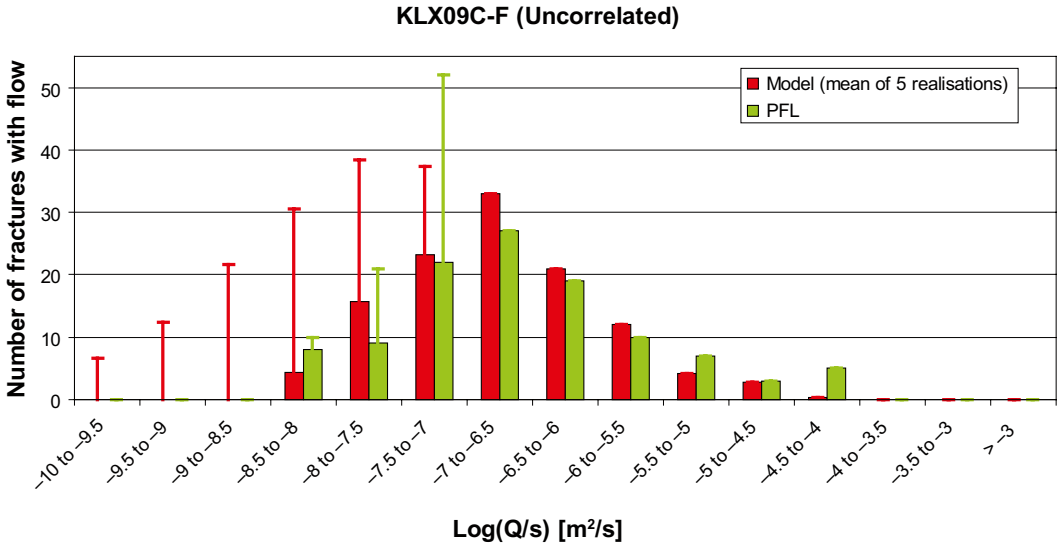

Figure 4-16. *A comparison of the distributions of individual fracture inflows, Q/s, for the PFL-f measurements from KLX09C–F against the mean over 5 realisations of the BH_DZ_min fracture size model and an uncorrelated transmissivity to size. For the PFL-f data, the error bars indicate values close to the detection limit which are estimated. For the model, the error bars indicate predicted flows below the measurement limit (Note the measurement limit varies between boreholes).*

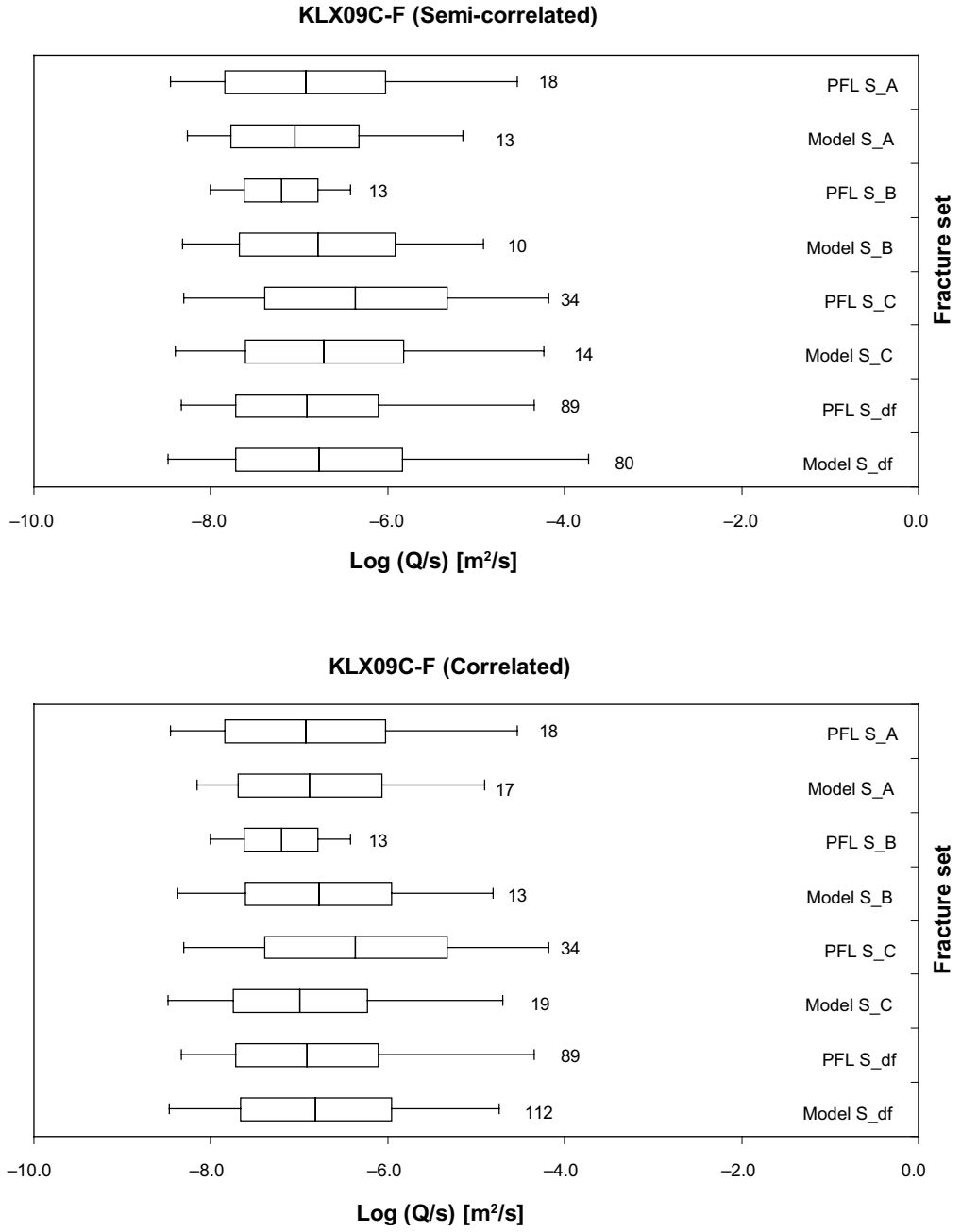

Figure 4-17. *Bar and whisker plot comparing statistics taken over each fracture set for the individual inflows, Q/s, for the PFL-f data from KLX09C–F against the mean over 5 realisations of the BH_DZ_min fracture size model. The centre of the bar indicates the mean value, the ends of the bar indicate ± 1 standard deviation, and the error bars indicate the minimum and maximum values. The total numbers of flows above the detection limits within each set are given. For the PFL-f data, the statistics are taken over the identified flow-anomalies within each set, and over the fractures generated within each set and over 5 model realisations. Top: semi-correlated transmissivity model; Bottom: correlated transmissivity model.*

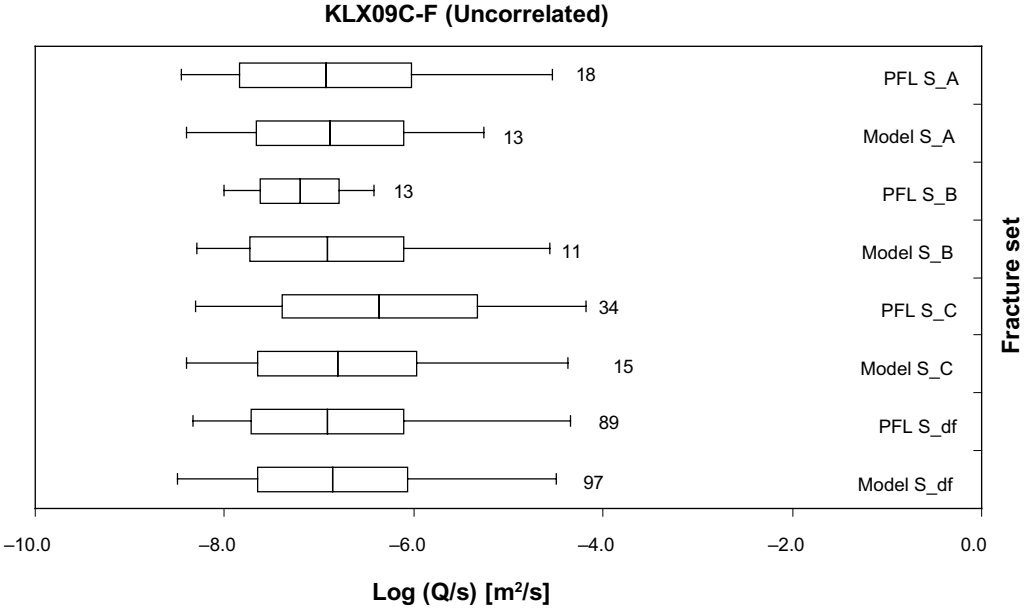

Figure 4-18. *Bar and whisker plots comparing statistics taken over each fracture set for the individual inflows, Q/s, for the PFL-f measurements from KLX09C–F against the mean over 5 realisations of the BH_DZ_min fracture size model. The centre of the bar indicates the mean value, the ends of the bar indicate ± 1 standard deviation, and the error bars indicate the minimum and maximum values. The total numbers of fractures with inflow above the detection limits within each set are also given. For the PFL-f data, the statistics are taken over the identified flow-anomalies within each set, and over the fractures generated within each set and over 5 model realisations. The uncorrelated transmissivity model is shown.*

Here, the statistics for the model are then taken over 5 realisations. To the right of each bar and whisker, the number of fracture flows is given. This is the actual number of anomalies within each set for the PFL-f data, but is based on an average over the realisations for the model, for fractures with flows above the measurement limit. The motivation for studying the individual sets in this way is to assess whether there is evidence for anisotropy in the connectivity or transmissivity between the different sets.

For S_A (ENE), the numbers of flows and the magnitude of flows are about correct for all transmissivity models. Set S_B (NS) has the correct numbers of flows, but the magnitude and spread are over-predicted since the data suggests a very tight distribution centred a bit less than 10^{-7} m^2/s. In contrast, S_C (NW) is under-predicted by about half an order of magnitude and has about half the number of flows as measured. The sub-horizontal S_df has about the correct magnitude and numbers of flows. Therefore, the simulations suggest the BH_DZ_min fracture size model with $r_0 = 0.04$ m performs well overall, but an isotropic model that has the same size and transmissivity parameters for all sets cannot match the flow responses in individual sets. Modelling suggests the S_C (NW) set is better connected (i.e. extensive) and more transmissive than the other sets, and the S_B (NS) set has a very tight distribution of transmissivity. These findings are consistent with the hypothesis that NW trending fractures are broadly subject to extensive in situ stress, whereas NS fractures tend to be subject to compression.

A summary of the total flow to each abstraction borehole for the PFL-f data and the geometric mean over 5 realisations are given in Table 4-15 for the 3 size-transmissivity relationships. Note: fine-tuning of the transmissivity parameters to match the total flows was not performed at this stage.

Table 4-15. Comparison of the total flow to the abstraction boreholes between the PFL data and the model averaged over 5 realisations for the BH_DZ_min fracture size model and 3 different size-transmissivity relationships. The values given for the model are geometric means over 5 realisations (a geometric mean is used as flows can be approximate by a log-normal distribution).

Total *Q/s* [m³/s]	KLX09B	KLX09C	KLX09D	KLX09E	KLX09F	Geometric mean KLX09B–F
PFL-f	$1.8\ 10^{-5}$	$1.0\ 10^{-4}$	$2.8\ 10^{-5}$	$8.9\ 10^{-5}$	$1.6\ 10^{-4}$	$6.0\ 10^{-5}$
Mean – model semi-correlated	$4.7\ 10^{-5}$	$4.6\ 10^{-5}$	$3.8\ 10^{-5}$	$3.4\ 10^{-5}$	$6.9\ 10^{-5}$	$4.6\ 10^{-5}$
Mean – model correlated	$3.3\ 10^{-5}$	$3.7\ 10^{-5}$	$3.8\ 10^{-5}$	$3.37\ 10^{-5}$	$3.4\ 10^{-5}$	$3.5\ 10^{-5}$
Mean – model uncorrelated	$3.9\ 10^{-5}$	$3.1\ 10^{-5}$	$2.1\ 10^{-5}$	$1.7\ 10^{-5}$	$3.4\ 10^{-5}$	$2.7\ 10^{-5}$

Considering the alternative fracture size distribution model, BH_DZ_outcrop, based on adjusting r_0 to match the outcrop P_{21}, this gives a network that is more connected since fractures have been made more extensive, especially sets S_A (ENE) and S_B(NS). Figure 4-19 shows the distribution of flow-rates *Q/s* for this size case, which indicates a reasonable match above $3\ 10^{-6}$ m²/s, but predicts a lot more fractures contributing to flow below this value. The consequence of increasing r_0, and so making fractures more extensive, is particularly evident in the numbers of flows and flow magnitudes in Figure 4-20. It can be seen that the adjustments to r_0 for sets S_A (ENE) has lead to a large over-prediction of the number of flows associated with this set, and to a lesser degree, sets S_B (NS) and S_df, while set S_C (NW) are still under-predicted. On the basis of these results, it was concluded that the matching to the outcrop P_{21} data did not guide a better choice of the size distribution for the flow conducting fractures. Hence, the BH_DZ_outcrop was not considered any further in matching the single-hole flow data.

The next step was to optimise the BH_DZ_min model starting from an r_0 of 0.04 m to achieve a better match across the individual sets was explored. The main steps taken were to change the power-law size parameters for set S_C (NW) to give $r_0 = 0.12$ m and $k_r = 2.69$, and to adjust the transmissivity of sets S_C (NW) and S_B (NS). It was necessary to adjust r_0 as well the transmissivity for set S_C (NW) since it was required to increase both the magnitude of flow and the numbers of flowing features. This case was named "BH_DZ_optbc". For this fine-tuning of the models and all subsequent simulations, 10 realisations were performed.

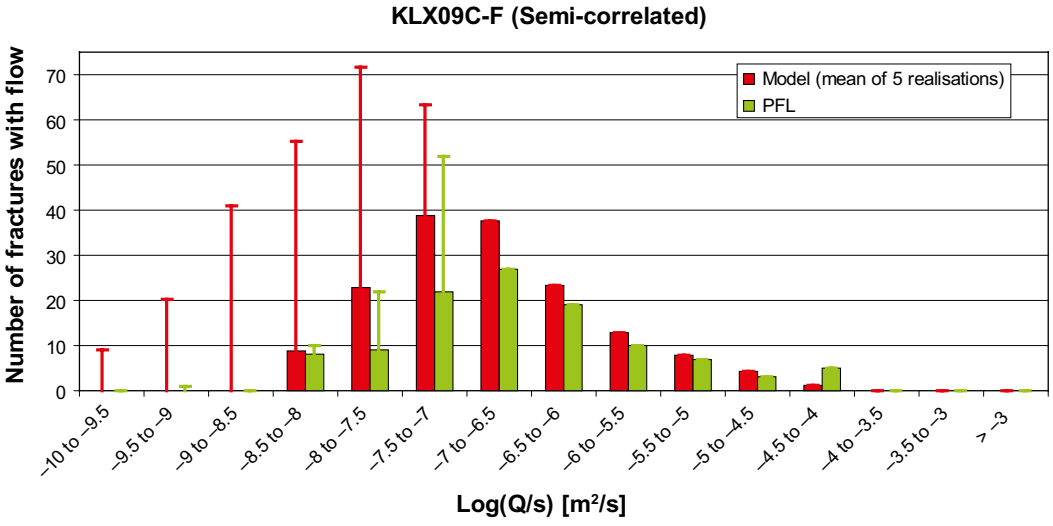

Figure 4-19. *A comparison of the distributions of individual fracture inflows, Q/s, for the PFL-f measurements from KLX09C–F against the mean over 5 realisations of the BH_DZ_outcrop fracture size model and a semi-correlated transmissivity to size. For the PFL-f data, the error bars indicate values close to the detection limit which are estimated. For the model, the error bars indicate predicted flows below the measurement limit (Note the measurement limit varies between boreholes).*

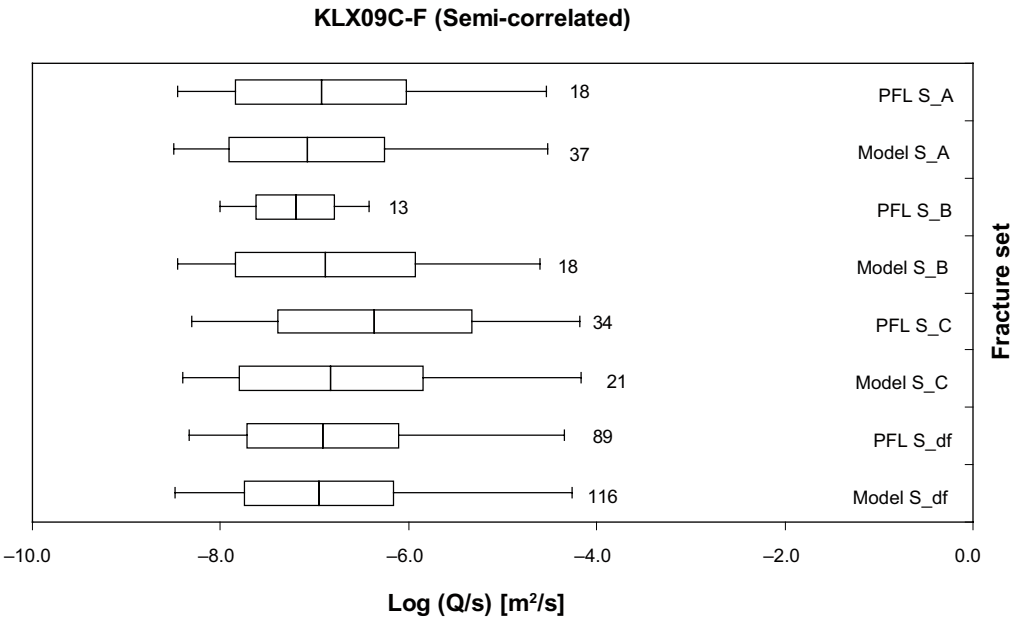

Figure 4-20. *Bar and whisker plots comparing statistics taken over each fracture set for the individual inflows, Q/s, for the PFL-f measurements from KLX09C–F against the mean over 5 realisations of the BH_DZ_outcrop fracture size model. The centre of the bar indicates the mean value, the ends of the bar indicate ± 1 standard deviation, and the error bars indicate the minimum and maximum values. The total numbers of fractures with inflow above the detection limits within each set are also given. For the PFL-f data, the statistics are taken over the identified flow-anomalies within each set, and over the fractures generated within each set and over 5 model realisations. The semi-correlated transmissivity model is shown.*

The calibration results for the optimised case BH_DZ_optbc with a semi-correlated transmissivity model are shown in Figure 4-21 and Figure 4-22. In Figure 4-22 it is shown that the adjustments made to the length and transmissivity distributions for sets S_B (NS) and S_C (NW) give a much improved match to the numbers and magnitude of flows in the individual sets. The parameter settings for this model are summarised in Section 4.5.3. Equivalent plots for the individual boreholes are given in Appendix D.1. Significantly, the predictions of the numbers of flows in each

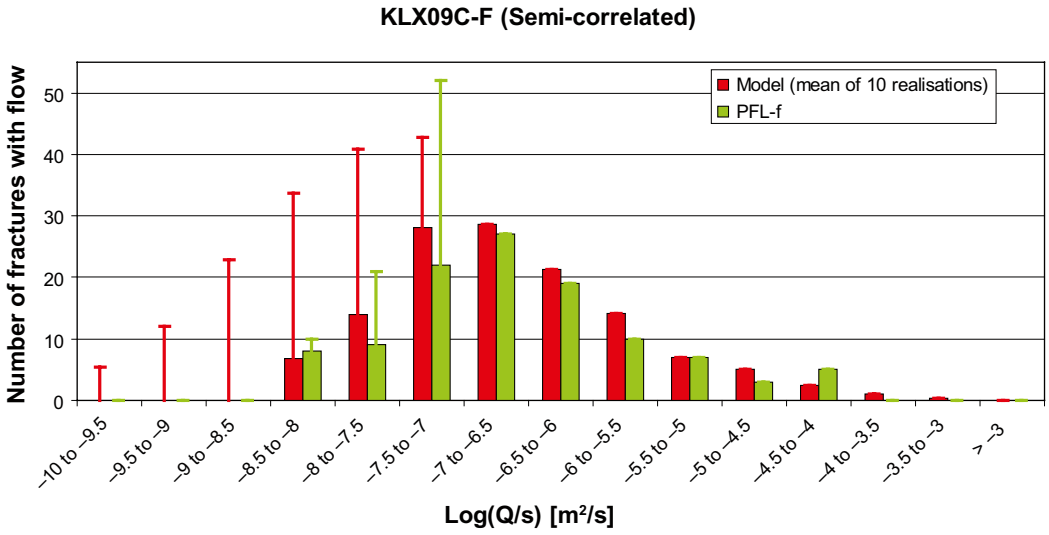

Figure 4-21. *A comparison of the distributions of individual fracture inflows, Q/s, for the PFL-f measurements from KLX09C–F against the mean over 10 realisations of the BH_DZ_optbc fracture size model and a semi-correlated transmissivity to size. For the PFL-f data, the error bars indicate values close to the detection limit which are estimated. For the model, the error bars indicate predicted flows below the measurement limit (Note the measurement limit varies between boreholes).*

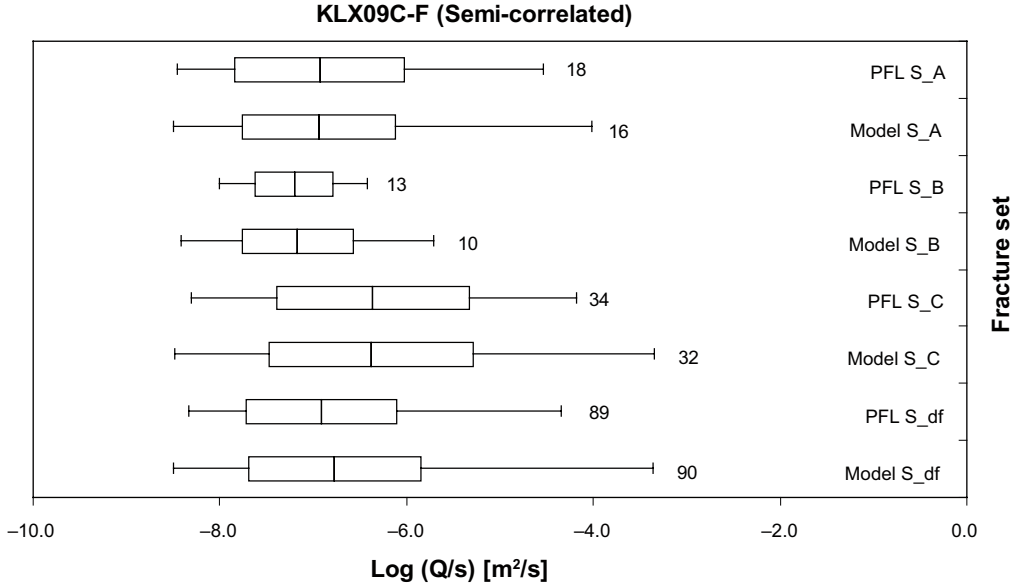

Figure 4-22. *Bar and whisker plots comparing statistics taken over each fracture set for the individual inflows, Q/s, for the PFL-f measurements from KLX09C–F against the mean over 10 realisations of the BH_DZ_optbc fracture size model. The centre of the bar indicates the mean value, the ends of the bar indicate ± 1 standard deviation, and the error bars indicate the minimum and maximum values. The total numbers of fractures with inflow above the detection limits within each set are also given. For the PFL-f data, the statistics are taken over the identified flow-anomalies within each set, and over the fractures generated within each set and over 10 model realisations. The semi-correlated transmissivity model is shown.*

set for each borehole are in remarkably good agreement considering that each borehole has a quite distinct trajectory and the stochastic nature of fracture occurrence. This confirms that the fracture set orientation definitions suggested by the Geo-DFN analysis reflect the fracture orientations. Alternative models based on the correlated and uncorrelated transmissivity models were simulated using the same BH_DZ_opt fracture size model to give a basis for analysing uncertainties with respect to the assumption about fracture size-transmissivity relationships. The results for these cases are shown in Figure 4-23 to Figure 4-26. Again, these cases do not match the shape of the flow distribution as well as the semi-correlated case. The numbers of flows for each set is reasonably consistent for each of the transmissivity models since this is mainly a function of the fracture connectivity, i.e. fracture size for a fixed intensity. A table comparing the total flows into the boreholes based on an average over 10 realisations is presented in Table 4-16. The uncorrelated model gives very little variability in total flow between boreholes, while the semi-correlated and correlated model vary significantly between boreholes despite being an average over 10 realisations. This illustrates how having a correlation between transmissivity and size with the power-law size distribution creates a lot of variability between realisations and between boreholes.

Table 4-16. Comparison of the total flow to the abstraction boreholes between the PFL data and the model averaged over 10 realisations for the BH_DZ_optbc fracture size model and 3 different size-transmissivity relationships. The values given for the model are geometric means over 10 realisations.

Total *Q/s* (m^3/s)	KLX09B	KLX09C	KLX09D	KLX09E	KLX09F	Geometric mean KLX09B–F
PFL-f	$1.8\ 10^{-5}$	$1.0\ 10^{-4}$	$2.8\ 10^{-5}$	$8.9\ 10^{-5}$	$1.6\ 10^{-4}$	$6.0\ 10^{-5}$
Mean – model semi-correlated	$1.4\ 10^{-4}$	$9.1\ 10^{-5}$	$1.2\ 10^{-4}$	$1.2\ 10^{-4}$	$5.4\ 10^{-5}$	$9.6\ 10^{-5}$
Mean – model correlated	$4.4\ 10^{-5}$	$2.6\ 10^{-4}$	$1.0\ 10^{-4}$	$8.0\ 10^{-5}$	$1.0\ 10^{-4}$	$1.0\ 10^{-4}$
Mean – model uncorrelated	$2.9\ 10^{-5}$	$5.6\ 10^{-5}$	$3.9\ 10^{-5}$	$4.7\ 10^{-5}$	$4.8\ 10^{-5}$	$4.3\ 10^{-5}$

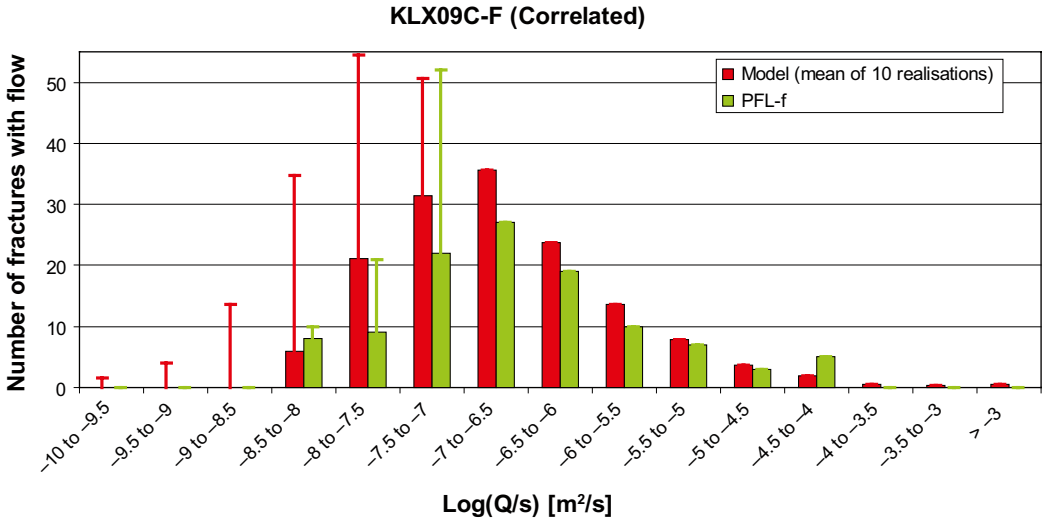

Figure 4-23. *A comparison of the distributions of individual fracture inflows, Q/s, for the PFL-f measurements from KLX09C–F against the mean over 10 realisations of the BH_DZ_optbc fracture size model and a correlated transmissivity to size. For the PFL-f data, the error bars indicate values close to the detection limit which are estimated. For the model, the error bars indicate predicted flows below the measurement limit (Note the measurement limit varies between boreholes).*

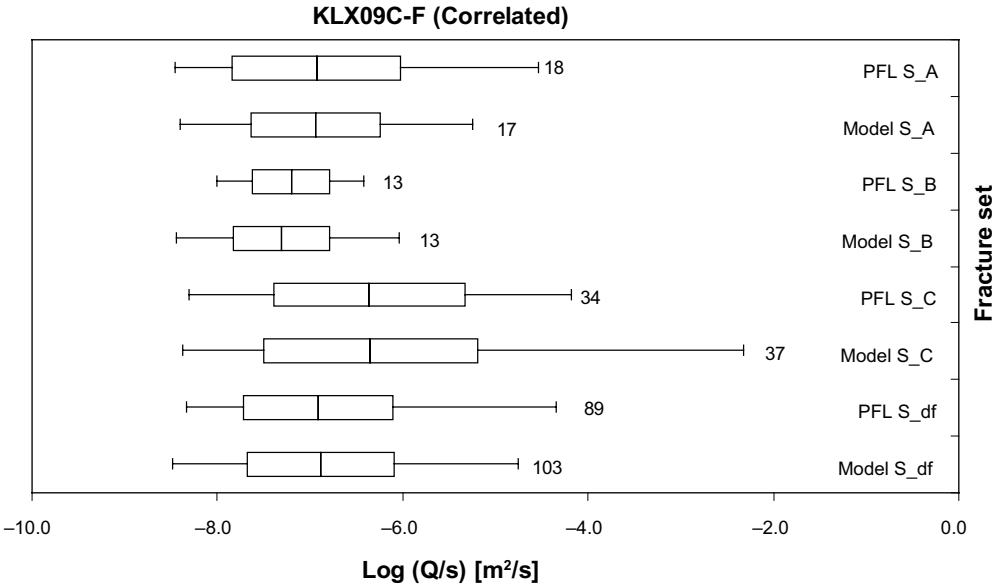

Figure 4-24. *Bar and whisker plots comparing statistics taken over each fracture set for the individual inflows, Q/s, for the PFL-f measurements from KLX09C–F against the mean over 10 realisations of the BH_DZ_optbc fracture size model. The centre of the bar indicates the mean value, the ends of the bar indicate ± 1 standard deviation, and the error bars indicate the minimum and maximum values. The total numbers of fractures with inflow above the detection limits within each set are also given. For the PFL-f data, the statistics are taken over the identified flow-anomalies within each set, and over the fractures generated within each set and over 10 model realisations. The correlated transmissivity model is shown.*

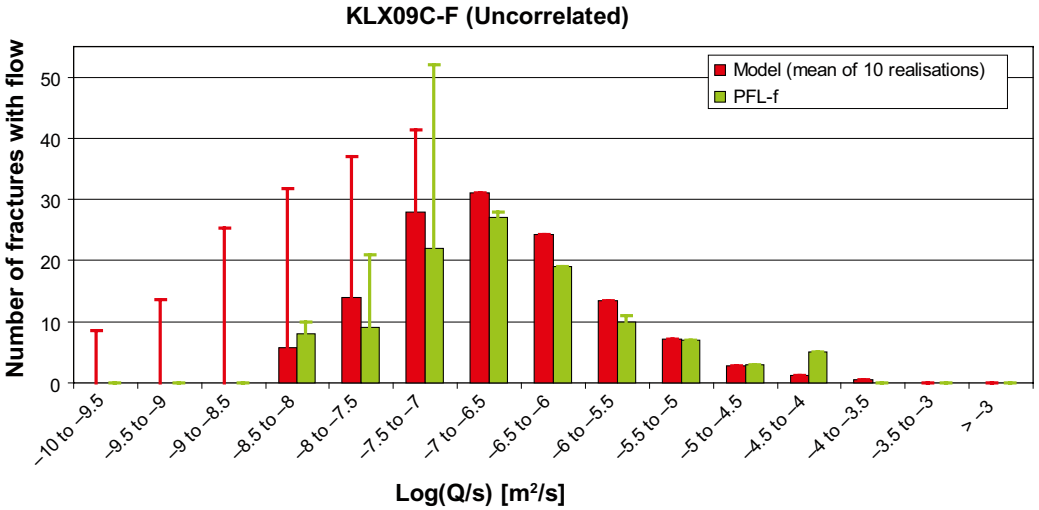

Figure 4-25. *A comparison of the distributions of individual fracture inflows, Q/s, for the PFL-f measurements from KLX09C–F against the mean over 10 realisations of the BH_DZ_opt fracture size model and an uncorrelated transmissivity to size. For the PFL-f data, the error bars indicate values close to the detection limit which are estimated. For the model, the error bars indicate predicted flows below the measurement limit (Note the measurement limit varies between boreholes).*

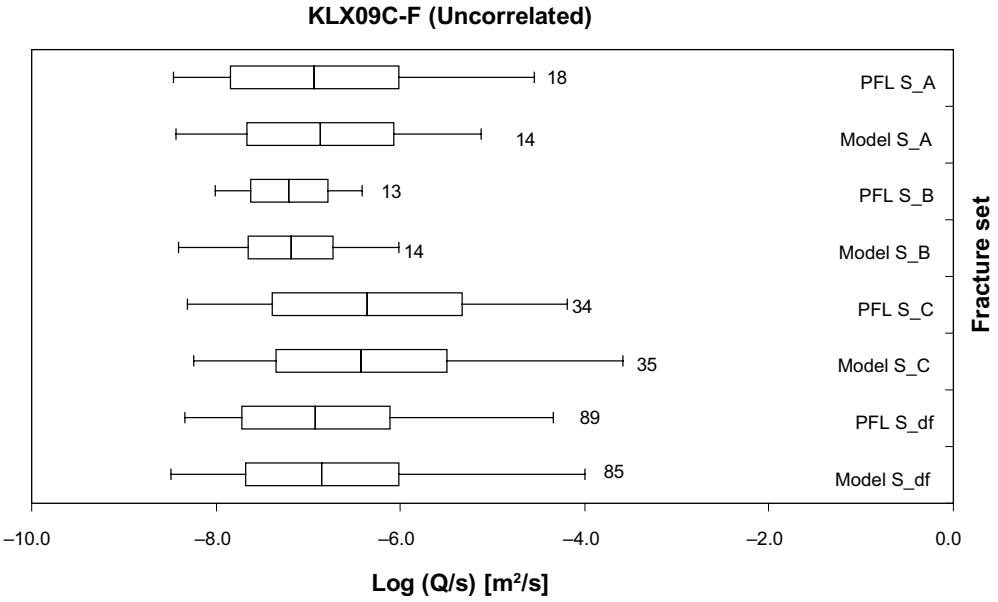

Figure 4-26. *Bar and whisker plots comparing statistics taken over each fracture set for the individual inflows, Q/s, for the PFL-f measurements from KLX09C–F against the mean over 10 realisations of the BH_DZ_optbc fracture size model. The centre of the bar indicates the mean value, the ends of the bar indicate ± 1 standard deviation, and the error bars indicate the minimum and maximum values. The total numbers of fractures with inflow above the detection limits within each set are also given. For the PFL-f data, the statistics are taken over the identified flow-anomalies within each set, and over the fractures generated within each set and over 10 model realisations. The uncorrelated transmissivity model is shown.*

One way of comparing the appropriateness of the transmissivity models is to quantify the variability in total flow, *Q/s*, over the abstraction boreholes within a single realisation, since in a sense reality is a single realisation. Table 4-17 to Table 4-19 present the mean and standard deviation of Log_{10}(total *Q/s*) within the individual realisations for each of the transmissivity models. For each model, the ensemble average of the total flow means is very similar to that for the PFL-f data for all 3 transmissivity models, as would be expected since the average total flow was one of the calibration targets. However, the magnitude of the standard deviation of total flows between abstraction boreholes is different between the 3 cases. For the semi-correlated model, the mean of standard deviations is 0.4, the same as the data. However, the variation in standard deviation between the realisations is large. Often when the mean total flow is high, then the variability between boreholes is low, suggesting the flow is dominated by a small number of horizontal fractures that intersect all 5 boreholes. For the semi-correlated model, the effect is similar, but slightly increased. For the uncorrelated model, the variability in total flow between boreholes is less than in the data, which suggests this model is less likely to produce realisations with the magnitude of variability in total flow rate seen in the hydraulic tests. This is because the random assignment of transmissivity tends to give a relatively homogeneous flow-field compared to when there is a correlation. This provides some evidence that the uncorrelated model is less consistent with the nature of the observed flow pattern.

Table 4-17. Variations in Log_{10}(total *Q/s*) in the abstraction boreholes between realisations. The columns show the difference in total flow between the abstraction boreholes for the same DFN realisation. The mean and standard deviation over the boreholes for the same realisation are given and compared to the mean standard deviation for the PFL-f data. Here, the DFN is based on the BH_DZ_optbc size model and a semi-correlated transmissivity model.

Pumping borehole	Realisation										Mean of mean and std.	PFL-f
	1	2	3	4	5	6	7	8	9	10		
KLX09B	–3.4	–3.7	–3.4	–3.8	–4.0	–3.8	–3.3	–3.7	–4.5	–5.0		–4.7
KLX09C	–3.3	–3.9	–3.7	–3.9	–4.9	–4.6	–4.3	–3.9	–4.1	–4.5		–4.0
KLX09D	–3.6	–3.8	–3.5	–4.0	–4.6	–4.1	–3.3	–4.2	–4.6	–3.5		–4.6
KLX09E	–3.3	–3.5	–3.6	–3.7	–4.7	–5.1	–3.3	–4.6	–4.0	–3.5		–4.0
KLX09F	–3.7	–4.0	–3.9	–3.7	–4.9	–4.6	–4.8	–4.3	–4.2	–3.7		–3.8
Mean	–3.5	–3.8	–3.6	–3.8	–4.6	–4.4	–3.8	–4.1	–4.3	–4.1	–4.0	–4.2
Std.	0.2	0.2	0.2	0.1	0.4	0.5	0.7	0.4	0.3	0.7	0.4	0.4

Table 4-18. Variations in Log_{10}(total *Q/s*) in the abstraction boreholes between realisations. The columns show the difference in total flow between the abstraction boreholes for the same DFN realisation. The mean and standard deviation over the boreholes for the same realisation are given and compared to the mean standard deviation for the PFL-f data. Here, the DFN is based on the BH_DZ_optbc size model and a correlated transmissivity model.

Pumping borehole	Realisation										Ensemble average	PFL-f
	1	2	3	4	5	6	7	8	9	10		
KLX09B	–4.3	–4.6	–5.0	–4.5	–4.7	–4.0	–3.5	–4.5	–4.3	–4.3		–4.7
KLX09C	–2.3	–2.9	–4.6	–3.8	–4.4	–2.6	–3.2	–4.1	–4.2	–3.8		–4.0
KLX09D	–4.1	–4.4	–4.9	–3.8	–4.3	–3.9	–3.2	–2.8	–4.2	–4.4		–4.6
KLX09E	–3.7	–4.4	–4.6	–4.7	–4.4	–3.8	–3.5	–3.5	–4.5	–3.9		–4.0
KLX09F	–4.2	–4.0	–4.4	–2.9	–4.7	–2.6	–4.8	–4.1	–3.8	–3.9		–3.8
Mean	–3.7	–4.1	–4.7	–3.9	–4.5	–3.4	–3.6	–3.8	–4.2	–4.1	–4.0	–4.2
Std.	0.8	0.7	0.2	0.7	0.2	0.7	0.7	0.7	0.2	0.3	0.5	0.4

Table 4-19. Variations in Log_{10}(total *Q/s*) in the abstraction boreholes between realisations. The columns show the difference in total flow between the abstraction boreholes for the same DFN realisation. The mean and standard deviation over the boreholes for the same realisation are given and compared to the mean standard deviation for the PFL-f data. Here, the DFN is based on the BH_DZ_optbc size model and an uncorrelated transmissivity model.

Pumping borehole	Realisation										Ensemble average	PFL-f
	1	2	3	4	5	6	7	8	9	10		
KLX09B	–4.7	–4.0	–5.2	–4.5	–4.8	–4.2	–4.4	–4.4	–4.6	–4.7		–4.7
KLX09C	–4.4	–3.5	–4.6	–3.7	–4.7	–4.5	–4.2	–4.0	–4.8	–4.1		–4.0
KLX09D	–4.5	–4.7	–4.8	–4.0	–4.7	–4.2	–4.1	–4.5	–4.4	–4.3		–4.6
KLX09E	–4.8	–3.9	–4.5	–4.9	–4.4	–4.3	–3.7	–3.8	–4.6	–4.3		–4.0
KLX09F	–4.5	–3.7	–5.0	–3.6	–4.8	–4.3	–4.7	–4.1	–4.3	–4.2		–3.8
Mean	–4.6	–4.0	–4.8	–4.2	–4.7	–4.3	–4.2	–4.1	–4.5	–4.3	–4.4	–4.2
Std.	0.2	0.5	0.3	0.6	0.2	0.1	0.4	0.3	0.2	0.2	0.3	0.4

4.5.3 Summary and parameterisation

The single-hole PFL-f hydraulic test guided the development of a Hydro-DFN model parameterisation. In order to honour the fracture intensity of open fractures in the borehole, intensity of regional-scale deformation zones, and frequency of PFL flow-anomalies, the fracture size model has converged on an r_0 of 0.04 m for sets S_A (ENE), S_B (NS) and S_df (HZ) and 0.12 m for the S_C (NW) set, and k_r between 2.59 and 2.69. The distribution of flow between the sets guided the choice of parameters for each set according to the 3 different transmissivity-size relationships. Generally, set S_C (NW) was assigned higher transmissivities than other sets, and set S_B (NS) was assigned lower. A summary of all Hydro-DFN settings for each set is given in Table 4-20. The different transmissivity relationships for each set and the alternative models are plotted in Figure 4-27. It should be noted that this does not represent a unique set of models that honour the data. Uncertainties remain in an appropriate choice of k_r for the sub-horizontal set S_df, for example. Also, a range of different combinations of the exponent b and standard deviation σ could be used for the semi-correlated model since by varying b, a continuous range of possible models can be obtained from fully correlated to uncorrelated. The smaller the value of b used, the higher the value of σ required to obtain a match to the inflow distribution. Another uncertainty is the effects of heterogeneity or channelling of flow within individual fractures. Here, it has been assumed that aperture/transmissivity is constant on a plane, which is equivalent to homogenising flow within a fracture plane. Some of these uncertainties are explored in the next section relating to the interference tests.

4.6 Interference tests

In addition to the single-hole flow differencing PFL-f tests, interference tests were performed between KLX09B–F /Sokolnicki and Pöllänen 2006/. While an abstraction test was being made in one of the boreholes KLX09B–F, each of the other 4 boreholes were monitored in terms of the drawdown in head relative to the head prior to the tests and intra-borehole flows associated with each PFL-anomaly identified in the single-hole tests. The monitoring holes were open during the interference tests. The interference tests were performed in all possible combinations, i.e. each of the five boreholes was pumped in turn. The drawdowns and inflows at the abstraction boreholes were identical to the single-hole tests reported in Section 4.5. For each test, the change in head and flow-rate between the values measured under pumped and un-pumped conditions at the locations associated with the PFL-anomalies, identified in the single-hole tests, were provided. The question was then how to use this additional information to better calibrate

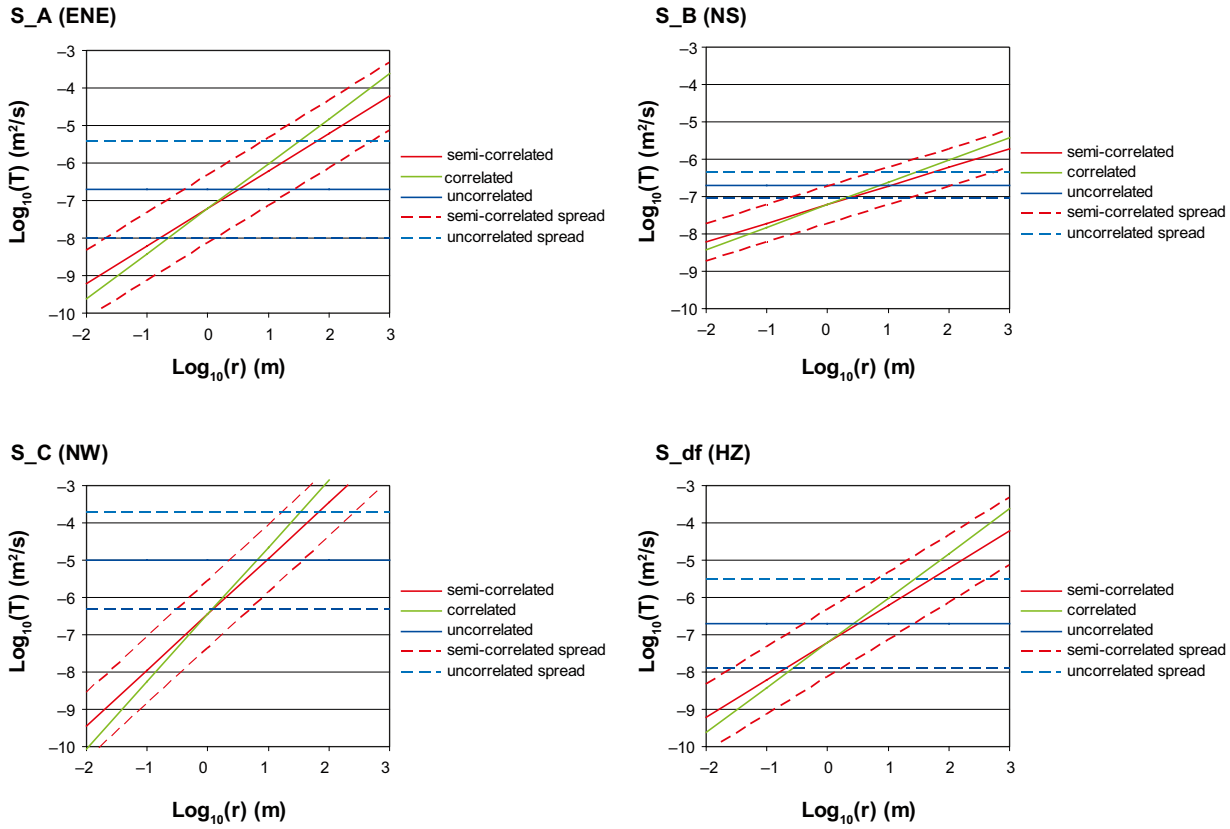

Figure 4-27. Transmissivity model relationships for each fracture set based on the calibration against single-hole tests as defined by the BH_DZ_optbc model given in Table 4-20. Relationships are shown for each of the three alternative models for transmissivity. For the semi-correlated and uncorrelated cases, the spread is displayed by the standard deviation, ± σ.

Table 4-20. Description of the Hydro-DFN input parameters for the BH_DZ_optbc fracture size model with transmissivity parameters calibrated on the single-hole test. The transmissivity parameters are given for each set and the semi-correlated (SC), correlated (C) and uncorrelated (UC) models.

Fracture set name	Orientation set pole: (trend, plunge), concentration	Fracture radius model power-law (r_0, k_r)	Intensity P_{32} (m^2/m^3); valid radius interval (r_{min}, r_{max})	Relative intensity of P32	Transmissivity model T (m^2/s)
S_A (ENE)	(350, 12) 19	(0.04, 2.59)		0.19	*SC: (a,b,σ)* = (6 10^{-8}, 1.0, 0.9)
					C: *(a,b)* = (6 10^{-8}, 1.2)
					UC:*(μ,σ)* = (–6.7, 1.3)
S_B (NS)	(92, 1) 17	(0.04, 2.62)		0.13	*SC: (a,b,σ)* = (6 10^{-8}, 0.5, 0.5)
					C: *(a,b)* = (6 10^{-8}, 0.6)
			3.99 (0.28, 564)		UC:*(μ,σ)* = (–6.7, 0.35)
S_C (NW)	(213, 5) 13	(0.12, 2.69)		0.21	*SC: (a,b,σ)* = (3.5 10^{-7}, 1.5, 0.9)
					C: *(a,b)* = (3.5 10^{-7}, 1.8)
					UC:*(μ,σ)* (–5.0, 1.3)
S_df (HZ)	(250, 77) 15	(0.04, 2.60)		0.47	*SC: (a,b,σ)* (6 10^{-8}, 1.0, 0.9)
					C: *(a,b)* (6 10^{-8}, 1.2)
					UC:*(μ,σ)* (–6.7, 1.2)

the Hydro-DFN and build confidence in its ability to mimic the flow characteristics of the upper 100 m of bedrock in this local area. One of the most important considerations was what measures to use when comparing the simulations with the field measurements. One decision that was made was that we should not aim to reproduce the exact same head and flow responses in the exact same positions as the data, since this would require developing an accurate structural model of the volume of rock immediate to KLX09, which implies an integration with geophysical data that was not available, and anyway we are more interested in deriving a stochastic Hydro-DFN model that could be used generally in the top section of Ävrö Granite rather than one particular to KLX09. Hence, effort was concentrated on deriving stochastic Hydro-DFN models that reproduced statistics and general trends in the measured responses. The main measures used were the distributions of intra-borehole flow rates, the distribution of heads in the monitoring holes in addition to the total inflows and inflow distribution at the abstraction boreholes already used in Section 4.5.3.

4.6.1 Modelling approach

Each of the interference tests were run for about 7 days by which time the responses were broadly in steady-state. Hence, the same steady-state simulations were used as in Section 4.5, but with some additional analysis of the results to compare with the interference tests.

One issue that was felt to be important though was to assess what effect the PFL tool had on the measured intra-borehole flows and how flow to and along the monitoring boreholes should be modelled. For the abstraction borehole, flow is convergent toward the pumped borehole and water has to enter the borehole via the fractures intersected. With the PFL-f measurements, water is abstracted from the top of the borehole and there is a bypass pipe for flow from below the tool's current position. An open hole has a diameter of about 76 mm, while the bypass pipe has a diameter of about 28 mm. During the measurement of inflow from a particular section or flow-anomaly, flow is channelled through a flow sensor of diameter 6 mm. Therefore, when the measurement is actually made for a particular flow-anomaly the flow is locally subject to a resistance created by the tool introducing a constriction. For the abstraction borehole, this constriction may reduce flow for very high transmissive fractures, but generally this is not a significant issue since the borehole being a sink, it forces flow to enter the borehole and overcome the resistance introduced by the presence of the tool. However, in the monitoring holes, flow will only enter the borehole if it provides a preferential connection to a more transmissive path to the downstream sink compared to flow carrying on passed the borehole. Clearly, a 76 mm diameter open hole has very little resistance to connect up fractures intersected, but when the tool measures the flow from a particular fracture, the 6 mm diameter constriction associated with the flow-sensor may inhibit flows as long as the tool is in position. Therefore, it is possible that open monitoring boreholes provide extra flow connections and enhance flow, but when the tool is inserted into the monitoring hole, it temporarily reduces the inflow/outflow for the measured flow-anomaly. This raises issues both in terms of how well the measured inflows in the monitoring holes reflect the intra-borehole flows occurring, and how flow within the boreholes should be modelled. Modelling the boreholes as 76 mm open holes may over-predict the intra-borehole flows, whereas modelling them as 6 mm holes may lead to a reduction of flow in the system overall. It is impractical to perform a simulation for each individual monitoring hole measurement with a constriction only at that position while all other parts of the borehole are fully open since this would require nearly 1,000 simulations.

To try to quantify the effect of the tool on flow, the flow-rates and heads in the monitoring holes were analysed to calculate the effective resistance in the boreholes based on the intra-borehole flow-rates and the head gradients. This was done by first calculating the net flux up the borehole given the inflow/outflows at each PFL-anomaly, and then using the formulae based on laminar Hagen-Poiseuille flow

$$K_E = \frac{Q_b}{\pi r_b^2} \Big/ \left(\frac{\Delta h}{\Delta L} \right) \qquad \text{Equation 4-5}$$

$$r_E = \left(\frac{8 Q_b}{\pi} \Big/ \left(\frac{\Delta h}{\Delta L} \right) \right)^{1/4} \qquad \text{Equation 4-6}$$

where K_E is the effective hydraulic conductivity of the borehole, r_E is the effective hydraulic borehole radius, Q_b is the flux along the borehole with pumping between each pair of flow-anomalies, r_b is the radius of the borehole, Δh is the head difference with pumping between each pair of flow-anomalies, and ΔL is the spacing between each pair of flow-anomalies. Using these formulae to calculate the effective hydraulic properties of the borehole between adjacent pairs of flow-anomalies gave consistent values between each pair of anomalies and between each monitored borehole of 7 10^{-2} – 0.8 m/s for the effective hydraulic conductivity, or an effective hydraulic radius of 5–11 mm, which is quite consistent with the actual physical hole size for flow-sensors. If the same calculations are made for the pumped borehole, the effective hydraulic conductivity is 5–30 m/s, and the effective hydraulic radius is about 15–28 mm. Hence, this analysis of the flux and head data confirms that the PFL tool creates more resistance in the monitoring holes under cross-flow conditions than at the pumped borehole when it acts as a radial sink.

Based on the above analysis a hydraulic conductivity of 0.3 m/s was assigned to the full length of all boreholes, being about the mean of that interpreted. In the DFN flow simulations, flow along a borehole is modelled as a 1D connection that provides a hydraulic connection between the fractures which it intersects. The flux along the borehole between any two adjacent fractures is then equal to the hydraulic conductivity multiplied by the cross-sectional area of the borehole times the head gradient between the fractures. For the pumped boreholes, the head was held at a uniform drawdown along the borehole as a boundary condition, and hence the flux along it is irrelevant. For the monitored holes, modelling the boreholes as additional hydraulic connections has the potential to enhance the flow field. To check that the above choice of hydraulic conductivity was appropriate, and quantify the sensitivity to the choice, the total intra-borehole flow was calculated by summing the magnitude of inflows/outflows for each PFL-anomaly interval over the monitoring holes for each set of interference tests. Also, the variability in head within each borehole was calculated as this would be expected to be zero for a borehole of infinite hydraulic conductivity. In the single-hole tests, a hydraulic conductivity of 10^4 m/s was used which is about correct for laminar flow in a 76 mm diameter open hole. When this hydraulic conductivity was decreased to 0.3 m/s, the mean total flow to the abstraction boreholes was reduced only slightly by 6%. However, much more significant effects were seen in the monitoring holes as shown in Table 4-21. The mean of the total inflows/outflows, *Q/s*, to the monitoring boreholes averaged over all test configurations reduced by nearly a half. The variability of head within each borehole also rose. The values for the total intra-borehole flows and head variability were similar to those for the PFL-f data when 0.3 m/s was used for the borehole hydraulic conductivity. Hence, for all the comparisons with interference test data, the Hydro-DFN simulations were modified to use this lower value for the boreholes.

Table 4-21. Comparison of variability in head and intra-borehole flow, *Q/s*, within the monitoring boreholes for different borehole hydraulic conductivities in the BH_DZ_optbc model with a semi-correlated transmissivity and the measured data.

Borehole conductivity	Mean (standard deviation in head within monitoring boreholes)	Mean (total intra-borehole flow *Q/s* within monitoring boreholes)
10^4 m/s	$7.3\ 10^{-4}$	$2.3\ 10^{-5}$ m²/s
0.3 m/s	0.09	$1.3\ 10^{-5}$ m²/s
PFL-f data	0.11	$1.0\ 10^{-5}$ m²/s

For the models derived from matching the single-hole tests, extra plots were generated of the distributions of fracture inflows/outflows in the monitoring holes and mean drawdowns in the monitoring holes to compare with the data.

Some additional cases were also studied to quantify uncertainties and sensitivities including different transmissivity parameters, different boundary conditions, heterogeneity within planes, and local conditioning of transmissivity.

4.6.2 Visualisation of flow responses

Before trying to obtain models consistent with the interference test data, it was instructive to try to visualise the main structures and flow connections that are responsible for the observed flow and head responses. This was done by identifying the PFL-anomalies that corresponded to the highest inflows/outflows measured during the interference tests, and visualising them as square fractures assumed to have a length of 15 m and centred on the borehole location where the flow was observed. 15 m was chosen as it gives fractures that extend approximately half the distance between boreholes. The orientation of the fractures was taken from Sweco Viak's work on associating PFL-f flow anomalies to the borehole image and core data. The result is shown in Figure 4-28 with fractures coloured by the transmissivity inferred from the single-hole tests. It should be remarked that the transmissivities interpreted from the single-hole tests are based on measuring the flow after many days of pumping, and so they reflect the response of the connected network as well as the localised transmissivity around the borehole. Also, the interpretation assumes radial flow through a homogeneous medium, and over an assumed radius of influence of c. twenty metres. It is possible that transmissivities of the fractures immediately adjacent to the borehole are substantially higher, but flow is limited by lower transmissivity fractures they intersect. The size of the discrepancy depends on the connectivity of the network and the heterogeneity in transmissivity between or within fractures.

Figure 4-28 reveals a number of interesting aspects, including that many of the highest transmissivities are associated with steeply dipping NW striking fractures, and that a number of pairs of fractures appear to be on a similar trajectory suggesting they could be part of the same structure. There are 3-4 pairs of fractures that could be parts of extensive structures, three of which are sub-horizontal. These potentially 'common' fractures tend to have different interpreted transmissivities in different boreholes varying by up to an order of magnitude suggesting heterogeneity within the planes. Hence, visualisation of the main flow-anomalies suggests:

- Set S_C has a very important role in flow.
- Relatively few structures are responsible for much of the flow, and also for the head distribution in the monitoring boreholes.
- Possible heterogeneity within some fracture planes between the boreholes at least in the sub-horizontal fractures.

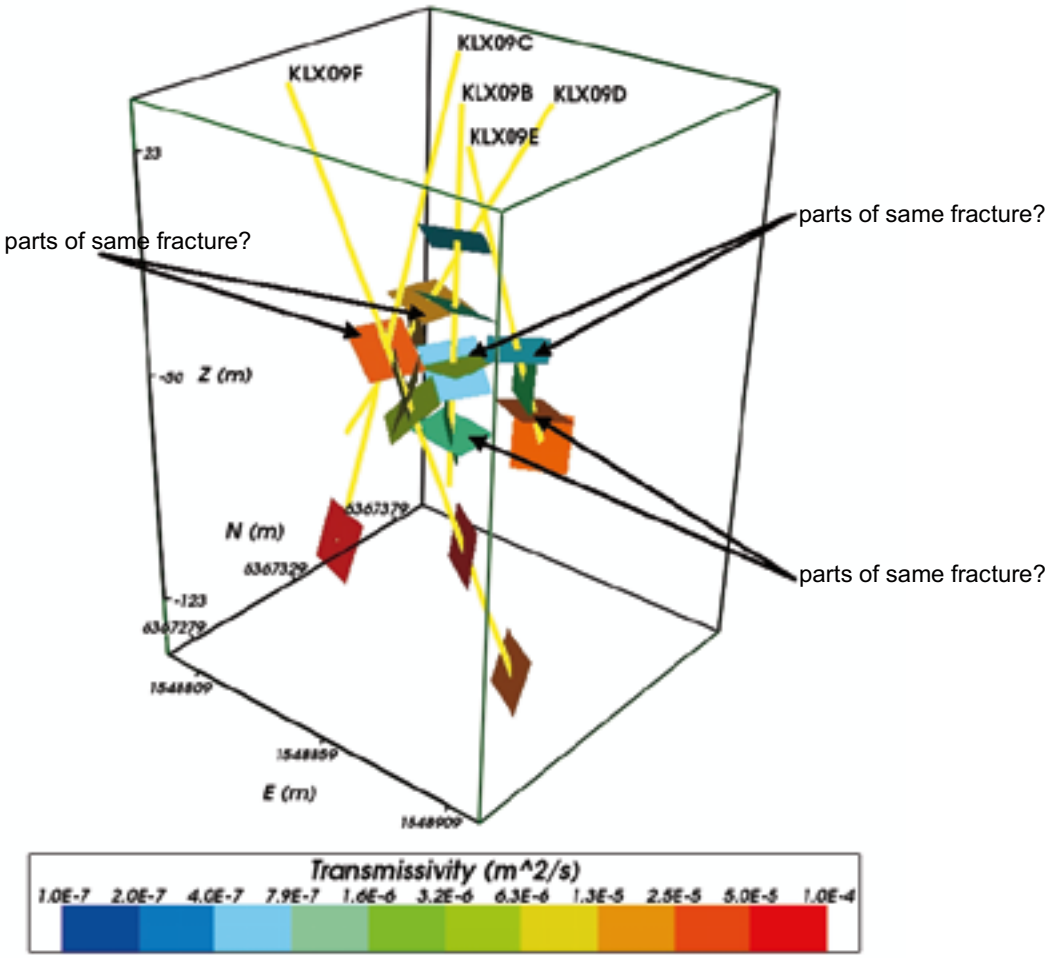

Figure 4-28. *Speculative visualisation of most transmissive fractures contributing to intra-borehole flows during the interference tests. The fractures are drawn as square fractures of length 15 m centred on the borehole with orientations taken from integration of PFL-f and borehole image analysis. The fractures are coloured according to the transmissivity interpreted from the single-hole test interpretations. Some potential 'common' fractures seen in the boreholes are indicated.*

It is also important to highlight that there are 5 fractures with transmissivities that have been interpreted from the single-hole test as being between 3 10^{-5} to 10^{-4} m^2/s. These are responsable for the small spike on the right side of the *Q/s* flux distribution for the PFL-f data plotted in Figure 4-21, for example. These flux values could be viewed as anomalous compared to the rest of the flux distribution and may correspond with minor deformation zones (no mapping of deformation zone was provided for these boreholes). Table 4-22 gives the orientations and transmissivities of these 5 fractures. Two of these are sub-horizontal belonging to set S_df (HZ), and 3 NW striking sub-vertical belonging to set S_C(NW). Of the boreholes they intercept, 2 are in KLX09C, 1 in KLX09E, and 2 in KLX09F. These 3 boreholes correspond to the ones with the highest total inflow during the single-hole tests, and the highest head responses seen in the monitoring holes during the interference tests. Therefore, it may be asserted that these 5 fractures with transmissivities around 10^{-4} m^2/s are responsible for the different magnitudes of flow and head response seen when pumping different borehole. Again, in the model calibration the aim was to not reproduce these exact responses in these particular boreholes, but to try to find model settings that gave significantly higher flows and head responses in about 3 of the 5 interference tests.

Table 4-22. Properties of the 5 fractures with highest interpreted transmissivities from the single-hole abstraction tests.

Borehole	Length	Anomaly number	Strike (°)	Dip (°)	Interpreted transmissivity (m^2/s)
KLX09C	73.71	25	20	37	$4.6\ 10^{-5}$
KLX09C	76.41	36	109	74	$6.3\ 10^{-5}$
KLX09E	79.89	27	293	13	$3.8\ 10^{-5}$
KLX09F	113.68	37	124	83	$6.5\ 10^{-5}$
KLX09F	145.78	43	122	76	$4.4\ 10^{-5}$

4.6.3 Model calibration

The first step in the model calibration on interference test data was to assess the performance of the model derived from the single-hole tests detailed in Table 4-20, and for each of the 3 transmissivity relationships. The performance of the model in simulating the data was measured in terms of a comparison of the distribution of fluxes within the monitoring boreholes, see Figure 4-29 for example. Here, the measured fluxes into or out of the monitoring holes at each PFL flow-anomaly location for all combinations of interference test (4 monitoring holes and 5 pumped boreholes) were collected together as an ensemble and the values divided into half order of magnitude bins to give a distribution. For the model, 10 model simulations were generated, and flow calculations made for pumping in each of the 5 boreholes to give equivalent set of histograms for each of the 10 simulations. An average histogram for the model was calculated by averaging the numbers of flows in each bin over the 10 realisations, and this average histogram was compared with the data, as in Figure 4-29.

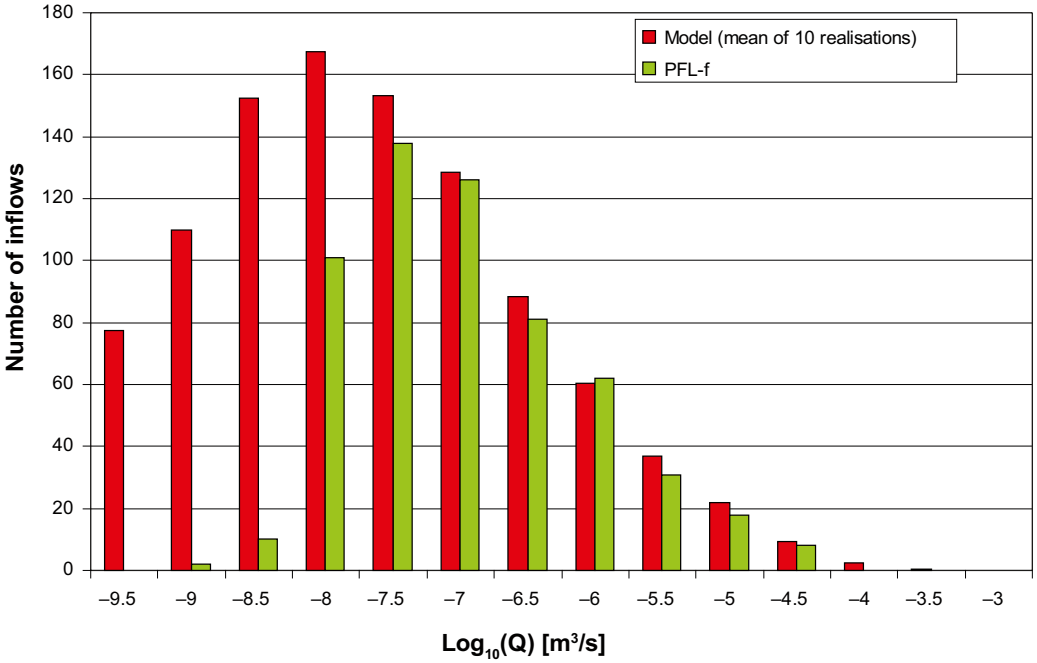

Figure 4-29. *Histogram comparing the distribution of the magnitude of inflows/outflows, Q, to the monitoring boreholes taken over an ensemble of all possible combinations, i.e. five abstraction boreholes multiplied by 4 monitoring boreholes each. The PFL-f interference measurements in KLX09C–F (green) are plotted against the mean over 10 realisations of the BH_DZ_optbc fracture size model (red) with a semi-correlated transmissivity (see Table 4-20 for parameter values).*

A second comparison was made against the drawdowns in the monitored boreholes, see Figure 4-30. Since for a particular pumped borehole, the average drawdowns in all of the monitoring holes are quite similar, the average drawdown over all the monitored boreholes (ordinate) is shown for each pumped borehole (abscissa). The first histogram bar represents the measured data for each of the 5 boreholes, followed by 10 data series for each of the model realisations. For the measured data, the drawdown in the monitored holes has been normalised linearly to a 10 m drawdown at the pumped borehole to make it easier to compare across the boreholes. Figure 4-29 and Figure 4-30 show results for the BH_DZ_optbc case with a semi-correlated transmissivity. The comparison of the inflow/outflow distribution in the monitoring holes appears to be very good, while the comparison of the drawdowns in the monitored holes is disappointing. Only Realisation 7 shows the right sort of characteristics with high drawdowns, 4–5 m, in three of the interference tests and low ones, around 1 m, in the other two. Generally, the model predicts drawdown responses around 1 m or less for all boreholes, i.e. more homogeneous and isotropic than the data suggests.

Some insight into what is important in order to obtain a match to the measured drawdowns can be gained by visualisation of Realisation 7. Figure 4-31 shows the highest transmissivity fractures in Realisation 7 of the BH_DZ_optbc fracture size model for a semi-correlated transmissivity model. This shows that there is a large fracture over 20 m in radius that intersects KLX09B, KLX09D and KLX09E with a transmissivity of about 5 10^{-4} m^2/s which is responsible for the high drawdowns responses seen in this realisation as shown in Figure 4-30. This suggests that the kinds of high drawdowns seen in the monitored holes when 3 of the boreholes are pumped, but not in the other 2, occur when there are 1 or 2 very transmissive extensive fractures in the NW set. The measurements give high drawdown responses for pumping in KLX09C, KLX09E and KLX09F. These 3 boreholes are on either sides of the study area, and so it's hard to envisage how a single fracture could be responsible for these 3 responses. Inspecting Figure 4-28, suggests the responses may be due to a NW sub-vertical fracture dipping SW at the base of KLX09E and one or more near vertical NW fractures near the base of KLX09C and KLX09F, all of which having high transmissivity and being extensive. These features could be several discrete features or be parts of unmapped minor deformations zones. From this, it can be surmised that a greater number of realisations with the desired types of drawdowns could be obtained if the size distribution of the NW set, S_C, were chosen to always give 1 or 2 fractures of radius greater than 20 m that intersect one or more boreholes. Hence, it is important to consider more the sensitivity to the size distribution of S_C as will be seen later.

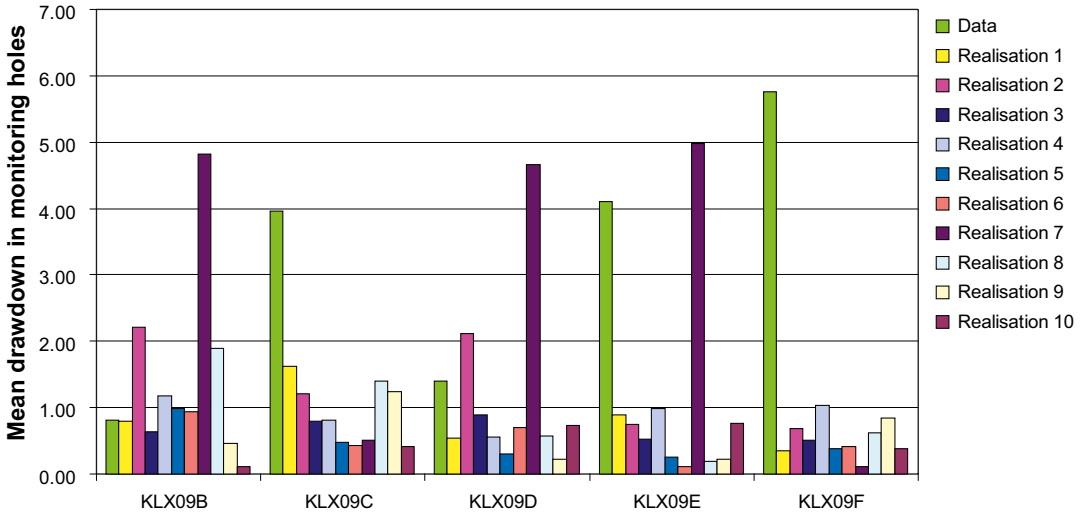

Figure 4-30. *Histogram comparing the mean drawdown response measured in the monitoring holes for pumping in the 5 abstraction boreholes KLX09B–F against the mean simulated head for each of 10 realisations. The model used is the BH_DZ_optbc fracture size model with a semi-correlated transmissivity (see Table 4-20 for parameter values).*

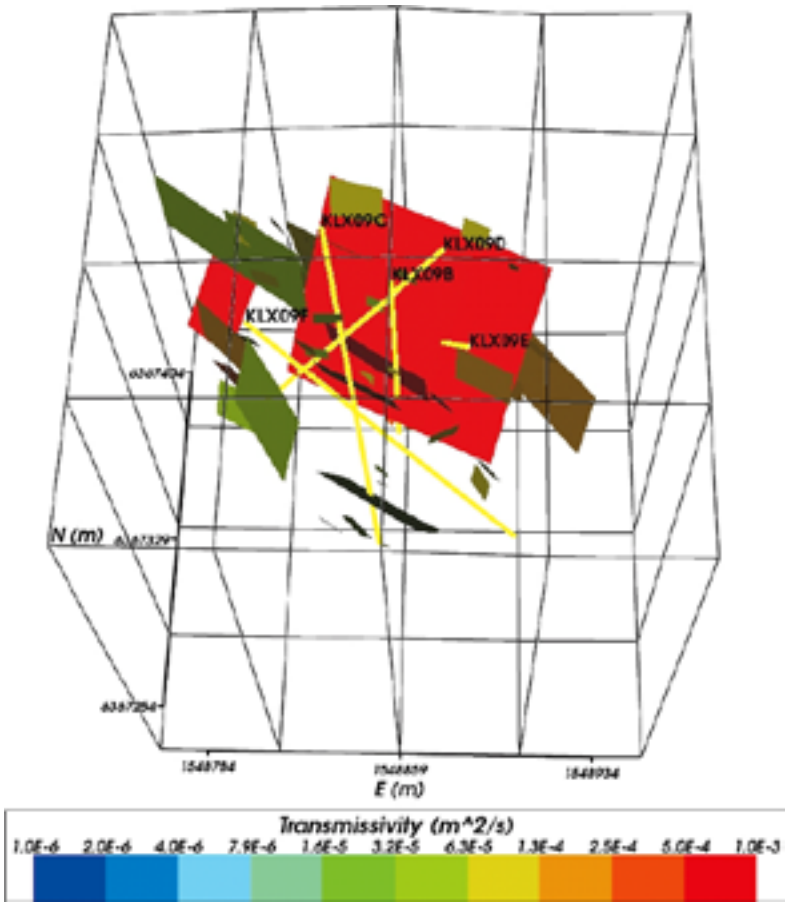

Figure 4-31. *Highest transmissivity fractures generated in Realisation 7 of the BH_DZ_optbc fracture size model with a semi-correlated transmissivity (see Table 4-20 for parameter values). Only fractures with transmissivity greater than 5 10^{-5} m^2/s are shown. The large high transmissivity fracture that intersects KLX09B, KLX09D and KLX09E is the one that causes the high head drawdown in the monitoring boreholes seen in Figure 4-30 for this realisation.*

Sensitivity to the top surface boundary condition

In modelling both the single-hole and interference tests it was assumed that appropriate boundary conditions for steady-state flow calculations were a fixed head of zero on all vertical sides and the top surface. The total abstraction rates at the pumped boreholes varies between about 14,000–48,000 l/day, which is clearly a significant amount of water to remove from the system and may be expected to result in some lowering of the watertable locally. For comparison, using an average infiltration of 200 mm over a year, would give a flux of about 12,300 l/day entering the top surface of the model which has a surface area of 150×150 m. Hence, a lot of the water abstracted at the boreholes is going to have to enter the model through the lateral surfaces rather than the top, at least for boreholes KLX09C, KLX09E and KLX09F. Therefore, it was thought important to assess the sensitivity of the results to the boundary condition set on the top surface. A simple test was to change the top surface boundary condition to no-flux, while maintaining a constant head of zero on the lateral sides of the model. For the BH_DZ_optbc size model with a semi-correlated transmissivity, the geometric mean flux into the abstraction boreholes reduced by only 10% with a no-flux boundary on the top surface, and the inflows/outflows to the monitored boreholes showed little effect comparing a no-flux with a specified head boundary condition on the top. However, the drawdowns in the monitored boreholes were found to be more sensitive to the top surface boundary condition for several realisations (compare Figure 4-32 with Figure 4-30). Realisations 5 and 6 show the most change, and many of the responses are increased by a factor of about 2. This implies that in order to simulate the drawdowns a realistic top surface boundary condition should be used rather specified head.

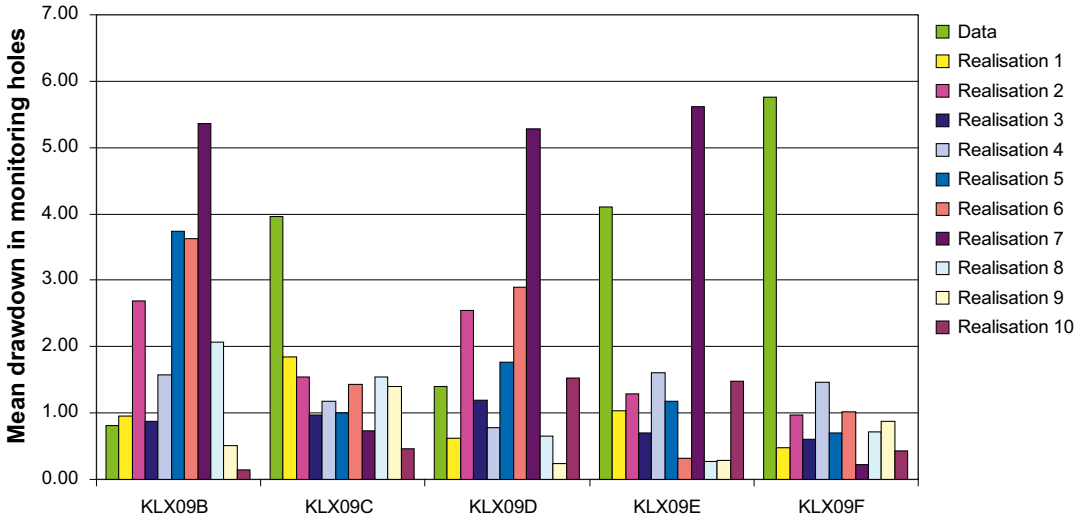

Figure 4-32. *Histogram comparing the mean drawdown response measured in the monitoring holes for pumping in the 5 abstraction boreholes KLX09B–F against the mean simulated head for each of 10 realisations. The model used is the BH_DZ_optbc fracture size model with a semi-correlated transmissivity (see Table 4-20 for parameter values) and a no flux boundary on the top surface.*

The sensitivity was examined further by comparing the results for a case with no-flux against one with a specified infiltration rate of 200 mm/year. For the specified flux case, the modelling procedure becomes a bit more complex. Two groups of models had to be run, one with a specified head of 13 m on the sides, specified infiltration of 200 mm/year on the top and no pumping at the boreholes, while the other group has pumping at each borehole. To specify the top surface flux in a discrete model, rules have to be defined for how much of this flux enters each fracture that intersects the top surface. The method used is to calculate the total flux entering the top surface of the model (i.e. infiltration multiplied by surface area), then apportion this total flux between individual fractures intersecting the top surface according to a weighting based on their trace length multiplied by transmissivity. Hence, more of the flux will enter long and/or more transmissive fractures. For each pair of simulations, with and without pumping, the drawdown was calculated as the difference between the heads in the monitored boreholes between the two simulations. The difference in the results for the specified flux case and the no-flux case were found to be small, just a few percent. Hence for simplicity, the remaining simulations were performed with a no flux condition.

Sensitivity to fracture size distributions

As discussed at the beginning of Section 4.6.3, it was thought a larger proportion of realisations with realistic head responses could be obtained if the frequency of large NW fractures in set S_C(NW) were increased such that there are about 2–3 borehole intersections with these fractures. This can be achieved by changing the size distribution parameters for set S_C(NW) to either (r_0, k_r) = (0.12 m, 2.6) or (0.23 m, 2.69), for example. Here, (r_0, k_r) = (0.12, 2.6) was used to create a case called "BH_DZ_optbc2". Along with fine-tuning the transmissivity versus size parameters to match the inflow distribution shown in Figure 4-33, these changes to the size parameters gave a greater number of realisations that give a distribution of head responses over the monitored boreholes similar to the observation as shown in Figure 4-34. Realisations 1, 3, 4, 6, 7 and 8 all give the heterogeneity of head responses, i.e. 2–3 high response > 2 m and the rest low, as seen in the tests. The transmissivity versus size relationships for this case were calibrated to reflect both the nature of the interference test and the single-hole tests. The agreement with the flow distribution between fracture sets in the pumped boreholes is demonstrated in Figure 4-35. The parameters used for this model are detailed in Table 4-23. It can be seen that the parameters chosen for the semi-correlated model actually uses different degrees of correlation for the different sets with a strong correlation for set S_C(NW), and no correlation for sets S_A(ENE), S_B(NS) and S_df(HZ).

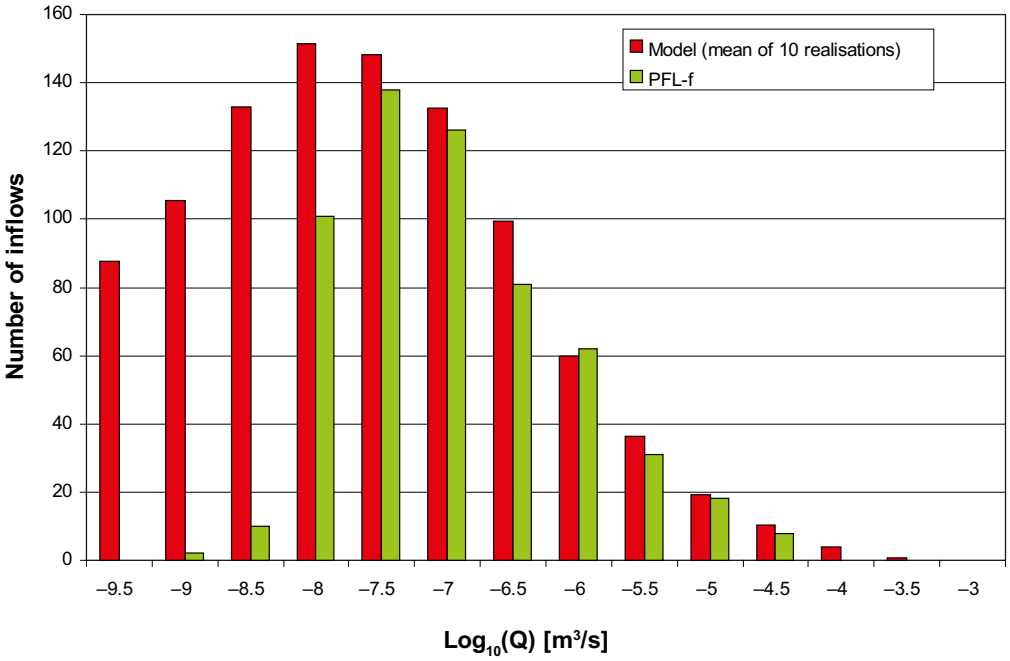

Figure 4-33. *Histogram comparing the distribution of the magnitude of inflows/outflows, Q, to the monitoring boreholes taken over an ensemble of all possible combinations, i.e. five abstraction boreholes multiplied by 4 monitoring boreholes each. The PFL-f interference measurements in KLX09C–F (green) are plotted against the mean over 10 realisations of the BH_DZ_optbc2 fracture size model (red) with a semi-correlated transmissivity (see Table 4-23 for parameter values) and no-flux boundary condition.*

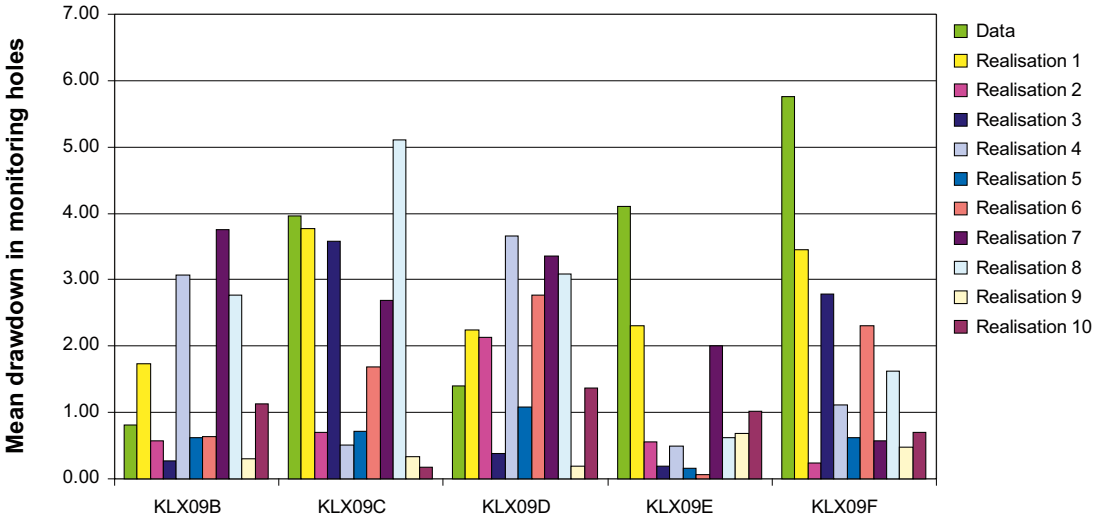

Figure 4-34. *Histogram comparing the mean drawdown response measured in the monitoring holes for pumping in the 5 abstraction boreholes KLX09B–F against the mean simulated head for each of 10 realisations. The model used is the BH_DZ_optbc2 fracture size model with a semi-correlated transmissivity (see Table 4-23 for parameter values) and no-flux boundary condition.*

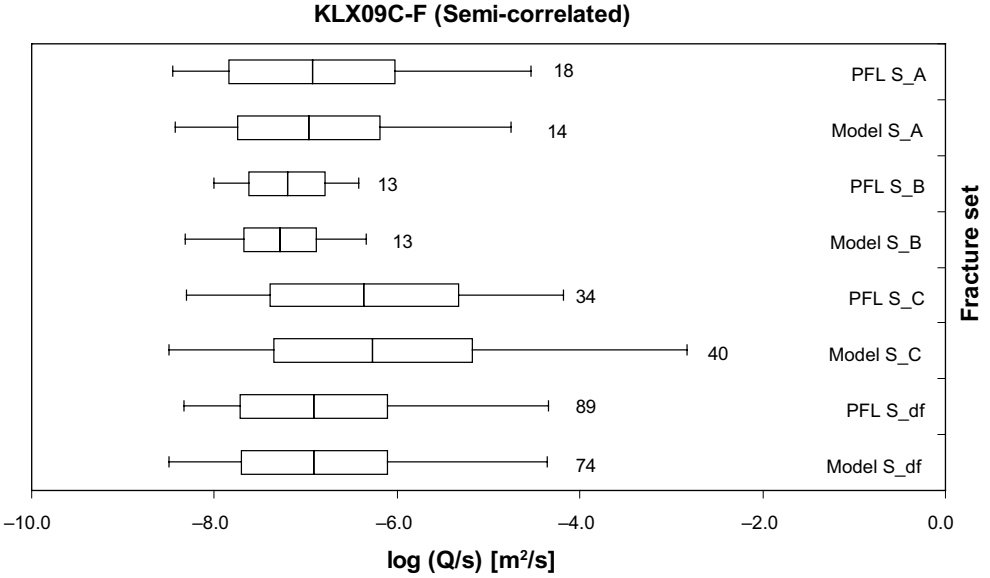

Figure 4-35. *Bar and whisker plots comparing statistics taken over each fracture set for the individual inflows, Q/s, for the PFL-f measurements from KLX09C–F against the mean over 10 realisations of the BH_DZ_optbc2 fracture size model. The centre of the bar indicates the mean value, the ends of the bar indicate ± 1 standard deviation, and the error bars indicate the minimum and maximum values. The total numbers of fractures with inflow above the detection limits within each set are also given. For the PFL-f data, the statistics are taken over the identified flow-anomalies within each set, and over the fractures generated within each set and over 10 model realisations. The semi-correlated transmissivity model is shown.*

Table 4-23. Description of the Hydro-DFN input parameters for the BH_DZ_optbc2 fracture size model with transmissivity parameters calibrated on the interference tests. The transmissivity parameters are given for each set and the semi-correlated (SC), correlated (C) and uncorrelated (UC) models.

Fracture set name	Orientation set pole: (trend, plunge), concentration	Fracture radius model power-law (r_0, k_r)	Intensity P_{32} (m^2/m^3); valid radius interval (r_{min}, r_{max})	Relative intensity of P32	Transmissivity model T (m^2/s)
S_A (ENE)	(350, 12) 19	(0.04, 2.59)		0.19	*SC: (a,b,σ)* = (1 10^{-7}, 0.0, 1.5)
					C: *(a,b)* = (4 10^{-8}, 1.0)
					UC:*(μ,σ)* = (–6.7, 1.3)
S_B (NS)	(92, 1) 17	(0.04, 2.62)		0.13	*SC: (a,b,σ)* = (1 10^{-7}, 0.0, 0.2)
			3.99		C: *(a,b)* = (4 10^{-8}, 0.5)
			(0.28, 564)		UC:*(μ,σ)* = (–6.7, 0.35)
S_C (NW)	(213, 5) 13	(0.12, 2.60)		0.21	*SC: (a,b,σ)* = (4 10^{-7}, 1.5, 0.3)
					C: *(a,b)* = (2 10^{-7}, 1.5)
					UC:*(μ,σ)* (–5.0, 1.3)
S_df (HZ)	(250, 77) 15	(0.04, 2.60)		0.47	*SC: (a,b,σ)* (7 10^{-8}, 0.0, 1.5)
					C: *(a,b)* (4 10^{-8}, 1.0)
					UC:*(μ,σ)* (–6.7, 1.2)

Sensitivity to transmissivity model

An important sensitivity to quantify is the effect of different relationships between fracture size and transmissivity. The 2 alternative models using a direct correlation between fracture size and transmissivity and a completely uncorrelated relationship derived in Table 4-23 were used to simulate the interference test. The distribution of intra-borehole flows and drawdowns for the correlated case are shown in Figure 4-36 and Figure 4-37, and the corresponding distribution of flow to the pumped boreholes for each fracture set is shown as a bar and whisker plot in Figure 4-38. Different correlation exponents were used for the different sets with 1.5 for set S_C (NW), 1.0 for sets S_A (ENE) and S_df (HZ), and 0.5 for S_B (NS). The numbers of inflow/outflows in the monitored boreholes are over-predicted above 10^{-7} m^3/s in this case, and generally a worse match than shown in Figure 4-33. The steepening of the distribution around the mode of the distribution for flow is typical of the correlated model. The distribution of drawdown in Figure 4-37 seems to show a reasonable number of realisations with the right sort of mix of head response magnitudes between the boreholes. Figure 4-38 suggests too many flows above the detection limit in set S_df (HZ), possibly suggesting that a direct correlation does not work well for the fractures in set S_df (HZ). For this instance of the correlated model the variability in flux to the pumped boreholes within individual boreholes is too high, an average standard deviation of 0.6 over the 10 realisations, compared to the measurements, a standard deviation of 0.4 in the flux between pumped boreholes. Hence, we conclude that the correlated model tends to focus flow too heavily in to large continuous fractures, at least in the horizontal set.

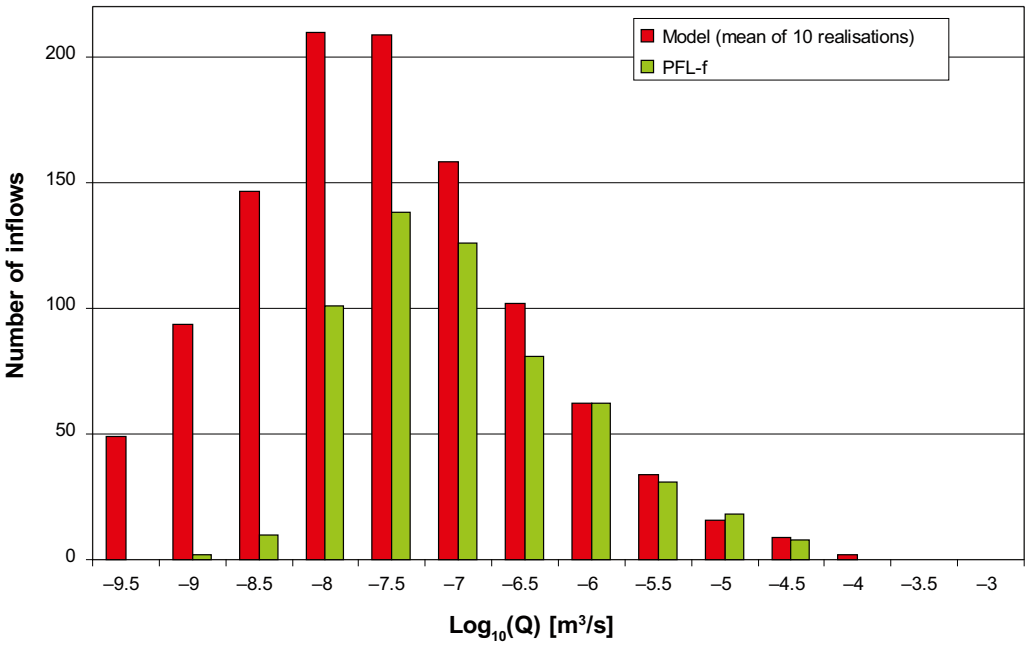

Figure 4-36. *Histogram comparing the distribution of the magnitude of inflows/outflows, Q, to the monitoring boreholes taken over an ensemble of all possible combinations, i.e. five abstraction boreholes multiplied by 4 monitoring boreholes each. The PFL-f interference measurements in KLX09C–F (green) are plotted against the mean over 10 realisations of the BH_DZ_optbc2 fracture size model (red) with a correlated transmissivity (see Table 4-23 for parameter values) and no-flux boundary condition.*

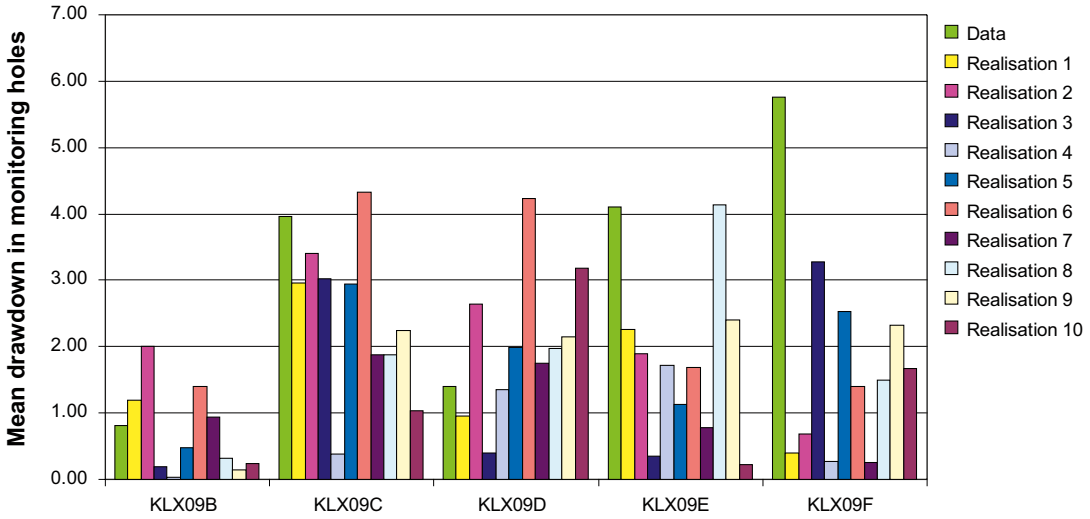

Figure 4-37. *Histogram comparing the mean drawdown response measured in the monitoring holes for pumping in the 5 abstraction boreholes KLX09B–F against the mean simulated head for each of 10 realisations. The model used is the BH_DZ_optbc2 fracture size model with a correlated transmissivity (see Table 4-23 for parameter values) and no-flux boundary condition.*

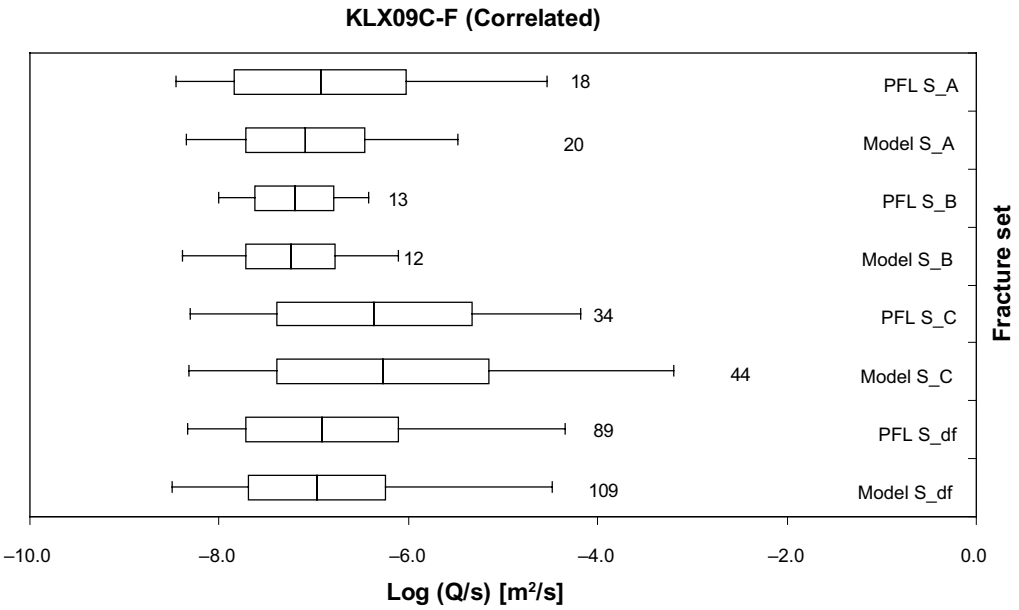

Figure 4-38. *Bar and whisker plots comparing statistics taken over each fracture set for the individual inflows, Q/s, for the PFL-f measurements from KLX09C–F against the mean over 10 realisations of the BH_DZ_optbc2 fracture size model. The centre of the bar indicates the mean value, the ends of the bar indicate ± 1 standard deviation, and the error bars indicate the minimum and maximum values. The total numbers of fractures with inflow above the detection limits within each set are also given. For the PFL-f data, the statistics are taken over the identified flow-anomalies within each set, and over the fractures generated within each set and over 10 model realisations. The correlated transmissivity model is shown.*

The equivalent plots for the uncorrelated case are shown in Figure 4-39 to Figure 4-41. This predicts a better match to the inflow/outflow rates in the monitored boreholes than the correlated model, but not good as the semi-correlated model, and probably the best match to the measured drawdowns of all the transmissivity models, although it was hard to predict any drawdowns above 4 m in this case. This is interesting since it suggests that models require substantial heterogeneity in the fracture transmissivity in the smaller fractures to simultaneously match both the intra-borehole flow-rates and drawdown in monitored holes. Because large transmissive sub-vertical fractures are sparse in these models, many of the flow-rate and drawdowns response in these boreholes are controlled by sub-horizontal fractures, and hence we hypothesise that the background flow is largely controlled by sub-horizontal fractures, while the high flow-rates, and consequent high drawdowns, result from the occasional extensive NW fracture. The variability in flux to the pumped boreholes within individual boreholes is a bit low again for this uncorrelated model, an average standard deviation of 0.3 over the 10 realisations, compared to 0.4 in the data.

Putting these remarks together with the previous ones on the semi-correlated case and Figure 4-28, we propose the ingredients required to get a good match to the data are a NW set S_C which has about 2-3 highly transmissivity and extensive fractures intersecting the boreholes in about 3 places, and a strongly heterogeneous sub-horizontal set S_df. To achieve this, the size distribution for set S_C (NW) needed to be modified to give a slightly higher intensity of long fractures than was suggested by matching to the L 1.2 deformation zone model, and have a strong correlation between size and transmissivity with exponent 1.5; while set S_df requires a weak correlation between size and transmissivity or heterogeneity within fracture planes on the scale of about 10 m, or so.

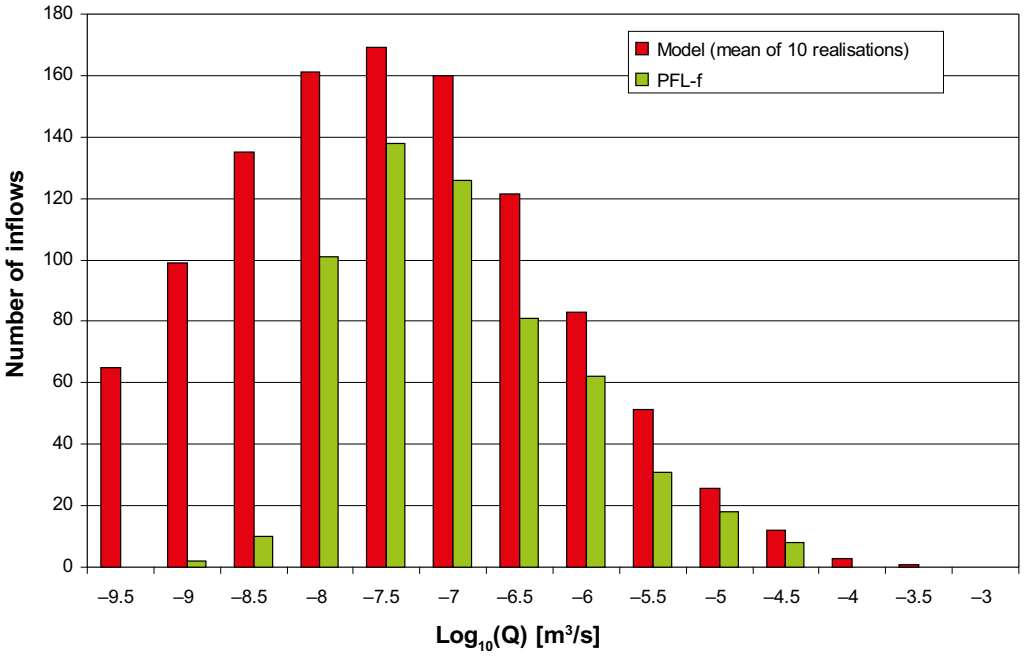

Figure 4-39. *Histogram comparing the distribution of the magnitude of inflows/outflows, Q, to the monitoring boreholes taken over an ensemble of all possible combinations, i.e. five abstraction boreholes multiplied by 4 monitoring boreholes each. The PFL-f interference measurements in KLX09C–F (green) are plotted against the mean over 10 realisations of the BH_DZ_optbc2 fracture size model (red) with an uncorrelated transmissivity (see Table 4-23 for parameter values) and no-flux boundary condition.*

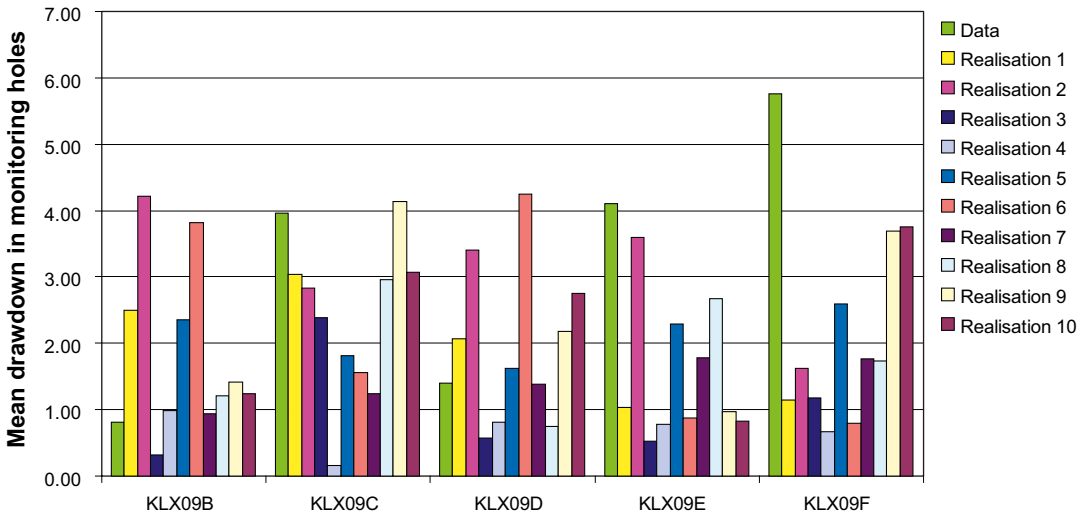

Figure 4-40. *Histogram comparing the mean drawdown response measured in the monitoring holes for pumping in the 5 abstraction boreholes KLX09B–F against the mean simulated head for each of 10 realisations. The model used is the BH_DZ_optbc2 fracture size model with an uncorrelated transmissivity (see Table 4-23 for parameter values) and no-flux boundary condition.*

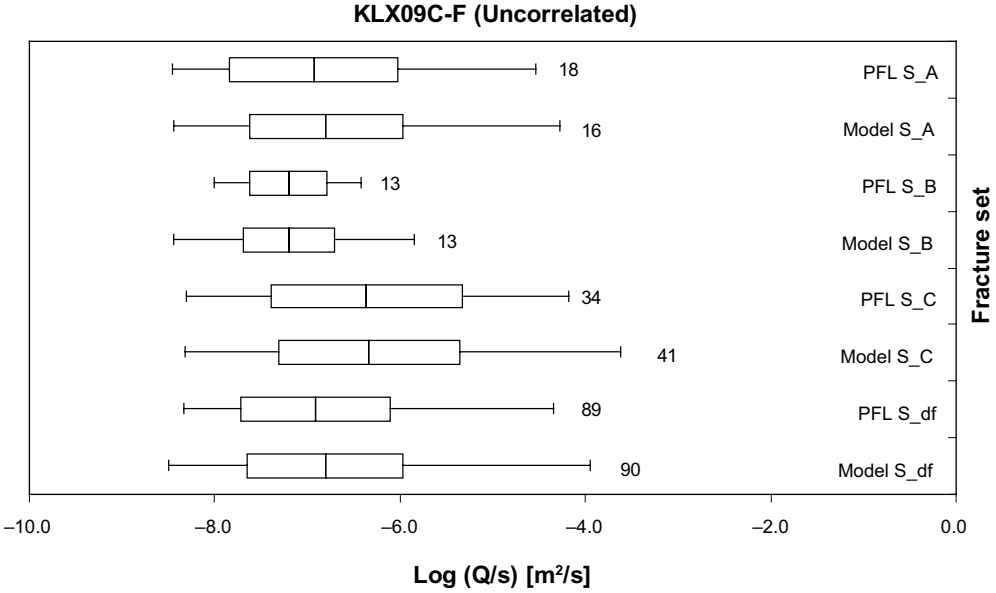

Figure 4-41. *Bar and whisker plots comparing statistics taken over each fracture set for the individual inflows, Q/s, for the PFL-f measurements from KLX09C–F against the mean over 10 realisations of the BH_DZ_optbc2 fracture size model. The centre of the bar indicates the mean value, the ends of the bar indicate ± 1 standard deviation, and the error bars indicate the minimum and maximum values. The total numbers of fractures with inflow above the detection limits within each set are also given. For the PFL-f data, the statistics are taken over the identified flow-anomalies within each set, and over the fractures generated within each set and over 10 model realisations. The uncorrelated transmissivity model is shown.*

In summary, the conclusions of considering transmissivity to size relationships suggests that the relationship may be different for different sets with strong correlations in sub-vertical sets parallel to the maximum in situ stress, while fractures in other directions are less well correlated or spatially heterogeneous, especially sub-horizontal fractures. It should be remembered that these remarks are based on the hydrogeology of fractures near the surface, so as yet it is not clear if such conclusions apply at also depth.

4.7 Summary and conclusions

This study has developed a Hydro-DFN model for the near surface Ävrö Granite based on one vertical and four inclined boreholes around the KLX09 drill site area and integrating core descriptions, borehole image and outcrop data together with hydraulic data from single-hole and multi-hole PFL-f tests. Fracture set classification and orientation models were provided by a local Geo-DFN model. Based on the power-law concept for fracture size, distribution parameters have been determined for DFN models consistent with the intensity of open fractures in the core-drilled boreholes, the intensity of deformation zones on the regional scale, and the frequency of connected fractures that provide the flows seen in the PFL-f tests. Briefly, the size models for open fractures that give the best overall performance are ones with a location parameter, r_0, similar to the borehole radius, 0.04 m, and an exponent k_r around 2.6. This is broadly consistent with the Geo-DFN model for the size distribution of all fractures in the sub-horizontal and NW sets, but quite different for the ENE and NS sets.

An analysis of the orientations of flow-anomalies suggests the sub-horizontal and NW (NE plunge) oriented fractures are responsible for the majority of higher flow-rates. This is reasonable since the sub-horizontal set is the most abundant and the NW set correlates with the direction of maximum horizontal in situ stress /SKB 2006a/, (Hakami 2007, personal communication based on KLX12A data).

Inspecting the interference tests revealed that the majority of the flow measured corresponds with only about 5 fractures intercepted by the boreholes. Two of these are sub-horizontal belonging to set S_df (HZ), and 3 NW striking sub-vertical belonging to set S_C. Of the boreholes they intercept, 2 are in KLX09C, 1 in KLX09E, and 2 in KLX09F. These 3 boreholes correspond to the ones with the highest total inflow during the single-hole tests, and the highest head responses seen in the monitoring holes during the interference tests. Therefore, it may be asserted that these 5 fractures with transmissivities around 10^{-4} m^2/s are responsible for the different magnitudes of flow and head response seen when pumping different boreholes. A local structural model of deformation zones was not available for the area around the boreholes, and hence the modelling did not aim to reproduce the exact responses in particular boreholes, but tried to find model settings that gave models that agreed with several statistics that quantified the nature of the flow system such as frequency, magnitudes and variability in flow-rates and head responses.

The fracture size distribution parameters were finely calibrated to obtain a good statistical match to the frequency and distribution in magnitudes of flows seen in the PFL-f tests for each fracture set based on numerical DFN simulations of connectivity and flow. The ultimate models were conditioned, based on several statistics that quantified the nature of flow in both the single-hole and multi-hole PFL-f tests, to give the parameterisation recommended in Table 4-24. Different relationships between fracture transmissivity and size were considered varying from direct correlations to completely uncorrelated, and due to the abundance of hydraulic data from a range of borehole orientations, different relationships were considered for different sets. It is hard to give a definitive answer as to which sort of relationship works best. The correlated model tends to provide a distribution of flow that is steeper than that measured, and has too much variability between the flow-rates at individual boreholes, while the uncorrelated model yields slightly too little variability. The relationships between fracture size and transmissivity are illustrated in Figure 4-42. The main actions taken to obtain a satisfactory stochastic model were to choose the size distribution for set S_C (NW) to give a slightly higher intensity of long fractures than was suggested by matching to the L 1.2 deformation zone model, and have a strong correlation between size and transmissivity with exponent 1.5; while set S_df (sub-horizontal) requires a weak correlation between size and transmissivity or heterogeneity within fracture planes on the scale of about 10 m, or so.

In summary, the KLX09 interference test data has allowed us to analyse differences between the geometrical and hydraulic properties between the different fracture sets much more thoroughly than has been possible using mainly vertical boreholes and single-hole tests. Key findings are a tendency toward distinctly more extensive and transmissive fracturing in the NW direction. It has also pointed towards possible subtleties such as that the relationship between transmissivity and size may be different for different sets with strong correlations in sub-vertical sets parallel to the maximum in situ stress (NW), while fractures in other directions (ENE and NS and sub-horizontal) are less well correlated or may be spatially heterogeneous. It should be remembered that these remarks are based on the hydrogeology of fractures near the surface, so as yet it is not clear if such conclusions apply at depth.

Table 4-24. Recommended parameter settings for a Hydro-DFN in the near-surface Ävrö Granite . The transmissivity parameters are given for each set and the semi-correlated (SC), correlated (C) and uncorrelated (UC) models. (Note: this is a copy of Table 4-23).

Fracture set name	Orientation set pole: (trend, plunge), concentration	Fracture radius model power-law (r_0, k_r)	Intensity P_{32} (m^2/m^3); valid radius interval (r_{min}, r_{max})	Relative intensity of P32	Transmissivity model T (m^2/s)
S_A (ENE)	(350, 12) 19	(0.04, 2.59)		0.19	*SC: (a,b,σ)* = (1 10^{-7}, 0.0, 1.5)
					C: *(a,b)* = (4 10^{-8}, 1.0)
					UC:*(μ,σ)* = (–6.7, 1.3)
S_B (NS)	(92, 1) 17	(0.04, 2.62)		0.13	*SC: (a,b,σ)* = (1 10^{-7}, 0.0, 0.2)
			3.99		C: *(a,b)* = (4 10^{-8}, 0.5)
			(0.28, 564)		UC:*(μ,σ)* = (–6.7, 0.35)
S_C (NW)	(213, 5) 13	(0.12, 2.60)		0.21	*SC: (a,b,σ)* = (4 10^{-7}, 1.5, 0.3)
					C: *(a,b)* = (2 10^{-7}, 1.5)
					UC:*(μ,σ)* (–5.0, 1.3)
S_df (HZ)	(250, 77) 15	(0.04, 2.60)		0.47	*SC: (a,b,σ)* (7 10^{-8}, 0.0, 1.5)
					C: *(a,b)* (4 10^{-8}, 1.0)
					UC:*(μ,σ)* (–6.7, 1.2)

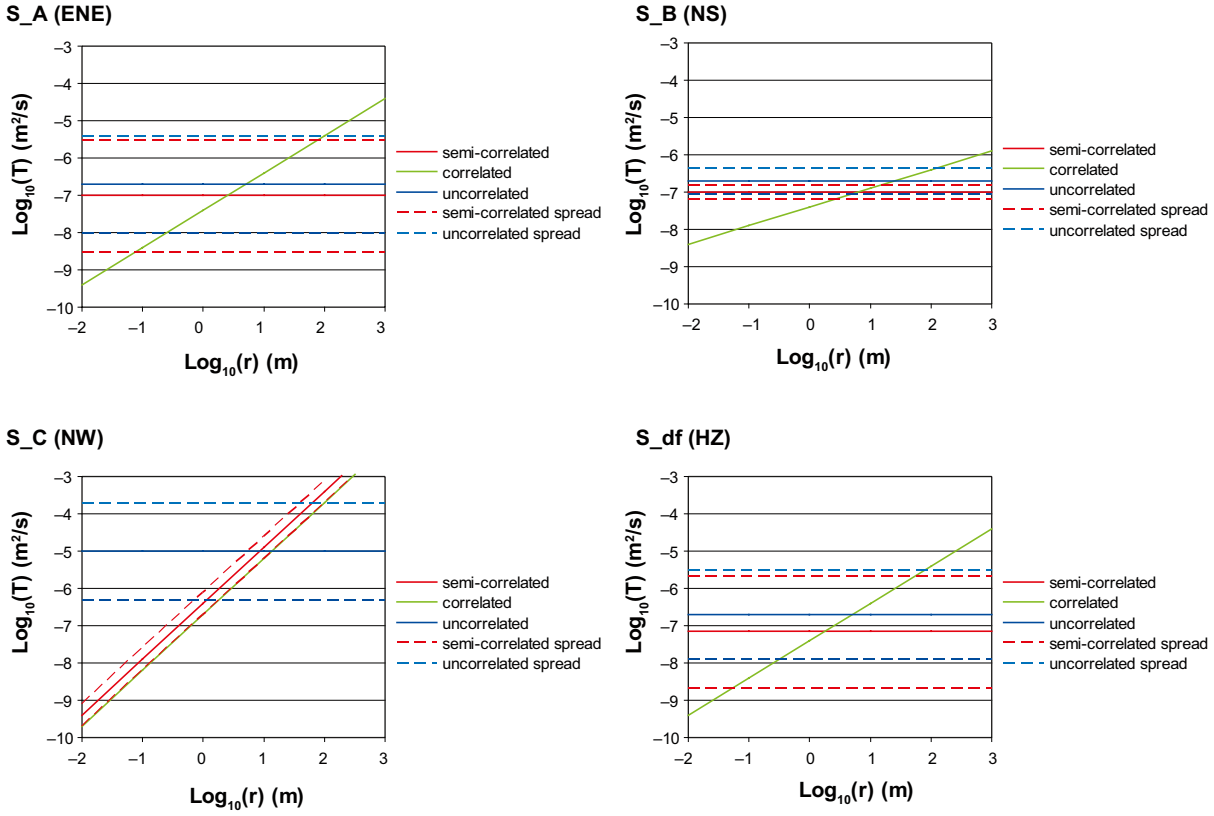

Figure 4-42. Transmissivity model relationships for each fracture set based on the calibration against interference tests as defined in Table 4-24. Relationships are shown for each of the three alternative models for transmissivity. For the semi-correlated and uncorrelated cases, the spread is displayed by the standard deviation, ± σ.

References

Byegård J, Gustavsson E, Tullborg E-A, 2006. Bedrock transport properties. Data evaluation and retardation model. Preliminary site description Simpevarp subarea – version 1.2, SKB R-06-27, Svensk Kärnbränslehantering AB.

Craig H, 1961. Isotope variations in meteoric waters. Science, 133: 1702–1703.

Dershowitz W, Lee G, Geier J, Foxford T, La Pointe P, Thomas A, 1998. FRACMAN, Interactive discrete feature data analysis, geometric modeling and exploration simulation. User documentation, version 2.6. Golder Associates, Inc. Redmond, Washington, USA.

Dershowitz W, Winberg A, Hermanson J, Byegård J, Tullborg E-L, Andersson P, Mazurek M, 2003. Äspö Hard Rock Laboratory. Äspö Task Force on modelling of groundwater flow and transport of solutes – Task 6C – A semi-synthetic model of block scale conductive structures at the Äspö HRL, SKB IPR-03-13, Svensk Kärnbränslehantering AB.

Follin S, Stigsson M, 2007. Hydrogeological pre-modelling for Forsmark version 2.2 – Sensitivity of the connected open fracture surface area per unit volume to the orientation, size and intensity of Poissonian discrete fracture network (DFN) models, SKB R-07-2, Svensk Kärnbränslehantering AB.

Follin S, Johansson P-O, Levén J, Hartlley L, Holton D, McCarthy R, Roberts D, 2007. Hydrogeological pre-modelling for Forsmark version 2.2, SKB R-07-20, Svensk Kärnbränslehantering AB.

Forssman I, Zetterlund M, Forsmark T, Rhén I, 2005. Oskarshamn site investigation. Correlation of Posiva Flow Log anomalies to core mapped features in KLX02, KLX03, KLX04, KAV04A and KAV04b. SKB P-05-241, Svensk Kärnbränslehantering AB.

Gómez J, Laaksoharju M, Skårman E, Gurban I, 2006. M3 version 3.0: Concepts, methods, and mathematical formulation. SKB TR-06-27, Svensk Kärnbränslehantering AB.

Gómez J, Laaksoharju M, Skårman E, Gurban I, 2007 (in prep.). M3 version 3.0: Verification and validation. SKB TR-07-xx, Svensk Kärnbränslehantering AB.

Hartley L, Hoch A, Hunter F, Jackson P, Gylling B, Marsic N, 2005. Regional hydrogeological simulations – Numerical modelling using Connectflow, Preliminary site description Simpevarp subarea – version 1.2, SKB R-05-12, Svensk Kärnbränslehantering AB.

Hartley L, Hoch A, Jackson P, Joyce S, McCarthy R, Swift B, Gylling B, Marsic N, 2006a. Groundwater flow and transport modelling during the temperate period for the SR-Can assessment – Laxemar subarea – version 1.2, SKB R-06-99, Svensk Kärnbränslehantering AB.

Hartley L, Hunter F, Jackson P, McCarthy R, Gylling B, Marsic N, 2006b. Regional Hydrogeological Simulations– Numerical Modelling Using CONNECTFLOW, Preliminary site description, Laxemar subarea – Version 1.2, SKB R-06-23, Svensk Kärnbränslehantering AB.

Hermanson J, Forssberg O, Fox A, La Point P, 2005. Statistical model of fractures and deformation zones: Preliminary site description, Laxemar subarea, version 1.2, SKB R-05-45, Svensk Kärnbränslehantering AB.

Jansson P, Näslund J-O, Rodhe L, 2007. Ice sheet hydrology – a review. SKB TR-06-34, Svensk Kärnbränslehantering AB.

Laaksoharju M, Skårman C, Skårman E, 1999. Multivariate mixing and mass balance (M3) calculations, a new tool for decoding hydrogeochemical information. App. Geoch. 14, 861–872.

Nyman H, 2005. Depth and stratigraphy of Quaternary deposits: Preliminary site description, Laxemar subarea – version 1.2, SKB R-05-454, Svensk Kärnbränslehantering AB.

Rhén I, Gustafson G, Wikberg P, 1997b. Äspö HRL – Geoscientific evaluation 1997/5. Models based on site characterization 1986–1995. SKB TR-97-06, Svensk Kärnbränslehantering AB.

Rhén I, Smellie J, 2003. Task force on modelling of groundwater flow and transport of solutes, Task 5 Summary report, SKB TR-03-01, Svensk Kärnbränslehantering AB.

Rhén I, Forsmark T, Forsman I, Zetterlund M, 2006. Evaluation of hydrogeological properties for Hydraulic Conductor Domains (HCD) and Hydraulic Rock Domains (HRD), Preliminary site description, Laxemar subarea – version 1.2. SKB R-06-22, Svensk Kärnbränslehantering AB.

SKB, 2006a. Preliminary site description, Laxemar subarea – version 1.2, SKB R-06-10, Svensk Kärnbränslehantering AB.

SKB 2006b. Hydrogeochemical Evaluation, Preliminary site description, Laxemar subarea – version 1.2, SKB R-06-12, Svensk Kärnbränslehantering AB.

SKB 2006c. Hydrogeochemical Evaluation, Preliminary site description, Laxemar subarea – version 2.1, SKB R-06-70, Svensk Kärnbränslehantering AB.

Sokolnicki M, Väisäsvaara J, 2006. Oskarshamn site investigation, Difference flow logging of boreholes KLX09B–F, Subarea Laxemar, SKB P-06-199, Svensk Kärnbränslehantering AB.

Sokolnicki M, Pöllänen J, 2006. Oskarshamn site investigation, Interference difference flow logging of boreholes KLX09B–F, Subarea Laxemar, SKB P-06-146, Svensk Kärnbränslehantering AB.

Terzaghi R, 1965. Sources of error in joint surveys. Geotechnique 15(3): 287–304.

Teurneau B, Forsmark T, Forssman I, Rhén I, 2007 (in prep.). Oskarshamn site investigation, Correlation of Posiva Flow Log anomalies to core mapped features in KLX09, KLX09B–G, KLX10, KLX11A–F, SKB P-07-xxx, Svensk Kärnbränslehantering AB.

Tullborg E-L, Larson S Å, 1984. $\delta^{18}O$ and $\delta^{13}C$ for limestones,calcite fissure infillings and calcite precipitates from Sweden. Geologiska Föreningens i Stockholm Förhandlingar, 106, 127–130.

Vidstrand P, 2003. Äspö Hard Rock Laboratory, Update of the Hydrogeological model 2002, SKB IPR-03-35, Svensk Kärnbränslehantering AB.

Vidstrand P, Svensson U, Follin S, 2006. Simulation of hydrodynamic effects of salt rejection due to permafrost. Hydrogeological numericalmodel of density-driven mixing, at a regional scale, due to a high salinity pulse, SKB R-06-101, Svensk Kärnbränslehantering AB.

Waber H N, Smellie J A T, 2006a. Borehole KLX03. Characterisation of pore water. Part 1: Methodology and analytical data. Oskarshamn site investigation. SKB P-06-12, Svensk Kärnbränslehantering AB.

Waber H N, Smellie J A T, 2006b. Borehole KLX08. Characterisation of pore water. Part 1: Methodology and analytical data. Oskarshamn site investigation. SKB P-06-163, Svensk Kärnbränslehantering AB.

Werner K, Bosson E, Berglund S, 2005. Laxemar 1.2. Background report for climate, surface hydrology and near-surface hydrogeology. SKB R-05-61, Svensk Kärnbränslehantering AB.

Appendix A

Additional information and data used in the HRL study

This section gives additional information and references to data sources. An attempt is made to record the data that has been used. File names refer to the files in the directory that was created for this pre-modelling exercise on the Project Place.

A.1 Tunnel geometry

File Tunnel-geometry.doc is basically the same as Tunnel-geometry_Aspo-HRL.doc. The files tunnel_surveying.xls and object_location.xls contain data of the geometry of the tunnel line of Äspö HRL. File Official_tunnel_IR-image3b.gif shows the tunnel and using a CAD system, and the tunnel can be visualized using Official_tunnel_V3(MS_V8_cd).dwg.

The influences of the ventilation shafts are included into the elevator shaft. Inflow to Tunnel G and F are added to the last part of tunnel TASA, and thus tunnels G and F are not modelled geometrically. All other short tunnels are excluded in the modelling.

The coordinates for the tunnel line for tunnel A is 0.25 m above the tunnel floor in the drill and blasted tunnel (tunnel section 0–3,191m) and 0.8 m above the tunnel floor in the TBM tunnel (tunnel section 3,191–3,600 m).

An observation or measurement in the tunnel is linked to a “Tunnel section”. “Tunnel section” is defined as the length of the projection of the tunnel line on a horizontal plane, called SECTION in the tables for tunnel A and other tunnel parts. All flow rates are related to SECTION for the tunnels.

The cross-section area of the drill and blasted tunnel is about 25 m^2 in the straight parts of the tunnel and about 43 m^2 in the bends. In the TBM assembly hall the cross-section area is about 100 m^2.

A.2 DZ – tunnel intersections

The file DZ_AHRL--tunnel.xls gives information on intersections between deformation zones and the HRL tunnel.

Table A-1. Examples of intersections of fracture zones intersecting the main Äspö HRL tunnel A.

DZ	Start-A (m)	End-A (m)	Comment – Eng
ZSMNE004A	276	378	
ZSMNW025A	286	301	
ZSMNS017A	327	327	The DZ touches, or is very close to, the tunnel at 327 m
ZSMNE012A	706	858	
ZSMEW038A	1,164	1,173	
ZSMNE006A	1,169	1,341	
ZSMEW009A	1,403	1,414	
ZSMNS017B	1,998	2,036	Local DZ, not implemented in the L 1.2 model
ZSMNS017B	2,095	2,142	Local DZ, not implemented in the L 1.2 model
ZSMNS017B	2,908	2,935	Local DZ, not implemented in the L 1.2 model
ZSMNS017B	3,132	3,152	Local DZ, not implemented in the L 1.2 model
ZSMNE005A	3,600	3,600	The DZ touches, or is very close to, the end of tunnel

A.3 Flow into the HRL

Weir flow – Äspö HRL

File: Weir-flow_Aspo-HRL.doc

Weir flowrate tot ver 3.xls contains data for the water flow into the Äspö HRL tunnel. The flow rates in the xls-file are plotted in Weir-flow_Aspo-HRL.doc. This file contain data of the monthly mean flow rates measured at the weirs along the Äspö tunnel during the excavation of Äspö Hard Rock Laboratory (HRL) and operation of Äspö HRL, for period: May 1991–Dec 2004.

Details about the flow measurements are found in SKB PR 25-95-28, Appendix 2:4. The flow rates have also been presented in SKB TR 97-06, Appendix 2. However minor adjustments of the flow rates reported in SKB TR 97-06 and in SKB PR 25-95-28 have been made for some of the monthly mean flow rates after August 1995. A few corrections of the measured flow rates have been made according to SKB PR 25-95-28.

A complete set of plots of the weir flow rates is given in Figure A-1.

The pump pit PG2 is losing water by leakage, which January 1994 was estimated to 42 L/min. The monthly mean flow rate measured at MA1030G has been reduced with this amount when PG2 was in operation.

The pump pit PG3 is probably losing water by leakage, which has been estimated to 5 L/min. The monthly mean flow rate measured at MA1745G has been reduced with this amount when PG3 was in operation.

The pump pit PG4 is possibly losing water by leakage when the water level is high in the pump pit. The leakage has been estimated to 10 L/min. The monthly mean flow rate measured at MA2699G has been reduced with this amount when PG4 was used for a drilling operation 22 November 1994–24 January 1995. When the water level is low in the pump pit, during normal operation, the leakage is probably small and no corrections have been made for other periods.

Water is flowing into the pump pit P5 which is not measured by MF0061G (down-stream the ditch (dam), the deepest part of tunnel F). Autumn 1995 this flow rate was estimated to 6 L/min. 6 L/min has been added to the monthly mean flow rate measured at MF0061G.

Table A-2. Explanations to the inflow data set.

Column	Unit	Description
Month	MMYY	Period for the estimated monthly mean flow rate.
MA682G etc	L/min	IDCODE for the weir. The figure (in this case 682) is the position in the tunnel A for the ditch (dam) that is collecting the water. Figures in the column show the estimated or mean value of the measured flow rate.
Total inflow	L/min	Sum of all measurements of the flow into the tunnel.

Table A-3. Definition of measurement sections.

Row	Unit	Description
SECUP	m	Upper measurement section along the tunnel line or depth in the shafts, which were defined in TUNNGEOM.zip.
SECLOW	m	Lower measurement section along the tunnel line or depth in the shafts, which were defined in TUNNGEOM.zip.
Tunnel part	–	IDCODE for tunnel or “shafts”.

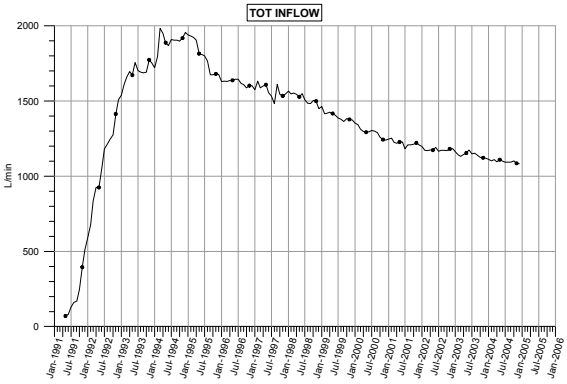
TOT INFLOW
L/min
2000
1500
1000
500
0

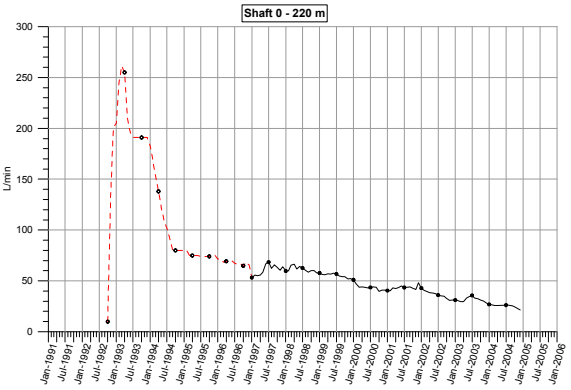
Shaft 0 - 220 m
L/min
300
250
200
150
100
50
0

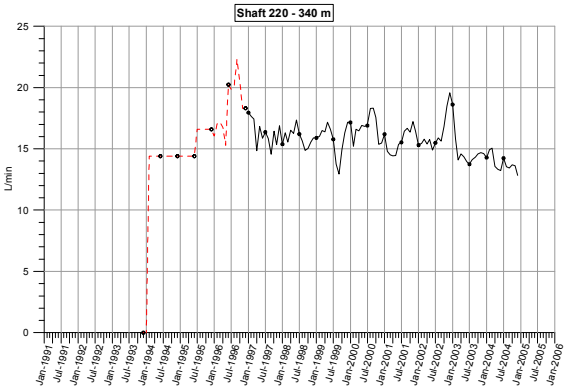
Shaft 220 - 340 m
L/min
25
20
15
10
5
0

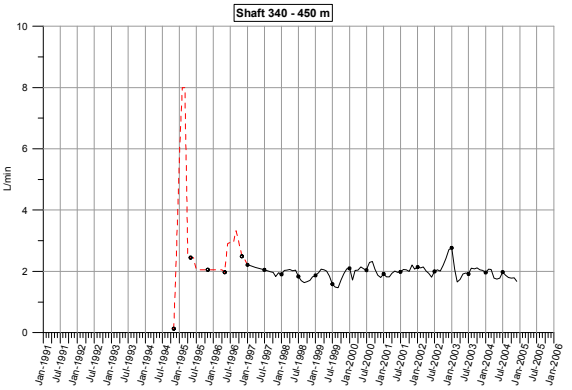
Shaft 340 - 450 m
L/min
10
8
6
4
2
0

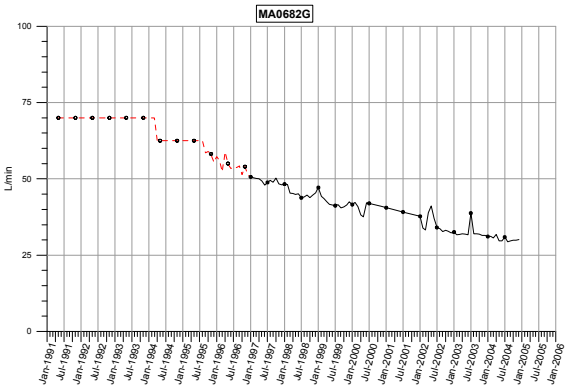
MA0682G
L/min
100
75
50
25
0

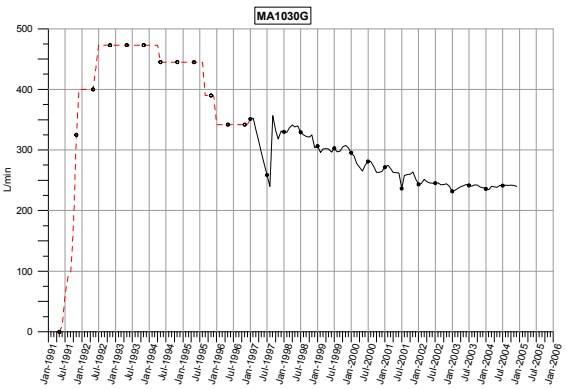
MA1030G
L/min
500
400
300
200
100
0

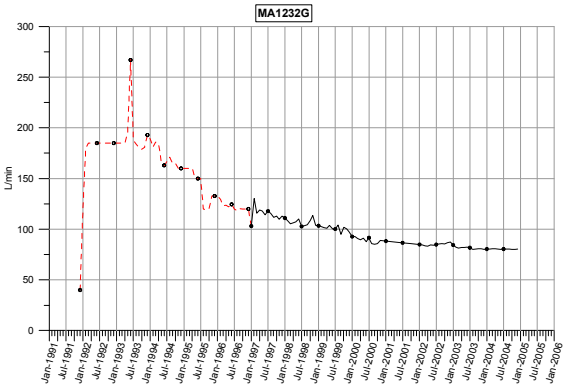
MA1232G
L/min
300
250
200
150
100
50
0

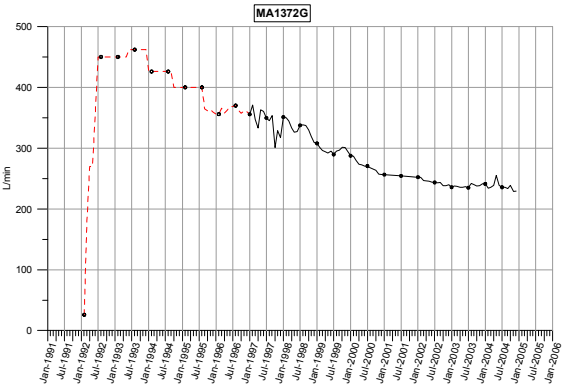
MA1372G
L/min
500
400
300
200
100
0

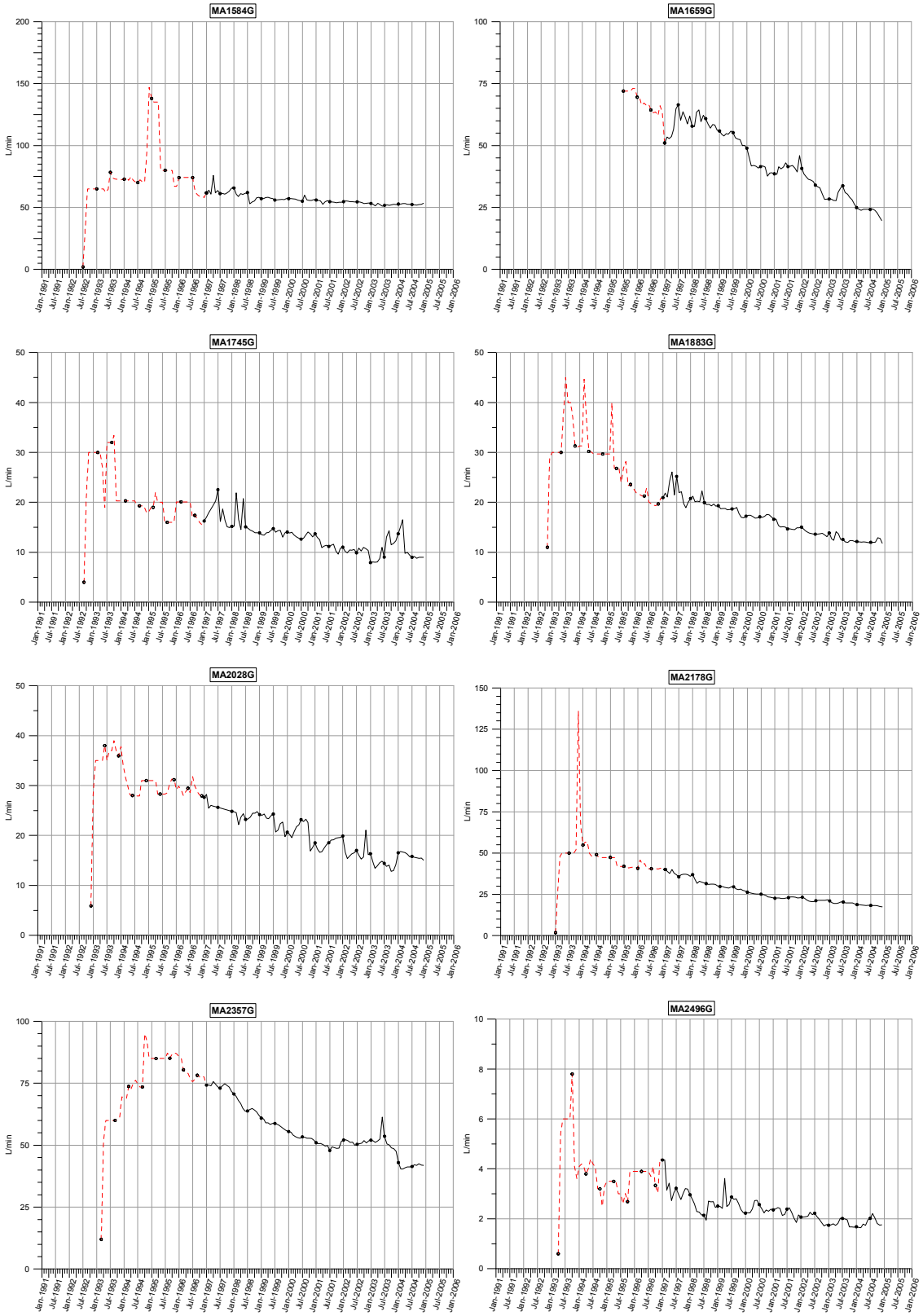
MA1584G
MA1659G
MA1745G
MA1883G
MA2028G
MA2178G
MA2357G
MA2496G
L/min

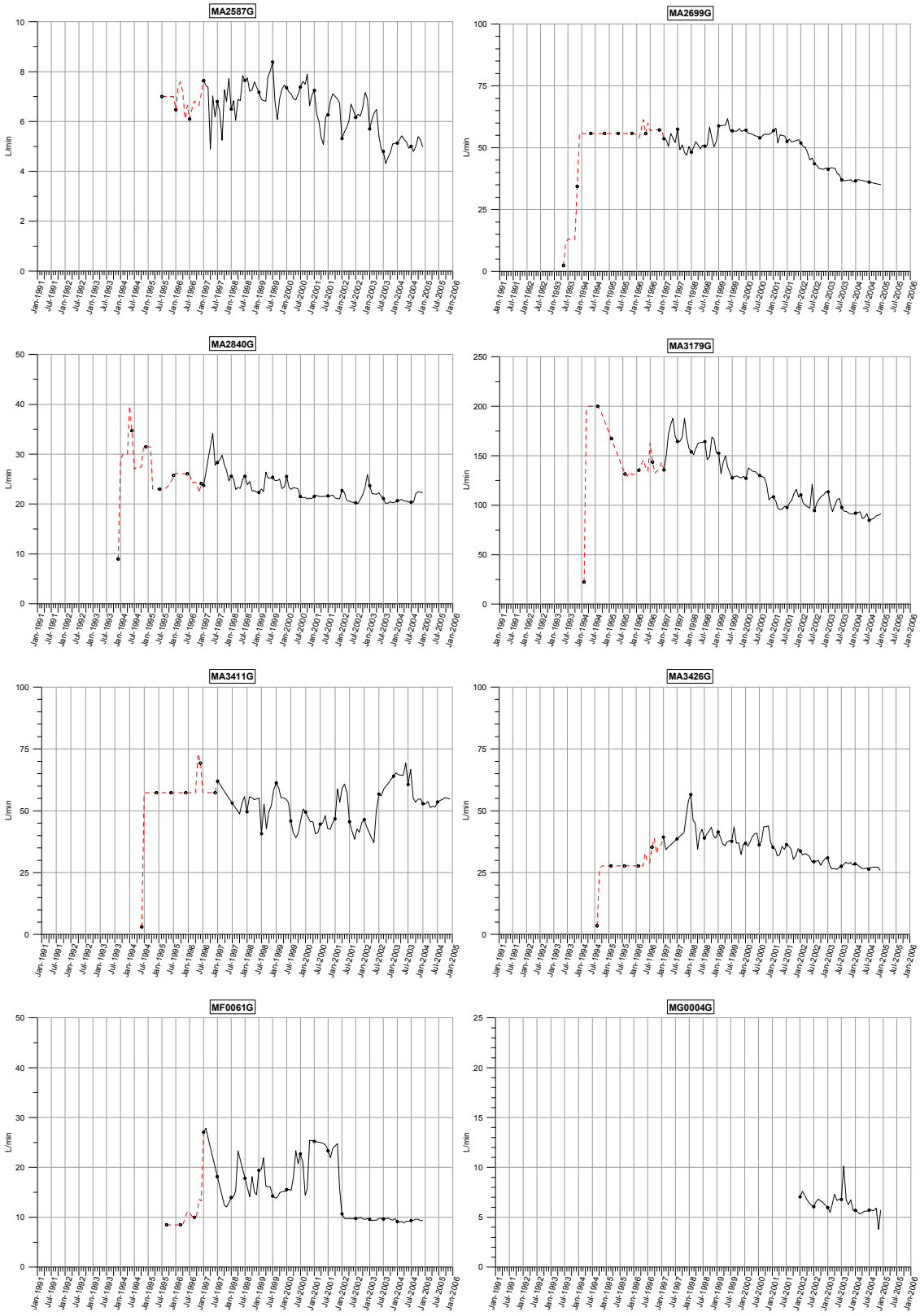

Figure A-1. *Complete set of weir measurements. The red dashed lines are Äspö Task Force, Task 5 data /Rhén and Smellie 2003/.*

The columns SHAFT220, SHAFT340, SHAFT450 represent the estimated flow rates for –z = 0–220 m, 220–340 m and 340–450 m respectively. In May 1995 the measurements with weirs started. Unfortunately not all shafts were equipped with water collecting devices at levels –220 m, –340 m and –450 m. Therefore must the measurements after May 1995 for the shafts be adjusted to depth levels. In SKB PR 25-95-28, Appendix 2:4 and in SKB TR 97-06, Appendix 2 a suggestion was made of how to make these adjustments. These calculations have been made in the file for Columns SHAFT220, SHAFT3340, SHAFT 450 for data collected after July 1995. The actual measurements at MA1659G, MA2587G and MA3384G are just provided to show the measured value AND SHALL NOT BE USED IN THE MODELLING.

MA3411G collects water from tunnel section 3,179–3,426 m in tunnel A.

MA3426G collects water from tunnel section 3,426–3,600 m in tunnel A.

Tunnel F and G are parallel and close to tunnel A, approximately section 3,400–3,510 m and 3,510–3,600 m. The flow rate shown in column MF0061G and MG0045 should be added to A3411G (50%) and MA3426G (50%) if tunnels F and G are not modelled. (For a short period, ca 2 month, the flow from tunnel G was measured by MF0061G before MG0045 was in operation.)

Data from May 1991 to Jan 1994 are from the Task 5 modelling exercise with the Äspö HRL Task Force. These data are used here. Data from later period are monthly mean values, calculated from SICADA data. Some spikes of inflow rates, with short duration, have been removed, as generally they can be assumed to be related to drill water when excavation new tunnels. It is possible that some of these spikes, totally or partly, can be related to true inflow from the rock, due e.g. hydraulic tests. No attempt has been made to sort this out as it was judged that it would only result in smaller changes of the total flow rate. At some occasions data are missing after 1995 or there is an indication that a weir has been clogged. Linear interpolation has been used to estimate flow rates for moths with missing or erroneous data. Flow rates are missing for 2005, but can be assumed to be more or less as Dec 2004.

A.4 Weir and chemistry data

File: WEIRCHEM.doc

Weirch02 bearb.xls contains hydochemistry data for the water flow into the Äspo HRL tunnel. This file contains data of Chloride, pH and electrical conductivity measured at the weirs along the Äspö tunnel during the excavation of Äspö Hard Rock Laboratory for period:

ÄspoHRL, for period: May 1991–ca 2003. Based on Cl and electrical conductivity (Cond) measured, TDS has been calculated based on relations:

TDS(Cl) = Cl·1.7

TDS(COND) = Cond·0.00467/0.741 (ref: TR-97-06)

TDS: g/L

Cl: g/L

Cond: mS/m

Table A-4. Explantions to the hydrochemistry data.

Column	Unit	Description
START_DATE	YYYYMMDD	Date for sampling
TIME	hhmmss	Hours, minutes, seconds for sampling
IDCODE	–	Code for measurement point
SECUP	m	Upper measurement section in the tunnel
SECLOW	m	Lower measurement section in the tunnel
SAMPLE_NO		The No of the sample
CL	mg/l	Cloride
PH	–	Ph
COND	mS/m	Electrical conductivity
TDS(COND)	g/L	Estimate of TDS based on COND
TDS(Cl)	g/L	Estimate of TDS based on Cl

A.5 Water table at Äspö

The file AspoHRL-drawdown_undist-1991-1994-1995-2000.doc contains extract from SKB IPR-03-35 /Vidstrand 2003/. Also, information from /Rhén et al. 1997b/ is included.

A.6 Water table at Ävrö and Laxemar

The estimated mean water levels in percussion boreholes based on data from HMS and soundings for three time periods, and calculated drawdowns in relation to the undisturbed conditions are shown in Table A-5. The estimated water levels are approximate, since other activities may have influenced the water levels as well.

Table A-5. Estimated mean water levels in percussion boreholes based on data from HMS and for three time periods, and calculated drawdowns in relation to the undisturbed conditions. Yellow indicates a significant drawdown. Note, that other activities may have influenced the water levels as well.

Borehole information			Undisturbed conditions 1989–1991		Max inflow conditions 1993–1995			Recent conditions 2000–2004			SKB Reference 910601–930521
BH-ID	Bh length Secup	Bh length Seclow	Water level (m.a.s.l.)	Comment	Water level (m.a.s.l.)	Drawdown	Comment	Water level (m.a.s.l.)	Drawdown	Comment	
HAV01	0	175	1.7		1.4	0.3		1.5	0.2	Uncertain	
HAV02	0	93	1		–0.3	1.3					PR 25-94-16
HAV02	94	163	1.7		–0.1	1.8					PR 25-94-16
HAV02	0	163						0.2	1.5	Uncertain	
HAV03	0	100	0.5	Uncertain			Uncertain				
HAV03	101	134	0.1	Uncertain							
HAV03	0	134			0.4		Uncertain	0.3		Uncertain	
HAV04	0	32	4.6	???							
HAV04	33	100	4.4		4.2						
HAV04	0	100						4.1		Uncertain	
HAV05	0	50	3.5	Uncertain							
HAV05	51	100	3.4		1	2.4					
HAV05	0	100						1.7	1.7		
HAV06	0	100	5.3		2.1	3.2		2.1	3.2	Uncertain	
HAV07	0	70	0.9								
HAV07	71	100	0.9								
HAV08	0	28	0.5								
HAV08	29	63	0.5								
HAV08	0	63			–4	4.5		–2.5	3		PR 25-94-16
HMJ01	0	33	0	Unknown, but should be close to +1 or 0	–8.5	8.5		–7	7		PR 25-94-16
HMJ01	34	46	0	Unknown, but should be close to + 1 or 1	–8.5	8.5		–7	7		PR 25-94-16
HLX01	0	55	6.8		6.8						
HLX01	56	100	7		7						
HLX01	0	100						6.8			
HLX02	0	15	5		5		Uncertain				

Borehole information			Undisturbed conditions 1989–1991		Max inflow conditions 1993–1995			Recent conditions 2000–2004			SKB Reference 910601–930521
BH-ID	Bh length Secup	Bh length Seclow	Water level (m.a.s.l.)	Comment	Water level (m.a.s.l.)	Drawdown	Comment	Water level (m.a.s.l.)	Drawdown	Comment	
HLX02	26	132	2.3		1.8	0.5	Possibly a drawdown				
HLX02	0	132						5.5		Uncertain	
HLX03	0	10	7		7						
HLX03	11	100	8.2		8.2						
HLX03	0	100						7.5			
HLX04	0	10	8		8.2						
HLX04	11	125	7.5		7.5						
HLX04	0	125						8			
HLX05	1	10	14.3		14.3						
HLX05	11	100	14		14						
HLX05	0	100						14			
HLX06	0	44	9		10						PR 25-94-16
HLX06	45	100	8		8						PR 25-94-16
HLX06	0	100						9			
HLX07	0	15	6.5		6.5						
HLX07	16	100	6.2		6.2						
HLX07	0	100						6.2		Uncertain	
HLX08	0	10	1	Unknown, but should be close to +1 or 0	0						
HLX08	11	40	1	Unknown, but should be close to +1 or 1	0						
HLX09	0	50	1	Uncertain	–0.5	1.5					PR 25-94-16
HLX09	51	151	0.5	Uncertain	–1.4	1.9					PR 25-94-16

Appendix B

Additional information on the hydrochemistry sensitivity study

The updated reference case

The complete set of hydrochemistry results for all simulated boreholes is given below for the updated reference case with revised reference waters given in Table 3-4.

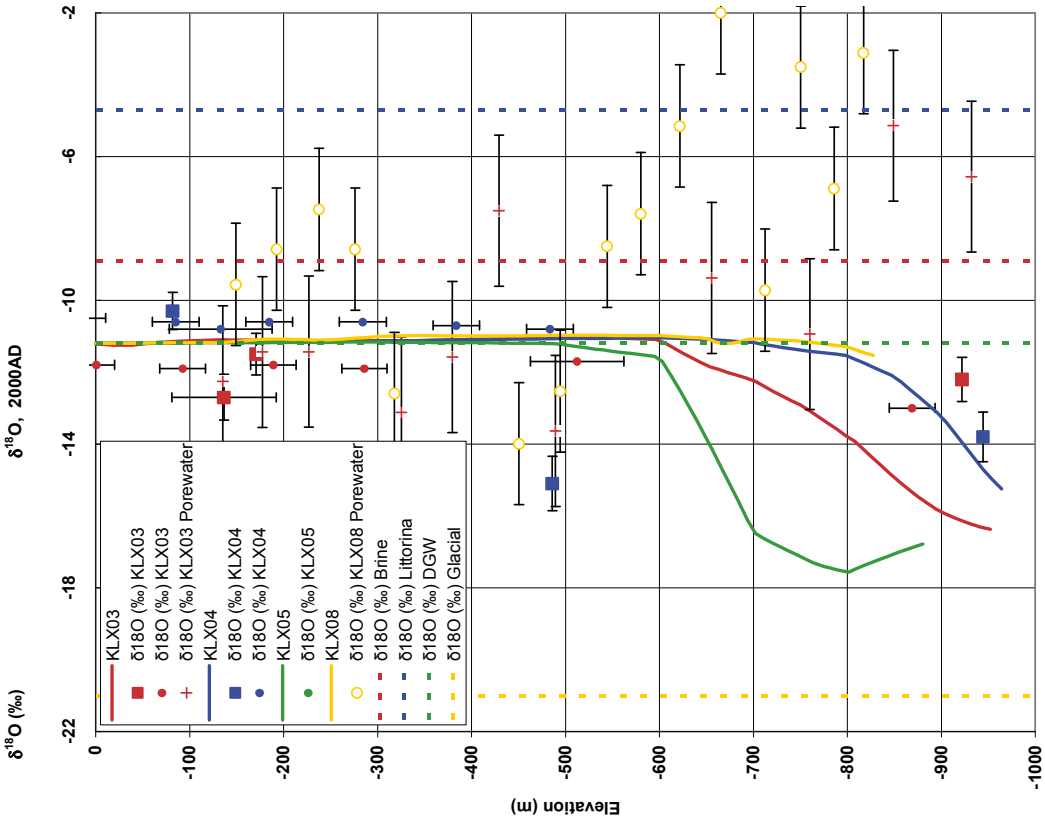
δ18O, 2000AD
δ18O (‰)
Elevation (m)
KLX03
δ18O (‰) KLX03
δ18O (‰) KLX03 Porewater
KLX04
δ18O (‰) KLX04
δ18O (‰) KLX04
KLX05
δ18O (‰) KLX05
KLX08
δ18O (‰) KLX08 Porewater
δ18O (‰) Brine
δ18O (‰) Littorina
δ18O (‰) DGW
δ18O (‰) Glacial

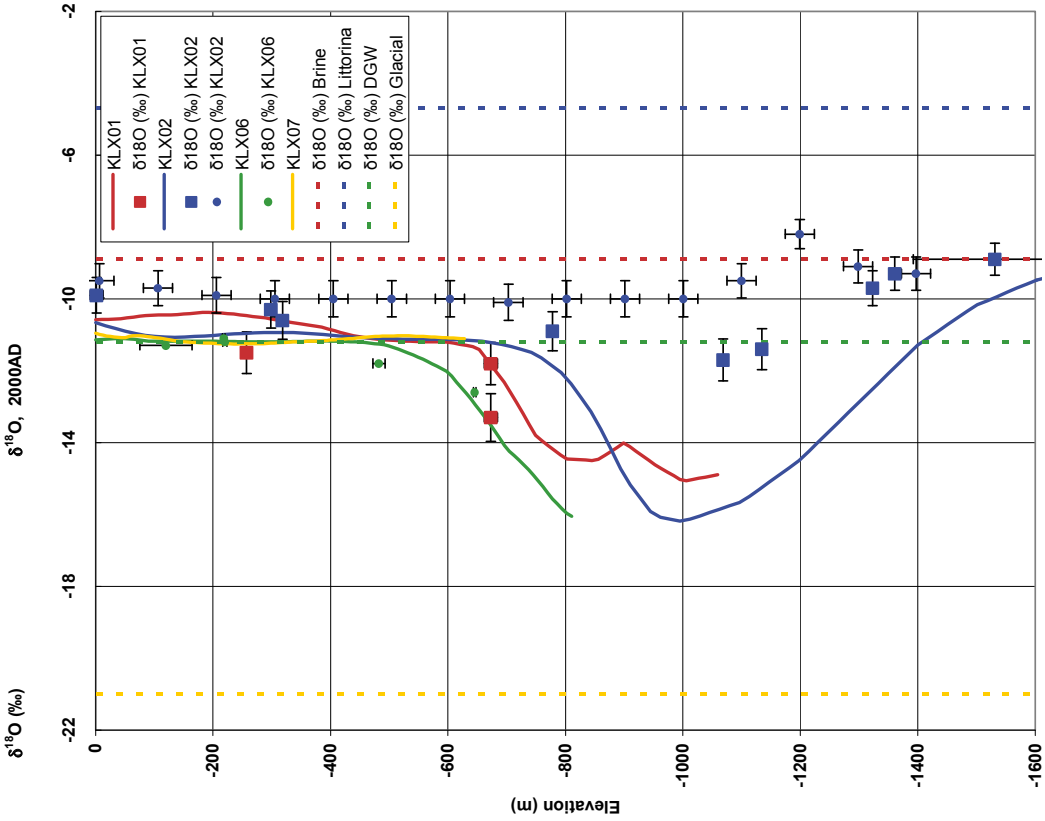
δ18O, 2000AD
δ18O (‰)
Elevation (m)
KLX01
δ18O (‰) KLX01
KLX02
δ18O (‰) KLX02
δ18O (‰) KLX02
KLX06
δ18O (‰) KLX06
KLX07
δ18O (‰) Brine
δ18O (‰) Littorina
δ18O (‰) DGW
δ18O (‰) Glacial

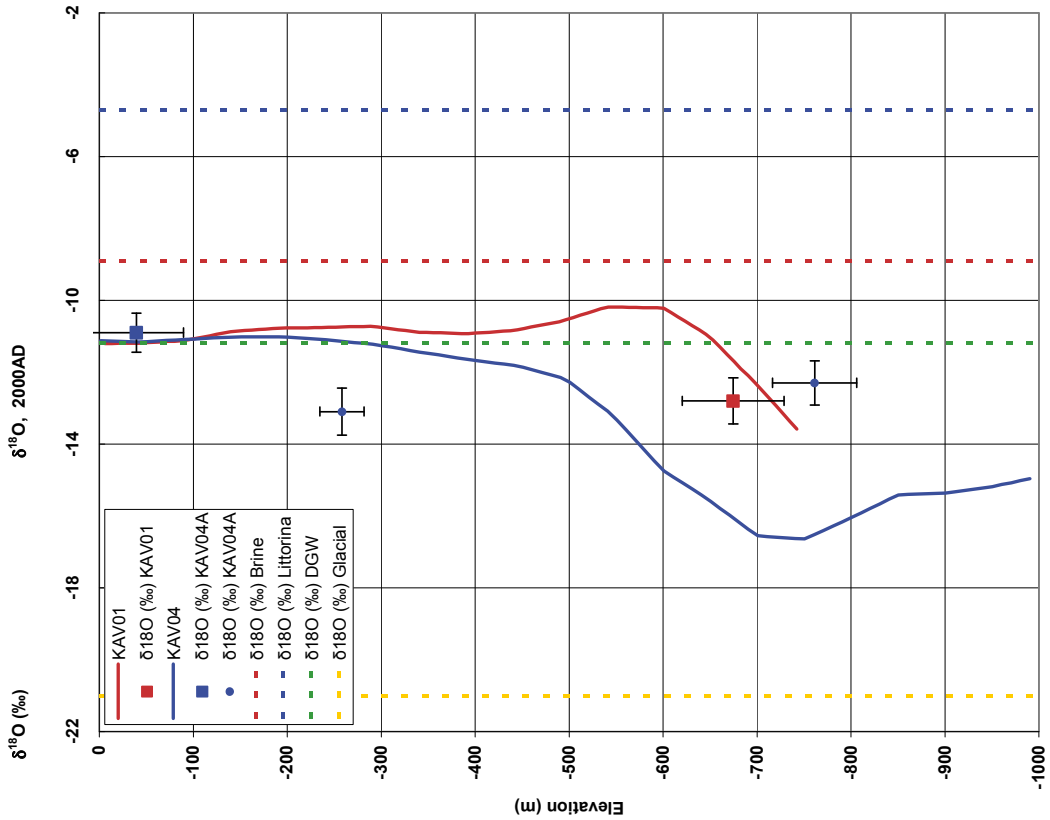
δ18O (‰)
δ18O, 2000AD
-2
-6
-10
-14
-18
-22
0
-100
-200
-300
-400
-500
-600
-700
-800
-900
-1000
Elevation (m)
KAV01
δ18O (‰) KAV01
KAV04
δ18O (‰) KAV04A
δ18O (‰) KAV04A
δ18O (‰) Brine
δ18O (‰) Littorina
δ18O (‰) DGW
δ18O (‰) Glacial

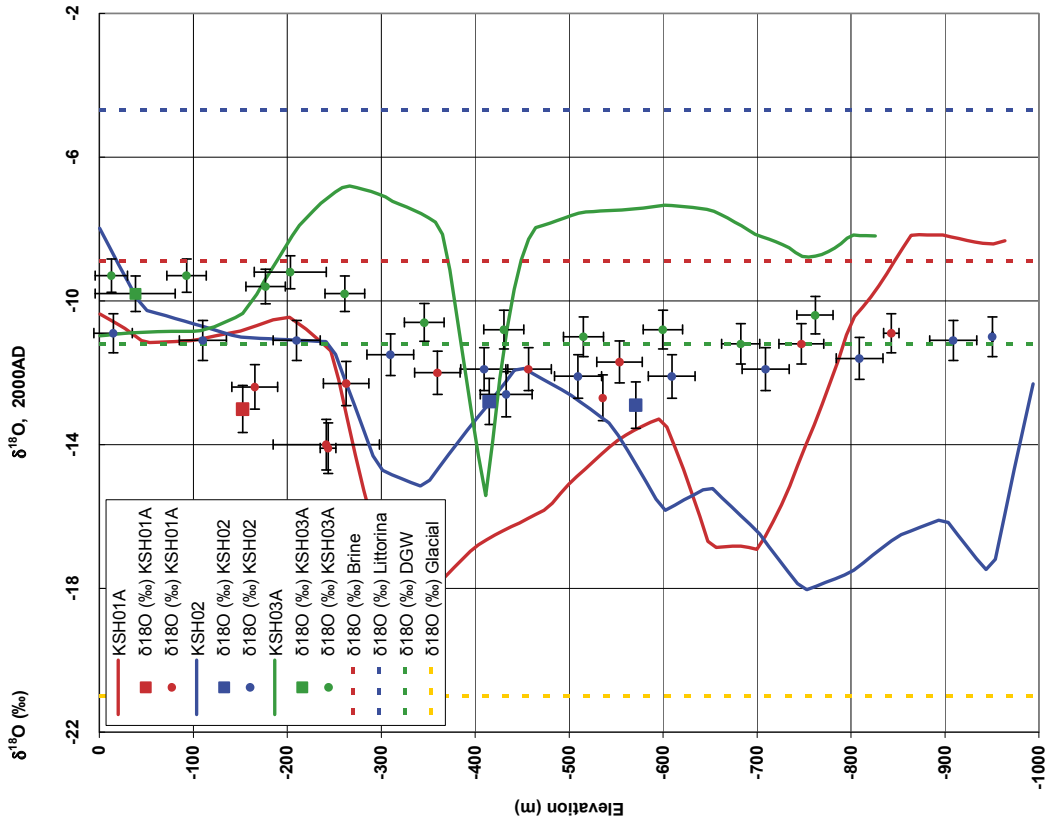
δ18O (‰)
δ18O, 2000AD
-2
-6
-10
-14
-18
-22
0
-100
-200
-300
-400
-500
-600
-700
-800
-900
-1000
Elevation (m)
KSH01A
δ18O (‰) KSH01A
δ18O (‰) KSH01A
KSH02
δ18O (‰) KSH02
δ18O (‰) KSH02
KSH03A
δ18O (‰) KSH03A
δ18O (‰) KSH03A
δ18O (‰) Brine
δ18O (‰) Littorina
δ18O (‰) DGW
δ18O (‰) Glacial

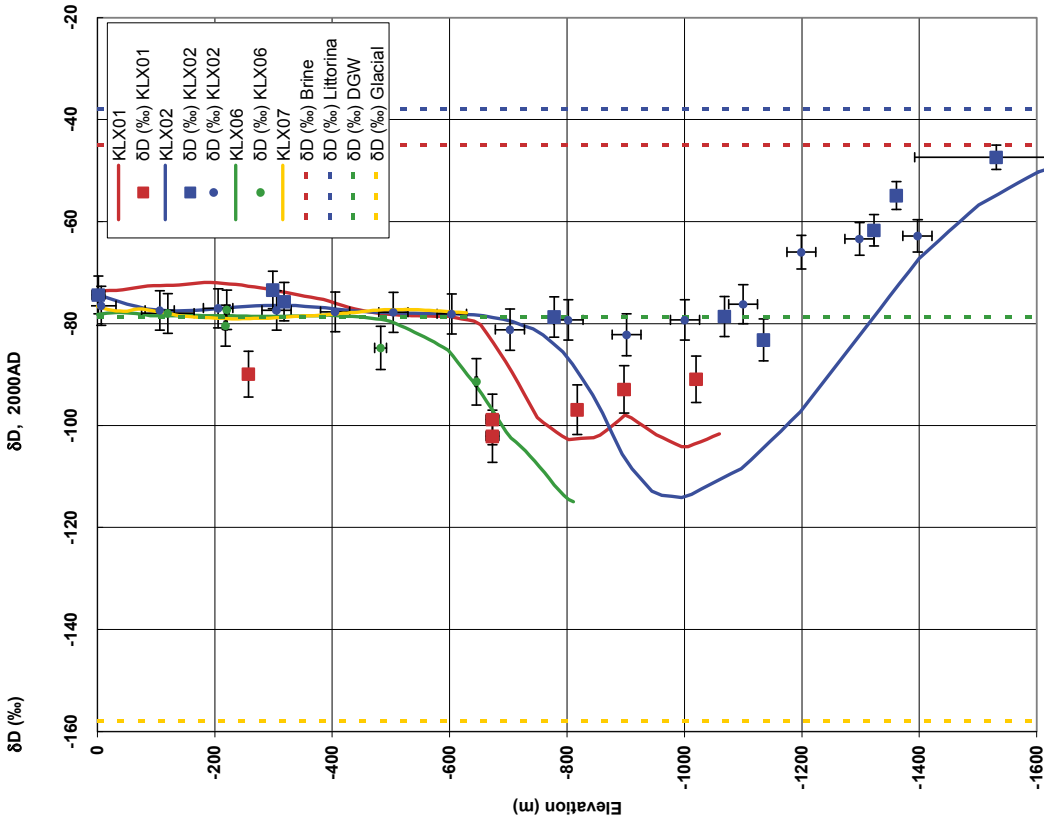
δD (‰)
δD, 2000AD
Elevation (m)
KLX01
δD (‰) KLX01
KLX02
δD (‰) KLX02
δD (‰) KLX02
KLX06
δD (‰) KLX06
KLX07
δD (‰) Brine
δD (‰) Littorina
δD (‰) DGW
δD (‰) Glacial

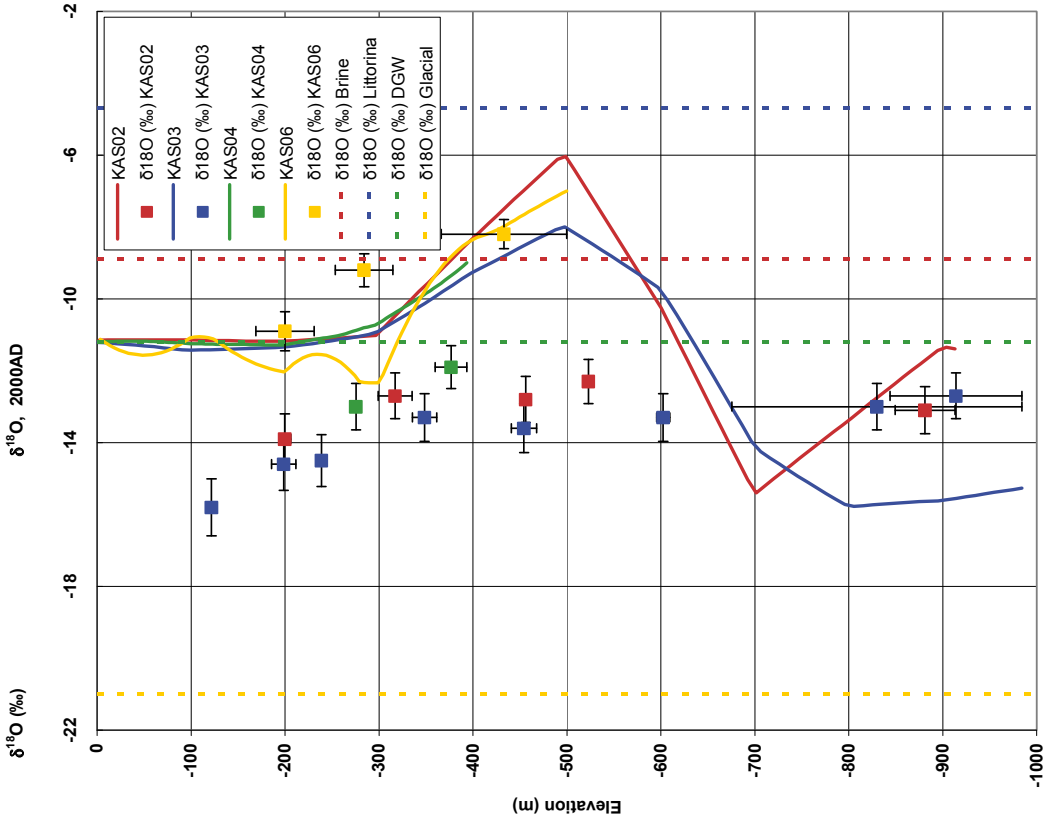
δ18O (‰)
δ18O, 2000AD
Elevation (m)
KAS02
δ18O (‰) KAS02
KAS03
δ18O (‰) KAS03
KAS04
δ18O (‰) KAS04
KAS06
δ18O (‰) KAS06
δ18O (‰) Brine
δ18O (‰) Littorina
δ18O (‰) DGW
δ18O (‰) Glacial

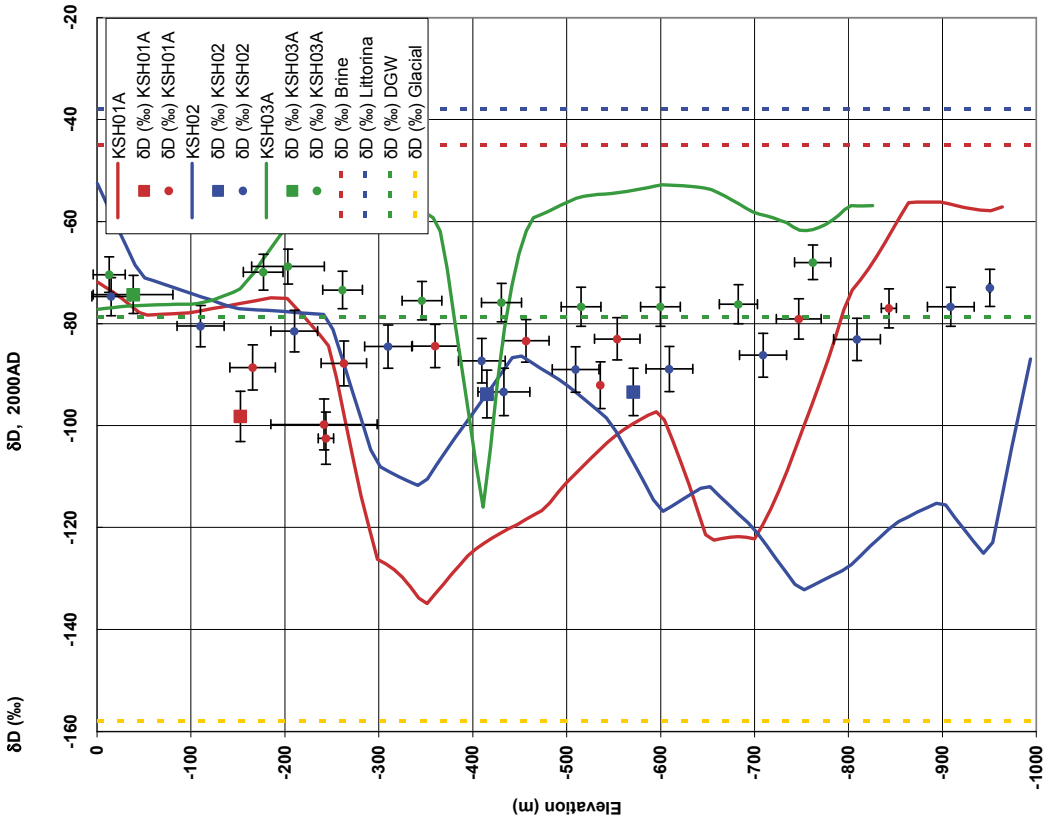
δD (‰)
δD, 2000AD
Elevation (m)
KSH01A
δD (‰) KSH01A
δD (‰) KSH01A
KSH02
δD (‰) KSH02
δD (‰) KSH02
KSH03A
δD (‰) KSH03A
δD (‰) KSH03A
δD (‰) Brine
δD (‰) Littorina
δD (‰) DGW
δD (‰) Glacial

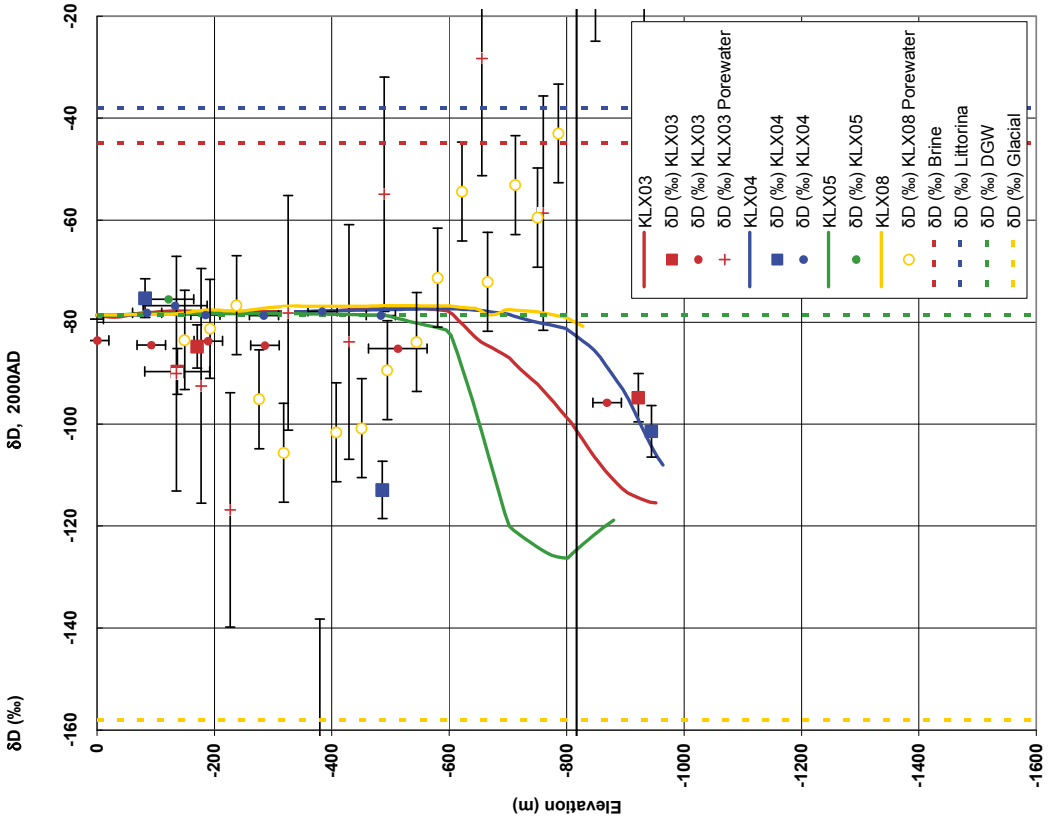
δD (‰)
δD, 2000AD
Elevation (m)
KLX03
δD (‰) KLX03
δD (‰) KLX03
δD (‰) KLX03 Porewater
KLX04
δD (‰) KLX04
δD (‰) KLX04
KLX05
δD (‰) KLX05
KLX08
δD (‰) KLX08 Porewater
δD (‰) Brine
δD (‰) Littorina
δD (‰) DGW
δD (‰) Glacial

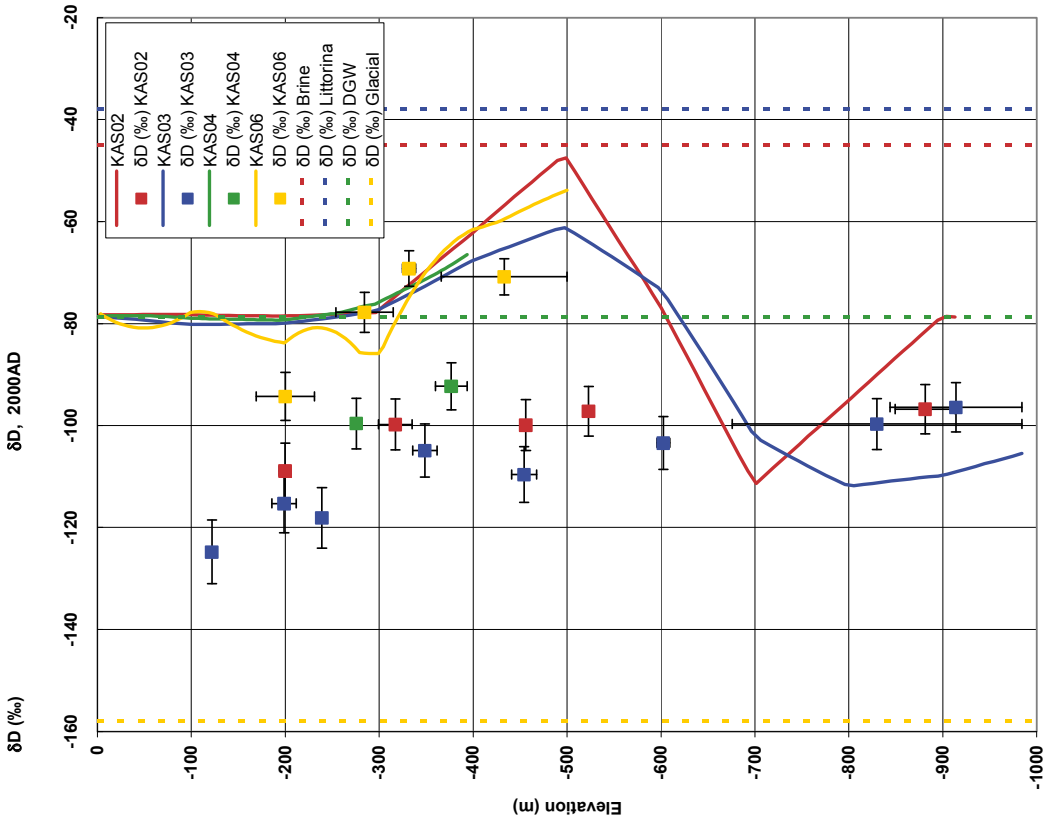
KAS02
δD (‰) KAS02
KAS03
δD (‰) KAS03
KAS04
δD (‰) KAS04
KAS06
δD (‰) KAS06
δD (‰) Brine
δD (‰) Littorina
δD (‰) DGW
δD (‰) Glacial
δD, 2000AD
δD (‰)
Elevation (m)
-20
-40
-60
-80
-100
-120
-140
-160
0
-100
-200
-300
-400
-500
-600
-700
-800
-900
-1000

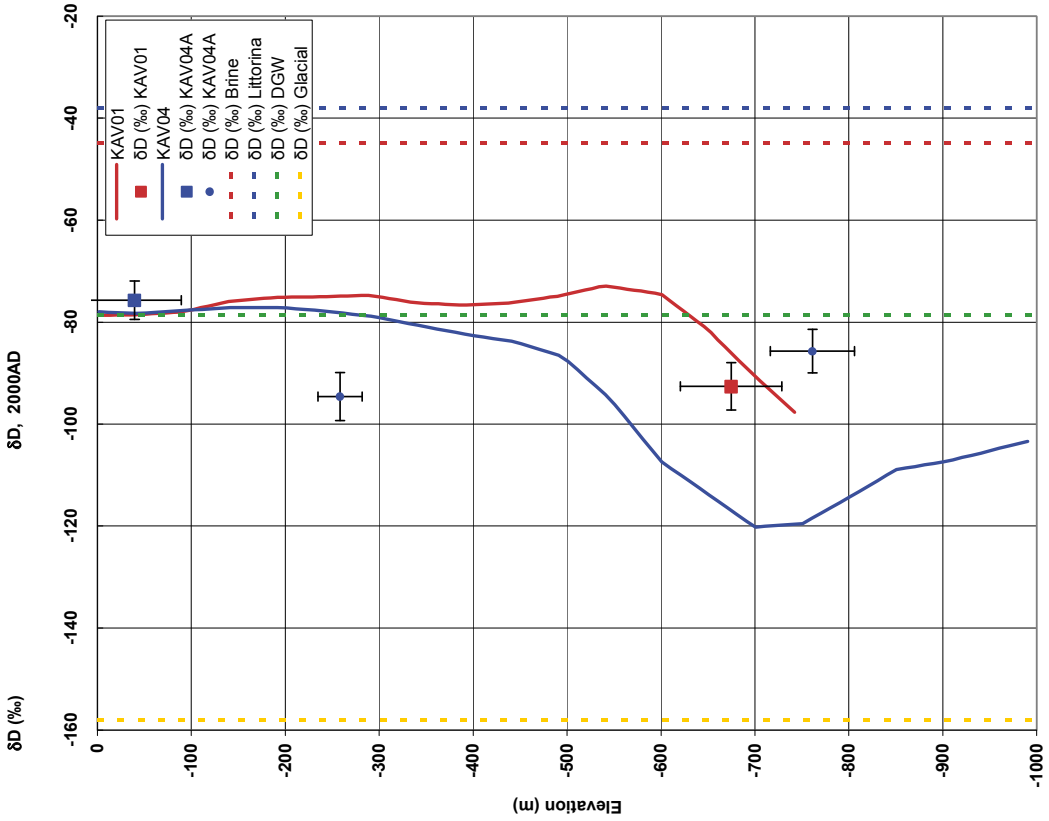
KAV01
δD (‰) KAV01
KAV04
δD (‰) KAV04A
δD (‰) KAV04A
δD (‰) Brine
δD (‰) Littorina
δD (‰) DGW
δD (‰) Glacial
δD, 2000AD
δD (‰)
Elevation (m)
-20
-40
-60
-80
-100
-120
-140
-160
0
-100
-200
-300
-400
-500
-600
-700
-800
-900
-1000

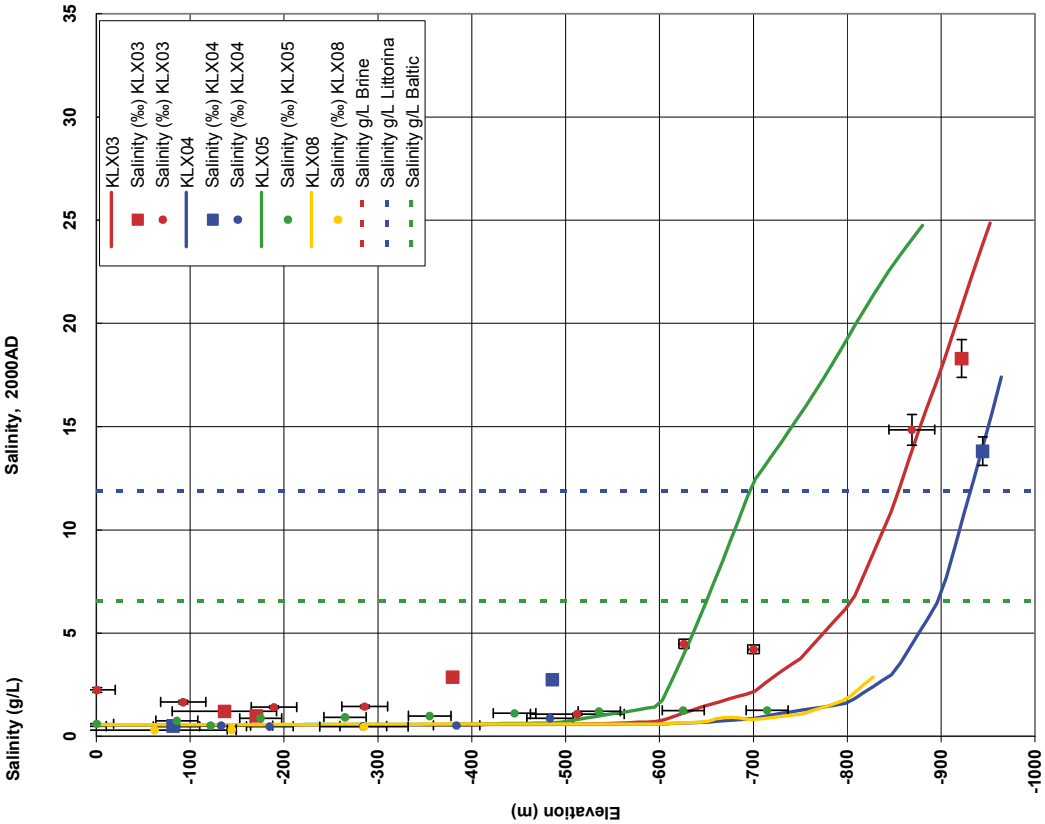
Salinity, 2000AD
Salinity (g/L)
Elevation (m)
KLX03
Salinity (‰) KLX03
Salinity (‰) KLX03
KLX04
Salinity (‰) KLX04
Salinity (‰) KLX04
KLX05
Salinity (‰) KLX05
KLX08
Salinity (‰) KLX08
Salinity g/L Brine
Salinity g/L Littorina
Salinity g/L Baltic

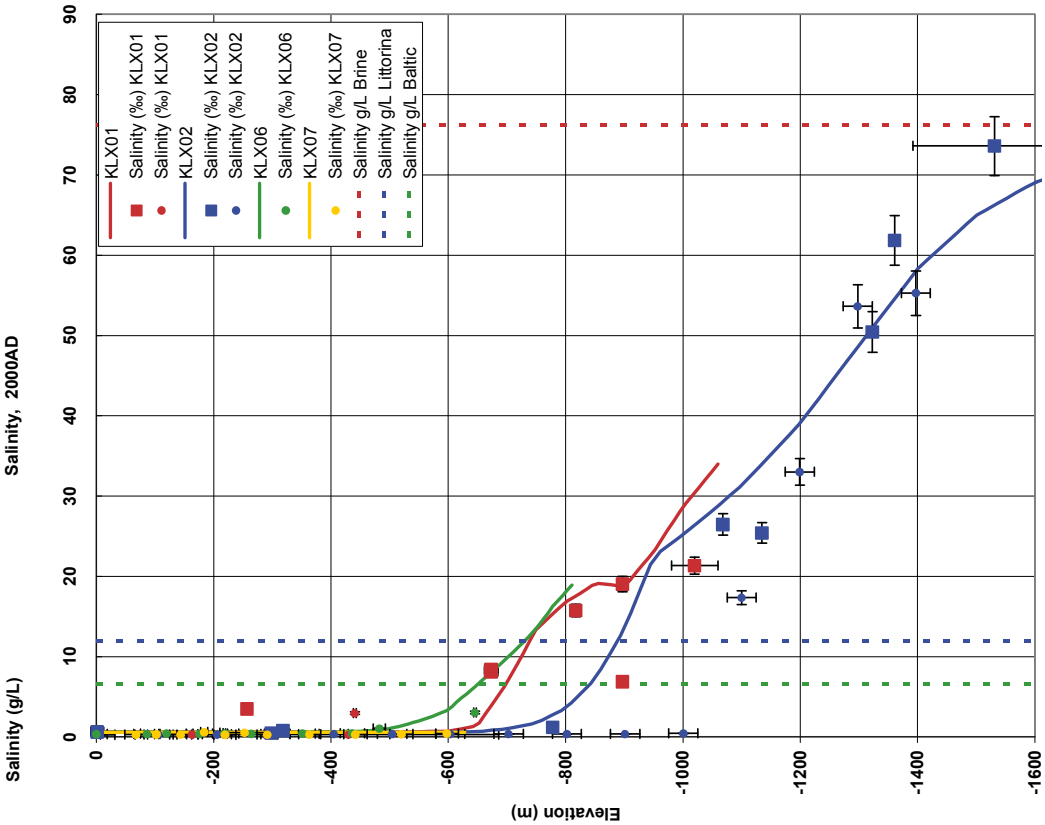
Salinity, 2000AD
Salinity (g/L)
Elevation (m)
KLX01
Salinity (‰) KLX01
Salinity (‰) KLX01
KLX02
Salinity (‰) KLX02
Salinity (‰) KLX02
KLX06
Salinity (‰) KLX06
KLX07
Salinity (‰) KLX07
Salinity g/L Brine
Salinity g/L Littorina
Salinity g/L Baltic

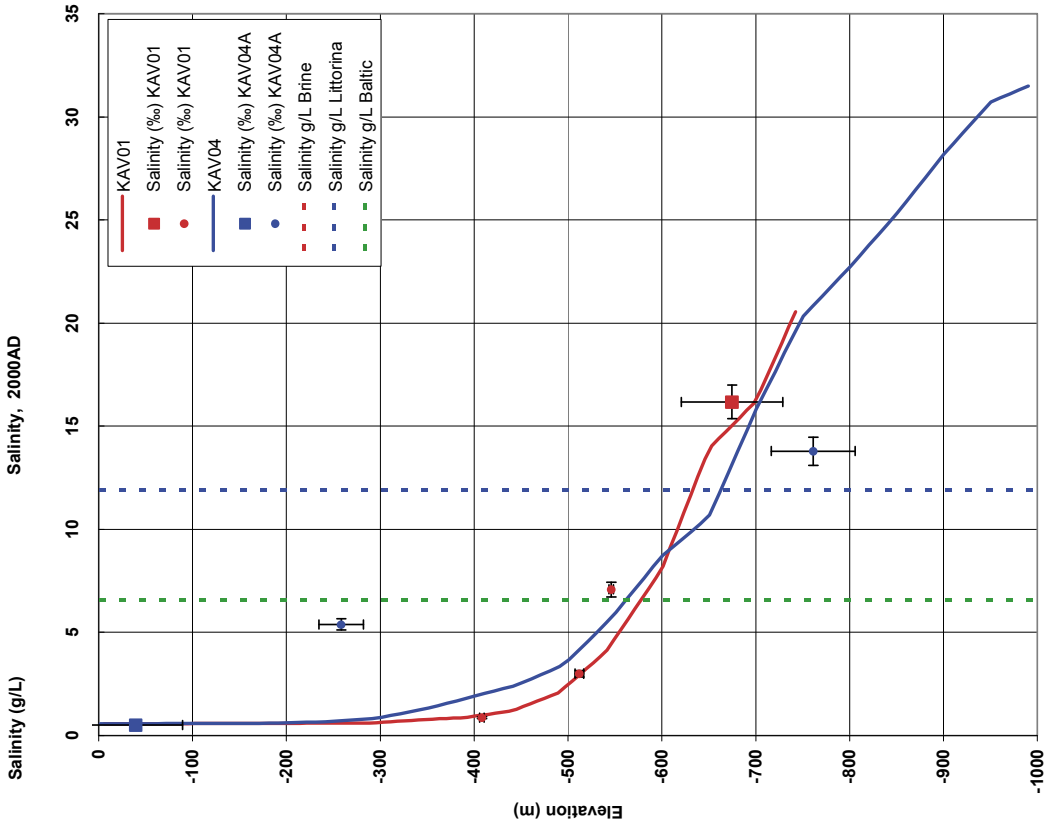
Salinity (g/L)
Salinity, 2000AD
Elevation (m)
KAV01
Salinity (‰) KAV01
Salinity (‰) KAV01
KAV04
Salinity (‰) KAV04A
Salinity (‰) KAV04A
Salinity g/L Brine
Salinity g/L Littorina
Salinity g/L Baltic

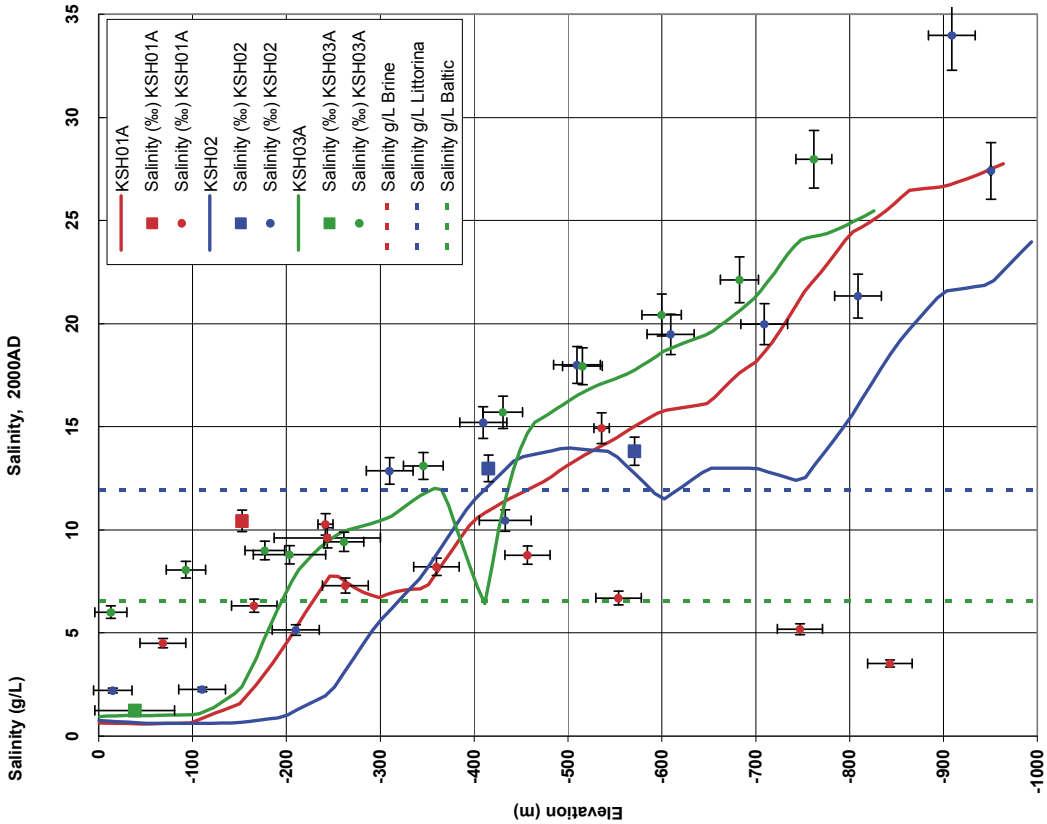
Salinity (g/L)
Salinity, 2000AD
Elevation (m)
KSH01A
Salinity (‰) KSH01A
Salinity (‰) KSH01A
KSH02
Salinity (‰) KSH02
Salinity (‰) KSH02
KSH03A
Salinity (‰) KSH03A
Salinity (‰) KSH03A
Salinity g/L Brine
Salinity g/L Littorina
Salinity g/L Baltic

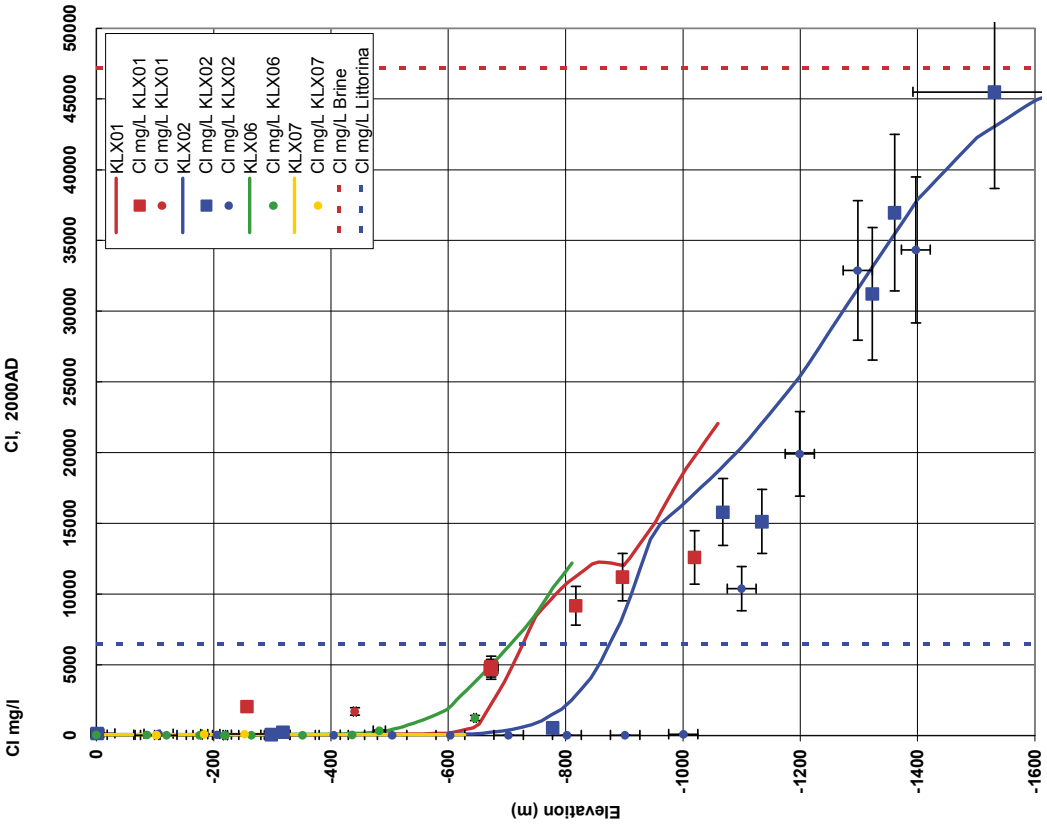
Cl, 2000AD
Cl mg/l
Elevation (m)
KLX01
Cl mg/L KLX01
Cl mg/L KLX01
KLX02
Cl mg/L KLX02
Cl mg/L KLX02
KLX06
Cl mg/L KLX06
KLX07
Cl mg/L KLX07
Cl mg/L Brine
Cl mg/L Littorina

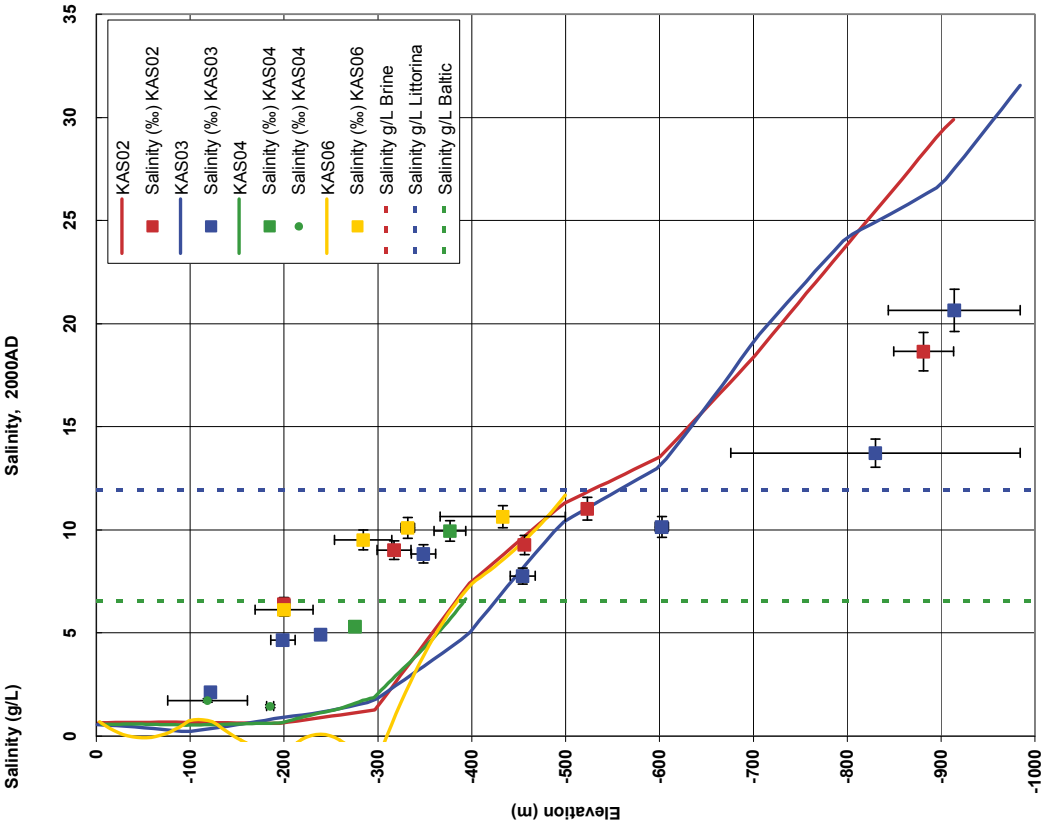
Salinity, 2000AD
Salinity (g/L)
Elevation (m)
KAS02
Salinity (‰) KAS02
KAS03
Salinity (‰) KAS03
KAS04
Salinity (‰) KAS04
Salinity (‰) KAS04
KAS06
Salinity (‰) KAS06
Salinity g/L Brine
Salinity g/L Littorina
Salinity g/L Baltic

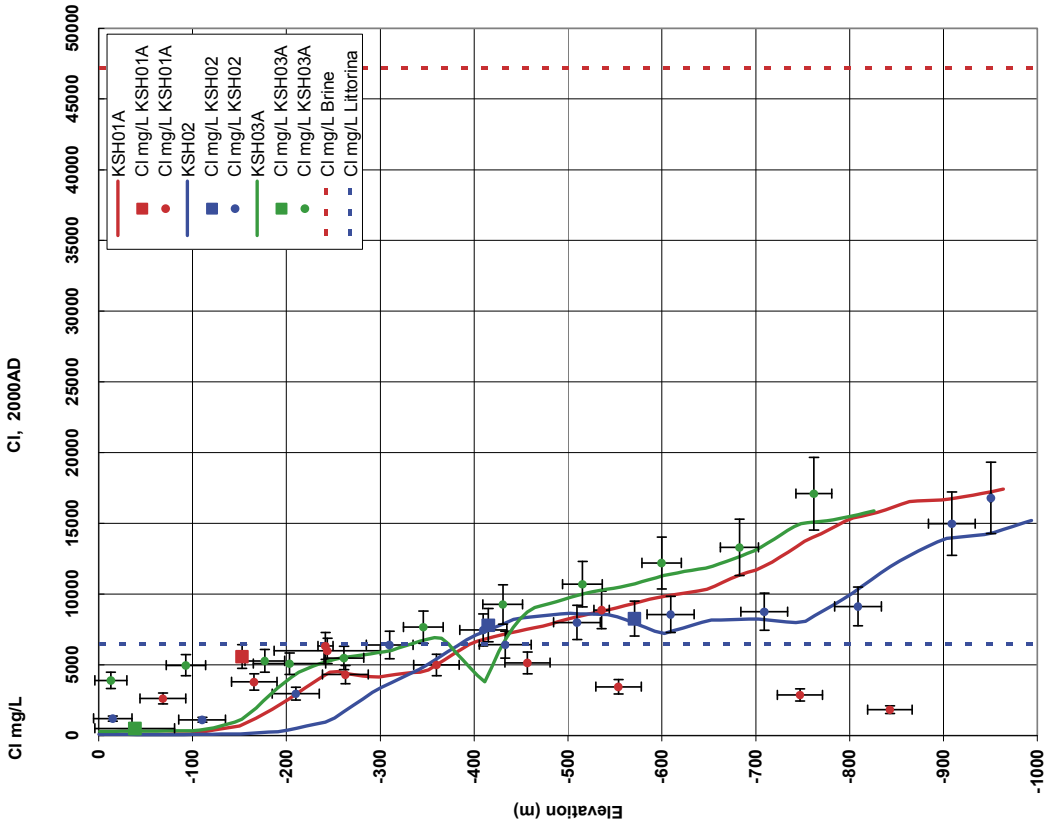
Cl mg/L
Cl, 2000AD
Elevation (m)
KSH01A
Cl mg/L KSH01A
Cl mg/L KSH01A
KSH02
Cl mg/L KSH02
Cl mg/L KSH02
KSH03A
Cl mg/L KSH03A
Cl mg/L KSH03A
Cl mg/L Brine
Cl mg/L Littorina

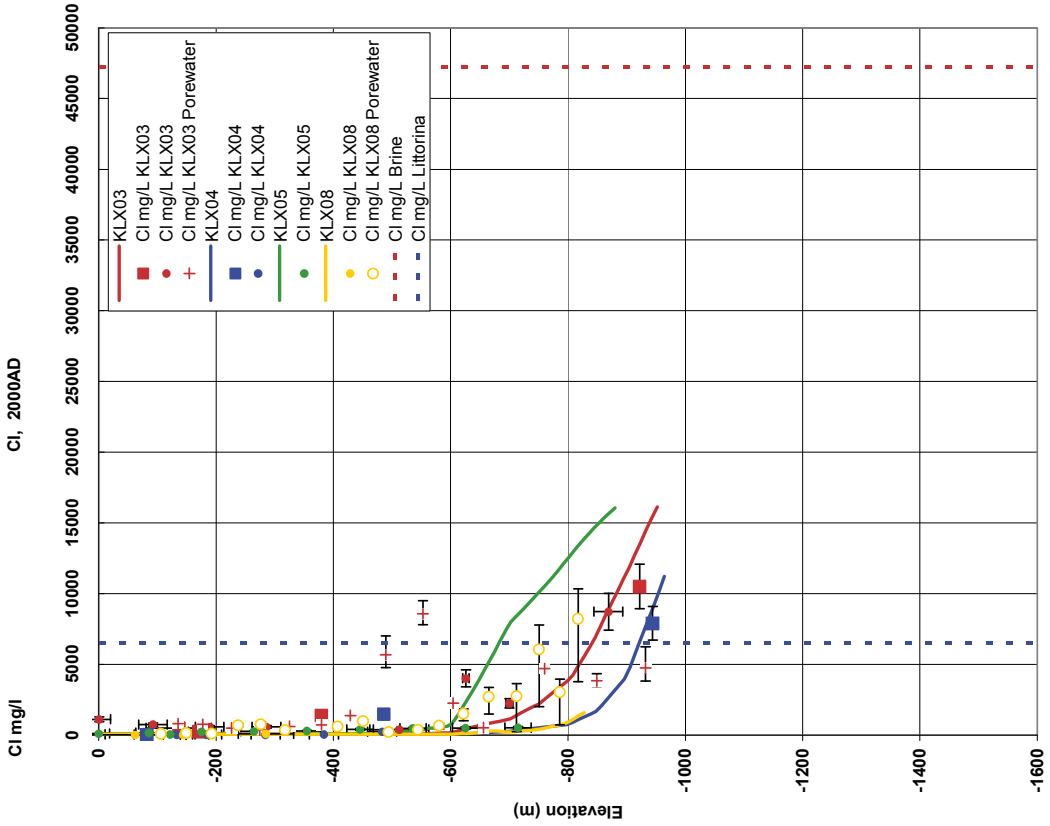
Cl mg/l
Cl, 2000AD
Elevation (m)
KLX03
Cl mg/L KLX03
Cl mg/L KLX03
Cl mg/L KLX03 Porewater
KLX04
Cl mg/L KLX04
Cl mg/L KLX04
KLX05
Cl mg/L KLX05
KLX08
Cl mg/L KLX08
Cl mg/L KLX08 Porewater
Cl mg/L Brine
Cl mg/L Littorina

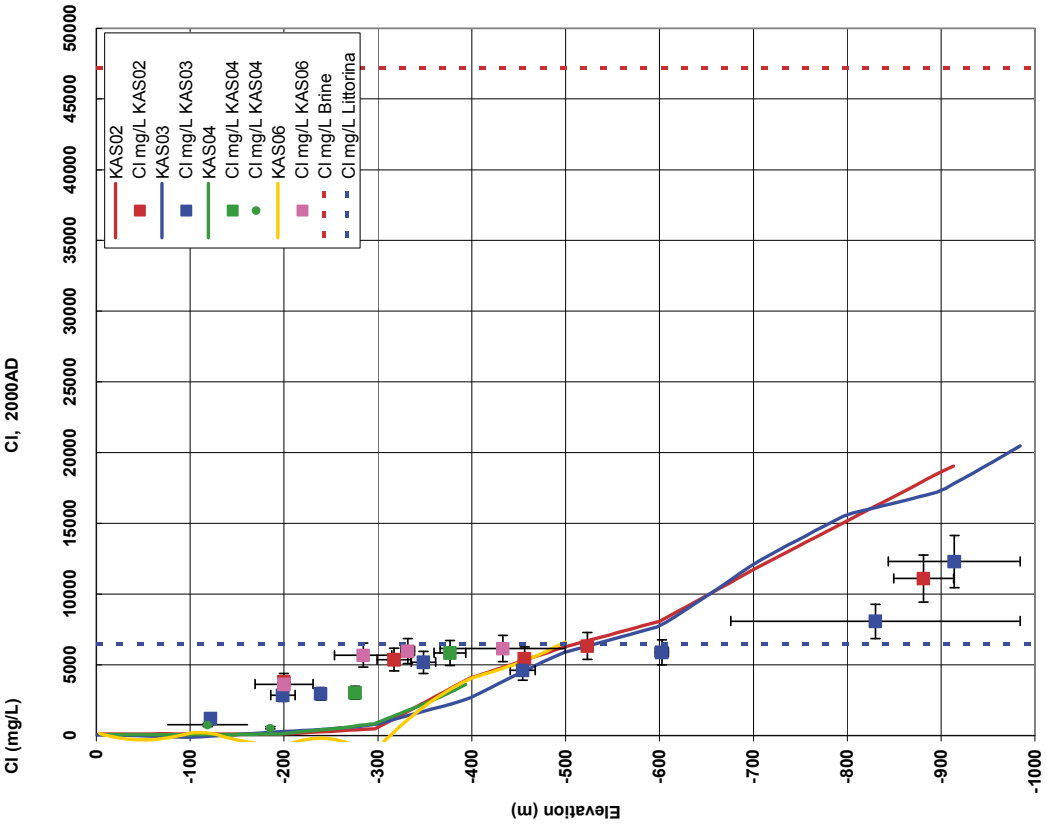
Cl, 2000AD
Cl (mg/L)
Elevation (m)
KAS02
Cl mg/L KAS02
KAS03
Cl mg/L KAS03
KAS04
Cl mg/L KAS04
Cl mg/L KAS04
KAS06
Cl mg/L KAS06
Cl mg/L Brine
Cl mg/L Littorina

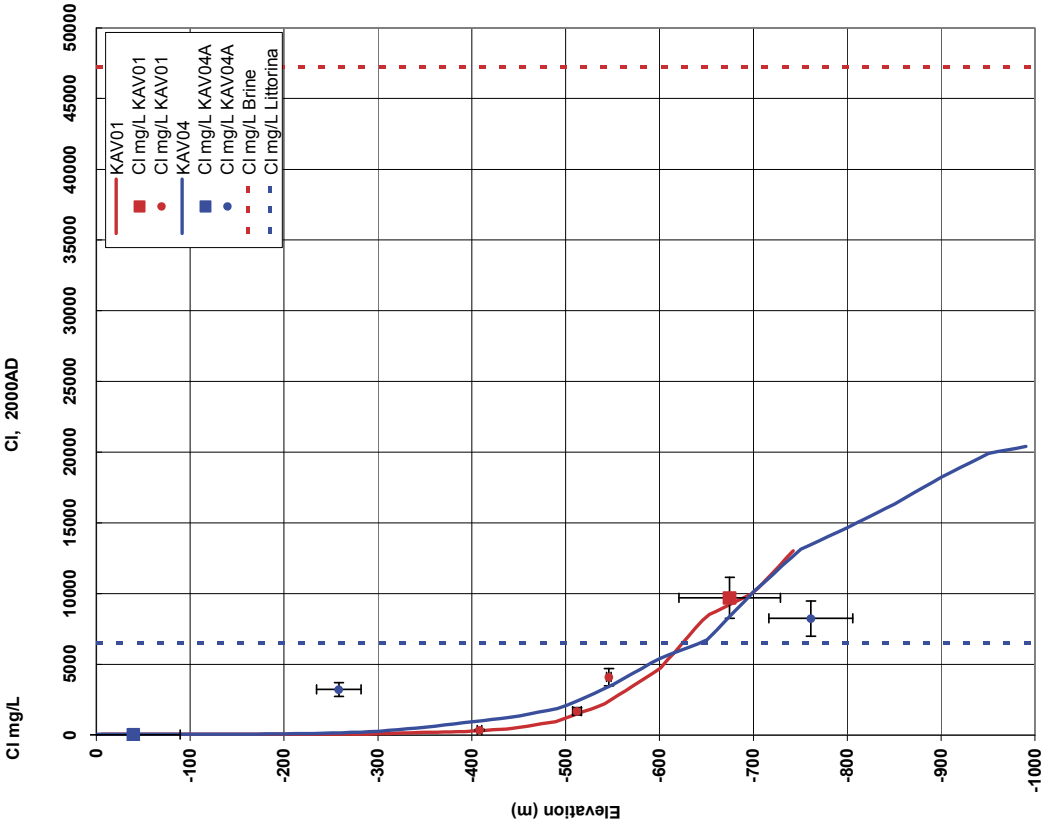
Cl, 2000AD
Cl mg/L
Elevation (m)
KAV01
Cl mg/L KAV01
Cl mg/L KAV01
KAV04
Cl mg/L KAV04A
Cl mg/L KAV04A
Cl mg/L Brine
Cl mg/L Littorina

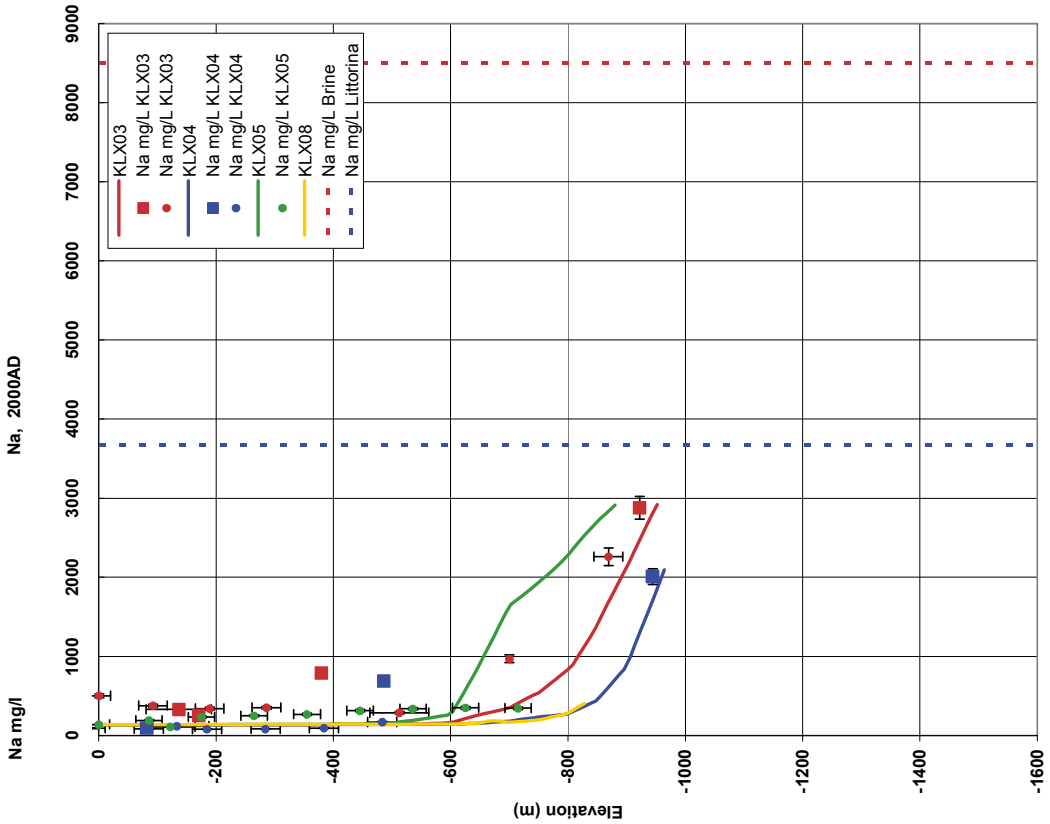
Na, 2000AD
Na mg/l
Elevation (m)
KLX03
Na mg/L KLX03
Na mg/L KLX03
KLX04
Na mg/L KLX04
Na mg/L KLX04
KLX05
Na mg/L KLX05
KLX08
Na mg/L Brine
Na mg/L Littorina

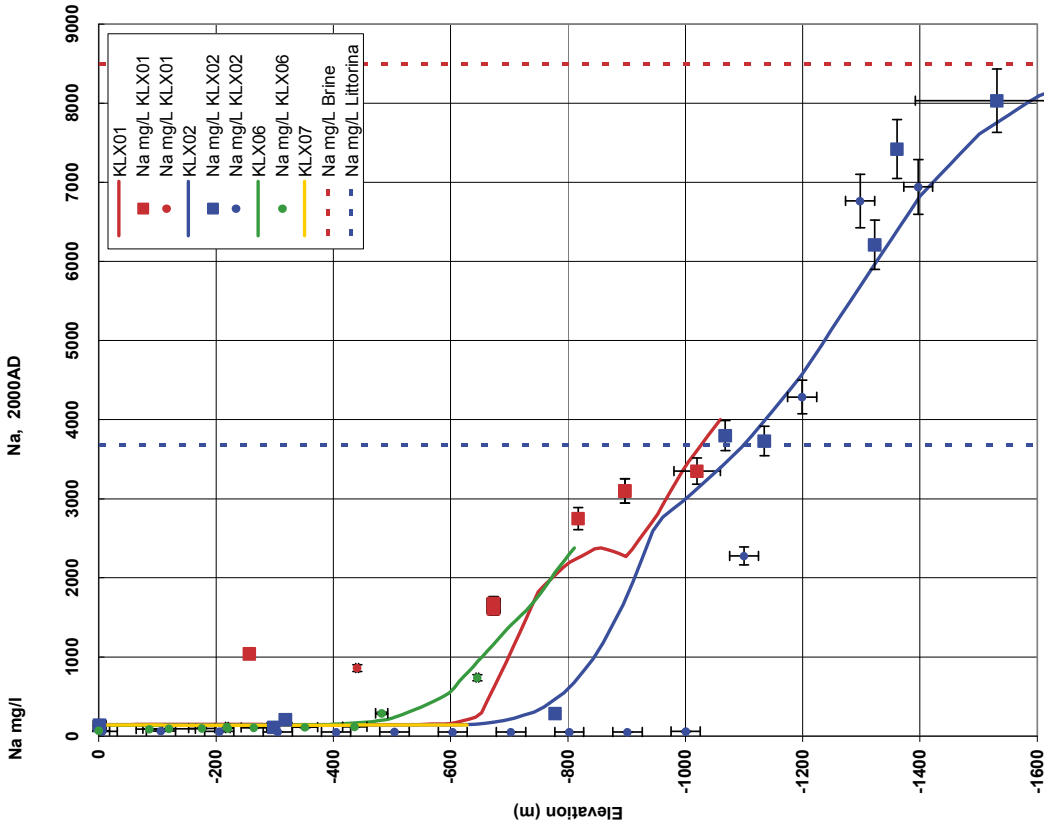
Na, 2000AD
Na mg/l
Elevation (m)
KLX01
Na mg/L KLX01
Na mg/L KLX01
KLX02
Na mg/L KLX02
Na mg/L KLX02
KLX06
Na mg/L KLX06
KLX07
Na mg/L Brine
Na mg/L Littorina

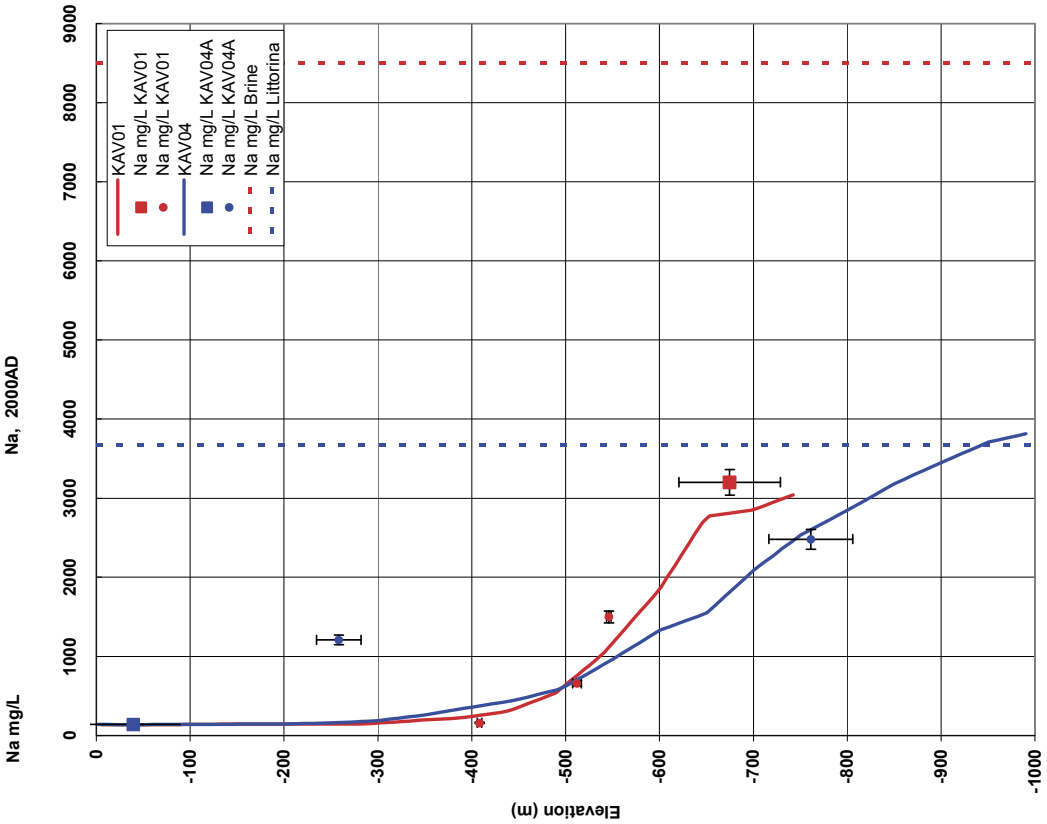
Na mg/L
Na, 2000AD
0
1000
2000
3000
4000
5000
6000
7000
8000
9000
Elevation (m)
0
-100
-200
-300
-400
-500
-600
-700
-800
-900
-1000
KAV01
Na mg/L KAV01
Na mg/L KAV01
KAV04
Na mg/L KAV04A
Na mg/L KAV04A
Na mg/L Brine
Na mg/L Littorina

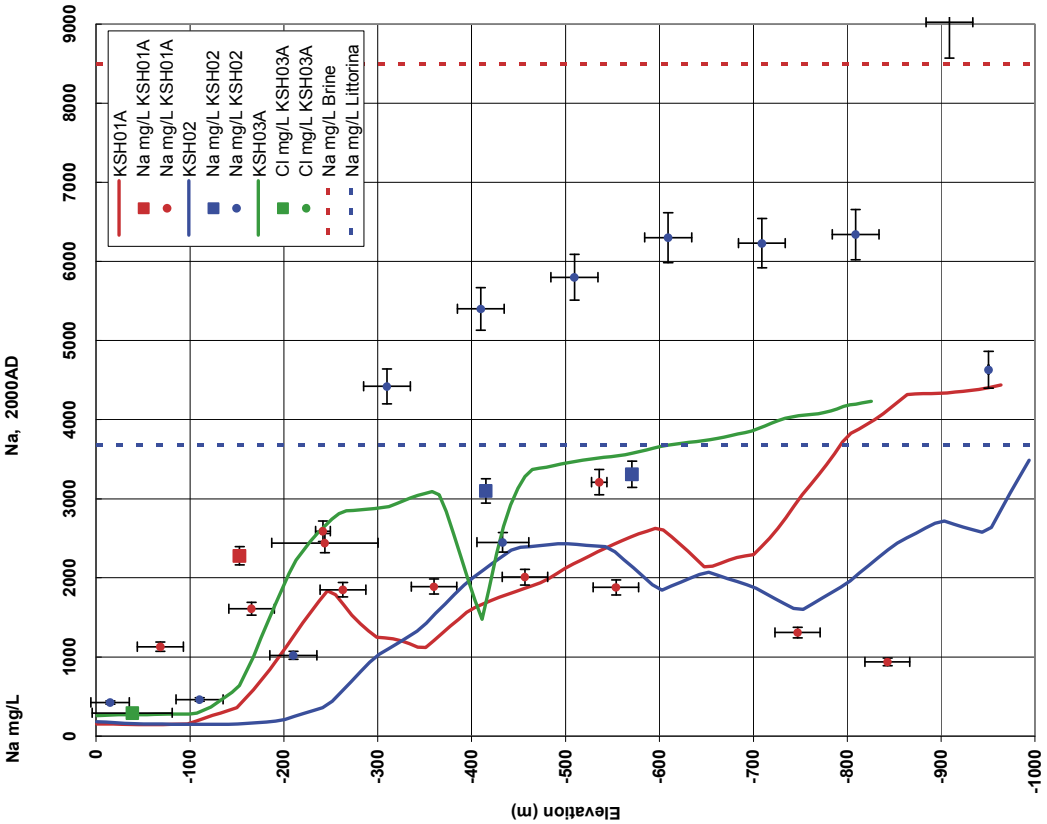
Na mg/L
Na, 2000AD
0
1000
2000
3000
4000
5000
6000
7000
8000
9000
Elevation (m)
0
-100
-200
-300
-400
-500
-600
-700
-800
-900
-1000
KSH01A
Na mg/L KSH01A
Na mg/L KSH01A
KSH02
Na mg/L KSH02
Na mg/L KSH02
KSH03A
Cl mg/L KSH03A
Cl mg/L KSH03A
Na mg/L Brine
Na mg/L Littorina

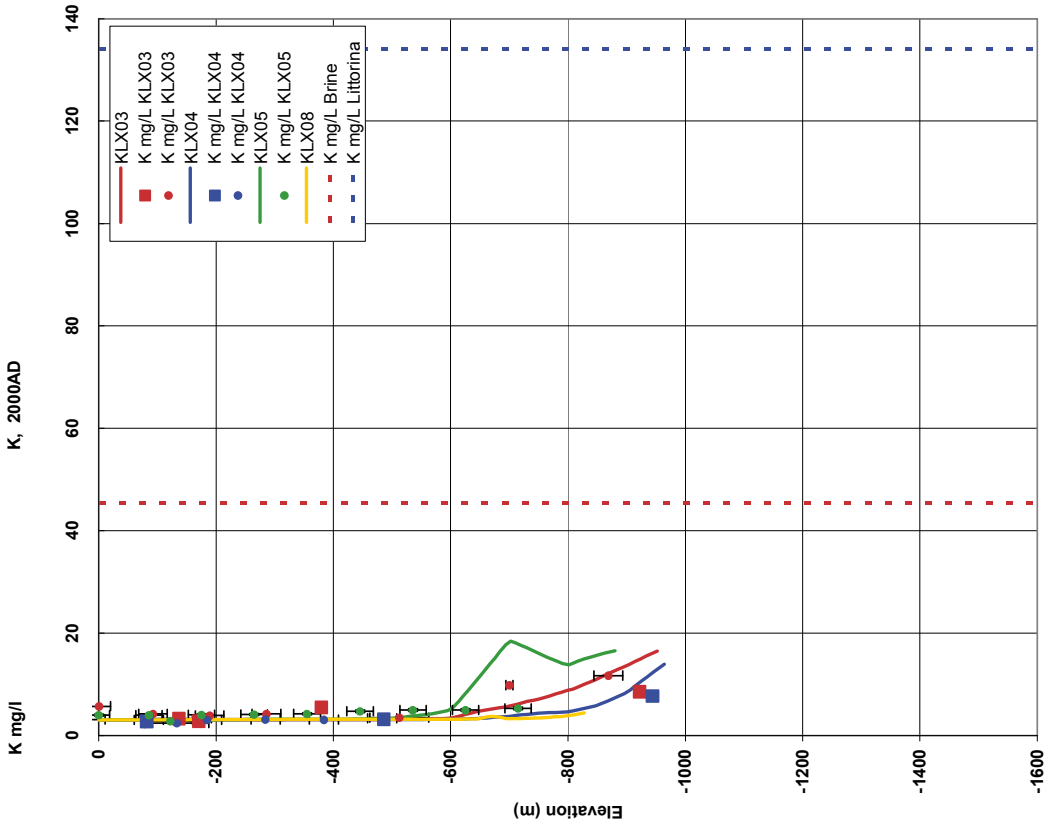
K, 2000AD
K mg/l
Elevation (m)
KLX03
K mg/L KLX03
K mg/L KLX03
KLX04
K mg/L KLX04
K mg/L KLX04
KLX05
K mg/L KLX05
KLX08
K mg/L Brine
K mg/L Littorina

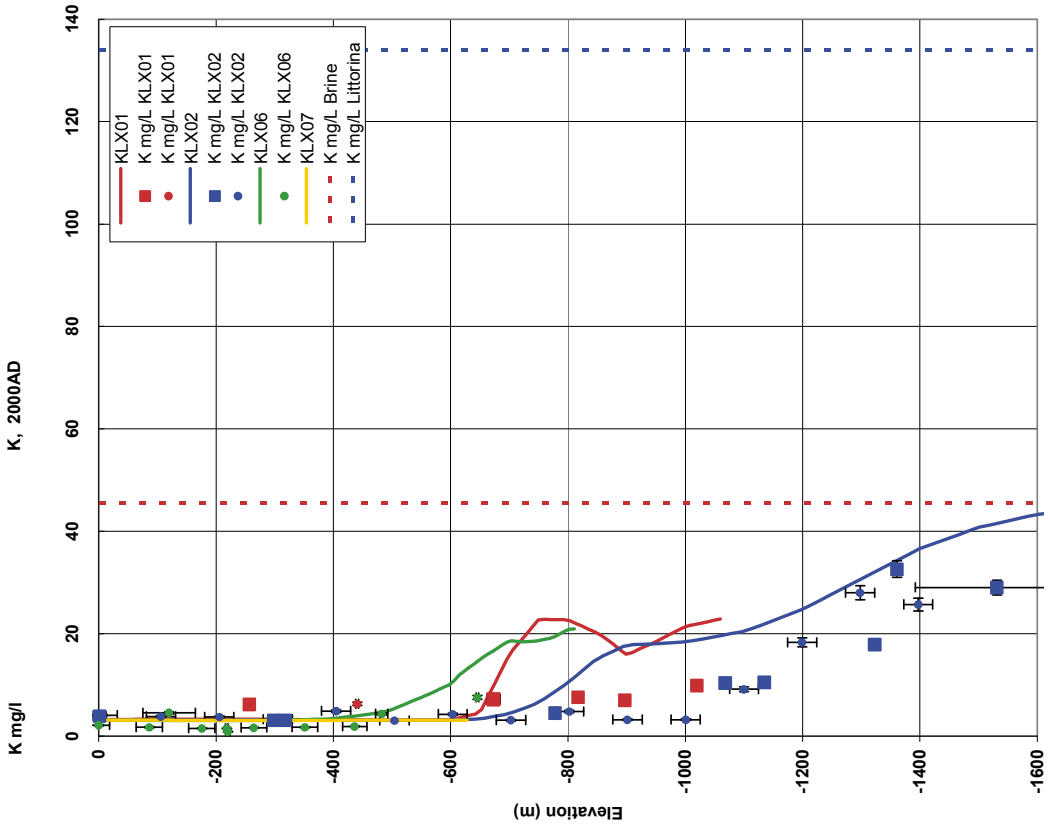
K, 2000AD
K mg/l
Elevation (m)
KLX01
K mg/L KLX01
K mg/L KLX01
KLX02
K mg/L KLX02
K mg/L KLX02
KLX06
K mg/L KLX06
KLX07
K mg/L Brine
K mg/L Littorina

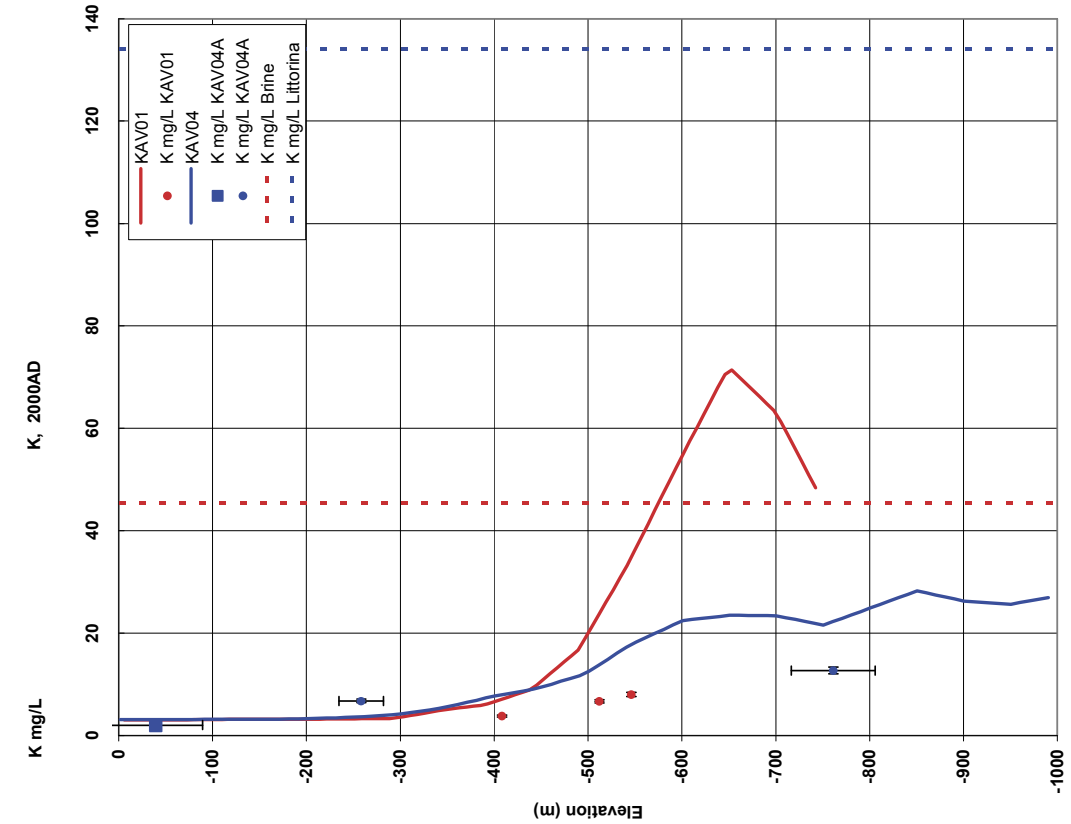
K, 2000AD
K mg/L
Elevation (m)
KAV01
K mg/L KAV01
KAV04
K mg/L KAV04A
K mg/L KAV04A
K mg/L Brine
K mg/L Littorina

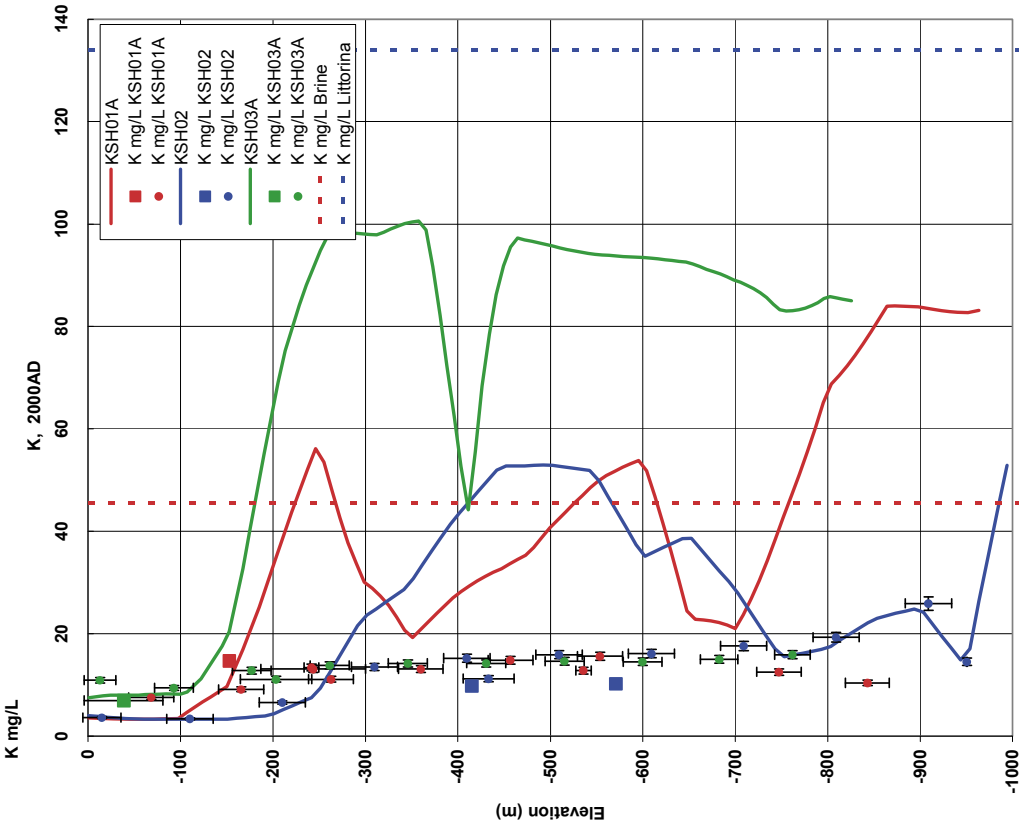
K, 2000AD
K mg/L
Elevation (m)
KSH01A
K mg/L KSH01A
K mg/L KSH01A
KSH02
K mg/L KSH02
K mg/L KSH02
KSH03A
K mg/L KSH03A
K mg/L KSH03A
K mg/L Brine
K mg/L Littorina

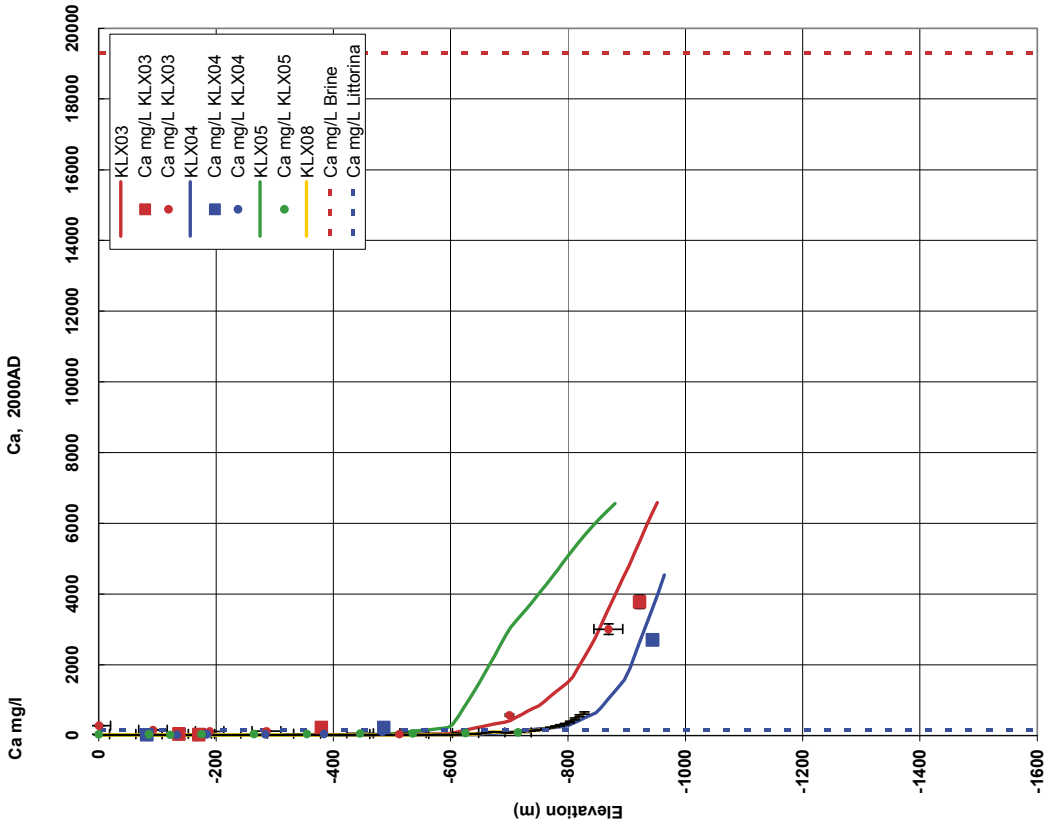
Ca, 2000AD
Ca mg/l
Elevation (m)
KLX03
Ca mg/L KLX03
Ca mg/L KLX03
KLX04
Ca mg/L KLX04
Ca mg/L KLX04
KLX05
Ca mg/L KLX05
KLX08
Ca mg/L Brine
Ca mg/L Littorina

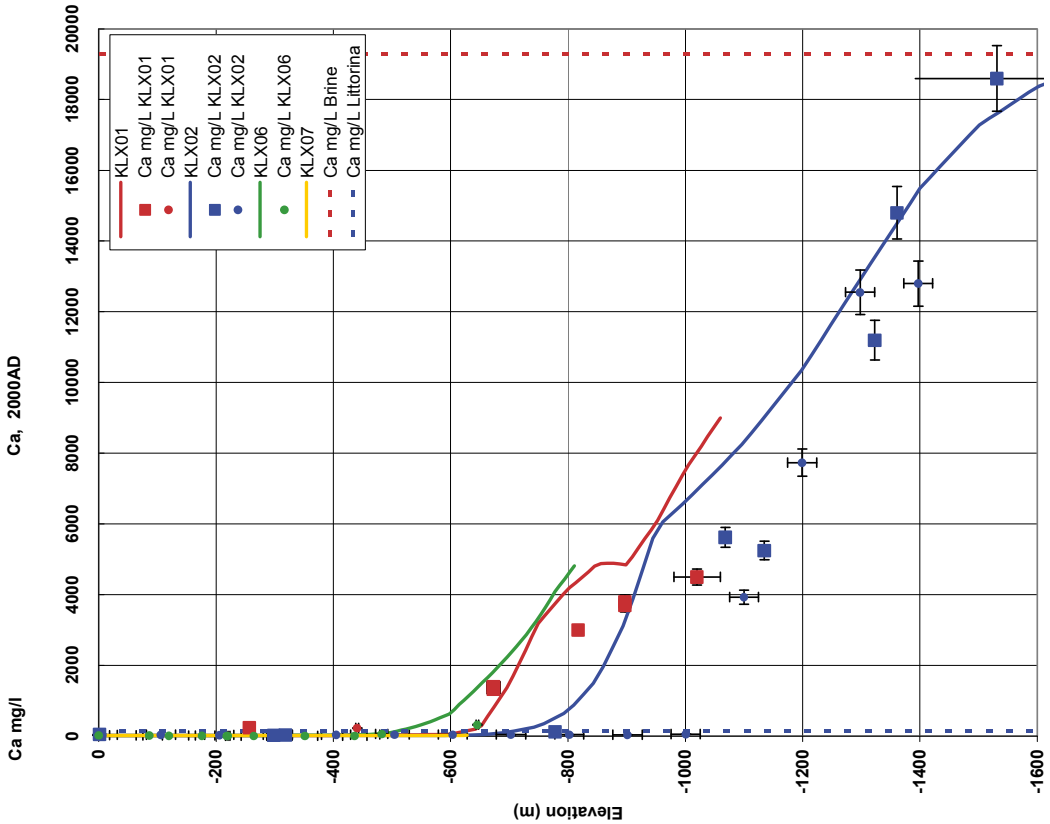
Ca, 2000AD
Ca mg/l
Elevation (m)
KLX01
Ca mg/L KLX01
Ca mg/L KLX01
KLX02
Ca mg/L KLX02
Ca mg/L KLX02
KLX06
Ca mg/L KLX06
KLX07
Ca mg/L Brine
Ca mg/L Littorina

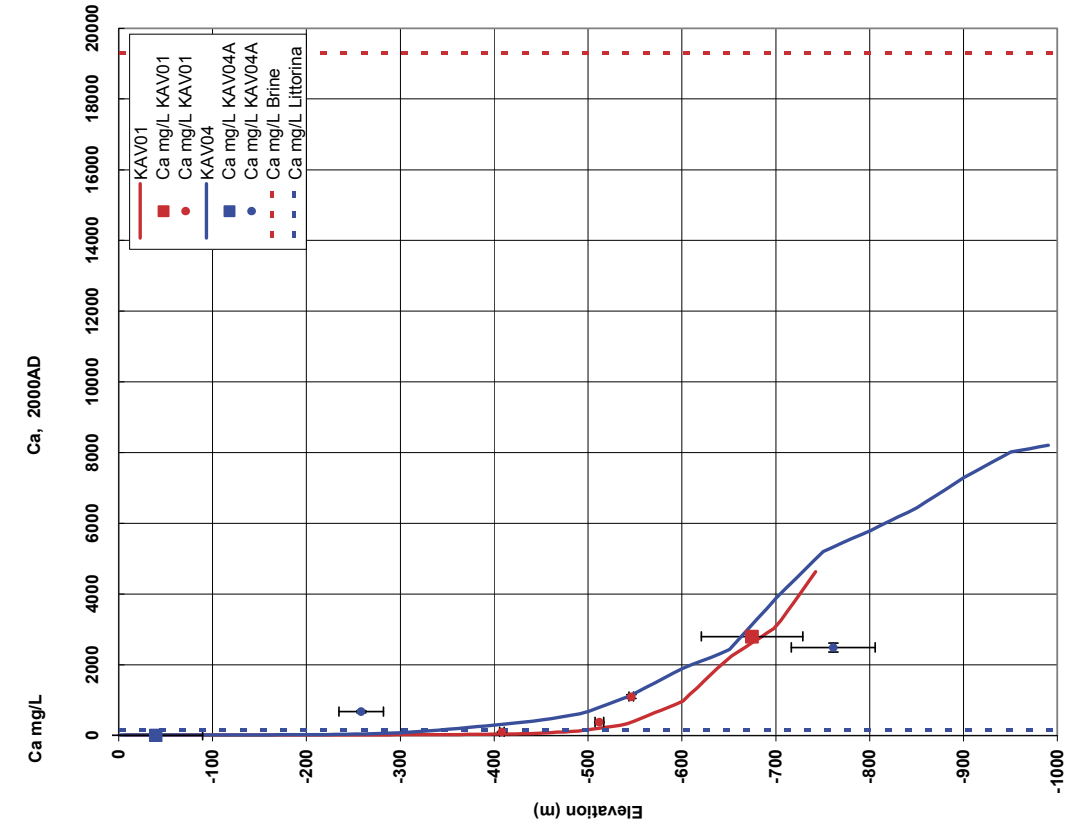
Ca mg/L
Ca, 2000AD
Elevation (m)
KAV01
Ca mg/L KAV01
Ca mg/L KAV01
KAV04
Ca mg/L KAV04A
Ca mg/L KAV04A
Ca mg/L Brine
Ca mg/L Littorina

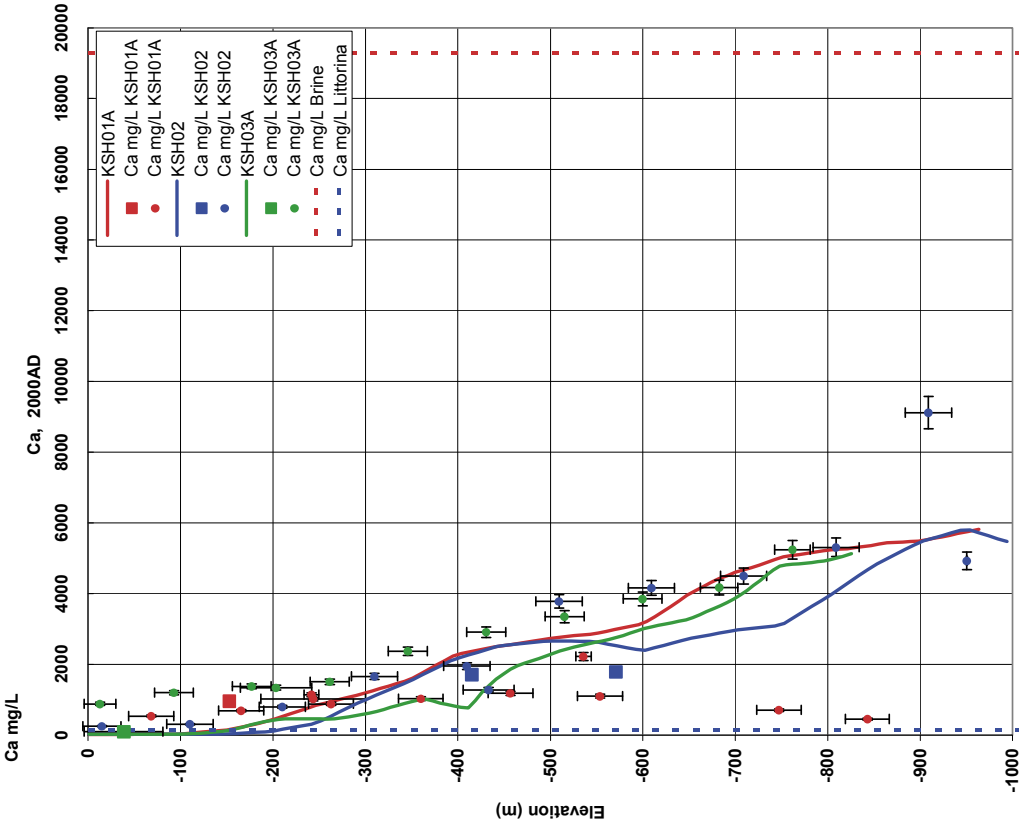
Ca mg/L
Ca, 2000AD
Elevation (m)
KSH01A
Ca mg/L KSH01A
Ca mg/L KSH01A
KSH02
Ca mg/L KSH02
Ca mg/L KSH02
KSH03A
Ca mg/L KSH03A
Ca mg/L KSH03A
Ca mg/L Brine
Ca mg/L Littorina

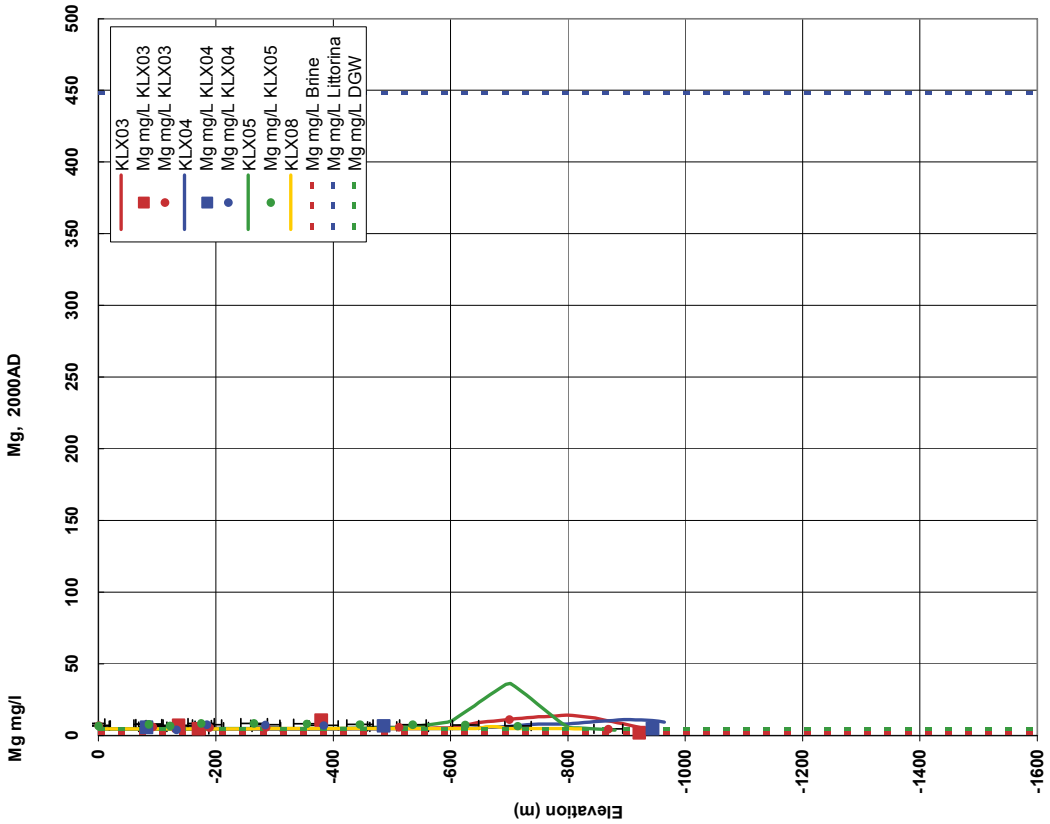
Mg, 2000AD
Mg mg/l
Elevation (m)
KLX03
Mg mg/L KLX03
Mg mg/L KLX03
KLX04
Mg mg/L KLX04
Mg mg/L KLX04
KLX05
Mg mg/L KLX05
KLX08
Mg mg/L Brine
Mg mg/L Littorina
Mg mg/L DGW

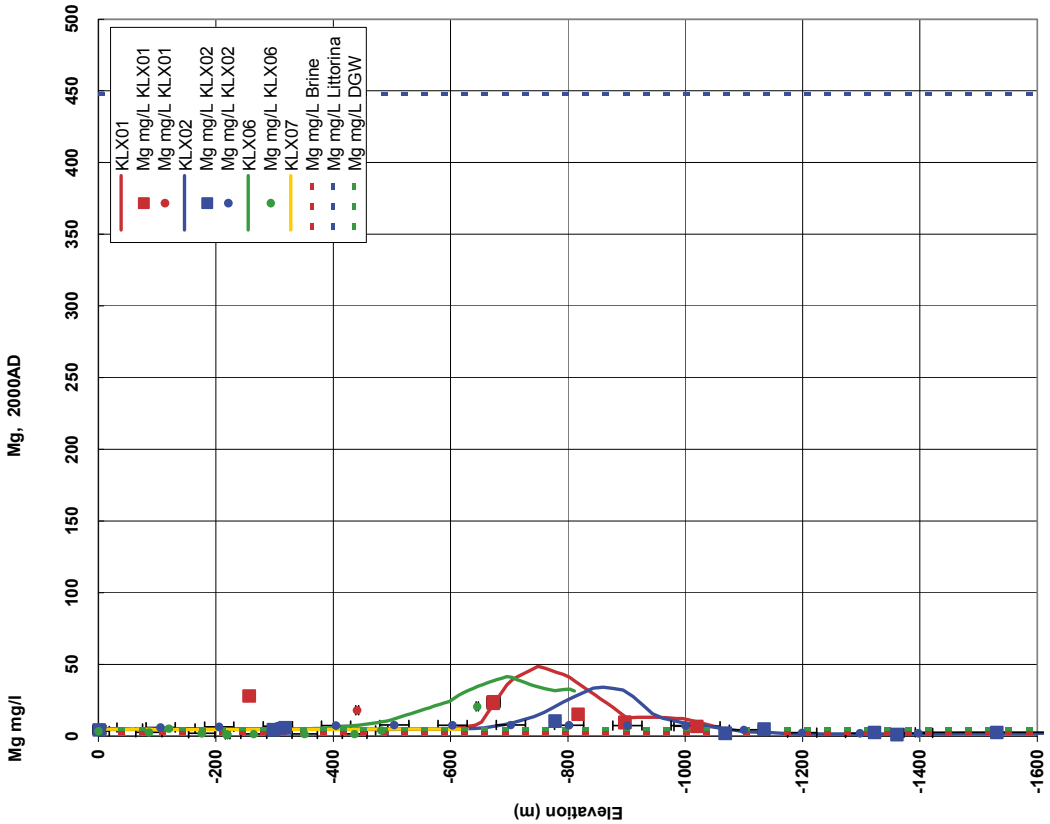
Mg, 2000AD
Mg mg/l
Elevation (m)
KLX01
Mg mg/L KLX01
Mg mg/L KLX01
KLX02
Mg mg/L KLX02
Mg mg/L KLX02
KLX06
Mg mg/L KLX06
KLX07
Mg mg/L Brine
Mg mg/L Littorina
Mg mg/L DGW

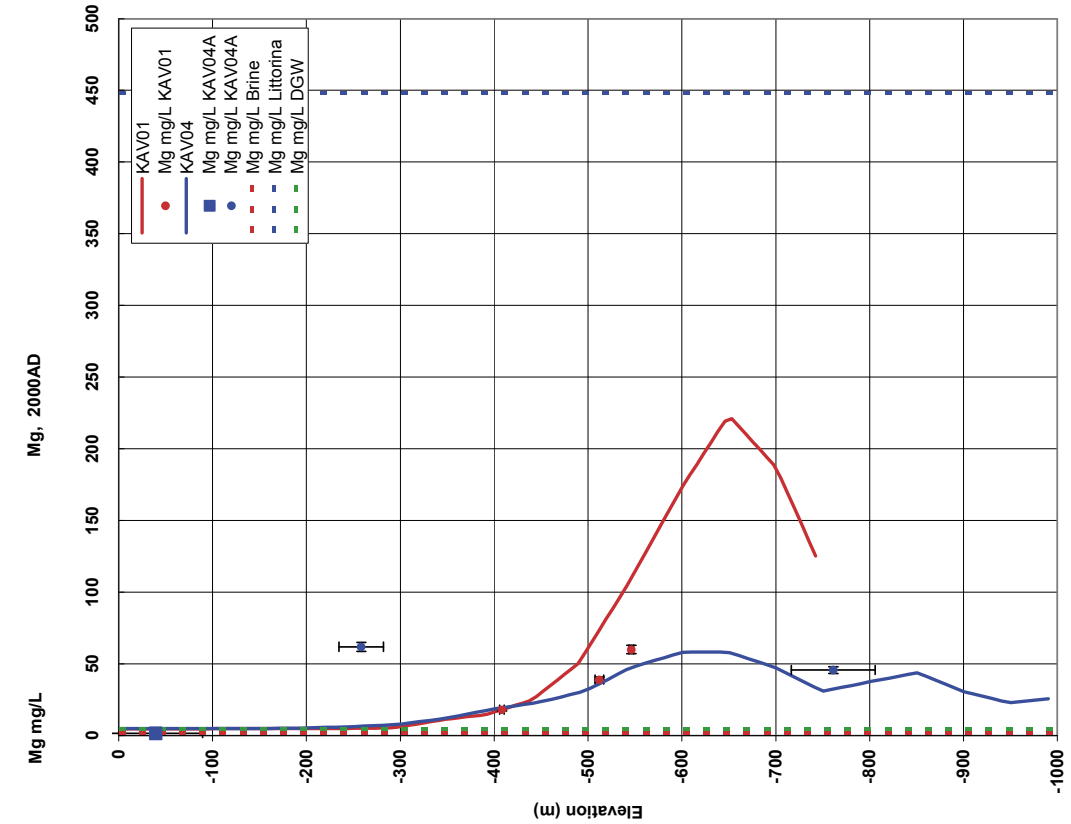
Mg, 2000AD
Mg mg/L
Elevation (m)
KAV01
Mg mg/L KAV01
KAV04
Mg mg/L KAV04A
Mg mg/L KAV04A
Mg mg/L Brine
Mg mg/L Littorina
Mg mg/L DGW

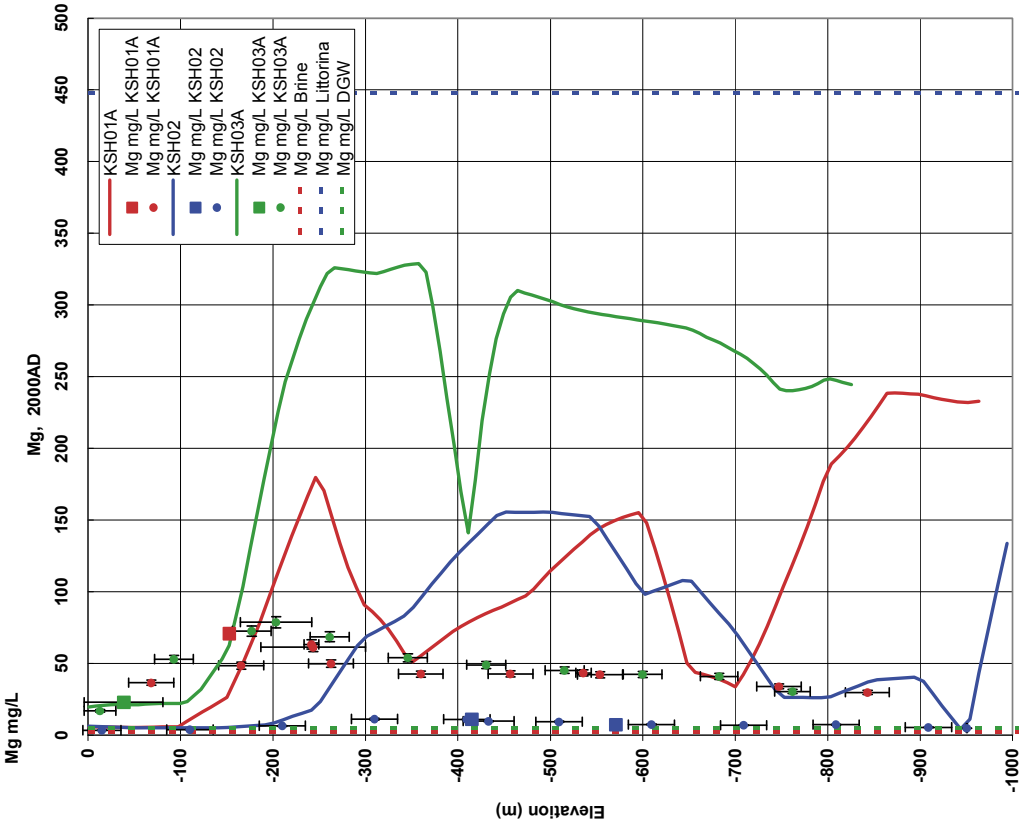
Mg, 2000AD
Mg mg/L
Elevation (m)
KSH01A
Mg mg/L KSH01A
Mg mg/L KSH01A
KSH02
Mg mg/L KSH02
Mg mg/L KSH02
KSH03A
Mg mg/L KSH03A
Mg mg/L KSH03A
Mg mg/L Brine
Mg mg/L Littorina
Mg mg/L DGW

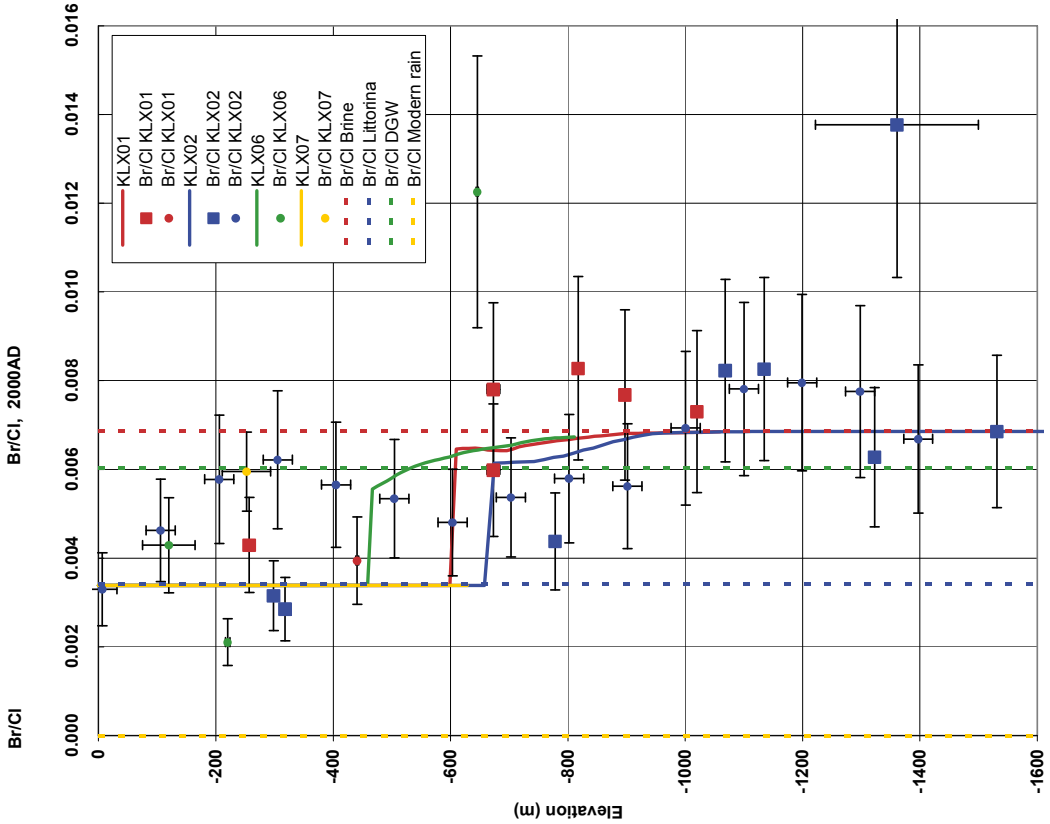
Br/Cl, 2000AD
Br/Cl
Elevation (m)
KLX01
Br/Cl KLX01
Br/Cl KLX01
KLX02
Br/Cl KLX02
Br/Cl KLX02
KLX06
Br/Cl KLX06
KLX07
Br/Cl KLX07
Br/Cl Brine
Br/Cl Littorina
Br/Cl DGW
Br/Cl Modern rain

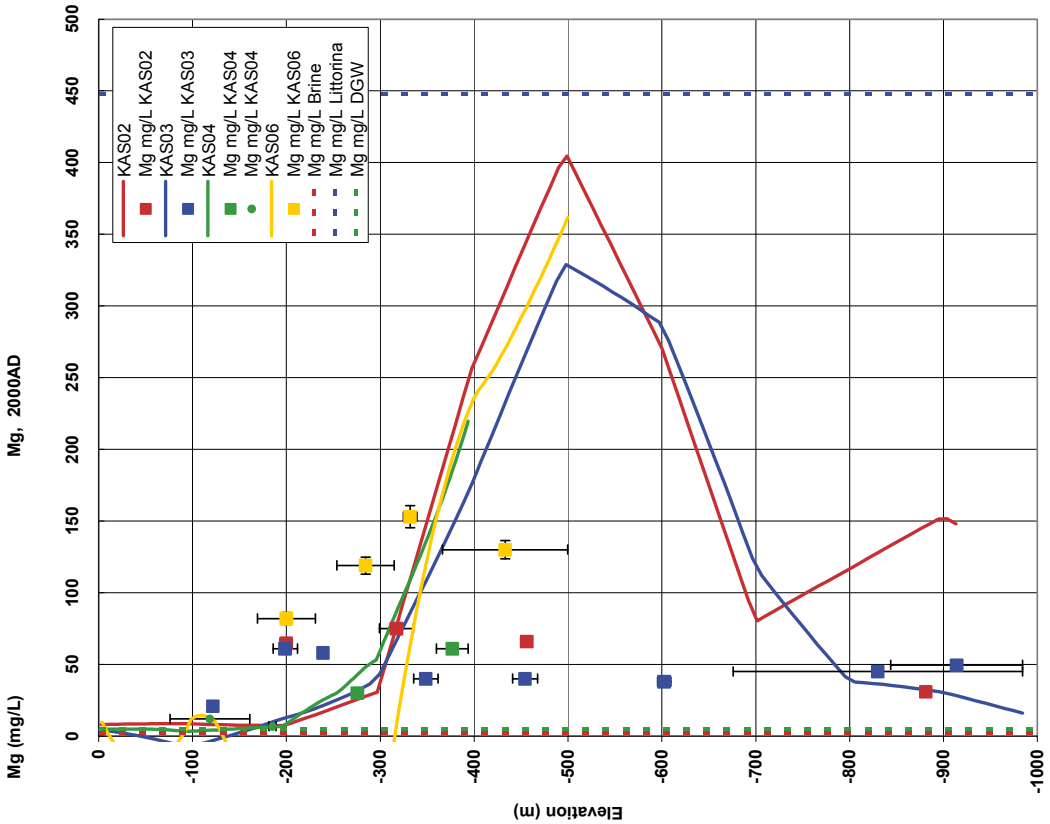
Mg, 2000AD
Mg (mg/L)
Elevation (m)
KAS02
Mg mg/L KAS02
KAS03
Mg mg/L KAS03
KAS04
Mg mg/L KAS04
Mg mg/L KAS04
KAS06
Mg mg/L KAS06
Mg mg/L Brine
Mg mg/L Littorina
Mg mg/L DGW

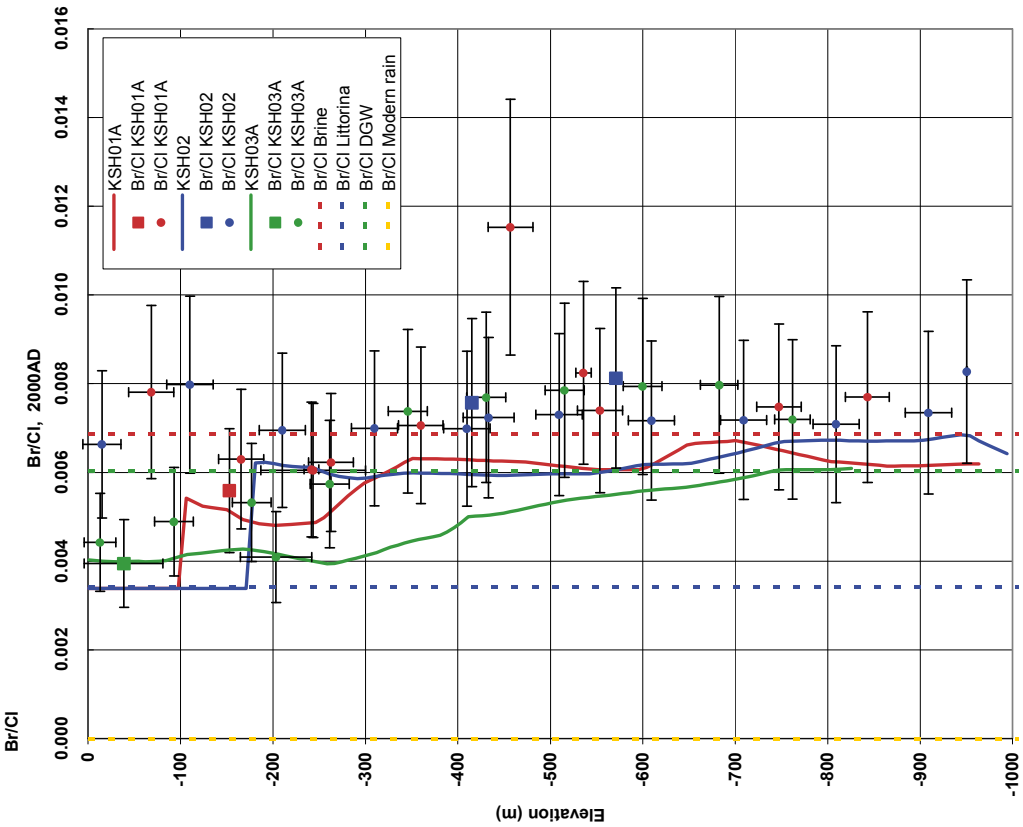
Br/Cl
Br/Cl, 2000AD
Elevation (m)
KSH01A
Br/Cl KSH01A
Br/Cl KSH01A
KSH02
Br/Cl KSH02
Br/Cl KSH02
KSH03A
Br/Cl KSH03A
Br/Cl KSH03A
Br/Cl Brine
Br/Cl Littorina
Br/Cl DGW
Br/Cl Modern rain

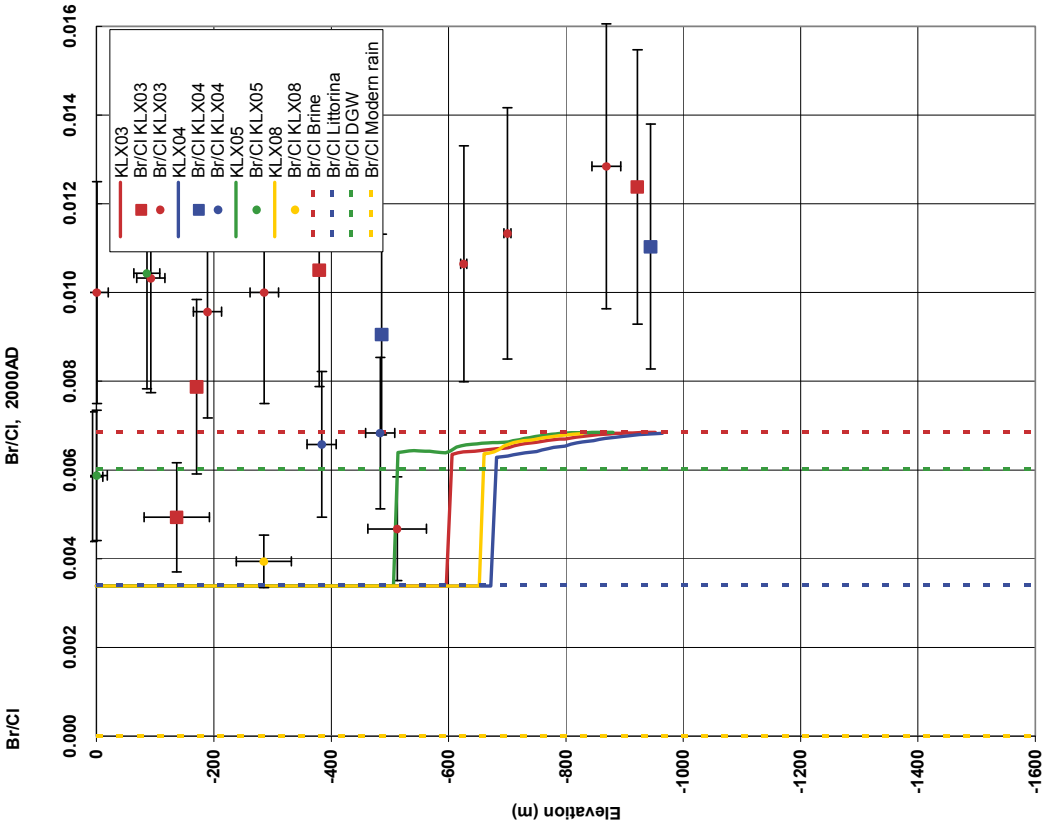
Br/Cl
Br/Cl, 2000AD
Elevation (m)
KLX03
Br/Cl KLX03
Br/Cl KLX03
KLX04
Br/Cl KLX04
Br/Cl KLX04
KLX05
Br/Cl KLX05
KLX08
Br/Cl KLX08
Br/Cl Brine
Br/Cl Littorina
Br/Cl DGW
Br/Cl Modern rain

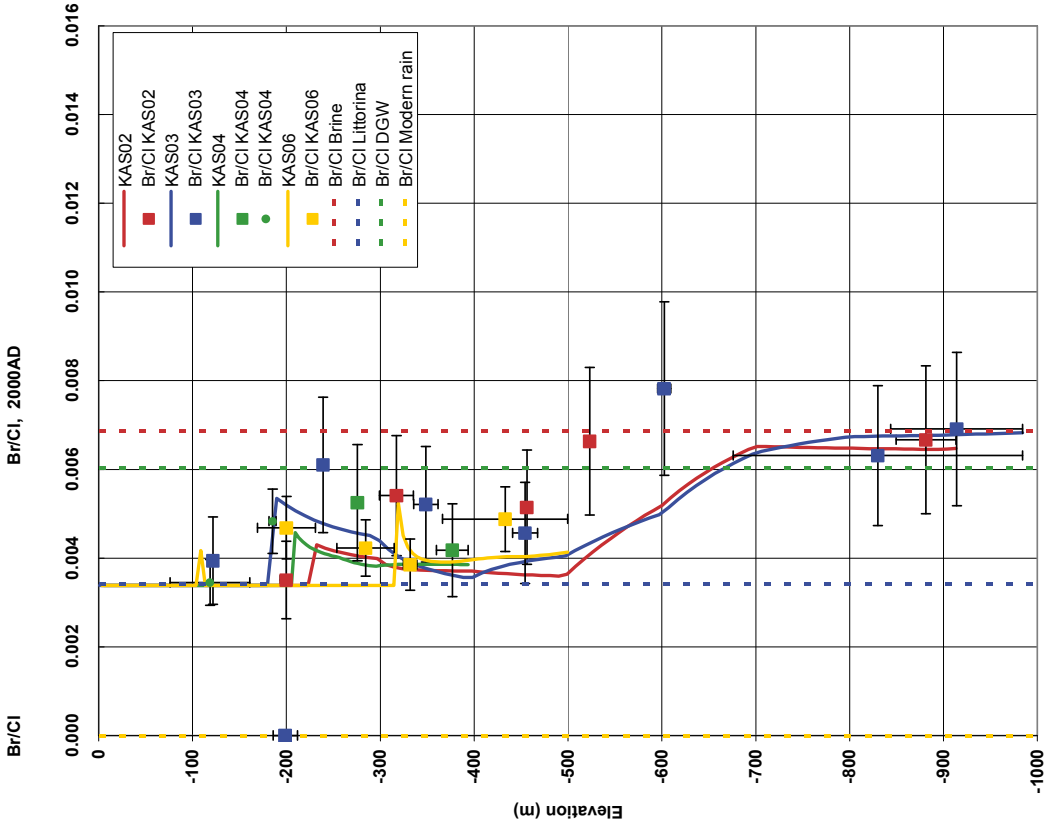
Br/Cl, 2000AD
Br/Cl
Elevation (m)
KAS02
Br/Cl KAS02
KAS03
Br/Cl KAS03
KAS04
Br/Cl KAS04
Br/Cl KAS04
KAS06
Br/Cl KAS06
Br/Cl Brine
Br/Cl Littorina
Br/Cl DGW
Br/Cl Modern rain

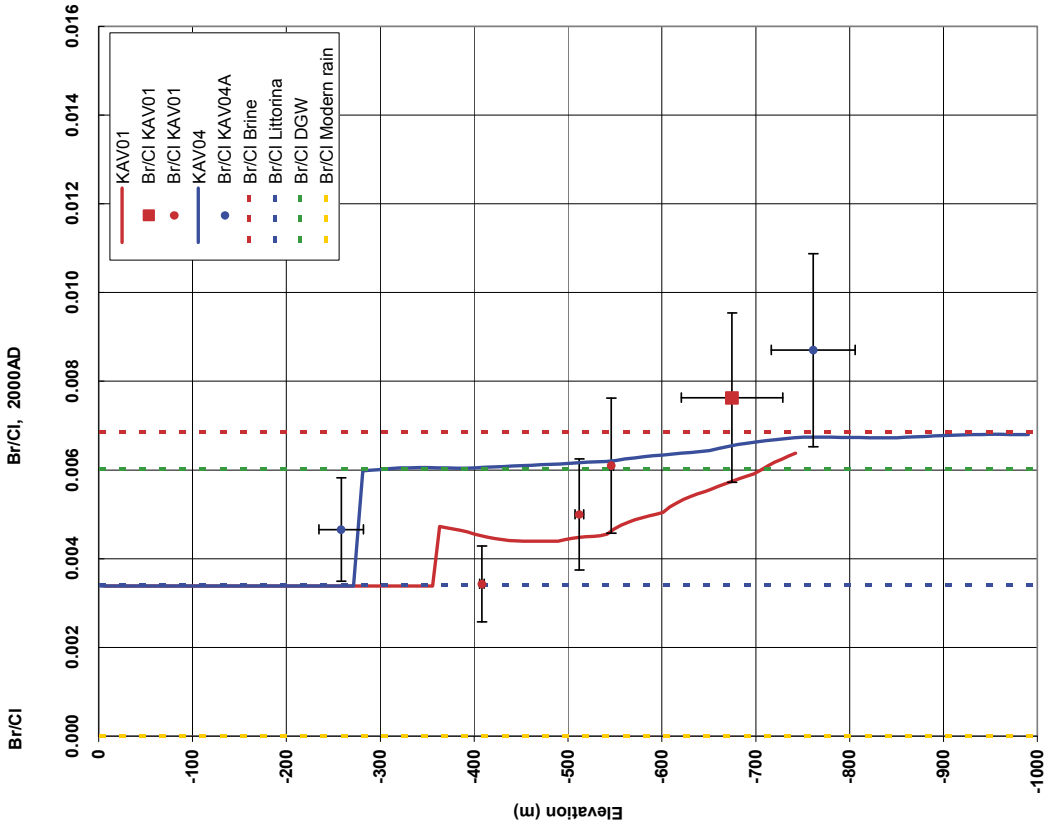
Br/Cl, 2000AD
Br/Cl
Elevation (m)
KAV01
Br/Cl KAV01
Br/Cl KAV01
KAV04
Br/Cl KAV04A
Br/Cl Brine
Br/Cl Littorina
Br/Cl DGW
Br/Cl Modern rain

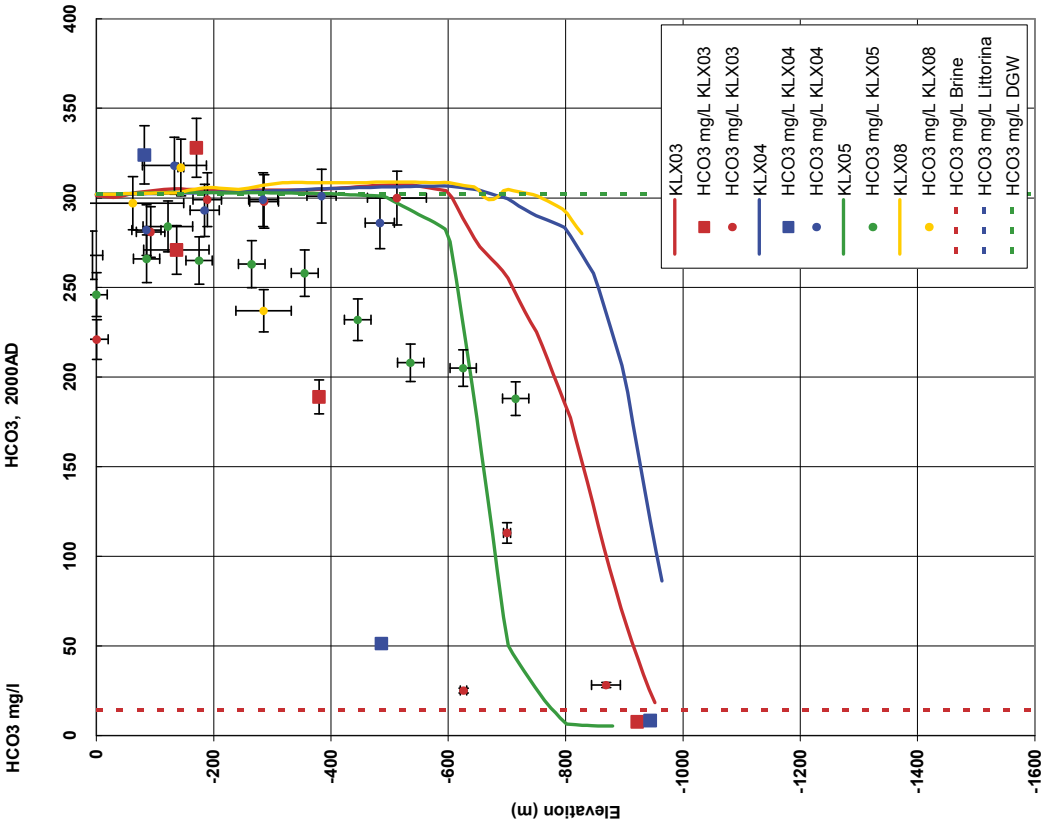
HCO3, 2000AD
HCO3 mg/l
Elevation (m)
0
50
100
150
200
250
300
350
400
-200
-400
-600
-800
-1000
-1200
-1400
-1600
KLX03
HCO3 mg/L KLX03
HCO3 mg/L KLX03
KLX04
HCO3 mg/L KLX04
HCO3 mg/L KLX04
KLX05
HCO3 mg/L KLX05
KLX08
HCO3 mg/L KLX08
HCO3 mg/L Brine
HCO3 mg/L Littorina
HCO3 mg/L DGW

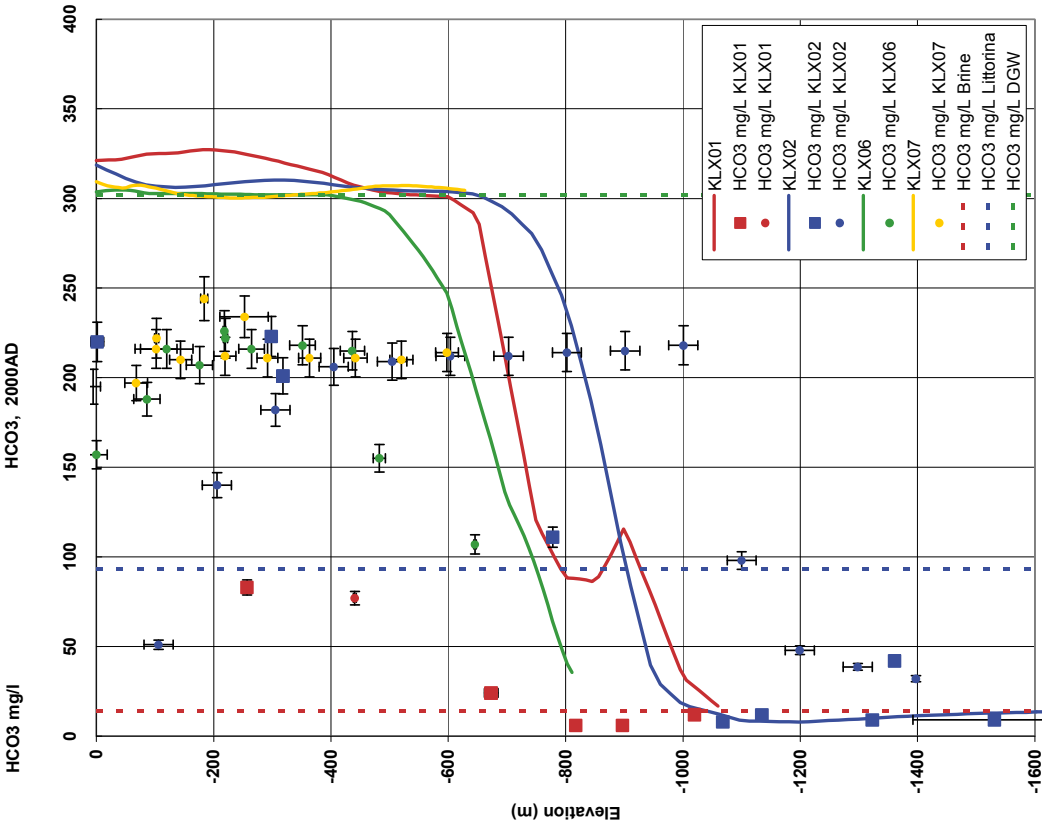
HCO3, 2000AD
HCO3 mg/l
Elevation (m)
0
50
100
150
200
250
300
350
400
-200
-400
-600
-800
-1000
-1200
-1400
-1600
KLX01
HCO3 mg/L KLX01
HCO3 mg/L KLX01
KLX02
HCO3 mg/L KLX02
HCO3 mg/L KLX02
KLX06
HCO3 mg/L KLX06
KLX07
HCO3 mg/L KLX07
HCO3 mg/L Brine
HCO3 mg/L Littorina
HCO3 mg/L DGW

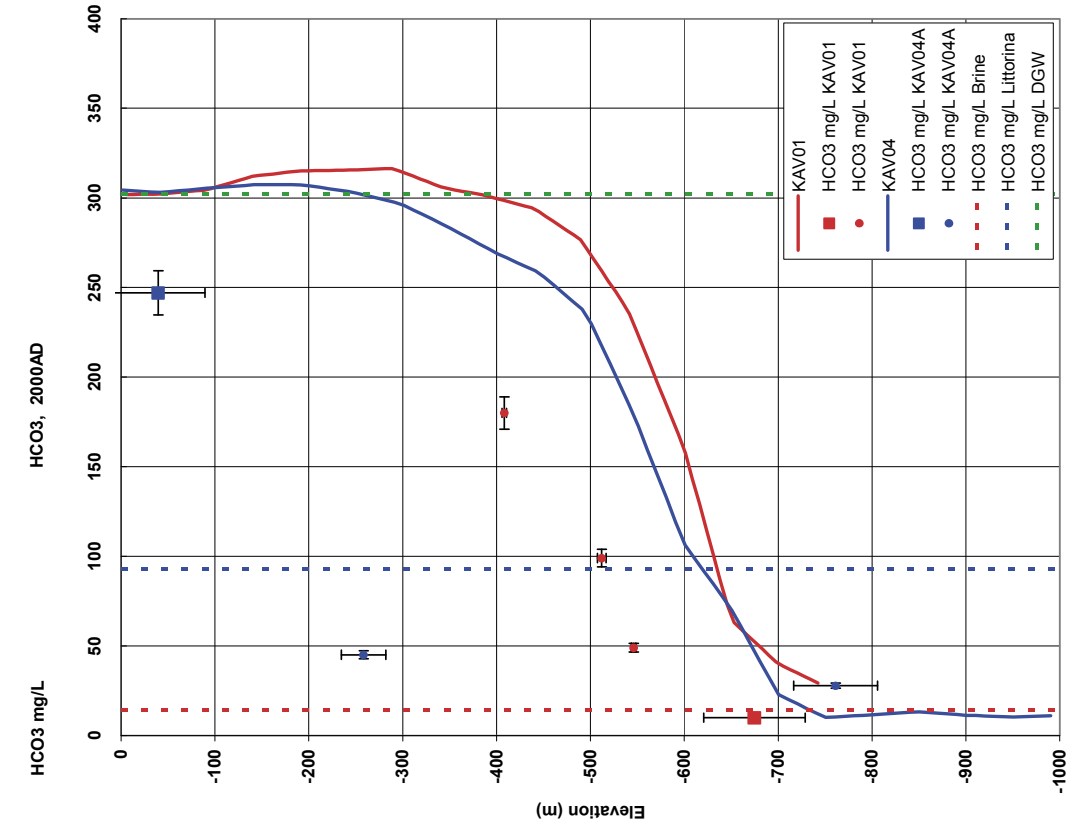
HCO3, 2000AD
HCO3 mg/L
Elevation (m)
KAV01
HCO3 mg/L KAV01
HCO3 mg/L KAV01
KAV04
HCO3 mg/L KAV04A
HCO3 mg/L KAV04A
HCO3 mg/L Brine
HCO3 mg/L Littorina
HCO3 mg/L DGW

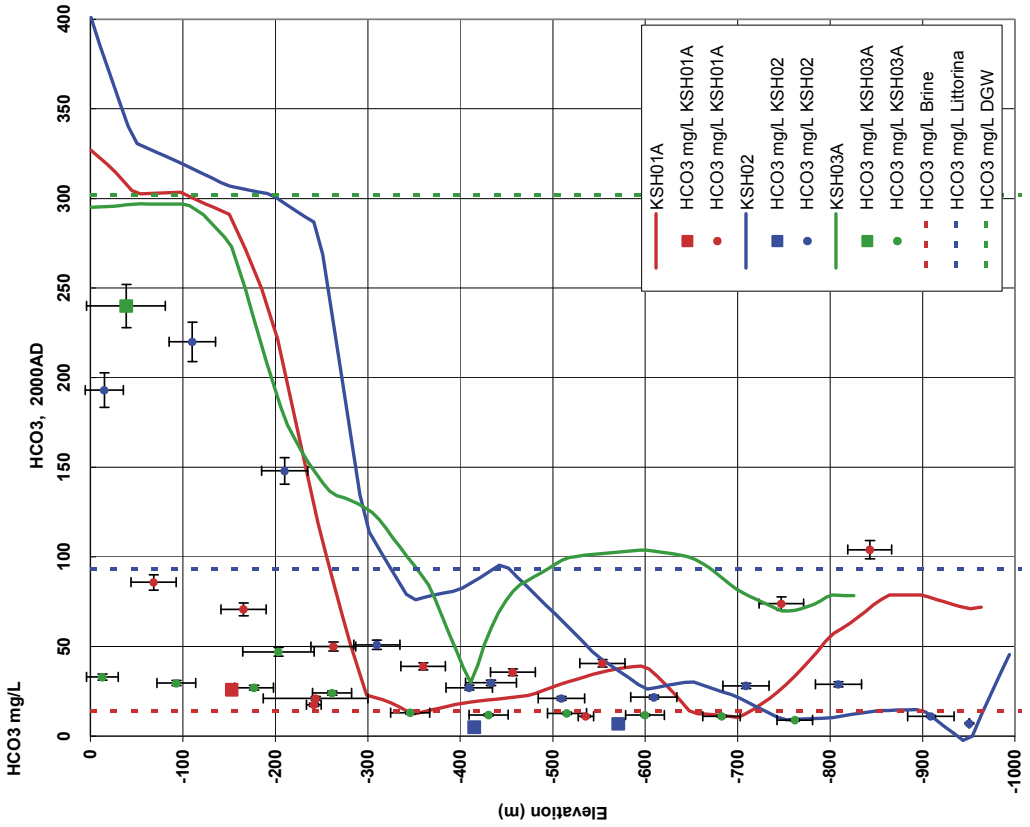
HCO3, 2000AD
HCO3 mg/L
Elevation (m)
KSH01A
HCO3 mg/L KSH01A
HCO3 mg/L KSH01A
KSH02
HCO3 mg/L KSH02
HCO3 mg/L KSH02
KSH03A
HCO3 mg/L KSH03A
HCO3 mg/L KSH03A
HCO3 mg/L Brine
HCO3 mg/L Littorina
HCO3 mg/L DGW

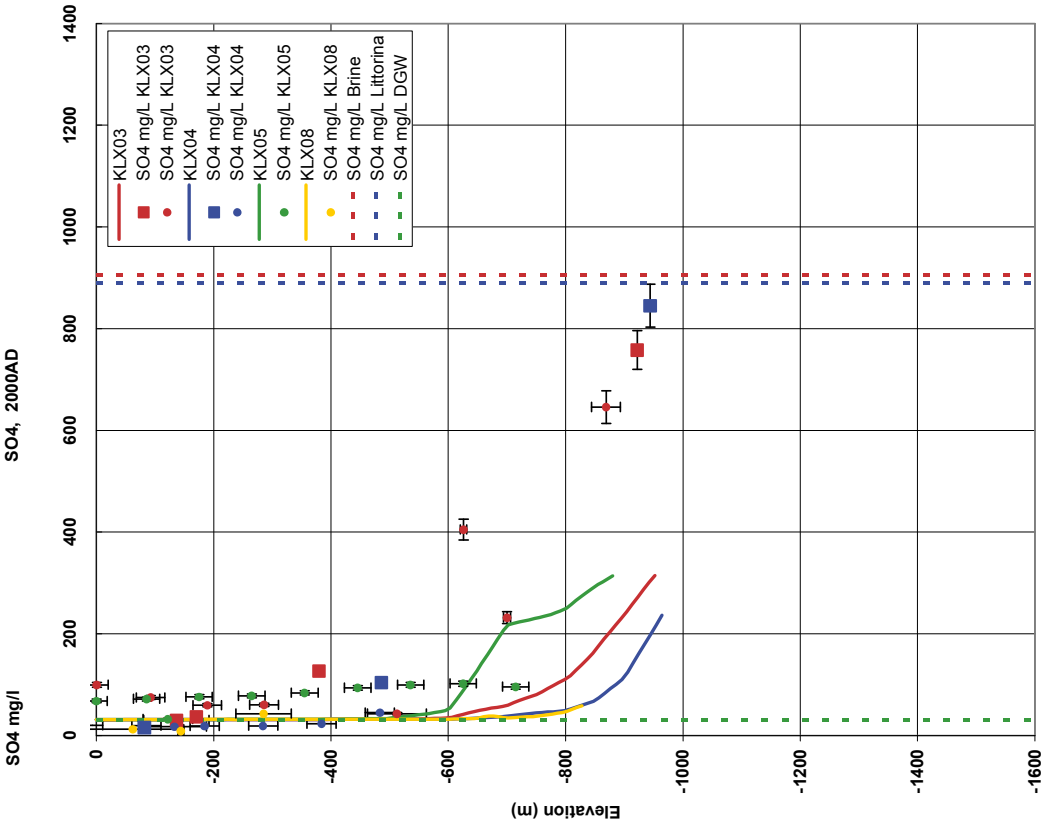
SO4, 2000AD
SO4 mg/l
Elevation (m)
KLX03
SO4 mg/L KLX03
SO4 mg/L KLX03
KLX04
SO4 mg/L KLX04
SO4 mg/L KLX04
KLX05
SO4 mg/L KLX05
KLX08
SO4 mg/L KLX08
SO4 mg/L Brine
SO4 mg/L Littorina
SO4 mg/L DGW

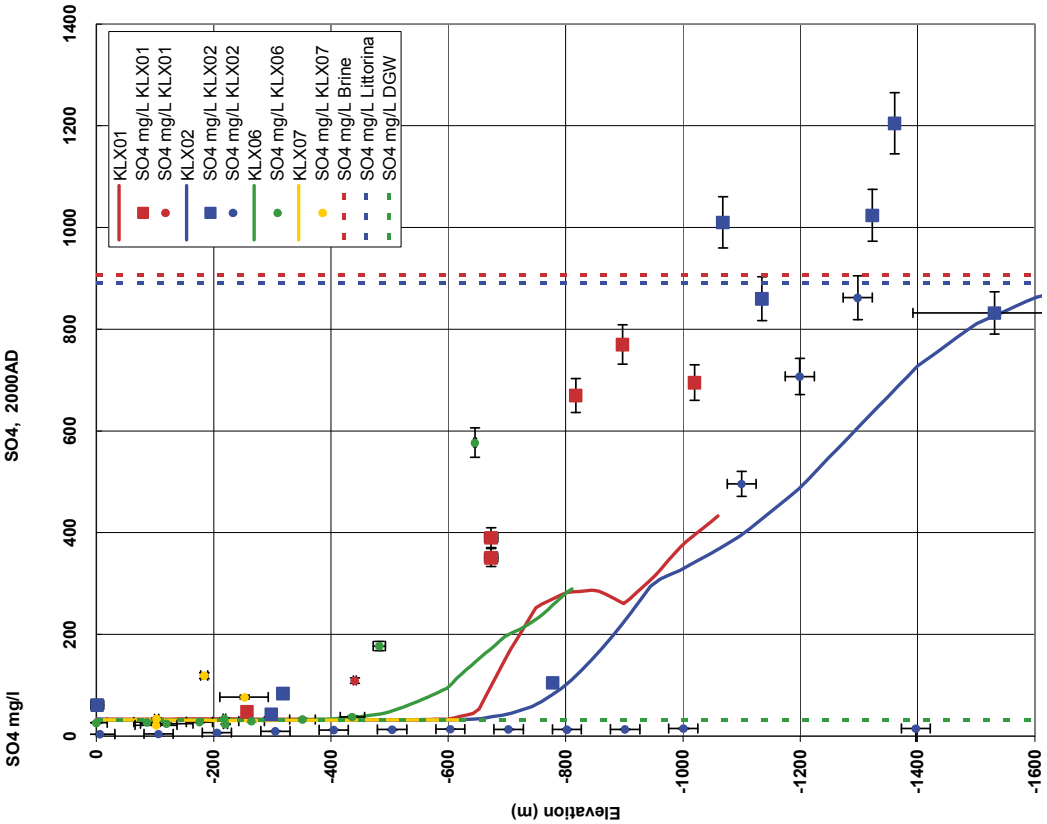
SO4, 2000AD
SO4 mg/l
Elevation (m)
KLX01
SO4 mg/L KLX01
SO4 mg/L KLX01
KLX02
SO4 mg/L KLX02
SO4 mg/L KLX02
KLX06
SO4 mg/L KLX06
KLX07
SO4 mg/L KLX07
SO4 mg/L Brine
SO4 mg/L Littorina
SO4 mg/L DGW

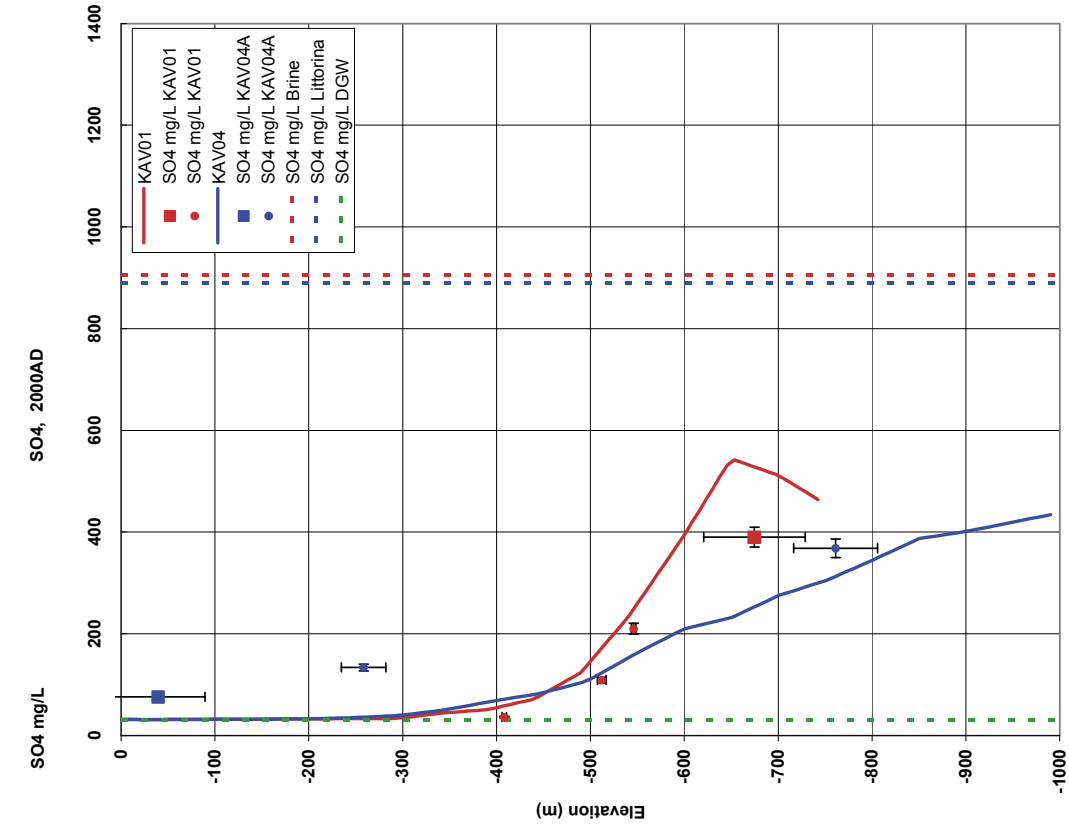
SO4 mg/L
SO4, 2000AD
Elevation (m)
KAV01
SO4 mg/L KAV01
SO4 mg/L KAV01
KAV04
SO4 mg/L KAV04A
SO4 mg/L KAV04A
SO4 mg/L Brine
SO4 mg/L Littorina
SO4 mg/L DGW

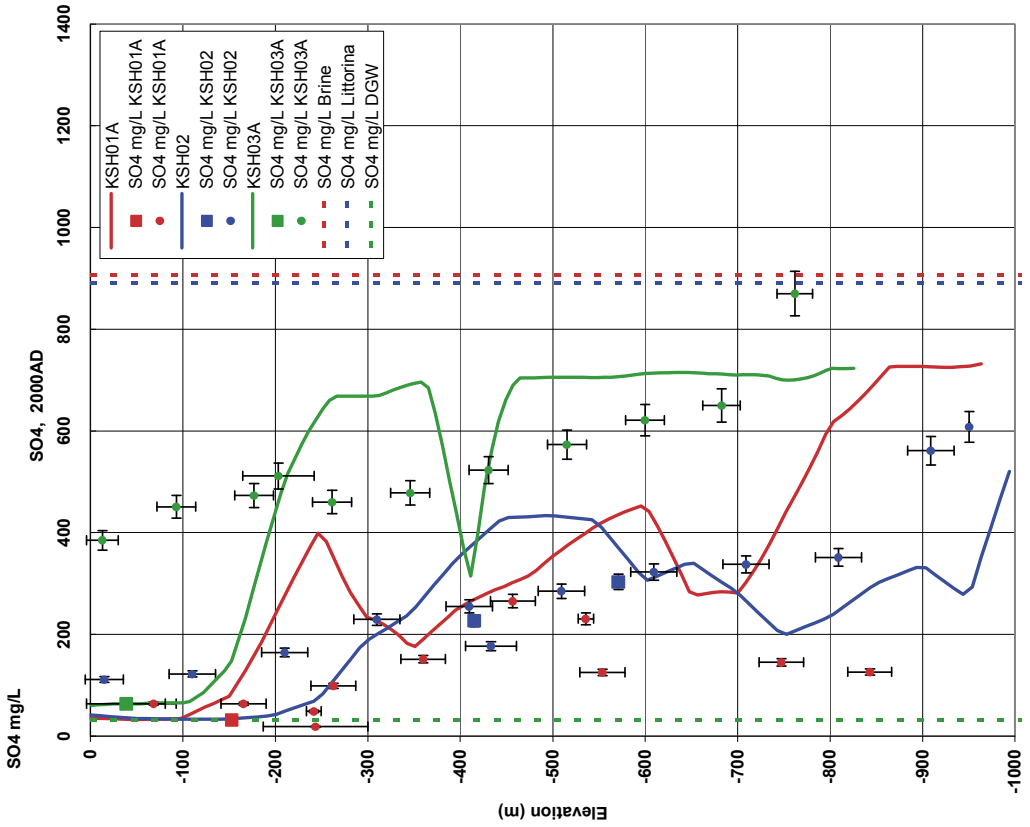
SO4 mg/L
SO4, 2000AD
Elevation (m)
KSH01A
SO4 mg/L KSH01A
SO4 mg/L KSH01A
KSH02
SO4 mg/L KSH02
SO4 mg/L KSH02
KSH03A
SO4 mg/L KSH03A
SO4 mg/L KSH03A
SO4 mg/L Brine
SO4 mg/L Littorina
SO4 mg/L DGW

Appendix C

Local Geo-DFN model of the KLX09 drill site

A local Geo-DFN model was developed for the KLX09 drill site area by Jan Hermanson and Johan Öhman, Golders Associates.

C.1 Objective

The objective of this PM is to define a local GeoDFN model of the KLX09 drill site. The approach involves two steps: 1) the identification and characterization of local fracture sets, which is followed by 2) the determination of set-specific DFN parameters. These DFN parameters are orientation distributions, size distributions and fracture intensities. Furthermore, the fracture intensity, P_{32}, is to be defined for two truncation levels:

- minimum fracture radius, *r_min* = 0.564 m, and
- minimum fracture radius, *r_min* = 1.0 m.

It should be emphasized that the GeoDFN model is valid only for the KLX09 drill site, and that it includes both open and closed fractures. It should also be noted that different possibilities of interpreting trace data are currently studied, by linking traces into larger features. Nevertheless, the size distributions used in the GeoDFN of this PM reflect non-linked trace data.

C.2 Presentation of available data from the site

Data available and spatial configuration

The near surface fracture data set consists of one outcrop (ASM100234) and five ambient boreholes (KLX09B–F). The boreholes are drilled at shallow angles and in "orthogonal" directions (see Figure C-1). The purpose of this is to provide an as complete sample of the overall fracture geometry as possible. These data were used for the calibration (and later evaluation) of the model, by constructing sampling structures used for simulated exploration (see Section C.4). In that simulated exploration, the sampling objects are given the same geometry as specified in (Table C-1).

Table C-1. Available data for the determination of the local GeoDFN model.

Sampling structure	Trend	Plunge	Upper bound[1)] [m]	Lower bound[2)] [m]	Mapped bh length[3)] [m]	Number of 25 m-sections
KLX09B	201.3	89.8	10.37	99.75	89.38	3
KLX09C	165.7	58.2	9.42	118.74	109.32	4
KLX09D	271.6	58.9	10.06	120.7	110.64	4
KLX09E	343.2	59.3	9.18	119.68	110.5	4
KLX09F	97.0	58.2	9.15	151.87	142.72	5
ASM100234[4)]	270	86				

[1)] Adjusted secup for the highest fracture with mapped orientation.

[2)] Adjusted secup for the lowest fracture with mapped orientation.

[3)] Borehole interval with fracture orientations being mapped.

[4)] The area of ASM100234 is 478.63 m^2.

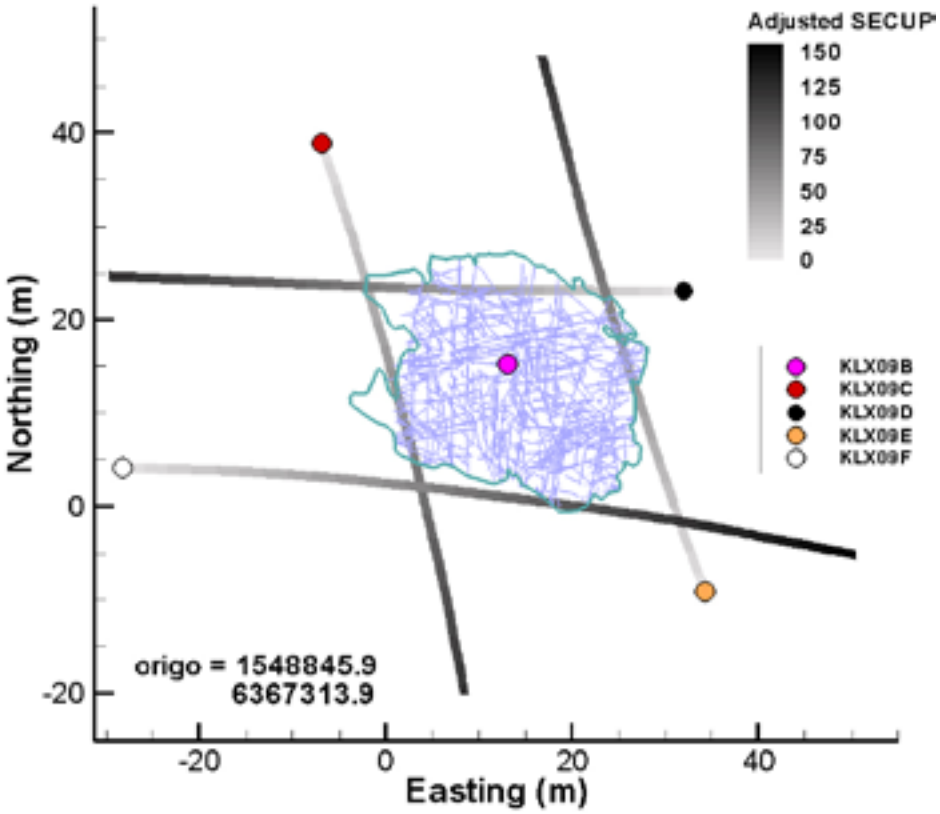

Figure C-1. *Geometry of the data types available for the KLX09 drill site (top view). Note that KLX09B is almost vertical, and that therefore its spatial extent does not show in this perspective.*

Calculation of borehole fracture frequency

Borehole fracture frequency, P_{10} [m^{-1}], was calculated over different borehole intervals for each borehole. These values are shown as functions of borehole depth (Figure C-2). Terzaghi weighing was used to compensate for the well-known sampling bias of boreholes (i.e. there is less probability in sampling fractures sub-parallel to the borehole orientation). The maximum Terzaghi correction factor was set to 5. However, it should be noted that Terzaghi correction is only used for visualization purposes. In the DFN calibration process, problems with borehole-sampling bias are circumvented by simulated exploration.

The calculation of P_{10} over 25-m borehole sections is of primary interest, as it provides convenient conditional data for the calibration of the model. The reason for calculating conditional data at the 25 m scale, is that it has been shown earlier that for the of the Laxemar subarea, RSMA, general fracture network exhibits Euclidean scaling at the 25-m scale.

Note that deformation zones have not yet been identified and that borehole data therefore may include deterministic data which do not belong in the DFN model.

C.3 Fracture orientation distributions

Examination of fracture orientations

Fracture orientation was first studied in terms of equal-area stereoplots of each data set [ASM100234, KLX09B, KLX09C, KLX09D, KLX09E, KLX09F]. The regional fracture sets are most clearly visible in the outcrop data set, while a sub-horizontal cluster is dominating in the borehole data (Figure C-3).

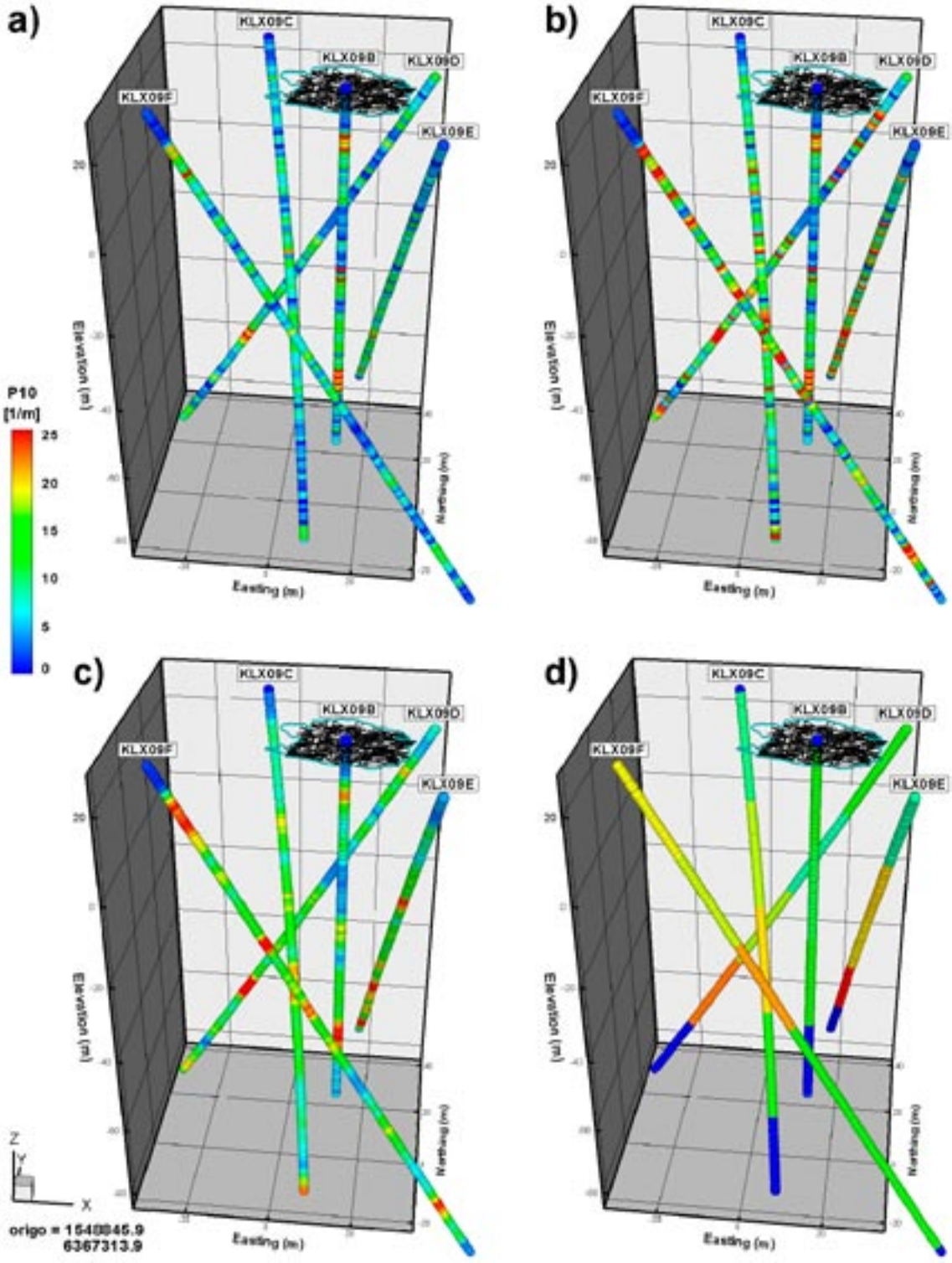

Figure C-2. *Three-dimensional visualization of borehole geometry and fracture frequency, P10 [1/m]: a) in 1-m sections, b) Terzaghi weighed frequency in 1-m sections, c) Terzaghi weighed frequency in terms of a 5-m moving average window, and d) Terzaghi weighed in 25-m sections.*

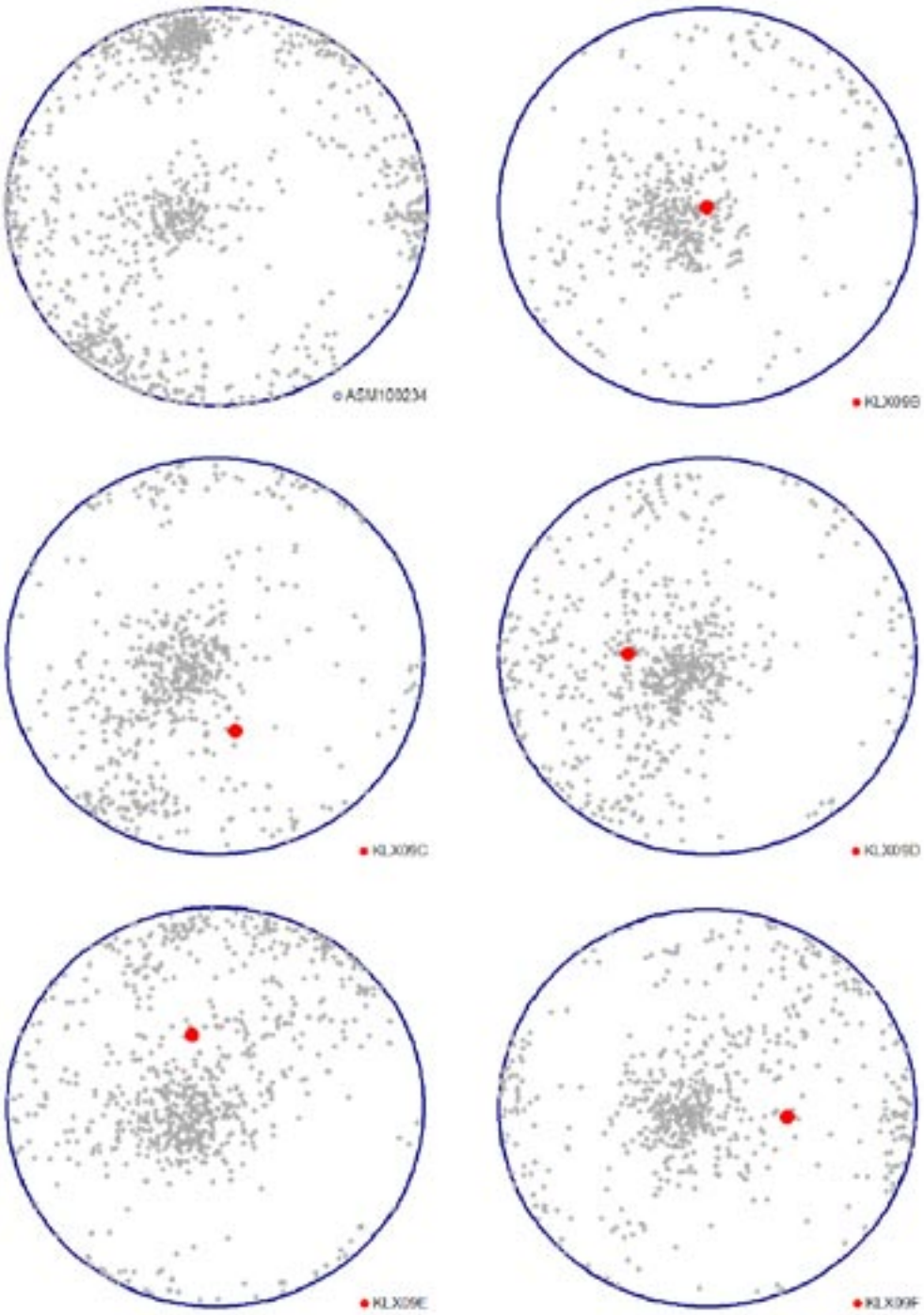

Figure C-3. *Equal-area stereoplots of outcrop and borehole data.*

Assigning fractures to Laxemar DFN model (1.2) fracture sets

Next, the fracture poles were divided into the hard-sector sets used in the derivation of the L1.2 GeoDFN model (see Table C-2) /Hermanson et al. 2005/, which were assumed to be valid for the Laxemar subarea, RSMA, in general.

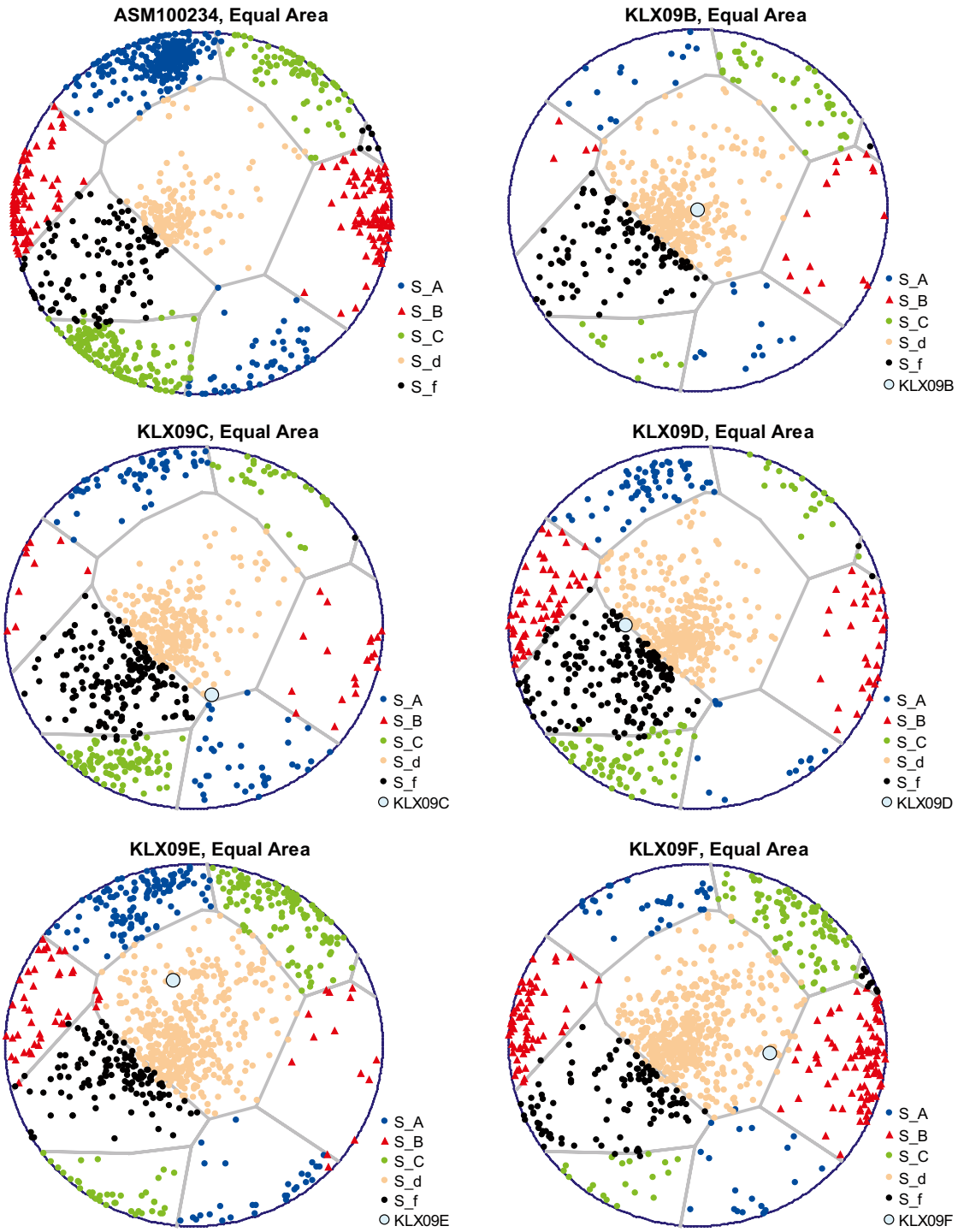

Figure C-4. *Fracture poles divided into the Laxemar subarea hard-sectors /Hermanson et al. 2005/. The fractures within S_d and S_f sectors appear to belong to the same population. Therefore new "local" sets were estimated for the current data set, where the two sets S_d and S_f are combined into a single sub-horizontal fracture set: S_df.*

Local re-interpretation of fracture sets

As sets S_d and S_f (L1.2 definitions; see /Hermanson et al. 2005/) appear to erroneously divide a fracture cluster into two, local sets were instead estimated for the KLX09 area (Figure C-5; Figure C-6; Table C-3). The procedure for determining these new sets are explained in Appendix A.

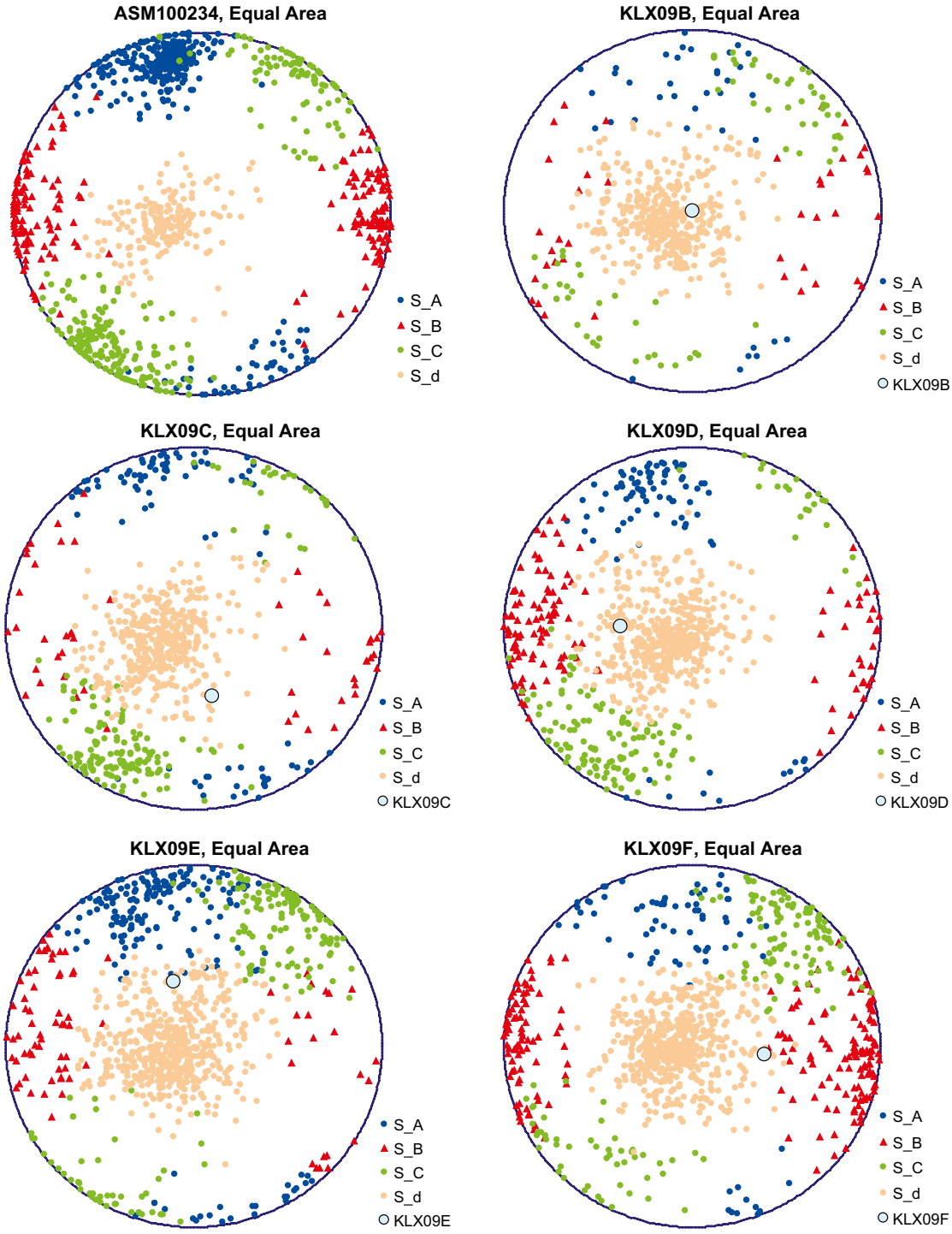

Figure C-5. *Fracture poles divided into "local" fracture sets. These sets were defined by visual fits in the FracMan/ISIS module.*

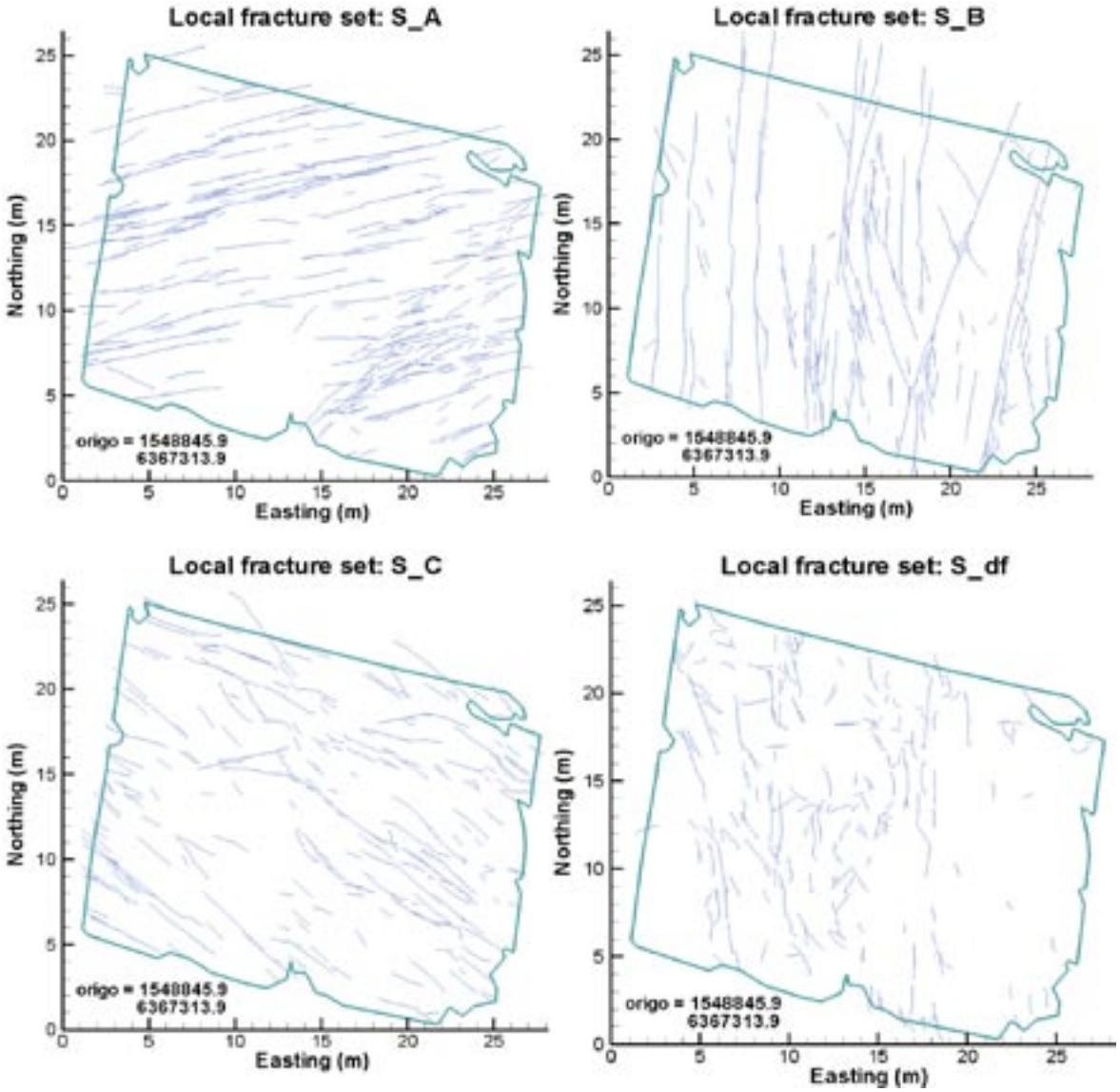

Figure C-6. *ASM100234 trace data divided into "local" soft sector set definitions (cf. Figure C-5, Table C-3).*

Table C-2. General set definitions for Laxemar subarea, RSMA, L1.2 (taken from /Hermanson et al. 2005/).

Fracture set	Trend	Plunge	Fisher κ	No. fractures in outcrop	No. fractures in boreholes
S_A	338	5	13	393	409
S_B	100	0	20	199	373
S_C	212	1	10	250	557
S_d	3	62	10	164	2,075
S_f	243	24	24	122	778

Table C-3. Local set definitions estimated for the KLX09-drilling-site data.

Fracture set	Orientation			Data	
	Trend	Plunge	Fisher κ	No. fracts in outcrop	No. fracts in borehole
S_A	350	12	19	397	464
S_B	92	1	17	231	499
S_C	213	5	13	293	712
S_df	250	77	15	207	2,517

An overall comparison between the L1.2 set definitions and the "local" KLX09 set definitions is shown in Figure C-7 and Figure C-8. These two figures also demonstrated that weighing outcrop orientation data by trace length, significantly enhances the appearance of mean poles, which supports the local set definitions.

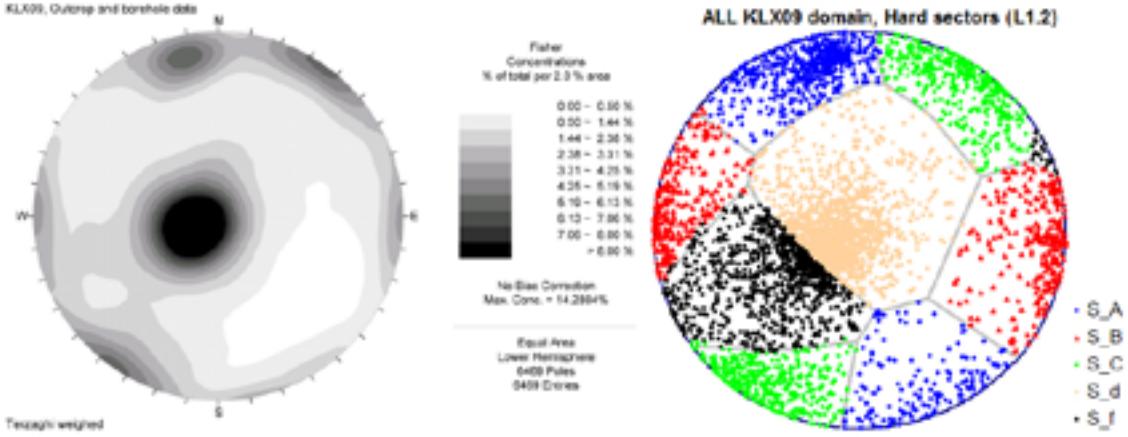

Figure C-7. *Terzaghi corrected stereoplot contours (left) and hard-sector divided orientation data (right), according to the overall Laxemar DFN model L1.2 (see Table C-2).*

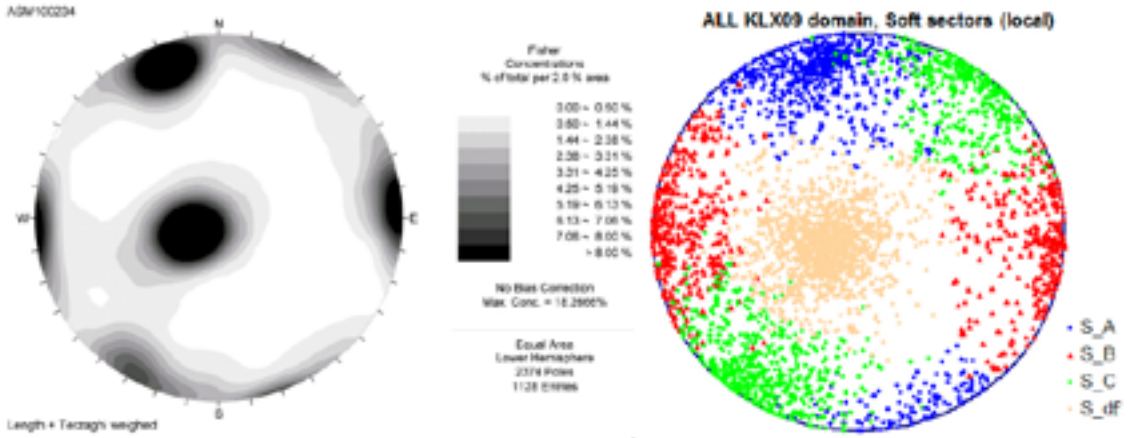

Figure C-8. *Terzaghi corrected and trace-length weighed stereoplot contours (left) and soft-sector divided orientation data (right), according to the local KLX09 DFN model (see Table C-3). Note that the lower contoured stereoplot involves weighing according to trace length (after a trace-linking procedure; see Section C.5).*

C.4 Model calibration: local DFN model of the KLX09 drill site

Preparation of conditional data

Having defined the local fracture sets in Section C.3, the borehole fracture intensity data (Figure C-2) were divided into set-specific P_{10} values, defined over 25 m-borehole sections (Table C-4). These were used as conditional data for the calibration process of the DFN model.

Note that deformation zones have not yet been identified in boreholes. Therefore these borehole data may contain data which should be excluded from the DFN model.

Similarly, aerial set-specific fracture intensities, P_{21} [m/m^2], could be calculated for the outcrop data (Figure C-6; Table C-5). Note that for the calculation of P_{21}, all mapped trace-sections extending beyond the 478.63 m^2-area (green line in Figure C-6) were removed from the calculations.

Table C-4. Set-specific borehole fracture intensity data in the KLX09-area.

P10 [m^{-1}] 25 m borehole\section	S_A	S_B	S_C	S_df
KLX09B(1)	0.36	0.44	0.8	4.24
KLX09B(2)	0.36	0.08	0.68	4.36
KLX09B(3)	0.40	1.08	1.16	6.44
KLX09C(1)	0.68	0.64	0.64	4.24
KLX09C(2)	0.88	0.2	2.4	4.8
KLX09C(3)	0.64	0.36	2.12	5.04
KLX09C(4)	0.96	0.56	0.84	1.96
KLX09D(1)	0.56	1.4	0.88	3.64
KLX09D(2)	0.16	0.32	0.8	4.84
KLX09D(3)	0.92	0.72	2.52	5.00
KLX09D(4)	1.04	1.8	1.04	4.40
KLX09E(1)	0.76	0.32	1.08	3.96
KLX09E(2)	1.76	0.32	2.04	4.12
KLX09E(3)	1.44	0.6	2	4.92
KLX09E(4)	2.28	1.12	1.16	7.32
KLX09F(1)	0.4	1.96	1.64	6
KLX09F(2)	0.48	1.12	1.52	4.12
KLX09F(3)	0.44	1.2	1.48	5.96
KLX09F(4)	0.56	1.16	0.52	2.32
KLX09F(5)	0.68	1.76	0.56	2.4

Table C-5. Set-specific outcrop fracture intensity data in the KLX09-area.

P_{21} [m^{-1}]	S_A	S_B	S_C	S_df
ASM100234	1.233	0.934	0.852	0.523

The DFN model parameters were calibrated by trial and error. Multiple realizations of fracture networks were generated within a 25 × 25 × 30 m^3 domain, and its characteristics in terms of P_{10} (25 m-scale), P_{21} and size distribution, were quantified by simulated exploration using synthetic boreholes and trace planes (see Figure C-9) with identical geometries and scales to the conditional data. In order to reduce simulation time, 9 replicas of each borehole (i.e. total 5 × 9 = 45) and 5 trace planes were used. The calibration process was iterated until the differences between results of simulated exploration and the real field data (conditional data) were minimized.

Size distribution and fracture intensities were calibrated so as to minimize the differences between the traces computed from the new local DFN through simulated exploration and the outcrop and borehole data recorded at KLX09. In order to simultaneously match $P_{10,}$ P_{21} and size distribution data, the minimum fracture radius, r^*_{min}, was used as a fitting parameter. This minimum radius was allowed to be small, although not less than borehole radius (0.04 m). The reason for this lower bound is that this is the minimum fracture size that can fully intersect the borehole core, and only such fractures are included in the conditional data set.

A simultaneous match to these three types of data builds confidence in the parameterization of the DFN model; however such a model is unfeasible for modeling purposes (as it includes too many small fractures, which are often are less significant for many processes being modeled). Therefore fracture intensity is specified for three cases:

2) the best fit truncation of the fracture network ($r_{min} = r^*_{min}$),
3) truncation of all fractures less than 1 m^2 ($r_{min} = 0.564$), and
4) truncation of all fractures with side-length or radius less than 1 m ($r_{min} = 1.0$ m).

The results are summarized in Table C-6 below.

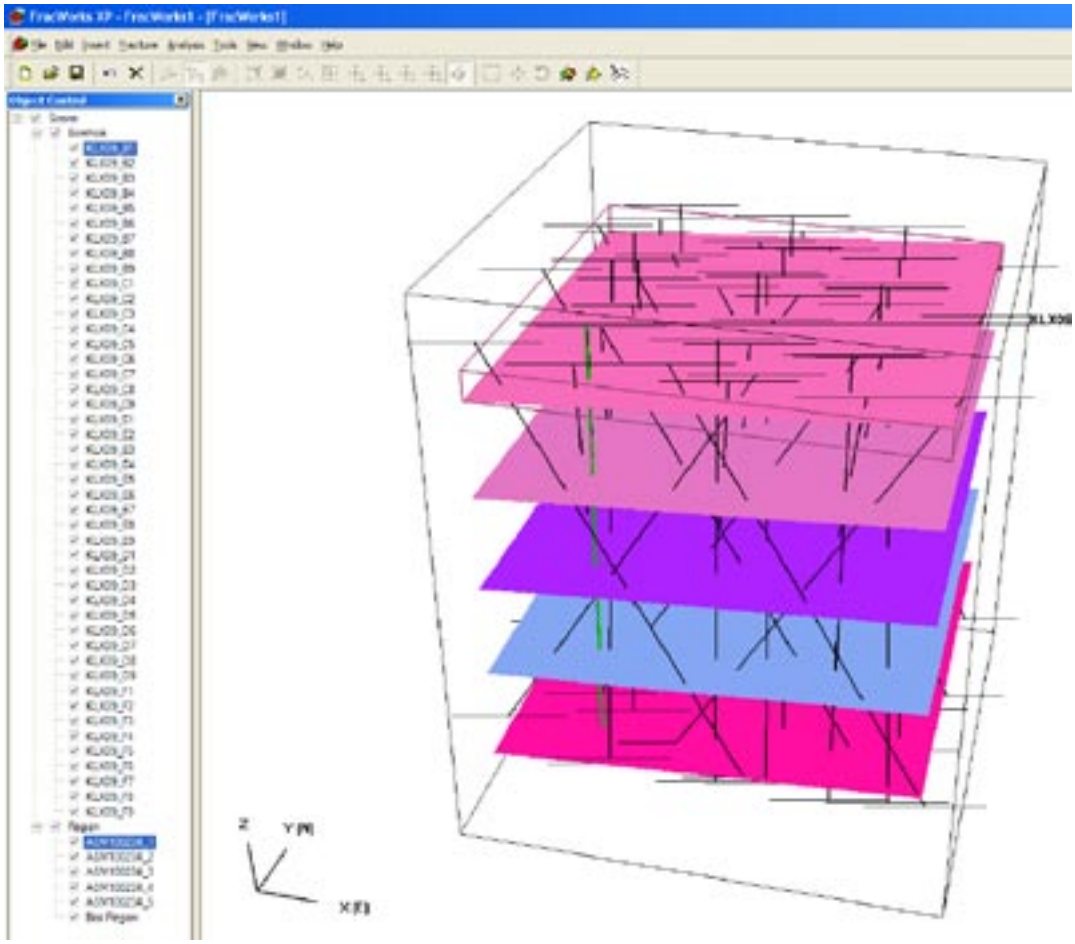

Figure C-9. *Sampling structures used to calibrate (and later evaluate) the local KLX09 DFN model: 5 trace planes and 45 boreholes. (Geometry of sampling structures according to Table C-1).*

Table C-6. Calibrated parameters for local KLX09 DFN model.

Fracture set	Orientation			Size		Intensity		
	Trend	Plunge	Fisher κ	k_r	r^*_{min} [m]	$P_{32}(r_{min} = r^*_{min})$ [m^2/m^3]	$P_{32}(r_{min} = 0.564)$ [m^2/m^3]	$P_{32}(r_{min} = 1.0)$ [m^2/m^3]
S_A	350	12	19	2.35	0.11	2.40	1.03	0.64
S_B	92	1	17	1.8	0.04	1.90	1.18	0.93
S_C	213	5	13	2.5	0.04	1.18	0.65	0.43
S_df	250	77	15	2.6	0.065	5.48	0.94	0.48

Evaluation of fitted local DFN model

The agreement in size distribution between simulated trace-plane exploration and outcrop data are demonstrated in Figure C-10 and Figure C-11.

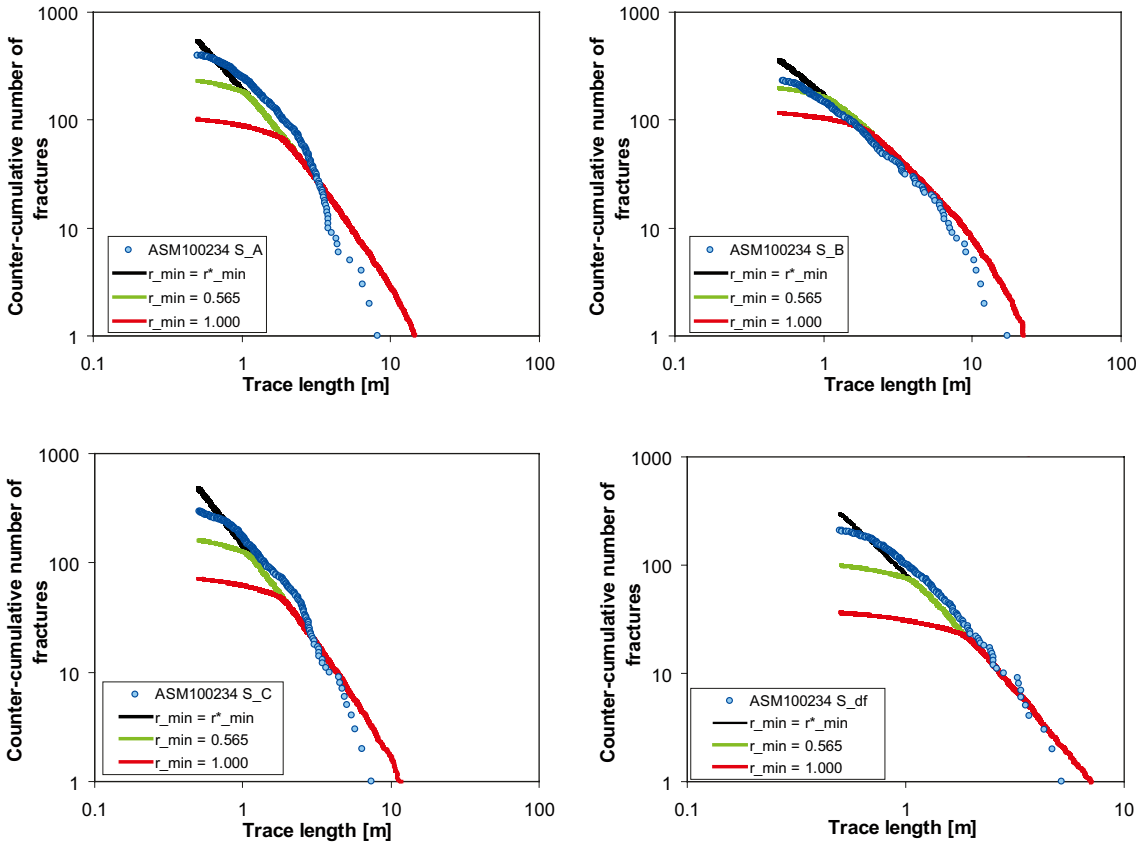

Figure C-10. *Set-specific size distributions obtained from simulated trace-plane exploration, arising from the three different cases of truncation radii, r_{min} (parameters specified in Table C-6). Simulated exploration agrees well with data, at least for the case $r_{min} = r^*_{min}$.*

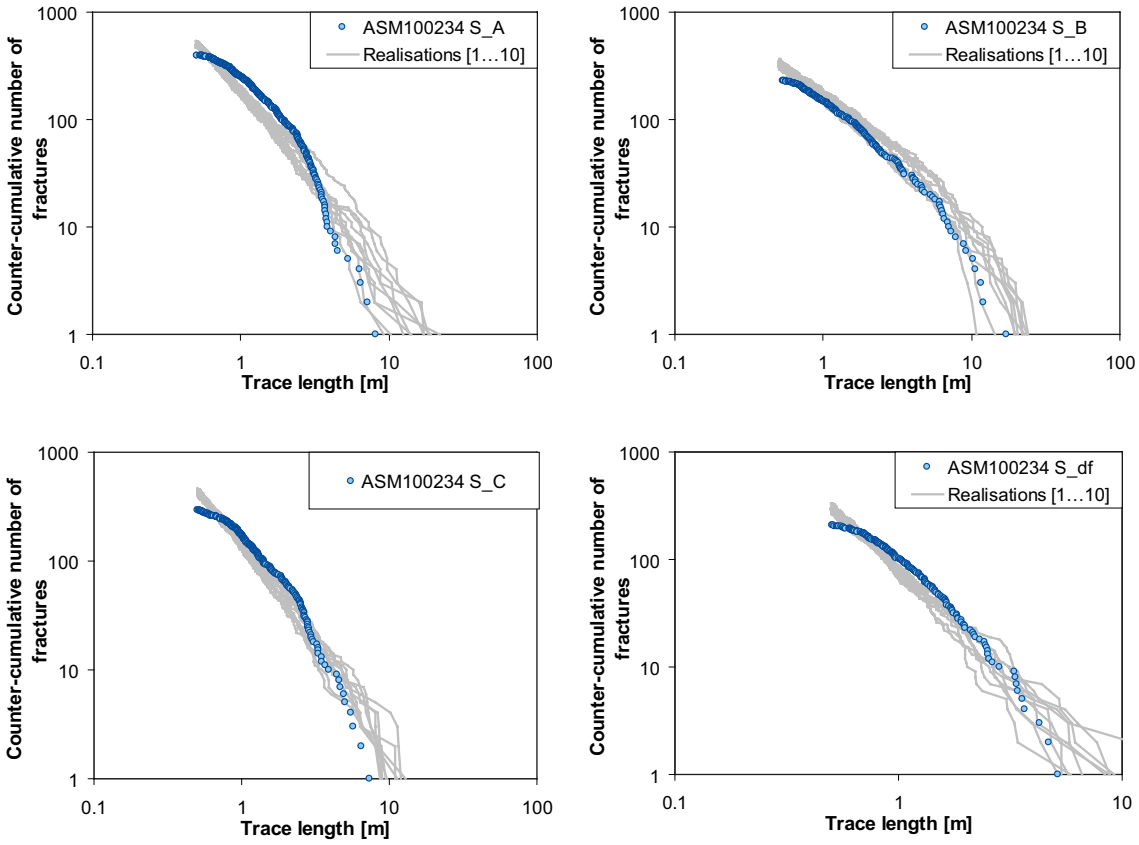

Figure C-11. *Ten size-distribution realizations run for each set (for $r_{min} = r^*_{min}$; see Table C-6).*

The match in fracture intensity between simulated exploration (trace planes and synthetic boreholes) and conditional data (outcrop and boreholes) are demonstrated in Figure C-12.

It should be noted that a perfect match would correspond to all points falling onto the target 1:1 slope. A data set with lower slope means that the model under-estimates variability in data (for example the range in P_{10} of S_df in KLX09F) and vice-versa for high slopes.

The mean of each data set (Table C-4) fall onto the 1:1 slope, although not all data points within a data set do. That is an indication that the variability of mean borehole P_{10} can be predicted, whereas its variability cannot. This is not surprising as in its current form deformation-zone data has not yet been excluded from the P_{10} data. It is also of interest to see that the relative orders of set-specific intensities, which vary with borehole orientations, are well predicted. The overestimation in P_{21} is due to the differences in size distributions for short fractures.

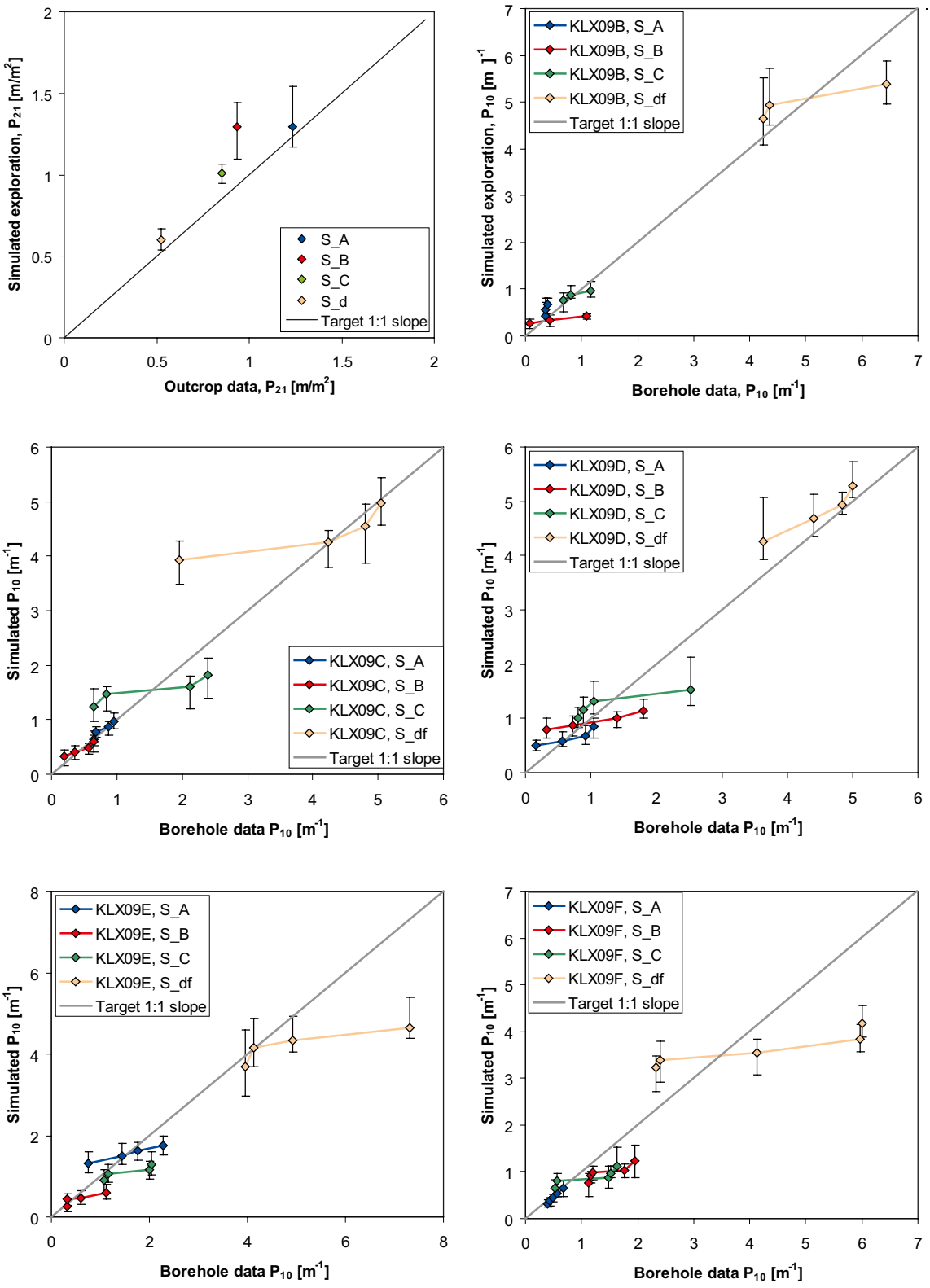

Figure C-12. *Cross-plots between simulated exploration results and conditional data: set-specific fracture intensity data in outcrop and in 25 m-borehole sections. Note that the target is that points should fall onto the 1:1 slope. A data set with lower slope means that the model under-estimates variability in data (for example the range in P10 of S_df in KLX09F).*

C.5 Addendum on linking traces, ASM100234

No statistically significant sets could be determined for the local sets of KLX09, by using the automatic fits in the FracMan/ISIS module /Dershowitz et al. 1998/. Therefore it was decided that the sets were to be estimated by visual fits.

The following procedure was pursued:

- Sequentially located, semi-parallel traces with closely located endpoints were linked to potentially form longer features.
- The orientation data was weighed by their trace lengths.
- The mean poles of fracture sets were estimated from trace data (i.e. primarily based on long features).

The rationale for this approach is an assumption that large traces deviate less from its set-mean-angle, and thereby serve as better estimators of the set mean pole. The linking procedure will be explained elsewhere – only its results are shown here (see figures).

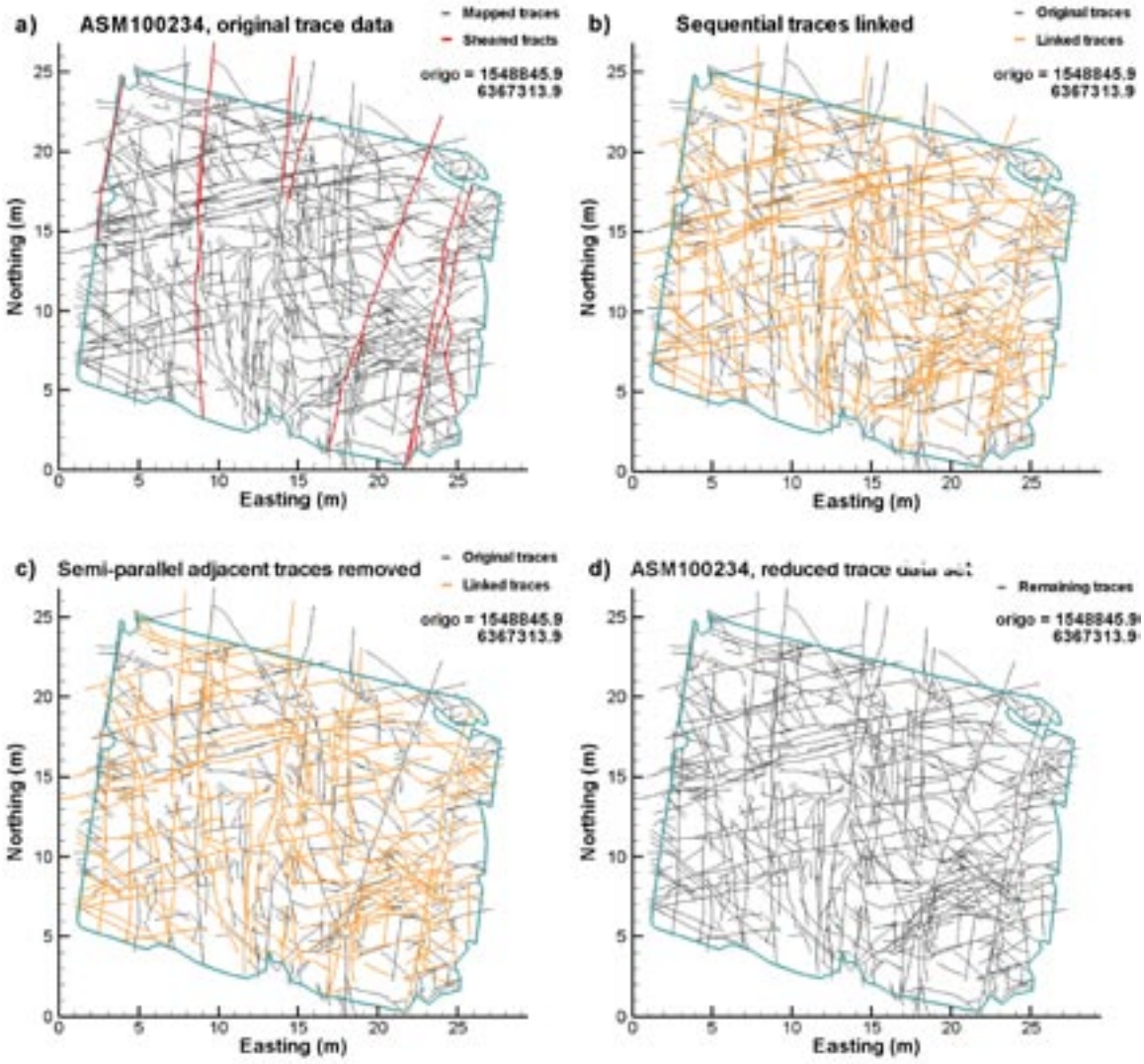

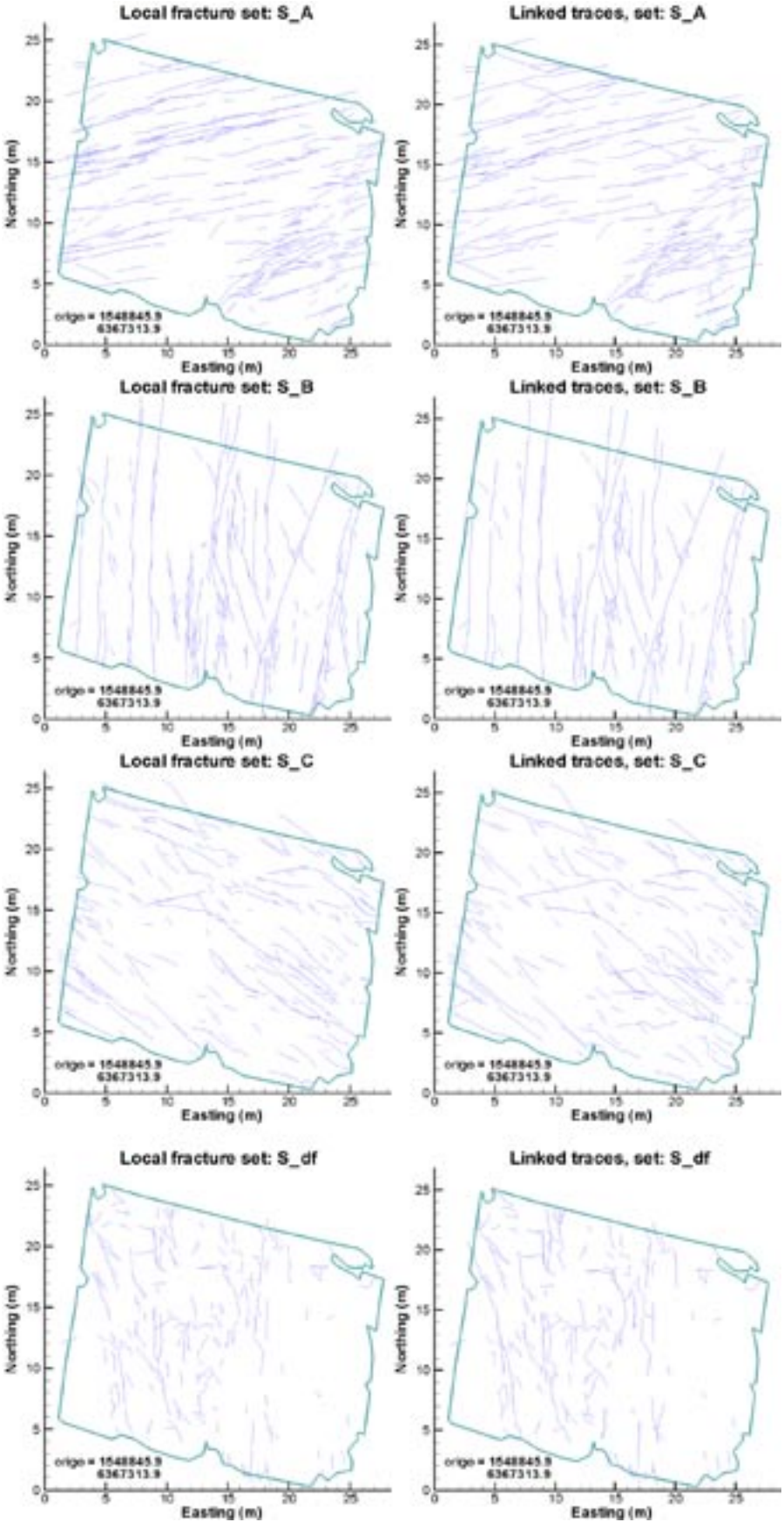
Local fracture set: S_A
Linked traces, set: S_A
Local fracture set: S_B
Linked traces, set: S_B
Local fracture set: S_C
Linked traces, set: S_C
Local fracture set: S_df
Linked traces, set: S_df
Northing (m)
Easting (m)
origo = 1548845.9
6367313.9

Effect on size distribution.

NOTE THAT: the size distribution of the current DFN model reflect non-linked trace lengths.

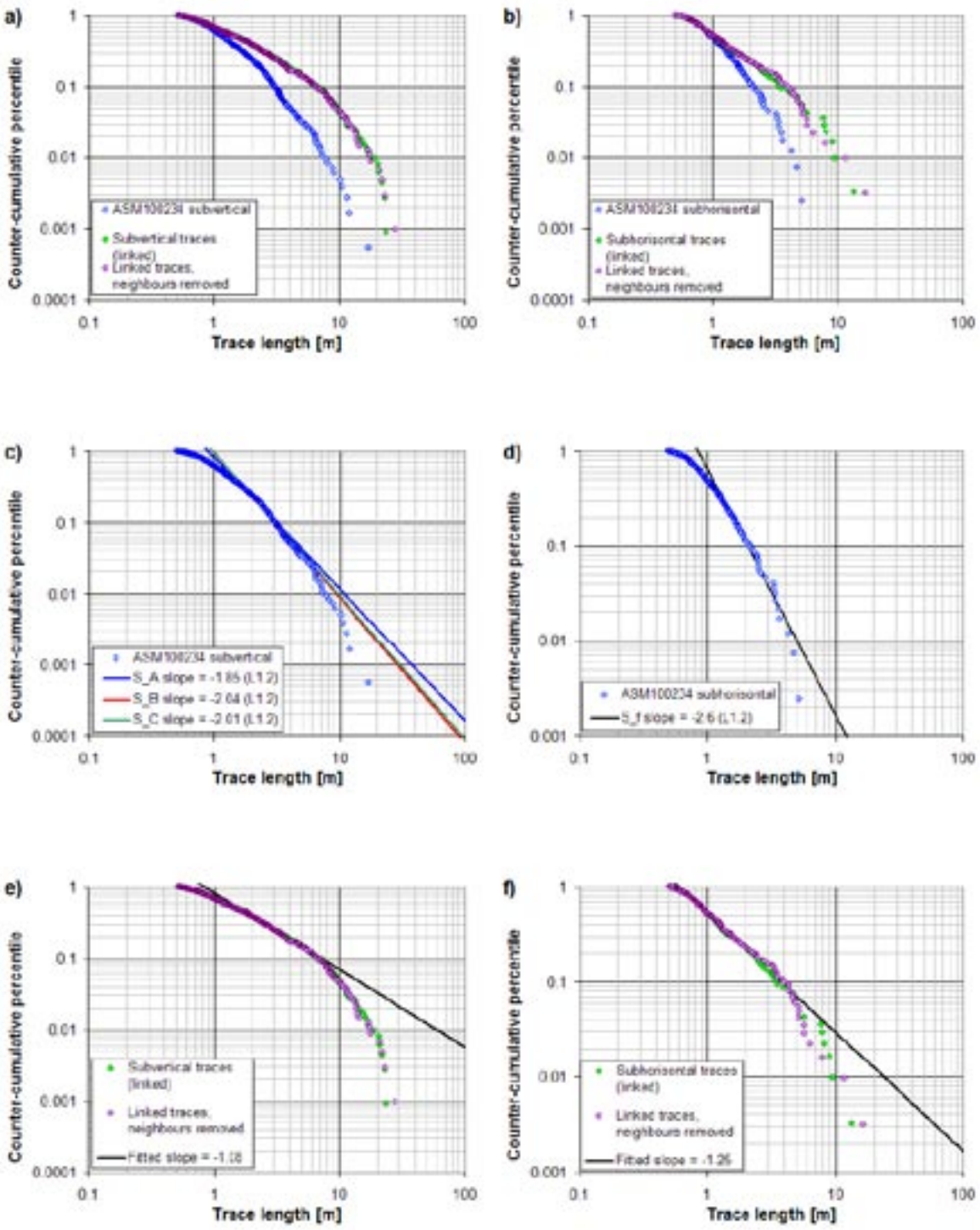

Appendix D

Additional results from KLX09B–F simulations

Here, some additional details of results used in calibrating the Hydro-DFN against hydraulic test data are presented.

D.1 Single hole PFL-f results

Figure D-1 to Figure D-5 give comparison of measured PFL-f flow-rates to the mean simulated flows averaged over 10 realisations for the individual abstraction boreholes KLX09B to KLX09F. The corresponding plots for the numbers and magnitudes of flows within each fracture set for boreholes KLX09B to KLX09F are given in Figure D-6 to Figure D-8. Plots are shown just for the BH_DZ_opt fracture size model and for the semi-correlated transmissivity relationship. The plots of flow-rate distribution illustrate that there is significant variation in the distribution of flow-rates between the boreholes, around an order magnitude in terms of total flow. The realisations are not conditioned to the flow-rate of each particular borehole, and hence individual realisation are likely to reproduce the variability between boreholes, but the distribution shown here are based on taking averages over 10 realisations, and therefore indicate a much smoother distribution than either the data or an individual model realisation. Figure D-6 to Figure D-8 for the individual sets show that the predictions of the numbers of flows in each set for each borehole are in remarkably good agreement considering that each borehole has a quite distinct trajectory and the stochastic nature of fracture occurrence. This suggests the fracture set orientation definitions suggest by the Geo-DFN analysis accurately reflect fracture orientations.

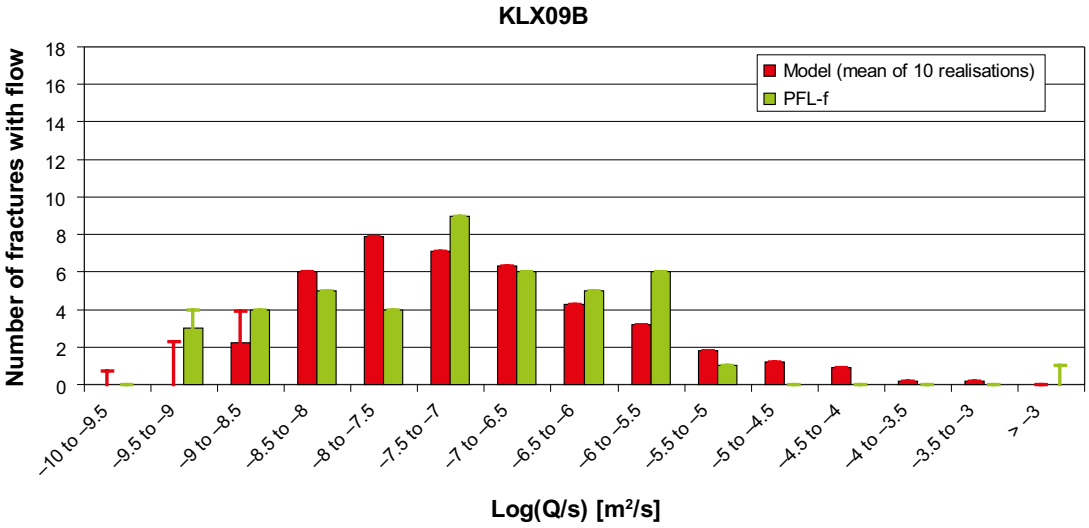

Figure D-1. *A comparison of the distributions of individual fracture inflows, Q/s, for the PFL-f measurements from KLX09B against the mean over 10 realisations of the BH_DZ_opt fracture size model and a semi-correlated transmissivity to size. For the PFL-f data, the error bars indicate values close to the detection limit which are estimated. For the model, the error bars indicate predicted flows below the measurement limit.*

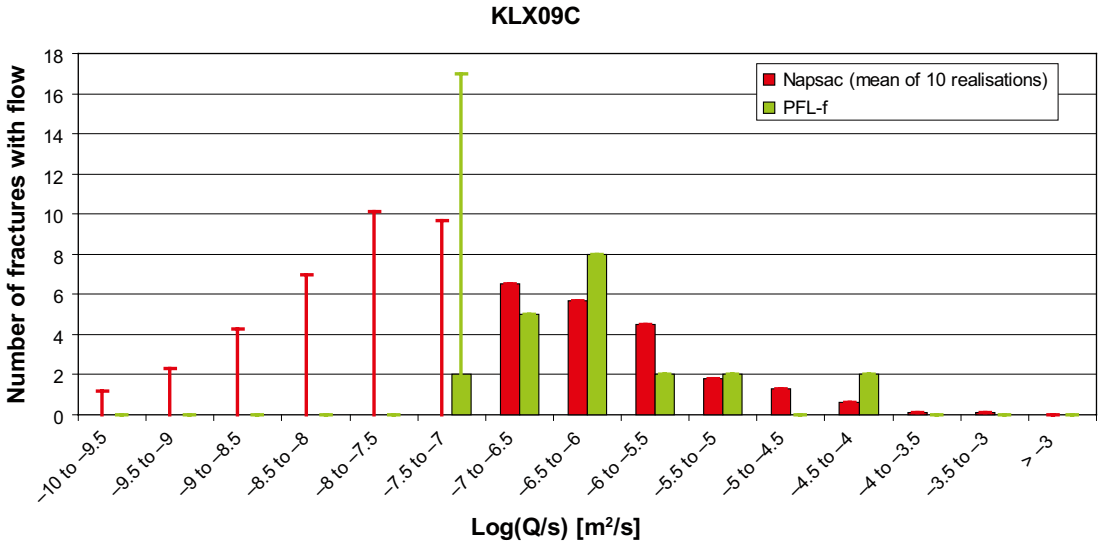

Figure D-2. *A comparison of the distributions of individual fracture inflows, Q/s, for the PFL-f measurements from KLX09C against the mean over 10 realisations of the BH_DZ_opt fracture size model and a semi-correlated transmissivity to size. For the PFL-f data, the error bars indicate values close to the detection limit which are estimated. For the model, the error bars indicate predicted flows below the measurement limit.*

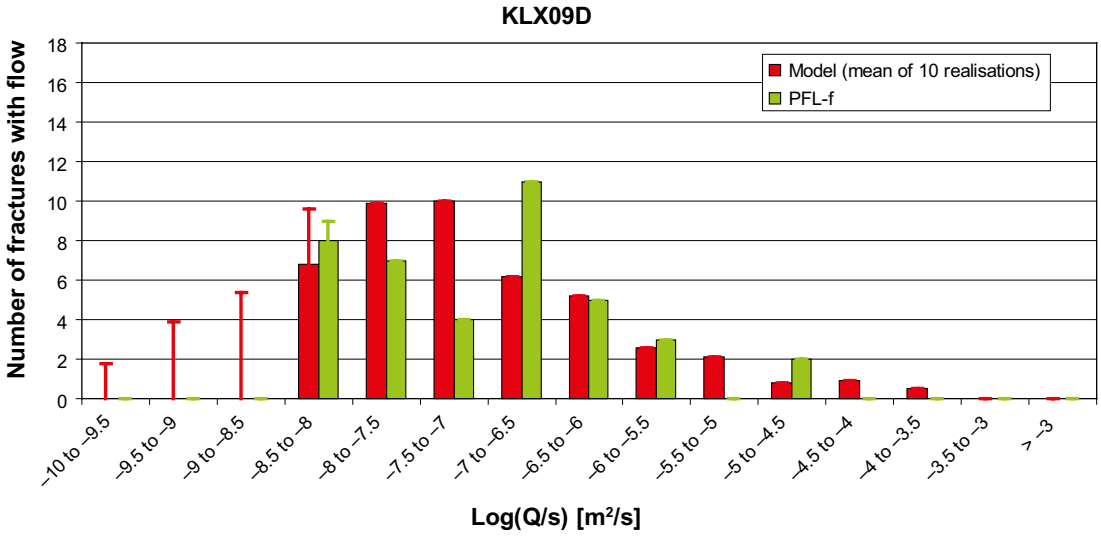

Figure D-3. *A comparison of the distributions of individual fracture inflows, Q/s, for the PFL-f measurements from KLX09D against the mean over 10 realisations of the BH_DZ_opt fracture size model and a semi-correlated transmissivity to size. For the PFL-f data, the error bars indicate values close to the detection limit which are estimated. For the model, the error bars indicate predicted flows below the measurement limit.*

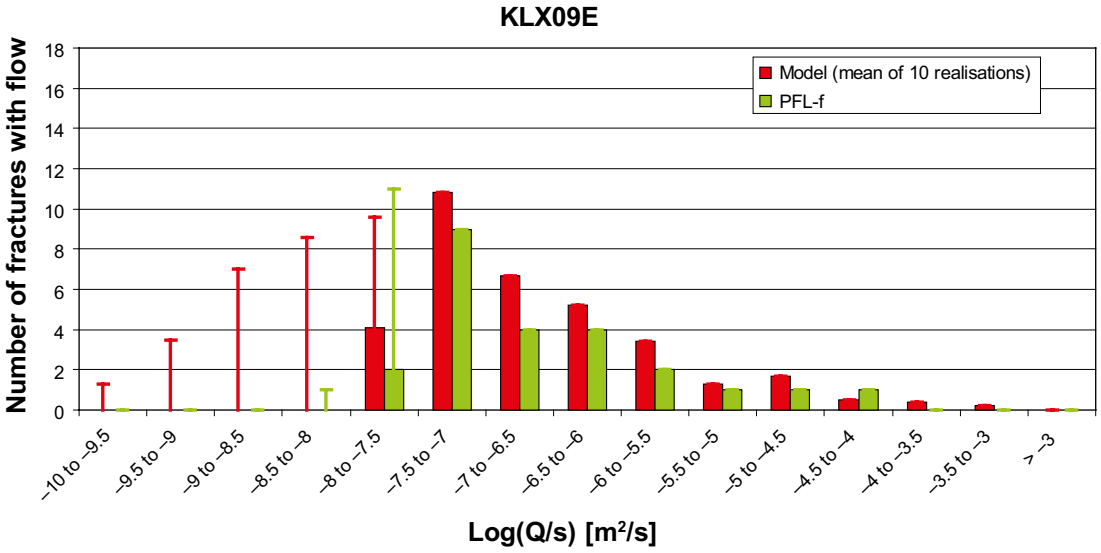

Figure D-4. *A comparison of the distributions of individual fracture inflows, Q/s, for the PFL-f measurements from KLX09E against the mean over 10 realisations of the BH_DZ_opt fracture size model and a semi-correlated transmissivity to size. For the PFL-f data, the error bars indicate values close to the detection limit which are estimated. For the model, the error bars indicate predicted flows below the measurement limit.*

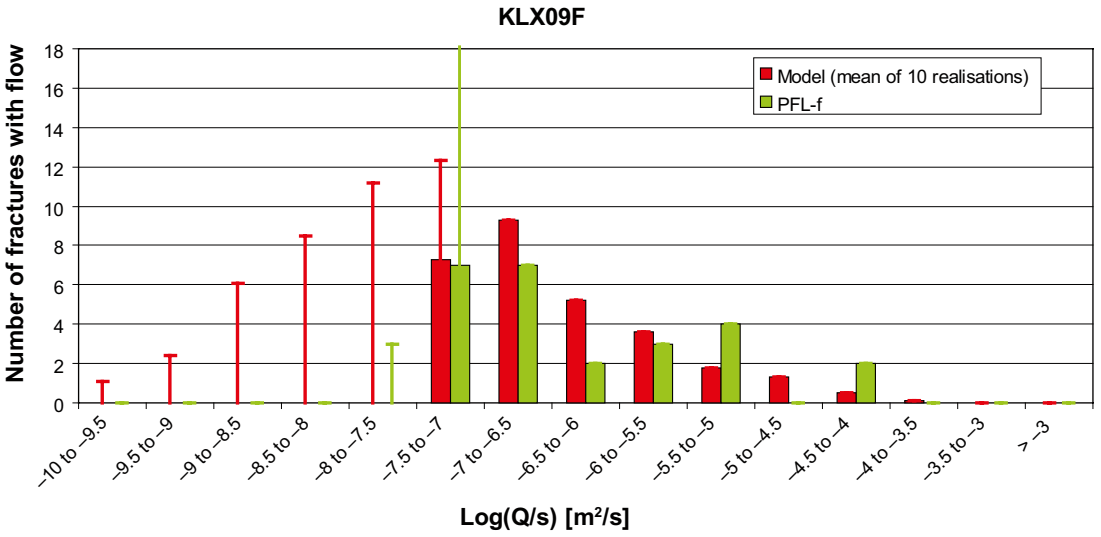

Figure D-5. *A comparison of the distributions of individual fracture inflows, Q/s, for the PFL-f measurements from KLX09F against the mean over 10 realisations of the BH_DZ_opt fracture size model and a semi-correlated transmissivity to size. For the PFL-f data, the error bars indicate values close to the detection limit which are estimated. For the model, the error bars indicate predicted flows below the measurement limit.*

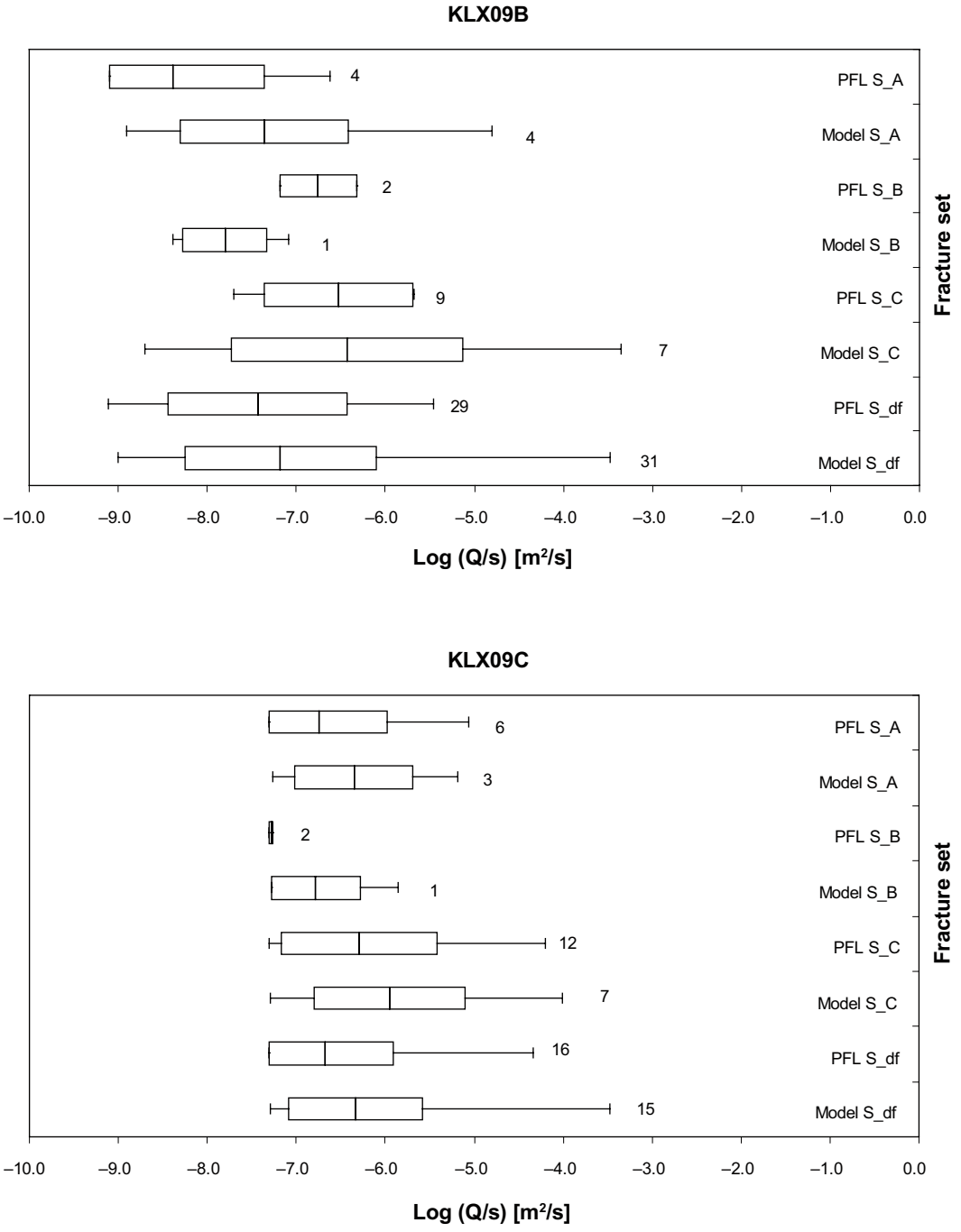

Figure D-6. *Bar and whisker plots comparing statistics taken over each fracture set for the individual inflows, Q/s, for the PFL-f measurements against the mean over 10 realisations of the BH_DZ_opt fracture size model. The centre of the bar indicates the mean value, the ends of the bar indicate ± 1 standard deviation, and the error bars indicate the minimum and maximum values. The total numbers of fractures with inflow above the detection limits within each set are also given. For the PFL-f data, the statistics are taken over the identified flow-anomalies within each set, and over the fractures generated within each set and over 10 model realisations. The semi-correlated transmissivity model is shown. Top: KLX09B; Bottom: KLX09C.*

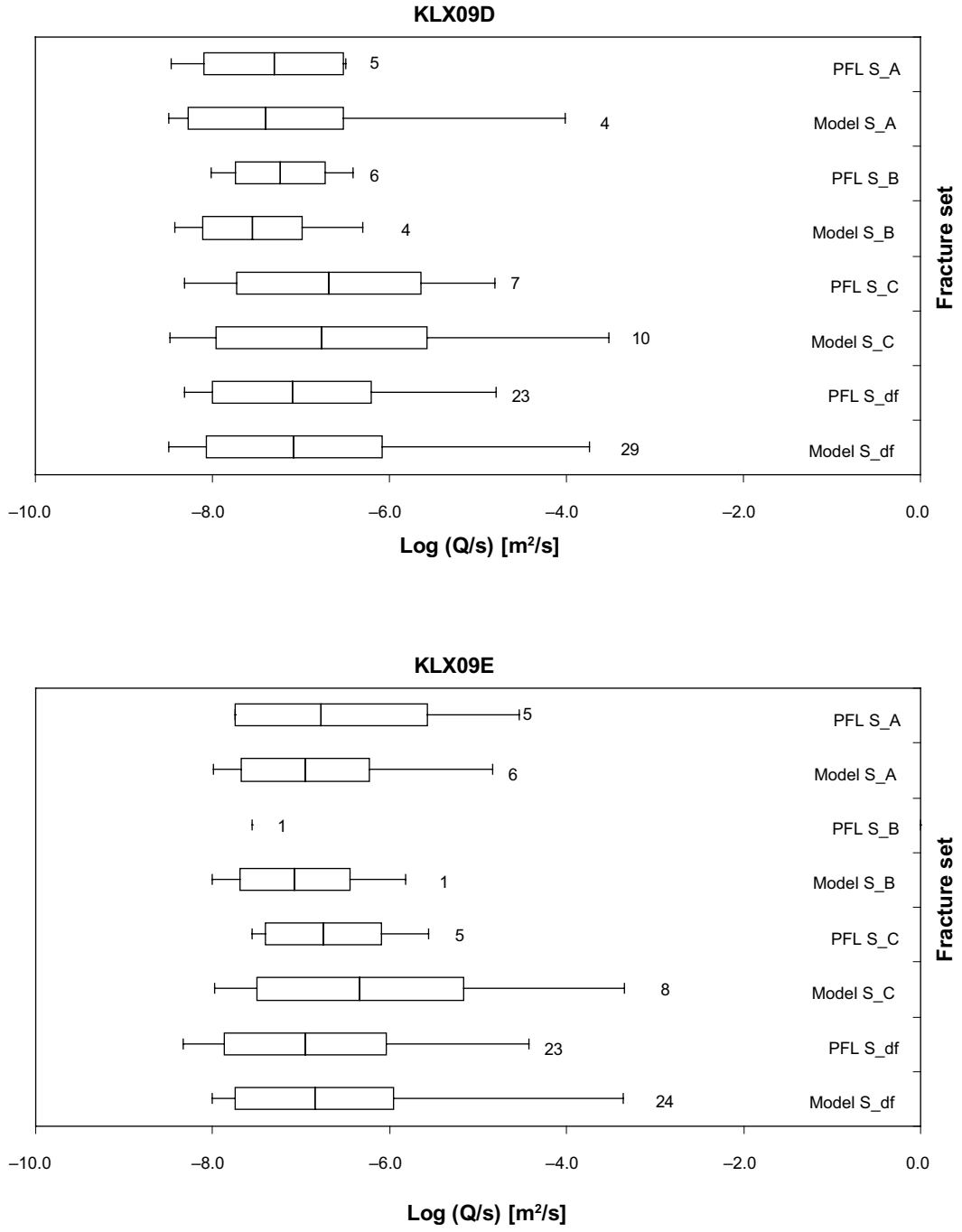

Figure D-7. *Bar and whisker plots comparing statistics taken over each fracture set for the individual inflows, Q/s, for the PFL-f measurements against the mean over 10 realisations of the BH_DZ_opt fracture size model. The centre of the bar indicates the mean value, the ends of the bar indicate ± 1 standard deviation, and the error bars indicate the minimum and maximum values. The total numbers of fractures with inflow above the detection limits within each set are also given. For the PFL-f data, the statistics are taken over the identified flow-anomalies within each set, and over the fractures generated within each set and over 10 model realisations. The semi-correlated transmissivity model is shown. Top: KLX09D; Bottom: KLX09E.*

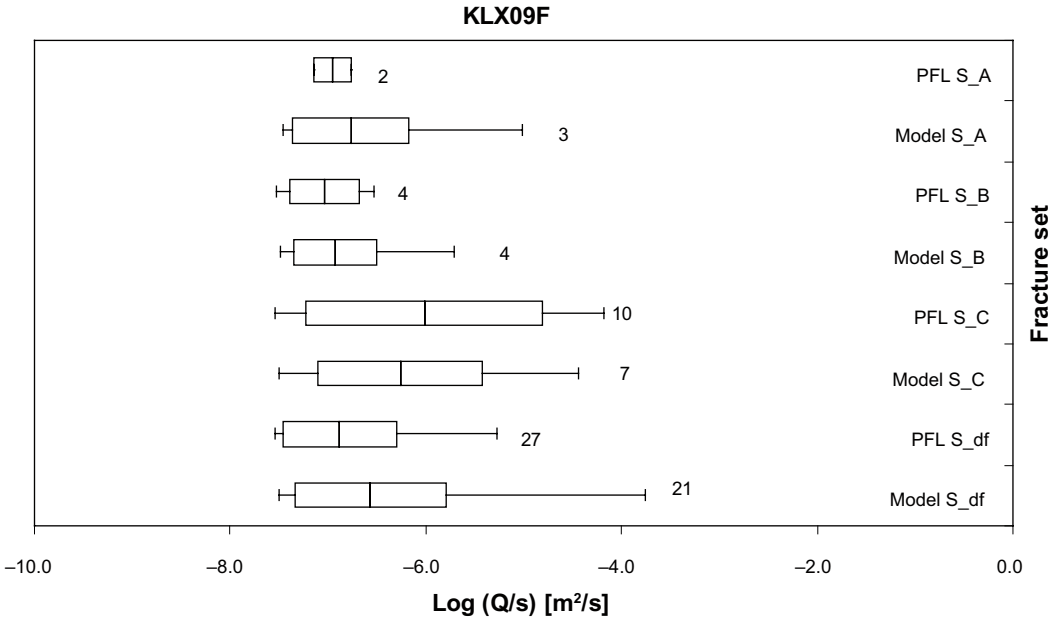

Figure D-8. *Bar and whisker plots comparing statistics taken over each fracture set for the individual inflows, Q/s, for the PFL-f measurements in KLX09F against the mean over 10 realisations of the BH_DZ_opt fracture size model. The centre of the bar indicates the mean value, the ends of the bar indicate ± 1 standard deviation, and the error bars indicate the minimum and maximum values. The total numbers of fractures with inflow above the detection limits within each set are also given. For the PFL-f data, the statistics are taken over the identified flow-anomalies within each set, and over the fractures generated within each set and over 10 model realisations. The semi-correlated transmissivity model is shown.*